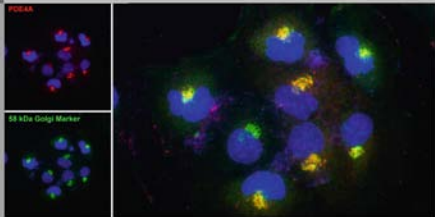



# Methods of Cancer Diagnosis, Therapy, and Prognosis

Volume 8  
Brain Cancer



M.A. Hayat  
*Editor*

 Springer

# Methods of Cancer Diagnosis, Therapy, and Prognosis

# Methods of Cancer Diagnosis, Therapy, and Prognosis

Volume 8

For other titles published in this series, go to  
[www.springer.com/series/8172](http://www.springer.com/series/8172)

# Methods of Cancer Diagnosis, Therapy, and Prognosis

Volume 8

# Methods of Cancer Diagnosis, Therapy, and Prognosis

Brain Cancer

Edited by

M.A. Hayat  
Distinguished Professor  
Department of Biological Sciences,  
Kean University, Union, NJ, USA

*Editor*

M.A. Hayat  
Distinguished Professor  
Department of Biological Sciences  
Kean University  
Union, NJ, USA

ISBN 978-90-481-8664-8

e-ISBN 978-90-481-8665-5

Library of Congress Control Number: 2010934642

© 2010 Springer Science + Business Media B.V.

No part of this work may be reproduced, stored in a retrieval system, or transmitted in any form or by any means, electronic, mechanical, photocopying, microfilming, recording or otherwise, without written permission from the Publisher, with the exception of any material supplied specifically for the purpose of being entered and executed on a computer system, for exclusive use by the purchaser of the work.

Printed on acid-free paper

springer.com

*New technology, for better or for worse, will be used, as that is our nature.*

Lewis Thomas

*You have been given the key that opens the gates of heaven; the same key opens the gates of hell.*

Writing at the entrance to a Buddhist temple



# Contributors

**Riyadh N. Alokaili**

Department of Radiology,  
University of Pennsylvania  
School of Medicine, 3400 Spruce Street,  
Dulles 2, Philadelphia, PA, 19104, USA

**Shiori Amemiya**

Department of Radiology,  
Graduate School of Medicine,  
University of Tokyo, 7-3-1, Hongo,  
Bunkyo-KuTokyo, 113-8655, Japan

**Filippo F. Angileri**

Clinica Neurochirurgica,  
Azienda Ospedaliera Universitaria  
Policlinico G. Martino, Via Consolare  
Valeria, 98100 Messina, Italy

**Alexandre Arcaro**

Neuro-Oncology Program,  
University Children's Hospital of Zürich  
Steinwiesstrasse 75, CH-8032 Zürich,  
Switzerland

**Carles Arus**

Grup d'Aplicacions Biomèdiques de la  
RMN (GABRMN), Departament de  
Bioquímica i Biologia Molecular, Facultat  
de Biociències, Universitat Autònoma de  
Barcelona, Campus de Bellaterra, 08193  
Cerdanyola del Vallès, Spain

**Susanna Asenbaum**

Nuclear Medicine Division,  
Mont-Godinne Medical Centre,  
Universite Catholique de Louvain,  
Dr. G. Therasse 1, 5530, Yvoir, Belgium

**Jerome Badaut**

Neurovascular Laboratory,  
Departments of Clinical and fundamental  
Neurosciences, Rue Michel-Servet 1,  
1211 Geneva 4, Switzerland

**Sergio Baldari**

Clinica Neurochirurgica,  
Azienda Ospedaliera Universitaria  
Policlinico G. Martino, Via Consolare  
Valeria, 98100 Messina, Italy

**Peter Bartenstein**

Nuclear Medicine Division,  
Mont-Godinne Medical Centre,  
Universite Catholique de Louvain,  
Dr. G. Therasse 1, 5530, Yvoir, Belgium

**Jaishri O. Blakeley**

Division of MR Research,  
Department of Radiology,  
Johns Hopkins University School  
of Medicine, 217 Taylor Building,  
720 Rutland Ave., Baltimore,  
MD 21205, USA



**William C. Broaddus**

Neuro-Oncology Laboratories,  
Department of Neurosurgery,  
School of Medicine, Virginia  
Commonwealth University, Box 980631,  
411 North 11th Street, ACC 6th Floor,  
Harold F. Young Neurosurgical Center,  
Richmond, VA 23298-0631, USA

**Jean-Francois Brunet**

Neurovascular Laboratory,  
Departments of Clinical and fundamental  
Neurosciences, Rue Michel-Servet 1,  
1211 Geneva 4, Switzerland

**Nail Bulakbasi**

Gulhane Military Medical Academy  
and Military Medical Faculty,  
Department of Radiology, Etlik 06018  
Ankara, Turkey

**Yue Cao**

Department of Radiology,  
University of Michigan Hospitals,  
1500 East Medical Center Drive,  
Room B2-A209, Ann Arbor,  
MI 48109-0030, USA

**Cacilda Casartelli**

Unidad de Investigacion, Hospital  
Universitario La Paz, Paseo Castellana  
261, 28046, Madrid, Spain

**Javier S. Castresana**

Unidad de Investigacion, Hospital  
Universitario La Paz, Paseo Castellana  
261, 28046, Madrid, Spain

**Thomas C. Chen**

Department of Pathology, Keck School  
of Medicine, University of Southern  
California, 2011 Zonal Avenue,  
Los Angeles, CA 90033, USA

**Thomas L. Chenevert**

Department of Radiology, University  
of Michigan Hospitals, 1500 East Medical  
Center Drive, Room B2-A209,  
Ann Arbor, MI 48109-0030, USA

**D. J. Coope**

Manchester Molecular Imaging Center,  
Academic Department of Radiation  
Oncology, University of Manchester,  
Christie Hospital NHS Trust,  
Withington, Manchester M20 4BX, UK

**Catherine Dumur**

Molecular Diagnostics Division,  
Department of Pathology, School of  
Medicine, Virginia Commonwealth  
University, Box 980631, 411 North 11th  
Street, ACC 6th Floor, Harold F. Young  
Neurosurgical Center, Richmond,  
VA 23298-0631, USA

**Andres J. M. Ferreri**

Medical Oncology Unit,  
Department of Oncology, San Raffaele  
Scientific Institute via Olgettina 60,  
20132, Milan, Italy

**Carmen Franco-Hernandez**

Unidad de Investigacion, Hospital  
Universitario La Paz, Paseo Castellana  
261, 28046, Madrid, Spain

**Gregory N. Fuller**

Department of Diagnostic Radiology,  
National Cancer Center, Cairo University,  
Cairo, Egypt

**Cole A. Giller**

Medical College of Georgia 1120  
15th St. B. 3088 Department  
of Neurosurgery, Augusta GA,  
30912, USA

**Michael A. Grotzer**

Neuro-Oncology Program,  
University Children's Hospital of Zürich  
Steinwiesstrasse 75, CH-8032 Zürich,  
Switzerland

**Christer Halldin**

Nuclear Medicine Division,  
Mont-Godinne Medical Centre,  
Universite Catholique de Louvain,  
Dr. G. Therasse 1, 5530, Yvoir, Belgium

**Dirk Hellwig**

Department of Nuclear Medicine,  
Saarland University Medical Center,  
66421, Hamburg/Saar, Germany

**K. Herholz**

Manchester Molecular Imaging Center,  
Academic Department of Radiation  
Oncology, University of Manchester,  
Christie Hospital NHS Trust,  
Withington, Manchester M20 4BX, UK

**Florence M. Hofman**

Department of Pathology, Keck School  
of Medicine, University of Southern  
California, 2011 Zonal Avenue,  
Los Angeles, CA 90033, USA

**Matthew A. Hunt**

Department of Neurosurgery,  
Oregon Health and Science University,  
3181 SW, Sam Jackson Park Road,  
CR137 Portland, OR 97239, USA

**Margarida Julia-Sape**

Grup d'Aplicacions Biomèdiques de  
la RMN (GABRMN), Departament de  
Bioquímica i Biologia Molecular, Facultat  
de Biociències, Universitat Autònoma de  
Barcelona, Campus de Bellaterra, 08193,  
Cerdanyola del Vallès, Spain

**Ozlem Kapucu**

Nuclear Medicine Division,  
Mont-Godinne Medical Centre,  
Universite Catholique de Louvain,  
Dr. G. Therasse 1, 5530, Yvoir, Belgium

**Leena M. Ketonen**

Department of Diagnostic Radiology,  
National Cancer Center, Cairo University,  
Cairo, Egypt

**Sungheon Kim**

Center for Biomedical Imaging, NYU  
Langone Medical Center, 660 First Ave.  
4th floor, New York, NY 10016, USA

**Murat Kocaoglu**

Gulhane Military Medical Academy  
and Military Medical Faculty, Department  
of Radiology, Etlik 06018 Ankara, Turkey

**Kaoru Kurisu**

Department of Neurosurgery,  
Graduate School of Biomedical Sciences,  
Hiroshima University, 1-2-3 Kasumi,  
Minami-ku, Hiroshima 734-8551, Japan

**Domenico La Torre**

Clinica Neurochirurgica,  
Azienda Ospedaliera Universitaria  
Policlinico G. Martino, Via Consolare  
Valeria, 98100 Messina, Italy

**Karl-Josef Langen**

Department of Nuclear Medicine,  
Munster University, Albert-Schweitzer-  
Strasse 33, 48149, Münster, Germany

**William P. J. Leenders**

Radboud University Nijmegen Medical  
Centre, Department of Pathology,  
P.O. Box 9101, 6500 HB Nijmegen,  
The Netherlands

**Fa-Hsuan Lin**

Athinoula A. Martinos Center  
for Biomedical Imaging, Department  
of Radiology, Massachusetts General  
Hospital, Building 149 Room 230,  
13th Street, Charlestown, MA 02129, USA

**Carles Majos**

Grup d'Aplicacions Biomèdiques de  
la RMN (GABRMN), Departament de  
Bioquímica i Biologia Molecular, Facultat  
de Biociències, Universitat Autònoma de  
Barcelona, Campus de Bellaterra, 08193,  
Cerdanyola del Vallès, Spain

**Victor Martinez-Glez**

Unidad de Investigacion, Hospital  
Universitario La Paz, Paseo Castellana  
261, 28046, Madrid, Spain

**Elena Mazza**

Medical Oncology Unit, Department  
of Oncology, San Raffaele Scientific  
Institute via Olgettina 60, 20132, Milan,  
Italy

**Elias R. Melhem**

Department of Radiology,  
University of Pennsylvania  
School of Medicine, 3400 Spruce Street.  
Dulles 2, Philadelphia, PA, 19104, USA

**Fabio Minutoli**

Clinica Neurochirurgica, Azienda  
Ospedaliera Universitaria Policlinico  
G. Martino, Via Consolare Valeria,  
98100 Messina, Italy

**Edward A. Neuwelt**

Department of Neurosurgery,  
Oregon Health and Science University,  
3181 SW, Sam Jackson Park Road,  
CR137 Portland, OR 97239, USA

**Carolina Pena-Granero**

Unidad de Investigacion, Hospital  
Universitario La Paz, Paseo Castellana  
261, 28046, Madrid, Spain

**Steve Pickup**

Center for Biomedical Imaging, NYU  
Langone Medical Center, 660 First Ave.  
4th floor, New York, NY 10016, USA

**Benoit Pirotte**

Department of Neurosurgery,  
Erasmus Hospital, Universite Libre de  
Bruxelles, 808 Route de Lennik,  
B-1070 Brussels, Belgium

**Harish Poptani**

Center for Biomedical Imaging, NYU  
Langone Medical Center, 660 First Ave.  
4th floor, New York, NY 10016, USA

**Suzanne Z. Powell**

Department of Pathology, Baylor College  
of Medicine, One Baylor Plaza, Suite  
286A, Houston, TX 77030-3498, USA

**P. Price**

Manchester Molecular Imaging Center,  
Academic Department of Radiation  
Oncology, University of Manchester,  
Christie Hospital NHS Trust,  
Withington, Manchester M20 4BX, UK

**Osama Raslan**

Department of Diagnostic Radiology,  
National Cancer Center, Cairo University,  
Cairo, Egypt

**Michele Reni**

Medical Oncology Unit, Department  
of Oncology, San Raffaele Scientific  
Institute via Olgettina 60, 20132, Milan,  
Italy

**Christof Renner**

University of Leipzig, Department  
of Neurosurgery, Liebigstrasse 20,  
D-04103 Leipzig, Germany

**Juan A. Rey**

Unidad de Investigacion,  
Hospital Universitario La Paz,  
Paseo Castellana 261, 28046, Madrid,  
Spain

**Joshua B. Rubin**

Division of Pediatric Hematology/  
Oncology, Department of Pediatrics,  
Washington University, School  
of Medicine, Campus Box 8208,  
660 South Euclid Avenue, St. Louis,  
MO 63110, USA

**Dawid Schellingerhout**

Department of Diagnostic Radiology,  
National Cancer Center, Cairo University,  
Cairo, Egypt

**Tarek Shalaby**

Neuro-Oncology Program,  
University Children's Hospital of Zürich  
Steinwiesstrasse 75, CH-8032 Zürich,  
Switzerland

**Kazuhiko Sugiyama**

Department of Neurosurgery,  
Graduate School of Biomedical Sciences,  
Hiroshima University, 1-2-3 Kasumi,  
Minami-ku, Hiroshima 734-8551, Japan

**Pia C. Sundgren**

Department of Radiology,  
University of Michigan Hospitals,  
1500 East Medical Center Drive,  
Room B2-A209, Ann Arbor,  
MI 48109-0030, USA

**Hidehiro Takei**

Department of Pathology,  
Baylor College of Medicine,  
One Baylor Plaza, Suite 286A,  
Houston, TX 77030-3498, USA

**Klaus Tatsch**

Nuclear Medicine Division,  
Mont-Godinne Medical Centre,  
Universite Catholique de Louvain,  
Dr. G. Therasse 1, 5530, Yvoir,  
Belgium

**Miguel Torres-Martin**

Unidad de Investigacion, Hospital  
Universitario La Paz, Paseo Castellana  
261, 28046, Madrid, Spain

**Shang-Yueh Tsai**

Athinoula A. Martinos Center  
for Biomedical Imaging, Department  
of Radiology, Massachusetts General  
Hospital, Building 149 Room 230,  
13th Street, Charlestown, MA 02129,  
USA

**Gary Tye**

Neuro-Oncology Laboratories,  
Department of Neurosurgery,  
School of Medicine, Virginia  
Commonwealth University, Box 980631,  
411 North 11th Street, ACC 6th Floor,  
Harold F. Young Neurosurgical  
Center, Richmond, VA 23298-0631,  
USA

**T. Vander Borgh**

Nuclear Medicine Division,  
Mont-Godinne Medical Centre,  
Universite Catholique de Louvain,  
Dr. G. Therasse 1, 5530,  
Yvoir, Belgium

**Koen Van Laere**

Nuclear Medicine Division,  
Mont-Godinne Medical Centre,  
Universite Catholique de Louvain,  
Dr. G. Therasse 1, 5530, Yvoir,  
Belgium

**Timothy E. Van Meter**

Neuro-Oncology Laboratories,  
Department of Neurosurgery,  
School of Medicine, Virginia  
Commonwealth University, Box 980631,  
411 North 11th Street, ACC 6th Floor,  
Harold F. Young Neurosurgical  
Center, Richmond, VA 23298-0631, USA

**Andrea Varrone**

Nuclear Medicine Division,  
Mont-Godinne Medical Centre,  
Universite Catholique de Louvain,  
Dr. G. Therasse 1, 5530, Yvoir, Belgium

**Matthias Weckesser**

Department of Nuclear Medicine,  
Munster University, Albert-Schweitzer-  
Strasse, 33, 48149, Münster, Germany

**Pieter Wesseling**

Radboud University Nijmegen Medical  
Centre, Department of Pathology,  
P.O. Box 9101, 6500 HB Nijmegen,  
The Netherlands

**B. Mark Woerner**

Division of Pediatric Hematology/  
Oncology, Department of Pediatrics,  
Washington University, School  
of Medicine, Campus Box 8208,  
660 South Euclid Avenue, St. Louis,  
MO 63110, USA

**Fumiyuki Yamasaki**

Department of Neurosurgery,  
Graduate School of Biomedical Sciences,  
Hiroshima University, 1-2-3 Kasumi,  
Minami-ku, Hiroshima 734-8551, Japan

**Jinyuan Zhou**

Division of MR Research, Department  
of Radiology, Johns Hopkins University  
School of Medicine, 217 Taylor Building,  
720 Rutland Ave., Baltimore, MD 21205,  
USA

# Preface

This volume discusses in detail various aspects of brain cancer in the series methods of cancer diagnosis, therapy, and prognosis, while the already published Volumes 1–7 detail similar aspects of the following cancers,

Volume 1: Breast Cancer

Volume 2: Lung Cancer

Volume 3: Gastrointestinal Cancer

Volume 4: Liver Cancer

Volume 5: Colorectal Cancer

Volume 6: Ovarian Cancer, Renal Cancer, Urinary Bladder cancer,

Adrenal Cancer, Cervical Cancer, Skin Cancer, Lymph Node Cancer,

Testicular Cancer, Wilms Tumor, Multiple Myeloma, and Sarcoma

Volume 7: General Overview, Head and Neck Cancer, and Thyroid Cancer

As in the previous seven volumes of this series, each chapter is written by distinguished, practicing clinicians/neurosurgeons/pathologists who provide meth-

odologies for diagnosis, and treatment of brain cancer. This volume was written by 74 oncologists representing 11 countries. Their practical experience highlights their writings, which should build and further the endeavors of the readers in this important area of disease. The text of each cancer type is divided into subheadings for the convenience of the readers. It is my hope that the current volume will join the preceding volumes of this series for assisting in the more complete understanding of globally relevant cancer syndromes. There exists a tremendous, urgent demand by the public in the scientific community to address cancer prevention, diagnosis, treatment, and hopefully cure.

I am grateful to the contributors for their promptness accepting my suggestions. I respect their dedication and diligent work in sharing their invaluable knowledge with the public through this series. Each chapter provides unique, individual knowledge based on the expertise and practical experience of the authors. The chapters contain the most up-to-date practical and theoretical information. I hope that these

handbooks will assist the practicing readers in their clinical work.

I am thankful to Dr. Dawood Farahi and Dr. Kristie Reilly for recognizing the importance of scholarship (research, writing, publishing) in an institution for higher education and for providing the resources

for completing this project. I appreciate receiving expert help from Myrna Ortiz, ZiphoraSam, and Amy Vitale in preparing this volume.

M. A. Hayat  
September 2009

# Contents of Volumes 1, 2, 3, 4, 5, 6 and 7

## **Volume 1**

- 1. Breast Cancer: An Introduction**
- 2. Breast Cancer: Computer-Aided Detection**
- 3. Sebaceous Carcinoma of the Breast: Clinicopathologic Features**
- 4. Breast Cancer: Detection by In-Vivo Imaging of Angiogenesis**
- 5. Breast and Prostate Biopsies: Use of Optimized High-Throughput MicroRNA Expression for Diagnosis (Methodology)**
- 6. Familial Breast Cancer: Detection of Prevalent High-Risk Epithelial Lesions**
- 7. Differentiation Between Benign and Malignant Papillary Lesions of Breast: Excisional Biopsy or Stereotactic Vacuum-Assisted Biopsy (Methodology)**
- 8. Multicentric Breast Cancer: Sentinel Node Biopsy as a Diagnostic Tool**
- 9. Breast Cancer Recurrence: Role of Serum Tumor Markers CEA and CA 15-3**
- 10. Breast Cancer Patients Before, During or After Treatment: Circulating Tumor Cells in Peripheral Blood Detected by Multigene Real-Time Reverse Transcriptase-Polymerase Chain Reaction**



- 11. Breast Cancer Patients: Diagnostic Epigenetic Markers in Blood**
- 12. Breast Cancer Patients: Detection of Circulating Cancer Cell-Related mRNA Markers with Membrane Array Method**
- 13. Prediction of Metastasis and Recurrence of Breast Carcinoma: Detection of Survivin-Expressing Circulating Cancer Cells**
- 14. Node-Negative Breast Cancer: Predictive and Prognostic Value of Peripheral Blood Cytokeratin-19 mRNA-Positive Cells**
- 15. Breast and Colon Carcinomas: Detection with Plasma CRIPTO-1**
- 16. Breast Cancer Risk in Women with Abnormal Cytology in Nipple Aspirate Fluid**
- 17. Tissue Microarrays: Construction and Utilization for Biomarker Studies**
- 18. Systematic Validation of Breast Cancer Biomarkers Using Tissue Microarrays: From Construction to Image Analysis**
- 19. Phyllodes Tumors of the Breast: The Role of Immunohistochemistry in Diagnosis**
- 20. Phyllodes Tumor of the Breast: Prognostic Assessment Using Immunohistochemistry**
- 21. Metaplastic Breast Carcinoma: Detection Using Histology and Immunohistochemistry**
- 22. Invasive Breast Cancer: Overexpression of HER-2 Determined by Immunohistochemistry and Multiplex Ligation-Dependent Probe Amplification**
- 23. Operable Breast Cancer: Neoadjuvant Treatment (Methodology)**
- 24. Chemotherapy for Breast Cancer**
- 25. Locally Advanced Breast Cancer: Role of Chemotherapy in Improving Prognosis**

26. **Relevance of Dose-Intensity for Adjuvant Treatment of Breast Cancer**
27. **Advanced Breast Cancer: Treatment with Docetaxel/Epirubicin**
28. **Systemic Therapy for Breast Cancer: Using Toxicity Data to Inform Decisions**
29. **Chemotherapy for Metastatic Breast Cancer Patients Who Received Adjuvant Anthracyclines (An Overview)**
30. **Estrogen Receptor-Negative and HER-2/neu-Positive Locally Advanced Breast Carcinoma: Therapy with Paclitaxel and Granulocyte-Colony Stimulating Factor**
31. **Breast Cancer: Side Effects of Tamoxifen and Anastrozole**
32. **Breast Cancer: Expression of HER-2 and Epidermal Growth Factor Receptor as Clinical Markers for Response to Targeted Therapy**
33. **Young Breast Cancer Patients Undergoing Breast-Conserving Therapy: Role of BRCA1 and BRCA2**
34. **Radiation Therapy for Older Women with Early Breast Cancer**
35. **Acute Side Effects of Radiotherapy in Breast Cancer Patients: Role of DNA-Repair and Cell Cycle Control Genes**
36. **<sup>18</sup>F-Fluorodeoxyglucose/Positron Emission Tomography in Primary Breast Cancer: Factors Responsible for False-Negative Results**
37. **Sentinel Lymph Node Surgery During Prophylactic Mastectomy (Methodology)**
38. **Breast Conservation Surgery: Methods**
39. **Lymph Node-Negative Breast Carcinoma: Assessment of HER-2/*neu* Gene Status as Prognostic Value**
40. **Multifocal or Multicentric Breast Cancer: Understanding Its Impact on Management and Treatment Outcomes**

- 41. Are Breast Cancer Survivors at Risk for Developing Other Cancers?**
- 42. Distant Metastasis in Elderly Patients with Breast Cancer: Prognosis with Nodal Status**
- 43. Concomitant Use of Tamoxifen with Radiotherapy Enhances Subcutaneous Breast Fibrosis in Hypersensitive Patients**
- 44. Malignant Phyllodes Tumor of the Breast: Is Adjuvant Radiotherapy Necessary?**
- 45. Locally Advanced Breast Cancer: Multidrug Resistance**
- 46. Breast Cancer: Diagnosis of Recurrence Using  $^{18}\text{F}$ -Fluorodeoxyglucose-Positron Emission Tomography/Computed Tomography**
- 47. Role of Sentinel Lymph Node Biopsy in Ductal Carcinoma In Situ: Diagnosis and Methodology**
- 48. Breast Conservation Treatment of Early Stage Breast Carcinoma: Risk of Cardiac Mortality**

## **Volume 2**

### **Part I General Methods and Overviews**

- 1. Metabolic Transformations of Malignant Cells: An Overview**
- 2. Detection of Recurrent Cancer by Radiological Imaging**
- 3. Tumor Gene Therapy: Magnetic Resonance Imaging and Magnetic Resonance Spectroscopy**
- 4. Assessment of Gene Transfer: Magnetic Resonance Imaging and Nuclear Medicine Techniques**
- 5. Role of Mutations in *TP53* in Cancer (An Overview)**
- 6. Personalized Medicine for Cancer**
- 7. Radiation Doses to Patients Using Computed Radiography, Direct Digital Radiography and Screen-Film Radiography**

- 8. Cancer Vaccines and Immune Monitoring (An Overview)**
- 9. New Insights into the Role of Infection, Immunity, and Apoptosis in the Genesis of the Cancer Stem Cell**
- 10. Successful Cancer Treatment: Eradication of Cancer Stem Cells**
- 11. Overexposure of Patients to Ionizing Radiation: An Overview**

## **Part II Lung Cancer**

- 12. Lung Carcinoma**
- 13. Extra-Pulmonary Small Cell Cancer: Diagnosis, Treatment, and Prognosis**
- 14. Magnetic Resonance Imaging of the Lung: Automated Segmentation Methods**
- 15. Peripheral Lung Lesions: Diagnosis Using Transcutaneous Contrast-Enhanced Sonography**
- 16. Small Pulmonary Nodules: Detection Using Multidetector-Row Computed Tomography**
- 17. Secondary Primary Cancer Following Chemoradiation for Non-Small-Cell Lung Cancer**
- 18. Advanced Non-Small Cell Lung Cancer: Second-Line Treatment with Docetaxel**
- 19. Non-Small Cell Lung Cancer with Brain Metastases: Platinum-Based Chemotherapy**
- 20. Non-Small Cell Lung Carcinoma: EGFR Gene Mutations and Response to Gefitinib**
- 21. Advanced Non-Small Cell Lung Carcinoma: Acquired Resistance to Gefitinib**
- 22. Prognostic Significance of [<sup>18</sup>F]-Fluorodeoxyglucose Uptake on Positron Emission Tomography in Patients with Pathological Stage I Lung Adenocarcinoma**

- 23. Non-Small Cell Lung Cancer: Prognosis Using the TNM Staging System**
- 24. Differentiation Between Malignant and Benign Pleural Effusions: Methylation Specific Polymerase Chain Reaction Analysis**
- 25. Pathological Distinction of Pulmonary Large Cell Neuroendocrine Carcinoma from Small-Cell Lung Carcinoma Using Immunohistochemistry**
- 26. Differentiating Between Pleuropulmonary Desmoid Tumors and Solitary Fibrous Tumors: Role of Histology and Immunohistochemistry**
- 27. Non-Small Cell Lung Cancer with Brain Metastasis: Role of Epidermal Growth Factor Receptor Gene Mutation**

### **Part III Prostate Cancer**

- 28. Prostate Carcinoma**
- 29. The Role of Intermediary Metabolism and Molecular Genetics in Prostate Cancer**
- 30. Array-Based Comparative Genomic Hybridization in Prostate Cancer: Research and Clinical Applications**
- 31. Prostate Cancer: Role of Vav3 Overexpression in Development and Progression**
- 32. Prostate Cancer: Detection and Monitoring Using Mitochondrial Mutations as a Biomarker**
- 33. Prognostic Markers in Prostate Carcinoma**
- 34. Prostate Cancer: Detection of Free Tumor-Specific DNA in Blood and Bone Marrow**
- 35. Prostate Carcinoma: Evaluation Using Transrectal Sonography**
- 36. Prostate Cancer:  $16\beta$ - $^{18}\text{F}$ Fluoro- $5\alpha$ -Dihydrotestosterone(FDHT) Whole-Body Positron Emission Tomography**
- 37. Effects of Standard Treatments on the Immune Response to Prostate Cancer**

- 38. Vinorelbine, Doxorubicin, and Prednisone  
in Hormone Refractory Prostate Cancer**
- 39. Locally Advanced Prostate Cancer Biochemical Recurrence  
After Radiotherapy: Use of Cyclic Androgen Withdrawal  
Therapy**

## **Volume 3**

### **Part I Gastrointestinal Cancers**

- 1. Introduction: Gastrointestinal Cancer**
- 2. Metastatic Gastrointestinal Cancer: Safety of Cisplatin  
Combined with Continuous 5-FU Versus Bolus 5-FU  
and Leucovorin (Methodology)**
- 3. Gastrointestinal Cancer: Endoscopic Submucosal  
Dissection (Methodology)**
- 4. Gastrointestinal Epithelial Neoplasms: Endoscopic  
Submucosal Dissection (Methodology)**
- 5. Inoperable Abdomino-Pelvic Tumors: Treatment  
with Radio-Frequency Ablation and Surgical Debulking**
- 6. Gastrointestinal Neuroendocrine Tumors:  
Diagnosis Using Gastrin Receptor Scintigraphy**

### **Part II Esophageal Cancer**

- 7. Distal Esophagus: Evaluation with 18F-FDG PET/CT  
Fusion Imaging**
- 8. Endoscopic Ultrasound and Staging of Esophageal Cancer**
- 9. Esophageal Cancer: Role of RNASEN Protein  
and microRNA in Prognosis**
- 10. Esophageal Cancer: Initial Staging**

**Part III Gastric Cancer**

- 11. Automated Disease Classification of Colon and Gastric Histological Samples Based on Digital Microscopy and Advanced Image Analysis**
- 12. Early Gastric Cancer: Prediction of Metachronous Recurrence Using Endoscopic Submucosal Dissection (Methodology)**
- 13. *Helicobacter pylori*-Infected Neoplastic Gastric Epithelium: Expression of MUC2 as a Biomarker**
- 14. Gastric Cancer: Role of Intestinal Metaplasia by Histochemical Detection Using Biopsy Specimens**
- 15. Gastric Cancer: Antitumor Activity of RUNX3**
- 16. Early Gastric Cancer: Laparoscopic Gastrectomy (Methodology)**
- 17. Gastric Cancer: Overexpression of Hypoxia-Inducible Factor 1 as a Prognostic Factor**

**Part IV Pancreatic Cancer**

- 18. Pancreatic Cancer: Hepatoma-Derived Growth Factor as a Prognostic Factor**
- 19. Pancreatic Cancer: 18F-Fluorodeoxyglucose Positron Emission Tomography as a Prognostic Parameter**
- 20. Imaging and Pathologic Findings of Peculiar Histologic Variants of Pancreatic Endocrine Tumors**
- 21. Periampullary Adenocarcinoma: Diagnosis and Survival After Pancreaticoduodenectomy**
- 22. Unresectable Locally Advanced Pancreatic Cancer: Concurrent Chemotherapy**

**Index**

## **Volume 4**

### **Part I Colorectal Cancer**

- 1. Introduction: Colorectal Cancer**
- 2. Poorly Differentiated Colorectal Adenocarcinoma: (Methodology)**
- 3. Colorectal Cancer: Immunohistochemical Diagnosis with Heterogenous Nuclear Ribonucleoprotein K**
- 4. Metastases and Recurrence of Colorectal Cancer: Diagnostic Role of Immunoscintigraphy**
- 5. Colorectal Cancer Diagnosis Using DNA Levels in Blood and Stool**
- 6. Colorectal Carcinoma: Identification of MicroRNAs Using Real-Time Polymerase Chain Reaction**
- 7. Colorectal Cancer: Optimization of the Combination of 5-Flouroracil and Irinotecan**
- 8. Detection of Abdominal Abscesses After Colorectal Surgery: Ultrasonography, Computed Tomography, and Gallium Scan**
- 9. Antimetastatic Therapy in Colorectal Cancer: Role of Tumor Cell Matrix Metalloproteinase 9 (Methodology)**
- 10. Endoscopic Resection of Early Colorectal Tumours: Novel Diagnostic and Therapeutic Techniques**
- 11. Role of Stromal Variables in Development and Progression of Colorectal Cancer**
- 12. Quantitative Assessment of Colorectal Cancer Perfusion: Perfusion Computed Tomography and Dynamic Contrast-Enhanced Magnetic Resonance Imaging**
- 13. Colorectal Cancer: Positron Emission Tomography**
- 14. Prognostic Significance of Protein Markers in Colorectal Cancer Stratified by Mismatch Repair Status**
- 15. Colorectal Cancer: Lactate Dehydrogenase (LDH) Activity as a Prognostic Marker**



**Part II Colon Cancer**

- 16. Detection of Tumor Cells in Lymph Nodes of Colon Cancer Patients Using Real-Time Quantitative Reverse Transcription-Polymerase Chain Reaction**
- 17. Colon Cancer: Laparoscopic Surgery**
- 18. Sentinel Node-Based Immunotherapy of Colon Cancer**

**Part III Rectal Cancer**

- 19. Rectal Cancer: Preoperative Staging Using Endorectal Ultrasonography (Methodology)**
- 20. Rectal Cancer: Spectral Imaging and Immunohistochemistry of Thymidylate Synthase**
- 21. Cancer of the Rectum: Abdominoperineal and Sphincter-Saving Resections**
- 22. Chemoradiation for Rectal Cancer**
- 23. Resectable Rectal Cancer: Preoperative Short-Course Radiation**
- 24. Preoperative Chemoradiotherapy Allows for Local Control in Rectal Cancer, but Distant Metastases Remain an Unsolved Problem**
- 25. Locally Advanced Rectal Cancer: Combined Chemotherapy During Preoperative Radiation Therapy**

**Part IV Colorectal Liver Metastases**

- 26. Colorectal Cancer Liver Metastases: Neoadjuvant Therapy with Bevacizumab**
- 27. Colorectal Liver Metastases: Radiofrequency Ablation**

**Part V Anal Cancer**

- 28. Anal Squamous Cell Carcinomas: Diagnosis Using p63 Immunohistochemistry**
- 29. Anorectal Melanoma: Prediction of Outcome Based on Molecular and Clinicopathologic Features**

## **Volume 5**

### **Part I Liver Cancer**

#### **A. Diagnosis**

- 1. Applications of Positron Emission Tomography in Liver Imaging: An Overview**
- 2. Localized Fibrous Tumor of the Liver: Imaging Features**
- 3. A Radial Magnetic Resonance Imaging Method for Imaging Abdominal Neoplasms**
- 4. Liver: Helical Computed Tomography and Magnetic Resonance Imaging**

### **Part II Resectable Liver Cancer**

#### **A. Diagnosis**

- 5. Selection of Patients for Resection of Hepatic Colorectal Metastases: 18F-Fluorodeoxyglucose/Positron Emission Tomography**

#### **B. Treatment**

- 6. Ultrasonography During Liver Surgery**

### **Part III Unresectable Liver Cancer**

#### **A. Treatment**

- 7. Intraoperative Magnetic Resonance Imaging for Radiofrequency Ablation of Hepatic Tumors**
- 8. Surgically Unresectable and Chemotherapy-Refractory Metastatic Liver Carcinoma: Treatment with Yttrium-90 Microsphere Followed by Assessment with Positron Emission Tomography**

#### **B. Prognosis**

- 9. Unresectable Liver Metastases from Colorectal Cancer: Methodology and Prognosis with Radiofrequency Ablation**

## **Part IV Hepatocellular Carcinoma**

### **A. Diagnosis**

- 10. Screening with Ultrasonography of Patients at High-Risk for Hepatocellular Carcinoma: Thrombocytopenia as a Valid Surrogate of Cirrhosis**
- 11. Hepatocellular Carcinoma: Contrast-Enhanced Sonography**
- 12. Focal Liver Lesion: Nonlinear Contrast-Enhanced Ultrasound Imaging**
- 13. Hepatocellular Carcinoma: Magnetic Resonance Imaging**
- 14. Expression of Vascular Endothelial Growth Factor in Hepatocellular Carcinoma: Correlation with Radiologic Findings**
- 15. Detection of Small Hepatic Lesions: Superparamagnetic Oxide-Enhanced Diffusion-Weighted T2 FSE Imaging**
- 16. Diagnosis of Hepatocellular Carcinoma: Multidetector-Row Computed Tomography and Magnetic Resonance Imaging**
- 17. Hepatocellular Carcinoma: Effect of Injection Rate/Injection Duration of Contrast Material on Computed Tomography**
- 18. Detection of Combined Hepatocellular and Cholangiocarcinomas: Enhanced Computed Tomography**
- 19. Hepatocellular Carcinoma and Adenomatous Hyperplasia (Dysplastic Nodules): Dynamic Computed Tomography and a Combination of Computed Tomography and Angiography**
- 20. Hepatocellular Cancer in Cirrhotic Patients: Radiological Imaging**

### **B. Treatment**

- 21. Treatment of Hepatocellular Carcinoma with Thalidomide: Assessment with Power Doppler Ultrasound**
- 22. Perfusion Scintigraphy with Integrated Single Photon Emission Computed Tomography/Computed Tomography in the Management of Transarterial Treatment of Hepatic Malignancies**
- 23. Postoperative Interferon Alpha Treatment of Patients with Hepatocellular Carcinoma: Expression of p48 Using Tissue Microarray**

**C. Prognosis**

- 24. Hepatocellular Carcinoma: Overexpression of Homeoprotein Six 1 as a Marker for Predicting Survival**
- 25. Hepatocellular Carcinoma: KiSS-1 Overexpression as a Prognostic Factor**
- 26. Hepatocellular Carcinoma: Prognosis Using Hepatoma-Derived Growth Factor Immunohistochemistry**
- 27. Hepatitis C Virus-Related Human Hepatocellular Carcinoma: Predictive Markers Using Proteomic Analysis (Methodology)**

**Part V Metastases****A. Diagnosis**

- 28. Liver Metastases from Colorectal Cancer: Ultrasound Imaging**
- 29. Preclinical Liver Metastases: Three-Dimensional High-Frequency Ultrasound Imaging**
- 30. Colorectal Liver Metastases: <sup>18</sup>F-Fluorodeoxyglucose-Positron Emission Tomography**

**Part VI Biliary Cancer****A. Diagnosis**

- 31. Biliary Cystic Tumors: Clinicopathological Features**
- 32. Cholangiocarcinoma: Intraductal Sonography**

**B. Prognosis**

- 33. Extrahepatic Bile Duct Carcinoma: Role of the p53 Protein Family**
- 34. Extrahepatic Bile Duct Carcinoma: Mucin 4, a Poor Prognostic Factor**

**C. Treatment**

- 35. Hilar Cholangiocarcinoma: Photodynamic Therapy and Stenting**

## **Part VII Splenic Cancer**

### **A. Diagnosis**

#### **36. Splenic Metastases: Diagnostic Methods**

## **Volume 6**

### **Part I Ovarian Cancer**

#### **A. Diagnosis**

- 1. Identification of Biomarkers for Clear Cell Ovarian Adenocarcinoma**
- 2. Ovarian Carcinoma: Diagnostic Immuno-histochemistry of MUCIN4 (MUC4)**
- 3. Distinguishing Benign from Malignant Complex Adnexal Masses in Ovarian Cancer: Two-Dimensional Power-Doppler Imaging**
- 4. Subgroups of Ovarian Carcinoma: Identification Using Differential Gene Expression**
- 5. Sertoliform Endometrioid Carcinoma of the Ovary: Diagnosis and Prognosis**

#### **B. Prognosis**

- 6. Role of MUC16 (CA125) in the Pathogenesis of Epithelial Ovarian Cancer**
- 7. Clear Cell Carcinoma of the Ovary: Prognosis Using Cytoreductive Surgery**
- 8. Advanced Ovarian Cancer: Prediction of Surgical Outcomes Using Computed Tomography**

### **Part II Renal Cancer**

#### **A. Treatment**

- 9. Renal Cell Carcinoma: Follow-Up with Magnetic Resonance Imaging After Percutaneous Radiofrequency Ablation**
- 10. Metastatic Kidney Cancer: Treatment with Infusional Interleukin-2 Plus Famotidine**

- 11. Renal Cell Carcinoma: Preoperative Treatment with Cytokines Followed by Surgery**
- 12. Metastatic Renal Cell Carcinoma: Use of Bcl-2 and Fas to Predict Responses to Immunotherapy**
- 13. Wilms Tumor: Prognosis Using Microvessel Density**

### **Part III Urogenitary Tract Cancer**

#### **A. Adrenal**

- 14. Adenomatoid Tumor of the Adrenal Gland: Differential Diagnosis Using Immunohistochemistry**
- 15. Testicular Cancer: Post-Chemotherapy Retroperitoneal Lymph Node Dissection**
- 16. Survivors of Germ-Cell Testicular Cancer: Increased Risk of Second Primary Tumors**

### **Part IV Urinary Bladder Cancer**

#### **Diagnosis**

- 17. Urothelial Bladder Cancer: Screening with Urine-Based Tumor Markers**
- 18. Detection of OCT-4 in Bladder Cancer: Role of Cancer Stem Cell**

### **Part V Cervical Uterine Cancer**

#### **Diagnosis**

- 19. Uterine Cervical Glandular Lesions: Differentiation Using Immunohistochemistry of Mucins**
- 20. Uterine Cervical Carcinoma: Preoperative Magnetic Resonance Imaging Staging**

#### **Treatment**

- 21. Cancer Imaging and Intracavitary Brachytherapy for Cervical Cancer**
- 22. Cervical Cancer: Methods for Assessing the Quality of Life**

**23. Cervical Cancer: Positron Emission Tomography and Positron Emission Tomography/Computed Tomography**

**24. Endometrial Cancer: Indoleamine 2,3-Dioxygenase as a Prognostic Indicator**

**Part VI Skin Cancer**

**Melanoma**

**25. Neurofibromatosis Type 1-Associated Malignant Melanoma: Molecular Evidence of Inactivation of the NF1 Gene**

**26. Malignant Melanoma: Localisation and Characterization Using Fluorodeoxyglucose-Positron Emission Tomography/Computed Tomography**

**27. Malignant Melanoma Versus Deep Penetrating Nevus: Diagnostic and Prognostic Immuno-Histochemistry of Dipeptidyl Peptidase IV (Methodology)**

**28. Nonmelanoma Skin Cancer: Use of EphA1 Receptor as a Prognostic Marker**

**Part VII Leukemia**

**29. Pretreated Chronic Lymphocytic Leukemia: Use of Alemtuzumab**

**Part VIII Multiple Myeloma**

**30. Immunotherapeutic Strategies, Radiotherapy, and Targeted Radionuclide Therapy Approaches for the Treatment of Multiple Myeloma**

**Part IX Sarcoma**

**Diagnosis**

**31. Low Grade Fibromyxoid Sarcoma: Diagnosis by Detecting FUS-CREB3L2 Fusion Gene Using Reverse Transcription-Polymerase Chain Reaction**

**32. Synovial Sarcoma: Role of TLE1 as a Diagnostic Immunohistochemical Marker**

- 33. The Immunohistochemistry of Kaposi's Sarcoma**
- 34. Synovial Sarcoma: Role of Immunohistochemistry and Molecular Genetics in Diagnosis and Prognosis**

#### **Treatment**

- 35. Sarcoma: Treatment with Ecteinascidin-743**

## **Volume 7**

### **Part I General Methods And Overviews**

#### **Diagnosis**

- 1. Role of RNA Interference in Understanding the Molecular Basis of Cancer**
- 2. Cancer Biomarkers (An Overview)**
- 3. Tumor Angiogenesis in Cancers: Expression of CD105 Marker**
- 4. Spindle Cell Oncocytoma of the Adenohypophysis: Integrated Clinicopathologic Diagnosis by Imaging, Histology, and Immunohistochemistry**
- 5. Disseminated Carcinoma of Unknown Primary Site: Detection with F-Fluorodeoxyglucose-Positron Emission Tomography**
- 6. Unknown Lymphadenopathy: Diagnosing Using an Endoscopic Ultrasound-Guided Fine-Needle Aspiration Biopsy**

#### **Therapy**

- 7. Pretargeted Radioimmunotherapy in Cancer: An Overview**
- 8. Chemotherapy-Induced Neurotoxicity**
- 9. Multidrug Resistance**
- 10. Role of Antibodies in Cancer Treatment (An Overview)**
- 11. Incorporating Pharmacogenomics into Cancer Therapy**



**12. Cancer Stem Cells: An Overview****13. Translating In Vitro Cell Lines Result into Clinical Practice****Prognosis****14. Classification of Cancer Stage Using Patient's Immune System****15. Late Relapse of Germ Cell Malignancies: Incidence, Management, and Prognosis****Part II Head and Neck Cancer****16. Head and Neck Squamous Cell Carcinoma: Therapy with Fusaric Acid/Paclitaxel****17. Early Stage Oral Squamous Cell Carcinoma: Use of Signal Transducer and Activator of Transcription 3 as a Risk Factor for Poor Diagnosis****18. Salivary Gland Tumors: Preoperative Tissue Characterization with Apparent Diffusion Coefficient Mapping****19. Role of Human Papillomavirus in Tonsillar Cancer****20. Quantitative Reverse Transcription–Polymerase Chain Reaction Based Assessment of the Candidate Biomarkers for Tongue Cancer Metastasis****21. Nasopharyngeal Carcinoma (Retropharyngeal Lymph Node Metastasis): Spread Pattern, Prognosis, and Staging****22. Retinoblastoma: Diagnosis, Treatment and Prognosis****Part III Thyroid Carcinoma****Diagnosis****23. Molecular Genetics of Thyroid Cancer****24. Thyroid Cancer: Identification of Gene Expression Markers for Diagnosis****25. Papillary Thyroid Carcinoma: Use of HBME1 and CK19 as Diagnostic Markers**

**26. Papillary Thyroid Carcinoma: Detection of Copy Gain of Platelet Derived Growth Factor B Using Array Comparative Genomic Hybridization in Combination with Laser Capture Microdissection**

**27. PET Imaging in Thyroid Carcinoma**

**Therapy**

**28. Metastasized Medullary Thyroid Carcinoma: Detection and Therapy Using Radiolabeled Gastrin Analogs**

**Prognosis**

**29. Medullary Thyroid Carcinoma: Prognosis based on Stage of Disease and Age**

**30. Overexpression of the Components of the Plasminogen Activating System as Prognostic Factors in Human Thyroid Carcinoma**



# Contents

<b>Contributors</b> .....	vii
<b>Preface</b> .....	xiii
<b>Contents of Volumes 1, 2, 3, 4, 5, 6 and 7</b> .....	xv
<b>1. The World Health Organization Classification of the Central Nervous System Tumors: An Update Using Imaging</b> .....	1
Shiori Amemiya	
Introduction .....	1
Astrocytic Tumors .....	1
Pilomyxoid Astrocytoma: WHO Grade II .....	1
Neuronal and Mixed Neuronal-Glial Tumors .....	2
Papillary Glioneuronal Tumor: WHO Grade I .....	2
Extraventricular Neurocytoma: WHO Grade II .....	2
Rosette-Forming Glioneuronal Tumor of the Fourth Ventricle: WHO Grade I .....	3
Other Neuroepithelial Tumors .....	3
Angiocentric Glioma: WHO Grade I .....	3
Tumors of the Pineal Region .....	4
Papillary Tumor of the Pineal Region: WHO Grade II/III .....	4
Embryonal Tumors .....	4
Medulloblastoma: WHO Grade IV .....	4
Medulloblastoma with Extensive Nodularity: WHO Grade IV .....	5
Anaplastic Medulloblastoma: WHO Grade IV .....	5
References .....	5

<b>2. Brain Tumor Imaging: European Association of Nuclear Medicine Procedure Guidelines</b> .....	9
Thierry Vander Borgh, Susanne Asenbaum, Peter Bartenstein, Christer Halldin, Özlem Kapucu, Koen Van Laere, Andrea Varrone, and Klaus Tatsch	
Background Information and Definitions .....	9
Common Indications .....	9
Indications.....	9
Contraindications (Relative) .....	11
Procedure .....	11
Patient Preparation .....	11
Information Pertinent to Performance of the Procedure .....	12
Precautions and Conscious Sedation .....	12
Radiopharmaceutical.....	12
Data Acquisition .....	13
Image Processing .....	15
Interpretation Criteria.....	15
Reporting.....	17
Issues Requiring Further Clarification .....	18
References.....	18
<b>3. Assessment of Heterogeneity in Malignant Brain Tumors</b> .....	21
Timothy E. Van Meter, Gary Tye, Catherine Dumur, and William C. Broaddus	
Introduction.....	21
The Problem of Heterogeneity and Its Clinical Significance.....	21
Previous Studies Assessing Molecular Heterogeneity of Tumors .....	21
Use of Stereotactic Neuroimaging Systems for Tumor Sampling .....	22
Methodology .....	22
Description of Method .....	22
MRI-Guided Stereotactic Biopsy.....	23
Integrated Histopathological Scoring .....	25
Use of Genomics Technologies for Regional Molecular Profiling .....	25
Microarray Data Analysis .....	26
Small Sample Size .....	26
Results.....	26
Histopathological Considerations .....	26
Assessing Quality of Biopsy Extracts.....	27
Genomic Assessment of Regional Tumor Phenotype.....	28
Validation Studies .....	29
Discussion .....	29
Utility of Stereotactic Biopsy for Tumor Characterization.....	29

Future Technical Applications .....	30
Clinical Impact of Improved Tumor Characterization .....	30
References .....	31
<b>4. Diagnosing and Grading of Brain Tumors: Immunohistochemistry .....</b>	<b>33</b>
Hidehiro Takei and Suzanne Z. Powell	
Introduction .....	33
Immunohistochemical Markers for Diagnosis and Differential	
Diagnosis of Brain Tumors .....	33
Immunohistochemical Markers Routinely Used	
in Diagnostic Neuro-oncology Practice .....	33
New Immunohistochemical Markers Applicable to Brain	
Tumor Diagnosis .....	39
Useful Immunohistochemical Markers for Differential	
Diagnosis of Brain Tumors .....	42
Immunohistochemistry as a Useful Adjunct in Grading	
of Brain Tumors: Ki-67 and Phospho-Histon H3 .....	44
Astrocytoma .....	45
Meningioma .....	45
Immunohistochemical and Analytical Methods	
(For Formalin-Fixed Paraffin-Embedded Tissue) .....	46
Formalin Fixation .....	46
Sectioning .....	46
Antigen Retrieval .....	46
Preparations for Retrieval Solutions .....	47
Immunohistochemical Staining of Formalin-Fixed	
Paraffin-Embedded Tissue .....	47
Protocol .....	48
Analysis .....	49
References .....	49
<b>5. Malignant Brain Tumors: Roles of Aquaporins .....</b>	<b>53</b>
Jérôme Badaut and Jean-François Brunet	
Introduction .....	53
AQP Expression in Normal Brain and its Function .....	54
AQP1 Distribution and Its Potential Role .....	54
AQP4 Astrocyte Endfeet Marker Involved in Brain	
Water Homeostasis .....	54
Involvement of AQP9 in Brain Energy Metabolism .....	55
AQP Distribution in Tumors: Roles in Prognosis and Treatment .....	56
AQP1 in Tumors: Water Homeostasis or Cell Migration? .....	56
AQP4 in Tumors: Biomarker for Tumor Classification .....	58
AQP9 in Brain Tumors: New Findings .....	61
References .....	62

<b>6. Brain Metastases: Gene Amplification Using Quantitative Real-Time Polymerase Chain Reaction Analysis</b> .....	65
Carmen Franco-Hernandez, Miguel Torres-Martin, Victor Martinez-Glez, Carolina Peña-Granero, Javier S. Castresana, Cacilda Casartelli, and Juan A. Rey	
Introduction.....	65
Objectives.....	66
Equipment and Procedure .....	66
DNA Extraction .....	66
Quantitative-PCR: Amplification Status .....	66
Procedure .....	67
Results.....	67
Further Considerations.....	68
References.....	69
<b>7. Cyclic AMP Phosphodiesterase-4 in Brain Tumor Biology: Immunochemical Analysis</b> .....	71
B. Mark Woerner and Joshua B. Rubin	
Introduction.....	71
Materials and Methods.....	72
Western Blotting .....	73
Materials .....	73
Methods.....	74
Immunohistochemistry .....	75
Materials .....	75
Methods.....	76
Immunocytochemistry .....	76
Materials .....	76
Methods.....	78
Results And Discussion .....	78
References.....	80
<b>8. Radiosurgical Treatment of Progressive Malignant Brain Tumors</b> .....	83
Cole A. Giller	
Introduction.....	83
Methodology of Treatment Philosophy .....	84
Methodology of Indications.....	84
Methodology of Choice of Fractionation Schedule .....	85
Methodology of Dosimetry.....	86
Construction of Hypofractionated Plans.....	91
Case Example.....	92
Cohort Study .....	94
References.....	95

<b>9. Anti-vascular Therapy for Brain Tumors.....</b>	<b>97</b>
Florence M. Hofman and Thomas C. Chen	
Introduction.....	97
Specific Drug Targets.....	99
Angiogenic Growth Factors.....	99
Growth Factor Receptor Inhibitors.....	100
Endothelial Cell Adhesion and Migration.....	102
Bone Marrow-Derived Endothelial Progenitor Cells.....	104
Conclusion.....	104
References.....	106
<b>10. Glial Brain Tumors: Antiangiogenic Therapy.....</b>	<b>109</b>
William P.J. Leenders and Pieter Wesseling	
Clinical Features of Glioma.....	109
Histopathology and Genetic Background of Gliomas.....	109
Current Treatment Modalities.....	110
Antiangiogenesis as Anti-Tumor Therapy.....	111
VEGF-A and angiogenesis.....	111
Preclinical Anti-Angiogenic Therapy of Brain Tumors.....	113
Consequences of Antiangiogenic Therapy for Diagnosis:	
Vessel Normalization.....	114
Clinical Experience with Anti-Angiogenic Therapy.....	114
Future Perspectives.....	116
References.....	117
<b>11. Brain Tumors: Amide Proton Transfer Imaging.....</b>	<b>121</b>
Jinyuan Zhou and Jaishri O. Blakeley	
Introduction.....	121
Chemical Exchange-Dependent Saturation Transfer Imaging:	
Principles and Applications.....	122
Magnetization Transfer Contrast (MTC), Cest, and APT.....	123
APT Imaging of Experimental Brain Tumor Models.....	123
APT Imaging of Human Brain Tumors.....	125
References.....	127
<b>12. Diffusion Tensor Imaging in Rat Models of Invasive Brain Tumors.....</b>	<b>131</b>
Sunghoon Kim, Steve Pickup, and Harish Poptani	
Introduction.....	131
Imaging Tissue Microstructure.....	132
Diffusion Tensor.....	132
Diffusion Tensor Metrics.....	134
Data Acquisition Methods.....	135
Rat Brain Tumor Models.....	136



9L Gliosarcoma.....	136
C6 Glioma.....	137
F98 Glioma .....	139
Mayo 22 Human Brain Tumor Xenograft.....	140
Future Considerations .....	140
Tractography .....	140
Tumor Cell Density and Diffusion Anisotropy.....	141
Other Challenges.....	142
References.....	143
<b>13. Brain Tumors: Diffusion Imaging and Diffusion Tensor Imaging .....</b>	<b>145</b>
Pia C. Sundgren, Yue Cao, and Thomas L. Chenevert	
Introduction.....	145
Imaging Techniques .....	146
Diffusion Weighted Imaging.....	146
Diffusion Tensor Imaging .....	147
Diffusion Imaging in Tissue Characterization .....	148
Diffusion Imaging in Tumor Grading .....	149
Diffusion Imaging in Pre-surgical Planning .....	150
Diffusion Imaging in Treatment Follow-Up .....	150
Diffusion Imaging in Differentiation of Recurrent Tumor from Radiation Injury and Post-surgical Injury .....	152
Pitfalls .....	153
Future Applications.....	154
References.....	154
<b>14. Brain Tumors: Planning and Monitoring Therapy with Positron Emission Tomography .....</b>	<b>157</b>
D.J. Coope, K. Herholz, and P. Price	
Introduction.....	157
Imaging Brain Tumors With Positron Emission Tomography and FDG .....	158
Amino Acid PET in Brain Tumors .....	159
Positron Emission Tomography Imaging in Less Common Tumor Types .....	161
Delineation of Tumor Extent for Treatment Planning .....	162
Minimizing Damage to Uninvolved Brain Structures.....	167
Monitoring Brain Tumors: When is the Best Time to Intervene?.....	170
Selection of Treatment Modalities.....	171
Assessing Response to Treatment and Prognosis .....	172
The Future of PET Imaging in Brain Tumors.....	174
References.....	176

<b>15. Clinical Evaluation of Primary Brain Tumor: O-(2-[<sup>18</sup>F]Fluorethyl)-L-Tyrosine Positron Emission Tomography .....</b>	<b>179</b>
Matthias Weckesser and Karl-Josef Langen	
Introduction.....	179
Intensity and Dynamics of O-(2-[ <sup>18</sup> F]Fluorethyl)-L-Tyrosine-Uptake .....	180
Correlation of O-(2-[ <sup>18</sup> F]Fluorethyl)-L-Tyrosine-Uptake with Morphological Imaging .....	184
Recommendations for Image Acquisition and Interpretation .....	185
Clinical Application .....	186
References.....	187
 <b>16. Combined Use of [F-18]Fluorodeoxyglucose and [C-11]Methionine in 45 PET-Guided Stereotactic Brain Biopsies.....</b>	<b>189</b>
Benoit Pirotte	
Introduction.....	189
Materials and Methods.....	189
Patient Selection.....	189
Stereotactic PET Data Acquisition .....	190
Analysis of Stereotactic PET Images and Target Definition.....	190
Data Analysis .....	192
Results.....	192
Discussion .....	195
PET for the Guidance of Stereotactic Brain Biopsy .....	195
Choice of Radiotracer .....	197
Accuracy of Stereotactic PET Coregistration .....	197
Comparison Between Met and FDG.....	198
References.....	199
 <b>17. Hemorrhagic Brain Neoplasm – <sup>99m</sup>Tc-Methoxyisobutyl Isonitrile-Single Photon Emission Computed Tomography.....</b>	<b>203</b>
Filippo F. Angileri, Fabio Minutoli, Domenico La Torre, and Sergio Baldari	
Introduction.....	203
Radiopharmaceutical and Technical Issues .....	203
<sup>99m</sup> Tc-MIBI-SPECT in Brain Tumors Evaluation.....	205
<sup>99m</sup> Tc-MIBI-SPECT in Hemorrhagic Brain Neoplasm.....	207
References.....	212
 <b>18. Brain Tumor Imaging Using p-[<sup>123</sup>I]Iodo-L-Phenylalanine and SPECT .....</b>	<b>215</b>
Dirk Hellwig	
Introduction.....	215

Imaging Method.....	216
Preparation of $^{123}\text{I}$ -IPA .....	216
Patient Preparation and Administration of $^{123}\text{I}$ -IPA .....	217
SPECT Acquisition.....	217
Correlative Nuclear Magnetic Resonance Imaging .....	217
Coregistration of SPECT and NMR Images .....	218
Qualitative Interpretation and Quantitative Image Analysis.....	218
Results of Brain Tumor Imaging Using $^{123}\text{I}$ -IPA .....	219
Initial Evaluation of Suspected Brain Tumors .....	219
Evaluation of Suspected Recurrence or Progression .....	221
Quantitative Criteria for the Evaluation of Brain Lesions by IPA-SPECT .....	222
Comparison of $^{123}\text{I}$ -IPA and $^{123}\text{I}$ -IMT .....	222
Dosimetry of $^{123}\text{I}$ -IPA.....	222
Discussion .....	222
Potential Advancements.....	225
References.....	225
<b>19. Diagnosis and Staging of Brain Tumours:</b>	
<b>Magnetic Resonance Single Voxel Spectra .....</b>	<b>227</b>
Margarida Julià-Sapé, Carles Majós, and Carles Arús	
Single Voxel Magnetic Resonance Spectroscopy .....	227
What Does Single Voxel MRS Tell us About a Brain Tumor?.....	228
Information Provided by a Single Voxel MR Spectrum .....	229
Methods.....	230
How to Perform a Single Voxel Magnetic Resonance Spectroscopy Study When a Brain Tumor Is Suspected.....	230
Acquisition Parameters for Single Voxel Magnetic Resonance Spectroscopy.....	231
Reporting on a Single Voxel Magnetic Resonance Spectroscopy Study.....	231
Quantifying a Magnetic Resonance Spectroscopy Study: Processing a Single Voxel Magnetic Resonance Spectrum .....	235
Quantifying an MRS Study: Ratio-Based Determinations .....	236
Quantifying an MRS Study: Classifiers and Decision-Support Systems.....	238
When There is an Indication for a SV MRS Exam.....	238
Discrimination Between Tumor and Pseudotumoral Lesion .....	239
Tumor Classification .....	240
Follow-Up of Brain-Tumors After Treatment.....	241
References.....	241

**20. Parallel Magnetic Resonance Imaging Acquisition and Reconstruction: Application to Functional and Spectroscopic Imaging in Human Brain** ..... 245

Fa-Hsuan Lin and Shang-Yueh Tsai

    Introduction..... 245

    Principles of Parallel MRI ..... 245

    Parallel MRI Acquisitions..... 246

    Parallel MRI Reconstructions ..... 248

    Mathematical Formulation..... 250

    Application – SENSE Human Brain Functional Magnetic Resonance Imaging..... 252

    Application – SENSE Proton Spectroscopic Imaging ..... 255

    References..... 259

**21. Intra-axial Brain Tumors: Diagnostic Magnetic Resonance Imaging** ..... 263

Elias R. Melhem and Riyadh N. Alokaili

    Introduction..... 263

    Classification and Overview of Central Nervous System Tumors ..... 263

    Intra-Axial Tumor Imaging Protocol ..... 264

    Diffusion Imaging ..... 267

    Diffusion Tensor Imaging ..... 267

    Perfusion Magnetic Resonance Imaging ..... 268

    Proton Magnetic Resonance Spectroscopy ..... 268

    Basics of Central Nervous System Tumor Image Interpretation..... 269

    General Conventional Magnetic Resonance Imaging Appearance of Intra-Axial Tumors ..... 270

    Appearance of Specific Intra-Axial Brain Tumors on Advanced Magnetic Resonance Imaging..... 270

        Primary (Non-lymphomatous) Neoplasms ..... 270

        Secondary Neoplasms (Metastases)..... 271

        Lymphoma ..... 272

        Tumefactive Demyelinating Lesions ..... 272

        Brain Abscess..... 273

        Encephalitis..... 274

    Approach to an Unknown Intra-Axial Brain Tumor..... 274

    Limitations and Future Direction..... 274

    References..... 276

<b>22. Brain Tumors: Apparent Diffusion Coefficient at Magnetic Resonance Imaging</b> .....	279
Fumiyuki Yamasaki, Kazuhiko Sugiyama, and Kaoru Kurisu	
Introduction .....	279
Diffusion-Weighted Imaging and T2 Shine-Through .....	279
Diffusion-Weighted Imaging Sequences .....	280
Cellularity and Apparent Diffusion Coefficient .....	280
Clinical Application of Apparnet Diffusion Coefficient in Brain Tumor Assessments .....	281
Tumor Grade and Apparent Diffusion Coefficient .....	282
Differentiation of Brain Tumors and Apparent Diffusion Coefficient .....	282
Astrocytomas, Oligodendrogliomas, and Ependymomas .....	282
Dysembryoplastic Neuroepithelial Tumors .....	283
Medulloblastomas, Primitive Neuroectodermal Tumors, and Ependymomas .....	283
Central Neurocytomas and Subependymomas .....	284
Hemangioblastomas and Other Posterior Cranial Fossa Tumors .....	284
Glioblastomas, Metastatic Tumors, and Malignant Lymphomas .....	284
Histologic Subtyping of Meningiomas and Schwannomas .....	285
Pituitary and Parasellar Tumors and Others .....	285
Visualizing Tumor Infiltration .....	286
Distinguishing Tumor Recurrence from Radiation Necrosis .....	287
Monitoring Treatment Effects .....	288
Distinguishing Tumor Recurrence from Resection Injury .....	289
Distinguishing Brain Abscesses from Cystic or Necrotic Malignant Tumors .....	290
Distinguishing Toxoplasma Abscesses and Malignant Lymphoma in AIDS .....	291
Study Limitations: Variations in Apparent Diffusion Coefficient Measurements, Selection of Regions of Interest .....	291
Future Directions .....	293
References .....	294
 <b>23. Magnetic Resonance Imaging of Brain Tumors Using Iron Oxide Nanoparticles</b> .....	297
Matthew A. Hunt and Edward A. Neuwelt	
Introduction .....	297
Biologic and Molecular Characteristics .....	297
Imaging Characteristics .....	298
Experimental Studies .....	298
Human Imaging .....	300
Intraoperative Magnetic Resonance Imaging .....	302

Future Directions .....	302
References.....	303
<b>24. Metastatic Solitary Malignant Brain Tumor: Magnetic Resonance Imaging .....</b>	<b>305</b>
Nail Bulakbasi and Murat Kocaoglu	
Introduction.....	305
Screening and Initial Evaluation.....	308
Imaging Protocol.....	308
Imaging Properties of Solitary Brain Metastasis .....	312
Differential Diagnosis of Solitary Brain Metastasis .....	317
Future Trends and Conclusion .....	320
References.....	321
<b>25. Brain Tumor Resection: Intra-operative Ultrasound Imaging.....</b>	<b>325</b>
Christof Renner	
Introduction.....	325
General Principles.....	326
Transducers (Arrays).....	326
Modes of Imaging .....	327
Image-Characteristics .....	327
Resolution .....	327
Principles of Intra-Operative Ultrasound Examination .....	329
Efficacy of Intra-Operative Ultrasound.....	329
Conclusion .....	334
References.....	334
<b>26. Primary Central Nervous System Lymphomas: Salvage Treatment .....</b>	<b>337</b>
Michele Reni, Elena Mazza, and Andrés J.M. Ferreri	
Introduction.....	337
Diagnostic Work up at Relapse.....	338
Prognostic Factors.....	338
Methodological Issues .....	339
Whole-Brain Radiotherapy .....	340
Chemotherapy .....	342
Single Agent Chemotherapy .....	342
Retreatment with Methotrexate.....	343
Combination Chemotherapy .....	344
Monoclonal Antibodies.....	345
High-Dose Chemotherapy and Autologous Stem-Cell Rescue .....	346
Intrathecal Chemotherapy .....	347
Conclusions.....	348
References.....	349

<b>27. Central Nervous System Atypical Teratoid/Rhabdoid Tumors: Role of Insulin-Like Growth Factor I Receptor .....</b>	<b>353</b>
Michael A. Grotzer, Tarek Shalaby, and Alexandre Arcaro	
Insulin-Like Growth Factor-I Receptor .....	353
Role in CNS Atypical Teratoid/Rhabdoid Tumor .....	353
Analytical Methods.....	354
Immunohistochemistry .....	354
Immunoprecipitation.....	355
Western Blotting .....	356
Quantitative RT-PCR.....	357
Cell Viability .....	358
Detection of Apoptosis .....	359
Evaluation of IGF-I/-II/IGF-IR in CNS AT/RT .....	359
Down-Regulation of IGF-IR.....	360
Therapeutic Significance of IGF-IR in CNS AT/RT .....	360
References.....	362
 <b>28. Central Nervous System Rosai–Dorfman Disease .....</b>	<b>365</b>
Osama Raslan, Leena M. Ketonen, Gregory N. Fuller, and Dawid Schellingerhout	
Introduction, Epidemiology and Etiology .....	365
Intracranial RDD: Clinical and Imaging Findings and Differential Diagnosis .....	366
Spinal RDD: Clinical and Imaging Findings and Differential Diagnosis .....	368
Histopathological and Definitive Diagnosis.....	370
Clinical Course and Treatment .....	370
References.....	371
 <b>Index.....</b>	<b>375</b>

# 1

## The World Health Organization Classification of the Central Nervous System Tumors: An Update Using Imaging

Shiori Amemiya

### INTRODUCTION

The fourth edition of the World Health Organization (WHO) classification of tumors was published in 2007. The essential alterations are based not only on histopathological findings but also on clinical behaviors and radiological findings of each tumor.

In this chapter, radiological aspects of eight newly recognized tumors of neuroepithelial tissue will be discussed. It should be noted that much work remains to formulate an ideal classification, and radiological findings based on limited previous reports are also susceptible to further alterations.

### ASTROCYTIC TUMORS

#### Pilomyxoid Astrocytoma: WHO Grade II

Pilomyxoid astrocytoma was first summarized by Tihen et al. (1999), and grouped as a variant of pilocytic astrocytoma, representing a comparatively more aggressive clinical course, with a higher dissemination rate than in WHO classification in 2007. Pilomyxoid astrocytoma typically presents in the very young (median 10 months),

but can also occur in older children. A few adult cases have also been reported (Linscott et al. 2008). Four cases of pilomyxoid astrocytoma in the setting of NF-1 were reported by Khanani et al. (2006), Rodriguez et al. (2008), and Linscott et al. (2008), suggesting that it may be another NF-1-associated tumor. In regard to the imaging findings, Linscott et al. (2008) reported the largest series ( $n = 21$ ), including five cases previously published as case reports. A large, solid hypothalamic tumor in a very young patient has been considered the classic pattern, because before 2004, few tumors were reported outside this region. Although pilomyxoid astrocytoma has a strong geographic predilection for the hypothalamic/chiasmatic region, other regions such as the parietal lobe, temporal lobe, cerebellum, basal ganglia, fourth ventricle, and spinal cord can also be involved. Pilomyxoid astrocytoma shows nonspecific signal intensity on MR images, i.e., high on T2-weighted and low on T1-weighted images with variable contrast enhancement. In contrast to the pilocytic astrocytoma, Linscott et al. (2008) reported that calcification is less frequent (10%) and intratumoral hemorrhage is more common (12–25%).



## NEURONAL AND MIXED NEURONAL-GLIAL TUMORS

### Papillary Glioneuronal Tumor: WHO Grade I

Papillary glioneuronal tumor (PGNT) was first described by Komori et al. (1996) as a pseudopapillary ganglioglioneurocytoma and, thereafter, designated as PGNT in expanded series detailing the clinical and pathologic features (Komori et al. 1998). Patients ranged in ages from 4 to 75 years, with the median age of 25 years. PGNT typically involves the cerebral hemispheres with or without involvement of the cortical gray matter. As noted by Komori et al. (1998), PGNT are usually well demarcated, composed mainly or partly of a cystic mass, with only mild peritumoral edema. In most cases, a variable enhancement in the solid part, a cyst wall, and a septum is seen. Intratumoral hemorrhage is sometimes seen (Figure 1.1), and this, in combination with high vascularity, may lead to a misdiagnosis as cavernous angioma as reported by Komori et al. (1998), and Buccoliero et al. (2006). One case with superficial siderosis, caused by intratumoral hemorrhage, ruptured into the ventricles were reported by Konya et al. (2006).

### Extraventricular Neurocytoma: WHO Grade II

Central neurocytoma-like tumors have been reported in a variety of locations outside of the supratentorial ventricular system. They have been termed extraventricular neurocytomas, and were mentioned in the 2000 WHO classification of tumors of the nervous system, but remained unclassified until the revision in 2007.

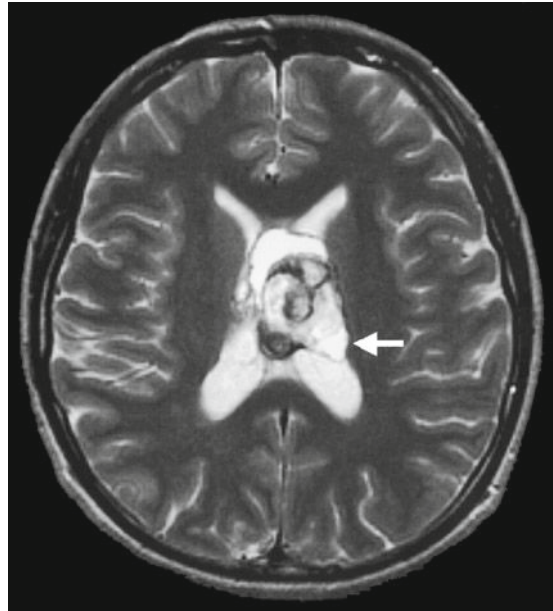


FIGURE 1.1. A 28-year-old woman with a papillary glioneuronal tumor involving the corpus callosum and lateral ventricles. A mass with mild peritumoral edema shows variable signal intensities on T2-weighted image because of intratumoral hemorrhage and calcification. The left dorsal portion (*arrow*) showing very high intensity on T2-weighted image was subacute hematoma. Rim-like low intensity reflects hemosiderin deposition

According to the largest series ( $n = 35$ ) reported by Brat et al. (2001), the patient age ranges from 5 to 76 years (median age 37 years). Tumors affected the frontal (46%), parietal (23%), temporal (14%), occipital (11%), thalamic (3%), or hypothalamic (3%) regions. Extraventricular neurocytomas are often well demarcated, partly or mainly cystic (57%), and variably enhancing masses, with or without peritumoral edema. They show nonspecific signal intensities or density, i.e., low on nonenhanced CT, low on T1-weighted images, and high on T2-weighted images; their solid portion may variably appear on CT and on

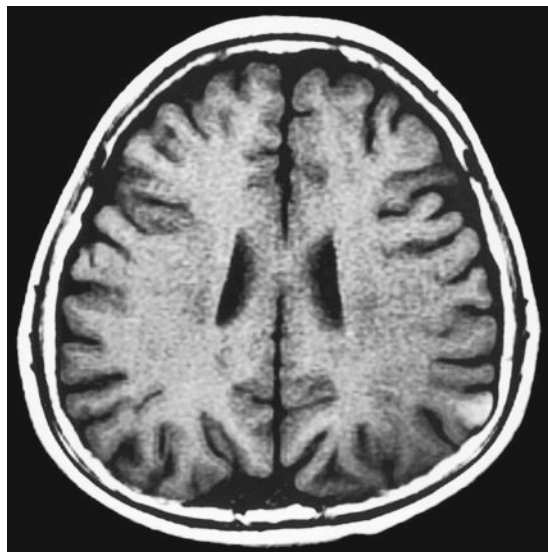


FIGURE 1.2. A 14-year-old boy with angiocentric glioma. Cortex and subcortical white matter in the left parietal lobe is involved. Reflecting its infiltrative nature, the lesion is seen as areas of abnormal intensity without displacement of surrounding structures. Thinning of the inner layer of adjacent cranial bone suggests slow growth of the tumor. The lesion shows high intensity on nonenhanced T1-weighted images

MRI depending on the cellularity and degree of calcification. Extraventricular neurocytomas, when mainly involve the brain surface, would radiologically resemble pilocytic astrocytoma, ganglioglioma, or oligodendroglioma.

#### Rosette-Forming Glioneuronal Tumor of the Fourth Ventricle: WHO Grade I

After the initial report in 1998, a detailed description of rosette-forming glioneuronal tumor of the fourth ventricle (RGNT) was reported by Komori et al. (2002). RGNT is a midline tumor. Not only fourth ventricle, but also aqueduct, pineal region, cerebellar vermis, midbrain, and thalamus are frequently involved. Despite its name, at least one case without involvement of the fourth

ventricle is reported. Patient age ranges from 12 to 59 years (mean age 33 years) (Preusser et al. 2007). The tumors are relatively circumscribed, heterogeneous, partially cystic, or multiloculate lesions. Dense calcification is sometimes seen (2 of 11 in the largest series reported by Komori et al. (2002)). Focal and curvilinear, ring, or spot-like enhancement scattered within the lesion (Figure 1.2) seems to be a characteristic feature of RGNT (Komori et al. 2002). Similar flaccid ring-like enhancement can sometimes be seen in pilocytic astrocytoma.

## OTHER NEUROEPITHELIAL TUMORS

### Angiocentric Glioma: WHO Grade I

Angiocentric glioma was proposed by two different groups as a distinctive epileptogenic neoplasm that shows features of both infiltrating astrocytoma and ependymoma (Lellouch-Tubiana et al. 2005; Wang et al. 2005). Patient age ranges from 2.3 to 70 years (mean age 17 years). Angiocentric glioma is located mainly in the cortex and the subcortical white matter in any cerebral lobe. Calcification is rare. It is reported that partial or total solid part of the tumor shows high intensity on non-enhanced T1-weighted images (Figure 1.3) (Lellouch-Tubiana et al. 2005; Preusser et al. (2007); Amemiya et al. 2008). This seems to be a characteristic feature of angiocentric glioma. The absence of hemorrhage and calcification has been pathologically proven (Preusser et al. 2007; Amemiya et al. 2008), and the causes of high intensity on T1-weighted images remain unknown. According to the report by Preusser et al. (2007), the tumor shows

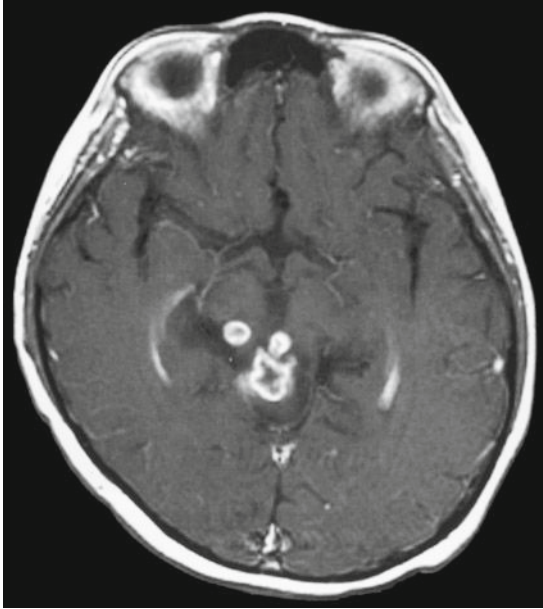


FIGURE 1.3. A 13-year-old girl with Rosette-Forming Glioneuronal Tumor of the fourth ventricle, presented with obstructive hydrocephalus. A heterogeneous mass with cystic part occupies the fourth ventricle and the aqueduct of cerebrum with brain stem involvement. Flaccid curvilinear enhancement scattered in the mass is seen on contrast-enhanced T1-weighted image

high intensity with or without high-intense stalk-like extension to the ventricle on T2-weighted images. None of the tumors reported by Lellouch-Tubiana et al. (2005), Preusser et al. (2007), and Amemiya et al. (2008) showed contrast enhancement.

## TUMORS OF THE PINEAL REGION

### Papillary Tumor of the Pineal Region: WHO Grade II/III

Papillary Tumors of the Pineal Region (PTPR) were first described as a distinctive entity and characterized by an epithelial-like growth pattern, strong staining for

cytokeratin and ultrastructural features, suggesting ependymal differentiation (Jouvet et al. 2003). Patient age ranges from 5 to 66 years (mean 32 years). They arise exclusively in the pineal region.

According to the limited radiological descriptions in previous reports, PTPR seems mildly lobulated and partially cystic, heterogeneously enhanced masses, and usually found with obstructive hydrocephalus (Kern et al. 2006). Jouvet et al. (2007) reported that PTPR shows nonspecific imaging features on MRI; i.e., iso or low on T1-weighted images, and iso to high on T2-weighted images with variable contrast enhancement. Chang et al. (2008) reported four cases demonstrating heterogeneous, high intensity on T1-weighted images. No calcification or hemorrhage or melanin was detected in their series. They concluded that the causes of the high intensity on T1-weighted images are unknown.

## EMBRYONAL TUMORS

### Medulloblastoma: WHO Grade IV

Typical appearance of a medulloblastoma is a well-defined vermian cerebellar mass, with a surrounding vasogenic edema, evidence of hydrocephalus and a homogeneous enhancement on contrast material-enhanced images in a child lower than 10 years of age. In a review of 233 cases of medulloblastoma, Nelson et al. (1991) found that 97% demonstrated at least some hyperdense region compared with normal cerebellar attenuation on nonenhanced CT, 95% had marginal vasogenic edema and 97% had at least some enhancement. However, variance from this imaging appearance is common. Typical 'uniformly hyperdense CT appearance' is considered

to reflect high cellular density of small round cells, which was seen only in 30% of the cases. Cyst formation and calcification were reported to be seen in 59% and 22% of the cases respectively. Also, reflecting its high cellular density, medulloblastoma often shows iso intensity on both T1- and T2-weighted images.

#### Medulloblastoma with Extensive Nodularity: WHO Grade IV

Medulloblastoma with extensive nodularity (MBEN) is a variant of medulloblastoma, which was previously known as cerebellar neuroblastoma. Giangaspero et al. (1999) reported 11 cases of this type of the tumor, and adopted the descriptive term medulloblastoma with extensive nodularity instead of cerebellar neuroblastoma to avoid confusion with supratentorial primitive neuroectodermal tumor known as cerebral neuroblastoma. MBEN occurs primarily in children lower than 3 years of age. As reported by Giangaspero et al. (1999) and Rutkowski et al. (2005), MBEN is associated with more favorable outcomes than those with classic medulloblastoma. A well demarcated, nodular grape-like appearance and a clearly depicted tumor extension on cross-sectional images characterize MBEN. In four of the ten lesions, the nodular structures were contained within a large well-delimited macrocyst separating the tumor from the surrounding brain (Giangaspero et al. 1999). The macrocyst grew in the vermis, compressing the fourth ventricle or in the cerebellar hemisphere, distorting and displacing the fourth ventricle.

Solid tumor components of MBEN are reported to be similar in density/ signal pattern to classic medulloblastoma on nonen-

hanced CT or MRI. MBEN shows iso- or slightly high density on CT scans, and iso- to low intensity on T1-weighted images, and iso- to high intensity on T2-weighted images. Surrounding edema may be seen as areas of high intensity on T2-weighted images. Solid components show marked to moderate contrast enhancement.

#### Anaplastic Medulloblastoma: WHO Grade IV

Anaplastic medulloblastoma was first proposed by Brown et al. (2000) who reviewed 495 medulloblastomas. Sharing some features with the large-cell variant, 17 of the tumors showed highly anaplastic features, and were characterized by marked nuclear pleomorphism, cell-cell wrapping, and high mitotic activity, often with atypical forms. These tumors were designated as anaplastic medulloblastoma. According to their studies, the prognosis of anaplastic medulloblastoma was markedly inferior compared to classic medulloblastoma. According to the report of Helton et al. (2004) that described five cases of a large cell/ anaplastic medulloblastoma, large cell/ anaplastic medulloblastoma can show similar characteristics to those shown by classic medulloblastomas. Because atypical imaging features are not rare in classic medulloblastomas, as mentioned above, discrimination between classic medulloblastomas and large cell/ anaplastic medulloblastoma is challenging.

#### REFERENCES

- Amemiya, S., Shibahara, J., Aoki, S., Takao, H., and Ohtomo, K. (2008) Recently established entities of central nervous system tumors: review of radiological findings. *J. Comput. Assist. Tomogr.* 32:279–285

- Brat, D.J., Scheithauer, B.W., Eberhart, C.G., and Burger, P.C. (2001) Extraventricular neurocytomas: pathologic features and clinical outcome. *Am. J. Surg. Pathol.* 25:1252–1260
- Brown, H.G., Kepner, J.L., Perlman, E.J., Friedman, H.S., Strother, D.R., Duffner, P.K., Kun, L.E., Goldthwaite, P.T., and Burger, P.C. (2000) “Large cell/anaplastic” medulloblastomas: a Pediatric Oncology Group Study. *J. Neuropathol. Exp. Neurol.* 59:857–865
- Buccoliero, A.M., Giordano, F., Mussa, F., Taddei, A., Genitori, L., and Taddei, G.L. (2006) Papillary glioneuronal tumor radiologically mimicking a cavernous hemangioma with hemorrhagic onset. *Neuropathology* 26:206–211
- Chang, A.H., Fuller, G.N., Debnam, J.M., Karis, J.P., Coons, S.W., Ross, J.S., and Dean, B.L. (2008) MR imaging of papillary tumor of the pineal region. *AJNR Am. J. Neuroradiol.* 29:187–189
- Giangaspero, F., Perilongo, G., Fondelli, M.P., Brisigotti, M., Carollo, C., Burnelli, R., Burger, P.C., and Garrè, M.L. (1999) Medulloblastoma with extensive nodularity: a variant with favorable prognosis. *J. Neurosurg.* 91:971–977
- Helton, K.J., Fouladi, M., Boop, F.A., Perry, A., Dalton, J., Kun, L., and Fuller, C. (2004) Medulloblastoma: a radiographic and clinicopathologic analysis of six cases and review of the literature. *Cancer* 101:1445–1454
- Jouvet, A., Fauchon, F., Liberski, P., Saint-Pierre, G., Didier-Bazes, M., Heitzmann, A., Delisle, M.B., Biassette, H.A., Vincent, S., Mikol, J., Streichenberger, N., Ahboucha, S., Brisson, C., Belin, M.F., and Fevre-Montange, M. (2003) Papillary tumor of the pineal region. *Am. J. Surg. Pathol.* 27:505–512
- Jouvet, A., Nakazato, Y., Scheithauer, B.W., and Paulus, W. (2007) Papillary tumour of the pineal region. World Health Organization classification of tumours of the nervous system. IARC, Lyon
- Kern, M., Robbins, P., Lee, G., and Watson, P. (2006) Papillary tumor of the pineal region – a new pathological entity. *Clin. Neuropathol.* 25:185–192
- Khanani, M.F., Hawkins, C., Shroff, M., Dirks, P., Capra, M., Burger, P.C., and Bouffet, E. (2006) Pilomyxoid astrocytoma in a patient with neurofibromatosis. *Pediatr. Blood Cancer* 46:377–380
- Komori, T., Scheithauer, B.W., Anthony, D.C., Scott, R.M., Okazaki, H., and Kobayashi, M.J. (1996) Pseudopapillary ganglioglioneurocytoma. *Neuropathol. Exp. Neurol.* 55:655
- Komori, T., Scheithauer, B.W., Anthony, D.C., Rosenblum, M.K., McLendon, R.E., Scott, R.M., Okazaki, H., and Kobayashi, M. (1998) Papillary glioneuronal tumor: a new variant of mixed neuronal-glial neoplasm. *Am. J. Surg. Pathol.* 22:1171–1183
- Komori, T., Scheithauer, B.W., and Hirose, T. (2002) A rosette-forming glioneuronal tumor of the fourth ventricle: infratentorial form of dysembryoplastic neuroepithelial tumor? *Am. J. Surg. Pathol.* 26:582–591
- Konya, D., Peker, S., Ozgen, S., Kurtkaya, O., and Necmettin, P.M. (2006) Superficial siderosis due to papillary glioneuronal tumor. *J. Clin. Neurosci.* 13:950–952
- Lellouch-Tubiana, A., Boddaert, N., Bourgeois, M., Fohlen, M., Jouvet, A., Delalande, O., Seidenwurm, D., Brunelle, F., and Sainte-Rose, C. (2005) Angiocentric neuroepithelial tumor (ANET): a new epilepsy-related clinicopathological entity with distinctive MRI. *Brain Pathol.* 15:281–286
- Linscott, L.L., Osborn, A.G., Blaser, S., Castillo, M., Hewlett, R.H., Wieselthaler, N., Chin, S.S., Krakenes, J., Hedlund, G.L., and Sutton, C.L. (2008) Pilomyxoid Astrocytoma: expanding the imaging spectrum. *AJNR Am. J. Neuroradiol.* 29:1861–1866
- Nelson, M., Diebler, C., and Forbes, W.S.C. (1991) Paediatric medulloblastoma: atypical CT features at presentation in the SIOP II trial. *Neuroradiology* 33:140–142
- Preusser, M., Hoischen, A., Novak, K., Czech, T., Prayer, D., Hainfellner, J.A., Baumgartner, C., Woermann, F.G., Tuxhorn, I.E., Pannek, H.W., Bergmann, M., Radlwimmer, B., Villagrán, R., Weber, R.G., and Hans, V.H. (2007) Angiocentric glioma: report of clinico-pathologic and genetic findings in 8 cases. *Am. J. Surg. Pathol.* 31:1709–1718
- Rodriguez, F.J., Perry, A., Gutmann, D.H., O'Neill, B.P., Leonard, J., Bryant, S., and Giannini, C. (2008) Gliomas in neurofibromatosis type 1: a clinicopathologic study of 100 patients. *J. Neuropathol. Exp. Neurol.* 67:240–249
- Rutkowski, S., Bode, U., Deinlein, F., Ottensmeier, H., Warmuth-Metz, M., Soerensen, N., Graf, N., Emser, A., Pietsch, T., Wolff, J.E., Kortmann, R.D.,

- and Kuehl, J. (2005) Treatment of early childhood medulloblastoma by postoperative chemotherapy alone. *N. Engl. J. Med.* 352:978–986
- Tihan, T., Fisher, P.G., Kepner, J.L., Godfraind, C., McComb, R.D., Goldthwaite, P.T., Burger, P.C. (1999) Pediatric astrocytomas with monomorphous pilomyxoid features and a less favorable outcome. *J Neuropathol Exp Neurol.* 58:1061–1068
- Wang, M., Tihan, T., Rojiani, A.M., Bodhireddy, S.R., Prayson, R.A., Iacuone, J.J., Alles, A.J., Donahue, D.J., Hessler, R.B., Kim, J.H., Haas, M., Rosenblum, M.K., and Burger, P.C. (2005) Monomorphous angiocentric glioma: a distinctive epileptogenic neoplasm with features of infiltrating astrocytoma and ependymoma. *J. Neuropathol. Exp. Neurol.* 64:875–881

*This page intentionally left blank*

# 2

## Brain Tumor Imaging: European Association of Nuclear Medicine Procedure Guidelines

Thierry Vander Borght, Susanne Asenbaum, Peter Bartenstein, Christer Halldin, Özlem Kapucu, Koen Van Laere, Andrea Varrone, and Klaus Tatsch

### BACKGROUND INFORMATION AND DEFINITIONS

The most widely used tracer in oncology is FDG, a glucose analogue. It is actively transported across the blood-brain-barrier (BBB) into the cells where it phosphorylated by hexokinase, then effectively ‘trapped’ intracellularly because dephosphorylation is slow. FDG uptake is enhanced in tumors due to both increased transport and phosphorylation. In the brain, however, high glucose utilisation by normal grey matter hampers the detection of tumor tissue by FDG-PET, depending on the metabolic grade of the tumor. Coregistration with structural data is then required for more sensitive analysis.

In comparison with FDG, better tumor delineation is reported for radiolabeled amino acid. Among them, [methyl-<sup>11</sup>C]-L-methionine (MET) used in conjunction with PET is the most frequently used (Chen 2005). In an effort to overcome the disadvantages of its short half-life and complex metabolism and despite a changed amino acid structure, several fluoro- and iodo-amino acid analogs have been developed. These agents include 3-[<sup>123</sup>I]iodo- $\alpha$ -methyl-L-tyrosine (IMT) for SPECT and O-(2-[<sup>18</sup>F]fluoroethyl)-L-tyro-

sine (FET) for PET, which are transported by the same specific amino acid transport system L as MET, but are not incorporated into proteins (Langen et al. 2002). Their rapid accumulation into brain tumors is independent of BBB disruption. Among the <sup>18</sup>F-labeled amino-acids, FET has been selected as a representative of this category due to ease of synthesis, high in vivo stability, and fast brain and tumor uptake kinetics. Other natural or artificial amino acids have been labeled to measure tumor metabolism, but they are beyond the scope of these guidelines. Despite differences in blood clearance, uptake kinetics, and relation to protein synthesis, MET, IMT, and FET show similar results in the diagnostic evaluation of cerebral tumors, supporting their parallel review in these guidelines.

### COMMON INDICATIONS

#### Indications

In the brain, glucose metabolism provides ~95% of adenosine triphosphate (ATP) required for brain function. Under physiological conditions glucose metabolism is tightly connected to neuronal activity. Besides neurooncology, FDG is indicated



for a number of diagnostic questions in dementing disorders, epilepsy, and movement disorders, which are beyond the scope of this chapter (Bartenstein et al. 2002).

#### *Detection of Viable Tumor Tissue*

Conventional CT and MRI techniques cannot reliably differentiate viable tumor tissue from treatment-induced nonneoplastic changes, such as oedema, postoperative changes or radiation necrosis. FDG-PET can be used in differential diagnosis of cerebral space occupying lesions and detection of viable tumor tissue (i.e., recurrence). Radiolabeled amino acid imaging is, however, superior to FDG-PET in confirming low-grade recurrence (Mehrkens et al. 2008; Van Laere et al. 2005).

#### *Tumor Delineation*

Radiolabeled amino acid tracers are superior to CT and MRI for estimation of true tumor extension in low as well as in high-grade gliomas (Kracht et al. 2004). In low grade tumors, oedema surrounding the tumor cannot be differentiated from tumor cell infiltration with MRI or CT. In anaplastic astrocytomas and glioblastomas, too, the area of contrast enhancement does not reflect tumor extent correctly. Radiolabeled amino acid tracers are also superior to FDG for tumor delineation in low-grade tumors, for which FDG uptake is found to be decreased compared with normal cortex or basal ganglia. The higher ratio for labeled amino acid tracers is due to the lower uptake of radioactivity in normal brain tissue. This is in sharp contrast with FDG with its high uptake in normal brain tissue, which can obscure delineation depending on the tumor glucose rate. With FET, however, large brain vessels might be visualised as blood pool radioactivity exceeds radioactivity in the normal brain tissue (Pauleit et al. 2003).

#### *Selecting the Best Biopsy Site*

Stereotactic biopsy remains the gold standard in the classification and grading of glioma. However, histopathological grading may be limited by sampling error due to well-known heterogeneity of gliomas or may not in all instances predict the biological behavior of brain tumors and thus the patient's prognosis. FDG as well as labeled amino acids imaging is recommended to guide the stereotactic biopsy (Pirrotte et al. 2004).

#### *Non-invasive Tumor Grading*

The role of labeled amino acids in the grading of cerebral gliomas is controversial and FDG-PET appears better suited to differentiate between tumor grades (Kaschten et al. 1998). MET and IMT uptake tends to correlate with cell proliferative activity and MET uptake with microvessel density (Kracht et al. 2003). Radiolabeled amino acid imaging may aid in differentiating high-grade gliomas from histologically benign brain tumors or nonneoplastic lesions (Floeth et al. 2008). The intensity of MET uptake may represent a prognostic factor for WHO Grade II and III tumors considered separately. Oligodendroglioma and oligo-astrocytoma could have greater uptake than high-grade gliomas. In contrast to MET (Moulin-Romsee et al. 2007), dynamic FET PET imaging has recently shown to allow differentiation of low versus high grade brain tumors on an individual patient basis. Time activity curves show slight increase in low grade gliomas, whereas high grade gliomas present with an early peak (10–20 min) followed by a decrease (Popperl et al. 2007).

#### *Therapy Planning*

In conjunction with anatomical imaging, radiolabeled amino acid imaging may be

used to better define the tumor volume to resect or irradiate (Levivier et al. 2004; Veas et al. 2009; Weber et al. 2008).

#### *Tumor Response*

FDG as well as labeled amino acid uptake changes may predict the response to loco-regional chemo- and radiotherapy as it may allow early detection of residual tumor after surgery (Brock et al. 2000; Galldiks et al. 2006).

#### Contraindications (Relative)

- Pregnancy (mothers should interrupt breast feeding for 24 h if PET is indicated; no data are available for IMT).
- Evident lack of cooperation or inability to cooperate.

## PROCEDURE

### Patient Preparation

#### *Prearrival*

Patients should be informed of the procedure to fully cooperate.

#### *Preinjection*

Patient should be fasting for at least 4 h for FDG as well as for radiolabeled amino acids: the former to allow for optimal cerebral FDG uptake not influenced by increased serum glucose levels and the latter to ensure stable metabolic conditions.

Prior to the *FDG administration*, blood glucose levels should be checked. When hyperglycemia is present (>160 mg/dL), there is increased competition of elevated plasma glucose with FDG at the carrier enzyme and, because it is usually associated with high intracellular glucose levels, also at hexokinase. Therefore, FDG uptake

is reduced in whole brain and stochastic noise is increased. In addition, decreased contrast of white and grey matter uptake can be expected, which might further decrease diagnostic accuracy. Acute correction of hyperglycemia with insulin usually does not improve brain image quality substantially, probably because the correction of increased intracellular glucose level lags behind the correction of the plasma glucose level. Quantitation of regional cerebral glucose metabolism with FDG-PET also requires steady state conditions which are not maintained during falling plasma glucose levels after application of insulin. Best results for clinical FDG-imaging in the brain of diabetics can be achieved in an euglycaemic situation during adequate therapeutic management.

To avoid variation of FDG uptake in normal brain tissue, several minutes before FDG administration and during the uptake phase of FDG (at least 20 min), patients should be positioned comfortably in a quiet, dimly lit room. They should be instructed not to speak, read or otherwise be active. It is desirable to have the cannula for i.v., administration in place 10 min before FDG administration.

Because the *L-type amino acid* transporter is an exchanging transporter the influence of plasma amino acid concentrations on the uptake of MET, FET, and IMT is complex. On the one hand, there is competitive inhibition of the transport system by natural L-amino acids, reducing radiolabeled amino acid uptake in tumor tissue. On the other hand, preloading with amino acids has been shown to increase tumor uptake of radiolabeled amino acids; the unlabeled intracellular amino acids being transported outside by the L-transporter in exchange for radiolabeled amino acids in the plasma (Lahoutte et al. 2002). For IMT, block the

thyroid gland by an adequate regimen (e.g., perchlorate 1,000 mg given at least 30 min prior to injection) to prevent possible thyroid uptake of free radioactive iodine.

#### Information Pertinent to Performance of the Procedure

- Patient history with particular focus on previous surgery and/or radiation therapy as well as current and past neurological or psychiatric status.
- History of diabetes, fasting state.
- Information regarding recent morphological imaging studies (CT, MRI).
- Current medication and when last taken, especially psychotropic pharmaceuticals. These may influence regional metabolic rate of glucose (rCMRGI).
- Patient's ability to lie still for 20–40 min for PET to ~1 h for SPECT.

#### Precautions and Conscious Sedation

- Continuous supervision of the patients during the whole scanning procedure is necessary. This is especially important for patients with tumor associated seizures.
- In uncooperative patients, it may be worthwhile to apply conscious sedation (e.g., by a short acting benzodiazepine such as i.v., midazolam). For FDG, administration should take place at least 20 min after tracer injection, preferably starting only a few minutes before data acquisition.
- Appropriate monitoring (pulse-oxymetry) should be performed to recognize the possibility of cardiopulmonary depression and appropriate antidote/emergency backup should be foreseen. Doses of sedation should be reduced in elderly patients.

#### Radiopharmaceutical

##### *Radiopharmaceutical*

- [<sup>18</sup>F]Fluoro-2-deoxyglucose (FDG).
- 3-[<sup>123</sup>I]Iodo- $\alpha$ -methyl-L-tyrosine (IMT).
- [Methyl-<sup>11</sup>C]-L-methionine (MET).
- *O*-(2-[<sup>18</sup>F]Fluoroethyl)-L-tyrosine (FET).

##### *Recommended Dosage*

The dose recommendations for FDG, MET, and FET mentioned here are valid for full ring dedicated PET-cameras with BGO-crystals in 3D-mode.

- FDG: in adults, 125–250 MBq (typically 150 MBq) in 3D-mode. In children, 2–4 MBq/kg in 3D-mode with a minimum of 10 MBq in newborn infants.
- IMT: 100–400 MBq (typically 185 MBq).
- MET: 200–250 MBq.
- FET: 200–250 MBq.

The administered dose may increase using 2D-mode and vary for other systems according to differences in sensitivity. For the radiolabeled amino acids, the activity to be administered to children should be a fraction of the adult activity calculated from body weight according to the factors given by the EANM Pediatric Task Group.

##### *Radiation Dosimetry (Table 2.1)*

##### *Radiation Dosimetry of Brain Transmission Scans*

Based on transmission scans of 10 min and CT-based scans of 5–10 s, the effective doses per scan are: 20–30  $\mu$ Sv for Germanium-based transmission, ~20  $\mu$ Sv for low-dose high-speed CT, and between 220 and 450  $\mu$ Sv for high-quality CT.

TABLE 2.1. Radiation dosimetry of FDG, IMT, MET, and FET

	Organ receiving the largest radiation dose (mGy/MBq)	Effective dose (mSv/MBq)
FDG adults	0.17 Bladder wall	0.019
FDG children (5 years)	0.48 Bladder wall	0.050
IMT	0.047 Bladder wall	0.0073
MET	0.091 Bladder wall	0.0074
FET	0.072 Bladder wall	0.023

Calculations based on (Schmidt et al. 1997), ICRP 53 (addenda 4 and 5) and ICRP 80.

## Data Acquisition

### *Time Delay from Injection to Beginning of Data Acquisition*

- Whatever the tracer, it is recommended to use a fixed acquisition period to ensure that data are comparable between subjects and in intraindividual follow-up studies.
- FDG: the acquisition should not start earlier than 30 min p.i. Better contrast between grey and white matter as well as between tumor and normal brain tissue can be achieved with a longer time interval between FDG administration and data acquisition (e.g., 3–8 h for tumors) (Spence et al. 2004).
- IMT: 15 min p.i.
- For MET or FET, many centers start a dynamic 40 min acquisition just after tracer injection. Image from 20 to 40 p.i. is used for the clinical reading.

### *Set Up for Data Acquisition*

Patients should void prior to acquisition for maximum comfort during the study and should be advised to void after the scan session to minimize radiation exposure. They should also be informed regarding the total acquisition time and positioned for maximum comfort. Because postprocessing routines allow correcting for minor obliquities of head orientation, patients' comfort (which reduces the probability of motion during acquisition) is more important than perfect alignment of the head. Careful

positioning of the patient's head may, however, become critical if tomographic cameras with a field of view similar to or smaller than the length of brain are used. The patient has to be informed regarding the necessity to avoid (voluntary) movements of the head and has to be asked for her/his active cooperation. If cooperation is poor sedation may be used. The patient's head should be only lightly restrained. If movement artefacts can be expected, it can be helpful to perform dynamic acquisition over the intended period of time, check the sinograms and add only the sinograms of the properly acquired time period prior to reconstruction.

### FDG, MET or FET Positron Emission Tomography

- *Transmission scan.* If attenuation correction is based on transmission images, better results are generally achieved when the images are acquired before tracer injection. If additional postprocessing like segmentation is performed, the images may be obtained after injection of radiotracer. Acquisition counts collected may vary between the PET-systems and the postprocessing procedures used. Institutions using standard full ring dedicated PET cameras with an axial field of view over 16 cm typically acquire transmission images of more than >100 million counts over 10–20 min. In the case of PET-CT system, the CT scan can be used for the

purpose of attenuation correction. The scanning parameters may vary according to the type of CT scanner. Usually the tube voltage is set at 140 kV, which permits the conversion of the Hounsfield units into attenuation coefficients at 511 keV. The CT scan can be performed after the injection of FDG and has the advantage to significantly reduce the total scan time (usual duration is <10 s). However, the dose of the CT scan to the patient can be reduced by lowering the tube current (see radiation dosimetry above) if anatomical information is not needed. When performing PET-CT of the brain it is recommended to check for movements between the CT and the PET sessions, which might produce artefacts in the attenuation correction.

- *Emission scan.* As semiquantitative estimates of tumor-to-background uptake ratios are typically used, it is recommended to use a standardized acquisition protocol with a fixed time for start of acquisition to make the data of different patients or repeated scans comparable. If data are acquired in 3-D mode, appropriate scatter correction is mandatory. The duration of emission image acquisition should be related to the minimum required number of counts. For FDG, typically data are acquired over 15–30 min aiming to collect 50–200 million counts. Even though shorter acquisition times can still be used for diagnostic pattern evaluation (Chen et al. 2005), a minimum of 15 min in 3D mode is advocated. For MET and FET typically data are acquired for 20 min (20–40 min p.i.), often supplemented by dynamic data starting directly with tracer injection.

#### IMT Single Photon Emission Tomography

- Multiple detectors (triple or dual head) or other dedicated SPECT cameras for brain imaging should be used for acquisition. Single detector units cannot generally be recommended. They may only be used if scan time is prolonged appropriately, a dose in the upper suggested range is applied, and meticulous care is taken to produce high-quality images.
- LEHR or LEUHR parallel-hole collimators are the mostly available collimator sets for brain imaging. All purpose collimators are not suitable. The use of medium energy collimators could be advantageous; however, usually they are hampered by a low sensitivity. They may only be used if acceptable count rates are obtained. If available, collimator sets specifically adapted to the characteristics of  $^{123}\text{I}$  may be used. Fan-beam collimators may be generally preferred over parallel-hole collimators due to the advantageous trade-off between resolution and count rate capability. The acquisition parameters are summarized in Table 2.2.

TABLE 2.2. Acquisition parameters for IMT-SPECT

- 
- Rotational radius: smallest possible with appropriate patient safeguard
  - Matrix:  $128 \times 128$
  - Angular sampling:  $\leq 3^\circ$  ( $360^\circ$  rotation)
  - Zoom: acquisition pixel size should be 1/3–1/2 of the expected resolution; therefore it may be necessary to use a hardware zoom to achieve an appropriate pixel size
  - Acquisition mode: Step and shoot mode is predominantly used. Continuous mode acquisition may provide shorter total scan time, reduce mechanical wear to the system and improve patient comfort
  - Total scan time: depending on the imaging device, typical scan time for a triple head camera is about 30–50 min (e.g., 120 projections; 40 projections per head; 60 s/projection)
-

## Image Processing

### *PET Reconstruction*

Images are reconstructed in the form of transaxial images of at least  $128 \times 128$  pixels, a usual pixel size is 2–4 mm. Commonly used filters are Hanning or Shepp-Logan but they should be fine-tuned depending on application, injected activity, camera and acquisition type and even physician's preference. Iterative reconstruction methods, including ordered-subset expectation maximization (OSEM) are also available, may improve target-to-background ratio and are used on many recent PET and PET-CT systems.

### *SPECT Reconstruction*

- Review of projection data: unprocessed projection data should be reviewed in cinematic display prior to filtering to assess presence and degree of motion artifacts, target-to-background ratios and other potential artifacts. Inspection of projection data in sinogram form may also be useful.
- *Reconstruction* of the entire brain volume at highest pixel resolution (i.e., one pixel thick) using filtered backprojection or iterative reconstruction.
- *Filtering*: data should be filtered in all three dimension (x,y,z). This can be achieved either by two-dimensional prefiltering the projection data or by applying a 3-dimensional postfilter to the reconstructed data. Low-Pass (e.g., Butterworth) filters should generally be used. Resolution recovery or spatially varying filters have to be used with caution, as they may produce artifacts. Therefore, the latter cannot be recommended for general use.
- *Attenuation correction*: Attenuation correction has to be performed. It could be performed either using a measured cor-

rection matrix or a calculated homogeneous correction matrix according to Chang (linear attenuation coefficient for  $^{123}\text{I}$ :  $\mu = 0.10\text{--}0.12 \text{ cm}^{-1}$ ). Shape contouring should be used if available. Contours should include scalp and not just grey matter. Contours should be defined for each individual transaxial slice. Correct shape and position of the contours should be reviewed prior to calculation of the corrected slices. In the case of SPECT-CT systems, the CT component of the scan can be used to perform the attenuation correction (Delbeke et al. 2006).

### *Reformatting of PET and SPECT Images*

Transaxial slices have to be reformatted into three orthogonal planes. Generate transverse sections parallel to a given anatomic orientation (e.g., AC-PC line), assuring a high degree of standardization in plane orientation. In addition, coronal sections orthogonal to the transverse sections and correct for obliquities should be created.

### *Comparative Evaluation*

ROI techniques need to be used to assess tumor uptake. ROI definition depends on the question to be answered (e.g., based on the area of maximal uptake or on the morphological information obtained by CT or MRI). When using quantitative criteria for image interpretation the same methods for ROI definition as described in the corresponding study in the literature should be applied.

## Interpretation Criteria

### *Visual Interpretation*

The images should be critically examined during interpretation for the presence of

movement, attenuation or camera related artefacts. Data evaluation must consider relevant morphologic information (CT, MRI). Morphologic changes should be known for the interpretation. In many cases it is recommended to fuse FDG or amino-acid images with the CT or MRI scan of the individual, especially to better delineate tumor extent or to identify accurately the metabolically most active part of a brain tumor prior to biopsy. In PET-CT or SPECT-CT systems, fused images can be immediately visualised after image reconstruction without the need of specific software for image registration. Images should be read on the computer screen rather than from hard copies, because this allows variation in color table and adjustments of background subtraction or contrast. However, inappropriate thresholding may result in artefacts and use of non-continuous color tables may overestimate findings due to abrupt color changes.

### *Quantification*

Quantification is helpful in assisting visual interpretation and to objectify tumor uptake of FDG or labeled amino acids. Usually transverse/oblique slices are picked for ROI definition. For evaluation either only the slices with the highest lesion uptake are picked or the entire tumor volume is taken into account. Interpretation of quantitative results is based on the comparison of tumor-to-background uptake ratio. The exact threshold value depends on the tracer, the techniques used for acquisition and ROI definition, and the question to be answered. It should be compared with the corresponding studies in the literature. For example, the best cutoff level of FDG uptake ratios in the differentiation of high-grade from low-grade tumors is 1.5

for tumor-to-white matter ratios and 0.6 for tumor-to-cortex ratios (Delbeke et al. 1995). 1.8 is the best cutoff value of the IMT uptake ratio between mean uptake in a 90% isocontour tumor ROI and that in the contralateral reference region, to differentiate between gliomas from nonneoplastic lesions (Kuwert et al. 1996) as well as between recurrent tumors and benign post-therapeutic lesions (Kuwert et al. 1998). Peak tumor activity-to-contralateral reference region  $>1.7$  after tumor resection with IMT (Weber et al. 2001) or  $>2.0$  in patients suspicious for recurrence with MET (Van Laere et al. 2005) is of poor prognosis. When using the ratio between the mean activity in a 25 mm<sup>2</sup> tumor ROI and that in the mirror reference region, 1.6 is the best threshold value to characterize neoplastic tissue with FET (Pauleit et al. 2005).

Estimation of the rCMRglc can be performed by compartmental modelling or using graphical analytic approaches. A correction factor, the so called “lumped constant”, can be used to convert the FDG values to values reflecting glucose metabolism. Such factor is however, lower in normal brain compared to that of glioma (Spence et al. 1998), so that semiquantitative estimates of glucose metabolism such as the SUV (standardised uptake value) are typically preferred for tumor imaging. For this kind of quantification, standardised acquisition times are mandatory. A static image is sufficient, typically acquired at 30 or 60 min p.i. (after FDG has reached a plateau concentration in the lesion). In addition, the exact total dose of FDG administered and the patient’s weight and height for measurement of body surface area are required. A calibration factor is also needed. These semiquantitative estimates can be corrected for blood glucose concentration.

## Reporting

### General

The report should include all pertinent information, including the name of the patient and other identifiers, such as birth date, name of the referring physician(s), potentially interfering medications, type of examination, date of examination, radiopharmaceutical, including administered dose, glycemia for FDG, and patient history, including reasons for requesting the study.

### Body of the Report

- Procedures and materials. Include in the report a brief description of the imaging procedure (i.e., type of transmission and emission imaging) and assessment of scan quality (if compromised give the reason, e.g., motion artifacts etc.). If sedation is performed, briefly describe the procedure, including type and time of medication given in relation to the radiotracer injection.
- Findings. Describe whether the FDG or amino acid imaging finding is normal or abnormal. If findings are abnormal, describe the location and intensity of abnormal radiotracer uptake. State what criteria were used for interpretation (visual assessment or semiquantitative measures).
- Limitations. Where appropriate, identify factors that can limit the sensitivity and specificity of the examination (i.e., movement, small lesions).
- Clinical issues. The report should address or answer any pertinent clinical issues raised in the request for the imaging examination.
- Comparative data. Results of morphological imaging modalities (CT, MRI) are essential for interpretation. Every

attempt should be made to obtain the images of these studies and not only the written interpretation for comparison with the PET or SPECT studies. Comparisons with these imaging modalities, previous examinations with radiolabeled amino acids or FDG-PET (if available), should be part of the report.

### Interpretation and Conclusion

A precise diagnosis should be given whenever possible. Interpretation should be based on the results of the visual and more important quantitative evaluation and conclude on whether an abnormal FDG or radiolabeled amino acid brain uptake is visualized (e.g., its extent and characteristics such as inhomogeneity) keeping in mind the potential sources of error (see Table 2.3). When appropriate, follow-up or additional studies should be recommended to clarify or confirm the suspected diagnosis.

TABLE 2.3. Sources of error (see also Cook et al. 1999)

- 
- Artifacts (patient movement, camera related, induced by inappropriate processing)
  - No or insufficient attenuation correction
  - Physiologic MET uptake in the pituitary gland, contrasting with that of IMT, and sometimes in choroids plexus
  - Small regional differences of normal brain uptake in normal brain emphasizing the careful choice of an appropriate reference region
  - False-negative results for radiolabeled amino acids in ~20% of untreated low-grade gliomas, especially those poorly vascularized. False-negative results are, however, very rare in pretreated recurrent low-grade gliomas
  - High tumor uptake does not always indicate high-grade glioma (oligodendroglioma, low-grade desmoplastic infantile ganglioglioma, pilocytic astrocytoma)
  - Mild uptake of radiolabeled amino acids can be observed in brain hematoma or close to surgery and/or radiation therapy, brain abscess, acute or subacute ischemic lesions, apparently in postischemic hyperperfusion areas, or focal cortical dysplasia
  - Soft tissue or skull uptake following surgery in the area of the skull or brain
  - Recent radio- or chemotherapy
-



## ISSUES REQUIRING FURTHER CLARIFICATION

In clinical diagnostic settings, the exact role of partial volume correction methods or of attenuation correction with MRI need to be further evaluated. The clinical impact of image fusion for planning stereotaxic surgery or radiotherapy (e.g., gamma-knife), especially for the treatment of patient with suspected recurrences, also requires further clarification. Other  $^{18}\text{F}$ -labeled amino acid analogues for brain tumor imaging are currently under development. Among them FDOPA is the most studied. When proofs of its clinical utility accumulate, FDOPA could be another tracer to include in an amended version of the guidelines.

## REFERENCES

- Bartenstein, P., Asenbaum, S., Catafau, A., Halldin, C., Pilowski, L., Pupi, A., and Tatsch, K. (2002) European Association of Nuclear Medicine procedure guidelines for brain imaging using [(18F)FDG]. *Eur. J. Nucl. Med. Mol. Imaging* 29:BP43–BP48
- Brock, C.S., Young, H., O'Reilly, S.M., Matthews, J., Osman, S., Evans, H., Newlands, E.S., and Price, P.M. (2000) Early evaluation of tumour metabolic response using [18F]fluorodeoxyglucose and positron emission tomography: a pilot study following the phase II chemotherapy schedule for temozolomide in recurrent high-grade gliomas. *Br. J. Cancer* 82:608–615
- Chen, W.P., Matsunari, I., Noda, A., Yanase, D., Yajima, K., Takeda, N., Yamada, M., Minoshima, S., and Nishimura, S. (2005) Rapid scanning protocol for brain (18F)-FDG PET: a validation study. *J. Nucl. Med.* 46:1633–1641
- Cook, G.J., Maisey, M.N., and Fogelman, I. (1999) Normal variants, artefacts and interpretative pitfalls in PET imaging with 18-fluoro-2-deoxyglucose and carbon-11 methionine. *Eur. J. Nucl. Med.* 26:1363–1378
- Delbeke, D., Meyerowitz, C., Lapidus, R.L., Maciunas, R.J., Jennings, M.T., Moots, P.L., and Kessler, R.M. (1995) Optimal cutoff levels of F-18 fluorodeoxyglucose uptake in the differentiation of low-grade from high-grade brain tumors with PET. *Radiology* 195:47–52
- Delbeke, D., Coleman, R.E., Guiberteau, M.J., Brown, M.L., Royal, H.D., Siegel, B.A., Townsend, D.W., Berland, L.L., Parker, J.A., Zubal, G., and Cronin, V. (2006) Procedure guideline for SPECT/CT imaging 1.0. *J. Nucl. Med.* 47:1227–1234
- Floeth, F.W., Sabel, M., Stoffels, G., Pauleit, D., Hamacher, K., Steiger, H.J., and Langen, K.J. (2008) Prognostic value of 18F-fluoroethyl-L-tyrosine PET and MRI in small nonspecific incidental brain lesions. *J. Nucl. Med.* 49:730–737
- Galldiks, N., Kracht, L.W., Burghaus, L., Thomas, A., Jacobs, A.H., Heiss, W.D., and Herholz, K. (2006) Use of 11C-methionine PET to monitor the effects of temozolomide chemotherapy in malignant gliomas. *Eur. J. Nucl. Med. Mol. Imaging* 33:516–524
- Kaschten, B., Stevenaert, A., Sadzot, B., Deprez, M., Degueldre, C., Del Fiore, G., Luxen, A., and Reznik, M. (1998) Preoperative evaluation of 54 gliomas by PET with fluorine-18-fluorodeoxyglucose and/or carbon-11-methionine. *J. Nucl. Med.* 39:778–785
- Kracht, L.W., Friese, M., Herholz, K., Schroeder, R., Bauer, B., Jacobs, A., and Heiss, W.D. (2003) Methyl-[11C]-l-methionine uptake as measured by positron emission tomography correlates to microvessel density in patients with glioma. *Eur. J. Nucl. Med. Mol. Imaging* 30:868–873
- Kracht, L.W., Miletic, H., Busch, S., Jacobs, A.H., Voges, J., Hoevens, M., Klein, J.C., Herholz, K., and Heiss, W.D. (2004) Delineation of brain tumor extent with [11C]L-methionine positron emission tomography: local comparison with stereotactic histopathology. *Clin. Cancer Res.* 10:7163–7170
- Kuwert, T., Morgenroth, C., Woesler, B., Matheja, P., Palkovic, S., Vollet, B., Samnick, S., Maasjosthusmann, U., Lerch, H., Gildehaus, F.J., Wassmann, H., and Schober, O. (1996) Uptake of iodine-123-alpha-methyl tyrosine by gliomas and non-neoplastic brain lesions. *Eur. J. Nucl. Med.* 23:1345–1353
- Kuwert, T., Woesler, B., Morgenroth, C., Lerch, H., Schafers, M., Palkovic, S., Matheja, P., Brandau, W., Wassmann, H., and Schober, O. (1998) Diagnosis of recurrent glioma with SPECT and iodine-123-alpha-methyl tyrosine. *J. Nucl. Med.* 39:23–27
- Lahoutte, T., Caveliers, V., Franken, P.R., Bossuyt, A., Mertens, J., and Everaert, H. (2002) Increased

- tumor uptake of 3-(123)I-Iodo-L-alpha-methyltyrosine after preloading with amino acids: an in vivo animal imaging study. *J. Nucl. Med.* 43:1201–1206
- Langen, K.J., Pauleit, D., and Coenen, H.H. (2002) 3-[(123)I]Iodo-alpha-methyl-L-tyrosine: uptake mechanisms and clinical applications. *Nucl. Med. Biol.* 29:625–631
- Levivier, M., Massager, N., Wikler, D., Lorenzoni, J., Ruiz, S., Devriendt, D., David, P., Desmedt, F., Simon, S., Van Houtte, P., Brotchi, J., and Goldman, S. (2004) Use of stereotactic PET images in dosimetry planning of radiosurgery for brain tumors: clinical experience and proposed classification. *J. Nucl. Med.* 45:1146–1154
- Mehrkens, J.H., Popperl, G., Rachinger, W., Herms, J., Seelos, K., Tatsch, K., Tonn, J.C., and Kreth, F.W. (2008) The positive predictive value of O-(2-[18F]fluoroethyl)-L-tyrosine (FET) PET in the diagnosis of a glioma recurrence after multimodal treatment. *J. Neurooncol.* 88:27–35
- Moulin-Romsee, G., D'Hondt, E., de Groot, T., Goffin, J., Sciot, R., Mortelmans, L., Menten, J., Bormans, G., and Van Laere, K. (2007) Non-invasive grading of brain tumours using dynamic amino acid PET imaging: does it work for 11C-methionine? *Eur. J. Nucl. Med. Mol. Imaging* 34:2082–2087
- Pauleit, D., Floeth, F., Herzog, H., Hamacher, K., Tellmann, L., Muller, H.W., Coenen, H.H., and Langen, K.J. (2003) Whole-body distribution and dosimetry of O-(2-[18F]fluoroethyl)-L-tyrosine. *Eur. J. Nucl. Med. Mol. Imaging* 30:519–524
- Pauleit, D., Floeth, F., Hamacher, K., Riemenschneider, M.J., Reifenberger, G., Muller, H.W., Zilles, K., Coenen, H.H., and Langen, K.J. (2005) O-(2-[18F]fluoroethyl)-L-tyrosine PET combined with MRI improves the diagnostic assessment of cerebral gliomas. *Brain* 128:678–687
- Pirrotte, B., Goldman, S., Massager, N., David, P., Wikler, D., Vandesteene, A., Salmon, I., Brotchi, J., and Levivier, M. (2004) Comparison of 18F-FDG and 11C-methionine for PET-guided stereotactic brain biopsy of gliomas. *J. Nucl. Med.* 45:1293–1298
- Popperl, G., Kreth, F.W., Mehrkens, J.H., Herms, J., Seelos, K., Koch, W., Gildehaus, F.J., Kretschmar, H.A., Tonn, J.C., and Tatsch, K. (2007) FET PET for the evaluation of untreated gliomas: correlation of FET uptake and uptake kinetics with tumour grading. *Eur. J. Nucl. Med. Mol. Imaging* 34:1933–1942
- Schmidt, D., Langen, K.J., Herzog, H., Wirths, J., Holschbach, M., Kiwit, J.C., Ziemons, K., Coenen, H.H., and Muller-Gartner, H. (1997) Whole-body kinetics and dosimetry of L-3--123I-iodo-alpha-methyltyrosine. *Eur. J. Nucl. Med.* 24:1162–1166
- Spence, A.M., Muzi, M., Graham, M.M., O'Sullivan, F., Krohn, K.A., Link, J.M., Lewellen, T.K., Lewellen, B., Freeman, S.D., Berger, M.S., and Ojemann, G.A. (1998) Glucose metabolism in human malignant gliomas measured quantitatively with PET, 1-[C-11]glucose and FDG: analysis of the FDG lumped constant. *J. Nucl. Med.* 39:440–448
- Spence, A.M., Muzi, M., Mankoff, D.A., O'Sullivan, S.F., Link, J.M., Lewellen, T.K., Lewellen, B., Pham, P., Minoshima, S., Swanson, K., and Krohn, K.A. (2004) 18F-FDG PET of gliomas at delayed intervals: improved distinction between tumor and normal gray matter. *J. Nucl. Med.* 45:1653–1659
- Van Laere, K., Ceyskens, S., Van Calenbergh, F., de Groot, T., Menten, J., Flamen, P., Bormans, G., and Mortelmans, L. (2005) Direct comparison of 18F-FDG and 11C-methionine PET in suspected recurrence of glioma: sensitivity, inter-observer variability and prognostic value. *Eur. J. Nucl. Med. Mol. Imaging* 32:39–51
- Vander Borgh, T., Asenbaum, S., Bartenstein, P., Halldin, C., Kapucu, O., Van Laere, K., Varrone, A., and Tatsch, K. (2006) EANM procedure guidelines for brain tumour imaging using labelled amino acid analogues. *Eur. J. Nucl. Med. Mol. Imaging* 33:1374–1380
- Vees, H., Senthamizhchelvan, S., Miralbell, R., Weber, D.C., Ratib, O., and Zaidi, H. (2009) Assessment of various strategies for 18F-FET PET-guided delineation of target volumes in high-grade glioma patients. *Eur. J. Nucl. Med. Mol. Imaging* 36:182–193
- Weber, W.A., Dick, S., Reidl, G., Dzewas, B., Busch, R., Feldmann, H.J., Molls, M., Lumenta, C.B., Schwaiger, M., and Grosu, A.L. (2001) Correlation between postoperative 3-[(123)I]iodo-L-alpha-methyltyrosine uptake and survival in patients with gliomas. *J. Nucl. Med.* 42:1144–1150
- Weber, D.C., Zilli, T., Buchegger, F., Casanova, N., Haller, G., Rouzaud, M., Nouet, P., Dipasquale, G., Ratib, O., Zaidi, H., Vees, H., and Miralbell, R. (2008) [(18)F]Fluoroethyltyrosine- positron emission tomography-guided radiotherapy for high-grade glioma. *Radiat. Oncol.* 3:44

*This page intentionally left blank*

# 3

## Assessment of Heterogeneity in Malignant Brain Tumors

Timothy E. Van Meter, Gary Tye, Catherine Dumur, and William C. Broaddus

### INTRODUCTION

#### The Problem of Heterogeneity and Its Clinical Significance

Primary malignant brain tumors are highly lethal cancers and vary in their histology, due to the many cell types in the brain and also the multipotent cells of origin (Singh et al. 2003, 2004). The most notorious among these is glioblastoma multiforme (GBM), the most aggressive glioma subtype, carrying the highest World Health Organization (WHO) grade of IV. As the name suggests, GBM can have features of several cell types, which can be regionally distinct, depending on the evolution of the tumor from CNS precursor cells. The varied cellular composition of these tumors can give rise to differences in phenotype, which alter therapeutic response. To better characterize the varied molecular phenotype of malignant brain tumors, we devised methodology which utilizes preoperative MR imaging to define areas of interest for stereotactic biopsy, image guided biopsy, followed by nucleic acid extraction with an “in-process” histopathological scoring during tissue processing. The procedure is followed by molecular phenotyping using any

highly reliable oligonucleotide microarray platform for molecular characterization. We have used Affymetrix gene expression microarrays due to the high reproducibility of these assays. The global gene expression profiling approach also allows a highly robust analysis to be performed on individual tumors, revealing a much more complete assessment of the overall molecular phenotype. Using this technique, significant differences in gene expression of important therapeutic targets were revealed, demonstrating the potential impact of the technique (Van Meter et al. 2006).

#### Previous Studies Assessing Molecular Heterogeneity of Tumors

Use of multiple biopsies for tumor assessment is regularly employed for histological assessment in routine diagnostic surgical pathology and has also been a feature of previous studies examining tumor associated gene expression. The examination of hallmark molecular genetic changes in gliomas, such as in the epidermal growth factor receptor (EGFR/ErbB1) gene alteration, were studied using multiple biopsy samples, some of which were defined regionally as tumor periphery or core samples

(von Deimling et al. 1993). Interestingly, mutations and gene amplification in the EGFR gene, a major therapeutic target, were increased in the tumor periphery of some of the tumors examined in a similar study, near the invasive, highly mitotic edge of growing glioblastomas. This perhaps demonstrates a difference in selection pressures in different tumor regions (Okada et al. 2003). This suggested to us that refined techniques might reveal other important aspects of tumor biology that derive from regional micro-environmental pressures and/or anatomical structures, including previously uncharacterized genes or metabolic processes. Other studies have looked at regional biopsies using immunohistochemistry to assess differences in protein expression of therapeutic targets. Vince et al. (1999) examined regional differences in tumor-associated matrix metalloproteinases (MMPs), and found that expression levels of the candidate MMPs varied considerably depending on the sampling area. Similarly, Raithatha et al. (2000) found that certain MMPs and their endogenous inhibitor proteins, the tissue inhibitors of MMPs (TIMPs), were preferentially associated with different tumor compartments, including association of MMP-9 primarily with the vasculature, whereas other MMP types were more widespread throughout the tumor. Each of these studies highlights the fact that important differences can exist in different tumor areas, which can impact both assessment of tumor pathology and therapeutic response. With the advent of global gene expression profiling techniques such as DNA microarrays, and the increasingly high throughput advances in tissue processing, a much more robust characterization of multiple tumor regions can be accomplished. Improving the success

of therapy for malignant brain tumors is imperative. The technique that follows represents one molecular diagnostic method that can define in exquisite detail the underlying biology of an unknown tumor, with great impact on the course of treatment.

### Use of Stereotactic Neuroimaging Systems for Tumor Sampling

There are two main stereotactic neuroimaging systems in widespread use for image-guided stereotactic neurosurgery, the first being the imaging station from BrainLab (Westchester, IL, USA), and the other, which we have used exclusively for the current techniques, from Medtronic, the Stealth Neuroimaging Station (Louisville, CO, USA). Each imaging console allows the use of preoperative MR image series to be uploaded and used for stereotactic navigation during surgery. One enabling feature of the neuroimaging stations is the ability to take snap shots of precise locations for biopsy during surgery. Using a foot pedal control, the neurosurgeon can gain a captured image (screen shot) of a specific location of interest, immediately prior to biopsy. The main difference between the two systems lies in the appearance of the software interface and its functionality. Both systems should perform equally well for the following protocols.

## METHODOLOGY

### Description of Method

The procedure consists of four main steps: (1) Neuroimaging guided stereotactic biopsy and storage of specimens; (2) cutting of serial frozen sections and in process histopathological assessment, (3) RNA

extraction from serial frozen sections and probe synthesis, and (4) microarray hybridization, imaging and data analysis. The nuances of each step are presented below.

### MRI-Guided Stereotactic Biopsy

Initial biopsy of the tumor is first obtained to allow full neuropathological evaluation and diagnosis, as required for the clinical management of the patient's disease. Following this, tumor samples are obtained that would otherwise have been discarded as surgical waste. The site of origin of tumor samples is planned preoperatively or intraoperatively by selecting areas of interest based on pre- and post contrast images. Figure 3.1a–c demonstrates

use of the Stealth Neuroimaging station to assess tumor pre- and intra-operatively. Generally, T1 weighted images are used. Biopsies can then be excised on the periphery of tumor, in the enhancing mass, in which a lower percentage of necrotic and hypoxic or peri-necrotic cells was expected, and selecting areas of tumor within the poorly enhancing central core of the tumor mass, in which a high percentage of necrosis is expected. The sites of origin of each biopsy are monitored by placement of the stereotactic probe within the tumor cavity and recorded during stereotactic tumor resection, utilizing the intraoperative neuro-navigation system (e.g., Medtronic Stealth Station) that is used routinely for these tumor

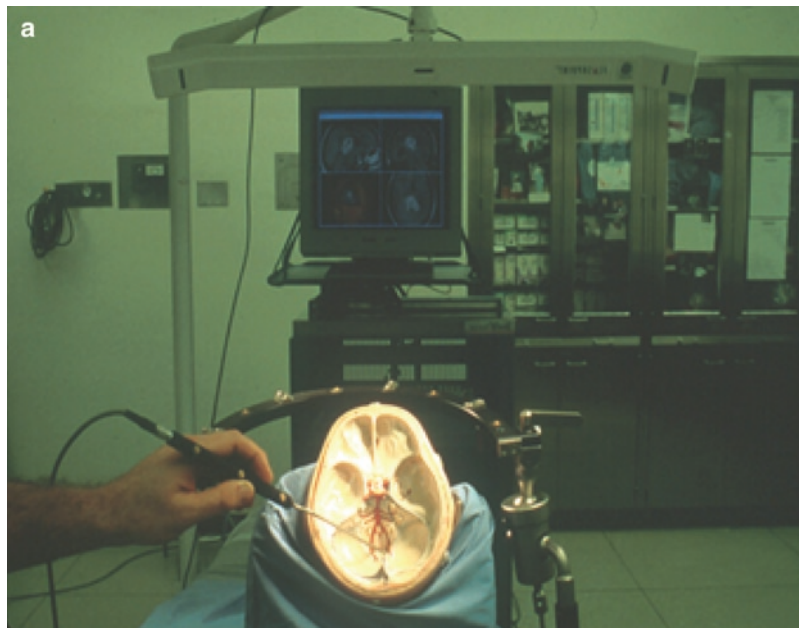


FIGURE 3.1. Neuro-navigation system used for stereotactic biopsy. (a) Mock positioning of the patient's head within the stereotactic frame. (b) Intraoperative screen shot from Medtronics' Stealth Station, demonstrating localization of stealth probe using infrared detection in relation to fixed caducels to verify positioning. (c) Intraoperative screen snapshots during tumor resection showing documentation of precise probe placement at biopsy sites within the tumor. Virtual probe trajectory is shown in the blue outline, and probe tip location is indicated by the red cross hairs

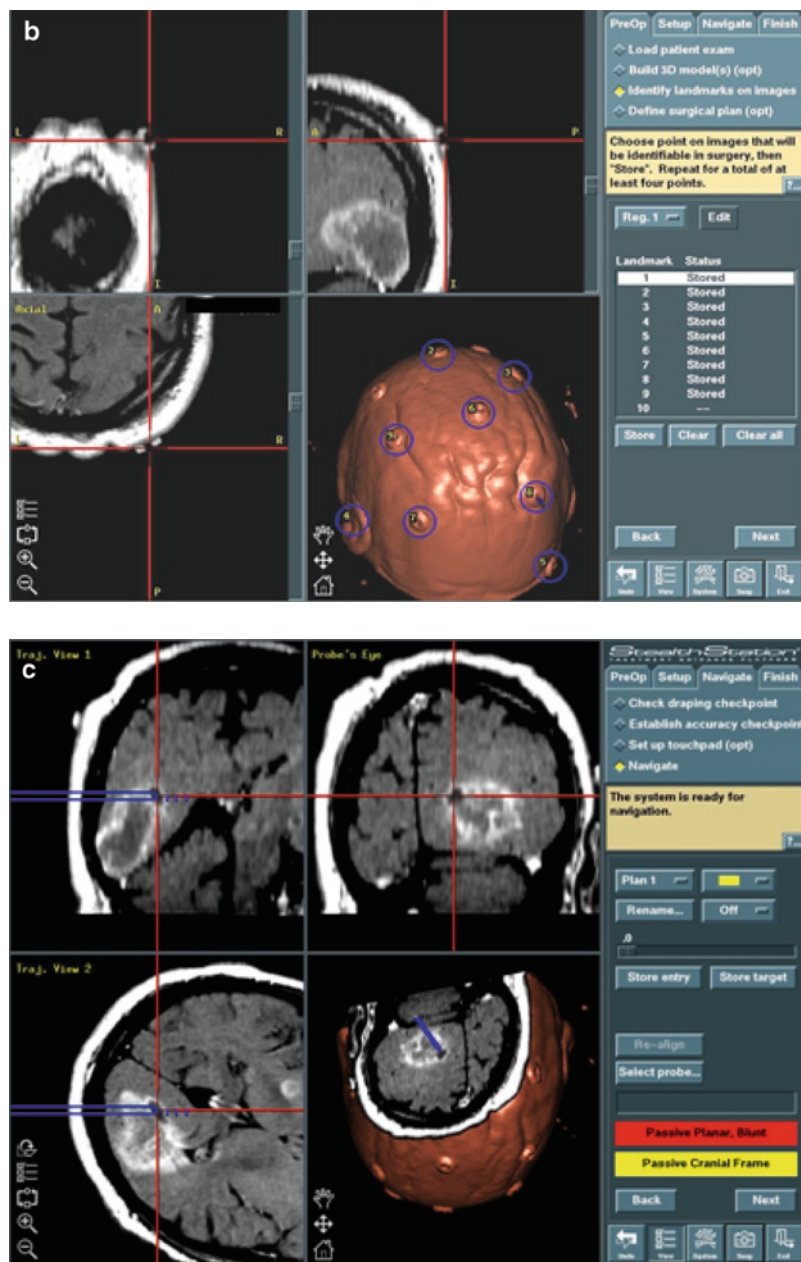


FIGURE 3.1. (continued)

resections at our institution. Using this procedure, we have removed as many as eight regional biopsies in a single surgery. Paired tumor core and periphery samples from the same patient, for example, can then be assessed and follow-on molecu-

lar assays and Histopathological features compared. Samples obtained are routinely snap-frozen in liquid nitrogen within 5 min of removal from the brain and stored at  $-86^{\circ}\text{C}$  or lower temperature until an appropriate time for further analysis.

### Integrated Histopathological Scoring

During processing, tumor samples are removed from storage and placed briefly on dry ice. Samples are then embedded in Tissue-Tek OCT compound and cooled for 10 min at  $-80^{\circ}\text{C}$  prior to sectioning on a cryostat (e.g., Leica, CM1850). Integral histopathological scoring of standard features (% tumor vs. normal cells, % necrosis, and extent of endothelial proliferation) is performed on flash-stained hematoxylin and eosin sections, in conjunction with an on-call neuropathologist. Routinely, 10  $\mu\text{M}$  serial frozen sections are analyzed at each 500–800  $\mu\text{M}$  increment during cryostat sectioning and the serial adjacent frozen sections are placed directly into Trizol Reagent (Invitrogen Life Sciences) for extraction. Polypropylene centrifuge tubes (15 mL) are used to contain the sections in Trizol reagent. Frozen sections (50–80  $\times$  10  $\mu\text{M}$ ) are prepared such that representative serial sections are available for staining at a minimum of three points throughout the specimen, with the remainder of the sections placed directly in Trizol Reagent (Invitrogen, Gaithersburg, MD) for extraction. This method yields high quality RNA extracts with detailed Histopathological classification for each biopsy piece for reference. Additional serial sections are routinely set aside for immunohistochemical or other studies.

Total RNA isolation is performed using Trizol reagent (Invitrogen<sup>TM</sup> Life Technologies, Carlsbad, CA), as reported previously (Dumur et al. 2004), followed by a cleanup process with RNeasy kits (Qiagen Inc., Valencia, CA) according to the manufacturer's protocols. The quality of total RNA sample as well as cDNA and cRNA synthesis products was assessed by running 1  $\mu\text{L}$  of every sample in RNA 6000 Nano or DNA

7500 LabChips<sup>®</sup> on the 2100 Bioanalyzer (Agilent, Palo Alto, CA), following the manufacturer's protocol. Furthermore, RNA integrity from high necrotic content samples was confirmed by monitoring cDNA and cRNA synthesis products following previously established quality control criteria (Dumur et al. 2004).

### Use of Genomics Technologies for Regional Molecular Profiling

The use of high density oligonucleotide DNA microarrays to assess tumor phenotype has become widespread since the technique was first described in the late 1990s, and significant improvements have been made in the reliability, the expense and ease of use of this technology over the last decade. We use Affymetrix microarray platforms due to the high reproducibility and tight correlation with probe set intensities and Taqman intensities in validation assays, but theoretically any similar technology can be used.

The Affymetrix<sup>®</sup> standard protocol has been extensively described elsewhere (Affymetrix 2001). Briefly, starting with 5  $\mu\text{g}$  of total RNA from every sample we generated double-stranded cDNA using a 24-mer oligodeoxythymidylic acid primer with a T7 RNA polymerase promoter site added to the 3' end (Superscript cDNA Synthesis System; Life Technologies, Inc., Rockville, MD). After second-strand synthesis, in vitro transcription was performed using the Enzo BioArray High Yield RNA Transcript Labeling Kit (Enzo Diagnostics, Farmingdale, NY) to produce biotin-labeled cRNA. Twenty microgram of the cRNA product was fragmented and hybridized for 18–20 h onto HG-U133A 2.0 microarrays, containing 22,283 probe sets. Each microarray was washed and stained with



streptavidin-phycoerythrin and scanned at a 6  $\mu\text{m}$  resolution by the Agilent G2500A Technologies Gene Array scanner (Agilent Technologies, Palo Alto, CA) according to the GeneChip<sup>®</sup> Expression Analysis Technical Manual procedures (Affymetrix, Santa Clara, CA). After scanning the chips, the raw intensities for every probe were stored in electronic files (in .DAT and .CEL formats) by the Microarray Suite 5.0 software (Affymetrix, Santa Clara, CA).

### Microarray Data Analysis

For every probe set, normalization, background subtraction, and expression summaries were calculated using three commonly used methods. First the Microarray Suite 5.0 (MAS5) method (Affymetrix, Santa Clara, CA) is used to obtain probe set summaries. A detailed description of this algorithm has been published elsewhere (Irizarry et al. 2003). Numerical expression summaries are stored in electronic files (in .CHP format). Second, model-based expression indexes (MBEI) are calculated, which uses a multiplicative model to account for probe affinity effects in calculating probe set expression summaries (described in Li and Wong 2001). Third, the robust multi-array average (RMA) method is used (Hubbell et al. 2002); this method uses quantile normalization followed by a median polish to remove probe affinity effects when calculating probe set summaries. Fold changes between core and periphery samples in our study can be obtained using the freely software BRB-ArrayTools, an Excel Add-in that performs analyses of microarray data (currently v3.7.0), which was developed and distributed by the National Cancer Institute of the US National Institutes of Health (<http://linus.nci.nih.gov/BRB-ArrayTools.html>).

### Small Sample Size

For a small number of biopsies from a single patient, statistical comparisons can be difficult. The “significance-score” algorithm (S-score), developed by Zhang et al. (2002), can be used to produce a score for the comparisons of the expression summaries between samples. The S-score produces a robust measure of gene expression changes by weighting oligonucleotide pairs according to their signal strength above empirically determined noise levels. The procedure produces scores centered on "0" (no change) with a standard deviation of 1. Thus, scores greater than 2 or less than  $-2$  from a single comparison have, on average, a 95% chance of being significant hybridization changes, corresponding to a p-value of  $p < 0.05$ . A p-value derived from S-score analysis, does not necessarily reflect that the observed changes in gene expression are biologically significant. To overcome this limitation, we perform additional validation assays, including quantitative polymerase chain reaction (QRT-PCR) for independent assessment of mRNA expression levels of candidate genes, and can do so with 1,000-fold greater dynamic range, making it an exquisitely sensitive technique for detecting mRNA and DNA quantification. We additionally validate any changes observed by evaluating a larger cohort of unrelated specimens to gain further statistical support for changes found to be significant differences in the hybridization-based oligonucleotide microarray assays.

## RESULTS

### Histopathological Considerations

Our analysis of different tumor regions from individual patients has detected wide variability in parameters, such as percent

TABLE 3.1. Regional differences in major histopathological criteria within individual glioblastoma tumors

Tumor case	Region	% Necrosis	Mitosis <sup>a</sup>	Vascular proliferation <sup>b</sup>
GBM1	Periphery	5	NP	3
GBM1	Periphery	5	NP	3
GBM1	Periphery	17	NP	3
GBM1	Core	30	NP	3
GBM1	Core	80	NP	3
GBM1	Core	0	3	3
GBM2	Periphery	50	1	2
GBM2	Core	10	3	4
GBM3	Periphery	0	1	2
GBM3	Core	63	1	4
GBM4	Periphery	0	3	3
GBM4	Core	22	2	3
GBM5	Periphery	10	3	3
GBM5	Core	94	1	2
GBM6	Periphery	35	2	3
GBM6	Core	96	2	3
GBM7	Periphery	10	3	4
GBM7	Core	28	3	3
GBM8	Periphery	25	1	3
GBM8	Core	75	1	3

<sup>a</sup>NP, not present, grading of 1–4 based on observation in less than 5% of cells (1), 5–20% (2) of cells, 15–40% (3), and greater than 40% of cells (4).

<sup>b</sup>Grading of 1–4 was based on degree observed by a neuropathologist, with 1 being minimal but present, 2–4 indicating increasing prevalence in the sections observed.

necrosis, percent tumor, and endothelial proliferation (Van Meter et al. 2006). An example of histopathological features that we have shown to differ between multiple MRI-guided stereotactic specimens from eight previously untreated glioblastoma patients is shown in Table 3.1. This is part of a larger series we are currently studying. Readers can appreciate that large regional differences are observed in parameters from separate regions of individual tumors, parameters that have major histopathological and prognostic significance. It can also be appreciated that surgical and post-surgical planning for complex drug delivery methods such as convection-enhanced drug delivery (CED) would be greatly informed by further molecular characterization of regional biopsy specimens, not only with regard to identifying appropriate molecular targeting agents for different

tumor regions, but also for issues such as optimal catheter placement. Both of these concerns are crucial to developing effective treatment regimens and to diminishing tumor recurrence.

#### Assessing Quality of Biopsy Extracts

As with any molecular biological study, the quality of the results obtained follow from the quality of the input material. Generally, adherence to strict quality control measures, as described above, will ensure that high quality and unbiased raw data will be generated in studies of regional biopsies. Figure 3.2 demonstrates an example of the preoperative MR scans and probe placement used to select and record the location of regional biopsy samples from tumor periphery (Figure 3.2a) and tumor core (Figure 3.2b), and the resulting histopa-

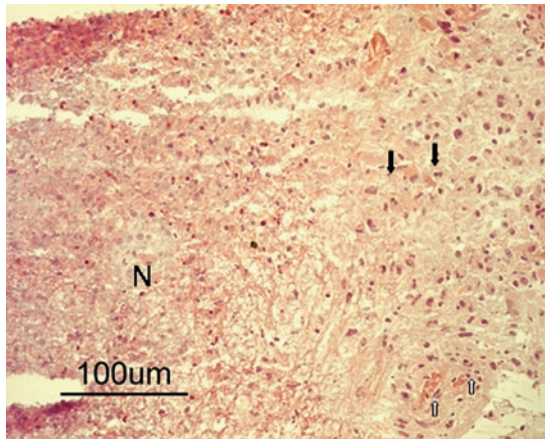


FIGURE 3.2. Example of stereotactic probe placement and resulting histopathology of snap-frozen biopsy sections. Precise locations can be identified and recorded using MR scans during tumor craniotomy to biopsy enhancing tumor periphery (a), and poorly enhancing tumor core (b) for molecular and biochemical studies. An example of histopathology seen in hematoxylin and eosin stained frozen sections during nucleic acid extraction is shown in C. N, Necrosis; *Open arrows*, areas of perinecrotic tissue with vascular proliferation; *Closed arrows*, mitotic figures

thology showing the pathognomic features of glioblastoma in one of the specimens of poorly enhancing tumor core (Figure 3.2c). For assessment of the quality and integrity of extracted nucleic acids, as well as the intermediate synthetic products such as cDNA and cRNA probes, and their dye labeling efficiencies, technologies such as the Agilent Bioanalyzer electropherogram, are critically important. We have provided detailed examples of the outcome of these strategies in recent published work (Van Meter et al. 2006). There are certain optimizations that should be mentioned when working with tumor biopsies. With glioblastoma biopsy samples in particular, we have performed detailed study of how the extent of necrosis can affect the success of unbiased cDNA and cRNA synthesis

in regional tumor studies (unpublished observations). In general, we have found that good quality RNA can be successfully obtained from islands of viable cells within necrotic and peri-necrotic areas of glioblastoma, provided there is no more than 80% necrosis in the tissue sections, as viewed in the histopathological scoring technique during RNA extraction from frozen sections. The “in-process” scoring approach also allows macrodissection of frozen biopsy regions after the initial viewing of hematoxylin and eosin stained cryosections when necessary, and prior to any further processing of tissue sections. One can see that this consideration has significance for tumor study in general, and especially for glioblastoma, given that the majority of cryopreserved tumor tissue may be derived from necrotic core areas during tumor debulking.

### Genomic Assessment of Regional Tumor Phenotype

Using the outlined methods, we have found that GBM cells located in perinecrotic areas of the tumor exhibit a gene expression profile consistent with highly aggressive and malignant cells. The significant association of the affected genes with cell motility and migration suggest a role for necrosis in tumor cell invasion from the necrotic core towards the periphery of the tumor. Moreover, we have found dramatic and significant down-regulation genes important to the differentiation state of neural cells, such as the ASCL1 (MASH1) transcription factor in perinecrotic areas. Using Ingenuity Pathway analysis software, we have been able to identify enrichment of stem cell-specific pathways (Wnt/b-catenin and Notch signaling pathways) suggesting that the necrotic microenvironment might host cancer stem

cells and promote cell-to-cell signaling that facilitates tumor progression and invasion towards peripheral regions of GBM.

More importantly, the results from studies utilizing these techniques demonstrate that the gene expression profiles of GBM samples strongly correlate with the histopathology of the sample, specifically with the necrotic content. This element becomes particularly important in an era where microarray analysis is set to offer unbiased, quantitative and reproducible tumor evaluation, as a promising ancillary tool for tumor classification and case prognosis. In that context, and considering the cellular heterogeneity and the important role of necrosis in GBM, a careful histopathological characterization of each sample subjected to microarray analysis is recommended. The increasing ease of use of microarray analysis software platforms offers greater accessibility to these complex datasets, which will likely be important for using this data to predict patient responses to therapeutic regimens in the future. Evaluation of multiple biopsy sites from a single patient will inform treatment decisions regarding the appropriateness of targeted therapeutics to a particular patient, or area of tumor.

#### Validation Studies

Use of genomic technologies may introduce bias to the study findings if, for instance, certain microarray probe sets perform better than others during hybridization. For this and other reasons it is necessary to perform additional assays to validate findings that emerge from genomic datasets. For both transcripts and genomic DNA findings, quantitative polymerase chain reaction (qPCR) techniques are generally used. The high sensitivity of these techniques and relative affordability make them accessible to

most institutions worldwide. Analyzing the concordance between probe set intensities and quantitative PCR fluorescence intensities using the  $\Delta\Delta CT$  method provide a good measure of the validity of the findings for both gene expression and chromosomal gain and loss (Livak and Schmittgen 2001).

## DISCUSSION

### Utility of Stereotactic Biopsy for Tumor Characterization

The utility of neuronavigation-guided, infrared imaging based stereotactic biopsy for regional tumor characterization has been highlighted here. The equipment for this technique is already available in many institutions around the world, and thus could be readily employed with molecular diagnostic techniques to characterize primary brain tumors. In the near future, the advent of more definitive molecular diagnostic tests for glioblastoma, based on smaller panels of diagnostic gene sets for tumor subtypes and treatment response profiles, and which are PCR based, would further simplify the technique and make it available for general clinical practice at most institutions equipped with a diagnostic pathology core facility.

The shortcomings of this approach should also be considered when planning any study. Minor inaccuracies can arise due to shifting of the brain volume during surgical debulking, generally within 1–3 cm of variation depending on the size and location of the tumor, and the extent of resection prior to sampling the biopsy site. Careful attention should therefore be paid to brain decompression and shifting during craniectomy, and close communication with the surgeon should prevent anomalies.

### Future Technical Applications

A number of other technologies used in neurosurgery and tumor resection could be combined with the current stereotactic biopsy technique, including MR-guided endoscopic biopsy or resection, which may be of particular use in difficult to access and otherwise delicate areas of the brain. Use of endoscopy has been used successfully in adult and pediatric brain tumor resection and could benefit from being coupled to neuro-navigation systems.

Pre-operative PET scans, MR angiography and MR spectroscopy studies could each add an additional level of information to molecular findings obtained through the stereotactic biopsy techniques described here, and combinations of such methods are being described in the literature (Hemm et al. 2005; Diehn et al. 2008). A number of novel molecular imaging agents are in development for real-time assessment of, for example, angiogenesis, protease activation (MMPs, Caspases), or other enzyme activities (e.g. Louie et al. 2000, and Genove et al. 2005; reviewed by Louie 2006 and Westmeyer and Jasanoff 2007). These imaging agents could therefore be validated or further studied at either the nucleic acid or functional protein level using the present stereotactic biopsy techniques. The potential for application during clinical trials to assess real-time molecular response or pro-drug conversion rates and metabolism in the brain is profound.

### Clinical Impact of Improved Tumor Characterization

There are at least two lines of evidence that support assessment of intratumoral heterogeneity as an important clinical consideration worthy of characterization in brain

tumors. The first is that a growing body of evidence has implicated transformed CNS stem or progenitor cells as the tumor initiating cells. Detailed intratumoral molecular phenotyping through prospective regional biopsy could help identify the more primitive cells of origin, which may be enriched in specific anatomical areas, and which may need to be selectively targeted with novel therapies to prevent recurrence. This ‘stem cell’ targeted approach will almost certainly be attempted within the next couple of years in malignant brain tumor clinical trials, during which the current techniques will be invaluable for determining phenotype and therapeutic response.

The second line of evidence regarding the clinical importance of tumor heterogeneity is that there appears to be a relationship between the degree of tumor heterogeneity and higher grades of malignancy, which may also be a reflection of a more primitive phenotype, or increased genetic instability. Notably, glioblastoma multiforme is a highly heterogeneous glial tumor carrying perhaps the worst prognosis of any primary brain tumor, and is reported to have a high percentage of primitive cancer stem cells (Singh et al. 2004). Again, detailed characterization of different tumor regions and further refinement of associated MR imaging techniques, may allow differential susceptibilities to be discerned within different tumor compartments and may uncover molecular profiles indicative of specific stages of cellular differentiation. Recent studies using microarray technologies have demonstrated the ability to discern precursor cells of origin in pediatric tumors such as ependymoma (Taylor et al. 2005), and to determine molecular profiles allowing diagnostic classification into prognostic subgroups in gliomas and

medulloblastomas (Mischel et al. 2003, Nutt et al. 2003, Hoelzinger et al. 2005; and Pomeroy et al. 2002, respectively), and in metastatic tumors of unknown primary origin (Dumur et al. 2008). Our own studies have detected specific highly proliferative tumor regions in glioblastoma that are enriched in cancer stem cells, suggesting cancer stem cell directed therapeutics should be targeted to these areas (Van Meter et al. 2007). Data on molecular profiles indicative of therapeutic response to specific treatment regimens are also emerging in many cancer types using microarray profiling and genetic markers (Buchholz et al. 2002). This type of detailed molecular analysis is increasingly being incorporated into clinical trials, and will aid in customization of therapeutic regimens in the post-surgical treatment phase.

In conclusion, the current method and derivative or similar techniques can be applied to better understand the underlying biology and clinical response of malignant brain tumors. Gradual decreases in the cost and time involved in global molecular profiling techniques will better enable medical centers to incorporate these technologies into treatment regimens and post-operative planning. These techniques should continue to be pursued, developed, and refined for their usefulness in uncovering important variations in the biology of individual tumors, and eventually, for enhanced mechanistic monitoring of tumor response or failure during treatment.

## REFERENCES

Affymetrix GeneChip®. Expression Analysis Technical Manual (2001) Affymetrix. Santa Clara, CA  
 Buchholz, T.A., Stivers, D.N., Stec, J., Ayers, M., Clark, E., Bolt, A., Sahin, A.A., Symmans,

W.F., Hess, K.R., Kuerer, H.M., Valero, V., Hortobagyi, G.N., and Pusztai, L. (2002) Global gene expression changes during neoadjuvant chemotherapy for human breast cancer. *Cancer J.* 8(6):461–468  
 Diehn, M., Nardini, C., Wang, D.S., McGovern, S., Jayaraman, M., Liang, Y., Aldape, K., Cha, S., and Kuo, M.D. (2008) Identification of noninvasive imaging surrogates for brain tumor gene-expression modules. *Proc. Natl. Acad. Sci. USA* 105(13):5213–5221  
 Dumur, C.I., Nasim, S., Best, A.M., Archer, K.J., Ladd, A.C., Mas, V.R., Wilkinson, D.S., Garrett, C.T., and Ferreira-Gonzalez, A. (2004) Evaluation of quality-control criteria for microarray gene expression analysis. *Clin. Chem.* 50(11):1994–2002  
 Dumur, C.I., Lyons-Weiler, M., Sciulli, C., Garrett, C.T., Schrijver, I., Holley, T.K., Rodriguez-Paris, J., Pollack, J.R., Zehnder, J.L., Price, M., Hagenkord, J.M., Rigl, C.T., Buturovic, L.J., Anderson, G.G., and Monzon, F.A. (2008) Interlaboratory performance of a microarray-based gene expression test to determine tissue of origin in poorly differentiated and undifferentiated cancers. *J. Mol. Diagn.* 10(1):67–77  
 Genove, G., DeMarco, U., Xu, H., Goins, W.F., and Ahrens, E.T. (2005) A new transgene reporter for in vivo magnetic resonance imaging. *Nat. Med.* 11(4):450–454  
 Hemm, S., Rigau, V., Chevalier, J., Picot, M.C., Bauchet, L., El Fertit, H., Rodriguez, M.A., Cif, L., Vayssière, N., Zanca, M., Baldet, P., Segnarbieux, F., and Coubes, P. (2005) Stereotactic coregistration of 201Tl SPECT and MRI applied to brain tumor biopsies. *J. Nucl. Med.* 46(7):1151–1157  
 Hoelzinger, D.B., Mariani, L., Weis, J., Woyke, T., Berens, T.J., McDonough, W.S., Sloan, A., Coons, S.W., and Berens, M.E. (2005) Gene expression profile of glioblastoma multiforme invasive phenotype points to new therapeutic targets. *Neoplasia* 7(1):7–16  
 Hubbell, E., Liu, W.M., and Mei, R. (2002) Robust estimators for expression analysis. *Bioinformatics* 18:1585–1592  
 Irizarry, R.A., Bolstad, B.M., Collin, F., Cope, L.M., Hobbs, B., and Speed, T.P. (2003) Summaries of Affymetrix GeneChip probe level data. *Nucleic Acids Res.* 31:e15

- Li, C., and Wong, W.H. (2001) Model-based analysis of oligonucleotide arrays: model validation, design issues and standard error application. *Genome Biol.* 2:RESEARCH0032
- Livak, K.J., and Schmittgen, T.D. (2001) Analysis of relative gene expression data using real-time quantitative PCR and the 2(-Delta Delta C(T)) Method. *Methods* 25(4):402–408
- Louie, A. (2006) Design and characterization of magnetic resonance imaging gene reporters. *Methods Mol. Med.* 124:401–417
- Louie, A.Y., Hüber, M.M., Ahrens, E.T., Rothbächer, U., Moats, R., Jacobs, R.E., Fraser, S.E., and Meade, T.J. (2000) In vivo visualization of gene expression using magnetic resonance imaging. *Nat. Biotechnol.* 18(3): 321–325
- Mischel, P.S., Shai, R., Shi, T., Horvath, S., Lu, K.V., Choe, G., Seligson, D., Kremen, T.J., Palotie, A., Liau, L.M., Cloughesy, T.F., and Nelson, S.F. (2003) Identification of molecular subtypes of glioblastoma by gene expression profiling. *Oncogene* 22(15):2361–2373
- Nutt, C.L., Mani, D.R., Betensky, R.A., Tamayo, P., Cairncross, J.G., Ladd, C., Pohl, U., Hartmann, C., McLaughlin, M.E., Batchelor, T.T., Black, P.M., von Deimling, A., Pomeroy, S.L., Golub, T.R., and Louis, D.N. (2003) Gene expression-based classification of malignant gliomas correlates better with survival than histological classification. *Cancer Res.* 63(7):1602–1607
- Okada, Y., Hurwitz, E.E., Esposito, J.M., Brower, M.A., Nutt, C.L., and Louis, D.N. (2003) Selection pressures of TP53 mutation and microenvironmental location influence epidermal growth factor receptor gene amplification in human glioblastomas. *Cancer Res.* 63(2):413–416
- Pomeroy, S.L., Tamayo, P., Gaasenbeek, M., Sturla, L.M., Angelo, M., McLaughlin, M.E., Kim, J.Y., Goumnerova, L.C., Black, P.M., Lau, C., Allen, J.C., Zagzag, D., Olson, J.M., Curran, T., Wetmore, C., Biegel, J.A., Poggio, T., Mukherjee, S., Rifkin, R., Califano, A., Stolovitzky, G., Louis, D.N., Mesirov, J.P., Lander, E.S., and Golub, T.R. (2002) Prediction of central nervous system embryonal tumour outcome based on gene expression. *Nature* 415(6870):436–442
- Raithatha, S.A., Muzik, H., Muzik, H., Rewcastle, N.B., Johnston, R.N., Edwards, D.R., and Forsyth, P.A. (2000) Localization of gelatinase-A and gelatinase-B mRNA and protein in human gliomas. *Neuro. Oncol.* 2(3):145–150
- Singh, S.K., Clarke, I.D., Terasaki, M., Bonn, V.E., Hawkins, C., Squire, J., and Dirks, P.B. (2003) Identification of a cancer stem cell in human brain tumors. *Cancer Res.* 63(18):5821–5828
- Singh, S.K., Hawkins, C., Clarke, I.D., Squire, J.A., Bayani, J., Hide, T., Henkelman, R.M., Cusimano, M.D., and Dirks, P.B. (2004) Identification of human brain tumour initiating cells. *Nature* 432(7015):396–401
- Taylor, M.D., Poppleton, H., Fuller, C., Su, X., Liu, Y., Jensen, P., Magdaleno, S., Dalton, J., Calabrese, C., Board, J., Macdonald, T., Rutka, J., Guha, A., Gajjar, A., Curran, T., and Gilbertson, R.J. (2005) Radial glia cells are candidate stem cells of ependymoma. *Cancer Cell* 8(4):323–335
- Van Meter, T., Dumur, C., Hafez, N., Garrett, C., Fillmore, H., and Broaddus, W.C. (2006) Microarray analysis of MRI-defined tissue samples in glioblastoma reveals differences in regional expression of therapeutic targets. *Diagn. Mol. Pathol.* 15(4):195–205
- Van Meter, T., Dumur, C., Tye, G., and Broaddus, W.C. (2007) Elevated Sox-11 expression is associated with proliferation, migration and poor overall survival in glioblastoma. *Neuro. Oncol.* 4 (9):591
- Vince, G.H., Wagner, S., Pietsch, T., Klein, R., Goldbrunner, R.H., Roosen, K., and Tonn, J.C. (1999) Heterogeneous regional expression patterns of matrix metalloproteinases in human malignant gliomas. *Int. J. Dev. Neurosci.* 17(5–6): 437–445
- von Deimling, A., von Ammon, K., Schoenfeld, D., Wiestler, O.D., Seizinger, B.R., and Louis, D.N. (1993) Subsets of glioblastoma multiforme defined by molecular genetic analysis. *Brain Pathol.* 3(1):19–26
- Westmeyer, G.G., and Jasanoff, A. (2007) Genetically controlled MRI contrast mechanisms and their prospects in systems neuroscience research. *Magn. Reson. Imaging* 25(6):1004–1010
- Zhang, L., Wang, L., Ravindranathan, A., and Miles, M.F. (2002) A new algorithm for analysis of oligonucleotide arrays: application to expression profiling in mouse brain regions. *J. Mol. Biol.* 317:225–235

# 4

## Diagnosing and Grading of Brain Tumors: Immunohistochemistry

Hidehiro Takei and Suzanne Z. Powell

### INTRODUCTION

Diagnostic neuro-oncology practice has benefited in the last 2 decades from the incorporation of, and recent advances in, immunohistochemistry (IHC). Although the mainstay of brain tumor diagnosis including its grading remains conventional hematoxylin-eosin (H&E)-stained histology, it is no doubt that IHC plays a major role in differential diagnosis and in improving the diagnostic accuracy. It is generally used for purposes of (1) identifying tumor cell type/origin, (2) assessing cell proliferation potential, (3) evaluating the boundary between tumor and the surrounding tissue (i.e., tumor “margin”), and (4) excluding reactive processes (e.g., demyelinating and infectious diseases). In the future, novel antibodies utilized as prognostic, predictive markers and as potential therapeutic targets for brain tumors will be developed.

Although there are several useful antibodies that are known to be relatively sensitive and specific for some tumor types, and thus are commonly used in the current neuropathology practice such as glial fibrillary acidic protein (GFAP) for gliomas and synaptophysin for neuronal tumors,

no diagnostic antibodies with absolute sensitivity and specificity for particular tumor types exist. Of note is that the judicious use of a panel of IHC antibodies in conjunction with thorough histological evaluation is unquestionably crucial for accurate diagnosis.

### IMMUNOHISTOCHEMICAL MARKERS FOR DIAGNOSIS AND DIFFERENTIAL DIAGNOSIS OF BRAIN TUMORS

#### Immunohistochemical Markers Routinely Used in Diagnostic Neuro-oncology Practice

Immunohistochemical markers that are routinely used for commonly encountered brain tumors in neuropathology practice are summarized in Table 4.1, listed according to the current WHO 2007 classification (Louis et al. 2007).

#### *Markers for Glial Tumors*

Gliomas comprise approximately 40% of primary central nervous system (CNS)



TABLE 4.1. Immunohistochemical markers commonly used for brain tumor diagnosis

		Immunohistochemical markers
<i>I. Tumors of neuroepithelial tissue</i>		
1. Gliomas	<b>Astrocytoma</b>	GFAP, S-100 protein, vimentin, p53
	<b>Oligodendroglioma</b>	S-100 protein (GFAP, Olig2)
	<b>Pleomorphic xanthoastrocytoma</b>	GFAP, S-100 protein, class III beta-tubulin, synaptophysin, neurofilament
	<b>Subependymal giant cell astrocytoma</b>	GFAP, S-100 protein, class III beta-tubulin, synaptophysin, neurofilament, alpha Beta crystallin
	<b>Ependymoma</b>	GFAP, EMA, S-100 protein, CD99
	<b>Choroid plexus tumor</b>	Cytokeratin, EMA, GFAP, transthyretin, S-100 protein, synaptophysin
2. Neuronal tumors	<b>Central neurocytoma</b>	Synaptophysin, NeuN
3. Mixed neuronal-glia tumors	<b>Ganglioglioma</b>	Synaptophysin, chromogranin A, class III beta-tubulin, NeuN, GFAP
4. Pineal tumors	<b>Pineocytoma</b>	Synaptophysin
5. Embryonal tumors	<b>Medulloblastoma</b>	Synaptophysin, NeuN, MAP-2 (GFAP)
	<b>Atypical teratoid/rhabdoid tumor</b>	EMA, cytokeratin, smooth muscle actin, GFAP, vimentin, INI-1
<i>II. Tumors of cranial and paraspinal nerves</i>		
	<b>Schwannoma</b>	S-100 protein
<i>III. Tumors of meninges</i>		
1. Tumors of meningotheial cells	<b>Meningioma</b>	EMA, progesterone receptor, claudin-1
2. Mesenchymal tumors	<b>Solitary fibrous tumor/ Hemangiopericytoma</b>	CD34, bcl-2, CD99
3. Other neoplasms related to the meninges	<b>Hemangioblastoma</b>	Alpha-Inhibin, aquaporin-1
<i>IV. Lymphomas</i>		
	<b>Primary CNS lymphoma</b>	CD20 (L26), CD79 alpha, EBER (immunocompromised cases)
<i>V. Germ cell tumors</i>		
	<b>Germinoma</b>	OCT4, c-kit, PLAP
<i>VI. Tumors of the seller region</i>		
	<b>Craniopharyngioma</b>	Beta-catenin, cytokeratin
<i>VII. Metastatic tumors</i>		
	<b>Metastatic Carcinoma</b>	Cytokeratin, organ specific markers
<i>VIII. Others</i>		
	<b>Chordoma</b>	S-100 protein, cytokeratin, EMA
	<b>Langerhans cell histiocytosis</b>	CD1a, S-100 protein, langerin (CD207)

tumors. GFAP and S-100 protein are the markers that are most commonly used for glial neoplasms. Immunoreactivity for GFAP in neoplastic cells clearly establishes the glial nature of the tumor. GFAP is a member of the class III intermediate filament protein family, and is expressed specifically in the astrocytic cytoplasm and, to a much lesser or variable degree, in the ependymal cytoplasm in normal mature brains. Reactive astrocytes are strongly

labeled with their radial array of often non-branching processes, and similarly, reactive ependymal cells show immunoreactivity. S-100 protein is a low molecular weight protein, characterized by two calcium binding sites of the helix-loop-helix (“EF-hand type”) conformation. There are many different types of S-100 proteins. Of these, S-100A1 and S-100B are the first members of this family that were purified from bovine brain, and are composed of

an alpha subunit combined with a beta subunit and of two beta subunits, respectively. In general practice, most clinical laboratories use heteroantisera against at least these two types of proteins, although dimer-specific monoclonal products are commercially available. S-100B labels many neural cell types (both nuclear and cytoplasmic labeling) including astrocytes, oligodendrocytes, ependymal cells, and choroid plexus epithelium, and thus is less astrocyte-specific than GFAP.

Vimentin is generally non-specifically immunoreactive in gliomas, and cannot be used to differentiate between gliomas and mesenchymal tumors. In general pathology practice, this antibody is used to confirm preservation of antigenicity of a specimen.

#### *Astrocytic Tumors*

In general, most astrocytomas are labeled with both GFAP and S-100 protein. As the degree of anaplasia is increased, GFAP reactivity tends to be reduced. Small cell glioblastoma is usually negative or minimally positive, while giant cell glioblastoma is immunoreactive for GFAP, and, in addition, is reportedly labeled with class III beta-tubulin (Martinez-Diaz et al. 2003). Malignant mesenchymal components of gliosarcoma are GFAP negative.

#### *Oligodendroglioma*

For oligodendrogliomas, no reliable or specific antibodies are currently available. Minigemistocytes and gliofibrillary oligodendrocytes, which are more frequently seen in anaplastic oligodendroglioma (WHO grade III) rather than in grade II oligodendroglioma, are usually strongly immunoreactive for GFAP. The antibody against Olig2 (oligodendrocyte transcription factor 2) stains nuclei of oligodendrocytes in normal brain as well as of oligodendrog-

lioma, however, it also labels those of astrocytic tumors, particularly glioblastomas and pilocytic astrocytomas.

#### *Well-Circumscribed Astrocytic Tumors*

In a group of well-circumscribed astrocytic tumors, pilocytic astrocytoma (WHO grade I) is GFAP immunoreactive with the compact areas being more strongly labeled than the loose areas with microcysts. Piloxyoid astrocytoma (WHO grade II), closely related to pilocytic astrocytoma, expresses GFAP, and some investigators reported synaptophysin immunoreactivity (de Chadarevian et al. 2006; Fuller et al. 2001). Pleomorphic xanthoastrocytoma (PXA) is immunoreactive for GFAP, labeling cells of different morphologies that range from spindle to pleomorphic, and xanthic cells, and the number of positive tumor cells varies from moderate to numerous. S-100 protein is diffusely and strongly immunoreactive. Immunoreactivity for neuronal markers (class III beta-tubulin, synaptophysin, and neurofilament) is usually present. Subependymal giant cell astrocytoma (SEGA) is frequently seen as a manifestation of tuberous sclerosis complex (TSC) and is composed of a mixture of spindle cells and ganglion-like/gemistocyte-like cells. As with PXA, SEGA often shows both glial (GFAP and S-100 protein) and neuronal (class III beta-tubulin, synaptophysin, and neurofilament) markers. GFAP positivity is observed in all these cellular components at variable intensity. Synaptophysin immunoreactivity may be weak and focal. Although renal angiomyolipoma and pulmonary lymphangiomyomatosis – PEComas (tumors showing perivascular epithelioid cell differentiation) – are known to be associated with TSC and to express HMB-45 Sharma et al. (2004) ZSEGA.

### *Ependymal Tumors*

According to WHO 2007 classification, ependymal tumors include four tumor entities; subependymoma (grade I), myxopapillary ependymoma (grade I), ependymoma (grade II), and anaplastic ependymoma (grade III) (Louis et al. 2007). In ependymomas, there are four histological variants recognized; cellular, papillary, clear cell, and tanycytic. All differentiated ependymal tumors are immunoreactive for GFAP and S-100 protein. GFAP is particularly prominently expressed in perivascular fibrillary processes featuring perivascular pseudorosettes. S-100 protein diffusely labels cellular lesions with epithelial-like features (Vege et al. 2000). Most of ependymomas show widespread immunoreactivity for pancytokeratin (AE1/AE3), however, other types of cytokeratin (CK) such as CK7, CAM5.2, CK903, and CK20 are focally positive (Vege et al. 2000). Epithelial membrane antigen (EMA), a highly glycosylated transmembrane protein, is known to be expressed in a relatively high proportion of cases. There are two patterns of EMA staining; intracytoplasmic dotlike and ring-like patterns. Hasselblatt and Paulus (2003) reported that the latter pattern was highly specific for the diagnosis of ependymoma compared with other glial tumors. The relationship between staining pattern/intensity and tumor subtype/grade is controversial. CD99, a product of MIC2 gene, is expressed in a membranous pattern with intracytoplasmic dots in ependymomas.

### *Choroid Plexus Tumors*

Choroid plexus papilloma (CPP, grade I), atypical choroid plexus papilloma (grade II), and choroid plexus carcinoma (CPC, grade III) are included in this group according to the current WHO 2007 classification

(Louis et al. 2007). Immunoreactivity of CPP shares with that of normal choroid plexus and is noted against cytokeratin, particularly low molecular forms, vimentin, S-100 protein, synaptophysin, and transthyretin. Although not seen in normal adult choroid plexus epithelium, GFAP and EMA immunoreactivity is observed in CPP. Of note is that the frequency of reaction of these markers varies greatly. CPC expresses cytokeratin, vimentin, GFAP, synaptophysin and S-100 protein (Louis et al. 2007). The reactivity of the latter three markers is greatly variable in CPC. The reader is referred to the discussion of AT/RT for differential diagnosis of CPC.

### *Markers for Neuronal Tumors*

Immunohistochemical neuronal markers include synaptophysin, chromogranin A, neurofilament (NF), microtubule associated protein (MAP)-2, NeuN, and class III beta-tubulin. Under certain neoplastic conditions, many of these are not neuron specific, calling for a cautious interpretation of cell phenotype. It is reported that MAP-2, NF and class III beta-tubulin are expressed in a high proportion of cases in glial tumors (Katsetos et al. 2001; Wharton et al. 2002).

Synaptophysin, a glycoprotein present in the membrane of neuronal presynaptic vesicles in brain and spinal cord, is a principal diagnostic marker for neurons. NFs are intermediate filament proteins exclusively found in neurons, and are obligate heteropolymers requiring the NF-L (low molecular weight) subunit together with either the NF-M (middle molecular weight) or the NF-H (high molecular weight) subunits for polymer formation. NF-M and NF-H contain phosphorylation sites for a large number of protein kinases. Extensively

phosphorylated NFs are involved in the establishment of a stationary cytoskeleton and are enriched in axons, while in the perikaryon and dendrites, NFs are unphosphorylated or poorly phosphorylated. There are specific antibodies against phosphorylated and non-phosphorylated NFs that highlight axons and, somata and dendrites in normal brains, respectively. Under damaged and disease conditions, it is known that the phosphorylated forms of NF-H accumulate in the neuronal perikarya.

#### *Ganglioglioma*

The immunohistochemical expression pattern of ganglioglioma (GG) reflects their dimorphic nature; neuronal and glial components highlighted with neuronal markers above mentioned and GFAP, respectively. Synaptophysin labels the neoplastic neurons with typical fine granular membrane-based positivity, and occasionally with pancytoplasmic immunoreactivity. This perisomatic synaptophysin immunoreactivity is often difficult to interpret because neuronal cells are embedded in a diffusely synaptophysin-positive neuropil background. Of note is that this surface reactive pattern is not pathognomonic for neoplastic neurons, although previously believed so, and is seen in certain large neurons in normal brains. Chromogranin A highlights granular cytoplasmic immunoreactivity, primarily within the perikarya of large neurons, which stand out among immunonegative surrounding neuropil and glial components. Normal neurons in the surrounding brain parenchyma are non-reactive to weakly immunoreactive. Hirose et al. (1997) reported that NF and class III beta-tubulin were immunoreactive in a high proportion (>80%) of GG cases in contrast to MAP-2, which was expressed in 14%.

NeuN labels the nuclei (and cytoplasm) of neuronal cells, although immunonegative cells are frequently encountered even when highly differentiated in appearance. Preusser et al. (2006) reported negative NeuN expression in approximately 70% of cases of GG and gangliocytoma.

#### *Neurocytic Tumors*

Central neurocytoma and extraventricular neurocytoma (EVN) occur supratentorially in young adults and both correspond to WHO grade II. Strong synaptophysin immunoreactivity for tumor cells is typical, and focal GFAP reactivity may be seen. Fine neuropil dispersed in broad zones that separate cell aggregates is also immunoreactive for synaptophysin. Nuclear NeuN reactivity is regularly seen, in contrast to neuronal cells in GG (Preusser et al. 2006). Chromogranin A immunoreactivity is usually absent except when neoplastic ganglion cells are present, which is more commonly seen in EVN.

#### *Medulloblastoma*

Medulloblastoma (MB) is defined as a malignant, invasive embryonal tumor of the cerebellum, and includes distinctive variants; desmoplastic/nodular, MB with extensive nodularity, anaplastic and large cell. Given that MB is derived from embryonal precursor cells with a capacity for divergent differentiation, of which neuronal differentiation is most consistently seen, MB is discussed in this section although listed in the embryonal tumor category in WHO 2007 classification (Louis et al. 2007). Neuronal differentiation in MBs is usually incipient in that neuronal immunohistochemical markers can detect it, although ganglion cells and “ganglioid” cells are rarely seen. Synaptophysin is mostly immunoreactive,

especially in fibrillary cores of Homer-Wright rosettes and intranodular fibrillary areas of pale islands in desmoplastic MBs, with reported positivity varying from 70% to 100% (Maraziotis et al. 1992; McLendon et al. 1999; Min et al. 2006). MAP-2 mirrors synaptophysin, although not as specific to cells with neuronal differentiation as synaptophysin, but shows a more intense granular or punctate pattern of reactivity. This marker is often helpful in those cases where the synaptophysin staining is weak or equivocal. Preusser et al. (2006) reported that NeuN immunoreactivity (at least focal staining) was seen in greater than three fourths of MB cases and that widespread expression was seen in ~80% of desmoplastic MB cases. Min et al. (2006) reported that no significant difference was observed in NeuN immunoreactivity (positive rate) between large cell/anaplastic (LC/A) and non-LC/A MB cases. Glial (astrocytic) cell differentiation with GFAP immunoreactivity is occasionally seen. Given the common presence of entrapped reactive astrocytes in MBs, interpretation of GFAP immunoreactive cells within the tumor should be done with caution.

#### *Markers for Meningeal Tumors*

The most diagnostically useful and commonly used immunohistochemical marker of meningiomas in all grades is EMA with a membranous pattern of immunoreactivity. Vimentin is typically expressed in all forms of meningioma. A considerable proportion of meningiomas, mostly fibrous type, express S-100 protein, although the extent and intensity of immunoreactivity is usually not comparable with that of schwannomas. Perry et al. (1997) reported that patchy and weak CD34 immunoreactivity was seen in 60% of fibrous meningiomas.

Surprisingly, Miettinen and Paetau (2002) reported that many meningiomas express cytokeratins (CKs), depending on specific subtypes of CK, usually with focal immunoreactivity seen except for microcystic and anaplastic meningiomas. Different types of meningiomas are commonly positive for CK18, one of simple epithelial CKs, but there is only limited immunoreactivity for other simple epithelial CKs (e.g., CK7, CK8, CK19) and for higher molecular weight CKs (e.g., CK14) in meningiomas (Miettinen and Paetau 2002). No CK20 positivity is reported. Interestingly, secretory meningioma (WHO grade I) has a unique and a most complex pattern of CK with immunoreactivity being almost confined to the cells lining the lumina often containing secretory droplets (pseudopsammomatous bodies). These tumor cells are consistently immunoreactive for simple epithelial keratins (including not only CK18 but also CK7, CK8, and CK19), and show focal limited immunoreactivity for a number of stratified epithelial CKs (e.g., CK5/6, CK14, CK16, CK17). In addition, carcinoembryonic antigen (CEA) is known to be expressed within the droplets as well as in the cells surrounding them.

The majority of meningiomas express progesterone receptor (PR), while much fewer cases express estrogen receptor (ER). Nuclear immunoreactivity of PR and ER was observed in 87.2% and 8.5%, respectively, in our series of non-malignant (i.e., grades I and II) meningiomas (Takei et al. 2008). Immunoreactivity is less prominent as the grade increases.

Claudin-1, an integral structural protein of tight junctions, has been used as a marker of perineurial cells and soft tissue perineuriomas. Bhattacharjee et al. (2003)

reported claudin-1 immunoreactivity in 85% of meningiomas with a crisp, punctate/granular membranous reactive pattern. Hahn et al. (2006) described similar results with lower positivity (53% of cases). All other histological mimics of meningiomas were negative.

#### New Immunohistochemical Markers

##### Applicable to Brain Tumor Diagnosis

##### *Craniopharyngioma (Beta-Catenin)*

Craniopharyngiomas (CPs) and Rathke's cleft cysts (RCCs) are space occupying lesions involving the sellar/suprasellar regions with significantly different post-surgical outcome (e.g., recurrence rate) (Figure 4.1). Clinical and histopathologic differentiation between these two entities is often challenging. Considerable proportions of purely cystic type of CPs, commonly encountered squamous metaplasia in RCCs, and rare ciliated CPs further complicate this problem.

Adamantinomatous CPs carry activating mutations in exon 3 of *beta-catenin* gene,

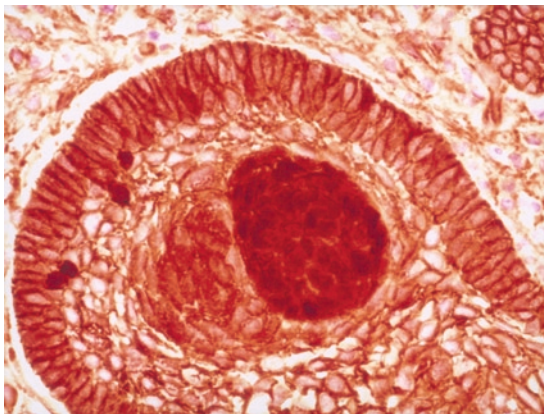


FIGURE 4.1. **Craniopharyngioma (adamantinomatous type)** with **beta-catenin** immunohistochemical stain, showing membranous labeling with the exception of the tumor whorls, which demonstrate nuclear labeling (original magnification:  $\times 200$ )

resulting in a shift from membrane-bound to nuclear accumulation of beta-catenin in greater than 90% of tumor specimens (Buslei et al. 2005). The characteristic immunoreactive tumor cells are not homogeneously distributed within the tumor, but are either clustered within the center of epithelial “whorls” or adjacent to ghost cells (Buslei et al. 2005; Hofmann et al. 2006). In contrast, papillary CPs reveal exclusively membranous immunoreactivity in a manner seen in RCCs as well as in mature, non-neoplastic epithelial cells. This distinctive pattern of aberrant nuclear beta-catenin immunoreactivity is a reliable marker for the identification of an adamantinomatous CP when present in small surgical specimens, and can be utilized for differential diagnosis between cystic adamantinomatous CP and RCC. However, this marker cannot be used for distinction of papillary CP from RCC (with squamous metaplasia).

##### *Germinoma (OCT 4)*

Primary intracranial germinomas occur predominantly in the pineal and suprasellar regions (Figure 4.2). The histologic evaluation can be challenging since the specimen is usually small and artifactually distorted. Further confounding factors often seen include marked lymphocytic infiltration and florid granulomatous reaction that obscures the typical histological features. Placental alkaline phosphatase (PLAP), a traditional marker of germinomas, shows surface membrane, or somewhat less commonly, diffuse cytoplasmic immunoreactivity. However, it has its shortcoming in that PLAP labeling is not constant with variable sensitivity, intensity, and extent of reactivity.

The *c-kit* proto-oncogene encodes a receptor tyrosine kinase that is required in

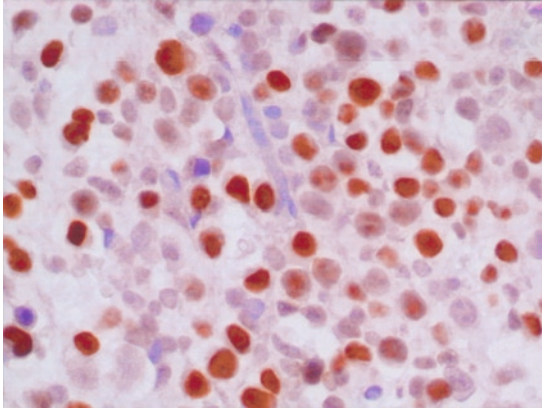


FIGURE 4.2. **Germinoma** with **OKT4** nuclear immunoreactivity (original magnification:  $\times 400$ )

normal spermatogenesis. Membranous c-kit (CD117) immunoreactivity is diffusely and strongly seen in germinoma cells.

OCT4, also known as POU5F1, OCT3, OCT3/4, or OFT3, is a nuclear transcription factor normally expressed in early embryonic cells and germ cells. Diffuse and strong nuclear labeling of OCT4 is regularly seen in germinoma. This staining pattern is more easily interpreted than membranous labeling of PLAP, especially in small, artifactually distorted specimens. Of note is that OCT4 also strongly labels tumor nuclei of embryonal carcinoma. Cytoplasmic CD30 immunoreactivity as well as diffuse and strong expression of various cytokeratins are typically seen in embryonal carcinoma, not germinoma. CD117 immunoreactivity for germinoma is also useful for this distinction.

#### *Atypical Teratoid/Rhabdoid Tumor (BAF47/INI1)*

Atypical teratoid rhabdoid tumor (AT/RT) is a highly malignant tumor frequently involving the posterior fossa in young children (often  $<1$  year old), with grave prognosis, and contains substantial areas

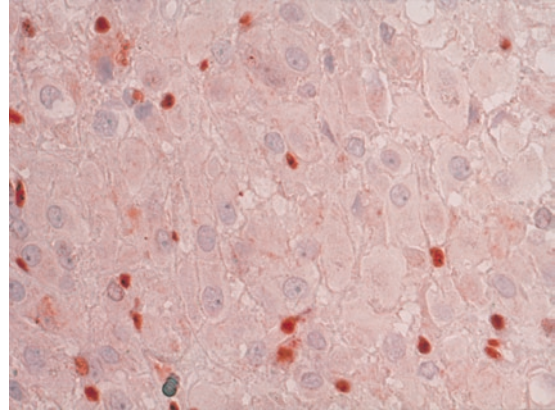


FIGURE 4.3. **Atypical teratoid rhabdoid tumor (AT/RT)** with **BAF47/INI-1** immunohistochemical stain, showing immunonegativity in tumor nuclei with scattered immunoreactive microglial cells and endothelial cells (original magnification:  $\times 400$ )

morphologically indistinguishable from CNS primitive neuroectodermal tumors (PNETs) along with a rhabdoid component (Figure 4.3). Given the association with rhabdoid predisposition syndrome, accurate diagnosis of AT/RT is mandated. This tumor is characterized by a well-known heterogeneous immunohistochemical profile with reactivity for a range of mesenchymal, epithelial, and neuroepithelial markers. Vimentin is consistently expressed, and the expression of smooth muscle actin, EMA, cytokeratin, and GFAP is frequently observed. Bouffard et al. (2004) reported in their double labeling study using some of these markers that most tumor cells demonstrated only single labeling. S-100 protein, synaptophysin, chromogranin, neurofilament and desmin may be variably and focally immunoreactive in AT/RTs. The germ cell markers as well as phenotypic markers specific for skeletal muscle differentiation, including MyoD, are negative.

The genetic hallmark of AT/RT is inactivation of hSNF5/INI1/SMARCB1/

BAF47, a tumor suppressor gene, located on chromosome 22q11.2, but it is found in only 70–75% of cases (Biegel 2006). An additional 20–25% of tumors have no detectable genomic alterations of INI1 with reduced expression at the RNA or protein level, and thus, immunohistochemistry using monoclonal antibody against BAF47 (with absent nuclear labeling in tumor cells in AT/RT) could be more relevant/potentially more sensitive for diagnosis than molecular studies. Complete absence of BAF47 nuclear reactivity of tumor cells with appropriate nuclear reactivity of included endothelial cells and reactive chronic inflammatory endogenous cellular constituents (as internal positive controls) is required for the purpose of diagnostic confirmation. In AT/RT with a substantial medulloblastoma (MB)/PNET-like component and scant rhabdoid component, differential diagnosis from MB/PNET, especially anaplastic variant, is difficult or often impossible on histologic grounds alone. A polyphenotypic immunohistochemical profile mentioned above raises the possibility of AT/RT, and BAF47 immunohistochemistry has a discriminative value in this setting since MBs retain its expression.

Choroid plexus carcinoma (CPC) shares several overlapping clinical, histologic, ultrastructural, and/or immunophenotypic features with AT/RT, and the distinction from AT/RT may not be clear in some poorly differentiated cases. Judkins et al. (2005) reported that seven (25%) of 28 cases with a diagnosis of CPC demonstrated loss of BAF47 expression, all of which exhibited features consistent with AT/RT, while the remaining cases had retained expression. BAF47 immunoreactivity can be used as a better differentiator

of CPP from AT/RT, with the latter having more aggressive clinical behavior.

Given the simple and sensitive marker of AT/RT, it is prudent that BAF47 immunohistochemical assessment should be applied to all malignant embryonal CNS tumors with the exception of desmoplastic/nodular MB, which is a distinctive variant of MB consistently retaining BAF47 expression.

Patil et al. (2008) recently reported that a mosaic pattern (i.e., mixed positive and negative nuclei) of INI1 expression, in contrast to a diffuse immunonegative pattern observed in AT/RT, in a large series of schwannomatosis (both familial and sporadic) and neurofibromatosis type 2-associated schwannomas, not in solitary, sporadic schwannomas.

#### *Hemangioblastoma*

*(Alpha-Inhibin, Aquaporin-1)*

Hemangioblastoma (HB) is a WHO grade I tumor of uncertain histogenesis and commonly involves the cerebellum, less frequently the spinal cord and brain stem, and rarely supratentorial regions. It occurs in sporadic forms and in association with von Hippel-Lindau syndrome (VHL). The histological differential diagnosis of HB includes metastatic clear cell renal cell carcinoma (MCCRCC), angiomatous meningioma, and capillary hemangioma. Of these, the distinction from MCCRCC is particularly crucial given that the prognostic and therapeutic significance is completely different. However, the histological distinction has long been a diagnostic challenge owing to striking morphologic similarities. This problem is further compounded in patients with VHL, in whom MCCRCC can occur synchronously, metachronously, or to HB (i.e., tumor-to-tumor metastasis).



To our surprise, Jarrell et al. (2006) reported that 8% of all HBs resected from patients with VHL had metastatic carcinoma within a CNS HB with the most common primary tumor being RCC. It is suggested that RCC-to-HB metastasis in VHL patients may have been under-recognized.

Weinbreck et al. (2008) recently confirmed the usefulness of alpha-inhibin and aquaporin-1 as positive markers of HBs, and reported sufficiently high sensitivity and specificity of these markers (88% sensitivity and 79% specificity, 97% sensitivity and 83% specificity, respectively) for the diagnosis of HB versus MCCRCC. In general, RCCs are immunoreactive for epithelial markers, such as EMA and cytokeratins (CAM5.2, AE1/AE3), as well as for CD10 (membranous staining). One study reported that 36% of HBs expressed EMA with a membranous staining of stromal cells, and that no immunoreactivity for AE1/AE3 and CD10 was seen in HBs (Weinbreck et al. 2008). An immunohistochemical panel of the positive HB markers combined with cytokeratins and/or CD10 can allow us to reliably distinguish between these two tumors. EMA alone is not sufficient for the differential diagnosis between HB and (angiomatous) meningioma given the considerable high proportion of immunoreactive HB cases.

#### Useful Immunohistochemical Markers for Differential Diagnosis of Brain Tumors

##### *Reactive Gliosis Versus Diffuse Astrocytoma*

One of the most commonly encountered dilemmas in diagnostic neuropathology is a distinction between benign reactive gliosis and diffuse astrocytoma (grade II), especially small biopsies such as stereotactic biopsies. Of note is that these are

not mutually exclusive, and that borders of diffuse astrocytoma are usually ill-defined with some surrounding gliosis. Almost evenly distributed, strongly GFAP immunoreactive cells with multiple delicate processes favor reactive astrocytes.

Ki-67 (MIB-1) and p53 immunohistochemical stains are commonly used in this setting, and are helpful if the expression is significantly high. Otherwise, given the unignorable overlap in the patterns of immunoreactivity between reactive gliosis and some astrocytomas, we believe that this distinction should be best handled on histologic grounds with available clinico-radiological and surgical information.

##### *Differential Diagnosis of Round Clear Cell (Oligodendroglioma-Like) Tumors*

Round clear cell (oligodendroglioma-like) tumors occurring in the brain parenchyma include oligodendroglioma, neurocytomas (central neurocytoma and extraventricular neurocytoma), clear cell ependymoma, dysembryoplastic neuroepithelial tumor (DNET), and pilocytic astrocytoma (focal) (Table 4.2). GFAP, Olig 2, NeuN and synaptophysin are very useful for the differential diagnosis. Diffuse and widespread immunoreactivity of NeuN and synaptophysin is typical of neurocytomas. Negative staining of Olig 2 favors neurocytoma, and can virtually exclude oligodendroglioma and oligodendroglioma-like areas of pilocytic astrocytoma, both of which show diffuse and strong immunoreactivity.

Dysembryoplastic neuroepithelial tumor (DNET) is characterized by the so-called "specific glioneuronal element" composed of oligodendroglia-like cells (OLCs), astrocytes and mature neurons that are orientated in columns perpendicularly to the cortical surface. OLCs show strong and widespread

TABLE 4.2. Differential immunohistochemical markers for round clear cell (oligodendrogloma-like) tumors

	GFAP	Olig 2	NeuN	Synaptophysin	EMA (dot-like positivity)
<b>Oligodendrogloma</b>	(-/+)	(+)	(-)	(-)	(-)
<b>Neurocytomas</b>	(-/+)	(-)	(+)	(+)	(-)
<b>Clear cell ependymoma</b>	(+)	(-/+)	(-)	(-)	(+)
<b>Dysembryoplastic neuroepithelial tumor (oligodendroglia-like cells)</b>	(-)	(+)	(+/-)	(+/-)	(-)
<b>Pilocytic astrocytoma (oligodendrogloma-like areas)</b>	(+)	(+)	(-)	(-)	(-)

TABLE 4.3. Differential immunohistochemical markers for malignant (small) blue cell tumors

	GFAP	S-100 protein	Synaptophysin	EMA	Cytokeratin	Others
<b>Medulloblastoma</b>	(-/+)	(+)	(+)	(-/+)	(-/+)	MAP-2
<b>Anaplastic ependymoma</b>	(+)	(+)	(-)	(+)	(-)	
<b>Atypical teratoid/rhabdoid tumor</b>	(+)	(+/-)	(-/+)	(+)	(+)	INI-1, smooth muscle actin, vimentin. (germ cell markers: Negative)
<b>Small cell glioblastoma</b>	(-/+)	(+)	(-/+)	(-)	(-)	
<b>Metastatic small cell carcinoma</b>	(-)	(-)	(+)	(-)	(+)	(Lung primary: TTF-1)
<b>Malignant lymphoma</b>	(-)	(-)	(-)	(-)	(-)	CD20, LCA

expression of Olig2 and S-100 protein, and rare expression of synaptophysin. Some, but not all, neuronal cells are immunoreactive for synaptophysin. Wolf et al. (1997) reported the striking difference in NeuN immunoreactivity in OLCs in DNET (44% positivity) and oligodendroglomas (0% positivity).

#### *Differential Diagnosis of Malignant (Small) Blue Cell Tumors in CNS*

Differential diagnosis of malignant (small) blue cell tumors includes medulloblastoma, anaplastic ependymoma, and atypical teratoid/rhabdoid tumor (AT/RT) in pediatric patients, and small cell glioblastoma, medulloblastoma, malignant lymphoma, and metastatic small cell carcinoma in adult patients (Table 4.3). The histological distinction between metastatic small cell carcinoma, medulloblastoma, and small

cell glioblastoma is particularly difficult, and the distinction between the former two tumors may be impossible on histologic ground alone without clinical information. Cytokeratin, not synaptophysin, is of great help for this distinction since metastatic small cell carcinomas exhibit immunoreactivity. Of note is that considerable numbers of glioblastomas, in general, are immunoreactive for pancytokeratin (AE1/AE3), and that other cytokeratins (e.g., CAM5.2) should be used for this purpose. Metastatic small cell carcinomas originating from lung often demonstrate thyroid transcription factor-1 (TTF-1), and this marker may also be helpful given that medulloblastomas are negative. Focal expression of epithelial markers (EMA and cytokeratins) can be rarely seen in medulloblastomas, primarily in anaplastic variant, but raises the possibility of AT/RT.

### Differential Diagnosis of Dural-Based Tumors

Dural-based tumors include meningioma, metastatic tumors, solitary fibrous tumor, hemangiopericytoma, Rosai-Dorfman disease, plasmacytoma, and (much less commonly) schwannoma (Table 4.4). Anaplastic meningiomas are EMA immunoreactive and can histologically simulate metastatic carcinoma, occasionally necessitating immunohistochemical staining for differential diagnosis, especially in some patients with no clinical history of carcinoma. Liu et al. (2004) reported common positivity of CAM5.2, AE1/AE3, and pancytokeratin in “malignant meningiomas”, but negative immunoreactivity in benign meningiomas tested. They proposed that a panel of epithelial markers, including Ber-EP4, CEA, B72.3 and CD15 (negative in malignant meningiomas), and vimentin (rarely positive in metastatic carcinomas) may be useful in separating malignant meningioma from metastatic carcinoma. CK20, which is present in lower gastrointestinal epithelia, urothelia, and Merkel cells, is also helpful since no meningiomas are reportedly immunoreactive (Miettinen and Paetau 2002).

The histological distinction between hemangiopericytoma (HPC) and solitary fibrous tumor (SFT) can be very difficult because of many overlapping morphological features. In contrast to soft tissue HPCs, which tend to merge into the SFT category,

in CNS they are now recognized as two distinct entities. Immunohistochemically, quantitative difference in CD34 and bcl-2 immunoreactivity is seen: diffuse and strong positivity in SFT and weak and focal positivity in HPC. Diffuse and strong immunoreactivity for CD34 is, in part, a diagnostic criterion for SFT. CD99 positivity is also observed in SFT.

### IMMUNOHISTOCHEMISTRY AS A USEFUL ADJUNCT IN GRADING OF BRAIN TUMORS: KI-67 AND PHOSPHO-HISTON H3

Histological grading is a means of predicting the biological behavior of a neoplasm, and in the clinical practice, is a key factor for deciding therapeutic strategies. The current WHO grading of CNS tumors establishes a “malignancy scale” (grade I–IV) ranging across a wide variety of neoplasms based on histological features on H&E-stained sections. It is known that the histology-based WHO grading system has some limitations in predicting clinical outcome and survival. Thus, many studies have focused on the clinical value of the proliferation activity assessed by various techniques in a given tumor, and of these, astrocytomas and meningiomas have been extensively studied.

TABLE 4.4. Differential immunohistochemical markers for dural-based tumors

	EMA	Claudin-1	S-100 protein	CD34	Bcl-2	Cytokeratin	CD138
<b>Meningioma</b>	(+)	(+)	(-/+)	(-/+)	(-)	(-/+)	(-)
<b>Hemangiopericytoma/Solitary fibrous tumor</b>	(-)	(-)	(-)	(+)	(+)	(-)	(-)
<b>Metastatic carcinoma</b>	(+)	(-)	(-)	(-)	(-)	(+)	(-)
<b>Rosai-Dorfman disease</b>	(-)	(-)	(+)	(-)	(-)	(-)	(-)
<b>Plasmacytoma</b>	(-/+)	(-)	(-)	(-)	(-)	(-)	(+)
<b>Schwannoma</b>	(-/+)	(-)	(+)	(-)	(-)	(-)	(-)

Ki-67 antigen is the prototypic cell cycle related nuclear protein, expressed by proliferating cells in non-G0 phases. Ki-67 antibodies (MIB-1) are routinely used in diagnostic neuro-oncology. The MIB-1 labeling index (MIB-1 LI) is calculated as a percentage of the Ki-67 positive cells to the total number of tumor cells, and enables such data to be incorporated into diagnostic algorithms for the estimation of biological behavior in brain tumors.

Of several histologic parameters on H&E-stained sections, mitotic figures (MFs) are particularly important in brain tumor grading. However, MFs are not as objective or diagnostic criterion as usually considered, since it is often difficult to distinguish MFs from similar chromatin changes observed in apoptotic cells or secondary to artifacts such as crush or distortion. A mitosis specific antibody against phospho-histone H3 (PHH3), which is negligible during interphase, but reaches a maximum during mitosis, is very sensitive and specific to detect MFs and allows for rapid and accurate identification of MFs. Of note, the significant difference in immunohistochemical staining techniques (e.g., antibody dilution, antibody clone, antigen retrieval method) among laboratories as well as in interpretation among pathologists makes it very difficult for both of these markers to apply specific cutoffs for grading in any types of brain tumors.

#### Astrocytoma

From a therapeutic point of view, aggressive treatment (i.e., maximum tumor resection followed by radiation therapy) is indicated for grade III astrocytomas, while observation following biopsy is usually appropriate for patients with grade II astrocytomas, especially in young patients

(under 35 or 40 years of age), unless the tumor shows a significant mass effect or causes neurological deficits. Thus, distinguishing between WHO grade II and III infiltrating astrocytomas is one of the most important differential diagnoses in diagnostic neuro-oncology practice, but the distinction is often challenging. According to the WHO 2007 guidelines, neither established number of MFs nor MIB-1 LI is indicated as a cutoff for this distinction. Colman et al. (2006) reported the following cutoffs for grade II versus, III, respectively: MFs per 10 HPFs ( $\leq 3$  versus,  $> 3$ ), PHH3 index ( $\leq 4$  versus,  $> 4$  per 1,000 cells), and MIB-1 LI ( $\leq 9\%$  versus,  $> 9\%$ ). Johannessen and Torp (2006) conducted a meta-analysis of 16 previous studies on diagnostic and prognostic significance of MIB-1 LI in astrocytomas (grade II-IV), all of which were classified based on WHO 2000 grading criteria, and reported that the mean MIB-1 LI ( $\pm$  SD) for grade II, III, and IV was 3.0 ( $\pm 2.1$ ), 11.8 ( $\pm 3.4$ ), and 15.8 ( $\pm 7.4$ ), respectively. Although most studies reviewed showed statistically significant differences in MIB-1 LI between high grade (grade III and IV) and low grade (grade II) astrocytomas, they stressed on the presence of considerable overlap in MIB-1 LI among the different grades, indicating that MIB-1 LI cannot be used alone as a diagnostic measure.

#### Meningioma

One of the WHO criteria in the assignment of grade in meningiomas is the number of MFs per ten high-power (400x) fields (HPFs, defined as  $0.16 \text{ mm}^2$ ); that is, grade I:  $< 4$ , grade II:  $\leq 4$ ,  $< 20$ , and grade III:  $\geq 20/10$  HPFs. Ribalta et al. (2004) studied 54 cases of meningiomas with PHH3 immunohistochemistry and reported that

this immunolabeling facilitated rapid reliable grading of meningiomas by showing quick focus of attention on the most mitotically active areas for quantification and by allowing easy and objective identification of MFs. Although MIB-1 LI is not included in the WHO 2007 criteria to grade meningiomas, it is particularly helpful for tumors that are histologically “on the fence” in terms of tumor grade. Based on 146 cases of meningiomas examined immunohistochemically, Amatya et al. (2001) reported the mean MIB-1 LI of benign, atypical, and anaplastic meningiomas was 1.5%, 8.1%, and 19.5%, respectively. Perry et al. (1998) studied 425 cases of meningiomas using image analysis and reported that the MIB-1 LI of 4.2% or more was strongly associated with a decreased recurrence-free survival rate in gross, totally resected meningiomas. By comparing two groups (54 cases of recurrent meningiomas versus 73 cases of non-recurrent meningiomas), Matsuno et al. (1996) mentioned that a MIB-1 LI of 3% was a cutoff point for recurrence, especially within the first 10-year follow-up period, although marked overlap of values was noted.

## IMMUNOHISTOCHEMICAL AND ANALYTICAL METHODS (FOR FORMALIN- FIXED PARAFFIN- EMBEDDED TISSUE)

### Formalin Fixation

Formaldehyde (10% neutral buffered formalin is most commonly used in surgical pathology laboratories) is a cross-linking fixative and can cause changes in the steric configuration of proteins, possibly resulting

in masking of antigenic sites (i.e., epitopes) for IHC. Of note, especially for clinicians, is that immediate formalin fixation of fresh (surgical and biopsy) tissue is crucial to avoid drying edge artifact, passive uptake of serum protein into the cytoplasm of specific cells, and extracellular antigen diffusion into the parenchyma due to autolysis, all of which can cause non-specific IHC reactions. Slicing large specimens prior to fixation is required for adequate and consistent fixation. Another important factor is fixation time; both over- and underfixation can affect IHC results. Subsequent processing usually includes dehydration using ethanol, and thus, the tissue is effectively double fixed with both formalin and ethanol. Areas underfixed with formalin may be fixed only with ethanol and cause artifactual IHC results since some antigenicity can be affected (i.e., enhanced or reduced) by alcohol fixation.

### Sectioning

IHC staining should be performed no later than a week, ideally as soon as possible, after sectioning the paraffin-embedded tissue placed on glass slides in order to minimize the loss of antigenicity (especially of nuclear antigens such as Ki-67, p53 protein, and estrogen receptor). Otherwise, the sections should be kept in an airtight bag at 4°C or following surface paraffin coating on the glasses.

### Antigen Retrieval

In response to the antigen-masking effects of formalin fixation, antigen retrieval (AR) is now extensively used. The technique whereby the application of heat for various lengths of time to formalin-fixed, paraffin-embedded tissue sections in an

aqueous solution (i.e., retrieval solution) is currently most popular and is referred to as “heat induced epitope retrieval (HIER)”. Microwave ovens, pressure cookers, and steamers are the most commonly used heating devices. Of these, pressure cookers permit attainment of higher temperature of the retrieval solution (~125°C) and the even nature of heating with no hot or cold spots unlike microwave ovens. The heating length of 20 min appears to be appropriate with the exception of pressure cookers, which require a much shorter time (only 2.5–3 min), and cooling usually takes about 20 min. Rapid cooling may decrease the staining intensity of some nuclear antigens, including Ki-67. The retrieval solutions are important for the effectiveness of antigen retrieval and include (sodium) citrate buffer (10 mM, pH 6.0), which is most commonly used, EDTA (1 mM, pH 8.0), and Tris-EDTA buffer (pH 9.0). Because the mechanism of HIER is not completely understood, there are no standards for the appropriate temperature, type of retrieval solution, or its pH. A test is probably the best way to know which one is the best for a specific antibody. Similar to its effect on protein epitopes, HIER produces variable degrees of enhancement of endogenous biotin activity, resulting in artifacts (i.e., nonspecific cytoplasmic staining) that commonly occur especially in mitochondria-rich tissue (e.g., liver, kidney, skeletal muscle, and brain) and tumors (e.g., oncocyoma) when used avidin-biotin complex method or labeled streptavidin biotin method for immunohistochemical staining. Another AR method is one using proteolytic enzymes (i.e., proteolytic induced epitope retrieval, PIER) such as trypsin, pronase, pepsin, ficin, proteinase K, etc.

#### Preparations for Retrieval Solutions

Sodium Citrate Buffer (10 mM sodium citrate, 0.05% Tween 20, pH 6.0)

Tri-sodium citrate (dihydrate)	2.94 g
Distilled water	1,000 mL

Mixed to dissolve. Adjust pH to 6.0 with 1N HCl and then add 0.5 mL of Tween 20 and mix well.

Citrate Buffer (10 mM citric acid, 0.05% Tween 20, pH 6.0)

Citric acid (anhydrous)	1.92 g
Distilled water	1,000 mL

Mixed to dissolve. Adjust pH to 6.0 with 1N HCl and then add 0.5 mL of Tween 20 and mix well.

EDTA Buffer (1 mM EDTA, 0.05% Tween 20, pH 8.0)

EDTA	0.37 g
Distilled water	1,000 mL

Mix to dissolve. Adjust pH to 8.0 with 1N NaOH and then add 0.5 mL of Tween 20 and mix well.

Tris-EDTA Buffer (10 mM Tris Base, 1 mM EDTA Solution, 0.05% Tween 20, pH 9.0)

Tris	1.21 g
EDTA	0.37 g
Distilled water	1,000 mL

Mix to dissolve. pH is usually at 9.0 and then add 0.5 mL of Tween 20 and mix well.

All these solutions can be stored at room temperature for 3 months or at 4°C for longer storage.

#### Immunohistochemical Staining of Formalin-Fixed Paraffin-Embedded Tissue

The most important factors for IHC staining include (1) type of primary antibody used

and its dilution, (2) specificity of the antibody, (3) type of detection system used and its sensitivity, and (4) chromogens or reaction products. The most appropriate conditions should be set for these factors in each laboratory.

## Protocol

1. Deparaffinization and rehydration:
  - Immerse the slides in xylene 3 × 3 min, in 100% ethanol 2 × 1 min, in 95% ethanol for 3 min, in 70% etha-

TABLE 4.5. Immunohistochemical stains commonly used for the diagnostic neuropathology

Primary antibody	Manufacture <sup>a</sup>	Clone <sup>a</sup>	Staining pattern <sup>b</sup>	Principal immunoreactive CNS lesions/normal tissue
<b>Aquaporin-1</b>	Santa Cruz	AQP1(B-11)	M	Hemangioblastoma
<b>BAF47 (hSNF5/INI-1)</b>	BD Biosciences	25	N	Atypical teratoid rhabdoid tumor (loss of nuclear expression)
<b>Bcl-2</b>	Dako	124	C + M	Solitary fibrous tumor, Hemangioblastoma
<b>Beta-catenin</b>	Ventana	14	N	Craniopharyngioma (adamantinomatous type)
<b>CD1a</b>	Immunotech	O10	M	Langerhans cells
<b>CD20</b>	Dako	B-Ly1	M	B lymphocytes
<b>CD34</b>	Becton Dickinson	HPCA-1	M (+C)	Solitary fibrous tumor, Hemangioblastoma/Endothelium
<b>CD79 alpha</b>	Dako	HM57	C	B lymphocytes
<b>CD99 (MIC2)</b>	Signet Laboratories	O13	M	Solitary fibrous tumor, Hemangioblastoma, Ependymoma
<b>CD138</b>	Serotec	B-B4	M	Plasma cells, Plasmacytoma
<b>Chromogranin A</b>	Dako	DAK-A3	C	Neuroendocrine cells
<b>c-kit (CD117)</b>	Dako	Polyclonal	M (+C)	Germinoma/Mast cells
<b>Claudin-1</b>	Zymed	Polyclonal	M	Meningioma/Perineurial cells
<b>Cytokeratin</b>	Signet Laboratories	OSCAR	C	Metastatic carcinomas
<b>Epithelial membrane antigen (EMA)</b>	Dako	E29	M (+C)	Meningioma (Atypical teratoid rhabdoid tumor)
<b>Glial fibrillary acidic protein (GFAP)</b>	Dako	Polyclonal	C	Astrocytes
<b>Inhibin alpha</b>	Dako	R1	C	Hemangioblastoma
<b>Ki-67</b>	Dako	MIB-1	N	Cells in non-G0 phase
<b>Langerin (CD207)</b>	Vision Biosystem	12D6	M + C	Langerhans cells
<b>Microtubule-associated protein (MAP) -2</b>	Chemicon	Polyclonal	C	Neurons
<b>Neuronal nuclear antigen (NeuN)</b>	Dako	NeuN	N	Neurons
<b>Neurofilament</b>	Dako	2F11	C	Neurons
<b>OCT3/4</b>	Santa Cruz	C-10	N	Germinoma, Embryonal carcinoma
<b>Olig 2</b>	Immuno-Biological Laboratories	Polyclonal	N	Oligodendroglioma, DNET
<b>p-53</b>	Dako	DO-7	N	
<b>Phospho-histone H3 (PHH3)</b>	Cell Signaling	Polyclonal	N	Mitotic nuclei
<b>Placental alkaline phosphatase (PLAP)</b>	BioGenex	PL8-F6	M	Germinoma/Villous trophoblasts
<b>S-100 protein</b>	Dako	Polyclonal	N + C	Neurons, Glia, Melanoma
<b>Smooth muscle actin</b>	BioGenex	1A4	C	(Atypical teratoid rhabdoid tumor)/ Blood vessel walls
<b>Synaptophysin</b>	Dako	SY38	C	Neurons, neuroendocrine cells
<b>Transthyretin</b>	Dako	Polyclonal	C	Choroid plexus
<b>Vimentin</b>	Dako	V9	C	Mesenchymal tissue

<sup>a</sup>Used at The Methodist Hospital, Houston, TX.

<sup>b</sup>C: cytoplasmic, M: membranous, N: nuclear.

- nol for 3 min, and in 50% ethanol for 3 min, and rinse with running tap water to remove ethanol.
- Keep the slides in tap water until ready to use for antigen retrieval.
2. Antigen retrieval (by HIER):
 

Preheat the heating device with retrieval solution.

    - Immerse the slides in the pre-heated solution and keep them in the device for appropriate time.
    - Cool gradually.
    - Rinse the slides in phosphate buffered saline (PBS) 3 × 2–3 min.
  3. Blocking the endogenous peroxidase activity to reduce the background staining if using a horseradish peroxidase (HRP) conjugate for detection:
    - Immerse the slides in methanol containing 0.2% hydrogen peroxidase for 20 min at room temperature.
    - Rinse the slides in PBS 3 × 3 min.
  4. Immunohistochemical staining
 

Incubate the slides with 2% normal serum (of the animal that was used to produce the secondary antibody) in PBS for 30 min in a humidity chamber at room temperature to block non-specific binding of the primary antibody, and discard residual fluid.

    - Apply the primary antibody to the slides and incubate for 60 min at room temperature or overnight at 4°C.
    - Rinse the slides 3 × 5 min in PBS.
    - Apply the enzyme-conjugated secondary antibody to the slides and incubate at room temperature for 30 min.
    - Rinse the slides 3 × 5 min in PBS.
    - Develop the colored product of the enzyme with chromogen for 10 min at room temperature.
    - Rinse the slides in running tap water for 5 min.

- Counterstain with hematoxylin (or methyl green).
- Dehydrate, clear and mount.

### Analysis

Both positive and negative controls should be used; the former is for control of all steps of the analysis and the latter is for detection of unintended background staining/nonspecific staining. The positive control should be examined first to ascertain that all reagents are properly functioning, and then, the negative control should be examined to verify the specificity of the primary antibody used.

For the evaluation of IHC staining, it is crucial to clarify the criteria for positive and negative results in terms of extent and intensity of staining for the given antibody. In addition, staining pattern (e.g., cytoplasmic membrane, nucleus, cytoplasm, or combination of these) is also important for evaluation. IHC stains commonly used for the diagnostic neuropathology with useful information including the expected staining pattern are listed in Table 4.5.

### REFERENCES

- Amatya, V.J., Takeshima, Y., Sugiyama, K., Kurisu, K., Nishisaka, T., Fukuhara, T., and Inai, K. (2001) Immunohistochemical study of Ki-67 (MIB-1), p53 protein, p21WAF1, and p27KIP1 expression in benign, atypical, and anaplastic meningiomas. *Hum. Pathol.* 32:970–975
- Bhattacharjee, M.B., Adesina, A.M., Goodman, J.C., and Powell, S.Z. (2003) Claudin-1 expression in meningiomas and schwannomas: possible role in differential diagnosis (abstract). *J. Neuropathol. Exp. Neurol.* 62:581
- Biegel, J.A. (2006) Molecular genetics of atypical teratoid/rhabdoid tumors. *Neurosurg. Focus* 20: 1–7
- Bouffard, J.P., Sandberg, G.D., Golden, J.A., and Rorke, L.B. (2004) Double immunolabeling of



- central nervous system atypical teratoid/rhabdoid tumors. *Mod. Pathol.* 17:679–683
- Buslei, R., Nolde, M., Hofmann, B., Meissner, S., Eyupoglu, I.Y., Siebzehnruhl, F., Hahnen, E., Kreutzer, J., and Fahlbusch, R. (2005) Common mutations of beta-catenin in adamantinomatous craniopharyngiomas but not in other tumors originating from the sellar region. *Acta Neuropathol.* 109:589–597
- Colman, H., Giannini, C., Huang, L., Gonzalez, J., Hess, K., Bruner, J., Fuller, G., Langford, L., Pelloski, C., Aaron, J., Burger, P., and Aldape, K. (2006) Assessment and prognosis significance of mitotic index using the mitosis marker phospho-histone H3 in low and intermediate-grade infiltrating astrocytomas. *Am. J. Surg. Pathol.* 30:657–664
- de Chadarevian, J.P., Halligan, G.E., Reddy, G., Bertrand, L., Pascasio, J.M., Faerber, E.N., and Katsetos, C.D. (2006) Glioneuronal phenotype in a diencephalic pilomyxoid astrocytoma. *Pediatr. Dev. Pathol.* 9:480–487
- Fuller, C.E., Frankel, B., Smith, M., Rodziewicz, G., Landas, S.K., Caruso, R., and Schelper, R. (2001) Suprasellar monomorphous pilomyxoid neoplasm: an ultrastructural analysis. *Clin. Neuropathol.* 20:256–262
- Hahn, H.P., Bundock, E.A., and Hornick, J.L. (2006) Immunohistochemical staining for claudin-1 can help distinguish meningiomas from histologic mimics. *Am. J. Clin. Pathol.* 125:203–208
- Hasselblatt, M., and Paulus, W. (2003) Sensitivity and specificity of epithelial membrane antigen staining patterns in ependymomas. *Acta Neuropathol. (Berlin)* 4:385–388
- Hirose, T., Scheithauer, B.W., Lopes, M.B.S., Gerber, H.A., Altermatt, H.J., and VandenBerg, S.R. (1997) Ganglioglioma: an ultrastructural and immunohistochemical study. *Cancer* 79:989–1003
- Hofmann, B.M., Kreutzer, J., Saeger, W., Buchfelder, M., Blumcke, I., Fahlbusch, R., and Buslei, R. (2006) Nuclear beta-catenin accumulation as reliable marker for the differentiation between cystic craniopharyngiomas and Rathke cleft cysts: a clinico-pathologic approach. *Am. J. Surg. Pathol.* 30:1595–1603
- Jarrell, S.T., Vortmeyer, A.O., Linehan, W.M., Oldfield, E.H., and Lonser, R.R. (2006) Metastases to hemangioblastomas in von Hippel-Lindau disease. *J. Neurosurg.* 105:256–263
- Johannessen, A.L., and Torp, S.H. (2006) The clinical value of Ki-67/MIB-1 labeling index in human astrocytomas. *Pathol. Oncol. Res.* 12:143–147
- Judkins, A.R., Burger, P.C., Hamilton, R.L., DeMasters, B.-K., Perry, A., Pomeroy, S.L., Rosenblum, M.K., Yachnis, A.T., Zhou, H., Rorke, L.B., and Biegel, J.A. (2005) INI1 protein expression distinguishes atypical teratoid/rhabdoid tumor from choroid plexus carcinoma. *J. Neuropathol. Exp. Neurol.* 64:391–397
- Katsetos, C.D., Del Valle, L., Geddes, J.F., Assimakopoulou, M., Legido, A., Boyd, J.C., Balin, B., Parikh, N.A., Maraziotis, T., de Chadarevian, J.P., Varakis, J.N., Matsas, R., Spano, A., Frankfurter, A., Herman, M.M., and Khalili, K. (2001) Aberrant localization of the neuronal class III beta-tubulin in astrocytomas. *Arch. Pathol. Lab. Med.* 125:613–624
- Liu, Y., Sturgis, C.D., Bunker, M., Saad, R.S., Tung, M., Raab, S.S., and Silverman, J.F. (2004) Expression of cytokeratin by malignant meningiomas: diagnostic pitfall of cytokeratin to separate malignant meningiomas from metastatic carcinoma. *Mod. Pathol.* 17:1129–1133
- Louis, D.N., Ohgaki, H., Wiestler, O.D., and Cavenee, W.K. (eds) (2007) WHO classification of tumours of the central nervous system. IARC Press, Lyon, France
- Maraziotis, T., Perentes, E., Karamitopoulou, E., Nakagawa, Y., Gessaga, E.C., Probst, A., and Frankfurter, A. (1992) Neuron-associated class II beta tubulin isotype, retinal S-antigen, synaptophysin, and glial fibrillary acidic protein in human medulloblastomas: a clinicopathological analysis of 36 cases. *Acta Neuropathol.* 84:355–363
- Martinez-Diaz, H., Kleinschmidt-DeMasters, B.K., Powell, S.Z., and Yachnis, A.T. (2003) Giant cell glioblastoma and pleomorphic xanthoastrocytoma show different immunohistochemical profiles for neuronal antigens and p53 but share reactivity for class III beta-tubulin. *Arch. Pathol. Lab. Med.* 127:1187–1191
- Matsuno, A., Fujimaki, T., Sasaki, T., Nagashima, T., Ide, T., Asai, A., Matsuura, R., Utsunomiya, H., and Kurino, T. (1996) Clinical and histopathological analysis of proliferative potentials

- of recurrent and non-recurrent meningiomas. *Acta Neuropathol.* 91:504–510
- McLendon, R.E., Friedman, H.S., Fuchs, H.E., Kun, L.E., and Bigner, S.H. (1999) Diagnostic markers in paediatric medulloblastoma: a Paediatric Oncology Group Study. *Histopathology* 34:154–162
- Miettinen, M., and Paetau, A. (2002) Mapping of the keratin polypeptides in meningiomas of different types: an immunohistochemical analysis of 463 cases. *Hum. Pathol.* 33:590–598
- Min, H.S., Lee, Y.J., Park, K., Cho, B.-K., and Park, S.-H. (2006) Medulloblastoma: histopathologic and molecular markers of anaplasia and biologic behavior. *Acta Neuropathol.* 112:13–20
- Patil, S., Perry, A., MacCollin, M., Dong, S., Betensky, R.A., Yeh, T.-H., Gutmann, D.H., and Stemmer-Rachamimov, A.O. (2008) Immunohistochemical analysis supports a role for INI1/SMARCB1 in hereditary forms of schwannomas, but not in solitary, sporadic schwannomas. *Brain Pathol.* 18:517–519
- Perry, A., Scheithauer, B.W., and Nascimento, A.G. (1997) The immunophenotypic spectrum of meningeal hemangiopericytoma: a comparison with fibrous meningioma and solitary fibrous tumor of meninges. *Am. J. Surg. Pathol.* 21:1354–1360
- Perry, A., Stafford, S.L., Scheithauer, B.W., Suman, V.J., and Lohse, C.M. (1998) The prognostic significance of MIB-1, p53, and DNA flow cytometry in completely resected primary meningiomas. *Cancer* 82:2262–2269
- Preusser, M., Laggner, U., Haberler, C., Heinzl, H., Budka, H., and Hainfellner, J.A. (2006) Comparative analysis of NeuN immunoreactivity in primary brain tumors: conclusions for rational use in diagnostic histopathology. *Histopathology* 48:438–444
- Ribalta, T., McCutcheon, I.E., Aldape, K.D., Bruner, J.M., and Fuller, G.N. (2004) The mitosis-specific antibody anti-phosphohistone-H3 (PHH3) facilitates rapid reliable grading of meningiomas according to WHO 2000 criteria. *Am. J. Surg. Pathol.* 28:1532–1536
- Sharma, M.C., Ralte, A.M., Gaekwad, S., Santosh, V., Shankar, S.K., and Sarkar, C. (2004) Subependymal giant cell astrocytoma- a clinicopathological study of 23 cases with special emphasis on histogenesis. *Pathol. Oncol. Res.* 10: 219–224
- Takei, H., Buckleair, L.W., and Powell, S.Z. (2008) Immunohistochemical expression of apoptosis regulating proteins and sex hormone receptors in meningiomas. *Neuropathology* 28:62–68
- Vege, K.D., Giannini, C., and Scheithauer, B.W. (2000) The immunophenotype of ependymomas. *Appl. Immunohistochem. Mol. Morphol.* 8:25–31
- Weinbreck, N., Marie, B., Bressenot, A., Montagne, K., Joud, A., Baumann, C., Klein, O., and Vignaud, J.M. (2008) Immunohistochemical markers to distinguish between hemangioblastoma and metastatic clear cell renal cell carcinoma in the brain: utility of aquaporin 1 combined with cytokeratin AE1/AE3 immunostaining. *Am. J. Surg. Pathol.* 32:1051–1059
- Wharton, S.B., Chan, K.K., and Whittle, I.R. (2002) Microtubule-associated protein 2 (MAP-2) is expressed in low and high grade diffuse astrocytomas. *J. Clin. Neurosci.* 9:165–169
- Wolf, H.K., Buslei, R., Blumcke, I., Wiesler, O.D., and Pietsch, T. (1997) Neuronal antigens in oligodendrogliomas and dysembryoplastic neuroepithelial tumors. *Acta Neuropathol.* 94:436–443

*This page intentionally left blank*

# 5

## Malignant Brain Tumors: Roles of Aquaporins

Jérôme Badaut and Jean-François Brunet

### INTRODUCTION

Water channels, renamed aquaporins (AQPs), were demonstrated in cells in 1992 and after the discovery of these water channels, water diffusion through the plasma membrane was revisited (Preston et al. 1992). The aquaporin (AQP) family is still growing with 13 members ubiquitously distributed in mammalian tissues. The functional roles of the AQPs are more complex than expected at their discovery (Badaut et al. 2007). In this chapter, we will review the latest reports on these AQPs and especially their contribution in brain tumors which may be useful for the prognosis and diagnostic of malignant brain tumors.

AQPs are water channel proteins with a molecular weight of ~30 kDa, and exhibit a common structure of six membrane spanning alpha helical domains with intracellular carboxyl (C) and amino (N) termini. They contain a consensus motif Asn-Pro-Ala (NPA), necessary for pore formation (Badaut et al. 2002). Despite a high sequence homology, the AQP family can still be divided into three subgroups: *aquaporin*, *aquaglyceroporin*, and *super-aquaporin*. The subgroup *aquaporin* is

composed of AQP0, 1, 2, 4, 5, 6, and is considered to be permeable to water. This permeability for water was recently revised as AQP6 is permeable for proton and AQP1 is permeable to volatile solutes such as NO (Herrera and Garvin 2007).

The second subgroup *aquaglyceroporins* is composed of AQP3, 7, 8, 9, 10 and the bacterial glycerol facilitator (Glpf) (Badaut et al. 2007). This subgroup of channels is permeable to water and glycerol. AQP9, a member of this group, is also surnamed the “neutral channel”. Indeed, injection of AQP9 into *Xenopus* oocytes or proteoliposomes facilitates the diffusion of water, polyols (glycerol, mannitol, and sorbitol), purines (adenine), pyrimidines (uracil and chemotherapeutic agent 5-fluorouracil), and monocarboxylates (lactate and  $\beta$ -hydroxybutyrate) (Badaut et al. 2007). However, the osmotic water coefficient for AQP9 is lower than for a pure water channel like AQP4. In addition, AQP9 facilitates metalloids transport, suggesting further that AQP9 may be a major route for arsenite uptake into mammalian cells (Badaut et al. 2007).

The last group, named *super-aquaporins*, is composed of AQP11 and 12 which were

recently described. Their specific feature is that they are localized in the cytoplasm. A study of AQP11 reconstitution into liposomes revealed an efficient water channel activity, comparable to AQP1 (Yakata et al. 2007). These *super-aquaporins* are involved in intracellular water transport and the regulation of organelle volume and intravesicular homeostasis (Nozaki et al. 2008). All of the water channel subgroups are widely distributed in several organs and in the brain for example, several subtypes co-exist.

## AQP EXPRESSION IN NORMAL BRAIN AND ITS FUNCTION

Water homeostasis is critical to sustain normal neural activity (Badaut et al. 2002). The discovery of the water channel family has motivated neuroscientists since 1994 to study the distribution and expression of the AQPs in normal and pathological brain. Seven aquaporin subtypes (AQP1, AQP3, AQP4, AQP5, AQP8, AQP9, AQP12) have been described in rodent brain cells. However, only three of these aquaporins have been well described in vivo: AQP1, AQP4, and AQP9 (Badaut et al. 2007). Their distribution and putative roles will be presented in normal and pathological brains. A review of our knowledge on AQP1, 4, and 9 will be useful to form hypotheses on functional roles for these channels in malignant brain tumors. These channels would potentially represent a future good marker for diagnosis and prognosis in malignant tumors.

### AQP1 Distribution and Its Potential Role

AQP1 is mainly expressed in epithelial cells of the choroid plexus in the rodent

brain, and is proposed to be involved in cerebrospinal fluid formation (Badaut et al. 2002). Interestingly, expression of AQP1 is seen in many non brain endothelia but its expression is suppressed in the specialized endothelial cells of the blood–brain barrier (BBB) (Dolman et al. 2005). Indeed, the presence of astrocytes inhibits the expression of AQP1 in endothelial cells.

In human brain diseases, astrocytic AQP1 expression is induced in the tissue after subarachnoid hemorrhage (SAH) (Badaut et al. 2003). Similar AQP1 induction was observed in a model of SAH in rats and correlated with edema formation (Yatsushige et al. 2007). A long term induction of AQP1 in neurons and astrocytes after spinal cord injury in the rat has been described, however, without evident edema formation (Nesic et al. 2008). These new results show the complexity of the roles of AQP1 in pathophysiology. In support of this, unexpected results have been obtained in AQP1-Knockout mice showing that AQP1 plays an important role in the neoangiogenesis of growing tumors (Saadoun et al. 2005), and recently several AQPs have been shown to be involved in the processes of cell migration. This function opens future avenues of research for AQPs. The roles of AQP1 in angiogenesis and cell migration in brain tumor development will be largely evoked later.

### AQP4 Astrocyte Endfeet Marker

#### Involved in Brain Water Homeostasis

AQP4 is one of the most studied aquaporins in the brain being the most abundant aquaporin. The AQP4 was first observed in the glia limitans, the ependymal lining system, the magnocellular hypothalamic nuclei, the cerebellum, the hippocampus, and the

neocortex (Badaut et al. 2002). The notable feature of AQP4 distribution is its presence on astrocyte endfeet in contact with blood vessels, and also on astrocytic processes in contact with synapses (Badaut et al. 2002). In the rodent brain, several regions show a strong AQP4 immunoreactive signal which may be due to the presence of the channel outside of the perivascular space, on astrocyte processes surrounding neuronal cells (Badaut et al. 2002). Such localizations of AQP4 and potassium inward rectifying channels 4.1 (KIR4.1), suggest that AQP4 may have a role in potassium homeostasis by facilitating water diffusion (Badaut et al. 2002). This hypothesis was confirmed in AQP4-KO mice where a delay in potassium reuptake during electrical activity is increased (Binder et al. 2006). The level of AQP4 expression in astrocyte endfeet varies in pathological conditions such brain ischemia, with a large induction of AQP4 within 1 h after stroke onset (de Castro Ribeiro et al. 2006). This rapid induction may be protective by a rapid removal of excess water in the perivascular space (Hirt et al. 2008). The importance of the AQP4 in water removal was also shown in vasogenic edema formation in a model of tumor implantation (Papadopoulos et al. 2004).

In addition to the brain water homeostasis, new functional roles were proposed for AQP4 in astrocytes. In fact, the high level of AQP4 protein in the hypothalamic glia lamellae may facilitate adhesion between the astrocyte processes (Hiroaki et al. 2006). On the other hand, AQP4 has recently been shown to be involved in glial scar formation with recruitment of the reactive astrocytes (Auguste et al. 2007). Indeed, astrocytes deficient in AQP4 migrated more slowly than wild type ones *in vitro*, using monolayer scratch and transwell assays and

*in vivo*, after injection of astrocytes with and without AQP4 distant to mechanical stab injury (Auguste et al. 2007).

In summary, AQP4 is a key player in brain water homeostasis and facilitates water movement through the astrocytic plasma membrane in contact with blood vessels and synapses. AQP4 will therefore be important in brain tumors, and the recent findings concerning the role of AQP4 in cell migration and adhesion will open possibilities for tumors.

### Involvement of AQP9 in Brain Energy Metabolism

AQP9 facilitates the diffusion of both water and several solutes such as glycerol, urea, and monocarboxylate. The highest level of AQP9 expression is in the liver and its expression is also observed in rodent brain (Badaut et al. 2004; de Castro Ribeiro et al. 2006). AQP9 mRNA and protein were detected in astrocyte cultures in rodent brain in three cell types (Badaut et al. 2004, 2008). Presently, AQP9 expression has been observed in: glial cells, in particular tanycytes and astrocytes, endothelial cells of subpial vessels and in one subtype of neurons, the catecholaminergic neurons (Badaut et al. 2004; de Castro Ribeiro et al. 2006). Two isoforms of AQP9 have been described in brain cells, the short isoform (26 kDa) is found in inner membrane of mitochondria and the long isoform (30 kDa) in the cell membrane (Badaut et al. 2007).

In hepatocytes, high plasma insulin suppresses glycerol uptake, which participates in neoglucogenesis to replenish blood glucose concentrations. AQP9 is down regulated by high insulin concentrations suggesting that AQP9 may play a key role

in the cellular energy balance as a glycerol channel in the liver (Badaut et al. 2007). AQP9 expression in liver is dramatically increased in models of diabetes induced by streptozotocin (STZ) injection (Badaut et al. 2008). Similarly, we showed that AQP9 protein levels were down regulated after insulin application and conversely levels of AQP9 were increased in catecholaminergic nuclei in brains of diabetic rats (Badaut et al. 2008). Therefore, it would appear that neuronal AQP9 expression is regulated by insulin concentrations similarly to the situation in hepatocytes. Based on these results, a sole role of AQP9 in water homeostasis was revised, and we postulated that AQP9 is involved in brain energy metabolism in catecholaminergic neurons, known to be involved in energy balance (Badaut et al. 2008). In astrocytes, AQP9 could facilitate diffusion of glycerol and monocarboxylates, which may serve as energy substrates for cells in the central nervous system (Badaut et al. 2004).

As shown for AQP1 and AQP4, it was recently shown that AQP9 is involved in leucocyte transmigration by facilitation of water entry during the formation of the filopodia (Loitto et al. 2007). This hypothesis may be true for astrocytes as we have already shown a huge increase of AQP9 in reactive astrocytes after stroke (de Castro Ribeiro et al. 2006) which may be involved in astrocyte migration during the glial scar formation. In summary, AQP9 is probably not involved directly in brain water homeostasis but rather in brain energy balance. In tumors, AQP9 could be a metabolite channel for glycerol and monocarboxylates; energy substrates potentially produced or used by tumor cells.

## AQP DISTRIBUTION IN TUMORS: ROLES IN PROGNOSIS AND TREATMENT

The expression of AQPs has been observed in different tumor cell types in humans and rodents. We will review the results concerning expression of AQP1, 4, and 9, which are the major AQPs in brain tumors.

### AQP1 in Tumors: Water Homeostasis or Cell Migration?

AQP1 is mainly localized in the choroids plexus in the normal brain. In many tumors, AQP1 has been shown to be overexpressed for example in astrocytomas (Saadoun et al. 2002a), gliomas (Badaut et al. 2003; Oshio et al. 2005) and also in meningiomas (Nagashima et al. 2006). Expression of AQP1 differs between tumor types, but it is always higher in tumors than in normal brains (Figure 5.1). AQP1 was observed in Glial Fibrillary Acid Protein (GFAP) and non GFAP positive cells in astrocytomas (Figure 5.1b) (Oshio et al. 2005). In this tumor type, AQP1 was observed in blood vessels. The level of expression of AQP1 increases with tumor grade, with a highest expression in World Health Organization (WHO) grade IV, suggesting that the level of AQP1 could be used as a prognostic factor.

Similarly, AQP1 was also strongly expressed at the invading front and dural attachment of meningiomas (Nagashima et al. 2006), suggesting the role of AQP1 in invasion and fixation of the tumor. Moreover, reactive astrocytes in contact with the tumor (such as glioma and astrocytoma)

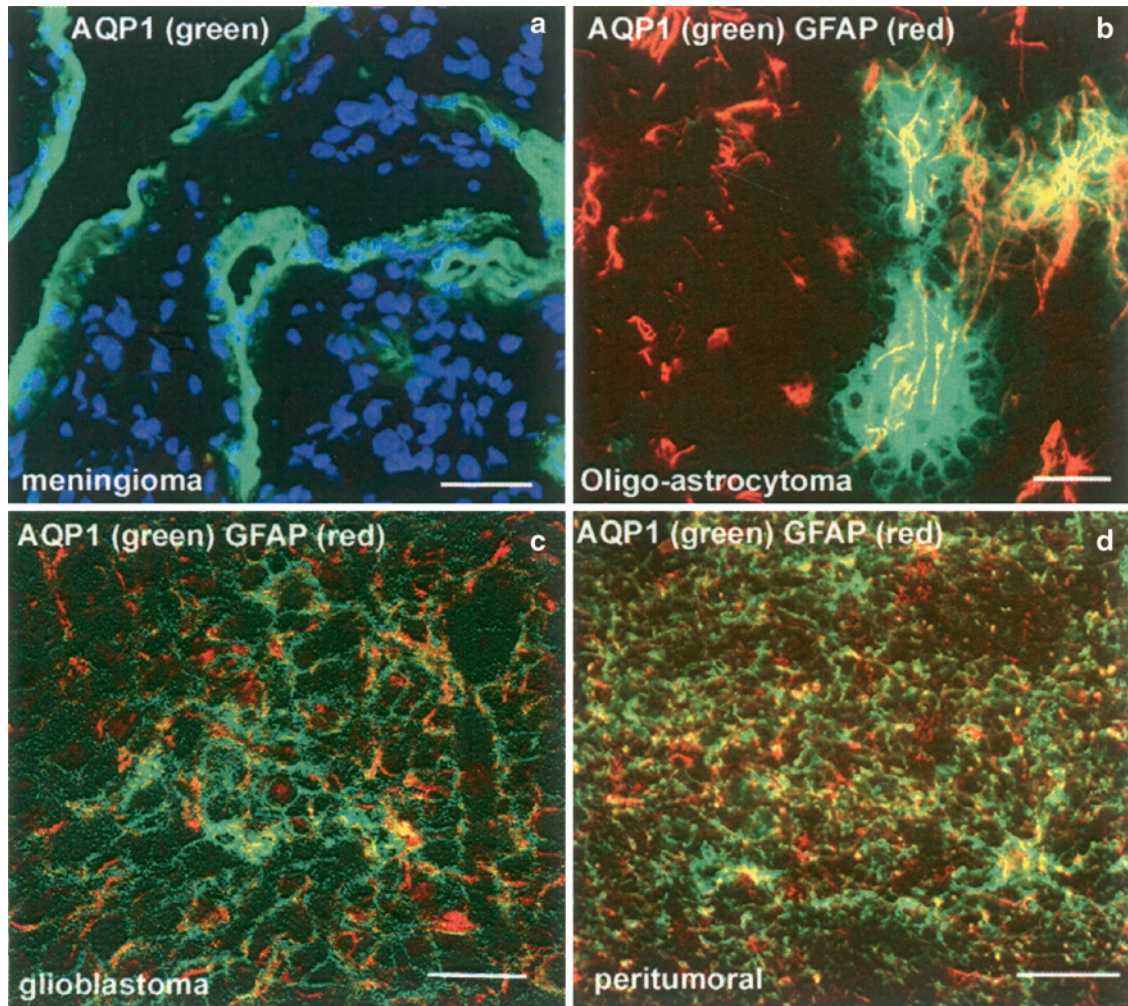


FIGURE 5.1. Representative distribution of AQP1 (**a**, **b**, **c**, **d**, green) in a meningioma (**a**), in oligoastrocytoma (**b**), in glioblastoma (**c**) and in peritumoral tissue in contact with the glioma (**d**). GFAP immunostaining (red) revealed tumor cells in the oligoastrocytoma (**b**) and glioblastoma (**c**). (**a**) AQP1 (green) is highly expressed at the edge of the meningioma that may correspond to the invading front of the tumor. (**b**) In the oligoastrocytoma, AQP1 expression is highly expressed in round cells, not necessarily GFAP positive. (**c**) In the glioblastoma, high GFAP immunoreactivity (in red) is colocalized with high AQP1 staining (in green). (**d**) The peritumoral tissue exhibited a reactive gliosis, observed by GFAP staining (red) and a high induction of AQP1 expression compared to normal astrocytes in human brain tissue. Bar A, B, C, D = 40  $\mu$ m

showed a strong induction of AQP1 expression compared to non reactive astrocytes (Figure 5.1d). This induction of its expression was thought to be correlated with

the glycolytic activity and associated with blood vessels at the tumor periphery. It was proposed that the combination of up regulation of AQP1, lactate dehydrogenase and



cathepsin B contributes to the acidification of the extracellular compartment and the invasive potential of glioma cells in the perivascular space (Hayashi et al. 2007).

AQP1 belongs to the family of the pure water channels and strong induction of this channel in tumors was first assumed to be related to water diffusion within compact tumors and perhaps contributing to the peri-tumoral edema formation (Badaut et al. 2003; Saadoun et al. 2002a). However, additional roles for AQP1 have recently been proposed; in particular a role of AQP1 in neoangiogenesis (Saadoun et al. 2005). Tumor growth was significantly reduced in AQP1-KO mice compared to wild type mice due to impairment of tumor neoangiogenesis. The absence of neovessels within the tumor caused extensive cell necrosis and a decrease in tumor size. The authors clearly demonstrated that the migration of endothelial cells in AQP1-KO mice was impaired, inducing an absence of neovessels during the tumor growing (Saadoun et al. 2005).

It was also shown *in vitro* that AQP1 expression facilitates tumoral cell migration, opposite to AQP4, which is involved in cell adhesion (McCoy and Sontheimer 2007). Therefore, the strong overexpression of AQP1 at the invading front and in tumoral cells may contribute to tumor growing and invasion (Nagashima et al. 2006) rather than water movement inside the tumor. In accordance with these hypotheses, the levels of expression of AQP1 reached a maximum in these gliomas with the highest WHO grade (Oshio et al. 2005) with possibly more infiltrating cells. Induction of AQP1 was shown to be dependent on hypoxic stress and contributes to the hypoxic-inducible angiogenesis in human retinal vascular endothelial cells

(Kaneko et al. 2008). Hypoxic events are observed in growing tumors and it can be envisaged that induction of angiogenesis in the tumor is the result of AQP1 induction as proposed by these authors. To summarize, AQP1 would be a good marker for the WHO tumor grade as well as for the invading front. However, possible roles for AQP1 are still undetermined and require further investigation. One of the future directions will be to study the synergy or collaboration between AQP1 and the other AQPs in water movement and in tumor invasion.

#### AQP4 in Tumors: Biomarker for Tumor Classification

As previously mentioned, AQP4, water-channel in the rodent brain, is likely to play an important role in extracellular water homeostasis, and thus may sustain normal neuronal activity (Badaut et al. 2002). A profound perturbation of the brain environment usually induces a regional cerebral edema, as observed in ischemia and also around brain tumor formation. Brain edema, which leads to an expansion in brain volume, has a crucial impact on morbidity and mortality after stroke, as it increases intracranial pressure, favours herniations, and contributes to additional ischemic injuries (Badaut et al. 2002). Results on AQP1 suggest that this channel may be involved in the tumor growth. What is the knowledge on AQP4 expression and its role in the malignant tumors?

In glioblastomas, AQP4 was highly expressed and the polarization usually observed in astrocyte endfeet is lost in tumoral cells (Figure 5.2) (Warth et al. 2004). This redistribution of AQP4 was studied in correlation with syntrophin, as

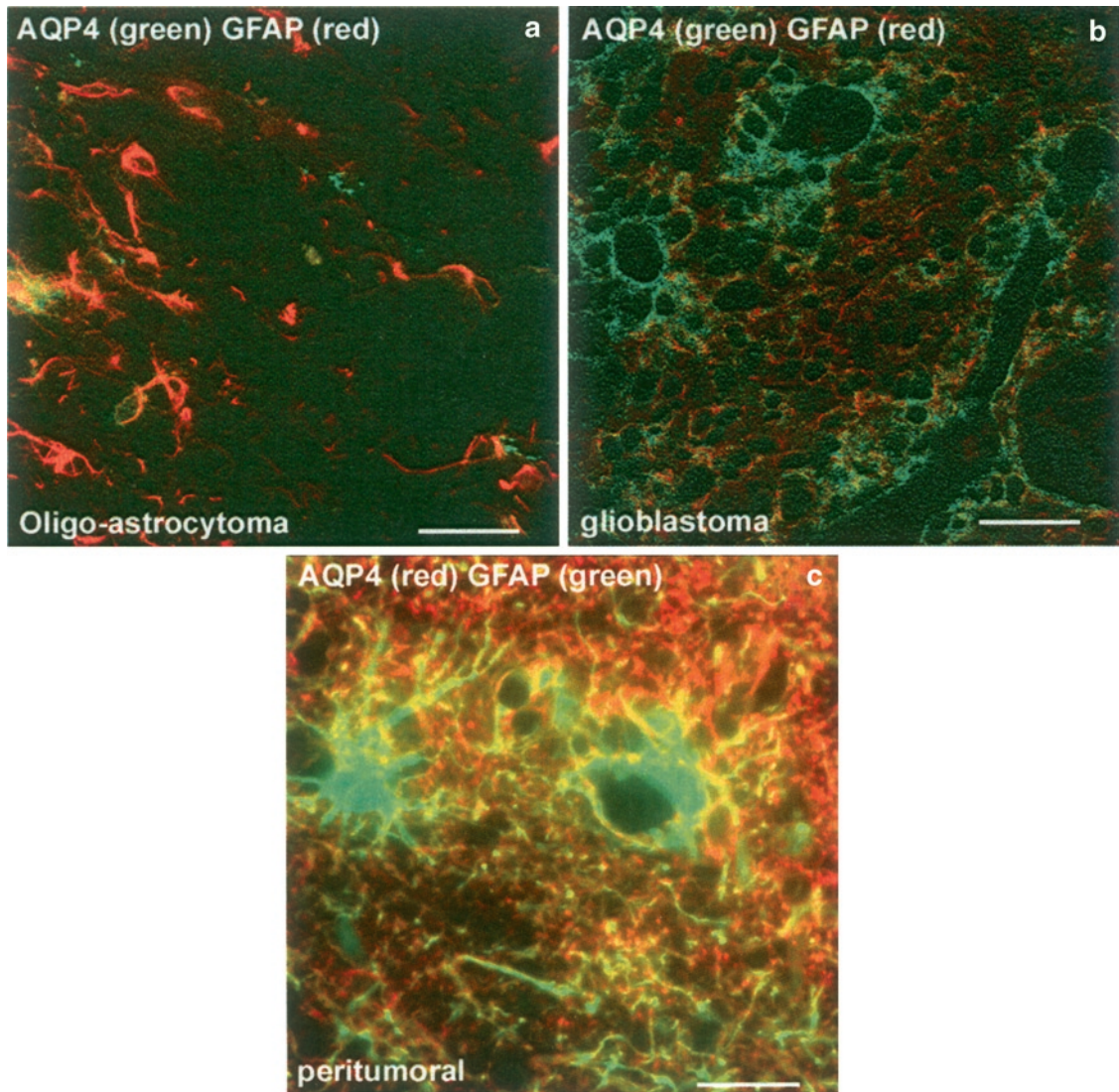


FIGURE 5.2. Representative distribution of AQP4 (a, b, c) in an oligoastrocytoma (a), in a glioblastoma (b) and in peritumoral tissue in contact with the glioma (c). GFAP immunostaining (red) revealed tumoral cells in the oligoastrocytoma (b) and glioblastoma (c). (a) AQP4 is expressed in some GFAP-positive cells in the oligoastrocytoma; however, the level of expression of AQP4 was lower than that of AQP1 (Figure 5.1b). (b) Similar to AQP1, AQP4 (green) is also highly expressed in all GFAP positive cells (red) in the glioblastoma. (c) AQP4 (red) expression is induced in the peritumoral tissue with expression in reactive astrocytes, revealed by GFAP staining (green). AQP4 is distributed on the whole astrocyte membrane contrary to that in normal tissue, where AQP4 is expressed only on astrocyte endfeet in contact with blood vessels A, B = 40  $\mu$ m and C = 20  $\mu$ m

well as proteins involved in the extracellular matrix such as agrin and dystroglycan. The decrease of agrin in glioblastomas

is concomitant with disorganization of the cellular distribution of AQP4. All these modifications in the perivascular

compartment were related to modifications of BBB properties, characterized by a leakage in tumors (Warth et al. 2004). The pattern and the level of expression of AQP4 showed differences between the tumor grades (Warth et al. 2007b). Tumors with a high WHO grade IV show the highest expression of AQP4, suggesting that AQP4 may be used as a marker to distinguish between astrocytic and oligodendroglial tumors (Ikota et al. 2006), and therefore facilitate classification into astroglial tumors of different WHO grades (Warth et al. 2007b). However, the level of AQP4 expression was not a good candidate for the survival prognosis in astroglial tumors.

The level of AQP4 expression was correlated with edema formation (Saadoun et al. 2002b; Warth et al. 2007b). To date the role of AQP4 in edema formation and resolution is still unclear (Badaut et al. 2007). All human studies depicted a relation between AQP4 expression and edema “scoring” at only one time point (Saadoun et al. 2002b; Warth et al. 2007b). However, on the basis of results in the literature, it would be important to have several time points to illustrate AQP4 variations over time during brain disease because functions of AQP4 may be different (Badaut et al. 2007). Thus, studies using AQP4-KO mice showed that AQP4 contributed to cytotoxic edema formation at early time points. On the other hand, the presence of AQP4 in brain tissue was critical to counteract vasogenic edema formation (Papadopoulos et al. 2004). In the report by these authors, AQP4 was proposed to remove excess of fluid from the tissue, pointing to a protective role by decreasing peritumoral edema formation.

Interestingly, brain edema formation was directly associated with mortality in both low- and high-grade gliomas (Pope et al. 2005). Despite the proposed correlation between the level of AQP4 expression and edema formation, Warth et al. (2007b) found no correlation between the levels of AQP4 expression and mortality rate. How may this discrepancy be explained? One of the possibilities is that the two principal AQP4 isoforms exhibit different forms of regulation in pathological conditions (Hirt et al. 2008). Moreover, it was recently shown that in humans, AQP4 exhibited more than two subtypes with new variants for AQP4 (Sorani et al. 2008). AQP4 variants had different water permeability; some of the mutations in the AQP4 gene induced a decrease in water permeability of 48% compared to AQP4-M23 protein (considered as a reference in the cited study). A straight consequence of these results is that a direct correlation between the level of expression of AQP4 and edema formation is not possible.

As described above, the repertoire of functional roles of AQP4 is increasing, AQP4 was shown to be involved in cell adhesion (Hiroaki et al. 2006) and in cell migration (Auguste et al. 2007). To date these other functions of AQP4 have not been investigated in astroglial tumors, but in vitro results suggest a role in cell adhesion (McCoy and Sontheimer 2007). To summarize, variability in AQP4 isoform expression in human brain tissue explains why it is difficult to find a direct correlation between AQP4 expression and edema formation and therefore survival rate. However, the level of expression of AQP4 may also be used in combination with AQP1 for the classification of tumors.

### AQP9 in Brain Tumors: New Findings

AQP9 is found in astrocytes and catecholaminergic neurons in normal brain (Badaut et al. 2007). Similarly to AQP4, AQP9 expression is increased after hyperosmotic stress by stimulation of the p38 mitogen-activated protein kinase-dependent pathway (Badaut et al. 2007). In the stroke disease, increase of AQP9 was proposed to be involved in the removal of lactate and glycerol excess (de Castro Ribeiro et al. 2006).

Recently, AQP9 expression was studied in human and rat gliomas which showed

an increase in AQP9 expression (Tan et al. 2008; Warth et al. 2007a) compared to non tumor tissue. Differences were observed in the pattern of distribution of AQP9 between rats and humans (Warth et al. 2007a). A strong staining of AQP9 was observed at the border of the tumor in rat gliomas in contrast to humans where AQP9 staining is increased throughout the whole tumor. As with AQP1 and AQP4, AQP9 expression increases with the grade of the tumor, with a maximum for grade IV (Tan et al. 2008). AQP9 over-expression may be related to energy metabolism. It was

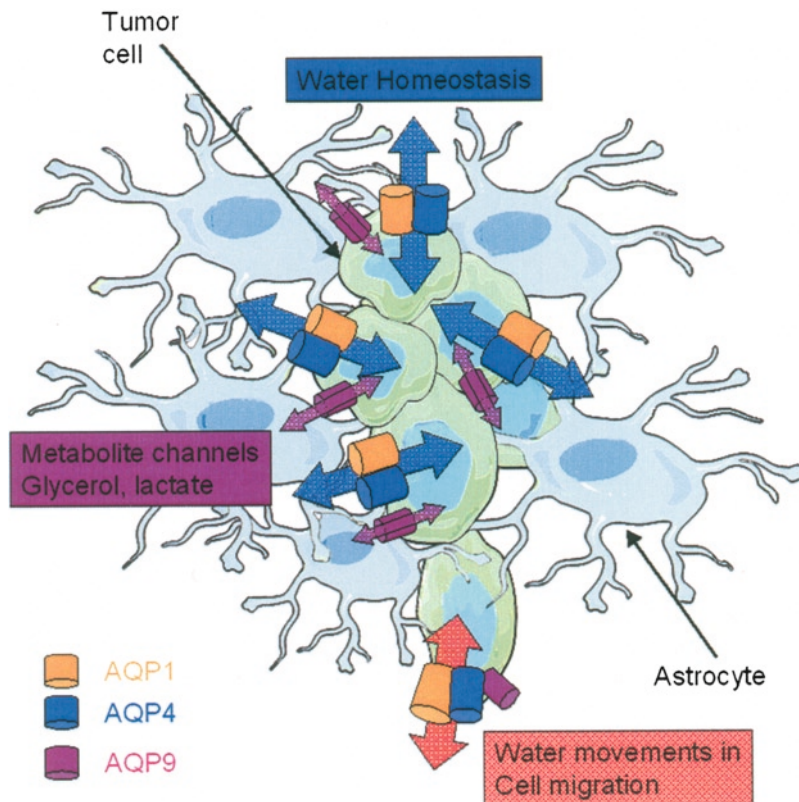


FIGURE 5.3. A schema depicting the distribution of AQP1, AQP4, and AQP9 in brain tumor cells (in green). AQP1 (orange) and AQP4 (blue) are pure water channels and are likely to be involved in water homeostasis in brain tumors. However, the presence of AQP1 and AQP4 may also be involved in tumor cell migration and in the growing phase of the tumor. AQP9 is an aquaglyceroporin which is known to facilitate diffusion of glycerol and monocarboxylates. This channel may be involved in the movement of these solutes within tumors. Recently, AQP9 was proposed to be involved in cell migration of leukocytes and this may also be a function in the tumor cells

proposed that presence of AQP9 in tumors correlates with the accumulated lactate which is increased in rat tumors (1.7-fold) (Warth et al. 2007a). It is interesting to note that mannitol or glycerol is clinically used for osmotic treatment to decrease the edema formation (Warth et al. 2007a) and AQP9 is known to transport both of these compounds. Therefore, AQP9 may facilitate their accumulation in cells to act positively in hyperosmotic treatment. However, the role of this aquaporin in tumors is still unclear. The involvement of AQP9 in leucocyte migration (Loitto et al. 2007) suggests that it is also involved in migration of tumor cells.

In conclusion, the expression of water channels is increased in malignant brain tumors compared to normal brain tissue (Badaut et al. 2003; Saadoun et al. 2002a, b; Warth et al. 2007a, b). However, at present the roles of these channels in tumoral cells are very speculative (Figure 5.3). The high level of expression of three AQPs is directly correlated to the grade of the tumor. In combination with AQP1, AQP4 and AQP9 staining can be used as a specific biomarker to define the WHO grades of brain tumor. However, the level of expression of these three AQPs was not positively or negatively correlated with patient survival. This negative result may be explained by the complexity of the channels in their number of isoforms as well as in their functional roles (i.e., water homeostasis, cell migration, cell adhesion, gas diffusion). A single tumor cell may express several AQP isoforms. At present, we have only a partial view of AQP expression in brain tumors, and it is becoming clear that other types of AQP can be expressed in tumor cells.

*Acknowledgements.* The authors wish to thank Dr M. Price for critical comments on the manuscript. This writing was supported by grants from the Swiss Science Foundation (FN 3100AO-108001; 31003A-122166); Novartis science foundation.

## REFERENCES

- Auguste, K.I., Jin, S., Uchida, K., Yan, D., Manley, G.T., Papadopoulos, M.C., and Verkman, A.S. (2007) Greatly impaired migration of implanted aquaporin-4-deficient astroglial cells in mouse brain toward a site of injury. *FASEB J.* 21: 108–116
- Badaut, J., Lasbennes, F., Magistretti, P.J., and Regli, L. (2002) Aquaporins in brain: distribution, physiology, and pathophysiology. *J. Cereb. Blood Flow Metab.* 22:367–378
- Badaut, J., Brunet, J.F., Grollmund, L., Hamou, M.F., Magistretti, P.J., Villemure, J.G., and Regli, L. (2003) Aquaporin 1 and 4 expression after human acute subarachnoid hemorrhage. *Acta Neurochir. Suppl.* 86:495–498
- Badaut, J., Petit, J.M., Brunet, J.F., Magistretti, P.J., Charriaut-Marlangue, C., and Regli, L. (2004) Distribution of Aquaporin 9 in the adult rat brain: preferential expression in catecholaminergic neurons and in glial cells. *Neuroscience* 128:27–38
- Badaut, J., Brunet, J.F., and Regli, L. (2007) Aquaporins in the brain: from aqueduct to “multi-duct”. *Metab. Brain Dis.* 22:251–263
- Badaut, J., Brunet, J.F., Petit, J.M., Guerin, C.F., Magistretti, P.J., and Regli, L. (2008) Induction of brain aquaporin 9 (AQP9) in catecholaminergic neurons in diabetic rats. *Brain Res.* 1188:17–24
- Binder, D.K., Yao, X., Zador, Z., Sick, T.J., Verkman, A.S., and Manley, G.T. (2006) Increased seizure duration and slowed potassium kinetics in mice lacking aquaporin-4 water channels. *Glia* 53:631–636
- de Castro Ribeiro, M., Hirt, L., Bogousslavsky, J., Regli, L., and Badaut, J. (2006) Time course of aquaporin expression after transient focal cerebral ischemia in mice. *J. Neurosci. Res.* 83:1231–1240
- Dolman, D., Drndarski, S., Abbott, N.J., and Rattray, M. (2005) Induction of aquaporin 1 but

- not aquaporin 4 messenger RNA in rat primary brain microvessel endothelial cells in culture. *J. Neurochem.* 93:825–833
- Hayashi, Y., Edwards, N.A., Proescholdt, M.A., Oldfield, E.H., and Merrill, M.J. (2007) Regulation and function of aquaporin-1 in glioma cells. *Neoplasia* 9:777–787
- Herrera, M., and Garvin, J.L. (2007) Novel role of AQP-1 in NO-dependent vasorelaxation. *Am. J. Physiol. Renal Physiol.* 292:F1443–1451
- Hiroaki, Y., Tani, K., Kamegawa, A., Gyobu, N., Nishikawa, K., Suzuki, H., Walz, T., Sasaki, S., Mitsuoka, K., and Kimura, K. (2006) Implications of the Aquaporin-4 Structure on Array Formation and Cell Adhesion. *J. Mol. Biol.* 355:628–639
- Hirt, L., Price, M., Ternon, B., Mastour, N., Brunet, J.F., and Badaut, J. (2008) Early induction of AQP4 contributes the limitation of the edema formation in the brain ischemia. *J. Cereb. Blood Flow Metab.* 29:423–433
- Ikota, H., Kinjo, S., Yokoo, H., and Nakazato, Y. (2006) Systematic immunohistochemical profiling of 378 brain tumors with 37 antibodies using tissue microarray technology. *Acta Neuropathol.* 111:475–482
- Kaneko, K., Yagui, K., Tanaka, A., Yoshihara, K., Ishikawa, K., Takahashi, K., Bujo, H., Sakurai, K., and Saito, Y. (2008) Aquaporin 1 is required for hypoxia-inducible angiogenesis in human retinal vascular endothelial cells. *Microvasc. Res.* 75:297–301
- Loitto, V.M., Huang, C., Sigal, Y.J., and Jacobson, K. (2007) Filopodia are induced by aquaporin-9 expression. *Exp. Cell Res.* 313:1295–1306
- McCoy, E., and Sontheimer, H. (2007) Expression and function of water channels (aquaporins) in migrating malignant astrocytes. *Glia* 55:1034–1043
- Nagashima, G., Fujimoto, T., Suzuki, R., Asai, J., Itokawa, H., and Noda, M. (2006) Dural invasion of meningioma: a histological and immunohistochemical study. *Brain Tumor Pathol.* 23:13–17
- Nesic, O., Lee, J., Unabia, G.C., Johnson, K., Ye, Z., Vergara, L., Hulsebosch, C.E., and Perez-Polo, J.R. (2008) Aquaporin 1 - a novel player in spinal cord injury. *J. Neurochem.* 105:628–640
- Nozaki, K., Ishii, D., and Ishibashi, K. (2008) Intracellular aquaporins: clues for intracellular water transport? *Pflugers Arch.* 456:701–707
- Oshio, K., Binder, D.K., Liang, Y., Bollen, A., Feuerstein, B., Berger, M.S., and Manley, G.T. (2005) Expression of the aquaporin-1 water channel in human glial tumors. *Neurosurgery* 56:375–381
- Papadopoulos, M.C., Manley, G.T., Krishna, S., and Verkman, A.S. (2004) Aquaporin-4 facilitates reabsorption of excess fluid in vasogenic brain edema. *FASEB J.* 18:1291–1293
- Pope, W.B., Sayre, J., Perlina, A., Villablanca, J.P., Mischel, P.S., and Cloughesy, T.F. (2005) MR imaging correlates of survival in patients with high-grade gliomas. *AJNR Am. J. Neuroradiol.* 26:2466–2474
- Preston, G.M., Carroll, T.P., Guggino, W.B., and Agre, P. (1992) Appearance of water channels in *Xenopus* oocytes expressing red cell CHIP28 protein. *Science* 256:385–387
- Saadoun, S., Papadopoulos, M.C., Davies, D.C., Bell, B.A., and Krishna, S. (2002a) Increased aquaporin 1 water channel expression in human brain tumours. *Br. J. Cancer* 87:621–623
- Saadoun, S., Papadopoulos, M.C., Davies, D.C., Krishna, S., and Bell, B.A. (2002b) Aquaporin-4 expression is increased in oedematous human brain tumours. *J. Neurol. Neurosurg. Psychiatry* 72:262–265
- Saadoun, S., Papadopoulos, M.C., Hara-Chikuma, M., and Verkman, A.S. (2005) Impairment of angiogenesis and cell migration by targeted aquaporin-1 gene disruption. *Nature* 434:786–792
- Sorani, M.D., Zador, Z., Hurowitz, E., Yan, D., Giacomini, K.M., and Manley, G.T. (2008) Novel variants in human Aquaporin-4 reduce cellular water permeability. *Hum. Mol. Genet.* 17:2379–2389
- Tan, G., Sun, S.Q., and Yuan, D.L. (2008) Expression of the water channel protein aquaporin-9 in human astrocytic tumours: correlation with pathological grade. *J. Int. Med. Res.* 36:777–782
- Warth, A., Kroger, S., and Wolburg, H. (2004) Redistribution of aquaporin-4 in human glioblastoma correlates with loss of agrin immunoreactivity from brain capillary basal laminae. *Acta Neuropathol. (Berlin)* 107:311–318

- Warth, A., Mittelbronn, M., Hulper, P., Erdlenbruch, B., and Wolburg, H. (2007a) Expression of the water channel protein aquaporin-9 in malignant brain tumors. *Appl. Immunohistochem. Mol. Morphol.* 15:193–198
- Warth, A., Simon, P., Capper, D., Goepfert, B., Tabatabai, G., Herzog, H., Dietz, K., Stubenvoll, F., Ajaaj, R., Becker, R., Weller, M., Meyermann, R., Wolburg, H., and Mittelbronn, M. (2007b) Expression pattern of the water channel aquaporin-4 in human gliomas is associated with blood-brain barrier disturbance but not with patient survival. *J. Neurosci. Res.* 85:1336–1346
- Yakata, K., Hiroaki, Y., Ishibashi, K., Sohara, E., Sasaki, S., Mitsuoka, K., and Fujiyoshi, Y. (2007) Aquaporin-11 containing a divergent NPA motif has normal water channel activity. *Biochim. Biophys. Acta* 1768:688–693
- Yatsushige, H., Ostrowski, R.P., Tsubokawa, T., Colohan, A., and Zhang, J.H. (2007) Role of c-Jun N-terminal kinase in early brain injury after subarachnoid hemorrhage. *J. Neurosci. Res.* 85: 1436–1448

# 6

## Brain Metastases: Gene Amplification Using Quantitative Real-Time Polymerase Chain Reaction Analysis

Carmen Franco-Hernandez, Miguel Torres-Martin, Victor Martinez-Glez, Carolina Peña-Granero, Javier S. Castresana, Cacilda Casartelli, and Juan A. Rey

### INTRODUCTION

Brain metastases represent an advanced step in the progression of multiple types of cancer and are associated with a poor prognosis. Approximately 20–40% of patients with systemic cancer develop metastasis involving the central nervous system. Metastases, therefore, represent ~5–15% of malignant brain tumors, and melanoma, lung, breast and colon carcinomas are the primary tumors most frequently involved in brain invasion (Wesseling et al. 2007). Recent studies suggest that the incidence of brain metastases may be increasing (Palmieri et al. 2007); several causes have been proposed.

Patients live longer due to the use of molecular therapies, and thus secondary brain metastases may occur. New therapies cannot cross the blood-brain barrier, thus the brain may represent a preferential site for metastasis. Early detection may be performed as a result of refined imaging diagnosis and increased attention given to neurological symptoms. Tumor metastasis is considered a complicated process involving cell motility, invasion, platelet aggregating ability, angiogenesis, and avoidance of host immune response. Accordingly, the metastatic mechanism most likely represents

a multistep process involving both genetic and epigenetic changes that activate or inactivate tumor-related genes (Brodeur and Hogarty 1998). Several genomic regions including: 1q23, 8p12, 8q24, 17q24~q25, and 20q13 (by gains), and 4q, 5q, 9p21, 17p12, 19q23~24, and 18q21~q22 (by losses) have been identified as recurrently gained/lost in brain metastases (Petersen et al. 2000). Although no candidate target genes have been identified in these genomic regions, decreased expression of certain genes (*DCC*, *KAI-1*, *MYO18B*, *BAI-1*) has been identified as associated with progression in endometrial, prostate, colon and lung cancer (Nathoo et al. 2005; Wesseling et al. 2007). Aberrant CpG island promoter methylation has been also identified at non-random frequencies in brain metastases (Gonzalez-Gomez et al. 2003, 2004; Martinez-Glez et al. 2007) suggesting that this epigenetic mechanism may participate in the process of tumor metastasis and brain invasion.

Overexpression of several genes, including *EGFR*, *CD44RI*, *S100A4* or *c-erbB2* appears to be associated with an increased potential for metastasis in lung, colon or breast carcinoma (Wesseling et al. 2007). Increased gene dosage through copy gains



or amplification is a common genetic mechanism for upregulation of gene expression and amplification of certain genes and is associated with a poor prognosis (Arai et al. 1994; Brodeur and Hogarty, 1998; Nathoo et al. 2005). Therefore, an accurate identification of gene dosage may become an important clue to discriminating clinical outcome in patients with brain metastasis. Along these lines, real-time quantitative PCR analysis of gene dosage has been used to determine amplification or copy gains of tumor-related genes that lead to altered expression of proteins with important roles in the regulation of cell proliferation, invasion or metastasis (Collins 1995).

## OBJECTIVES

In this study, we used quantitative real-time polymerase chain reaction to determine gene dosage (copy gains/amplification) of eight tumor-related genes in a series of 18 brain metastases. This methodology allows detection of gene copy gains in addition to gene amplification.

## EQUIPMENT AND PROCEDURE

### DNA Extraction

Eighteen samples derived from brain metastases were available for this study. Tumors were immediately frozen and conserved at  $-80^{\circ}\text{C}$  after surgical removal. The metastases originated from lung cancer (six cases), breast carcinoma (three cases), melanoma (three samples), ovarian carcinoma (two cases), and one each from colon, bladder, and kidney carcinoma. The primary tumor origin in one sample could not be determined; accordingly it was diagnosed as undifferentiated carci-

noma. With mortar and pestle, tumor samples were homogenized for posterior DNA isolation according to the Wizard Genomic DNA Purification KIT (Promega Corporation, WI, USA) protocol for animal tissue. Briefly: For each sample Nuclei Lysis solution (0.5M EDTA pH 8.0) and Proteinase K (20 mg/mL) are added, and incubated over night at  $55^{\circ}\text{C}$ . RNase solution is added and incubated for 10–30 min at  $37^{\circ}\text{C}$ . At room temperature the Protein precipitation solution is added and vortexed. Chill sample on ice for 5 min. After centrifugation (4 min  $13,000\text{--}16,000 \times g$ ) carefully remove the supernatant containing the DNA (leaving the protein pellet behind) and transfer to a micropcentrifuge tube containing 600  $\mu\text{L}$  of room temperature isopropanol; gently mix and centrifuge 1 min at  $13,000\text{--}16,000 \times g$  at room temperature. Aspirate ethanol and air-dry the pellet for 10–15 min. Rehydrate the DNA with DNA rehydration solution: 10 mM Tris-HCL (pH 7.4)/1 mM EDTA (pH 8.0), and incubate at  $65^{\circ}\text{C}$  for 1 h, and overnight at  $4^{\circ}\text{C}$ .

### Quantitative-PCR: Amplification Status

This technique has been widely used by us for gene copy dosage screening in gliomas and brain metastases (Alonso et al. 2005; Arjona et al. 2005; Franco-Hernandez et al. 2007, 2008). In this report we used quantitative PCR to determine the dosage status of eight tumor-related genes that participate in the control of key cellular functions such as signal transduction control, regulation of cell proliferation, or encoding transcriptional factors. The genes analyzed were: *ELF3* (E74-like factor 3), *MDM4* (transformed 3T3 cell double minute 4) and *LRRN2* (leucine rich repeat neuronal 2; alias glioma amplified on chromosome 1 *GAC1*) (all three located at 1q32); *PDGFRA* (platelet derived growth factor

receptor alpha polypeptide) (at 4q11~q13); *EGFR* (epidermal growth factor receptor) (at 7p12); *MYC* (v-myc myelocytomatosis viral oncogene homolog; alias *c-MYC*) (8q24.12~q24.13); *MDM2* (transformed 3T3 cell double minute 2)(located at 12q13~q14); and *ERBB2* (erythroblastic leukemia viral oncogene homolog 2) (located at 17q21.2). For *ERBB2* and *EGFR*, the specific amplification status of the extracellular (EC) and intracellular (IC) domains was analyzed. Quantitative real-time PCR was performed using the LightCycler Fast Start DNA Master SYBR Green I kit and LightCycler (Roche Molecular Biochemical, Mannheim, Germany). As control we used the *18S* gene because its amplification and expression levels remain steady in both normal and tumoral tissues (Blanquicett et al. 2002). Primer sequences used for all genes have been described previously (Alonso et al. 2005; Arjona et al. 2005).

#### Procedure

PCR was performed in a volume of 20  $\mu$ L reaction containing 12  $\mu$ L of water, 2  $\mu$ L of  $MgCl_2$  stock solution 25 mM, 1  $\mu$ L of each primer 5.5 nM, 2  $\mu$ L of LC FastStart Reaction Mix and 100 ng of DNA tumor sample. All samples were loaded three times: first pipetted into capillary reservoir, then forced into glass capillary by centrifugation in LightCycler Centrifuge Adapters and run in a LightCycler 1.0 Instrument with capacity for 32 samples per run. PCR was carried out as follows: after an initial incubation step at 95°C, 45 amplification cycles of 10 s at 95°C, 10 s at 60–68°C, and a final extension cycle of 10 s at 72°C were performed. To confirm the specificity of the amplification signal, we considered the gene dissociation curve

in each case. To normalize the fluorescent signal of the differentially sized fragments, a ratio was calculated between each sample and a non-tumoral DNA, on the assumption that the gene dosage in normal tissue would be one. The relative amounts of each gene with respect to the control gene, *18S*, were determined using the LightCycler Relative Quantification Software provided by Roche Molecular Biochemical. The final results were calculated as a ration for each normalized gene dosage versus the reference dosage for every sample. A ratio between 1.2 and 5 was considered as a low amplification rate (copy gains), and values higher than 5.1 were considered positive for high amplification rates. All samples were analyzed in triplicate.

## RESULTS

Of the 18 samples, six (33%) were positive for amplification and ten (55%) positive for copy gains in at least one gene. Among the genes located at 1q, the most frequently involved was *LRRN2*: it was amplified in two cases (derived from lung carcinoma and from malignant melanoma), and copy gains of this gene were identified in a lesion derived from one lung carcinoma. Also, two samples derived from breast carcinoma displayed copy gains of *MDM4*, but no amplification was observed for this gene. *ELF3* showed neither amplification nor copy gains in any sample. Copy gains were identified for *MDM2* (two samples derived from undifferentiated and from lung carcinoma), *PDGFRA* and *MYC* (one sample each, from lung carcinoma); the last one was also amplified in a lesion derived from an ovarian carcinoma.

*EGFR* and *ERBB2* were analyzed at both EC and IC domains. *EGFR* alterations were obtained in six samples; amplification (ten- to 100-fold) was detected in at least one of the studied domains in four of 18 metastases (22%); these cases derived from kidney, ovarian and lung (two samples) carcinomas. Also, low gene amplification rates were identified in four cases: they derived from kidney, lung ( $\times 2$ ) carcinomas, and from malignant melanoma. In summary, one sample displayed amplification and another copy gains at both *EGFR* domains. Different patterns of gene dosage were found in the remaining four metastases: two cases displayed amplification at the IC region with copy gains in the corresponding EC regions; one tumor presented copy gains at the IC domain and normal dosage for the EC domain. Finally, amplification at the EC region and normal IC domain dosage characterized an ovarian carcinoma. *ERBB2* was positive for amplification of the IC domain, together with copy gains in the EC domain, in one sample. IC domain copy gains and normal EC domain dosage characterized an additional metastasis. Both lesions derived from lung carcinomas.

## FURTHER CONSIDERATIONS

Quantitative PCR has been demonstrated to be a more sensitive technique than others, such as Southern blot, which were previously used to determine gene amplification. Furthermore, quantitative PCR allows differentiation between copy gains and gene amplification; thus, providing important clues regarding various possible implications of gene dosage on tumor development and progression. Our work demonstrated the usefulness of this meth-

odology for identifying the presence of both gene dosage variations in brain metastasis lesions. We also identified distinct amplification patterns for the genes located at 1q32 (*LRRN2*, *ELF3* and *MDM4*); these genes are not always necessarily coamplified as was suggested to occur for *ELF3* and *LRRN2* in other brain tumors (Alonso et al. 2005).

Concurrent alterations of the genes we studied occurred in only three samples in our series: two derived from lung carcinoma and the third from an ovarian carcinoma. One lesion derived from a lung carcinoma accumulated copy gains of *LRRN2*, *MDM2*, *PDGFRA*, and the IC domain of *ERBB2*. The second lesion displayed copy gains of *EGFR* and *ERBB2* (IC and EC domains, respectively) and amplification of *LRRN2* and *ERBB2* (IC region). Finally, the lesion derived from an ovarian carcinoma presented amplification of *MYC* and of the EC region of *EGFR*.

Quantitative PCR allowed identification of a heterogeneous pattern of involvement in *EGFR* and *ERBB2* that generates distinct degrees of copy dosage for different gene regions: EC versus IC domains. This anomaly has also been described in malignant gliomas, specially involving *EGFR* (Malden et al. 1998; Alonso et al. 2005; Arjona et al. 2005). Amplification of the EC domain has been suggested to be associated with the genesis of mutant deletion forms; on the other hand amplification of the IC domain was proposed to be associated with increased expression of an independent ligand-binding truncated receptor (Malden et al., 1998).

In summary, quantitative PCR appears to be an important methodology to detect not only gene amplification, but also low-grade copy gains. Since gene amplifica-

tion appears to be associated with greater tumor aggressiveness early detection, even in brain metastatic lesions, may be of interest for clinical management and treatment.

## REFERENCES

- Alonso, M.E., Bello, M.J., Arjona, D., Martinez-Glez, V., de Campos, J.M., Isla, A., Kusak, M.E., Vaquero, J., Gutierrez, M., Sarasa, J.L., and Rey, J.A. (2005) Real-time quantitative PCR analysis of gene dosages reveals amplification in low-grade oligodendrogliomas. *Am. J. Clin. Pathol.* 123:900–906
- Arai, T., Ichimura, K., Hirakawa, K., and Yuasa, Y. (1994) DNA amplifications and elevated expression of proto-oncogenes in addition to altered DNA ploidy in metastatic brain tumors. *Clin. Exp. Metastasis* 12:267–275
- Arjona, D., Bello, M.J., Alonso, M.E., Isla, A., de Campos, J.M., Vaquero, J., Sarasa, J.L., Gutierrez, M., and Rey, J.A. (2005) Real-time quantitative PCR análisis of regions involved in gene amplification reveals gene overdose in low-grade astrocytic gliomas. *Diagn. Mol. Pathol.* 14:224–229
- Blanquicett, C., Johnson, M.R., Heslin, M., and Diasio, R.B. (2002) Housekeeping gene variability in normal and carcinomatous colorectal and liver tissues: application in pharmacogenomic gene expression studies. *Anal. Biochem.* 19:209–214
- Brodeur, G.M., and Hogarty, M.D. (1998) Gene amplification in human cancers: biological and clinical significance. In: Vogelstein, B., Kinzler, K.W. (eds) *The genetic basis of human cancer*. McGraw-Hill, New York, pp. 161–172
- Collins, V.P. (1995) Gene amplification in human gliomas. *Glia* 15:289–296
- Franco-Hernandez, C., Martinez-Glez, V., Arjona, D., de Campos, J.M., Isla, A., Gutierrez, M., Vaquero, J., and Rey, J.A. (2007) EGFR sequence variations and real-time quantitative polymerase Caín reaction análisis of gene dosage in brain metastases of solid tumors. *Cancer Genet. Cytogenet.* 173:63–67
- Franco-Hernandez, C., Martinez-Glez, V., de Campos, J.M., Isla, A., Vaquero, J., and Rey, J.A. (2008) Detection of gene amplification and copy gains in brain metastases of solid tumors using quantitative real-time polymerase Caín reaction. *Cancer Genet. Cytogenet.* 182:61–62
- Gonzalez-Gomez, P., Bello, M.J., Alonso, M.E., Lomas, J., Arjona, D., Amiñoso, C., de Campos, J.M., Isla, A., Gutierrez, M., and Rey, J.A. (2003) Frequent *death-associated protein-kinase* promoter hypermethylation in brain metastases of solid tumors. *Oncol. Rep.* 10:1031–1033
- Gonzalez-Gomez, P., Bello, M.J., Alonso, M.E., Amiñoso, C., Lopez-Marin, I., de Campos, J.M., Isla, A., Gutierrez, M., and Rey, J.A. (2004) Promoter methylation of multiple genes in brain metastases of solid tumors. *Int. J. Mol. Med.* 13:93–98
- Malden, M.T., Novak, U., Kaye, A.H., and Burgess, A.W. (1998) Selective amplification of the cytoplasmic domain of the epidermal growth factor receptor gene in glioblastoma multiforme. *Cancer Res.* 48:2711–2714
- Martinez-Glez, V., Franco-Hernandez, C., Gonzalez-Gomez, P., Isla, A., de Campos, J.M., Vaquero, J., Gutierrez, M., Casartelli, C., and Rey, J.A. (2007) *DAPK1* promoter hypermethylation in brain metastases and peripheral blood. *Neoplasia* 54:123–126
- Nathoo, N., Chahlavi, A., Barnett, G.H., and Toms, S.A. (2005) Pathobiology of brain metastases. *APMIS* 100:713–719
- Palmieri, D., Chambers, A.F., Felding-Habermann, B., Huang, S., and Steeg, P.S. (2007) The biology of metastasis to a sanctuary site. *Clin. Cancer Res.* 13:1656–1662
- Petersen, I., Hidalgo, A., Petersen, S., Schlüns, K., Schewe, C., Pacyna-Gengelbach, M., Goeze, A., Krebber, B., Knösel, T., Kaufmann, O., Szymas, J., and von Deimling, A. (2000) Chromosomal imbalances in brain metastasis of solid tumors. *Brain Pathol.* 10:395–401
- Wesseling, P., von Deimling, A., and Aldape, K.D. (2007) Metastatic tumours of the CNS. In: Luois, D.N., Ohgaki, H., Wiestler, O.D., Cavenee, W.K. (eds) *WHO classification of tumours of the Central Nervous System*. IARC, Lyon, pp. 247–252

*This page intentionally left blank*

# 7

## Cyclic AMP Phosphodiesterase-4 in Brain Tumor Biology: Immunochemical Analysis

B. Mark Woerner and Joshua B. Rubin

### INTRODUCTION

Furman and Shulman (1977) first recognized the relationship between abnormally low levels of cAMP and brain tumor growth. They found that both the activity of the cAMP synthetase, adenylate cyclase, and cAMP levels were inversely correlated with the degree of malignancy of brain tumors. The importance of PDE4 to tumor biology was first suggested by the antitumor activity of the PDE4 inhibitor Rolipram when tested *in vitro* against breast and lung carcinoma cell lines (Drees et al. 1993; Merz et al. 1998). More recently, McEwan et al. demonstrated Rolipram activity against colon carcinoma cells (McEwan et al. 2007), and we found that decreased cAMP levels stimulate brain tumor growth *in vivo* and that drugs that can elevate cAMP, including Rolipram, exhibit significant antitumor effects (Goldhoff et al. 2008; Yang et al. 2007). These studies strongly suggest that the PDE4 family of enzymes and PDE4 inhibitors be vigorously evaluated as vital targets to oncology.

Phosphodiesterases hydrolyze intracellular cAMP and cGMP to their respective 5' monophosphate forms, and thereby

function as negative regulators of multiple cyclic nucleotide-dependent processes. The PDE superfamily contains 11 subfamilies that are distinguished by sequence homology, substrate affinity, enzyme kinetics, and modulation by specific regulators (Conti and Jin 1999). The PDE4 subfamily is highly specific for cAMP and abundant in the brain (Cherry and Davis 1999). PDE4 was found to be the predominant isoform expressed in approximately two-thirds of 60 human tumor cell lines (Marko et al. 2000), and expression correlated with malignancy in mouse keratinocyte derived carcinoma lines (Marko et al. 1998). PDE4 expression was also evaluated in six human glioblastoma multiforme (GBM) cell lines where it was found to be present, but at lower levels than PDE1, a combined cAMP/cGMP hydrolase (Marko et al. 2000). We found that several histological subtypes of brain tumors expressed high levels of PDE4 and that PDE4 inhibition, in combination with standard radiation and chemotherapy, promoted a unique tumor regression in an intracranial xenograft model of GBM (Goldhoff et al. 2008).

The PDE4 family of phosphodiesterases can be further subdivided into four subfamilies derived from separate genes

(A–D). From these four genes at least 35 different functional isoforms are generated (Lugnier 2006). Through distinct combinations of localization motifs, regulatory sites and protein–protein interacting domains, the multiplicity of PDE4 isoforms performs a wide array of tissue and subcellular compartment specific functions (Lynch et al. 2006). For instance, only PDE4D5 regulates PKA-dependent heterotrimeric G protein switching by  $\beta_2$  – adrenergic receptors (Lynch et al. 2005). Similarly, PDE4D3 and PDE4C2, but not PDE4A4 or PDE4B1, are required for basal AKAP450-tethered protein kinase type II activity (McCahill et al. 2005).

The range of function and form within the PDE4 family constitutes an experimental challenge for those interested in evaluating changes in expression or localization as a basis for a difference in PDE4 activity. It is likely that functionally significant variations in PDE4 activity result from modulation in the expression or localization of a limited number of isoforms. Thus, antibody reagents that cannot distinguish between isoforms may, in some circumstances, be less useful than those that can. In this regard some consideration for the domain organization of the PDE family is warranted. The fundamental domain organization of PDE4 includes unique, isoform specific amino-terminal regions, two regulatory domains referred to as upstream conserved regions (UCR1 and UCR2), a highly conserved catalytic unit, and a subfamily or gene specific carboxy terminal domain (Figure 7.1). The multiplicity of PDE4 isoforms arises from splice variants that are derived from the four PDE4 genes (A–D). This results in three groups of PDE4 molecules: the long isoforms which include complete UCR1 and UCR2, the short

isoforms which contain only UCR2, and the super-short isoforms which contain a truncated UCR2. Thus, while the potential exists to utilize isoform specific reagents directed against the unique amino termini, most commercially available antibodies are directed against the carboxy-terminus and recognize all the members of one PDE4 subfamily without further distinction. Finally, while the carboxy-termini of PDE4B, PDE4C, and PDE4D are conserved between humans and rodents, the carboxy termini of human and rodent PDE4A diverge considerably.

## MATERIALS AND METHODS

Phosphodiesterase function is dependent upon which PDE4 isoforms are expressed, what their subcellular localization is, and what other proteins they are in complex with. Each of these elements of PDE4 function can be assessed with immunochemical methods. It is imperative that only the appropriate antibody reagents be utilized. Commercially available antibodies include those directed against a synthetic peptide common to most of the PDE4 subtypes and belonging to the PDE4A and D subfamilies. Alternatively, there are antibodies directed against the carboxy-terminus that can distinguish between members of different subfamilies. Furthermore, there are some isoform specific antibodies as well as antibodies against phosphorylated PDE4, such as the phospho-PDE4A-selective antibody. Finally, while many commercial antibody specifications indicate cross-reaction between human and animal PDE4, the sequence divergence between murine and human PDE4A can make this less likely, and caution should be used when identification of the immunizing peptide is treated as proprietary information.

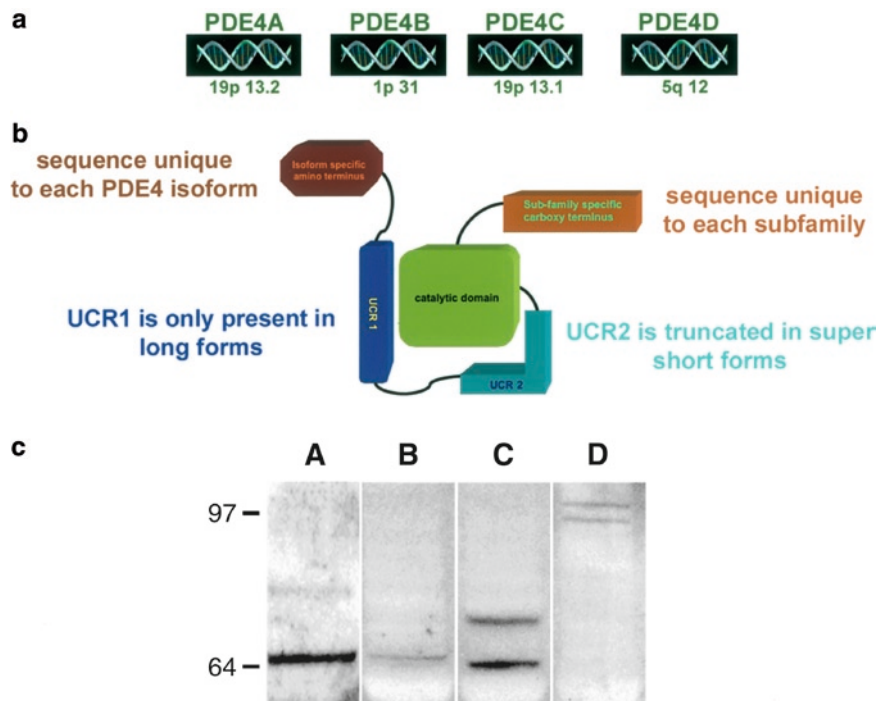


FIGURE 7.1. PDE4 exists as multiple isoforms. (a) Chromosomal location of the four PDE4 genes (A–D). (b) Domain organization of PDE4 isoforms consisting of unique isoform specific amino terminus, upstream conserved regions (UCR) 1 and 2, catalytic domain and subfamily (A–D) specific carboxy terminus. Long forms contain all five domains. Short and supershort forms do not contain UCR1. Supershort forms contain a truncated UCR2. (c) Western Blots of U87 glioblastoma cells probed with the human specific antibody for PDE4A (Houslay) and with PDE4 subfamily specific antibodies from FabGennix lanes 2 through 4. U87 cells express PDE4A isoforms of 66 and 80 kDa likely corresponding to PDE4A1 and PDE4Ax. The PDE4B antibody also reveals a band at 66 kDa indicating that U87 cells also express PDE4B4. Two isoforms of PDE4C are evident in U87 cells at 64 and 73 kDa. These correspond PDE4C2 and PDE4C3, respectively. Finally, the PDE4D antibody reveals a high molecular weight doublet corresponding to PDE4D3 at 95 kDa and PDE4D5 at 105 kDa

In the following sections we provide detailed protocols for investigating PDE4 protein expression.

## WESTERN BLOTTING

### Materials

1. Cell lysates were obtained from U87 cells, an established human brain tumor cell lines (ATTC)
2. Phosphate buffered saline (PBS), pH 7.35
3. RIPA Buffer: 150 mM NaCl, 10 mM Tris (pH 7.2), 0.1% SDS, 1.0% Triton X-100, 1% deoxycholate and 5 mM EDTA
4. Protease inhibitor cocktail: (1 mM phenylmethylsulfonyl fluoride, 10 mM benzamidine, aprotinin 5  $\mu$ g/mL, leupeptin 5  $\mu$ g/mL)
5. Protein Assay Bio-Rad DC Bradford system



6. NuPAGE LDS Sample Buffer (4X) Invitrogen (NP0007)
7. NuPAGE DTT Sample Reducing Agent Invitrogen (NP0004)
8. Molecular weight marker SeeBlue Plus2 Invitrogen (LC5925)
9. NuPAGE 10% Bis-Tris Gel Invitrogen (NP0301)
10. NuPAGE MOPS SDS Running Buffer Invitrogen (NP0001)
11. Gel running apparatus
12. Nitrocellulose Membrane Amersham
13. Transfer apparatus
14. NuPAGE Transfer Buffer Invitrogen (NP0006)
15. Tris buffered saline with 0.01% Tween-20 in TBST (pH 7.6)
16. Bovine serum albumin (BSA)
17. Antibodies used and their concentrations were as follows:
  - (a). hPDE4A-PDE-46 noncommercial polyclonal antibody made against human PDE4A (GST 788–886) used at a dilution of 1:400 (kind gift from M.D. Houslay)
  - (b). PDE4B- FabGennix (PD4-201AP) made against undisclosed synthetic peptides corresponding to N- & C-terminal region common to all PDE4B proteins, used at used at a concentration of 1  $\mu\text{g}/\text{mL}$
  - (c). PDE4C- FabGennix (PD4-301AP) made against an undisclosed synthetic peptide common to all PDE4C subtypes, used at a concentration of 1  $\mu\text{g}/\text{mL}$
  - (d). PDE4D- FabGennix (PD4-401AP) made against an undisclosed synthetic peptide common to all PDE4D subtypes, used at a concentration of 1  $\mu\text{g}/\text{mL}$
1. Goat anti-Rabbit-HRP Biorad (170–6515) used at a dilution of 1:25,000

2. Chemiluminescent Detection Super-Signal West Pico Pierce (34080)

## Methods

Western blotting is a method for quantifying protein expression in cell or tissue lysates. Under the denaturing conditions described below, electrophoresis of proteins through an acrylamide gel will result in their separation based on size. Immunolabeling of separated protein bands provides a reliable method for identification of individual proteins such as specific isoforms of PDE4. The coupling of antibody labeling to photon-emitting reactions or fluorescent tags supports the quantitation of relative protein abundance. Thus, Western blotting can identify which PDE4 isoforms are expressed and provide information regarding relative levels of expression between different cell lines or tissues as well as information regarding up- or down-regulation of specific isoforms under different growth conditions or in response to different stimuli (Figure 7.1).

1. Human astrocytoma cells (U87) are grown in serum supplemented media on 10 cm plates. When the cells are confluent, the plates are removed from the incubator and placed onto ice and rinsed two times with ice cold PBS.
2. Remove the PBS and add 0.5 mL RIPA lysis buffer supplemented with protease inhibitor cocktail to each 10 cm plate.
3. Scrape cells with a cell scraper into the RIPA buffer and transfer to microfuge tube.
4. Incubate on ice for 10 min. Vortex every few minutes to dissolve cell membranes. Alternatively, cells and tissue can be solubilized in a sonicator.

5. Centrifuge samples at 10,000 rpm for 5 min in a microfuge to pellet insoluble material.
6. Remove supernatant and discard the pellet.
7. Determine protein concentration of the supernatant with an assay kit according to manufacturer's instructions. We typically utilize the Bradford Assay (Bio-Rad).
8. Take a volume of supernatant that corresponds to 25  $\mu\text{g}$  of protein, add 4X concentrate of Sample Buffer and 10% by volume of DTT and heat to 70°C in boil proof Eppendorf tube for 10 min.
9. Load cooled mixture onto a 10% Bis-Tris gel. Load 5  $\mu\text{L}$  of molecular weight markers into a separate lane.
10. Run gels at 100 V for 115 min or until a 17 kDa marker has run off the gel.
11. Prepare the gel and nitrocellulose membranes for transfer by equilibrating in transfer buffer for 10 min.
12. Gels and nitrocellulose paper are then mounted into a transfer apparatus.
13. Transfer of proteins occurs at 150 V for 120 min.
14. Membranes (now blots) are removed from transfer apparatus. Non-specific antibody labeling is reduced by soaking the membrane for 1 h at room temperature (RT) in 4% BSA in TBST.
15. Primary antibodies are added to blots for overnight incubation at R.T. in 5 mL plastic sealable baggies and placed onto a nutator.
16. The next day, blots are rinsed in TBST three times for 10 min/wash.
17. Secondary antibody conjugated to HRP is added to blots at a concentration of 1:25,000 for 90 min at R.T. on the nutator.
18. Blots are rinsed in TBST three times for 10 min/wash and then developed in chemiluminescent reaction system according to manufacturers instructions; we prefer the West Pico Substrate from Pierce.
19. Blots are finally wrapped in Saran wrap, placed into a light tight cassette and developed with X-ray film in the dark room. Start with a 2 min exposure and change time as appropriate to develop bands on film.
20. Use molecular weight marker lane to gauge molecular weights of the bands.
21. To quantify protein expression, scan blots and quantify bands using Image J software from the NIH, a free imaging software that can be downloaded at <http://rsbweb.nih.gov/ij/download.html>.

## IMMUNOHISTOCHEMISTRY

### Materials

1. Tissue sections were obtained from archival tissue blocks sectioned to 5  $\mu\text{m}$  and placed onto positively coated (+) slides. Slides were dried in an oven for 1 h at 35°C.
2. Antigen Retrieval Solution Citrate buffer (pH 6.0) DAKO (S1699)
3. PAP Pen hydrophobic marker Vector (H-4000)
4. Tris buffered saline with 0.01% Tween-20 in TBST (pH 7.6)
5. Hydrogen Peroxide 30 wt.% solution in water Sigma-Aldrich (216763)
6. Avidin/Biotin Blocking Kit Vector (SP-2001)
7. Antibody Diluent: 1% Milk in TBS (pH 7.6) heated to and held at 60° C for 1

- h. After cooling, add 2% BSA, 0.1% Triton X-100, and 0.01% sodium azide
8. Normal swine serum Jackson ImmunoResearch (014-000-121)
9. Antibodies used and their concentrations were as follows:
  - (a). hPDE4A- PDE-46 (GST 788–886) used at a dilution of 1:400
  - (b). Swine anti-Rabbit Biotin Conjugate DAKO (E0431) used at a dilution of 1:450
10. Streptavidin-HRP DAKO (P0397) used at a dilution of 1:450
11. Diaminobenzidine Chromogen DAKO (K4366)
12. Hematoxylin Counterstain Gill 2 Richard-Allan Scientific (72504)
13. Permunt Fisher Scientific (SP15)
14. Xylenes and alcohols found in a typical histology staining system
2. Antigen Retrieve in 0.01 M Sodium Citrate (pH 6.0) at 95°C for 10 min, cool down on desktop for 10 min.
3. Rinse slides briefly in dH<sub>2</sub>O, circle tissue with PAP Pen.
4. Block endogenous peroxide with H<sub>2</sub>O<sub>2</sub> (3% in TBST for 15 min at RT).
5. Wash briefly in TBST.
6. Block with Avidin/Biotin for 15 min at RT, each reagent following manufacturers instructions.
7. Wash briefly in TBST after each block.
8. Block with 10% normal swine serum in diluent for 1 h at R.T.
9. Drain blocking solution and incubate in primary antibody overnight at R.T.
10. The next day, wash three times in TBST for 10 min/wash at RT
11. Incubate in Secondary Swine  $\alpha$  Rabbit Biotin conjugate for 90 min at a dilution of 1:450 at R.T.
12. Wash three times in TBST for 5 min/wash at R.T.
13. Incubate in Streptavidin-HRP for 60 min at a dilution of 1:450 at RT
14. Wash three times in TBST for 5 min/wash at RT
15. Develop in DAB following manufacturers instructions for 5 min or until there is sufficient staining.
16. Counterstain with hematoxylin.
17. Dehydrate through a series of alcohols and xylenes.
18. Mount with Permunt, allow to dry overnight and photograph.

## Methods

Immunohistochemistry is a method for detecting and localizing proteins of interest in tissue sections. Investigators can determine which cell types express a particular protein through colocalization of that protein and a second protein whose expression is limited to a specific cell type. As an example (Figure 7.2), we found that hPDE4A was localized to cells that had been found to express glial fibrillary acidic protein (GFAP) in serial sections (data not shown). In this fashion we were able to conclude that astrocytoma cells express PDE4A.

1. Deparaffinize slides and bring to H<sub>2</sub>O (two washes in xylene 5 min/wash, two washes in 100% EtOH 5 min/wash, one wash in 90% EtOH for 5 min and then place into 100% dH<sub>2</sub>O. All washes are done at R.T.

## IMMUNOCYTOCHEMISTRY

### Materials

1. DAOY cells, an established human medulloblastoma cell line (ATCC) engineered to express murine PDE4A1.

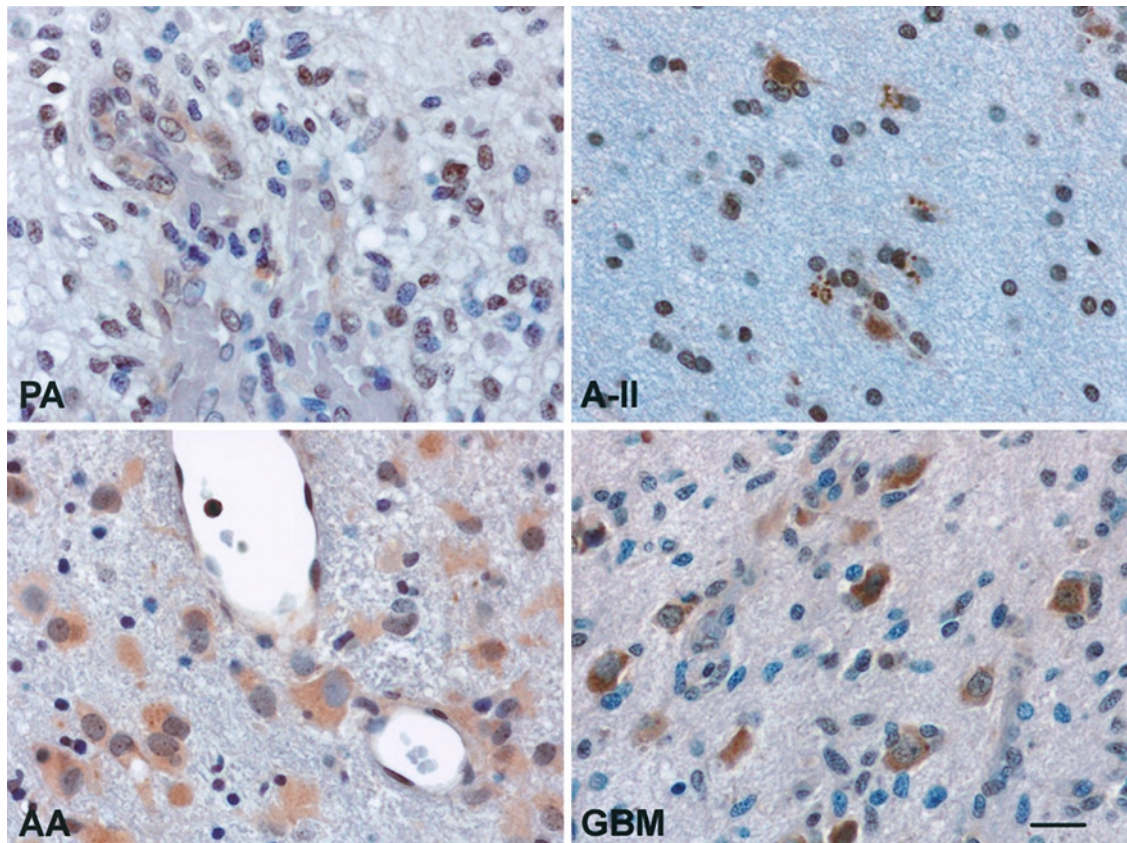


FIGURE 7.2. Astrocytomas of all grades express PDE4. – Immunohistochemical staining of human tumor specimens. PA- Grade I Pilocytic Astrocytoma, A-II Grade II Astrocytoma, AA- Grade III Anaplastic Astrocytoma and GBM- Grade IV Glioblastoma stained using a human specific PDE4A antibody. In all cases positive staining for PDE4A appears *brown*. Scale bar is 20  $\mu$ m

2. Fixative, Prefer, an aqueous glyoxal fixative obtained from Anatech Ltd.
3. Tris buffered saline with 0.01% Tween-20 in TBST (pH 7.6)
4. Antibody Diluent: pH 7.6 Tris Buffered Saline (TBS) with 2% IgG free BSA Jackson ImmunoResearch (001-000-161), 0.1% Triton X-100 and 0.01% sodium azide
5. Normal Donkey serum Jackson ImmunoResearch (017-000-121)
6. Antibodies used and their concentrations were as follows:
  - (a). PDE4A- Abcam (ab 14607) C-terminal region specific anti-body raised against an undisclosed peptide, used at a concentration of 4  $\mu$ g/mL
  - (b). 58K Golgi Protein- Abcam (ab27043) made against full length purified native rat protein and used at a concentration of 1 mg/mL
  - (c). Donkey anti-Rabbit AlexaFluor 555 Molecular Probes (A-31572) used at a dilution of 1:2000
  - (d). Donkey anti-Mouse AlexaFluor 488 Molecular Probes (A-21202) used at a dilution of 1:2000
7. DAPI 4', 6-diamidino-2-phenyl-indole dihydrochloride Molecular Probes

(D-1306) 14.3 mM stock at a dilution of 1:10,000

8. Immu-Mount mounting media Thermo Scientific (9990402)

## Methods

Immunocytochemistry is a method for detecting and localizing proteins of interest in cells grown in culture. Through the use of multiple antibodies and fluorophore detection techniques, more than one protein can be detected simultaneously. Thus, co-localization of a protein of interest with a marker of a subcellular organelle can identify that organelle as a domain in which the protein functions. As an example, the subcellular localization of virally encoded murine PDE4A1 to the Golgi membranes of Daoy cells was achieved by double labeling cells with an antibody directed against murine PDE4 and a second antibody directed against the 58KD Golgi Marker. The use of green and red fluorophores allows for the detection of protein colocalization through the merging of the green and red images and the generation of a yellow signal in the regions of co-localization (Figure 7.3).

1. Human DAOY medulloblastoma cells expressing murine PDE4A1 are grown on coverslips.
2. Rinse with ice cold TBS twice briefly.
3. Fix with ice-cold fixative for 15 min on ice.
4. Wash two times with TBST for 1 min/wash at RT.
5. Permeabilize cells with 0.5% Triton X-100 for 10 min at RT.
6. Wash three times in TBST for 10 min/wash at RT.
7. Block with 5% normal donkey serum in diluent for 60 min at RT.

8. Remove blocking solution without rinsing.
9. Incubate in both primaries overnight at 4°C.
10. The next day, wash three times in TBST for 10 min/wash.
11. Incubate in both secondary Alexafluors for 90 min at RT.
12. Remove antibody solution and incubate with DAPI for 10 min at RT.
13. Wash three times TBST for 10 min/wash at RT.
14. Mount with Immu-Mount.

## RESULTS AND DISCUSSION

A strong relationship exists between malignant brain tumor growth and low levels of cAMP (Furman and Shulman 1977; Racagni et al. 1983). In general, low levels of cAMP may be attained through either inhibition of adenylate cyclase as occurs downstream of Gi-coupled G protein coupled receptors (Sunahara and Taussig 2002), or through increased action of phosphodiesterases (Lugnier 2006). We have generated data to support both mechanisms for maintaining low levels of cAMP (Goldhoff et al. 2008; Warrington et al. 2007; Yang et al. 2007) and present data here that indicate PDE4 is highly expressed in both astrocyomas and medulloblastomas (Figures 7.1–7.3).

It is not realistic to speak of cAMP levels as if a single level applies to the entire cell. Indeed, fluorescent probes for cAMP levels have made it clear that cAMP levels change within microdomains suggesting that it is microdomains of cAMP that regulate cellular function (Ponsioen et al. 2004). In this regard the described functions of the PDE4 family are particularly relevant. The

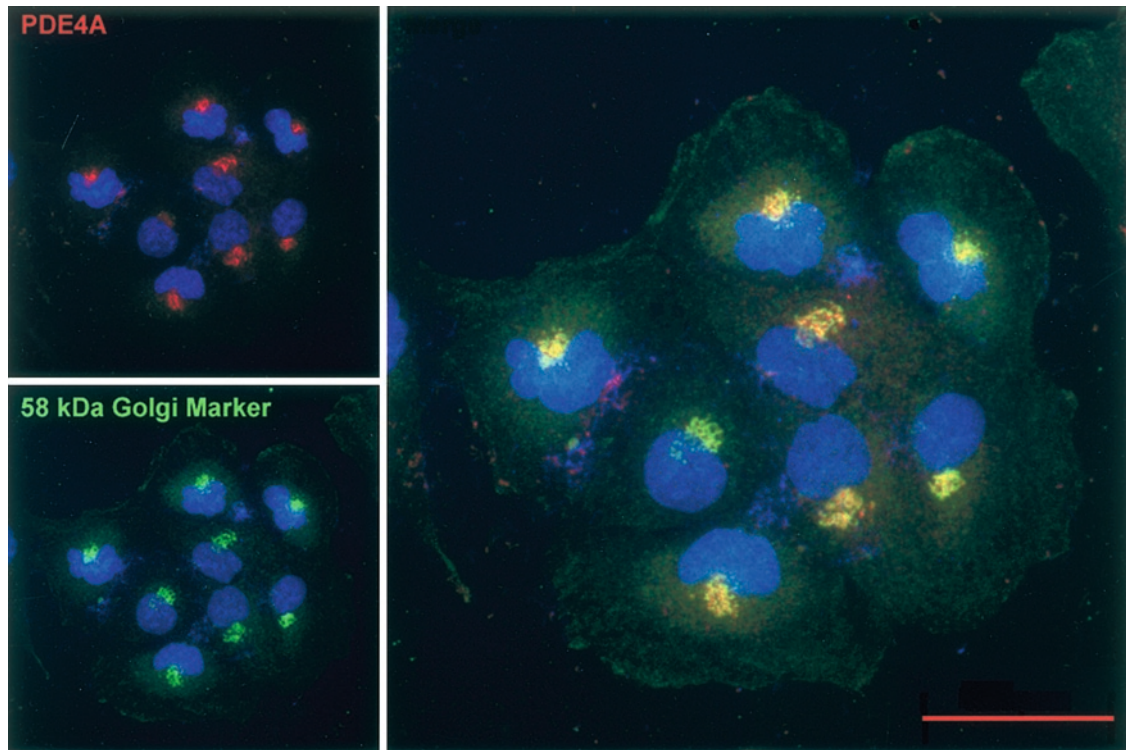


FIGURE 7.3. PDE4A1 is localized to the Golgi. Daoy medulloblastoma cells were infected with lentivirus encoding murine PDE4A1. Immunofluorescent co-localization of murine PDE4A (red) and a 58 kDa Golgi Marker (green) reveals that the two proteins are co-localized as evidenced by yellow appearance when the color channels are combined. Nuclei are stained with DAPI. *Scale bar* is 20  $\mu$ m

extended family of PDE4 isoforms allows not only for tissue specific expression of PDE4 activity but subcellular localization of different isoforms, which support the spatial resolution of cAMP signaling. As an example, we have found that PDE4A1 stimulates brain tumor growth (Goldhoff et al. 2008; Yang et al. 2007). This particular isoform of PDE4 is localized to the Golgi (Figure 7.3). Thus, the cAMP-sensitive mediators of PDE4A1 effects must also be localized to this domain.

Utilizing the methods described above it is possible to detect individual PDE4 isoforms in tissue and cells and to localize PDE4 to particular cells and to subcellular compartments (Figures 7.2 and 7.3).

These studies provide the foundation for generating hypotheses about specific PDE4 isoforms and function. Coupled with techniques to generate mutant PDE4 isoforms in which localization, catalytic and protein-protein interacting domains are disrupted, these kinds of studies allow investigators to dissect out the dependence of specific PDE4 functions on particular PDE4 domains (Huston et al. 2006; Scotland and Houslay 1995; Shakur et al. 1993).

Among the most attractive aspects of PDE4 inquiry is the number of clinically available PDE4 inhibitors. Currently there is an active program for the evaluation of PDE inhibition in the treatment of chronic obstructive pulmonary disease (Spina

2008). There are nearly twenty clinically available, some with known isoform specificity. This has the advantage of efficacy for specific indications without excessive toxicity or off target effects. Ample preclinical investigation, demonstrating a potential application would stand the chance of rapid translation.

Rolipram, a pan-PDE4 inhibitor, was developed as an anti-depressant (Wachtel and Schneider 1986) and has also been evaluated as an anti-inflammatory in multiple sclerosis (Dyke and Montana 2002). It is relatively well tolerated with nausea and emesis the limiting toxicities. Rolipram penetrates into the central nervous system and does not induce its own metabolism. Based on the activity of cAMP analogues as antitumor cell agents, Rolipram has been evaluated for antitumor cell activity in a limited number of in vitro studies. Antitumor activity has been described for chronic B-cell leukemia cells (Siegmond et al. 2001), acute lymphocytic leukemia (Ogawa et al. 2002) as well as for an astrocytoma cell line (Chen et al. 2002). Further, we have evaluated Rolipram in an extensive in vivo study in which we compared the antitumor effect of Rolipram alone to Rolipram in combination with conformal radiotherapy and temozolomide in an intracranial xenograft model of glioblastoma multiforme. Rolipram, in combination with radiation and temozolomide was observed to promote significant tumor regression (Goldhoff et al. 2008). These data again emphasize the importance of cAMP to brain tumor growth and the importance of PDE4 to cAMP regulation in brain tumors.

The scope of investigations into identifying individual PDE4 isoforms, their physiological roles, their subcellular local-

ization, associated interacting proteins and the impact of specific inhibitors on numerous biological functions and in diseases will be a richly promising and rewarding line of work for some time to come.

*Acknowledgements.* The authors thank Nicole Warrington for critical reading of the manuscript. This work was supported by the NCI/NIH (CA118389) to JBR.

## REFERENCES

- Chen, T.C., Wadsten, P., Su, S., Rawlinson, N., Hofman, F.M., Hill, C.K., and Schonthal, A.H. (2002) The type IV phosphodiesterase inhibitor rolipram induces expression of the cell cycle inhibitors p21(Cip1) and p27(Kip1), resulting in growth inhibition, increased differentiation, and subsequent apoptosis of malignant A-172 glioma cells. *Cancer Biol. Ther.* 1:268–276
- Cherry, J.A., and Davis, R.L. (1999) Cyclic AMP phosphodiesterases are localized in regions of the mouse brain associated with reinforcement, movement, and affect. *J. Comp. Neurol.* 407:287–301
- Conti, M., and Jin, S.L. (1999) The molecular biology of cyclic nucleotide phosphodiesterases. *Prog. Nucl. Acid Res. Mol. Biol.* 63:1–38
- Drees, M., Zimmermann, R., and Eisenbrand, G. (1993) 3',5'-Cyclic nucleotide phosphodiesterase in tumor cells as potential target for tumor growth inhibition. *Cancer Res.* 53:3058–3061
- Dyke, H.J., and Montana, J.G. (2002) Update on the therapeutic potential of PDE4 inhibitors. *Expert Opin. Investig. Drugs* 11: 1–13
- Furman, M.A., and Shulman, K. (1977) Cyclic AMP and adenylyl cyclase in brain tumors. *J. Neurosurg.* 46:477–483
- Goldhoff, P., Warrington, N.M., Limbrick, D.D. Jr., Hope, A., Woerner, B.M., Jackson, E., Perry, A., Piwnica-Worms, D., and Rubin, J.B. (2008) Targeted inhibition of cyclic AMP phosphodiesterase-4 promotes brain tumor regression. *Clin. Cancer Res.* 14: 7717–7725

- Huston, E., Gall, I., Houslay, T.M., and Houslay, M.D. (2006) Helix-1 of the cAMP-specific phosphodiesterase PDE4A1 regulates its phospholipase-D-dependent redistribution in response to release of Ca<sup>2+</sup>. *J. Cell Sci.* 119:3799–3810
- Lugnier, C. (2006) Cyclic nucleotide phosphodiesterase (PDE) superfamily: a new target for the development of specific therapeutic agents. *Pharmacol. Ther.* 109:366–398
- Lynch, M.J., Baillie, G.S., Mohamed, A., Li, X., Maisonneuve, C., Klussmann, E., van Heeke, G., and Houslay, M.D. (2005) RNA silencing identifies PDE4D5 as the functionally relevant cAMP phosphodiesterase interacting with beta arrestin to control the protein kinase A/AKAP79-mediated switching of the beta2-adrenergic receptor to activation of ERK in HEK293B2 cells. *J. Biol. Chem.* 280:33178–3389
- Lynch, M.J., Hill, E.V., and Houslay, M.D. (2006) Intracellular targeting of phosphodiesterase-4 underpins compartmentalized cAMP signaling. *Curr. Top. Dev. Biol.* 75:225–259
- Marko, D., Pahlke, G., Merz, K.H., and Eisenbrand, G. (2000) Cyclic 3',5'-nucleotide phosphodiesterases: potential targets for anticancer therapy. *Chem. Res. Toxicol.* 13:944–948
- Marko, D., Romanakis, K., Zankl, H., Furstenberger, G., Steinbauer, B., and Eisenbrand, G. (1998) Induction of apoptosis by an inhibitor of cAMP-specific PDE in malignant murine carcinoma cells overexpressing PDE activity in comparison to their nonmalignant counterparts. *Cell Biochem. Biophys.* 28:75–101
- McCahill, A., McSorley, T., Huston, E., Hill, E.V., Lynch, M.J., Gall, I., Keryer, G., Lygren, B., Tasken, K., van Heeke, G., and Houslay, M.D. (2005) In resting COS1 cells a dominant negative approach shows that specific, anchored PDE4 cAMP phosphodiesterase isoforms gate the activation, by basal cyclic AMP production, of AKAP-tethered protein kinase A type II located in the centrosomal region. *Cell Signal* 17:1158–1173
- McEwan, D.G., Brunton, V.G., Baillie, G.S., Leslie, N.R., Houslay, M.D., and Frame, M.C. (2007) Chemoresistant KM12C colon cancer cells are addicted to low cyclic AMP levels in a phosphodiesterase 4-regulated compartment via effects on phosphoinositide 3-kinase. *Cancer Res.* 67:5248–5257
- Merz, K.H., Marko, D., Regiert, T., Reiss, G., Frank, W., and Eisenbrand, G. (1998) Synthesis of 7-benzylamino-6-chloro-2-piperazino-4-pyrrolidinopteridine and novel derivatives free of positional isomers. Potent inhibitors of cAMP-specific phosphodiesterase and of malignant tumor cell growth. *J. Med. Chem.* 41:4733–4743
- Ogawa, R., Streiff, M.B., Bugayenko, A., and Kato, G.J. (2002) Inhibition of PDE4 phosphodiesterase activity induces growth suppression, apoptosis, glucocorticoid sensitivity, p53, and p21(WAF1/CIP1) proteins in human acute lymphoblastic leukemia cells. *Blood* 99: 3390–3397
- Ponsioen, B., Zhao, J., Riedl, J., Zwartkruis, F., van der Krogt, G., Zaccolo, M., Moolenaar, W.H., Bos, J.L., and Jalink, K. (2004) Detecting cAMP-induced Epac activation by fluorescence resonance energy transfer: Epac as a novel cAMP indicator. *EMBO Rep.* 5:1176–1180
- Racagni, G., Pezzotta, S., Giordana, M.T., Iuliano, E., Mocchetti, I., Spanu, G., Sangiovanni, G., and Paoletti, P. (1983) Cyclic nucleotides in experimental and human brain tumors. *J. Neurooncol.* 1:61–67
- Scotland, G., and Houslay, M.D. (1995) Chimeric constructs show that the unique N-terminal domain of the cyclic AMP phosphodiesterase RD1 (RNPDE4A1A; rPDE-IVA1) can confer membrane association upon the normally cytosolic protein chloramphenicol acetyltransferase. *Biochem. J.* 308 (Pt 2):673–681
- Shakur, Y., Pryde, J.G., and Houslay, M.D. (1993) Engineered deletion of the unique N-terminal domain of the cyclic AMP-specific phosphodiesterase RD1 prevents plasma membrane association and the attainment of enhanced thermostability without altering its sensitivity to inhibition by rolipram. *Biochem. J.* 292 (Pt 3):677–686
- Siegmund, B., Welsch, J., Loher, F., Meinhardt, G., Emmerich, B., Endres, S., and Eigler, A. (2001) Phosphodiesterase type 4 inhibitor suppresses expression of anti-apoptotic members of the Bcl-2 family in B-CLL cells and induces caspase-dependent apoptosis. *Leukemia* 15:1564–1571
- Spina, D. (2008) PDE4 inhibitors: current status. *Br. J. Pharmacol.* 155:308–315



- Sunahara, R.K., and Taussig, R. (2002) Isoforms of mammalian adenylyl cyclase: multiplicities of signaling. *Mol. Interv.* 2:168–184
- Wachtel, H., and Schneider, H.H. (1986) Rolipram, a novel antidepressant drug, reverses the hypothermia and hypokinesia of monoamine-depleted mice by an action beyond postsynaptic monoamine receptors. *Neuropharmacology* 25:1119–1126
- Warrington, N.M., Woerner, B.M., Dagainakatte, G.C., Dasgupta, B., Perry, A., Gutmann, D.H., and Rubin, J.B. (2007) Spatiotemporal differences in CXCL12 expression and cyclic AMP underlie the unique pattern of optic glioma growth in neurofibromatosis type 1. *Cancer Res.* 67:8588–8595
- Yang, L., Jackson, E., Woerner, B.M., Perry, A., Piwnica-Worms, D., and Rubin, J.B. (2007) Blocking CXCR4-mediated cyclic amp suppression inhibits brain tumor growth *in vivo*. *Cancer Res.* 67:651–658

# 8

## Radiosurgical Treatment of Progressive Malignant Brain Tumors

Cole A. Giller

### INTRODUCTION

This chapter will focus on one of the most feared scenarios in clinical medicine: the neurologically well patient who harbors an unresectable malignant brain tumor that is growing despite extensive adjuvant therapy. All proven therapeutic avenues have been exhausted and the patient is doomed to a crushing neurological death, despite, at least for the moment, being neurologically normal. Far from occasional curiosities, these scenarios are becoming commonplace in busy oncology centers as advances in surgical technique, chemotherapy, and conformal radiotherapy allow patients to live long enough to develop these serious intracranial tumors. The clinician, therefore, is faced with a disturbing dilemma: what can be offered to these desperate patients when all proven methods of treatment have failed?

A common suggestion is to offer more radiosurgery. Radiosurgery is the treatment of tumors with fields of radiation focused so precisely that the amount of radiation received by the surrounding normal tissue and nearby critical structures

is negligible. The dose to the tumor can, therefore, be extraordinarily high, yielding a high efficacy augmented by a radiobiology that is different than conventional fractionated schedules. Radiosurgery is commonly suggested in these desperate situations because it is both efficacious and noninvasive.

A full discussion of the management of progressive malignant brain tumors would consider all treatment modalities, but is beyond the scope of this chapter. We will instead limit our attention to how radiosurgery might be used in the setting described earlier, and in keeping with the theme of this book, i.e. the methodology used for such radiosurgical treatment. It is important to remember that we are assuming that standard radiosurgery has either already failed to control the tumor progression or is considered inappropriate. Our task, therefore, is not only to discuss the radiosurgical technique, but also to develop a methodology of clinical thinking for these dire situations. The methodologies include treatment philosophy, indications, choice of fractionation schedule, and dosimetry.

## METHODOLOGY OF TREATMENT PHILOSOPHY

It may seem odd to suggest a methodology for a component of a treatment philosophy, but the setting we have chosen is one for which all accepted therapy has been exhausted and for which there is no Class I evidence to support treatment. How then can further radiosurgery be offered? What is the methodology of thinking that could justify such a decision? We believe that treatment can be philosophically justified by the following three 'methodological' aspects. First, note that the situation is desperate, the patient will not be neurologically well for much longer, and there is little to lose. One might argue that uncertain treatment should be withheld in order to allow the patient to enjoy what is left of his or her life. However, as long as there is some hope of efficacy, and we will show later in this Chapter that this is the case for some types of radiosurgical treatment, it seems reasonable to offer treatment to these desperate patients. Such discussions are common in oncology clinics, and in fact, some believe that clinicians are obligated to offer such options. Furthermore, we do not believe that patients are too frightened or too naive to weigh the options or to make good medical decisions. After all, people make shrewd financial decisions and face critical family issues when they are not busy being our patients, and most are not easily swayed against their best interests in their normal lives. It has been our experience that patients and their families make appropriate decisions, even when confronted by complex uncertainty. Many have said yes, while many others have said no.

Second, although a common argument against treatment is the availability of research protocols, enrollment may not be appropriate for all patients for at least two reasons: (1) appropriate protocols are frequently not available to a particular patient for reasons of time, distance, and eligibility, (2) many protocols do not address real clinical circumstances, but instead address simplified versions of the disease, for example, single intracranial metastatic lesions, while most patients suffer from more complex versions. In other words, protocols might not fit the needs of the individual patient. The issue is admittedly intricate, requiring the clinician to make the difficult choice of whether an uncertain treatment is preferable to enrollment in a formal protocol for each particular patient.

Finally, there are humanistic reasons to offer uncertain therapies in desperate situations. When faced with an outwardly healthy patient who is enjoying life but knows that a neurological end is near, we find it difficult to take the purist's position and say 'there is nothing we can do' because of the lack of strong data. Instead, we find it more appropriate to explain the pros and cons of various uncertain options, provided we believe there is a reasonable hope of safety and efficacy. The agonizing problem for the clinician is that the judgment of what constitutes an adequate 'reasonable hope' is often a matter of personal judgment, philosophy, and taste.

## METHODOLOGY OF INDICATIONS

Even when the philosophical decision has been made to offer radiosurgical treatment despite significant uncertainties,

a methodology for choosing indications may be helpful in our setting, especially when there are traditionally no indications. In particular, one may consider three particular indications.

The first indication for further radiosurgery is that there is no other available therapy that is less uncertain. For example, it makes little sense to offer a course of hypofractionated radiosurgery (i.e., radiosurgery using a small number of fractions) to treat a brain tumor with mass effect if the surgeon believes the tumor can be safely resected. Likewise, it may be best to withhold radiosurgery if the medical oncologist believes that further chemotherapy is safe and highly likely to induce a favorable response. In other words, before offering uncertain therapy we must make sure that the situation is appropriately desperate.

A second indication is the requirement that tumor control would make a meaningful difference in either survival or quality of life for the individual patient. For example, further radiosurgery is not indicated for the cachectic patient in the end stages of metastatic cancer, nor is it necessarily indicated to treat a small, asymptomatic tumor that has grown only 1 mm during the past year. Decisions for scenarios between these extremes can be difficult, but radiosurgery is not indicated unless successful tumor control would make a clinical difference.

Finally, there must be some chance that further radiosurgery will lead to a meaningful degree of tumor control for a reasonable length of time. Because we have assumed that there are no definitive data in support of such treatment, the decision is necessarily subjective. Nevertheless, we will present an experience later in this chapter that can justify a cautious optimism.

## METHODOLOGY OF CHOICE OF FRACTIONATION SCHEDULE

Having made the difficult decision to treat and having satisfied appropriate indications, the clinician must choose a fractionation schedule. In practice, the number of fractions will range between one and five. This is because the effect of a higher number of fractions is close to that of conventional radiotherapy, which we have assumed has either failed or cannot be offered. This choice is reflected by the definition of radiosurgery sanctioned by the AANS, CNS and ASTRO as ‘typically ... performed in a single session ... but can be performed in a limited number of sessions, up to a maximum of five’ (Barnett et al. 2007).

‘Single shot’ radiosurgery, i.e., radiosurgery given as a high dose in a single fraction, is the schedule used by the inventors of radiosurgery and used for Gamma Knife treatments. It is often more effective than conventional fractionation, and can be effective even after conventional radiotherapy has failed. For example, tumors such as renal cell carcinoma, melanoma, and sarcoma are usually ‘radioresistant’ to conventional radiotherapy but respond well to single shot radiosurgery (Brown et al. 2002). Because of these radiobiological differences, and because there is an extensive experience with single shot dosimetry, one might argue that single shot radiosurgery should be the optimum choice for every tumor.

In the previous section, however, we agreed to limit our consideration to tumors not amenable to standard single shot radiosurgery. Moreover, single shot treatment of many tumors in our scenario would

have significant risks of radionecrosis and neurological morbidity for several reasons. For a given dose, the risk of radionecrosis is higher for tumors larger than 2 or 3 cm in diameter (Shaw et al. 2000), and many of the tumors found in our desperate scenario are of this size. Tumors surrounded by edema, accompanied by mass effect, or those that have been heavily pretreated with radiation also pose significant problems because of the risk of radionecrosis after single shot radiosurgery. Treatment of tumors in infants or young children may be accompanied by higher risk because of the fragility of the pediatric cerebral tissue, and treatment of tumors located in eloquent areas, such as the brainstem or motor cortex, pose special problems because even a small amount of radiation induced toxicity can produce unacceptable clinical symptoms.

This means that for the scenarios under consideration, circumstances encourage the clinician to use radiosurgery schedules with two to five fractions, i.e., to choose hypofractionation. Although there is no Class I data proving that hypofractionated radiosurgery is safer or more efficacious in our desperate scenarios, hypofractionation is commonly chosen for reasons outlined above (Adler et al. 1999; Giller et al. 2004, 2005, 2007; Nishizaki et al. 2006).

Although hypofractionation is a natural choice for our chosen scenario, we do not know of data that would help to decide between three, four or five fractions. The decision for three fractions is sometimes made based on the belief that a fewer number of fractions better approximates the radiobiology of single shot radiosurgery, but this assumption is unproven. Decisions are also made according to what other groups have done, although the data

for these decisions may not be compelling and some groups alter their fractionation schedules with time. We use three fractions when we want to enhance efficacy and use five fractions when we want to enhance safety, but admit that this is one of the important uncertainties motivating the discussions earlier in this chapter.

## METHODOLOGY OF DOSIMETRY

Dosimetry refers to the doses of radiation chosen for the radiation field and the choice of how that field is constructed. It, therefore, encompasses the most critical decision in the delivery of radiosurgery, high doses represent aggressive therapy with a higher probability of tumor control but carry a higher risk of damage to normal tissues, whereas low doses represent safer therapy with less chance of tumor control. Most of the important clinical tradeoffs are embedded within dosimetric decisions, and so we will elaborate upon this subject.

We consider four types of important dosimetric considerations: the summary of past empirical experience, consideration of late versus, early effects, the equivalence of fractionation schedules, and the effects of different treatment isodose lines. We will discuss each of these considerations and then show how they can be combined to construct a radiosurgical plan for progressive malignant brain tumors.

*Dosimetry Consideration #1: Past Experience.* The first factor that must be considered when choosing a dosage is the past experience of other groups. Some of this experience may have been gathered empirically and some may be justified by

theory, but a well documented experience can be invaluable in choosing dosimetry for the individual patient. We can summarize much of the prior experience with hypofractionation used to treat malignant brain tumors as follows: many groups use three fractions of 5–6 Gy each, and many groups use five fractions of 4–5 Gy each ('Gy' refers to Gray, the unit of dose). Our experience is similar, and we consider a schedule of five fractions of 5 Gy each to be a standard starting point for difficult tumors, and consider five fractions of 6 Gy each to be aggressive. As stated before, we will use three fractions when we want to closely approach the radiobiology of single shot radiosurgery, and view this as a more aggressive regimen. These heuristics provide an empiric starting point, and are of course modified by the size of the tumor, the estimated fragility of the tissue, and the wishes of the patient regarding aggressive treatment.

*Dosimetry Consideration #2: Late versus Early Effects.* The second consideration for dosimetry is the realization that different tissues respond differently to radiation. Traditionally, this has been expressed by dividing tissues into 'early responders' and 'late responders', indicating the time required to observe a biological response to the radiation. Because malignant tumors are composed of rapidly dividing cells, they are early responders, a brisk early response is equivalent to good tumor control. Because the cells of normal tissue divide more slowly, they are late responders and so a brisk late response is equivalent to unwanted damage to normal tissues. Theoretically, a schedule with a higher number of fractions should affect early responding tissue (i.e., the tumor) more strongly than late responding tissue

(i.e., normal surrounding tissue). The goal of radiosurgery is to choose a fractionation schedule that optimizes this difference.

*Dosimetry Consideration #3: Fractionation Schedules.* The third consideration for dosimetry is the comparison of different fractionation schedules. Rational choice of dose and number of fractions requires accurate comparison of different schedules to assess the effects on both early and late responding tissues. Radiation oncologists have developed various theoretical methods to make such comparisons when comparing conventional schedules in which the number of fractions is relatively high (Hall 2000; Liu et al. 2003). A popular such method is the 'linear-quadratic' theory, in which a 'biological equivalent dose' (BED) is calculated, and used to compare the effects of different fractionation schedules. BED is given by

$$\text{BED} = nD(1 + D/r) = T(1 + T/(nr))$$

where  $n$  is the number of fractions,  $D$  is the dose per fraction,  $T = nD$  is the total dose, and  $r$  is a quantity (the 'alpha over beta') that is low for late responding tissues and high for early responding tissues. Reasonable values of  $r$  for malignant brain tumors and normal brain tissue are 10 and 3, respectively.

In order to assess a fractionated schedule, we express the effects upon early and late responding tissues as an equivalent single shot plan, and use our experience with single shot dosimetry to guide the final choice of dose. To do this, we calculate the single shot dose  $T_1$  that has the same BED as a fractionated schedule using  $n$  fractions with total dose  $T_n$ . The BED for the single shot plan is

$$T_1 (1 + T_1 / r),$$

whereas the BED for the fractionated plan is

$$T_n (1 + T_n / (nr)).$$

Setting these expressions equal to one another and doing some algebra yields

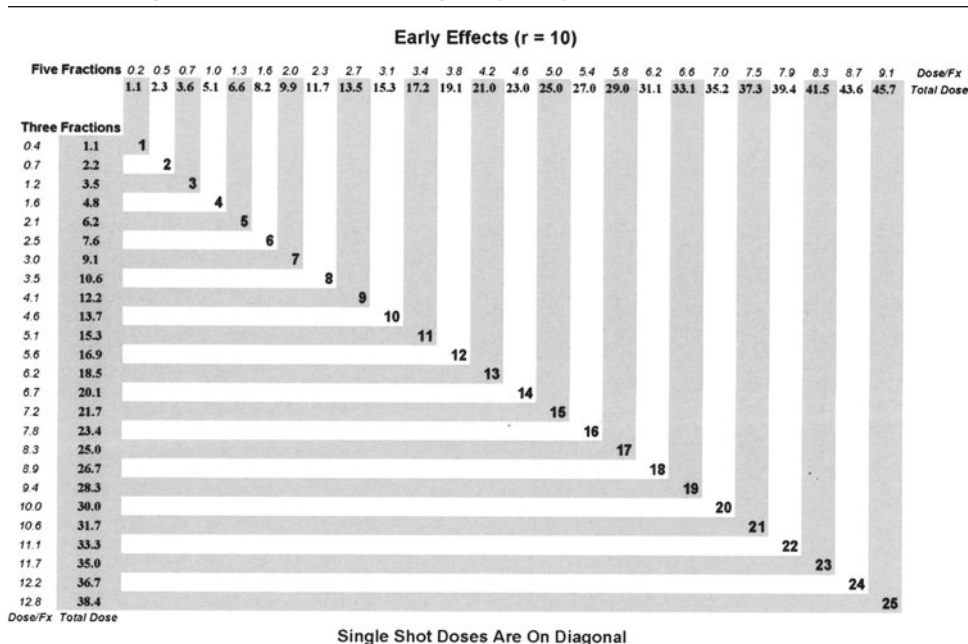
$$T_1 = (T_n (r + T_n / n) + r^2 / 4)^{1/2} - r / 2. \quad (8.1)$$

This equation was used to create Tables 8.1, 8.2, and Figure 8.1, and similar tables have been constructed by others (Liu et al. 2003). The graphs in Figure 8.1 show that for a particular total dose for the fractionated plan, the single shot equivalent doses for early responding tissues are higher than those for late responding tissues. This is advantageous because the tumor is receiving a higher equivalent dose than the surrounding normal tissue, and hence these

calculations confirm the advantage of fractionation. The graphs show that plans using three fractions yield single shot equivalent doses that are ~1.5 Gy less for normal tissue than for the target for plans with three fractions, and that are ~2 Gy less for normal tissue than for the target for plans with five fractions. In other words, hypofractionation ‘buys’ us 1–2 Gy.

One strategy that takes advantage of these calculations is to choose a single shot dose felt to be efficacious, and use Table 8.1 to calculate the equivalent fractionated total dose for early responding tissue. This dose is then converted to a single shot equivalent dose for late responding tissue using Table 8.2 in order to assess the effect on the nearby surrounding brain and critical structures. For example, suppose we believe that an appropriate single-shot marginal dose to treat a particular tumor is 15 Gy. Table 8.1 shows that the equivalent total dose for

TABLE 8.1. Single Shot Doses are shown diagonally: Early Effects (r = 10)



Single Shot Doses Are On Diagonal

TABLE 8.2. Single Shot Doses are shown diagonally: Early Effects ( $r = 3$ )

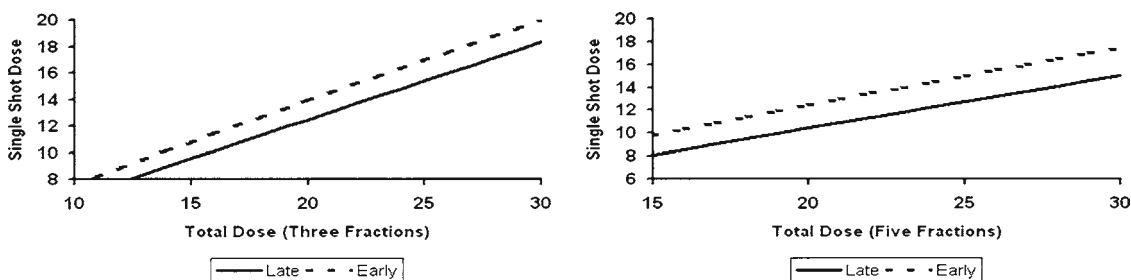
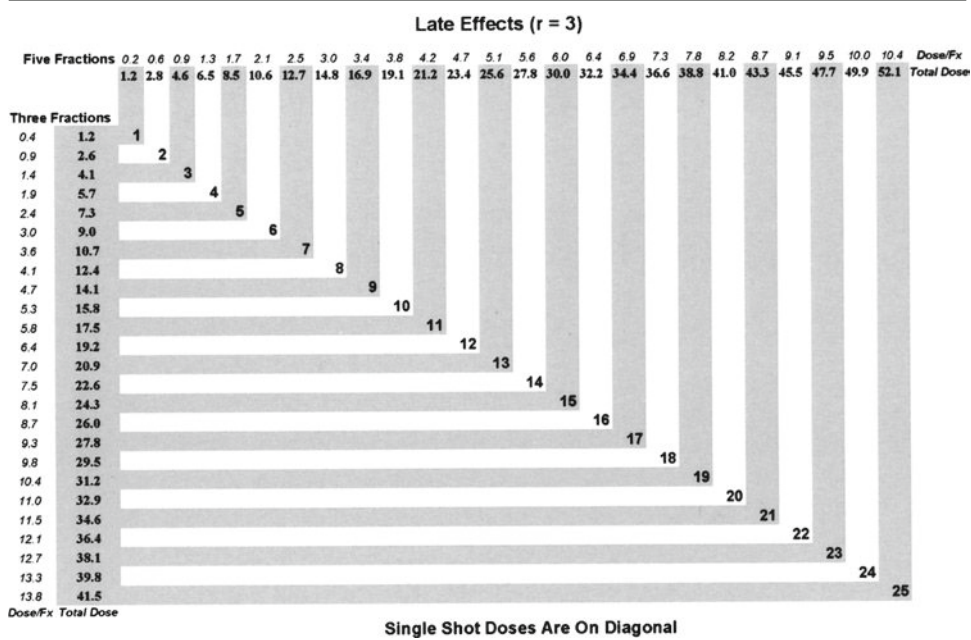


FIGURE 8.1. Graphs showing the single shot dose plotted against the equivalent dose delivered in three fractions (left) or five fractions (right). Dotted lines indicate relationship for early responding tissues, solid lines for late responding tissues

early responding tissues using a schedule with five fractions is 25 Gy delivered in five fractions of 5 Gy each (Find 15 on the diagonal and read 25 Gy in the top shaded row in the same column). Using Table 8.2, we see that the single-shot equivalent dose for late responding tissue (such as our critical structures) to this fractionated schedule is ~13 Gy (find 25.6 on the top shaded row and read 13 Gy in the diagonal lying on

that same column). As desired, the effects of this regimen on the normal critical structures are less than upon the tumor by ~2 Gy. Hypofractionation permits higher doses to the tumor with a lower risk to surrounding structures.

Unfortunately, this method is not completely accurate because the linear-quadratic formalism may not work well for all radiosurgical plans using the low



numbers of fractions found in radiosurgery (Astrahan 2008). However, the differences may not be large for doses used commonly in clinical practice. He gives modified equations for the BED of each fraction, yielding the same value given by the linear-quadratic formalism ( $d + d^2/r$ ) when the dose per fraction  $d$  is less than a threshold  $D_T$ , and yielding

$$d + d^2 / r + g(d - D_T)$$

when  $d$  is greater than  $D_T$ . Astrahan (2008) shows that  $g$  is  $\sim 5$  for clinically relevant doses and that  $D_T$  is  $\sim 6$  Gy for late responding tissues and 20 Gy for early responding tissues. The modified BED is, therefore, the same for early tissues because the dose per fraction is almost never as large as 20 Gy, whereas the modified BED begins to be larger than the linear-quadratic value when the dose per fraction is larger than 6 Gy. In other words, these data suggest that the use of the linear-quadratic equations is accurate for tumors, but underestimates the effects of radiation upon late responding tissues when the dose per fraction is  $>6$  Gy, consistent with our previously mentioned observation of changes noted at this threshold. These are also the findings suggested by comparison of the BED and modified BED values for plans using three or five fractions shown in Table 8.1 of Astrahan (2008).

Despite these arguments, uncertainty remains about the single shot equivalent doses calculated by the linear-quadratic equations (Guerrero and Li 2004; Hall 2000; Jones et al. 2001). Because there is no foolproof method to evaluate hypofractionated plans, we must rely upon experience and the best theoretical formalism available. These uncertainties must be accepted if we are to offer treatment to

patients in the desperate scenarios under consideration, and so we again refer to our preliminary comments regarding treatment philosophy and indications.

*Dosimetry Consideration #4: Isodose Lines.* The fourth and final dosimetric consideration is that of the choice of treatment isodose line. An isodose line corresponding to a dose  $d$  is defined as the set of points receiving exactly  $d$  Gy. On a two dimensional MRI or CT slice, isodose lines are typically concentric circles surrounding the point of maximum dose and in which the smaller circles correspond to larger doses. In practice, an isodose line is not labeled by its corresponding dose  $d$ , but instead is labeled by the percentage that  $d$  represents relative to the maximum dose. For example, if the maximum dose is 24 Gy, the isodose corresponding to 12 Gy is said to be the 50% isodose line ( $12/24 = 0.50$ ). This convention is followed to facilitate scaling with different choices of the maximum dose.

The goal of radiosurgery is to create a field of radiation precisely contoured to the tumor, typically achieved by creating a plan so that a specific isodose line, the treatment isodose line, closely approximates the tumor outline. In conventional radiotherapy the 90% (or higher) isodose line is used, so that doses within the isodose line range between 90% and 100% and so approximate each other. Such a plan is said to be homogeneous and delivers approximately the same amount of radiation to each point within the treatment isodose line. In contrast, the treatment isodose lines used in radiosurgery are typically low, usually from 40% to 60%. This means that the range of doses within the tumor will be broad, and that some areas will receive much higher doses than others.

For example, if 15 Gy is delivered to a 90% treatment isodose line, the doses within that line will range between 15 and 16.7 Gy ( $15/0.9 = 16.7$ ). On the other hand if 15 Gy is delivered to a 50% treatment isodose line, the doses within that line will range between 15 and 30 Gy ( $15/0.5 = 30$ )

The efficacy of radiosurgery is in part due to these internal high doses, and so one might think that the treatment isodose line should always be chosen as low as possible. However, the risk of radionecrosis rises as more tissue receives more radiation, forcing the use of higher isodose lines for larger tumors. As we will see later, a judicious choice of the value of the treatment isodose line allows these gradients to be exploited to deliver small doses to nearby normal structures while maximizing the tumor dose.

## CONSTRUCTION OF HYPOFRACTIONATED PLANS

We now show how to combine the principles previously described to create a hypofractionated plan for these difficult tumors. The first step is to specify the desired treatment isodose line, choosing a low value (typically 40–50%) if the tumor is small enough so that high doses will be tolerated, otherwise choosing a higher value. The next step is to construct a plan so that the treatment isodose line is as conformal to the tumor outline as possible. Different planning systems achieve this in different ways, and this step is often performed by a dosimetrist or physicist.

We then choose the single shot dose that would best control the tumor if we were constructing a single shot plan. We start with the choice of a single shot dose because these

choices are more established than those published for hypofractionated plans. The number of fractions is then chosen, using three fractions rather than five fractions if we wish to be more aggressive and more closely approximate the radiobiology associated with single shot plans. The single shot dose is then converted to a fractionated dose for early responding tissues using Table 8.1 as described in the previous section.

Although the plan is now optimal for the tumor, we must ensure that the doses delivered to the surrounding normal structures are not too high. These structures are first identified along with the isodose lines running through them, and this information is then used to calculate the total dose to these structures. That dose is then converted back to its single shot equivalent using Table 8.2 for late responding tissues, and compared to known tolerances. For example, suppose our plan delivers 15 Gy to a 50% treatment isodose line in five fractions, and that the 30% isodose line touches the optic chiasm. The dose to the chiasm is, therefore, 9 Gy ( $((0.3) \cdot (15)) / (0.50) = 9$ ), which (using Table 8.2) corresponds to a single shot dose of <6 Gy. Because 6 Gy is less than the generally accepted threshold for chiasmatic injury of 8 Gy, this plan would be accepted. Again, we use single shot doses for critical structures because the thresholds for injury are more established than those for hypofractionation.

If the single shot doses to critical structures are too high, the clinician has several options. One option is to reduce the treatment dose, knowing that this may decrease the tumor response. A second option is to alter the plan so that the isodose lines are pulled away from the critical structure, although this may worsen the tumor coverage and may not always be possible.

A third choice is to use a higher number of fractions to further exploit the differences between late and early equivalent doses, although we believe that the radiosurgical advantage is lost beyond five fractions. Several of these options are often tried using a variety of plans before an acceptable compromise is attained.

An alternative and perhaps more common method is to choose the isodose line and construct the plan as before, but then to first examine the isodose lines touching the critical structures and to choose the treatment dose based on the critical structure thresholds. For example, suppose we are using three fractions and a 50% treatment isodose line, and that the 30% isodose line touches the optic chiasm. The single shot threshold for chiasmatic injury is 8 Gy, which we see corresponds to a total dose of 12.4 Gy by using Table 8.2 for late responding tissues receiving three fractions. The dose delivered to the treatment isodose line is, therefore, 20.7 Gy  $[(0.5)(12.4)/(0.3) = 20.7]$ , which corresponds to a single shot equivalent dose of 14.4 Gy (using the formulas for early responding tissues). The clinician then decides if 14.4 Gy is an appropriate dose for the given tumor. The advantage of this method is that it yields the maximum dose that can be given to the tumor while respecting the injury thresholds of the critical structures. These considerations focus on the marginal dose, i.e., the minimal dose delivered to the tumor and the critical structures. Similar calculations could be made for each of the inner isodose lines to yield different single shot equivalent doses for each shell. Some authors recommend doing so routinely (Liu et al. 2003; Jones et al. 2000).

Regardless of the order of these steps, consideration must also be made to the

volume of the treatment isodose line. As mentioned before, the risk of radionecrosis is greater for larger tumors, and so we ensure that the dose we have chosen for the tumor is appropriate for its size. Again, we find that converting to single shot equivalent doses allows the use of established thresholds for dose-volume considerations (Shaw et al. 2000).

## CASE EXAMPLE

A 20 year old man presented with headaches and an MRI scan showing abnormal FLAIR signal in the was brainstem believed to be due to a brainstem glioma. He did well for 3 years until he developed left upper extremity paresthesias, left facial weakness and ataxia. An MRI scan showed diffuse enlargement of the pons and diencephalon with a small enhancing nodule. He underwent conventional radiotherapy, receiving 54 Gy to the brainstem region in 30 fractions. Both his symptoms and MRI findings improved. Subsequent treatment with temazolamide could not be completed because of intractable vomiting, a Mallory-Weiss tear, and a renal stone. His symptoms returned, and 5 months after his initial presentation he required a wheelchair and developed progressive hemiparesis, facial droop, dysarthria, and diplopia despite administration of steroids. An MRI scan showed a larger brainstem mass with extensive enhancement (left frame of Figure 8.2), and he was referred for consideration of radiosurgery.

It was believed that the risk of surgical resection was prohibitively high. Because the tumor was progressing despite chemotherapy and radiotherapy; he was offered hypofractionated radiosurgery. The uncer-

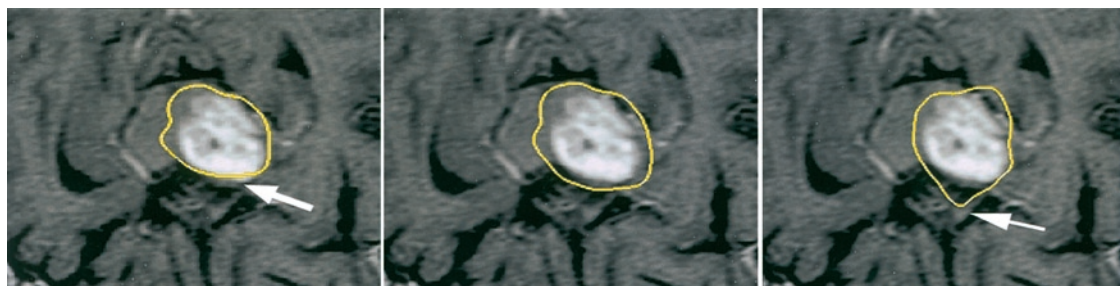


FIGURE 8.2. Image on left shows enhancing lesion in diencephalon at time of radiosurgical treatment. Center image was obtained 6 months after radiosurgery, and image on right was obtained 16 months after radiosurgery. Note the serial improvement in enhancement

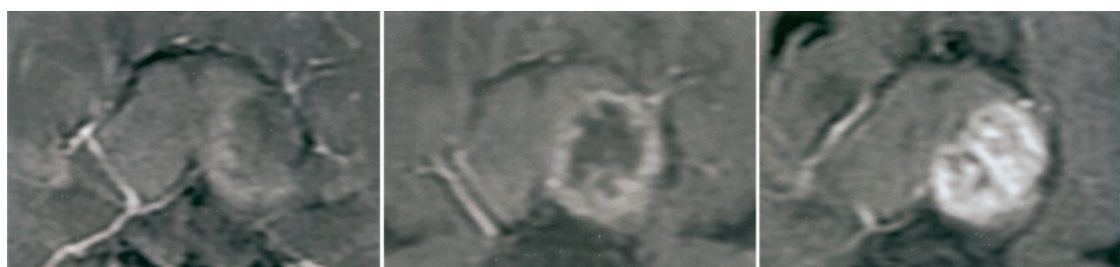


FIGURE 8.3. Image on left shows treatment isodose line (yellow) touches the optic chiasm (*arrow*). In the middle image, the plan has been modified so that the treatment isodose line (the 46% isodose line) is further away from the optic chiasm. However, the 20% isodose line touches the chiasm and represents its maximum dose. Imposing the desired limit of 4 Gy as a late single-shot equivalent dose to the chiasm would result in a total dose of 5.7 Gy delivered in three equal fractions. The tumor boundary would therefore receive 13.1 Gy delivered in three fractions, a schedule equivalent to a single shot plan delivering (to the early responding tumor) 9.6 Gy. Because the dose was considered too low, the plan was further modified as shown in the image on the right. The 46% treatment isodose line is even further from the chiasm, and the 12% isodose line now represents the maximum dose to the chiasm. Again, limiting the total dose of a three fraction schedule to 5.7 Gy, the tumor boundary will receive 21.9 Gy divided into three fractions. The early single-shot equivalent to this dose is 15.1 Gy, considered adequate. Arrow in the image on the right indicates a portion of the tumor not contained within the treatment isodose line. See text

tainties of this approach were explained to the patient and his family as has been discussed earlier in this chapter. A fractionation schedule using three fractions was chosen in order to offer aggressive therapy, and a first radiosurgical plan constructed. The treatment isodose line of the initial plan made contact with the optic chiasm (left frame of Figure 8.3). Because the threshold dose for injury of the chiasm

is low, i.e., 8 Gy if there has not been prior radiation, this plan was modified so that the 46% isodose line surrounded the tumor without contact with the chiasm (middle frame of Figure 8.3). The minimum dose to the chiasm was represented by the 20% isodose line in this plan. Because the chiasm had received prior radiation, it was desired to limit the single shot equivalent dose (as a late responding tissue) to the

chiasm to 4 Gy. Using Table 8.2, this threshold was calculated as equivalent to 5.7 Gy delivered in three fractions. This meant that the tumor boundary, described by the 46% isodose line, would receive a total dose of 13.1 Gy  $[(0.46).(5.7)/(0.20) = 13.1]$ . Use of Eq. 8.1 showed that this dose is equivalent to 9.6 Gy delivered as a single shot to early responding tissue, which was felt to be too low for effective treatment of this aggressive tumor.

The plan was, therefore, modified again to shrink the 46% isodose line further from the chiasm (right frame of Figure 8.3). At this time the minimum dose to the chiasm was represented by the 12% isodose line, so that 5.7 Gy delivered to the chiasm meant that 21.9 Gy would be delivered to the tumor margin  $[(0.46).(5.7)/(0.12) = 21.9]$ . Using Eq. 8.1 and Table 8.1 as before, this dose was seen to be equivalent to a single shot dose of 15.1 Gy delivered to early responding tissue. This dose was considered adequate for tumor control and so the final prescription was 21.9 Gy delivered to the 46% isodose line in three equal fractions of 7.3 Gy each. The maximum dose to the chiasm was 5.7 Gy and the volume of the 46% isodose line was 19.4 cc.

Figure 8.3 shows that the treatment isodose line did not cover a small portion of the tumor (arrow) and covered some of the normal brainstem to the left of mid-line. However, because the geometry of the plans could not be improved despite intense effort, and because a high dose could be delivered to the majority of the tumor while sparing the optic chiasm, we accepted these compromises and delivered the treatment plan. Other groups might choose other compromises, but we feel that compromises of some form are unavoidable when treating these difficult tumors.

The patient was then given a course of bevacizumab and carboplatin. Six months later, his diplopia had resolved and he was walking with assistance with significant improvement in his left hemiparesis. An MRI scan (middle frame of Figure 8.2) showed less enhancement and mass effect. Six months later his diplopia had returned but he could ambulate. His MRI was unchanged. Four months later his walking had improved and the enhancement had diminished further (right frame of Figure 8.2).

## COHORT STUDY

A small cohort of patients with progressive malignant brain tumors who had exhausted their major treatment options has been reported (Giller et al. 2007). Eighteen tumors in 15 patients were treated with hypofractionated CyberKnife radiosurgery (Adler et al. 1999). Six of the tumors were high grade gliomas and 12 were metastatic lesions. All patients had received chemotherapy, ten had undergone craniotomy, and 12 had received conventional radiotherapy. Despite these measures, all tumors were progressing at the time of radiosurgical treatment, and the clinical situation for each of these patients was that described in the beginning of this chapter. Furthermore, hypofractionation was chosen for each tumor because of complicating factors for each – five were large (volume > 14 cc), five had received prior radiation and were located either in the diencephalon or brainstem, and seven were surrounded by significant edema.

The mean total dose delivered was  $21 \pm 4$  Gy (sd), the mean number of fractions was  $5 \pm 0.6$ , and the mean treatment isodose line was  $57\% \pm 13\%$ . The majority of

the tumors received 20 or 25 Gy as a total dose delivered in five equal fractions, providing single shot equivalent doses to the (early responding) tumor of ~15 Gy and to the (late responding) normal structures of ~12.5 Gy. Fifteen Gray was considered a reasonable dose for palliation of these aggressive tumors. With a median follow-up period of 172 days, local control was achieved in 72% of the tumors. Seven of the nine tumors followed longer than 6 months showed a decrease in size. There was one toxicity presenting with dysarthria and increased T2 signal on an MRI scan. These symptoms resolved with steroids, and the tumor volume subsequently decreased by 50%. These are short-term results, but given the aggressive nature of these progressive tumors that had failed other multimodality therapy, we believe the outcomes are encouraging.

In conclusion, any proposal to offer radiosurgery to a neurologically well patient in the face of so many uncertainties and without benefit of randomized trials should produce some degree of anxiety in every thoughtful clinician. Questions such as the proper dosimetry, the validity of the linear-quadratic model, and the assessment of risk have not been fully explored for this group of difficult tumors that have already been so aggressively treated. For some clinicians, these issues are prohibitive, and we have witnessed significant resistance to treatment based on the principle of *primum non nocere* – first do no harm. On the other hand, there are patients to which a greater harm is inflicted by doing nothing by allowing nature to quickly take its inevitable and ugly course. For these patients, the chance of receiving an additional allotment of high quality time can outweigh the risk of treatment that is not fully tested. Finding

an appropriate balance requires thoughtful discussions with the patient combined with a great deal of introspective judgment. It is hoped that this chapter not only provided the methodology for delivery of radiosurgical treatment in these circumstances, but also a framework for discussion of these more thorny issues.

## REFERENCES

- Adler, J.R. Jr., Murphy, M.J., Chang, S.d., and Hancock, S.L. (1999) Image-guided robotic radiosurgery. *Neurosurgery* 44:1299–1307
- Astrahan, M. (2008) Some implications of linear-quadratic-linear radiation dose-response with regard to hypofractionation. *Med. Phys.* 35:4161–4172
- Barnett, G.H., Linskey, M.E., Adler, J.R., Cozzens, J.W., Friedman, W.A., Heilbrun, M.P., Lunsford, L.D., Schulder, M., and Sloan, A.E. (2007) American Association of Neurological Surgeons, Congress of Neurological Surgeons Washington Committee Stereotactic Radiosurgery Task Force. *J. Neurosurg.* 106:1–5
- Brown, P.D., Brown, C.A., Pollock, B.E., Gorman, D.A., and Foote, R.L. (2002) Stereotactic radiosurgery for patients with “radioresistant” brain metastases. *Neurosurgery* 51:656–665
- Giller, C.A., Berger, B.D., Gilio, J.P., Delp, J.L., Gall, K.P., Weprin, B., and Bowers, D. (2004) Feasibility of radiosurgery for malignant brain tumors in infants by use of image-guided robotic radiosurgery: preliminary report. *Neurosurgery* 33:916–924
- Giller, C.A., Berger, B.D., Pistenmaa, D.A., Sklar, F., Weprin, B., Shapiro, K., Winick, N., Mulne, A.F., Delp, J.L., Gilio, J.P., Gall, K.P., Dicke, K.A., Swift, D., Sacco, D., Harris-Henderson, K., and Bowers, D. (2005) Robotically guided radiosurgery for children. *Pediatr. Blood Cancer* 45:304–310
- Giller, C.A., Berger, B.D., Fink, K., and Bastian, E. (2007) A volumetric study of CyberKnife hypofractionated stereotactic radiotherapy as salvage for progressive malignant brain tumors: initial experience. *Neurol. Res.* 29:563–568
- Guerrero, M., and Li, X. (2004) Extending the linear-quadratic model for large fraction doses

- pertinent to stereotactic radiotherapy. *Phys. Med. Biol.* 49:4825–4835
- Hall, E.J. (2000) Time, dose and fractionation in radiotherapy. In: Hall, E.J. (ed) *Radiobiology for the radiologist*, 5th edn, Chapter 22. Lippincott Williams and Wilkins, Philadelphia, PA, pp. 397–418
- Jones, B., Dale, R.G., Finst, P., and Khaksar, S.J. (2000) Biological equivalent dose assessment of the consequences of hypofractionated radiotherapy. *Int. J. Radiat. Oncol. Biol. Phys.* 47:1379–1384
- Jones, L., Hoban, P., and Metcalfe, P. (2001) The use of the linear quadratic model in radiotherapy: a review. *Australas Phys. Eng. Sci. Med.* 24:132–146
- Liu, L., Bassano, D.A., Prasad, S.C., Hahn, S.S., and Chung, C.T. (2003) The linear-quadratic model and fractionated stereotactic radiotherapy. *Int. J. Radiat. Oncol. Biol. Phys.* 57:827–832
- Nishizaki, T., Saito, K., Jimi, Y., Harada, N., Kajiwara, K., Nomura, S., Ishihara, H., Yoshikawa, K., Yoneda, H., Suzuki, M., and Gibbs, I.C. (2006) The role of cyberknife radiosurgery/radiotherapy for brain metastases of multiple or large-size tumors. *Minim. Invasive Neurosurg.* 49:203–209
- Shaw, E., Scott, C., Souhami, L., Dinapoli, R., Kline, R., Loeffler, J., and Farnan, N. (2000) Single dose radiosurgical treatment of recurrent previously irradiated primary brain tumors and brain metastases: final report of RTOG protocol 90–05. *Int. J. Radiat. Oncol. Biol. Phys.* 47:291–298

# 9

## Anti-vascular Therapy for Brain Tumors

Florence M. Hofman and Thomas C. Chen

### INTRODUCTION

The formation of new blood vessels, a normal process in fetal development, wound healing and during the menstrual cycle, functions to provide expanding tissues with nutrients, oxygen, and waste removal. The extent of vasculature development defines the survival and growth of tissues. Tumor growth also depends on the expansion of the vasculature. Tumor cells can survive only within a specific distance from the blood vessels; beyond this point the cells become hypoxic and die (Hlatky et al. 2002). In the absence of a parallel expansion of the blood supply, the tumor will stop growing and remain dormant for years or die (Folkman 2007). Studies suggest that activation of the dormant tumor cells cause a change in the balance of pro- and anti-angiogenic factors present in the tumor microenvironment, triggering the blood vessels in the surrounding normal tissue to become activated and invade the tumor (angiogenesis) (Folkman 2007). The growth factors responsible for the “switch” may be unique, appearing early in tumor growth and different from the growth factors detected later in tumor development. In addition to the already

existing vasculature surrounding the tumor, blood vessels may arise from the circulating bone-marrow-derived progenitor cells (Nolan et al. 2007). The initiation of blood vessel growth in tumors is currently under investigation. Ultimately both processes are involved in the formation of the tumor vasculature. How these processes are connected is not known; what is clear, however, is that tumors require a dynamic ever expanding vascular system for growth and survival. Thus, targeting the vasculature as an antitumor therapy can be an effective approach to treatment of solid tumors, particularly brain tumors.

Angiogenesis involves a sequence of events, initiated by the activation of endothelial cells already in tubule formation. Blocking or interfering with any of these events will inhibit or decrease the formation of new vessels. Endothelial cells can be activated by a number of stimulatory signals including hypoxia, decreased nutrients, changes in flow rate, and inflammation (Bergers and Benjamin 2003). Once this activation process occurs, endothelial cells release an array of enzymes which break down the extracellular matrix (ECM) surrounding the endothelial cells, the basement membrane; thus, enabling



the endothelial cells to migrate out of the existing blood vessel causing sprouting. The enzymes responsible for sprouting include matrix metalloprotease MMP2, MMP9, and urokinase plasminogen activator (uPA). In addition to disrupting the physical barrier around the vessels to allow vessel growth, the destruction of the ECM releases proangiogenic factors which further stimulate the endothelial cells. These proangiogenic factors include vascular endothelial growth factor (VEGF), interleukin-8 (IL-8), platelet-derived growth factor (PDGF), placental growth factor (PGF), and endothelin-1 (Et-1) (Kerbel and Folkman 2002). These factors provide the proangiogenic environment which continues to stimulate blood vessel growth. Proangiogenic factors can function to induce endothelial cells to sprout, migrate, and proliferate, thereby culminating in the formation of new vessels. Several of these angiogenic factors (i.e., VEGF and IL-8) have somewhat redundant functions; thus, therapeutic agents eliminating one angiogenic factor will ultimately lose effectiveness because other proangiogenic factors are present and functional. Inhibition of endothelial cell activity during any of these processes will block vessel formation. In the normal process of angiogenesis, once the tubules have formed and blood is flowing within the vessel lumen, the process of angiogenesis is halted by several endogenous antiangiogenic factors. Thrombospondin-1 (TSP-1), produced by the tumor stromal tissue, is the critical agent which is very effective in inhibiting angiogenesis (Fernando et al. 2008). The breakdown products of the ECM (i.e., endostatin, and tumstatin) when accumulated at the surface of the endothelial cells, also block further

endothelial cells migration and tubule formation. It is these anti-angiogenic factors that keep the endothelial cells in their quiescent state under normal conditions.

In sharp contrast to normal blood vessels, the tumor vasculature is morphologically and functionally different; especially so in brain tumors. Morphologically, the glioma vessels exhibit increased numbers of caveolae, abnormal pericyte distribution, and discontinuous basement membranes. The vasculature in gliomas, for example, is considerably denser as compared to normal brain tissue. The vessels are also irregular in distribution, thicker walled with blind out-pouchings, and shunts from arterioles to venuoles, without the typical capillary structures (McDonald and Choyke 2003). These abnormalities cause decreased blood flow and blood pooling. Tumor vessels are also more permeable, resulting in a loss of interstitial pressure. On the cellular level, endothelial cells isolated from brain tumors function very differently from normal brain endothelial cells. These tumor-associated endothelial cells constitutively produce a variety of proangiogenic cytokines and growth factors, and migrate more rapidly, but proliferate less rapidly than control endothelial cells (Charalambous et al. 2005). What is particularly critical for cancer therapy is that these tumor-associated endothelial cells are generally resistant to chemotherapeutic agents (Charalambous et al. 2007). The mechanism of this chemoresistance is not clear. However, unlike normal tissues, tumor cells produce a large variety of proangiogenic growth factors, resulting in a pro-angiogenic microenvironment surrounding the tumor. Thus, the surrounding blood vessels invading the adjacent tumor are being continuously activated by growth

factors for months and even years. This constant activation of cells may be responsible for the observed senescent-like phenotype of tumor-associated endothelial cells (Charalambous et al. 2007). A common characteristic of senescent cells is resistant to apoptosis (Effros 2003). Studies focusing on chemosensitivity of tumor-associated endothelial cells have shown that these cells are more resistant to drugs compared to normal, activated endothelial cells (Charalambous et al. 2007). Therefore, any antiangiogenic therapy must consider the properties of these established tumor-associated endothelial cells, as well as the newly invading, activated endothelial cells.

## SPECIFIC DRUG TARGETS

Because the angiogenic process is so critical to tumor development, any method that reduces or blocks endothelial cell function or inhibits tumor cells from producing the appropriate proangiogenic growth factors can be an effective antiangiogenic agent. Furthermore, as a target for therapy, the tumor vasculature has distinct advantages because endothelial cells are easily accessible, and genetically stable; these cells are, therefore, less likely to develop drug resistance, as compared to the tumor cells. Currently there are over ten different anti-vascular drugs in preclinical studies or in clinical trials. Presented here are examples of the types therapeutic agents directed against different angiogenic functions.

### Angiogenic Growth Factors

*Vascular Endothelial Growth Factor (VEGF)* is critical for endothelial cell survival as well as other endothelial cell functions (Dvorak

2002). Thus, the direct approach to blocking angiogenesis is to reduce levels of VEGF in the tumor. This was implemented by preparing a recombinant, humanized monoclonal antibody directed against VEGF, bevacizumab (Avastin), which binds to and inactivates secreted VEGF; this drug was approved by the Federal Drug Administration (FDA) for patient use (Ma and Waxman 2008). Clinical trial demonstrated that bevacizumab has significant efficacy in several types of tumors, including colorectal cancer, renal cell cancer, breast cancer, non-small cell lung cancer, and gliomas (Stupp et al. 2007). Using an orthotopic glioma model, studies showed that anti-VEGF treatment alone increased survival; however, this therapy also caused greater tumor infiltration and the cooption of normal blood vessels. These data suggest that anti-VEGF therapy cannot be used alone, but may also require the administration of anti-invasion and antitumor agents. In human trials, the effects of bevacizumab were modest, but did exhibit a significant increase in patient survival, especially in combination with drugs targeting tumor cells. Administration of bevacizumab and irinotecan (CPT-11) already in phase II trials of grade II and IV glioma treatment showed the 6 month progression-free survival (PFS) probability to be 38% and 6 month overall survival probability to be 72%. This is compared to the 6 month rate PFS of 21% for patients receiving temozolomide (Temodar) alone, the standard of care for glioma therapy. In addition, the combination of bevacizumab and CPT-11 appeared to be effective for recurrent grade III-IV glioma, with acceptable toxicity (Ma and Waxman 2008).

The mechanisms responsible for the effects of bevacizumab are not completely understood. Recent studies have suggested

that anti-VEGF agents work by decreasing peritumoral edema, through decreasing vascular permeability; thereby, reducing intracranial pressure, and thus reducing the corticosteroid dose requirement (Wen and Kesari 2008). Unfortunately, bevacizumab has also been associated with toxicities, such as neutropenia, pulmonary hemorrhage, hypertension, poor wound healing, and renal toxicity (Socinski 2008), as well as the upregulation of other potent proangiogenic factors (i.e., platelet-derived growth factor (PDGF), or basic fibroblast growth factor (bFGF) (LoRusso and Eder 2008).

*Placental growth factor (PGF)* levels have been reported to increase with tumor progression (Jansen et al. 2004). PGF binds to VEGF Receptor 1 (VEGFR1), thus, activating this VEGF signaling pathway. Anti-PGF antibodies induce endothelial cell apoptosis and reduce infiltration of VEGFR1 positive macrophages, responsible for tumor expansion. A potential advantage of anti-PGF therapy is that this agent does not induce genes involved in angiogenic rescue, as is the situation with anti-VEGF; nor does anti-PGF appear to affect capillary growth or pruning in healthy tissues, as does anti-VEGF (Jansen et al. 2004). Thus, the anti-PGF targeting drug appears to have the positive qualities of anti-VEGF without the negative side effects (Fischer et al. 2007).

*Thrombospondin-1 (TSP)* is an antiangiogenic growth factor normally expressed by stromal cells for stabilizing the newly formed blood vessels and inhibition of further angiogenesis (Rege et al. 2005). TSP-1 ensures appropriate vessel density during development and wound repair. This large molecule has several different inhibitory functions. TSP-1 binds to CD36 scavenger receptor on the surface of endothelial cells causing inhibition of

endothelial cell migration. TSP-1 inhibits endothelial cell proliferation causing cell cycle arrest in G0/G1, and binds to MMP-2 and MMP-9 resulting in enzyme inactivation (Rege et al. 2005). TSP-1 also induces apoptosis in endothelial cells by upregulating FasL on endothelial cells (Volpert et al. 2002). Endothelial cells normally express low levels of Fas (death receptor) and FasL (Fas ligand). VEGF acts as a survival factor for these cells by downregulating FasL. However, TSP-1 induces transcriptional upregulation of FasL resulting in surface expression of this apoptotic molecule within 4 h. The Fas receptor is highly expressed on newly formed vessels; but once activated endothelial cells form tubules, Fas receptor levels go down. Thus, the increased presence of TSP-1 causing upregulation of FasL results in the elimination of the endothelial cells actively participating in angiogenesis. TSP-1 expression is localized to vascular cells in the tumor microenvironment, with little expression in tumor cells, suggesting that the antiangiogenesis activity of TSP-1 is the host response to tumors. In preclinical studies, nude mice implanted with human glioma cells that stably expressed TSP-1, exhibited smaller tumors with fewer blood vessels as compared to controls (Kragh et al. 2002). Unfortunately, lack of specificity of this agent may be a problem for further clinical evaluation. However, these data suggest that TSP-1 or CD36, the receptor to which TSP-1 binds, may be used as therapeutic targets.

#### Growth Factor Receptor Inhibitors

*Vascular Endothelial Growth Factor (VEGF) Receptor-2 inhibitors:* Another approach to decreasing the effects of proangiogenic factors is to block the recep-

tor signaling pathways by using small molecule inhibitors to inhibit the phosphorylation of the protein tyrosine kinase (PTK) (Jansen et al. 2004). SU5416 is a PTK inhibitor specific for the VEGF receptor -2 (VEGFR-2). This drug was shown to cause a 70% decrease in tumor volume in the rat glioma xenograft model. SU5416 targets the actively, proliferating vasculature at the tumor periphery, but not the blood vessels within the tumor or the endothelial progenitor cells. SU5416 apparently has no effect on already formed tumors, but was effective at the very early stage of tumor growth (LoRusso and Eder 2008). The VEGFR inhibitor, cediranib, used in patients with recurrent glioblastoma, showed response rates in excess of 50% and prolongation of the 6-month rate of progression-free survival (Jansen et al. 2004). Other agents, PTK787 and ZD6474, target VEGFR-2 as well as VEGFR-1 (Jansen et al. 2004). ZD1839 (Iressa) is a PTK-inhibitor of epithelial growth factor receptor (EGFR)-tyrosine kinase which has antiangiogenic activity in human tumor xenografts (Hirata et al. 2002).

*Multiple Receptor Inhibitors:* Since there are a multitude of growth factors responsible for angiogenesis in tumors, small molecule inhibitors with more global activity have been used to block multiple growth factors signal transduction processes. Sorafenib, active against VEGFR-2 and Platelet-Derived Growth Factor receptor (PDGFR), has been approved by the FDA for therapy in renal cell and hepatocellular cancer, and is in the process of phase II/III clinical evaluation for melanoma and non-small cell lung cancer (LoRusso and Eder 2008). Sorafenib is a small molecule inhibitor of the raf/ serine/ threonine kinase isoforms, and receptor tyrosine kinase. Because PDGF is critical for pericyte sta-

bilization of blood vessels in the absence of PDGF receptor activity, endothelial cells become more susceptible to apoptosis (Wilhelm et al. 2008). Sorafenib was shown to be active in patients that did not respond to bevacizumab (Wilhelm et al. 2008). Sunitinib (SU11248) (XL880) is an inhibitor of tyrosine kinase activity which blocks multiple angiogenic receptors, such as VEGFR, PDGFR, cKit, SDF-1 receptor, Flt3, and c-MET (Zhou et al. 2008). This broad spectrum agent has antiangiogenic and antitumor activities, and can be used alone, or in combination with docetaxel, fluorouracil, doxorubicin, and cisplatin to potentiate these chemotherapeutic agents.

Sunitinib reduces tumor microvessel density and collagen IV density in a dose-dependent way with no effect on the pericyte density. Sunitinib appears to enhance penetration of drugs, such as temozolomide (Zhou et al. 2008). These authors suggest that sunitinib “normalizes” and stabilizes the vessels, making the vessels more functional and, therefore, enhances the distribution of temozolomide into the tissue. Sunitinib prunes the most immature newly formed microvessels, leaving the other vessels with increased blood flow, reduced basement membrane thickness, and relatively efficient “normal” vessels covered by pericytes. Temozolomide penetration correlates with the number of functioning vessels in the tumor (Zhou et al. 2008). It was noted that drug penetration decreases after 14 days, suggesting that continuous sunitinib treatment beyond a normalization window may be disruptive to the vessels. Therefore, sunitinib is likely to be useful initially, with reduced efficacy over longer periods of treatment. Another aspect to be considered is dose. Perhaps long term treatment at low doses, referred to as metronomic dosing of sunitinib would prolong

the useful period of this drug (Kerbel and Folkman 2002). However, presently, none of these agents are curative when used alone or in combination (Zhou et al. 2008).

### Endothelial Cell Adhesion and Migration

Survival of endothelial cells is dependent on cell adhesion to the extracellular matrix substrate. This binding, mediated by integrins expressed on the cell surface, is predominantly of the  $\alpha v B1$ ,  $\alpha v B3$ ,  $\alpha v B5$ , and  $\alpha 5 B1$  subtypes (Rege et al. 2005). Blocking this binding over a period of time will trigger the apoptotic pathway. Endothelial cell migration requires integrin binding to substrate; therefore, blocking this migration, will inhibit sprouting and tubule formation, critical functional components of angiogenesis (Bergers and Benjamin 2003). Therefore, agents interfering with the integrin adhesion process can be effective antiangiogenic agents.

*Cilengitide* is a synthetic integrin-targeting arginine-glycine-aspartic acid peptide (RGD) (Reardon et al. 2008). Cilengitide blocks  $\alpha v B3$  and  $\alpha v B5$  on endothelial cells, thus interfering with binding to vitronectin and tesascin, matrix proteins found in high levels in brain tumors (Reardon et al. 2008). Cilengitide induces apoptosis of endothelial cells by blocking the survival pathway (Stupp et al. 2007). Clinical trials using this agent showed minimal toxicity, effective delivery into the glioma tissue in human brain, good retention for at least 24 h, and clinical activity in newly diagnosed brain tumors (Reardon et al. 2008).

*Angiostatin*: Antagonists directed against the integrin  $\alpha v B3$ , which binds to fibronectin, vitronectin, and degraded collagen, have been shown to inhibit tumor neovas-

cularization in several animal models of cancer (Jansen et al. 2004). Angiostatin is an internal fragment of plasminogen which binds to  $\alpha v B3$  (Rege et al. 2005). Treatment of endothelial cells with angiostatin inhibits cell migration and capillary tube formation. Recombinant angiostatin has been reported to inhibit growth and neovascularization of intracerebral glioma xenografts, as well as to increase tumor cell apoptosis (Joe et al. 1999).

*Endostatin*, a cleavage fragment of collagen type XVIII produced by the proteases, elastase and cathepsin-L (Ma and Waxman 2008), specifically inhibits proliferating endothelial cells and does not affect other cell types. Endostatin interacts with several cell surface molecules, including heparin sulfate proteoglycan (HSPG),  $\alpha 5 B1$ , tropomyosin, and VEGFR-2; thus, affecting proliferation via different mechanisms. Basic FGF, an important growth factor in endothelial cell proliferation, requires binding to cell surface HSPG for activation to take place. Endostatin interferes with this bFGF binding; thus, selectively blocking subsequent bFGF signaling and bFGF-mediated proliferation (Kerbel and Folkman 2002). Endostatin binding to  $\alpha 5 B1$  integrin results in inhibition of focal adhesion kinase and Erk signaling that are required for endothelial cell survival and motility. Furthermore, focal adhesion kinase is necessary for brain microvessel tube formation and migration (Haskell et al. 2003). Endostatin binding to tropomyosin causes disruption of microfilament integrity and inhibits cell motility (Kerbel and Folkman 2002). Finally, endostatin blocks VEGFR 2 activity, which results in reduced blood vessel density within tumors (Jansen et al. 2004). In experimental rodent cancer models, genetically engineered tumor cells

overexpressing endostatin demonstrated decreased tumor growth, as compared with control tumor cells (Fernando et al. 2008). For endostatin, the site of drug administration may be critical. In phase I trials, continuous intracerebral delivery of endostatin via an osmotic minipump connected to an intracranial catheter resulted in higher antitumor efficacy compared to continuous systemic administration or daily injections (Jansen et al. 2004). Thus, with endostatin, the most effective regimen, requires a constant level of inhibitor to be maintained locally, within the tumor environment. The fact that endostatin has a relatively short half-life in plasma (2–10 h) may be responsible for this requirement. Thus, strategies which result in sustained delivery of endostatin would be desirable. A novel strategy to enhance local delivery of angiogenic inhibitors is implantation of encapsulated producer cells that have been engineered to express endostatin or the reformulation of endostatin in the form of a slow-releasing product (Jansen et al. 2004).

*Survivin*: Studies from this laboratory have shown that the glioma-derived endothelial cells are considerably more chemoresistant to a wide variety of drugs, compared to normal endothelial cell (Charalambous et al. 2007). The mechanism(s) of this resistance are not well understood. Survivin, a protective protein which inhibits caspase activity, has been found in a variety of tumor cells including gliomas (Altieri 2003). Our studies showed that survivin is expressed in tumor vessels, as well as in tumor cells (Virrey et al. 2008a). Furthermore, blocking survivin expression in these tumor-associated endothelial cells increased the sensitivity of these cells to drugs. Thus, agents that block the phosphorylation of survivin (e.g., roscovitine) or those that increase the

proteasome degradation of survivin would be excellent drugs to provide enhanced efficacy of known chemotherapeutic agents.

*Glucose regulated protein 78/Binding immunoglobulin protein (GRP78/BiP)*: While blocking survivin expression was effective in increasing tumor endothelial cell sensitivity to chemotherapeutic drugs, cell death did not reach 100%, suggesting that more than one mechanism of cell protection may be active in these endothelial cells. The unfolded protein response (UPR) is an evolutionarily conserved mechanism that activates both proapoptotic and survival pathway to allow eukaryotic cells to adapt to endoplasmic reticulum (ER) stress (Lee 2007). A major UPR protective response is the induction of the ER chaperone protein GRP78/BIP, that is required for the proper folding and assembly of membrane and secretory proteins. Overexpression of GRP78 is prominent in a wide variety of tumors, and was correlated with, the resistance of tumor cells to a range of cancer therapeutic agents. GRP78 is highly elevated in the tumor vasculature, both in situ in tissue and in vitro in primary cell cultures, in contrast to the minimal expression in normal brain vasculature (Virrey et al. 2008b). Knockdown of GRP78 by siRNA significantly sensitizes the glioma-associated endothelial cells to a variety of chemotherapeutic agents, whereas upregulation of GRP78 in control endothelial cells renders these cells drug resistant. Recently, it was discovered that the green tea component (-)-epigallocatechin gallate (EGCG) blocks the ATPase domain of GRP78 and suppresses its antiapoptotic property (Lee 2007). Our studies have shown that EGCG mimics siRNA against GRP78 in sensitizing the tumor vasculature to chemotherapeutic agents, suggesting that small molecules

targeting GRP78 may enhance the efficacy of chemotherapeutic drugs by eliminating the chemoresistant tumor vasculature (Virrey et al. 2008b).

### Bone Marrow-Derived Endothelial Progenitor Cells

Studies have shown that bone marrow (BM)-derived endothelial progenitor cells (EPC) contribute to the vasculature of developing tumors, particularly during the initial stages of tumor growth (Nolan et al. 2007). These BM-derived EPCs differentiate into mature endothelial cells by incorporating into the sprouting new vessels; in the later tumors the EPCs are diluted by non-bone marrow-derived cells from the periphery (Nolan et al. 2007). The number of EPCs participating in tumor blood vessel growth depends on the tumor type; the highly vascular gliomas recruit relatively high numbers of these cells (Moore et al. 2004). Because of their relevance to the tumor vasculature, one approach to antivasular therapy is to block circulating EPCs from migrating to the tumors. The directional migration of BM-EPCs is dependent on the release of specific angiogenic growth factors from the tumor site. These growth factors: VEGF, PGF, TSP-1, and PDGF, together with (stromal cell-derived factor) SDF-1/CXCL12 promote cell replication and recruitment of the EPC from their quiescent state in the bone marrow to the tumor (Nolan et al. 2007). Upregulation of SDF-1 and PDGF are particularly critical for this homing process. Platelets contain VEGF, TSP-1, and SDF-1; therefore, blocking platelet aggregation at the tumor site by decreasing PDGF will reduce the accumulation of EPCs and thus reduce tumor blood vessel density (Rafii

et al. 2008). Thus, by reducing the quantity or activity of these growth factors, the migration of EPCs to the tumor is diminished. However, our current understanding of EPC activity would suggest that any increase in TSP-1 production as a treatment to inhibit angiogenesis would have the undesirable side effect of stimulating EPC accumulation and vasculogenesis.

A second approach to the use of EPCs for cancer therapy is based on the capacity of these cells to be genetically manipulated and still competent to migrate to the tumor (Moore et al. 2004). The fact that EPCs home to the tumor suggest that these cells may be used to carry antiangiogenic genes that have the potential to retard and destroy the tumor vasculature. EPCs can be isolated from bone marrow or peripheral blood and amplified ex vivo (Debatin et al. 2008). These cells can then be bioengineered to express antiangiogenic protein, i.e., endostatin (Dudek et al. 2007), resulting in decreased angiogenesis. EPCs can also be infected with retrovirus, lentivirus vectors, or non-integrating vectors such as adenovirus and herpes simplex virus to carry suicide genes that could metabolize a nontoxic prodrug to a cancer drug. (Debatin et al. 2008). The main advantage of EPCs in cancer therapy is that these cells can be generated from autologous blood; thus, eliminating histoincompatibility. The disadvantage is the relatively low numbers of EPCs that actually incorporate into the tumor vasculature.

### CONCLUSION

Common antiangiogenic strategies target the growth and infiltration of newly forming blood vessels, which contain endothelial

cells highly sensitive to agents blocking proliferation and migration. However, we and others have shown that the tumor-associated endothelial cells function differently from activated brain-derived endothelial cells (Charalambous et al. 2005; Hida et al. 2004). Because these tumor-associated endothelial cells proliferate more slowly, this population is less sensitive to growth inhibition. Furthermore, these cells produce VEGF and express the VEGF receptor, resulting in autocrine activation; thus, suggesting that VEGF withdrawal may not be as effective for the mature tumor vasculature as compared to the newly forming vessels. Microarray studies have provided potential targets for the glioma vasculature; Pen et al. (2007) have shown that IBFBP-7 is overexpressed in glioma blood vessels, and is a highly selective biomarker for the glioma vasculature. Thus, more studies need to be performed to identify distinguishing characteristics of these tumor-associated endothelial cells for identification and drug target purposes.

Combination therapies which focus on both tumor cells and the tumor vasculature may be more effective for therapy than single agents (Ma and Waxman 2008). Targeting both cell populations with different drugs may increase tumor regression efficiency because the mechanisms responsible for the cell death of tumor cells are not likely to be those active in blocking blood vessel growth. The dosage regimens of the drugs are also important. Traditional high dose-schedule protocols cannot provide sustained blockade of angiogenesis because endothelial cells that proliferate rapidly are vulnerable to conventional chemotherapy, while the mature intra-tumoral endothelial cells do not proliferate and, therefore, are not susceptible

to these drugs (Jansen et al. 2004). In conventional therapy, during the intervals between cycles, the fraction of blood vessels that survive can regrow, causing a persistence of tumor vasculature in spite of the antiangiogenic therapy. Studies show that because of the nature of new blood vessel formation, fine-tuning doses and schedule of combination therapy are critical. Thus, the continuous low-dose chemotherapy, metronomic scheduling, maintains a constant level of drug for the endothelial cells and cancer cells, resulting in minimal regrowth of vessels (Kerbel and Folkman 2002).

Another rationale for using tumor blood vessels as a target for therapy is based on the normalization of tumor blood vessels (Ma and Waxman 2008). Because tumor vessels are disorganized and leaky, “pruning” these abnormal vessels would result in a higher density of more normal-like vessels. The interstitial pressure in malignant tumors is elevated and normalizing the vasculature would lower this interstitial fluid pressure (Jansen et al. 2004). Thus, “normalizing” the vessels would provide more effective drug delivery. Confirming this notion, it was shown that VEGFR-2 inhibitor SU5416 increases the intratumoral concentrations of temozolomide in orthotopically implanted glioma xenografts. The optimal antiangiogenic effects would, therefore, be after “normalization” of the vascular physiology and before the total destruction of the new blood vessels. Increasing vascular function, even temporarily, may be important in improving drug delivery due to alteration of interstitial pressure.

Gene therapy targeting the vasculature has advantages because of easy access to the blood supply. However, the lentiviral



approach has certain restrictions, particularly the host response to the lentiviral infection. Ideally, the administration of siRNA would be safe and effective; however, siRNA is easily degradable and, therefore, has poor bioavailability. The new approach of inserting siRNA into neutral liposomes, combines the specificity of the genetic therapy with the safe delivery system of liposomes (Villares et al. 2008). These neutral liposomes are able to enter endothelial cells without significant activation. Another challenge to drug therapy, especially in the brain, is the blood-brain-barrier (BBB). Within the glioma, the blood vessels are noticeably permeable, and drugs which may not ordinarily enter normal brain, do enter into the tumor tissue. However, in the areas closer to the border of the tumor, the BBB inhibits the entry of a wide range of agents. Thus, delivering the drug to the tumor is critical. To approach this, convection enhanced delivery has been used with various targeted toxins (Raghavan et al. 2006).

We are still exploring the regulatory mechanisms involved in tumor angiogenesis, particularly the interaction of the endothelial cells with the tumor environment, and the unique qualities of the tumor-associated endothelial cells. As we learn more regarding the developing tumor system, we will be able to design specific drugs, therapeutic regimens, and delivery systems to better target the appropriate cellular functions. The constant appearance of new drugs for clinical trials provides evidence that the field of anti-vascular therapy is moving rapidly forward.

## REFERENCES

- Altieri, D.C. (2003) Validating survivin as a cancer therapeutic agent. *Nat. Rev. Cancer* 3:46–54

- Bergers, G., and Benjamin, L.E. (2003) Tumorigenesis and the angiogenic switch. *Nat. Rev. Cancer* 3:401–410
- Charalambous, C.C., Hofman, F.M., and Chen, T.C. (2005) Functional and phenotypic differences between glioblastoma multiforme-derived and normal human brain endothelial cells. *J. Neurosurg.* 102(4):699–705
- Charalambous, C.C., Virrey, J.J., Kardosh, A., Jabbour, M.N., Qazi-Abdullah, L., Pen, L., Zidovetzki, R., Schonthal, A.H., Chen, T.C., and Hofman, F.M. (2007) Glioma-associated endothelial cells show evidence of replicative senescence. *Exp. Cell Res.* 313(6):1192–1202
- Debatin, K.M., Wei, J., and Beltinger, C. (2008) Endothelial progenitor cells for cancer gene therapy. *Gene. Ther.* 15(10):780–786
- Dudek, A.Z., Bodempudi, V., Welsh, B.W., Jasinski, P., Griffin, R.J., Milbauer, L., and Hebbel, R.P. (2007) Systemic inhibition of tumour angiogenesis by endothelial cell-based gene therapy. *Br. J. Cancer* 97(4):513–522
- Dvorak, H.F. (2002) Vascular permeability factor/vascular endothelial growth factor: a critical cytokine in tumor angiogenesis and a potential target for diagnosis and therapy. *J. Clin. Oncol.* 20(21):4368–4380
- Effros, R.B. (2003) Replicative senescence: the final stage of memory T cell differentiation? *Curr. HIV Res.* 1:153–165
- Fernando, N.T., Koch, M., Rothrock, C., Gollogly, L.K., D'Amore, P.A., Ryeom, S., and Yoon, S.S. (2008) Tumor escape from endogenous, extracellular matrix-associated angiogenesis inhibitors by up-regulation of multiple proangiogenic factors. *Clin. Cancer Res.* 14(5):1529–1539
- Fischer, C., Jonckx, B., Mazzone, M., Zacchigna, S., Loges, S., Pattarini, L., Chorianopoulos, E., Liesenborghs, L., Koch, M., De Mol, M., Autiero, M., Wyns, S., Plaisance, S., Moons, L., van Rooijen, N., Giacca, M., Stassen, J.M., Dewerchin, M., Collen, D., and Carmeliet, P. (2007) Anti-PlGF inhibits growth of VEGF(R)-inhibitor-resistant tumors without affecting healthy vessels. *Cell* 131(3):463–475
- Folkman, J. (2007) Angiogenesis: an organizing principle for drug discovery? *Nat. Rev. Drug Disc.* 6(4):273–286
- Haskell, H., Natarajan, M., Hecker, T.P., Ding, Q., Stewart, J. Jr., Grammer, J.R., and Gladson, C.L.

- (2003) Focal adhesion kinase is expressed in the angiogenic blood vessels of malignant astrocytic tumors in vivo and promotes capillary tube formation of brain microvascular endothelial cells. *Clin. Cancer Res.* 9(6):2157–2165
- Hida, K., Hida, Y., Amin, D.N., Flint, A.F., Panigrahy, D., Morton, C.C., and Klagsbrun, M. (2004) Tumor-associated endothelial cells with cytogenetic abnormalities. *Cancer Res.* 64(22):8249–8255
- Hirata, A., Ogawa, S., Kometani, T., Kuwano, T., Naito, S., Kuwano, M., and Ono, M. (2002) ZD1839 (Iressa) induces antiangiogenic effects through inhibition of epidermal growth factor receptor tyrosine kinase. *Cancer Res.* 62(9):2554–2560
- Hlatky, L., Hahnfeldt, P., and Folkman, J. (2002) Clinical application of antiangiogenic therapy: microvessel density, what it does and doesn't tell us. *J. Nat. Cancer Inst.* 94(12):883–893
- Jansen, M., de Witt Hamer, P.C., Witmer, A.N., Troost, D., and van Noorden, C.J. (2004) Current perspectives on antiangiogenesis strategies in the treatment of malignant gliomas. *Brain Res.* 45(3):143–163
- Joe, Y.A., Hong, Y.K., Chung, D.S., Yang, Y.J., Kang, J.K., Lee, Y.S., Chang, S.I., You, W.K., Lee, H., and Chung, S.I. (1999) Inhibition of human malignant glioma growth in vivo by human recombinant plasminogen kringle 1–3. *Int. J. Cancer* 82(5):694–699
- Kerbel, R., and Folkman, J. (2002) Clinical translation of angiogenesis inhibitors. *Nat. Rev. Cancer* 2(10):727–739
- Kragh, M., Quistorff, B., Tenan, M., Van Meir, E.G., and Kristjansen, P.E. (2002) Overexpression of thrombospondin-1 reduces growth and vascular index but not perfusion in glioblastoma. *Cancer Res.* 62(4):1191–1195
- Lee, A.S. (2007) GRP78 induction in cancer: therapeutic and prognostic implications. *Cancer Res.* 67:3496–3499
- LoRusso, P.M., and Eder, J.P. (2008) Therapeutic potential of novel selective-spectrum kinase inhibitors in oncology. *Expert Opin. Invest. Drugs* 17(7):1013–1028
- Ma, J., and Waxman, D.J. (2008) Combination of antiangiogenesis with chemotherapy for more effective cancer treatment. *Mol. Cancer Ther.* 7:3670–3684
- McDonald, D.M., and Choyke, P.L. (2003) Imaging of angiogenesis: from microscope to clinic. *Nat. Med.* 9(6):713–725
- Moore, X.L., Lu, J., Sun, L., Zhu, C.J., Tan, P., and Wong, M.C. (2004) Endothelial progenitor cells' "homing" specificity to brain tumors. *Gene Ther.* 11(10):811–818
- Nolan, D.J., Ciarrocchi, A., Mellick, A.S., Jaggi, J.S., Bambino, K., Gupta, S., Heikamp, E., McDevitt, M.R., Scheinberg, D.A., Benezra, R., and Mittal, V. (2007) Bone marrow-derived endothelial progenitor cells are a major determinant of nascent tumor neovascularization. *Genes Dev.* 21(12):1546–1558
- Pen, A., Moreno, M.J., Martin, J., and Stanimirovic, D.B. (2007) Molecular markers of extracellular matrix remodeling in glioblastoma vessels: microarray study of laser-captured glioblastoma vessels. *GLIA* 55(6):559–572
- Rafii, D.C., Psaila, B., Butler, J., Jin, D.K., and Lyden, D. (2008) Regulation of vasculogenesis by platelet-mediated recruitment of bone marrow-derived cells. *Arterioscler Thromb. Vasc. Biol.* 28(2):217–222
- Raghavan, R., Brady, M.L., Rodriguez-Ponce, M.I., Hartlep, A., Pedain, C., and Sampson, J.H. (2006) Convection enhanced delivery of therapeutics for brain disease, and its optimization. *Neurosurg. Focus* 20(4):1–13
- Reardon, D.A., Nabors, L.B., Stupp, R., and Mikkelsen, T. (2008) Cilengitide: an integrin-targeting arginine-glycine-aspartic acid peptide with promising activity for glioblastoma multiforme. *Expert Opin. Invest. Drugs* 17(8):1225–1235
- Rege, T.A., Fears, C.Y., and Gladson, C.L. (2005) Endogenous inhibitors of angiogenesis in malignant gliomas: nature's antiangiogenic therapy. *Neuro. Oncol.* 7(2):106–121
- Socinski, M.A. (2008) Bevacizumab as first-line treatment for advanced non-small cell lung cancer. *Drugs Today* 44(4):293–301
- Stupp, R., Hegi, M.E., Gilbert, M.R., and Chakravarti, A. (2007) Chemoradiotherapy in malignant glioma: standard of care and future directions. *J. Clin. Oncol.* 25(26):4127–4136
- Villares, G.J., Zigler, M., Wang, H., Melnikova, V.O., Wu, H., Friedman, R., Leslie, M.C., Vivas-Mejia, P.E., Lopez-Berestein, G., Sood, A.K., and Bar-Eli, M. (2008) Targeting melanoma growth and

- metastasis with systemic delivery of liposome-incorporated protease-activated receptor-1 small interfering RNA. *Cancer Res.* 68:9078–9086
- Virrey, J.J., Guan, S., Li, W., Schonthal, A.H., Chen, T.C., and Hofman, F.M. (2008a) Increased survivin expression confers chemoresistance to tumor-associated endothelial cells. *Am. J. Pathol.* 173(2):575–585
- Virrey, J.J., Dong, D., Stiles, C., Patterson, J.B., Pen, L., Ni, M., Schonthal, A.H., Chen, T.C., Hofman, F.M., and Lee, A.S. (2008b) Stress chaperone GRP78/BiP confers chemoresistance to tumor-associated endothelial cells. *Mol. Cancer Res.* 6(8):1268–1275
- Volpert, O.V., Zaichuk, T., Zhou, W., Reiher, F., Ferguson, T.A., Stuart, P.M., Amin, M., and Bouck, N.P. (2002) Inducer-stimulated Fas targets activated endothelium for destruction by anti-angiogenic thrombospondin-1 and pigment epithelium-derived factor. *Nat. Med.* 8(4):349–357
- Wen, P.Y., and Kesari, S. (2008) Malignant gliomas in adults. *N. Engl. J. Med.* 359(5):492–507
- Wilhelm, S.M., Adnane, L., Newell, P., Villanueva, A., Llovet, J.M., and Lynch, M. (2008) Preclinical overview of sorafenib, a multikinase inhibitor that targets both Raf and VEGF and PDGF receptor tyrosine kinase signaling. *Mol. Cancer Ther.* 7(10):3129–3140
- Zhou, Q., Guo, P., and Gallo, J.M. (2008) Impact of angiogenesis inhibition by sunitinib on tumor distribution of temozolomide. *Clin. Cancer Res.* 14(5):1540–1549

# 10

## Glial Brain Tumors: Antiangiogenic Therapy

William P.J. Leenders and Pieter Wesseling

### CLINICAL FEATURES OF GLIOMA

Gliomas comprise a heterogeneous group of tumors of the central nervous system (CNS), encompassing many different histological types and malignancy grades. Most gliomas, the so-called ‘diffuse gliomas’, are characterized by extensive diffuse infiltrative growth. The most malignant type, glioblastoma multiforme (GBM), is by far the most common, accounting for 60–70% of all primary CNS gliomas. Other diffuse glioma types are low grade and anaplastic astrocytomas, oligodendrogliomas and oligoastrocytomas (Wen and Kesari 2008). The incidence of GBM in the Western world is relatively low with five cases per 100,000 people per year, as compared to lung, breast, and colorectal cancer which have an annual incidence of ~60–85 cases per 100,000 people. Despite this relatively low incidence, high grade gliomas represent a very important and devastating tumor type because they often occur relatively early in life and are always fatal, with a median survival rate of only 12–15 months for patients with GBM, and 2–5 years for patients with anaplastic astrocytoma. In fact, astrocytic tumors are the third leading cause of cancer-

related deaths among middle aged men and the fourth leading cause of death for women between 15 and 34 years of age.

Glioma symptoms vary depending on tumor phenotype, size and location and may consist of edema with increased intracranial pressure and headache, and neural damage resulting in vision loss, seizures, progressive failure in mental functioning and sometimes even hemiparesis. Diffuse low grade gliomas may go unnoticed for years before neural damage becomes symptomatic.

### HISTOPATHOLOGY AND GENETIC BACKGROUND OF GLIOMAS

Diffuse gliomas can be classified in three main subtypes: astrocytic, oligodendroglial, and mixed oligoastrocytic tumors (Louis et al. 2007). The nomenclature is based on the resemblance of the tumor cells with non-neoplastic astrocytes and oligodendrocytes, which however does not necessarily imply that these tumors originate from mature glial cells. In fact, there is quite some evidence that gliomas originate from neural stem cells (NSCs) or progenitor cells (Canoll and Goldman

2008). Astrocytic and oligodendroglial tumors differ in the genetic aberrations encountered. 60–70% of oligodendroglial tumors show a combined loss of chromosomal arms 1p and 19q, whereas high-grade astrocytic tumors often show amplification of chromosome 7 and loss of chromosome 10. Chromosome 7 contains the Epidermal Growth Factor Receptor (EGFR) gene (7p12), which indeed is frequently overexpressed in these tumors resulting in overactivation of signaling pathways and increased proliferation. Chromosome 10 harbours the tumor suppressor gene PTEN. These combined genetic alterations may, therefore, directly contribute to tumorigenesis. Noteworthy is that an auto-activating deletion variant of EGFR, EGFR-vIII, is frequently expressed by glioma cells (Sampson et al. 2008). Proper discrimination between different subtypes of glial tumors has high prognostic and predictive relevance: patients with malignant oligodendroglial tumors with 1p/19q loss show better survival and better response to chemotherapy.

Glial brain tumors are classified in four malignancy grades according to the WHO-2007 classification, non-diffuse pilocytic astrocytoma (WHO grade I) being the least and GBM (WHO grade IV) the most aggressive tumor. Histopathological hallmarks to classify glial tumors as GBM include necrosis and angiogenesis. A peculiar type of angiogenesis, called florid microvascular proliferation, is frequently encountered. The angiogenic response occurs especially in the perinecrotic regions and can be attributed to hypoxia-induced expression of Vascular Endothelial Growth Factor-A (VEGF-A), the most important angiogenic factor known to date and prime candidate for targeted anti-angiogenic therapies.

A unique characteristic of gliomas in WHO grades II to IV is their extensive diffuse infiltrative growth along myelinated fibers in white matter tracts. Also, perivascular growth in the Virchow-Robin space is frequently observed. The most extreme example of diffuse infiltrative glioma growth is represented by gliomatosis cerebri which involves at least three cerebral lobes, usually bilaterally (Louis et al. 2007). Of importance, it seems that infiltrative growth of gliomas in all grades is not dependent on angiogenesis, as the high vessel density in normal brain tissue allows the tumors to progress via incorporation of preexistent blood vessels, a process which is referred to as vessel cooption (Leenders et al. 2002).

## CURRENT TREATMENT MODALITIES

Diffuse infiltrative growth in the brain parenchyma enormously complicates treatment of glioma. Current standard of care is surgery to the maximum feasible extent, based on contrast-enhanced MR images. Surgery is never curative, due to the presence of individual migrating glioma cells within centimeters from the tumor core. Eventually, these remaining tumor cells will give rise to recurrent tumor. An additional complication is that current diagnostic modalities only allow visualization of parts of the tumor. Indeed, contrast-enhanced MRI-based diagnosis is based on the extravasation of small paramagnetic compounds, such as gadolinium diethylenetriaminepenta-acetic acid (Gd-DTPA). Such extravasation occurs only at sites where the blood brain barrier (BBB) is disrupted, i.e., especially in angiogenic areas. This explains the frequent finding of a

ring-like enhancement pattern in GBM, representing a non-enhancing necrotic core surrounded by an enhancing rim of angiogenic tumor. More distant areas with dispersed coopting tumor cells are not visualized because the BBB in the coopted vasculature in these areas is often intact. For first line treatment, surgery is followed by radiotherapy but, again, effective radiotherapy is problematic because the extended margins that are needed to kill all tumor cells would lead to unacceptable toxicity.

Except for oligodendrogliomas, gliomas are relatively insensitive to most chemotherapeutic agents like DNA-alkylating agents (carmustine, procarbazine, lomustine and vincristine) and topoisomerase I inhibitors (irinotecan) which do have prominent activity against other tumor types (Prados et al. 2006). This resistance may be intrinsic and related to a high capacity to restore therapy-induced DNA-damage. The subgroup of GBM patients with low levels of the DNA repair enzyme O<sup>6</sup>-methylguanine methyltransferase (MGMT), resulting from methylation of the MGMT promoter and silencing of the gene, has a relatively good response to temozolomide (Temodar/Temodal<sup>®</sup>, TMZ). TMZ is an orally-available DNA-alkylating agent with minimal toxicity, which is converted in the circulation into its active derivative MTIC (3-methyl-(1H-1,2,4-triazen-1-yl)imidazole-4-carboxamide). MTIC transfers alkylgroups to the DNA, and thereby interferes with the DNA replication machinery. Continuous exposure to TMZ may deplete MGMT pools, also in cells with unmethylated promoter, and ultimately result in sufficient DNA damage to kill the cell. Since TMZ treatment results in modest improvements of progression free and overall survival of GBM patients, combination of TMZ with

radiotherapy has become the standard first line treatment for these gliomas (Stupp et al. 2007).

A second important factor in determining chemoresistance of brain tumors is the BBB which is actually designed to keep away toxic substances from the brain parenchyma. In GBM there are regions that will be readily accessible to drugs because of prominent angiogenesis and concomitant absence of a functional BBB. However, in the same tumor there may be a high volume of infiltrative cancer in which incorporated vessels have an intact BBB, resulting in poor drug penetration in these regions. In such cases only a small proportion of the tumor is effectively treated when drugs are used that do not (or only partially) pass the intact BBB. The leakiness of vasculature in angiogenic tumor parts results in edema which may become clinically symptomatic and very aggravating when it leads to high intracranial pressure. To relieve these symptoms, patients are often treated with corticosteroids.

## ANTIANGIOGENESIS AS ANTI-TUMOR THERAPY

### VEGF-A and angiogenesis

It is commonly accepted that tumors need sufficient blood supply to be able to progress. As early as the 1970s, Folkman proposed that tumors induce their own blood supply via angiogenesis (Folkman 1971). Since then, research was boosted to elucidate the mechanisms behind induction of angiogenesis. This research revealed that cells in a growing tumor that become deprived of blood, sense hypoxia via a mechanism that results in activation of hypoxia-sensitive genes, among which VEGF-A, a chemotactic

factor for endothelial cells. VEGF-A activates the transmembrane tyrosine kinase VEGF receptors VEGFR1 and VEGFR2. In particular, activation of the latter results in signal transduction cascades, involving PI3 kinase-pAKT (leading to cell survival), MAPK (leading to cell proliferation) and the small Rac/RhoA GTPases (leading to cell migration) (Chan et al. 2005). VEGFR2 activation is also responsible for vascular hyperpermeability, induced via endothelial fenestrations or vesiculo-vacuolar organelles (VVOs) (Dvorak and Feng 2001). Indeed, preclinical work has shown that VEGF-A expression is sufficient to induce vessel permeability, and that inhibition of VEGF-A activity effectively annihilates this phenomenon (Leenders et al. 2004).

The knowledge on mechanisms of angiogenesis induction by tumors has been translated into numerous compounds that effectively inhibit the process. These can be put in two categories: antibodies and small compound tyrosine kinase inhibitors. Bevacizumab (Avastin, developed by Genentech) is a humanized monoclonal antibody against human VEGF-A (Kerbel 2008). Bevacizumab neutralizes VEGF-A activity by preventing binding to its receptors. A similar mode of action is accomplished by IMC-1121, an antibody against VEGFR2 (developed by Imclone) and by the VEGF neutralizer VEGF-TRAP, a chimeric soluble VEGF-receptor protein consisting of the VEGF binding domains of VEGFR1 and VEGFR2 (developed by Regeneron) (Gomez-Manzano et al. 2008). Both antibodies and receptor chimera prevent dimerization and subsequent autophosphorylation of VEGFR2. Tyrosine kinase inhibitors (TKIs) prevent downstream signal transduction from VEGF receptors. These orally available small

compounds are ATP analogues which bind to the ATP binding pocket of kinase receptors, competitively preventing binding of normal ATP and, thus, receptor phosphorylation. A number of VEGF receptor TKIs has been developed, which also have activity against other tyrosine kinase receptors, such as platelet-derived growth factor receptor (PDGFR) and Epidermal Growth Factor Receptor (EGFR) (Batchelor et al. 2007; Norden et al. 2008). The latter are of particular interest because these may allow simultaneous targeting of angiogenesis and other oncogenic pathways in tumor cells (e.g., the EGFR pathway in GBMs).

The approach of inhibiting angiogenesis has proven very effective as anti-tumor therapy in animal tumor models in which tumor stabilization and even regression are observed on a regular basis (Wedge et al. 2002). Most studies in which potent anti-tumor effects have been demonstrated, were performed in animal models in which tumor xenografts, also gliomas, were grown in the subcutaneous space of mice (Goldbrunner et al. 2000). Such studies have resulted in clinical trials and, for some tumor types, even in inclusion of anti-angiogenic therapies in standard care. Bevacizumab in combination with chemotherapy is now approved for first line treatment of patients with advanced colorectal carcinoma (Hurwitz et al. 2004), non-small cell lung cancer (Sandler et al. 2006) and metastatic breast cancer (Miller et al. 2007). Sunitinib, a tyrosine kinase inhibitor of, among others, VEGFRs and PDGFRs, is now approved for treatment of metastatic clear cell renal cell carcinoma (Motzer et al. 2007). In general, it can be stated that in these tumor types antiangiogenic therapy in combination with chemotherapy does lead to prolonged progression free

survival, as well as to some prolonged overall survival. However, it is now also clear that these new modalities have not yet resulted in durable control.

### PRECLINICAL ANTI- ANGIOGENIC THERAPY OF BRAIN TUMORS

Where do the discrepancies between pre-clinical and clinical results come from? It is important to realize that many preclinical models utilizing subcutaneous xenografts are not representative of clinical glioma because a relevant tumor micro-environment is lacking (Goldbrunner et al. 2000), and this may result in misinterpretation of therapeutic effects. For instance, as the subcutaneous space is avascular with limited potential for vessel cooption, when using subcutaneous xenograft models, one selects for a tumor's capacity to induce angiogenesis and thereby, for an intrinsic susceptibility to anti-angiogenic agents. Indeed, our experience with glioma xenografts is that angiogenesis-incompetent tumors exist and that, upon direct transplantation into the subcutaneous space, these tumors do not grow, whereas the same specimens rapidly induce tumors when implanted intracerebrally (Claes et al. 2008b). Furthermore, we have shown that melanoma cell lines which show slow growth and extensive necrosis when grown subcutaneously, grow vividly and without any evidence of necrosis or even hypoxia when grown in the brain parenchyma upon intracarotid injection (Kusters et al. 2002, 2007). In this case, these non-angiogenic tumors develop in the brain micro-environment by cooption of preexistent vasculature (Leenders et al. 2002).

In our centre we developed a number of human glioma xenograft lines, such as E98. This xenograft line was initiated in the early 1990s and is maintained as subcutaneous tumors which develop within 2 months after grafting to tumors of approximately 1 cm<sup>3</sup>. Subcutaneous E98 tumors contain dispersed areas of hypoxia. Intracerebral injection of a cell homogenate, prepared from these subcutaneous tumors, results in a heterogeneous tumor phenotype with very few hypoxic areas and which actually contains all the hallmarks of a high grade malignant human glioma, i.e., microvascular proliferations in more compact tumor areas with leaky vasculature, but also diffuse infiltrative growth in white matter tracts and perivascular growth (Claes et al. 2008b).

We have subjected mice bearing intracerebral E98 tumors to anti-angiogenic therapies using the VEGFR2/EGFR tyrosine kinase inhibitor vandetanib (ZD6474), sunitinib, avastin or combinations of these. The results of these studies confirmed previous results of our laboratory with angiogenic melanoma in brain (Leenders et al. 2004). All compounds effectively inhibited angiogenesis and accompanying vessel leakiness, an effect that is best illustrated by the fact that tumor visibility was drastically reduced in Gd-DTPA-enhanced MRI scans (Claes et al. 2008a, 2008c). Angiogenesis was also effectively inhibited by VEGF-TRAP or anti-VEGFR2 antibodies in orthotopic models of glioma (Gomez-Manzano et al. 2008). A common result of all these studies is that anti-angiogenic compounds are indeed unequivocally inhibiting angiogenesis, but that anti-angiogenic therapy is not effective against the diffuse infiltrative tumor components (Claes et al. 2008c). It has



even been postulated that antiangiogenic compounds may force a tumor into a more infiltrative growth mode (Lamszus et al. 2003; Rubenstein et al. 2000). In our tumor models, mice did not survive longer when under vandetanib therapy. It must be realized, however, that the diffuse infiltrative growth in E98 is extensive, generally involving both hemispheres (Claes et al. 2008b). Therefore, in this model the relative decrease in tumor burden due to eradication of the angiogenic component may be too low to result in survival advantage.

### CONSEQUENCES OF ANTIANGIOGENIC THERAPY FOR DIAGNOSIS: VESSEL NORMALIZATION

Uncontrolled VEGF-A activity in tumors results in a tortuous, irregularly dilated and hyperpermeable vasculature and edema. A high interstitial pressure, together with poor blood flow in these vessels has been proposed to counteract the effective uptake of drugs from the circulation. Anti-VEGF-A therapies result in pruning of newly formed vessels, sparing the more matured and non-leaky ones. This phenomenon is termed vessel normalization and presumably results in an overall reduced interstitial pressure and better tumor perfusion (Jain 2005). The hypothesis of vessel normalization has been used to explain the synergistic effects of antiangiogenic therapies and chemotherapies in advanced colorectal cancer patients.

Vessel normalization in brain tumors is both a blessing and a curse (Claes and Leenders 2008). Firstly, reduction of edema is expected to be beneficial for patients with (glial) brain tumors, since a high intracranial pressure can be very aggravating and

ultimately life threatening. On the other hand, the annihilation of vessel leakage complicates evaluation of therapies, as contrast-enhanced MRI investigations depend on this vessel leakage. Indeed, experimental tumors in a brain setting become undetectable after anti-VEGF therapies, while still progressing via infiltration, resulting in enormous overestimation of therapeutic efficacy (Claes et al. 2008a, c; Leenders et al. 2004).

Another complication relates to the BBB. It is known that the BBB is meant to keep toxic substances away from the very sensitive neurons. However, normalization of the BBB in tumor vessels may also hamper delivery of chemotherapeutic drugs to the tumor cells. We recently described that this is a relevant danger, as a higher percentage of mice carrying intracerebral E98 tumors was completely cured when treated with TMZ, compared to mice that received TMZ and vandetanib (Claes et al. 2008c). As TMZ combined with radiotherapy is now the standard of care for glioma patients (Stupp et al. 2005), we are facing the problem that combining this treatment with antiangiogenic compounds might indeed adversely affect tumor response to therapy. Meanwhile, anti-VEGF therapies may result in a significant but temporarily improved quality of life. These different beneficial and adverse effects of antiangiogenic compounds need careful attention before antiangiogenic therapy is implemented in the routine treatment of glioma patients.

### CLINICAL EXPERIENCE WITH ANTI-ANGIOGENIC THERAPY

As of now, no large phase III trials on angiogenesis inhibition in glioma patients have been performed. A number of antian-

giogenic approaches has been tested in phase I and II trials including thalidomide and its analogue lenalidomide (targeting the fibroblast growth factor [FGF] pathway) (Groves et al. 2007), the integrin antagonist cilengitide (Reardon et al. 2008), and metronomic chemotherapy, targeting proliferating endothelial cells rather than tumor cells (Kerbel 2008). Most reports on effective treatment involve phase II studies in which bevacizumab was administered in combination with (radio) chemotherapy for recurrent GBM.

In a number of studies investigating combination therapy of bevacizumab with irinotecan for recurrent GBM and anaplastic astrocytoma, ~60–80% of patients showed a partial response (Ali et al. 2008; Narayana et al. 2008; Vredenburgh et al. 2007). However, as these responses were defined by radiological criteria (Macdonald et al. 1990), i.e., by post-contrast MRI as discussed earlier, the actual efficacy of this treatment may be overestimated. Importantly, in these patients tumors frequently recur at some distance from the primary tumor mass, corroborating the concept that under bevacizumab therapy, diffuse tumor infiltration can continue (Zuniga et al. 2008).

Also, these trials showed improvements on the 6-month progression free survival (PFS) rate as compared to historical controls. Again, the status of progression-free is established by post-contrast MRI criteria and absence of neurological worsening. The better performance of patients under bevacizumab therapy may be related to diminished edema and intracranial pressure, rather than anti-angiogenesis. Of interest, these effects are not limited to gliomas but also appear to apply to brain metastases of other tumors (Mathews et al. 2008).

An involvement of an autocrine PDGF/PDGFR loop in glioma has been suggested

(Guha et al. 1995), and this has been the rationale for testing the PDGFR tyrosine kinase inhibitor imatinib, either alone or in combination with hydroxyurea in phase II studies (Raymond et al. 2008). Besides a potential effect on tumor cell proliferation, PDGF signaling is involved in maturation of newly formed vessels (Bergers et al. 2003). Imatinib as monotherapy did not significantly improve 6 month PFS in these studies (Raymond et al. 2008; Wen et al. 2006), and in combination with hydroxyurea had only modest activity (Reardon et al. 2005). Of importance, other studies described an increased incidence of intratumoral hemorrhage upon imatinib treatment of GBM (Wen et al. 2006). It may be hypothesized that inhibition of PDGF signaling without diminishing VEGF-A activity results in the continuous presence of tortuously dilated and immature vasculature in the tumor with increased chance of vessel rupture. These results indicate that caution is warranted with such targeted therapies. Simultaneous targeting of both VEGFR and PDGFRs may therefore be more effective.

TKIs, targeting both of these receptors are available and have been tested. A phase II study in 16 patients with recurrent GBM showed that cediranib (AZD2171, a tyrosine kinase inhibitor targeting both VEGF and PDGF receptors) transiently normalized tumor vasculature resulting in decreased MRI visibility and reduced edema-related clinical symptoms (Batchelor et al. 2007). The reduction of edema greatly reduced the need for corticosteroid treatment in these patients. Despite these positive effects, significant effects on median progression-free survival and overall survival seemed absent, although the number of patients in this study was obviously too small to reach definite conclusions.

It seems, therefore, that patients benefit from anti-VEGF-A treatment. As previously indicated, one of the main problems in evaluating the efficacy of VEGF-A targeting is that the diagnostic possibilities to monitor the nature of the response are limited. Several recent articles have analyzed effects of bevacizumab on tumor behavior on the histological level, and first results confirm preclinical findings: although contrast-enhanced MRI suggests response to therapy, analysis of surgically obtained post-therapy specimens reveals the presence of highly infiltrative tumor, even with increased expression levels of migration-related genes (Narayana et al. 2008). Whether antiangiogenesis truly induces an invasive phenotype or leaves the invasive tumor compartment unaffected remains to be determined. In any case, these data show that antiangiogenesis should ideally be combined with therapies that target the diffuse infiltrative tumor component.

## FUTURE PERSPECTIVES

Although normalization of the BBB by antiangiogenic therapy has clear positive effects for glioma patients, up till now these effects only seem to be temporary and palliative. However, for a tumor which is currently incurable, this may be an important improvement in care. Unfortunately, there are also adverse effects associated with antiangiogenic therapy, and ironically these are also associated with the BBB normalization. Whereas the underestimation of tumor burden after anti-angiogenic therapy may be resolved in the future by employing alternative imaging modalities such as positron emission tomography (PET), diffusion-weighted imaging, perfusion MRI,

magnetic resonance spectroscopy (MRS) or blood volume imaging (Gambarota et al. 2008; Jenkinson et al. 2007), the potential interference with chemodistribution needs careful attention. To this end, extensive further preclinical work is needed to help elucidate optimal timing and dosing schedules of antiangiogenic therapy, radiotherapy, and chemotherapy.

In fact, there are rational arguments to combine anti-VEGF therapy with radiation therapy. VEGF-A promotes cell survival via induction of AKT phosphorylation. As such, it will protect endothelial cells against radiation-induced apoptosis. In this respect, angiogenesis inhibitors or inhibitors of mTOR may enhance efficacy of radiation therapy (Chi et al. 2007; Duda et al. 2007; Lee et al. 2000). Furthermore, radiation therapy temporarily disrupts the BBB, possibly improving concomitant chemotherapy.

It is clear from preclinical and clinical work that, despite progress in attacking the tumor's blood supply, the presence of migrating tumor cells which can progress by incorporating preexisting blood supply, is a fundamental problem. Targeting of cell migration, for instance by interfering with c-MET induced Rac-RhoA small GTPase signaling (Martens et al. 2006) may therefore represent an important next step towards effective glioma therapy. Also a direct attack of tumor cells by immunotherapy with vaccines, specifically targeting the constitutively active EGFR-vIII on tumor cells has been considered for the subgroup of gliomas that overexpress this deletion mutant, and such studies have already yielded encouraging results (Sampson et al. 2008). How the BBB is involved in allowing access of cytotoxic T-cells to the tumor cells is currently unclear.

In conclusion, a number of approaches has been developed for therapy of diffuse glioma. No modality has yet been shown to result in a more than modest improvement of overall survival, and curation of these tumors is still not possible. A multimodality approach, simultaneously targeting different molecular characteristics of the glioma cells (e.g., those involved in oncogenesis, angiogenesis, migration, and DNA-repair) may lead to improved therapy of diffuse gliomas. Preclinical studies using genotypically and phenotypically relevant glioma models may be of great help in exploring how the different treatment modalities interact in order to optimize combination therapies with respect to timing and dosage.

## REFERENCES

- Ali, S.A., McHayleh, W.M., Ahmad, A., Sehgal, R., Braffet, M., Rahman, M., Bejjani, G., and Friedland, D.M. (2008) Bevacizumab and irinotecan therapy in glioblastoma multiforme: a series of 13 cases. *J. Neurosurg.* 109:268–272
- Batchelor, T.T., Sorensen, A.G., di Tomaso, E., Zhang, W.T., Duda, D.G., Cohen, K.S., Kozaki, K.R., Cahill, D.P., Chen, P.J., Zhu, M., Ancukiewicz, M., Mrugala, M.M., Plotkin, S., Drappatz, J., Louis, D.N., Ivy, P., Scadden, D.T., Benner, T., Loeffler, J.S., Wen, P.Y., and Jain, R.K. (2007) AZD2171, a pan-VEGF receptor tyrosine kinase inhibitor, normalizes tumor vasculature and alleviates edema in glioblastoma patients. *Cancer Cell* 11:83–95
- Bergers, G., Song, S., Meyer-Morse, N., Bergsland, E., and Hanahan, D. (2003) Benefits of targeting both pericytes and endothelial cells in the tumor vasculature with kinase inhibitors. *J. Clin. Invest.* 111:1287–1295
- Canoll, P., and Goldman, J.E. (2008) The interface between glial progenitors and gliomas. *Acta Neuropathol.* 116:465–477
- Chan, A.Y., Coniglio, S.J., Chuang, Y.Y., Michaelson, D., Knaus, U.G., Philips, M.R., and Symons, M. (2005) Roles of the Rac1 and Rac3 GTPases in human tumor cell invasion. *Oncogene* 24:7821–7829
- Chi, A., Norden, A.D., and Wen, P.Y. (2007) Inhibition of angiogenesis and invasion in malignant gliomas. *Expert Rev. Anticancer Ther.* 7:1537–1560
- Claes, A., and Leenders, W. (2008) Vessel normalization by VEGF inhibition. *Cancer Biol. Ther.* 7:7
- Claes, A., Gambarota, G., Hamans, B., van Tellingen, O., Wesseling, P., Maass, C., Heerschap, A., and Leenders, W. (2008a) Magnetic resonance imaging-based detection of glial brain tumors in mice after antiangiogenic treatment. *Int. J. Cancer* 122:1981–1986
- Claes, A., Schuurings, J., Boots-Sprenger, S., Hendriks-Cornelissen, S., Dekkers, M., van der Kogel, A.J., Leenders, W.P., Wesseling, P., and Jeuken, J.W. (2008b) Phenotypic and genotypic characterization of orthotopic human glioma models and its relevance for the study of anti-glioma therapy. *Brain Pathol.* 18:423–433
- Claes, A., Wesseling, P., Jeuken, J., Maass, C., Heerschap, A., and Leenders, W.P. (2008c) Antiangiogenic compounds interfere with chemotherapy of brain tumors due to vessel normalization. *Mol. Cancer Ther.* 7:71–78
- Duda, D.G., Jain, R.K., and Willett, C.G. (2007) Antiangiogenics: the potential role of integrating this novel treatment modality with chemoradiation for solid cancers. *J. Clin. Oncol.* 25:4033–4042
- Dvorak, A.M., and Feng, D. (2001) The vesiculo-vacuolar organelle (VVO). A new endothelial cell permeability organelle. *J. Histochem. Cytochem.* 49:419–432
- Folkman, J. (1971) Tumor angiogenesis: therapeutic implications. *N. Engl. J. Med.* 285:1182–1186
- Gambarota, G., Leenders, W., Maass, C., Wesseling, P., van der Kogel, A., van Tellingen, O., and Heerschap, A. (2008) Characterization of tumor vasculature in mouse brain by USPIO contrast-enhanced MRI. *Br. J. Cancer* 98:1784–1789
- Goldbrunner, R.H., Wagner, S., Roosen, K., and Tonn, J.C. (2000) Models for assessment of angiogenesis in gliomas. *J. Neurooncol.* 50:53–62
- Gomez-Manzano, C., Holash, J., Fueyo, J., Xu, J., Conrad, C.A., Aldape, K.D., de Groot, J.F., Bekele, B.N., and Yung, W.K. (2008) VEGF Trap induces antiglioma effect at different stages of disease. *Neuro. Oncol.* 10:940–945

- Groves, M.D., Puduvalli, V.K., Chang, S.M., Conrad, C.A., Gilbert, M.R., Tremont-Lukats, I.W., Liu, T.J., Peterson, P., Schiff, D., Cloughesy, T.F., Wen, P.Y., Greenberg, H., Abrey, L.E., DeAngelis, L.M., Hess, K.R., Lamborn, K.R., Prados, M.D., and Yung, W.K. (2007) A North American brain tumor consortium (NABTC 99-04) phase II trial of temozolomide plus thalidomide for recurrent glioblastoma multiforme. *J. Neurooncol.* 81:271–277
- Guha, A., Dashner, K., Black, P.M., Wagner, J.A., and Stiles, C.D. (1995) Expression of PDGF and PDGF receptors in human astrocytoma operation specimens supports the existence of an autocrine loop. *Int. J. Cancer* 60:168–173
- Hurwitz, H., Fehrenbacher, L., Novotny, W., Cartwright, T., Hainsworth, J., Heim, W., Berlin, J., Baron, A., Griffing, S., Holmgren, E., Ferrara, N., Fyfe, G., Rogers, B., Ross, R., and Kabbinavar, F. (2004) Bevacizumab plus irinotecan, fluorouracil, and leucovorin for metastatic colorectal cancer. *N. Engl. J. Med.* 350:2335–2342
- Jain, R.K. (2005) Normalization of tumor vasculature: an emerging concept in antiangiogenic therapy. *Science* 307:58–62
- Jenkinson, M.D., Du Plessis, D.G., Walker, C., and Smith, T.S. (2007) Advanced MRI in the management of adult gliomas. *Br. J. Neurosurg.* 21:550–561
- Kerbel, R.S. (2008) Tumor angiogenesis. *N. Engl. J. Med.* 358:2039–2049
- Kusters, B., Leenders, W.P., Wesseling, P., Smits, D., Verrijp, K., Ruiter, D.J., Peters, J.P., van Der Kogel, A.J., and de Waal, R.M. (2002) Vascular endothelial growth factor-A (165) induces progression of melanoma brain metastases without induction of sprouting angiogenesis. *Cancer Res.* 62:341–345
- Kusters, B., Kats, G., Roodink, I., Verrijp, K., Wesseling, P., Ruiter, D.J., de Waal, R.M., and Leenders, W.P. (2007) Micronodular transformation as a novel mechanism of VEGF-A-induced metastasis. *Oncogene* 26:5808–5815
- Lamszus, K., Kunkel, P., and Westphal, M. (2003) Invasion as limitation to anti-angiogenic glioma therapy. *Acta Neurochir. (Suppl. 88)*:169–177
- Lee, C.G., Heijn, M., di Tomaso, E., Griffon-Etienne, G., Ancukiewicz, M., Koike, C., Park, K.R., Ferrara, N., Jain, R.K., Suit, H.D., and Boucher, Y. (2000) Anti-Vascular endothelial growth factor treatment augments tumor radiation response under normoxic or hypoxic conditions. *Cancer Res.* 60:5565–5570
- Leenders, W., Kusters, B., and De Waal, R. (2002) Vessel co-option: How tumors obtain blood supply in the absence of sprouting angiogenesis. *Endothelium* 9:83–87
- Leenders, W.P., Kusters, B., Verrijp, K., Maass, C., Wesseling, P., Heerschap, A., Ruiter, D., Ryan, A., and de Waal, R. (2004) Antiangiogenic therapy of cerebral melanoma metastases results in sustained tumor progression via vessel co-option. *Clin. Cancer Res.* 10:6222–6230
- Louis, D.N., Ohgaki, H., Wiestler, O.D., and Cavenee, W.K. (2007) Classification of tumours of the central nervous system. IARC Press, Lyon
- Macdonald, D.R., Cascino, T.L., Schold, S.C. Jr., and Cairncross, J.G. (1990) Response criteria for phase II studies of supratentorial malignant glioma. *J. Clin. Oncol.* 8:1277–1280
- Martens, T., Schmidt, N.O., Eckerich, C., Fillbrandt, R., Merchant, M., Schwall, R., Westphal, M., and Lamszus, K. (2006) A novel one-armed anti-Met antibody inhibits glioblastoma growth in vivo. *Clin. Cancer Res.* 12:6144–6152
- Mathews, M.S., Linskey, M.E., Hasso, A.N., and Fruehauf, J.P. (2008) The effect of bevacizumab (Avastin) on neuroimaging of brain metastases. *Surg. Neurol.* 7:7
- Miller, K., Wang, M., Gralow, J., Dickler, M., Cobleigh, M., Perez, E.A., Shenkier, T., Cella, D., and Davidson, N.E. (2007) Paclitaxel plus bevacizumab versus paclitaxel alone for metastatic breast cancer. *N. Engl. J. Med.* 357:2666–2676
- Motzer, R.J., Hutson, T.E., Tomczak, P., Michaelson, M.D., Bukowski, R.M., Rixe, O., Oudard, S., Negrier, S., Szczylik, C., Kim, S.T., Chen, I., Bycott, P.W., Baum, C.M., and Figlin, R.A. (2007) Sunitinib versus interferon alfa in metastatic renal-cell carcinoma. *N. Engl. J. Med.* 356:115–124
- Narayana, A., Kelly, P., Golfinos, J., Parker, E., Johnson, G., Knopp, E., Zagzag, D., Fischer, I., Raza, S., Medabalmi, P., Eagan, P., and Gruber, M.L. (2008) Antiangiogenic therapy using bevacizumab in recurrent high-grade glioma: impact on local control and patient survival. *J. Neurosurg.* published online October 3, 2008. doi:10.3171/2008.4.17492
- Norden, A.D., Drappatz, J., and Wen, P.Y. (2008) Antiangiogenic therapy in malignant gliomas. *Curr. Opin. Oncol.* 20:652–661

- Prados, M.D., Lamborn, K., Yung, W.K., Jaeckle, K., Robins, H.I., Mehta, M., Fine, H.A., Wen, P.Y., Cloughesy, T., Chang, S., Nicholas, M.K., Schiff, D., Greenberg, H., Junck, L., Fink, K., Hess, K., and Kuhn, J. (2006) A phase 2 trial of irinotecan (CPT-11) in patients with recurrent malignant glioma: a North American Brain Tumor Consortium Study. *Neuro. Oncol.* 8:189–193
- Raymond, E., Brandes, A.A., Dittrich, C., Fumoleau, P., Coudert, B., Clement, P.M., Frenay, M., Rampling, R., Stupp, R., Kros, J.M., Heinrich, M.C., Gorlia, T., Lacombe, D., and van den Bent, M.J. (2008) Phase II study of imatinib in patients with recurrent gliomas of various histologies: a European Organisation for Research and Treatment of Cancer Brain Tumor Group Study. *J. Clin. Oncol.* 26:4659–4665
- Reardon, D.A., Egorin, M.J., Quinn, J.A., Rich, J.N., Gururangan, S., Vredenburgh, J.J., Desjardins, A., Sathornsumetee, S., Provenzale, J.M., Herndon, J.E. II, Dowell, J.M., Badruddoja, M.A., McLendon, R.E., Lagattuta, T.F., Kicielinski, K.P., Dresemann, G., Sampson, J.H., Friedman, A.H., Salvado, A.J., and Friedman, H.S. (2005) Phase II study of imatinib mesylate plus hydroxyurea in adults with recurrent glioblastoma multiforme. *J. Clin. Oncol.* 23:9359–9368
- Reardon, D.A., Nabors, L.B., Stupp, R., and Mikkelsen, T. (2008) Cilengitide: an integrin-targeting arginine-glycine-aspartic acid peptide with promising activity for glioblastoma multiforme. *Expert Opin. Investig. Drugs* 17:1225–1235
- Rubenstein, J.L., Kim, J., Ozawa, T., Zhang, M., Westphal, M., Deen, D.F., and Shuman, M.A. (2000) Anti-VEGF antibody treatment of glioblastoma prolongs survival but results in increased vascular cooption. *Neoplasia* 2:306–314
- Sampson, J.H., Archer, G.E., Mitchell, D.A., Heimberger, A.B., and Bigner, D.D. (2008) Tumor-specific immunotherapy targeting the EGFRvIII mutation in patients with malignant glioma. *Semin. Immunol.* 20:267–275
- Sandler, A., Gray, R., Perry, M.C., Brahmer, J., Schiller, J.H., Dowlati, A., Lilienbaum, R., and Johnson, D.H. (2006) Paclitaxel-carboplatin alone or with bevacizumab for non-small-cell lung cancer. *N. Engl. J. Med.* 355:2542–2550
- Stupp, R., Mason, W.P., van den Bent, M.J., Weller, M., Fisher, B., Taphoorn, M.J., Belanger, K., Brandes, A.A., Marosi, C., Bogdahn, U., Curschmann, J., Janzer, R.C., Ludwin, S.K., Gorlia, T., Allgeier, A., Lacombe, D., Cairncross, J.G., Eisenhauer, E., and Mirimanoff, R.O. (2005) Radiotherapy plus concomitant and adjuvant temozolomide for glioblastoma. *N. Engl. J. Med.* 352:987–996
- Stupp, R., Hegi, M.E., Gilbert, M.R., and Chakravarti, A. (2007) Chemoradiotherapy in malignant glioma: standard of care and future directions. *J. Clin. Oncol.* 25:4127–4136
- Vredenburgh, J.J., Desjardins, A., Herndon, J.E. 2nd, Marcello, J., Reardon, D.A., Quinn, J.A., Rich, J.N., Sathornsumetee, S., Gururangan, S., Sampson, J., Wagner, M., Bailey, L., Bigner, D.D., Friedman, A.H., and Friedman, H.S. (2007) Bevacizumab plus irinotecan in recurrent glioblastoma multiforme. *J. Clin. Oncol.* 25:4722–4729
- Wedge, S.R., Ogilvie, D.J., Dukes, M., Kendrew, J., Chester, R., Jackson, J.A., Boffey, S.J., Valentine, P.J., Curwen, J.O., Musgrove, H.L., Graham, G.A., Hughes, G.D., Thomas, A.P., Stokes, E.S., Curry, B., Richmond, G.H., Wadsworth, P.F., Bigley, A.L., and Hennequin, L.F. (2002) ZD6474 inhibits vascular endothelial growth factor signaling, angiogenesis, and tumor growth following oral administration. *Cancer Res.* 62:4645–4655
- Wen PY, and Kesari S (2008) Malignant gliomas in adults. *N. Engl. J. Med.* 359:492–507
- Wen, P.Y., Yung, W.K., Lamborn, K.R., Dahia, P.L., Wang, Y., Peng, B., Abrey, L.E., Raizer, J., Cloughesy, T.F., Fink, K., Gilbert, M., Chang, S., Junck, L., Schiff, D., Lieberman, F., Fine, H.A., Mehta, M., Robins, H.I., DeAngelis, L.M., Groves, M.D., Puduvalli, V.K., Levin, V., Conrad, C., Maher, E.A., Aldape, K., Hayes, M., Letvak, L., Egorin, M.J., Capdeville, R., Kaplan, R., Murgu, A.J., Stiles, C., and Prados, M.D. (2006) Phase I/II study of imatinib mesylate for recurrent malignant gliomas: North American Brain Tumor Consortium Study 99–08. *Clin. Cancer Res.* 12:4899–4907
- Zuniga, R.M., Torcuator, R., Jain, R., Anderson, J., Doyle, T., Ellika, S., Schultz, L., and Mikkelsen, T. (2008) Efficacy, safety and patterns of response and recurrence in patients with recurrent high-grade gliomas treated with bevacizumab plus irinotecan. *J. Neurooncol.* doi:10.1007/s11060-008-9718-y

*This page intentionally left blank*

# 11

## Brain Tumors: Amide Proton Transfer Imaging

Jinyuan Zhou and Jaishri O. Blakeley

### INTRODUCTION

Currently, gliomas are generally evaluated using gadolinium (Gd)-enhanced  $T_1$ -weighted ( $T_1w$ ) MRI in combination with  $T_2$ -weighted ( $T_2w$ ) or fluid-attenuated inversion recovery (FLAIR)  $T_2w$  MRI, which are used to determine the extent of involvement, to plan treatments, and to assess a therapeutic response. However, existing MRI techniques are not sufficiently tissue-specific and suffer from several limitations. First, Gd enhancement reveals focal areas of tumor where the blood-brain barrier (BBB) is disrupted, but it does not show large areas of an infiltrating tumor (Kelly et al. 1987; Burger et al. 1988). Another limitation is that some high-grade gliomas (roughly 10% of glioblastoma multiforme and 30% of anaplastic astrocytoma) demonstrate no Gd enhancement (Scott et al. 2002). Therefore, it can be difficult to identify the most malignant portions of tumor prior to surgery or local therapies. Third, Gd enhancement is not always specific for tumor grade, as low-grade gliomas occasionally enhance (Knopp et al. 1999). Fourth, Gd enhancement occurs in any area of BBB disruption, such as that caused by radiation necrosis, regardless of etiology

(Mullins et al. 2005). Finally, glioma patients require frequent MRIs, and Gd exposure has recently been indicated as a risk factor for renal toxicity (Ersoy and Rybicki 2007). These imaging limitations have immediate clinical repercussions that may cause diagnosis problematic and render local therapies ineffectual. Notably, standard brain MRI cannot distinguish between treatment-related injury and tumor progression. This distinction is critical for appropriate treatment planning and assessment of tumor response. In recent years, there has been much progress in tumor assessment using more advanced MRI approaches, including MR spectroscopy (Vigneron et al. 2001), diffusion imaging (Chenevert et al. 1997), perfusion imaging (Law et al. 2003), and combinations of these techniques. However, additional MR approaches, especially tissue-specific ones that use endogenous contrast, are much needed.

The extension of MR neuroimaging to the cellular and molecular level has introduced new possibilities for imaging malignant gliomas. Currently, however, most molecular and cellular MRI studies have been limited to the preclinical setting, because they rely on the administration of paramagnetic or super-paramagnetic



metal-based substrates that are potentially toxic. Ideally, molecular imaging would exploit endogenous molecules that can be probed noninvasively using existing hardware. Amide proton transfer (APT) imaging (Zhou et al. 2003a, b) is a new MRI technique that detects endogenous mobile proteins and peptides in tissue using the principle of chemical exchange-dependent saturation transfer (CEST) sensitivity enhancement (Wolff and Balaban 1990; Ward et al. 2000). The preclinical studies and pilot clinical data have suggested that there is an increased APT signal in malignant brain tumors, potentially providing unique information regarding the presence and grade of brain tumors based on the increased cellular content of proteins and peptides. This is in line with existing knowledge that malignant gliomas and other cancers have high cellularity (Gauvain et al. 2001), as well as increased cellular protein and peptide levels (Hobbs et al. 2003; Howe et al. 2003). APT-MRI has the potential to expand the range of molecular MRI techniques to the endogenous protein and peptide level and to enhance the noninvasive identification and classification of brain cancers before and after treatment.

## CHEMICAL EXCHANGE-DEPENDENT SATURATION TRANSFER IMAGING: PRINCIPLES AND APPLICATIONS

Using NMR concepts of chemical exchange, Wolff and Balaban (1990), and Ward et al. (2000) demonstrated that the process of saturation transfer from exchangeable protons to water can be used for metabolite

sensitivity enhancement, an approach dubbed CEST. In CEST imaging, low-concentration solute molecules are selectively labeled by saturating specific exchangeable protons (e.g., hydroxyl, amine, amide, or imino protons) with radiofrequency (RF) irradiation. When such saturation-labeled protons exchange with water protons, the water signal becomes slightly saturated. In view of the low concentration of solute ( $\mu\text{M}$  to  $\text{mM}$  range), a single transfer of saturation would be insufficient to show any effect on water (100 M). However, because the water pool is much larger than the saturated solute proton pool, each exchanging saturated solute proton is replaced by a non-saturated water proton, which is then again saturated. If the solute protons have a sufficiently fast exchange rate (tens of Hz) and if the  $T_1$  of water is sufficiently long (sec range), prolonged irradiation leads to substantial enhancement of this saturation effect.

Following the pioneering work by Wolff and Balaban (1990), and Ward et al. (2000), Goffeney et al. (2001) showed that large increases in sensitivity can be obtained for macromolecules, such as poly-L-lysine, dendrimers, and polynucleotides, which contain a large number of exchangeable protons with a similar chemical shift. Zhang et al. (2001), and Aime et al. (2002) simultaneously reported several paramagnetic CEST (paraCEST) agents that made the approach more flexible by significantly enlarging the frequency range for the exchanging sites that need to be saturated selectively.

Based on these CEST results, Zhou et al. (2003a, b) hypothesized that it should be possible to detect mobile proteins and peptides in tissue via the water signal using the CEST approach, and subsequently demonstrated this amide proton transfer (APT) process *in vivo*. For the APT

approach, the composite amide resonance at  $\sim 8.3$  ppm in the proton spectrum of the brain is saturated and detected through water to image the pH level (Zhou et al. 2003a) or the endogenous protein and peptide content of tissue (Zhou et al. 2003b). APT imaging is one of the first examples of the successful *in vivo* application of CEST-based techniques.

The CEST approach presents a large and specific detection sensitivity enhancement through progressive saturation of the water signal, and the contrast can be switched on-and-off by simply changing the RF irradiation frequency or by turning it on and off. Currently, many important CEST-type applications are being evaluated by different researchers, including pH imaging (Aime et al. 2002; Zhou et al. 2003a; Sun et al. 2007; Jokivarsi et al. 2007), metabolite detection (Zhang et al. 2003), imaging of cellular proteins and peptides (Zhou et al. 2003b; Ling et al. 2008), cell labeling (Aime et al. 2005), detection of enzyme activity (Yoo and Pagel 2006), CEST reporter genes (Gilad et al. 2007), and imaging of sugars (van Zijl et al. 2007). The CEST technology allows multiple new types of applications, and the development of new imaging approaches is progressing rapidly on many fronts.

## MAGNETIZATION TRANSFER CONTRAST (MTC), CEST, AND APT

When discussing *in vivo* CEST effects, it is important to understand the contributing mechanism and terminology. Notably, all phenomena discussed here are magnetization transfer (MT) effects, but they have different mechanisms and origins. CEST

(Wolff and Balaban 1990; Ward et al. 2000) and APT (Zhou et al. 2003a, b) employ a chemical exchange as a single transfer pathway to accomplish MT. APT is a special type of CEST, with selective irradiation at 3.5 ppm from water to saturate amide protons. Unlike CEST, conventional MTC imaging (Balaban and Ceckler 1992) is based on protons in immobile semi-solid macromolecules (such as structural proteins, membranes, and myelins), where saturation transfer occurs through multiple pathways, such as dipolar coupling and chemical exchange. These solid-like protons have a very short  $T_2$  and, therefore, resonate over a very large spectral width ( $\pm 100$  kHz) that does not allow selective RF irradiation of individual resonances. Thus, the MT spectrum appears to be symmetric. In contrast, the frequency offset in CEST or APT experiments is limited to a small range around the water resonance, and two proton pools can be distinguished from each other on the NMR time scale. This leads to a clear asymmetry in the MT-spectrum with respect to the water resonance, such that the APT effect can be separated from MTC and direct saturation, by determining the asymmetry in the magnetization transfer ratio (MTR) (Zhou et al. 2003a, b).

## APT IMAGING OF EXPERIMENTAL BRAIN TUMOR MODELS

The possibility of producing APT contrast in brain tumors was first demonstrated in a rat 9L glioma model at 4.7T (Zhou et al. 2003b; Salhotra et al. 2008). As seen in Figure 11.1a, RF irradiation over an 11-ppm range around water produces a large decrease in water signal intensity. This is due mainly

to direct water saturation close to the water frequency, and the conventional solid-like MTC effect over the whole spectral range. Interestingly, there is a very small dip at a frequency difference of 3.5 ppm from water, corresponding to about 8.3 ppm in a standard MR spectrum, where the exchangeable amide protons are located. To reduce interference from MTC and direct saturation effects, MTR asymmetry ( $MTR_{\text{asym}}$ ) analysis was used. Interestingly, the resulting  $MTR_{\text{asym}}$  curves show a more complex

asymmetry pattern in vivo than in phantoms (Goffeney et al. 2001). This is due to the MTC effect that also has a slight asymmetry. This complicates interpretation in vivo, but one can compare a tumor with contralateral normal tissue. The results (Figure 11.1b) show an increase in the tumor  $MTR_{\text{asym}}$  with respect to normal brain over a range of offsets between 2 and 5 ppm, which is the frequency range for exchangeable amide protons. A maximum APT effect was found at an offset of 3.5 ppm, exactly corresponding

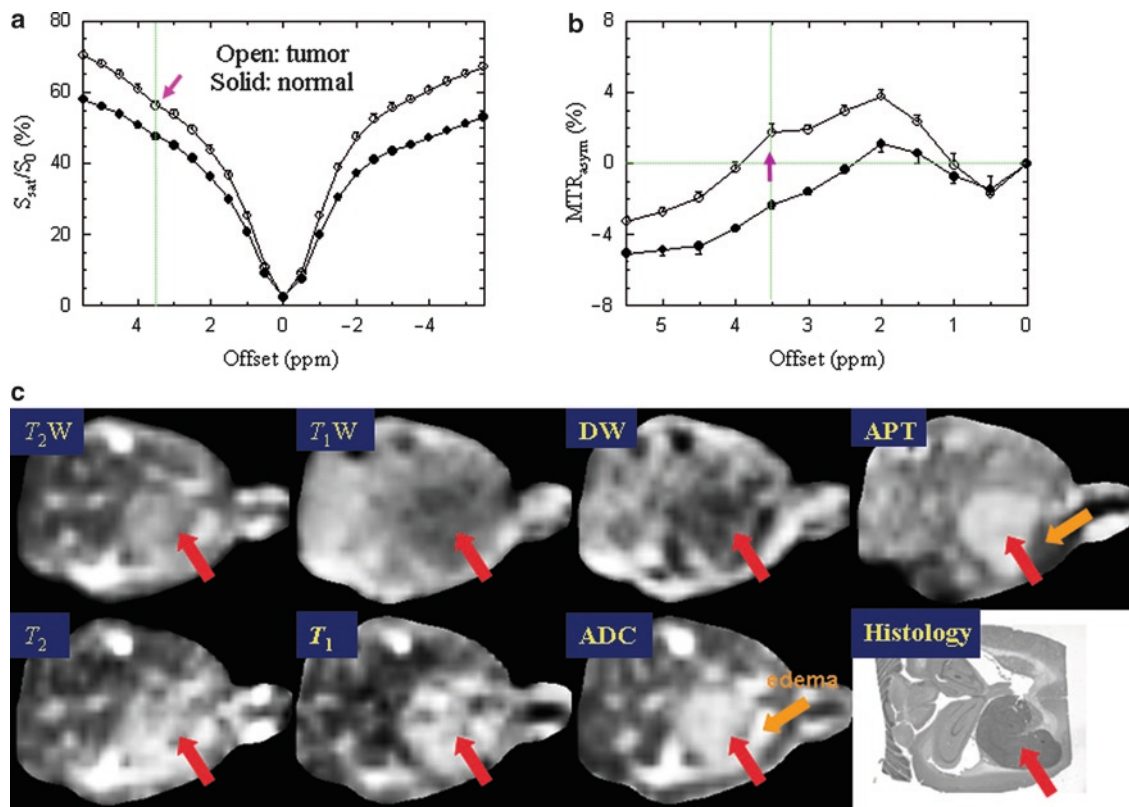


FIGURE 11.1. MT (a) and  $MTR_{\text{asym}}$  (b) spectra for the 9L brain tumor model (post-implantation day 12;  $n = 6$ ). The APT effect is stronger (about 5% of the water signal intensity) in tumor (*open*) than in the contralateral normal-appearing region (*solid*), which maximizes at the offset of 3.5 ppm from the water resonance. (c) MR and histology images for a 9L glioma (10 days) in a rat. The glioma is visible (*red arrow*) in all the MR images, as confirmed by histology, but it is much clearer in the APT-weighted image. Data were acquired on a 4.7T animal MRI scanner, using the experimental parameters: imaging matrix =  $64 \times 64$ ; slice thickness = 1.5 mm; field of view (FOV) =  $32 \times 32$  mm<sup>2</sup>; TR = 10 s; TE = 30 ms; saturation time = 4 s; and saturation power = 1.3 or 2  $\mu$ T (Reprinted from Zhou et al. 2003b; Salhotra et al. 2008. With permission from Wiley-Liss, Inc. and John Wiley & Sons, Ltd., respectively)

to the spectral frequency of the broad backbone amide proton resonance.

Following the acquisition of the MT spectra, APT images were acquired using frequency-labeling offsets of  $\pm 3.5$  ppm. In Figure 11.1c, the processed APT-weighted image (defined by  $MTR_{\text{asym}}$  at 3.5 ppm) is compared with several commonly used MR images and histology. The image quality in these first studies was low (echo planar imaging at 4.7T), but was sufficient to show the difference between various contrasts. It was concluded that APT defines a more reliable tumor profile in the animal glioma model, based on histology as the gold standard. These first APT imaging results also suggested that APT has the potential to differentiate peritumoral tissue from a tumor.

When interpreting these data, it is important to keep the CEST mechanism in mind. According to the theory (Zhou et al. 2004), changes in the APT intensities can also be due to changes in the exchange rate (e.g., if pH changes). Such contributions cannot be excluded completely. Solid tumors have a unique microenvironment (low blood flow, hypoxia, high lactate, and low extracellular pH) (Gillies et al. 2000). It is important to note that the intracellular pH of tumors has been found to remain neutral to slightly alkaline (Ross et al. 1988), as measured by  $^{31}\text{P}$  MRS. Tissue water content and water longitudinal relaxation are also contributing factors, but their effects partially compensate for each other. In addition, MRS in isolated tumor cells confirmed a large resonance at the amide proton frequency. Based on these qualitative assessments, it was concluded that increased protein and peptide content is the most likely explanation. Although further investigation is needed, the increase in APT signal in malignant gliomas has been found to be

reproducible in both animal models and in humans thus far.

## APT IMAGING OF HUMAN BRAIN TUMORS

The APT imaging approach was recently implemented on the 3T human MRI scanner to assess the clinical applicability of this approach (Jones et al. 2006; Zhou et al. 2008). Figure 11.2 (top row) shows the MR images for a patient with a pathologically-proven WHO grade III anaplastic astrocytoma. In this patient, there is a clear increase in APT signal intensity in tumor (red arrow) compared to surrounding normal appearing brain tissue. The high APT signal is likely associated with the most solid aspects of the lesion. Regions of increased APT extend outside the very small core (signified by Gd-enhancement) and into the peripheral zones; however, these increased APT regions do not include the full extent of the FLAIR hyperintensity, which may include peritumoral edematous regions. These early results suggest that APT-MRI based on molecular imaging of endogenous mobile proteins and peptides would be a particularly promising technique for localizing brain tumors and defining their spatial extent.

Unlike Gd-enhanced MRI, APT-enhanced MRI depends on the endogenous cytosolic protein and peptide content that is directly associated with tumor cellularity and tumor cell proliferation. The early data indicate that APT enhancement is always present for high-grade tumors. Moreover, the highest APT intensity is associated with the most malignant portions of tumor (Gd-enhancing areas, if present). Therefore, APT imaging may help to better distinguish the heterogeneous portions of tumor

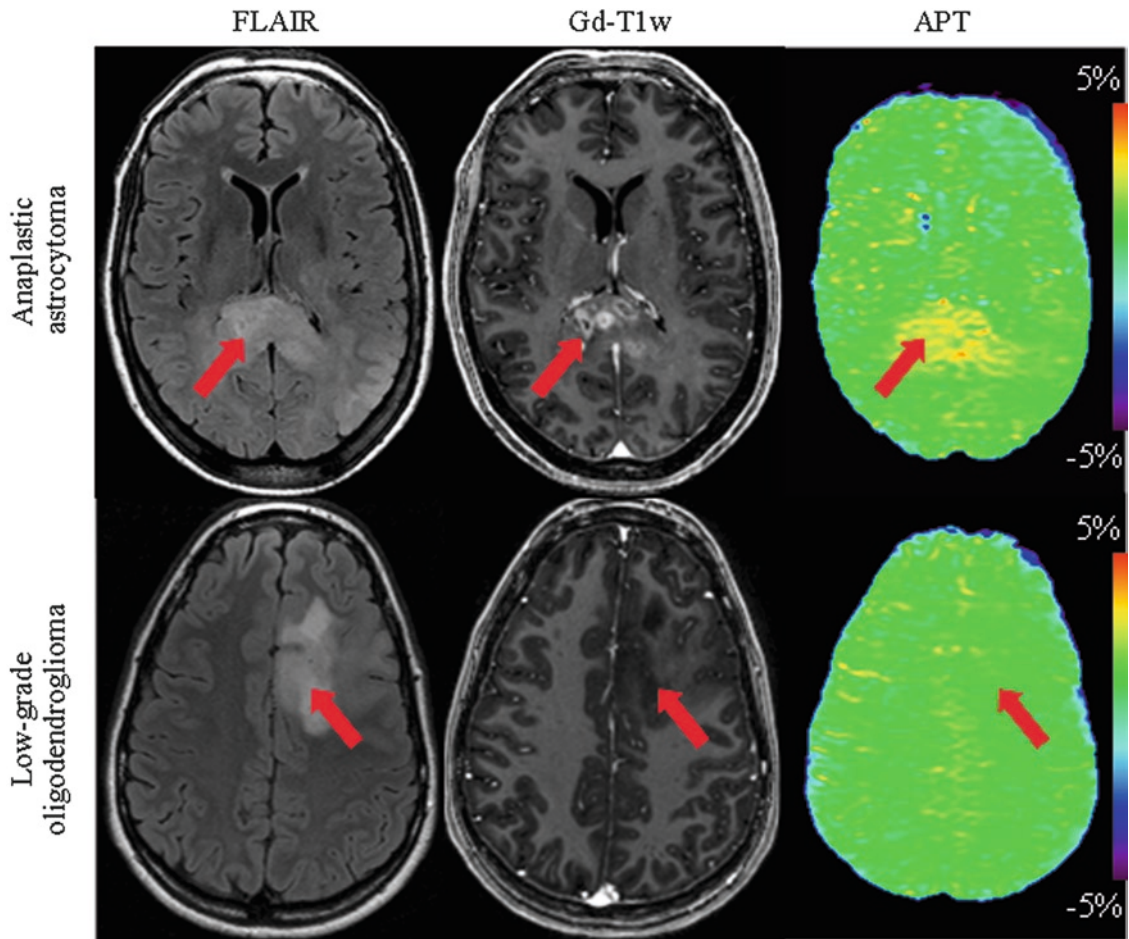


FIGURE 11.2. *Top row:* MR images of a patient with an anaplastic astrocytoma. It can be seen clearly that hyperintensity is present on APT and Gd-T<sub>1</sub>w. The hyperintense APT area is smaller, or comparable in size to the lesion identified on FLAIR, but larger than that on the Gd-T<sub>1</sub>w image. *Lower row:* MR images of a patient with a low-grade oligodendroglioma. Despite clear abnormalities on FLAIR, there is no visible signal enhancement in tumor on either the Gd-T<sub>1</sub>w or APT images. Data were acquired on a 3T Philips MRI scanner with a six-channel phased-array coil for reception. A six-offset APT data acquisition approach (Zhou et al. 2008) was used to correct for the artifacts induced by B<sub>0</sub>-inhomogeneity. The experimental parameters used were: TR = 3 s; TE = 30 ms; matrix = 128 × 128; FOV = 230 × 230 mm<sup>2</sup>; single-slice; slice thickness = 5 mm; RF saturation time = 500 ms; and saturation power = 4 μT. The total scan time was about 4.5 min (Reprinted from Zhou et al. 2008. With permission from Wiley-Liss, Inc.)

(both contrast-enhanced and non-contrast-enhanced) to assist with treatment planning by providing targets for tissue sampling to yield the most accurate diagnosis.

APT-based imaging may potentially provide a useful complementary MRI modality to better characterize the heterogeneous

portions of a tumor. This could be extremely helpful in planning maximal tumor resections, which is particularly important, because ~80% of recurrent brain tumors occur at the resection margin (Albert et al. 1994). Moreover, although still controversial, several studies indicate that the degree

of resection is correlated with survival. Similar arguments for maximizing the tumor targeting area apply to radiation therapy planning, where an increased dose could be given to tumor-infiltrating areas, while the rest of the brain could receive a reduced dose. Hence, the additive data provided by APT may complement existing image-guided approaches to allow maximal targeting of active tumor. The hope is that this may ultimately improve survival for brain cancer patients.

Figure 11.2 (lower row) shows the MR images of a pathologically confirmed, low-grade oligodendroglioma. Although FLAIR shows hyperintensity, there is negligible signal enhancement and, thus, no obvious lesion in this region on either the APT or Gd- $T_1$ w images for this patient. As previously noted, the presence or absence of Gd enhancement is not an absolute measure of tumor grade. Although more studies are required to evaluate whether APT hyperintensity is specific for high-grade gliomas, early quantitative data analysis (Zhou et al. 2008) has shown that the correlation between APT intensity and tumor grade is clearly visible ( $n = 9$ ,  $r$ -squared = 0.92). When combined with the standard  $T_2$ w or FLAIR- $T_2$ w sequences, APT-enhanced MRI may be able to provide visual information about the presence and grade of a tumor, based on the increased content of proteins and peptides. Since low-grade and high-grade gliomas have distinct characteristics on APT imaging, the APT technology, without the need for exogenous contrast agents, may help in predicting early malignant transformation allowing more accurate timing for initiation of various therapies targeted to high grade gliomas.

In conclusion, living in the early dawn of an era of proteomics and molecular

imaging, it is exciting that we have the potential to perform noninvasive imaging at the protein and peptide level in a clinical setting. APT imaging has the potential to introduce to the clinic an entirely new MRI methodology that can detect endogenous mobile proteins and peptides in biological tissue noninvasively. Pre-clinical and early clinical data suggest that APT may have unique features to better characterize brain tumors. The APT technique can be incorporated into standard MRI acquisition protocols without the need for exogenous contrast. This specific MRI modality would be able to aid in the diagnosis and treatment of tumors and, potentially, of several other diseases of the brain.

*Acknowledgments.* This work was supported in part by grants from NIH (RR015241 and EB002634) and the Dana Foundation.

## REFERENCES

- Aime, S., Barge, A., Delli Castelli, D., Fedeli, F., Mortillaro, A., Nielsen, F.U., and Terreno, E. (2002) Paramagnetic Lanthanide(III) complexes as pH-sensitive chemical exchange saturation transfer (CEST) contrast agents for MRI applications. *Magn. Reson. Med.* 47:639–648
- Aime, S., Carrera, C., Delli Castelli, D., Geninatti Crich, S., and Terreno, E. (2005) Tunable imaging of cells labelled with MRI-PARACEST agents. *Angew. Chem. Int. Ed.* 44:1813–1815
- Albert, F.K., Forsting, M., Sartor, K., Adams, H.-P., and Kunze, S. (1994) Early postoperative magnetic resonance imaging after resection of malignant glioma: objective evaluation of residual tumor and its influence on regrowth and prognosis. *Neurosurgery* 34:45–60
- Balaban, R.S., and Ceckler, T.L. (1992) Magnetization transfer contrast in magnetic resonance imaging. *Magn. Reson. Q.* 8:116–137

- Burger, P.C., Heinz, E.R., Shibata, T., and Kleihues, P. (1988) Topographic anatomy and CT correlations in the untreated glioblastoma multiforme. *J. Neurosurg.* 68:698–704
- Chenevert, T.L., McKeever, P.E., and Ross, B.D. (1997) Monitoring early response of experimental brain tumors to therapy using diffusion magnetic resonance imaging. *Clin. Cancer Res.* 3:1457–1466
- Ersoy, H., and Rybicki, F.J. (2007) Biochemical safety profiles of gadolinium-based extracellular contrast agents and nephrogenic systemic fibrosis. *J. Magn. Reson. Imaging* 26:1190–1197
- Gauvain, K.M., McKinstry, R.C., Mukherjee, P., Perry, A., Neil, J.J., Kaufman, B.A., and Hayashi, R.J. (2001) Evaluating pediatric brain tumor cellularity with diffusion-tensor imaging. *Am. J. Roentgenol.* 177:449–454
- Gilad, A.A., McMahan, M.T., Walczak, P., Winnard, P.T., Raman, V., van Laarhoven, H.W.M., Skoglund, C.M., Bulte, J.W.M., and van Zijl, P.C.M. (2007) Artificial reporter gene providing MRI contrast based on proton exchange. *Nature Biotech.* 25:217–219
- Gillies, R.J., Bhujwala, Z., Evelhoch, J., Garwood, M., Neeman, M., Robinson, S.P., Sotak, C.H., and van der Sanden, B. (2000) Applications of magnetic resonance in model systems: tumor biology and physiology. *Neoplasia* 2:139–151
- Goffeney, N., Bulte, J.W.M., Duyn, J., Bryant, L.H., and van Zijl, P.C.M. (2001) Sensitive NMR detection of cationic-polymer-based gene delivery systems using saturation transfer via proton exchange. *J. Am. Chem. Soc.* 123:8628–8629
- Hobbs, S.K., Shi, G., Homer, R., Harsh, G., Altlas, S.W., and Bednarski, M.D. (2003) Magnetic resonance imaging-guided proteomics of human glioblastoma multiforme. *J. Magn. Reson. Imaging* 18:530–536
- Howe, F.A., Barton, S.J., Cudlip, S.A., Stubbs, M., Saunders, D.E., Murphy, M., Wilkins, P., Opstad, K.S., Doyle, V.L., McLean, M.A., Bell, B.A., and Griffiths, J.R. (2003) Metabolic profiles of human brain tumors using quantitative in vivo <sup>1</sup>H magnetic resonance spectroscopy. *Magn. Reson. Med.* 49:223–232
- Jokivarsi, K.T., Grohn, H.I., Grohn, O.H., and Kauppinen, R.A. (2007) Proton transfer ratio, lactate, and intracellular pH in acute cerebral ischemia. *Magn. Reson. Med.* 57:647–653
- Jones, C.K., Schlosser, M.J., van Zijl, P.C., Pomper, M.G., Golay, X., and Zhou, J. (2006) Amide proton transfer imaging of human brain tumors at 3T. *Magn. Reson. Med.* 56:585–592
- Kelly, P.J., Daumas-Duport, C., Kispert, D.B., Kall, B.A., Scheithauer, B.W., and Illig, J.J. (1987) Imaging-based stereotaxic serial biopsies in untreated intracranial glial neoplasms. *J. Neurosurg.* 66:865–874
- Knopp, E.A., Cha, S., Johnson, G., Mazumdar, A., Golfinos, J.G., Zagzag, D., Miller, D.C., Kelly, P.J., and Kricheff, I.I. (1999) Glial neoplasms: dynamic contrast-enhanced T2\*-weighted MR imaging. *Radiology* 211:791–798
- Law, M., Yang, S., Wang, H., Babb, J.S., Johnson, G., Cha, S., Knopp, E.A., and Zagzag, D. (2003) Glioma grading: sensitivity, specificity, and predictive values of perfusion MR imaging and proton MR spectroscopic imaging compared with conventional MR imaging. *Am. J. Neuroradiol.* 24:1989–1998
- Ling, W., Regatte, R.R., Navon, G., and Jerschow, A. (2008) Assessment of glycosaminoglycan concentration in vivo by chemical exchange-dependent saturation transfer (gagCEST). *Proc. Natl. Acad. Sci. USA* 105:2266–2270
- Mullins, M.E., Barest, G.D., Schaefer, P.W., Hochberg, F.H., Gonzalez, R.G., and Lev, M.H. (2005) Radiation necrosis versus glioma recurrence: conventional MR imaging clues to diagnosis. *AJNR Am. J. Neuroradiol.* 26:1967–1972
- Ross, B.D., Higgins, R.J., Boggan, J.E., Knittel, B., and Garwood, M. (1988) <sup>31</sup>P NMR spectroscopy of the in vivo metabolism of an intracerebral glioma in the rat. *Magn. Reson. Med.* 6:403–417
- Salhotra, A., Lal, B., Larterra, J., Sun, P.Z., van Zijl, P.C.M., and Zhou, J. (2008) Amide proton transfer imaging of 9L gliosarcoma and human glioblastoma xenografts. *NMR Biomed.* 21:489–497
- Scott, J.N., Brasher, P.M., Sevic, R.J., Rewcastle, N.B., and Forsyth, P.A. (2002) How often are nonenhancing supratentorial gliomas malignant? A population study. *Neurology* 59:947–949
- Sun, P.Z., Zhou, J., Sun, W., Huang, J., and van Zijl, P.C.M. (2007) Delineating the boundary between the Ischemic Penumbra and regions of Oligemia using pH-weighted Magnetic

- Resonance Imaging (pHWI). *J. Cereb. Blood Flow Metab.* 27:1129–1136
- van Zijl, P.C.M., Jones, C.K., Ren, J., Malloy, C.R., and Sherry, A.D. (2007) MRI detection of glycogen in vivo by using chemical exchange saturation transfer imaging (glycoCEST). *Proc. Natl. Acad. Sci. USA* 104:4359–4364
- Vigneron, D., Bollen, A., McDermott, M., Wald, L., Day, M., Moyher-Noworolski, S., Henry, R., Chang, S., Berger, M., Dillon, W., and Nelson, S. (2001) Three-dimensional magnetic resonance spectroscopic imaging of histologically confirmed brain tumors. *Magn. Reson. Imaging* 19:89–101
- Ward, K.M., Aletras, A.H., and Balaban, R.S. (2000) A new class of contrast agents for MRI based on proton chemical exchange dependent saturation transfer (CEST). *J. Magn. Reson.* 143:79–87
- Wolff, S.D., and Balaban, R.S. (1990) NMR imaging of labile proton exchange. *J. Magn. Reson.* 86:164–169
- Yoo, B., and Pagel, M.D. (2006) A PARACEST MRI contrast agent to detect enzyme activity. *J. Am. Chem. Soc.* 128:14032–14033
- Zhang, S., Winter, P., Wu, K., and Sherry, A.D. (2001) A novel europium(III)-based MRI contrast agent. *J. Am. Chem. Soc.* 123:1517–1578
- Zhang, S., Trokowski, R., and Sherry, A.D. (2003) A paramagnetic CEST agent for imaging glucose by MRI. *J. Am. Chem. Soc.* 125:15288–15289
- Zhou, J., Payen, J., Wilson, D.A., Traystman, R.J., and van Zijl, P.C.M. (2003a) Using the amide proton signals of intracellular proteins and peptides to detect pH effects in MRI. *Nature Med.* 9:1085–1090
- Zhou, J., Lal, B., Wilson, D.A., Larterra, J., and van Zijl, P.C.M. (2003b) Amide proton transfer (APT) contrast for imaging of brain tumors. *Magn. Reson. Med.* 50:1120–1126
- Zhou, J., Wilson, D.A., Sun, P.Z., Klaus, J.A., and van Zijl, P.C.M. (2004) Quantitative description of proton exchange processes between water and endogenous and exogenous agents for WEX, CEST, and APT experiments. *Magn. Reson. Med.* 51:945–952
- Zhou, J., Blakeley, J.O., Hua, J., Kim, M., Larterra, J., Pomper, M.G., and van Zijl, P.C.M. (2008) Practical data acquisition method for human brain tumor amide proton transfer (APT) imaging. *Magn. Reson. Med.* 60:842–849



*This page intentionally left blank*

# 12

## Diffusion Tensor Imaging in Rat Models of Invasive Brain Tumors

Sungheon Kim, Steve Pickup, and Harish Poptani

### INTRODUCTION

Since their introduction in early 1960s, intra-cranial rat brain tumor models have been extensively used for studying tumor growth characteristics and for development of therapeutic strategies (Barth 1998). These models have also been used for development and testing of magnetic resonance (MR) imaging and spectroscopy techniques. MR methods have been used not only for anatomical imaging, but also for assessing functional parameters, such as oxygenation and metabolism. Paramagnetic MR contrast agents, such as Gd-DTPA, have been effectively used in rat tumor models for accurate demarcation of the tumor boundary and for measurement of blood–brain barrier integrity and vascularity. However, in the clinic, diagnostic MRI techniques are often found to be inadequate for detecting infiltrating tumor cells in the normal brain parenchyma, which often leads to tumor regrowth even after complete resection and radiotherapy. Magnetic resonance spectroscopy studies have reported abnormal choline metabolism (indicating tumor regions) in regions beyond contrast-enhanced areas (McKnight et al. 2002). Since MR spectroscopic

imaging requires a long acquisition time to cover the whole brain (~20 min) and provides only low resolution images ( $\sim 1 \times 1 \times 1$  cm), it is necessary to develop alternative imaging methods with shorter scan times and higher spatial resolution suitable for clinical application.

Diffusion-weighted (DW)-MRI, or simply referred to as DWI, offers a way to probe the diffusion of water molecules within the intra- and extra-cellular environment and can thus provide microscopic structural information of tissue *in vivo*. Due to its specificity for probing the diffusivity of water molecules, DWI is often found to be more sensitive in detecting pathology earlier than conventionally used T1 or T2 weighted MRI. The enhanced sensitivity of DW-MRI in detection of early onset of an ischemic event, prior to the lesion being visible by other imaging methods, was initially reported in 1990 (Moseley et al. 1990) and DWI has now become the modality of choice for detection of stroke. DWI has also been used extensively in diagnosis and monitoring early therapeutic response of brain tumors (Kauppinen 2002). Although a promising role of DWI in brain tumors has been demonstrated, the technique only provides measurement of average diffusivity of water molecules in three dimensions. It is possible that some tissues have orientation dependent diffusivity, also known as anisotropic diffusion. In tissues

with a fibrous structure, such as white matter, multiple DWI measurements with different diffusion weighting directions can be combined to describe the phenomenon of anisotropic diffusion in three dimensions using diffusion tensor, and the imaging technique is referred as diffusion tensor imaging (DTI) (Basser et al. 1994b). DTI is the only available non-invasive imaging modality that allows visualization of the white matter fiber tracts of the brain (Le Bihan et al. 2001).

During last decade, development of DTI techniques have significantly benefited from the availability of fast scanning methods on commercial MRI scanners. At present, DTI has become the modality of choice for anatomical study of the white matter and for the detection of pathologies with striking details describing the white matter tracts. However, physiological/biological interpretation of changes detected by DWI/DTI and quantification of DTI tractography remain challenging, largely due to the complex nature of the biological tissue of interest and the absence of histological validation in clinical DTI studies.

Animal models can be used in bridging the gap between imaging findings and pathological features. Particularly for cancer research, in vivo DTI studies of well-established rat brain tumor models would greatly benefit from the advantages of having greater experimental control, histological confirmation, and follow-up studies of underlying cellular and molecular mechanisms. However, in vivo DTI of the rat brain is not trivial, considering the small size of the rat brain (~1 cc) in comparison to the human brain (~1,500 cc). In the following sections, we will briefly discuss the background of DTI, practical considerations for DTI of the rat brain, and its applications in rat brain tumor models.

## IMAGING TISSUE MICROSTRUCTURE

A full description of diffusion tensor imaging is beyond the scope of this chapter, which can be found in the literature (Basser et al. 1994a; Le Bihan et al. 2001; Pierpaoli and Basser 1996). However, a brief description of the method is provided below as it is helpful in understanding DTI studies of rat tumor models and their findings in general.

### Diffusion Tensor

Self-diffusion of water molecules can be used to probe microscopic structural information about tissue. The mean displacement distance ( $L$ ) of particles by random Brownian motion in three dimensions is estimated by the Einstein diffusion equation;  $\langle L^2 \rangle = 6Dt_d$  where  $D$  is diffusion coefficient and  $t_d$  is diffusion time. For instance, the  $D$  of the cerebrospinal fluid in the ventricles of the brain is about  $3 \mu\text{m}^2/\text{ms}$ . Using the Einstein diffusion equation,  $L$  is expected to be about  $13 \mu\text{m}$  when  $t_d$  of 10 ms is used. This distance is close to the size of typical mammalian cells, such that random motion of water molecules during this 10 ms can be hindered or restricted by cellular structures, such as cell membrane, leading to reduction of the actual displacement by diffusion. Diffusion measurement using a typical clinical or animal MR scanner is usually performed with a diffusion time longer than 10 ms. Thus, the diffusion coefficient measured by a diffusion weighted MRI experiment reflects a combination of self-diffusivity of water molecules and its surrounding tissue microstructure.

The principal of probing tissue microstructure using self-diffusion of water molecules is elaborated by a cartoon shown in Figure 12.1. Figure 12.1a shows a simplified fibrous tissue and random motion of water molecules. When the diffusion time is short with respect to the mean displacement of particles within the shortest distance between the adjacent restricting structures ( $<L1$ ), the measured displacement distance will be same in all directions, i.e. isotropic diffusion, as depicted by a sphere in Figure 12.1b. If the diffusion time increases such that water molecules can travel more than  $L1$ , the mean displacement distance increases along the fiber direction, but apparently remains same in the direction perpendicular to the fiber, i.e., anisotropic diffusion. The measured displacement distance can be described in three dimensions as an elongated ellipsoid,

as shown in Figure 12.1c. This type of an ellipsoid representing the mean displacement of water molecules in 3D space can be described as a rank-2 tensor,  $3 \times 3$  matrix as in Eq. (12.1).

$$D = \begin{vmatrix} D_{xx} & D_{xy} & D_{xz} \\ D_{yx} & D_{yy} & D_{yz} \\ D_{zx} & D_{zy} & D_{zz} \end{vmatrix} \quad (12.1)$$

Diffusional displacement of water molecules leads to a decrease in MRI signal intensity. In addition, MRI can be made more sensitive to such diffusion by increasing the diffusion time and the degree of diffusion weighting (Stejskal and Tanner 1965) as shown in Eq. (12.2) below.

$$S = S_0 \exp(-bD) \quad (12.2)$$

where  $S_0$  is the MR signal without diffusion weighting and  $b$  is the degree of diffu-

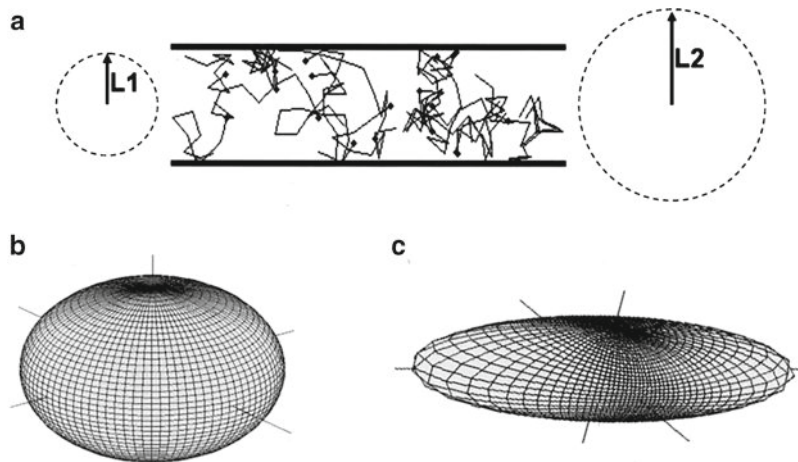


FIGURE 12.1. Principal of probing tissue microstructure using water diffusion. (a) An example of simplified fibrous tissue structure.  $L1$  and  $L2$  indicate the mean diffusion distances of two different diffusion times. Measured 3D diffusion pattern depends on the allowed diffusion time. When the diffusion time is short enough to have the mean displacement of particles within the shortest distance between the adjacent restricting structures ( $<L1$ ), an isotropic diffusion is expected as depicted by a sphere in (b). If diffusion time is considerably long such that the mean diffusion distance is longer than the restricting structure, like  $L2$ , then the estimated 3D diffusion pattern will look like an ellipsoid as shown in (c)

sion weighting determined by the duration and magnitude of diffusion sensitizing gradients. In practice, the diffusion tensor  $D$  is a symmetric matrix (i.e.  $D_{xy} = D_{yx}$ ;  $D_{zx} = D_{xz}$ , and  $D_{zy} = D_{yz}$ ), leaving only six unknown parameters. Therefore, if there are more than six measurements along the non-collinear directions with a reference image for  $S_0$ , the diffusion tensor can be estimated using weighted multivariate linear regression or nonlinear estimation.

Diffusion measurement for non-fibrous tissues can be simplified to estimate a scalar diffusion coefficient rather than a tensor. In this case, diffusion experiment is conducted with diffusion weighting along one direction alone or in three orthogonal directions to estimate the averaged diffusion coefficient. Apparent diffusion coefficient (ADC) measured in this way has been used for preclinical and clinical tumor studies. In contrast, diffusion tensor MRI can be used to measure more complex 3D pattern than a simple ellipsoid shape represented by diffusion tensor. Diffusion tensor is a valid model when all the fibers in the voxel are parallel. In regions with crossing or radiating fibers, diffusion tensor fails to represent the diffusional displacement pattern adequately. Thus, it is necessary to use more complex models which also require a large number of diffusion measurements. These methods include diffusion kurtosis imaging (Jensen et al. 2005), Q-ball imaging (Tuch 2004) and diffusion spectrum imaging (Wedeen et al. 2005). Therefore, a diffusion MRI study needs to be tailor fitted to specific tissue type and study objectives. In this chapter, we will limit our discussion to DTI, which is to approximate complex 3D diffusion pattern by diffusion tensor.

## Diffusion Tensor Metrics

For a symmetric and positive definite diffusion tensor, three principal coordinate vectors can be found with effective diffusivities along orthogonal directions by diagonalizing the diffusion tensor (Eq. (12.3)):

$$DE = EA \quad (12.3)$$

where  $E = [\varepsilon_1 \ \varepsilon_2 \ \varepsilon_3]$  is a matrix of the eigenvectors ( $\varepsilon_1$ ,  $\varepsilon_2$ , and  $\varepsilon_3$ ) and  $\Lambda$  is the diagonal matrix of the eigenvalues ( $\lambda_1$ ,  $\lambda_2$ , and  $\lambda_3$ ). The size and shape of the diffusion tensor can then be measured using eigenvalues that are rotationally invariant quantities. The mean diffusivity (MD) or  $\langle \lambda \rangle$  is measured as the average of the eigenvalues. Several scalar indices have been proposed to characterize the diffusion anisotropy and the most commonly used index is known as the fractional anisotropy (FA) (Basser and Pierpaoli 1996):

$$FA = \frac{\sqrt{3 \left( (\lambda_1 - \langle \lambda \rangle)^2 + (\lambda_2 - \langle \lambda \rangle)^2 + (\lambda_3 - \langle \lambda \rangle)^2 \right)}}{\sqrt{2(\lambda_1^2 + \lambda_2^2 + \lambda_3^2)}} \quad (12.4)$$

While FA is a good indicator of the fraction of diffusivity due to anisotropic diffusion, it does not provide information on the shape of the anisotropic diffusion. As described in Figure 12.1 above, the geometric shape associated with a diffusion tensor is assumed to be ellipsoidal, defined as the iso-surface of the multivariate normal probability distribution of diffusivity. Thus, there are two possible anisotropic shapes of the ellipsoid; prolate (linear) and oblate (planar) for a rank-2 positive definite diffusion tensor. Closeness of a

diffusion tensor to these two anisotropic shapes can be measured using linear (CL) and planar (CP) anisotropy coefficients (Westin et al. 2002):

$$CL = (\lambda_1 - \lambda_2) / \sqrt{(\lambda_1^2 + \lambda_2^2 + \lambda_3^2)} \quad (12.5)$$

$$CP = 2(\lambda_2 - \lambda_3) / \sqrt{(\lambda_1^2 + \lambda_2^2 + \lambda_3^2)}. \quad (12.6)$$

DTI data can also be used to generate other useful parameters, such as lattice index and volume ratio (Pierpaoli and Basser 1996), depending on the tissue property of interest in individual studies.

## DATA ACQUISITION METHODS

While diffusion anisotropy is a valuable tool for probing tissue microstructure, it is to be noted that diffusion anisotropy may also be observed in the noise of the MRI signal. Thus acquisition of good quality images (signal to noise ratio (SNR) > 20) is one of the most critical requirements for a successful DTI experiment. In comparison to the human brain (~1,500 cc), the substantially smaller size of the rat brain (~1 cc) poses specific challenges in the acquisition of diffusion weighted (i.e. attenuated) MR images with high SNR. Furthermore, MR scanners have hardware limitations on the gradient strength, which is necessary to achieve sub-millimeter resolution images for the rat brain. Despite a rapid increase in clinical and research applications of the human brain DTI studies in the last decade, DTI for small animal models has been limited by these issues.

Mori and colleagues at the Johns Hopkins University have pioneered the development of high resolution *ex vivo* DTI of the rodent brains (Mori et al. 2001;

Mori and van Zijl 1998). These investigators have developed a diffusion weighted MR technique based on a multiple spin echo sequence in order to increase SNR by adding multiple echo signals and have used the last two echoes as navigator to correct for phase errors induced by eddy-current or any systemic artifact (Mori and van Zijl 1998). This pulse sequence, along with dedicated radiofrequency (RF)-coils and a high field magnet (9.4 T), has been successfully used to acquire high resolution *ex vivo* DTI images of the fixed mouse brain (Mori et al. 2001). The drawback for high-resolution DTI is the long acquisition times (>12 h) per sample, which although is not a limitation for *ex vivo* studies of the brain, such long scan times cannot be used for *in vivo* imaging.

Most DTI studies of the human brain are performed using echo-planar imaging (EPI) based diffusion sequences. EPI methods acquire an entire 2D image in a few hundred milliseconds as a long train of gradient echoes following a single RF pulse excitation. This rapid acquisition time facilitates acquisition of images with diffusion weighting in many directions in a time that is practical for clinical applications. However, the EPI technique is very sensitive to inhomogeneities in the static magnetic field. The main source of static field inhomogeneity is the spatial variation in magnetic susceptibility of the patient/animal. These distortions scale with the magnitude of the static magnetic field. At the field strength typically employed for small animal studies (>4.7 T), the image distortions in EPI studies due to field inhomogeneity are often excessive and severely limit its use. In addition, EPI based techniques do not provide the high-spatial resolution necessary to probe the smaller

rat brain. Hence, *in vivo* DTI experiments of rat brain are usually performed using a single or multiple spin-echo sequence. Since water diffusion is highly sensitive to motion and temperature, rodent DTI experiments are typically performed under isoflurane (1–2%) anesthesia together with temperature control. To further reduce the effects of respiratory or any other unexpected motion, a stereotactic headset (ear pins and bite bar) is used to confine the animal's head within the imaging coil.

Recently, the feasibility of monitoring intra-cranial brain tumors in the rat brain using *in vivo* DTI has also been reported by different research groups (Kim et al. 2008; Lope-Piedrafita et al. 2008; Zhang et al. 2007). The imaging setup and parameters for these studies share many common features. All these studies were performed using 4.7 T horizontal scanners with a 25 mm surface coil for RF signal receive and a 70 mm volume coil for RF transmit to accommodate the rat with the receive coil mounted on the head inside. Spin echo or fast spin echo diffusion pulse sequences were used with 14–25 ms diffusion time and b-value around 1,000 s/mm<sup>2</sup>. Within the total scan time about 2 h, these investigators were able to achieve 0.16–0.33 mm in-plane resolution with 1–1.5 mm slice thickness. The results from these studies are discussed in the following section which suggest the feasibility of using *in vivo* DTI for the study of rat tumor models.

## RAT BRAIN TUMOR MODELS

Rat brain tumor models have been used for a variety of MRI studies. However, there are only a limited number of *in vivo* DTI

studies on rat brain tumor models (Kim et al. 2006, 2008; Lope-Piedrafita et al. 2008; Zhang et al. 2007). These studies demonstrate that *in vivo* DTI can be used to delineate the changes in orientation and anisotropy of the tissues due to tumor progression.

### 9L Gliosarcoma

The 9L gliosarcoma model was originally generated by intravenous injection of N-methylnitrosourea (MNU) in Fisher rats (Barth 1998). MRI studies in this model report presence of vasogenic edema on T2-weighted images, however, administration of a contrast agent, such as Gd-DTPA was found to be necessary for accurate tumor delineation. These tumors exhibit non-infiltrative, well demarcated boundaries. In comparison to the contralateral normal brain, the tumor demonstrates significantly increased T1, T2, and ADC (Vonarbourg et al. 2004). This model has also been used to investigate therapeutic response using various MRI techniques, such as spectroscopy, diffusion, and perfusion weighted imaging.

Zhang et al. (2007) performed a DTI study on 9L tumors implanted in the caudate-putamen of Fisher rats. These authors reported that the tumor grew to occupy most of the caudate-putamen area of the implanted site within 10 days, as observed by an increase in the T2 and ADC (Figure 12.2a). While T2-weighted (T2W) and ADC images exhibited a homogeneous signal across the tumor, the FA image showed decreased anisotropy in the central region of the tumor with increased anisotropy being observed in the rim. The high diffusion anisotropy in the tumor rim was attributed to a circular pattern of tumor

cell arrangement as shown by the vector map in Figure 12.2a, which was confirmed by histology.

In a separate study, Kim and colleagues used *in vivo* DTI to observe the growth of 9L tumor when the cells were inoculated in the corpus callosum of Fisher rats (Kim et al. 2006; Kim et al. 2008). Figure 12.2b shows longitudinal DTI parameter maps from one slice through the tumor. On post-injection day 7, the tumor was not evident on T2w or ADC images. However, the FA image shows reduced anisotropy near the injection site, where the tumor was subsequently observed on later imaging studies. On days 14 and 21, the tumor was seen above and below the CC on all images (T2w, ADC and FA). The tumor growing in the cortical ribbon above the CC displayed similar FA characteristics of a core and rim, as reported by Zhang et al. (2007), however, no circular pattern of cells was observed in the rim. Below the CC, the tumor also grew, however, it was confined to the hippocampal region between the CC and the fimbria. Of note is the portion of the CC within the tumor, which displayed a high anisotropy on day 14. The tumor volume almost doubled by day 21, and a disruption of the CC within the tumor was observed. The tumor in the hippocampus did not grow further and was still confined between the CC and the fimbria. It appears that this tumor does not infiltrate through the white matter as easily as through the gray matter. In addition, it was reported that the mean primary eigenvalues ( $\lambda_1$ ) increased while the mean tertiary eigenvalues ( $\lambda_3$ ) decreased significantly between days 14 and 21. This observation suggests that the tumor tends to grow along the fibrous structure. Histological studies demonstrated

the tumor as a homogeneous mass with non-diffused boundaries.

### C6 Glioma

The C6 glioma is another popular rat brain tumor model that has been used for MRI studies. This tumor model was developed in a similar way to 9L, by administering MNU to outbred Wistar rats and is histologically classified as an astrocytoma (Barth 1998). Similar to the 9L gliosarcoma, the C6 glioma grows as a homogeneous mass, as reported by conventional MRI techniques. Bennett et al. (2004) used this tumor model for a DWI study with diffusion-weighting factor  $b = 500\text{--}6,500$  s/mm<sup>2</sup> and reported that the peritumoral region had a stretched-exponential diffusion decay similar to that of the tumor and different from those of the normal appearing white and gray matter. This phenomenon was not caused by vasogenic edema as the peritumoral region had no change in proton density or T2-weighted images. Presence of infiltrating tumor cells outside of the main tumor was confirmed by histology in this study.

The C6 tumor model has been used for a longitudinal DTI study by Lope-Piedrafita et al. (2008). In this study, the C6 glioma cells were inoculated into the caudate-putamen of female adult Wistar rats. Figure 12.2c shows the DTI maps of a rat brain 8 days after tumor cell inoculation. This is a rapidly growing tumor, which occupies the whole putamen within a week after transplantation. In comparison to the 9L tumor (shown in Figure 12.2a, b), this tumor had a large central area with very low anisotropy and a thin rim with high planar anisotropy. The primary eigenvectors in the rim formed a circular pattern. In H&E stained slides, the entire tumor



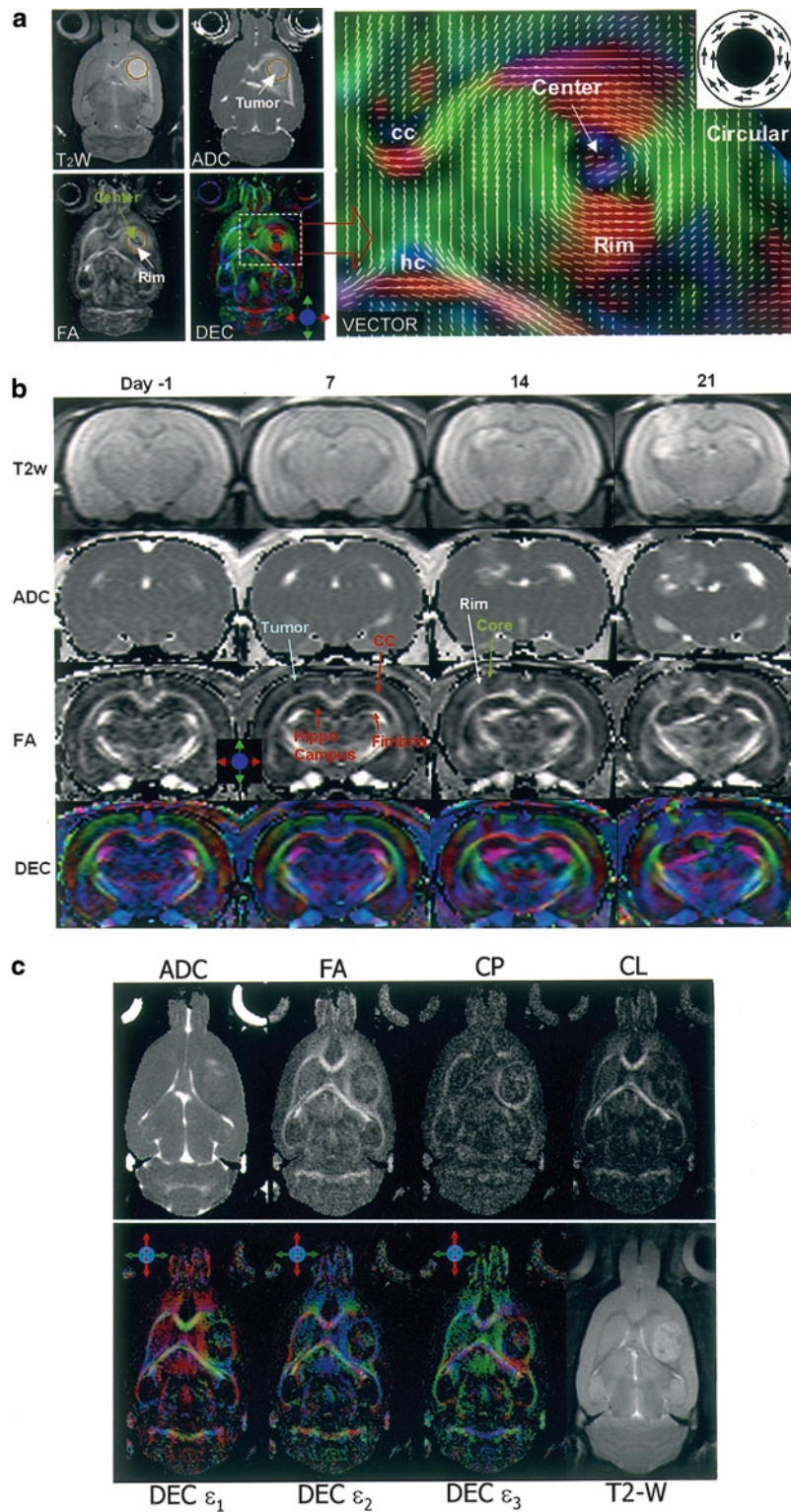


FIGURE 12.2. (a) In vivo MR images of 9L gliosarcoma brain tumor model at post-implantation day 11. cc, corpus callosum; hc, hippocampal commissure. The tumor regions are hyperintense

appeared solid and the tumor cells were arranged in a circular pattern, similar to what was observed in the DTI parameter maps. As the tumor grew quite rapidly, it apparently displaced the surrounding white matter tracts. Significantly lower FA in the external capsule near the tumor was observed indicating the presence of infiltrating tumor into the normal appearing external capsule.

### F98 Glioma

The F98 glioma is an undifferentiated glioma and is known to have an infiltrative pattern of growth and is weakly immunogenic. It was developed by injecting N-ethyl-N-nitrosourea into a pregnant CD Fischer rat. It is also reported that implantation of F98 cells in Fisher rats results in large infiltrative neoplasms with a necrotic core. Since these characteristics resemble to human glioblastomas, the F98 model has been used widely for a variety of MRI studies.

DTI studies on the F98 gliomas were reported by Zhang et al. (2007) and Kim et al. (2008). Zhang et al. (2007) found

that the F98 tumor had a growth pattern similar to that of the 9L tumor. At post-implantation day 10, the F98 tumor exhibited a similar growth pattern to that of the 9L tumor in terms of size and the circular pattern of primary eigenvectors in the rim. One of the interesting findings was that the FA in the central region of F98 was significantly lower than the contralateral striatum, which is in contrast to the 9L tumor where no such differences in FA values were observed. There were no other differences between the F98 and the 9L tumors reported in this study indicating a similar growth pattern of the two tumor models.

In contrast, Kim et al. (2008) found that the F98 grew more aggressively than the 9L tumor. Within 1 week after transplantation, the F98 tumors grew rapidly and the tumor volume matched the size of a 2- to 3-week-old 9L tumors. A significant reduction in the anisotropy of the corpus callosal area within the tumor was observed by day 7, unlike the 9L tumor which demonstrated reduced anisotropy in the corpus callosal area after the third week of transplantation. At subsequent scans, the F98 tumors continued to grow

←  
 FIGURE 12.2. (continued) on the T2W and ADC images. The boundaries of T2W hyperintense tumor regions were manually defined and overlaid on other images. In FA maps the *tumors* show high contrasts and various degrees of high-level diffusion anisotropy. In DEC and vector images the tumor areas exhibit a *circular orientation*. (Zhang et al. 2007) (b) Longitudinal in vivo DTI maps of rat brain bearing a 9L tumor. T2w images are the T2-weighted images without diffusion weighting. Tumor was implanted near the corpus callosum and can be seen from day 7 in FA map. However, disruption of the CC was observed only at day 21 (Kim et al. 2008). (c) Representative images and parametric DTI maps of a rat brain bearing the C6 glioma acquired at day 8 of tumor growth. The *CP* and *CL maps* indicate relative amounts of planar and linear anisotropy, respectively. In the tissue surrounding the tumor, there is a slight decrease in the mean diffusivity and increase in anisotropy as seen in ADC and FA maps, respectively. This anisotropy surrounding the tumor also exhibits higher values of CP, and lower values of CL, indicating a planar geometry to water diffusion, i.e. water motion is restricted in one direction more than the other two orthogonal directions. This is also seen in the DEC maps where the two major diffusion directions ( $\epsilon_1$  and  $\epsilon_2$ ) are parallel to the surface of the tumor, and the direction of the lowest diffusion direction ( $\epsilon_3$ ) is perpendicular to the surface (Lope-Piedrafita et al. 2008)

rapidly and became necrotic in the core. In addition, it was found that all three eigenvalues in the tumor rim increased significantly between day 14 and day 21, indicating that the tumor grew in all directions regardless of the existing fibrous structure of the tissue. On histology, the F98 tumor exhibited diffused boundaries probably due to the tumor cells invading the normal brain parenchyma. Some of the differences in the FA characteristics of the F98 tumor reported in these two studies may be due to the difference in the tumor implantation method or mutagenic differences in the cell lines used at the two research sites. Nevertheless, the results from both studies indicate that DTI parameters reflect the pathology accurately as confirmed by histology in each case, thereby suggesting that DTI can be used as an adequate tool to monitor the tumor growth.

#### Mayo 22 Human Brain Tumor Xenograft

Zhang et al. (2007) also reported a DTI study in a human brain tumor xenograft, Mayo 22, in nude rats. DTI maps of a rat with a Mayo 22 tumor at day 27 post-implantation when the tumor size was about same as those of 9L and F98. The Mayo 22 tumor exhibited homogeneously increased signal intensity on T2w and ADC maps. However, the central region had significantly lower FA than the contralateral striatum and the rim had higher FA than the contralateral striatum. Most interestingly, the primary eigenvectors in the rim were aligned in a radial direction in the vector map. The radial orientation of tumor cells in the boundary of the tumor was confirmed by histology. Although this human tumor xenograft grew relatively slower than the rat tumor models, it

displays typical characteristic of an infiltrating tumor, as observed by the radial pattern of diffusion tensors.

## FUTURE CONSIDERATIONS

As discussed in the previous section, recent studies have demonstrated the potential of DTI as a noninvasive tool for longitudinal *in vivo* study of rat brain tumor models. While DWI is increasingly being used for differential diagnosis of tumors and for monitoring therapeutic response, the use of DTI for such applications is still in its infancy and requires more studies in preclinical and clinical environment. In this section, we would like to look at some of the important questions still in debate and discuss how DTI studies in rat brain tumor models can contribute in answering them.

#### Tractography

In addition to the micro-structural and physiological information provided by the rotationally invariant measures, such as MD and FA, the eigenvectors can also provide information about the fibrous structure of the tissue. Based on the assumption that the primary eigenvector (i.e., direction with the largest diffusivity) represents the direction of the underlying fiber, fiber-tracking methods have been developed to reconstruct and visualize the white matter tracts in the brain. A number of algorithms have been proposed to propagate lines through tensor fields to reconstruct these tracts. One of relatively simple ways is to draw a line parallel to the major eigenvector for each voxel. This has been proposed by Mori et al. (1999) and referred

to as Fiber Assignment by Continuous Tracking (FACT) method. More complex methods have also been proposed to generate streamlined fiber tracts (Basser et al. 2000) or probabilistic maps to show the likelihood of individual tracts in each voxel (Behrens et al. 2003). To date, white matter tractography is the only non-invasive technique to generate the morphological connectivity information of the white matter tracts.

Gliomas are known to spread diffusely through the brain, preferentially infiltrating along white matter tracts. Infiltrated white matter tracts may thus lose their directional organization and orientation. DTI tractography can detect subtle disruption in the white matter as well as abnormality in the contralateral white matter. As demonstrated in Figure 12.2 the directionally encoded color (DEC) maps can show the structural changes in not only the white matter, but also in the entire brain. Field and colleagues categorized the structural disruption in the white matter by the invading tumor, based on MD, FA, and DEC maps (Field et al. 2004). Neuronal fiber tractography can also assist in pre-surgical planning as well as post-surgical assessment. Although a visual estimation of the disruption/displacement of white matter tracts is possible, it is to be noted that fiber-tracking methods may not accurately estimate the size of the fiber bundle passing through a tumor (Kinoshita et al. 2005).

DTI of small animal models has a great potential in advancing our understanding of fiber orientation and for further development and refinement of imaging technology. In Figure 12.3, an example of the white matter tractography of the rat brain is shown, which demonstrates the feasibility of using in vivo DTI to evaluate the

integrity of specific white matter tracts in the rat brain (Kim et al. 2006). With further development in data acquisition and processing methods, this technology may be used to assist in probing the infiltrative tumor growth within the white matter tracts of rodent brain tumor models. The ease in histopathological validation of rodent tumor models will further help in establishing DTI-based tractography as a robust clinical diagnostic and research tool.

### Tumor Cell Density and Diffusion Anisotropy

In many studies including the ones discussed in the previous section, it has been reported that the solid portions of the tumors have significantly higher cell density than the neighboring normal parenchyma. However, a positive correlation between FA and cell density has been reported for human astrocytic tumors (Beppu et al. 2003) and glioblastomas (Beppu et al. 2005). In a recent DTI study with malignant tumors (grade 2, 3, or 4 gliomas and malignant lymphoma) (Kinoshita et al. 2008), a positive correlation ( $R = 0.75$ ) between FA and the tumor cell density of H&E stained biopsy specimens from the corresponding location was reported. FA also has a good positive correlation ( $R = 0.71$ ) with the Ki-67 labeling percentage. However, it is still not clear as to why an aggressively growing tumor maintains certain directionality (increased anisotropy), instead of growing in a random fashion. The availability of in vivo DTI techniques for rat tumor models and human tumor xenograft models exhibiting growth characteristics similar to human brain tumors may further assist in better understanding of DTI parameters in brain tumors.

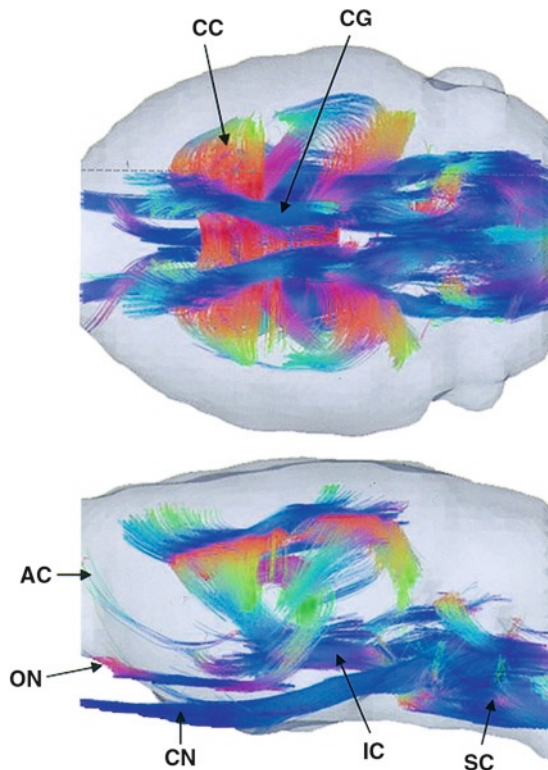


FIGURE 12.3. Major white matter tracts of the rat brain reconstructed using in vivo DTI data. CC, corpus callosum; CG, cingulum; AC, anterior commissure; ON, optic nerve; CN, cranial nerve; IC, internal capsule; SC, cortico-spinal tract. The color of the tracts represents the tangential orientation of tract at each point: *red, left-right; green, dorsal-ventral; blue, caudal-rostral*. The reconstructed tracts are overlaid on top of the rendered images of the segmented brain parenchyma (Presented at the 14th annual meeting of international society of magnetic resonance in medicine, Seattle 2006, by Kim et al.)

### Other Challenges

There are many advantages in using the currently available rat brain tumor models for DTI studies. However, there is also a need to further characterize and standardize the animal models, for better understanding of the DTI measurements, in testing the reproducibility of the exist-

ing methods and for investigation of new therapeutic strategies. In addition to the genetic variability in the cell lines across different research sites, there is a considerable difference in the methods for tumor inoculation and site of implantation, which makes it difficult to compare the results from different groups. A systematic investigation of each cell line is desired to characterize the tumor uptake and progression pattern depending on tumor implantation method. Such an exercise will also help in comparing responses to treatment methods from independent studies.

Future DTI studies of rodent brain will continue to benefit from the recent hardware and software developments in MRI technologies. Of particular interest is the development of parallel imaging, which leads to a substantial reduction in image acquisition times. The reduced scan time can be used to increase the imaging quality by allowing more repetitions or to increase the number of diffusion weighting directions toward Q-ball or diffusion spectrum imaging methods in order to measure the complete 3D pattern of diffusion. Another potential area of improvement is the improvement in SNR by using a quadrature coil to maximize the efficiency or using a cryogenic coil to minimize the thermal noise. Improved SNR will allow achieving better spatial resolution for small brain structures and also improve the accuracy of diffusion tensor estimation which is sensitive to the noise level. With these exciting developments on the horizon, an increase in the number and quality of DTI studies of rat brain tumor models is anticipated which will further aid in understanding brain tumor progression and development of therapeutic methods.

## REFERENCES

- Barth, R.F. (1998) Rat brain tumor models in experimental neuro-oncology: the 9L, C6, T9, F98, RG2 (D74), RT-2 and CNS-1 gliomas. *J. Neurooncol.* 36: 91–102
- Basser, P.J., and Pierpaoli, C. (1996) Microstructural and physiological features of tissues elucidated by quantitative-diffusion-tensor MRI. *J. Magn. Reson. B.* 111: 209–219
- Basser, P.J., Mattiello, J., and LeBihan, D. (1994a) Estimation of the effective self-diffusion tensor from the NMR spin echo. *J. Magn. Reson. B.* 103: 247–254
- Basser, P.J., Mattiello, J., and LeBihan, D. (1994b) MR diffusion tensor spectroscopy and imaging. *Biophys. J.* 66: 259–267
- Basser, P.J., Pajevic, S., Pierpaoli, C., Duda, J., and Aldroubi, A. (2000) *In vivo* fiber tractography using DT-MRI data. *Magn. Reson. Med.* 44: 625–632
- Behrens, T.E., Johansen-Berg, H., Woolrich, M.W., Smith, S.M., Wheeler-Kingshott, C.A., Boulby, P.A., Barker, G.J., Sillery, E.L., Sheehan, K., Ciccarelli, O., Thompson, A.J., Brady, J.M., and Matthews, P.M. (2003) Non-invasive mapping of connections between human thalamus and cortex using diffusion imaging. *Nat. Neurosci.* 6: 750–757
- Bennett, K.M., Hyde, J.S., Rand, S.D., Bennett, R., Krouwer, H.G., Rebro, K.J., and Schmainda, K.M. (2004) Intravoxel distribution of DWI decay rates reveals C6 glioma invasion in rat brain. *Magn. Reson. Med.* 52: 994–1004
- Beppu, T., Inoue, T., Shibata, Y., Kurose, A., Arai, H., Ogasawara, K., Ogawa, A., Nakamura, S., and Kabasawa, H. (2003) Measurement of fractional anisotropy using diffusion tensor MRI in supratentorial astrocytic tumors. *J. Neurooncol.* 63: 109–116
- Beppu, T., Inoue, T., Shibata, Y., Yamada, N., Kurose, A., Ogasawara, K., Ogawa, A., and Kabasawa, H. (2005) Fractional anisotropy value by diffusion tensor magnetic resonance imaging as a predictor of cell density and proliferation activity of glioblastomas. *Surg. Neurol.* 63: 56–61
- Field, A.S., Alexander, A.L., Wu, Y.C., Hasan, K.M., Witwer, B., and Badie, B. (2004) Diffusion tensor eigenvector directional color imaging patterns in the evaluation of cerebral white matter tracts altered by tumor. *J. Magn. Reson. Imaging* 20: 555–562
- Jensen, J.H., Helpert, J.A., Ramani, A., Lu, H., and Kaczynski, K. (2005) Diffusional kurtosis imaging: the quantification of non-gaussian water diffusion by means of magnetic resonance imaging. *Magn. Reson. Med.* 53: 1432–1440
- Kauppinen, R.A. (2002) Monitoring cytotoxic tumour treatment response by diffusion magnetic resonance imaging and proton spectroscopy. *NMR Biomed.* 15: 6–17
- Kim, S., Pickup, S., Hsu, O., and Poptani, H. (2006). *In vivo* DTI-based tractography of intracranial rat brain tumors. Paper presented at: 14th Annual meeting ISMRM (Seattle)
- Kim, S., Pickup, S., Hsu, O., and Poptani, H. (2008) Diffusion tensor MRI in rat models of invasive and well-demarcated brain tumors. *NMR Biomed.* 21: 208–216
- Kinoshita, M., Yamada, K., Hashimoto, N., Kato, A., Izumoto, S., Baba, T., Maruno, M., Nishimura, T., and Yoshimine, T. (2005) Fiber-tracking does not accurately estimate size of fiber bundle in pathological condition: initial neurosurgical experience using neuronavigation and subcortical white matter stimulation. *Neuroimage* 25: 424–429
- Kinoshita, M., Hashimoto, N., Goto, T., Kagawa, N., Kishima, H., Izumoto, S., Tanaka, H., Fujita, N., and Yoshimine, T. (2008) Fractional anisotropy and tumor cell density of the tumor core show positive correlation in diffusion tensor magnetic resonance imaging of malignant brain tumors. *Neuroimage* 43: 29–35
- Le Bihan, D., Mangin, J.F., Poupon, C., Clark, C.A., Pappata, S., Molko, N., and Chabriat, H. (2001) Diffusion tensor imaging: concepts and applications. *J. Magn. Reson. Imaging* 13: 534–546
- Lope-Piedrafita, S., Garcia-Martin, M.L., Galons, J.P., Gillies, R.J., and Trouard, T.P. (2008) Longitudinal diffusion tensor imaging in a rat brain glioma model. *NMR Biomed.* 21: 799–808
- McKnight, T.R., von dem Bussche, M.H., Vigneron, D.B., Lu, Y., Berger, M.S., McDermott, M.W., Dillon, W.P., Graves, E.E., Pirzkall, A., and Nelson, S.J. (2002) Histopathological validation of a three-dimensional magnetic resonance

- spectroscopy index as a predictor of tumor presence. *J. Neurosurg.* 97: 794–802
- Mori, S., and van Zijl, P.C. (1998) A motion correction scheme by twin-echo navigation for diffusion-weighted magnetic resonance imaging with multiple RF echo acquisition. *Magn. Reson. Med.* 40: 511–516
- Mori, S., Crain, B.J., Chacko, V.P., and van Zijl, P.C. (1999) Three-dimensional tracking of axonal projections in the brain by magnetic resonance imaging. *Ann. Neurol.* 45: 265–269
- Mori, S., Itoh, R., Zhang, J., Kaufmann, W.E., van Zijl, P.C., Solaiyappan, M., and Yarowsky, P. (2001) Diffusion tensor imaging of the developing mouse brain. *Magn. Reson. Med.* 46: 18–23
- Moseley, M.E., Cohen, Y., Mintorovitch, J., Chileuitt, L., Shimizu, H., Kucharczyk, J., Wendland, M.F., and Weinstein, P.R. (1990) Early detection of regional cerebral ischemia in cats: comparison of diffusion- and T2-weighted MRI and spectroscopy. *Magn. Reson. Med.* 14: 330–346
- Pierpaoli, C., and Basser, P.J. (1996) Toward a quantitative assessment of diffusion anisotropy. *Magn. Reson. Med.* 36: 893–906
- Stejskal, E.O., and Tanner, J.E. (1965) Spin diffusion measurements: spin echoes in the presence of a time-dependent field gradient. *J. Chem. Phys.* 42: 288–292
- Tuch DS (2004) Q-ball imaging. *Magn Reson Med* 52: 1358–1372
- Vonarbourg, A., Sapin, A., Lemaire, L., Franconi, F., Menei, P., Jallet, P., and Le Jeune, J.J. (2004) Characterization and detection of experimental rat gliomas using magnetic resonance imaging. *Magma* 17: 133–139
- Wedeen, V.J., Hagmann, P., Tseng, W.Y., Reese, T.G., and Weisskoff, R.M. (2005) Mapping complex tissue architecture with diffusion spectrum magnetic resonance imaging. *Magn. Reson. Med.* 54: 1377–1386
- Westin, C.F., Maier, S.E., Mamata, H., Nabavi, A., Jolesz, F.A., and Kikinis, R. (2002) Processing and visualization for diffusion tensor MRI. *Med. Image Anal.* 6: 93–108
- Zhang, J., van Zijl, P.C., Laterra, J., Salhotra, A., Lal, B., Mori, S., and Zhou, J. (2007) Unique patterns of diffusion directionality in rat brain tumors revealed by high-resolution diffusion tensor MRI. *Magn. Reson. Med.* 58: 454–462

# 13

## Brain Tumors: Diffusion Imaging and Diffusion Tensor Imaging

Pia C. Sundgren, Yue Cao, and Thomas L. Chenevert

### INTRODUCTION

Introduction of magnetic resonance imaging (MRI) into clinical practice has been among the most important of all advances in the diagnosis of patients with brain tumor. Excellent soft tissue differentiation and wide availability of clinical MR scanners have resulted in crucial roles of anatomic MRI. However the radiological specification and grading of a brain tumor is still limited despite the information provided by conventional MR with contrast-enhanced T1-weighted and T2-weighted sequences to characterize the location and extent of the tumor. In recent years a new MRI technique, diffusion-weighted MR imaging (DWI), has become part of the routine neuroimaging protocol worldwide. DWI measures the mobility of water molecules and the principles for the measurement of diffusion with MRI are well described (Le Bihan 1991; Moseley et al. 1990). Further technical improvements have led to more complex diffusion tensor imaging (DTI) that allows direct examination in vivo of some aspects of tissue microstructure. DTI yields quantitative measures reflecting the integrity of white matter fiber tracts by taking advantage of

the intrinsic properties of directionality of water diffusion in human brain tissue. Both diffusion-weighted imaging and analysis from DTI may provide new possibilities in the work-up of patients with brain neoplasm in terms of tissue characterization, to evaluate different tumor components, to grade tumor in high-grade or low-grade, to differentiate tumor invasion from normal brain tissue or edema, surgical planning, and treatment follow-up (Field and Alexander et al. 2004 Field et al. 2004).

New and more aggressive treatment modalities and combined modalities are constantly being investigated for brain tumor treatment at institutions around the world to obtain optimal treatment schemes for different brain tumors. Therefore, it has become crucial to the treatment of patients with brain tumors to better define tumor margins, to determine the most aggressive tumor regions for intensified radiation treatment, and to obtain reliable information regarding tumor response to therapy or tumor progression for reoptimization of treatment, and to predict treatment toxicity early. Recent data from both animal models and human studies suggest that diffusion imaging may be a sensitive tool in the



evaluation of tumor response to therapy (Chenevert et al. 1997; Mardor et al. 2003).

We have to keep in mind that these possibilities are only just beginning to be fully explored and that the analysis of diffusion-weighted images and the tensor data shall be done in combination with conventional neuroimaging. Also, other MRI techniques such as MR perfusion imaging and magnetic resonance spectroscopy (MRS) may add valuable information when used separately or combined with the diffusion-weighted MR imaging.

This chapter will give a brief introduction to the DWI and DTI techniques and summarize the current knowledge on the use of DWI and DTI in brain tissue characterization, brain tumor grading and presurgical planning. The possibility to differentiate recurrent tumor from radiation injury and the use of diffusion imaging in treatment follow-up, as well as the pitfalls and future prospective will be discussed.

## IMAGING TECHNIQUES

### Diffusion Weighted Imaging

DWI has a well-established advantage over essentially all modern MRI systems, and is implemented as a part of routine neuroimaging protocols. This imaging measures the mobility of water molecules and the principles for the measurement of diffusion with magnetic resonance imaging (MRI) are well described by others (Le Bihan 1991). In DWI, water mobility is described using a scalar parameter, the diffusion coefficient  $D$  which is known to be dependent on systematic effects such as the time-scale of the diffusion measurement. As such, usually only an “apparent” diffusion coefficient (ADC) is calculable

in complex systems such as cellular tissue. Apparent diffusion coefficients can be computed from a pair of images with or without additional diffusion sensitization gradient pulses. The ADC takes into consideration the heterogeneous environment of brain cytoarchitecture as well as factors other than diffusion such as temperature, perfusion, and presence of membranes and macromolecules that affect microscopic thermal motion (Cha 2005).

The most widely used diffusion-weighted image acquisition method is single-shot echo-planar imaging (EPI) (Turner et al. 1990) because it is fast and allows the entire set of echoes needed to generate an image to be collected within one single acquisition period of 25–100 ms, thereby essentially freezing bulk tissue motion that would otherwise overwhelm measurement of molecular motion. The technique is efficient, and insensitive to small motions, as well as readily available on most modern clinical MRI scanners. EPI virtually eliminates motion artifacts but due to the long readout time for Echo planar imaging the images are sensitive to artifacts, such as misregistration of the data due to eddy currents, and signal loss due to susceptibility variations both of which cause distortion in the image data. Hardware issues such as background gradients, gradient non-linearity, and miscalibration also are taken into consideration in image reconstruction routines. However, improvements in image resolution and reduction of distortion have been made using motion-corrected multi-shot EPI PROPELLER (Periodically Rotated Overlapping Parallel Lines with Enhanced Reconstruction) and sensitivity-encoding (SENSE) EPI techniques (Bammer et al. 2002; Pipe et al. 2002).

### Diffusion Tensor Imaging

Not even the most anatomically detailed conventional neuro-MR imaging allows an assessment of specific white matter fiber tracts. However, further improvements in the imaging of water diffusion have led to a more complete probing of water motions in anisotropic media, such as tissue via DTI. In other words, water mobility is highly dependent on directionality of tissue structures that impede water movement, and DTI allows direct examination in vivo of some aspects of directional tissue microstructure. Diffusion tensor imaging yields quantitative measurements, reflecting the integrity of white matter fiber tracts by taking advantage of the intrinsic properties of directionality of water diffusion in human brain tissue. Brownian motion characterizes the diffusion of water molecules. When water molecules are unconstrained, the direction of motion of a given molecule is random. A Gaussian distribution describes the displacement of water molecules over time. The diffusion is called isotropic when the motion is equal and unconstrained in all directions. However, the microstructure of brain tissue forms physical boundaries that impede the Brownian motion of water molecules, resulting in directional anisotropy in the amount of water molecule migration. In high directionally ordered tissues, such as the white matter fibers, the diffusion of water molecules will be relatively more impeded perpendicular than parallel to the multiple myelin layers encasing the neuron; thus, diffusion is anisotropic (Le Bihan 1993).

In standard DWI-MRI, diffusion is described using a scalar parameter, the diffusion coefficient  $D$ . In tissues, such as gray matter, where the measured apparent diffusivity is largely isotropic, it is sufficient to describe the diffusion characteris-

tics with a single scalar ADC along with relevant acquisition settings. In the presence of anisotropy, the diffusion can no longer be characterized by a single scalar coefficient, but requires a tensor  $\underline{D}$  that more fully describes the mobility of the molecules along each direction and the correlation between these directions. The mathematical construct used to characterize anisotropic Gaussian diffusion is a second-order diffusion tensor (Le Bihan et al. 2001). Because the tensor is symmetric, six unique elements are required to fully characterize the tensor. The tensor can be diagonalized such that only three non-zero elements ( $\lambda_1$ ,  $\lambda_2$ , and  $\lambda_3$ ) remain along the diagonal. These elements are known as the eigenvalues. Each eigenvalue is associated with an eigenvector ( $\varepsilon_1$ ,  $\varepsilon_2$  and  $\varepsilon_3$ ), where the largest of the three eigenvalues ( $\lambda_1$ ) corresponds to the eigenvector  $\varepsilon_1$  and describes the principal direction of the diffusion at that point.

Diffusion tensor measurements result in a rich data set. Metrics of diffusion anisotropy can be measured in different ways by applying simple or more complicated mathematical formulas and recalculations using the underlying eigenvectors (Le Bihan et al. 2001; Basser and Jones 2002). A common way to summarize diffusion measurements in DTI is the calculation of parameter for the overall diffusivity and another parameter that reflects anisotropy. As before, the ADC serves for overall diffusivity and is derived from the trace of the diffusion tensor. Anisotropy is represented by the fractional anisotropy (FA) or alternatively the relative anisotropy (RA). The FA is a measure of the portion of the magnitude of the diffusion tensor due to anisotropy. The RA is derived from a ratio between the anisotropic portion of the diffusion tensor and

the isotropic portion. Another commonly used value is the volume ratio (VR), which expresses the relationship between the diffusion ellipsoid volume to the volume of a sphere with radius equal to the average of eigenvalues (Pierpaoli et al. 1996). From previous work it is known that both the water ADC and the diffusion anisotropy differ markedly between pediatric brain and adult brain, and also both parameters vary with increasing age as well as in different regions of the brain (Pfefferbaum et al. 2000; Mukherjee et al. 2001)

The differences between these measurements lie in their sensitivity to anisotropy: FA is more sensitive for low anisotropy values, whereas VR is sensitive to high values of diffusion anisotropy, and RA scales linearly for different levels of anisotropy. Both FA and RA are 0.0 for a purely isotropic medium. For a highly anisotropic medium FA tends towards 1, while RA tends towards  $\sqrt{2}$ . Both FA and RA maps can be presented as gray scale images for the purpose of visual evaluation of patterns of tissue anisotropy. As for VR, the range is from 1 (isotropic diffusion) to 0; therefore, some authors prefer to use  $(1-VR)$ . In contrast to aforementioned measurements, which represent intravoxel anisotropy, the lattice anisotropy index, another way to evaluate diffusion, measures the intervoxel anisotropy. The lattice measures of diffusion anisotropy allow neighboring voxels to be considered together in a region of interest, without losing anisotropy effects that result from different fiber orientations across voxels (Pierpaoli et al. 1996).

DTI allows us to look at the anisotropic diffusion within the white matter tracts but is limited in demonstrating the spatial, directional diffusion anisotropy. Therefore, new and or more sophisticated methods to

demonstrate diffusion directions such as color-coding and fiber tracking have been proposed (Pierpaoli and Basser 1996; Pajevic and Pierpaoli 1999; Mori and van Zijl 2002; Mori et al. 2004). By choosing the eigenvector associated with the largest eigenvalue, the principal diffusion direction of the brain structure to be examined can be encoded with color, resulting in directionally-encoded FA maps (DEC FA maps). In these color-encoded maps the fibers have been given different colors (red, green and blue), depending on their different diffusion directions (Pajevic and Pierpaoli 1999).

#### Diffusion Imaging in Tissue Characterization

Apparent diffusion coefficient maps that can be generated from both DWI and/or DTI data have proved to be helpful in defining solid enhancing tumor, non-contrast enhancing lesion, peritumoral edema, and necrotic and/or cystic regions from normal surrounding brain tissue. It has been suggested in several studies that ADC values can be helpful to discriminate edema from tumor (Bastin et al. 2002; Sinha et al. 2002), but there are several examples of the contrary (Stadnik et al. 2001; Provenzale et al. 2004). Field et al. 2004, suggested that one likely explanation for all the contradictory results of the value of ADC to discriminate edema for tumor is the lack of standardized methods not only for the diffusion image acquisition but also for post processing and ROI analysis, and concluded that when considering all the evidence it seems appears unlikely that ADC values alone can with certainty differentiate between peritumoral edema and noncontrast enhancing neoplasm in individual patient. It has been shown that cystic or necrotic regions have highest ADC

values (Sinha et al. 2002), while contrast-enhancing part of the tumor has lower ADC than both the cystic or the necrotic areas and edema (Krabbe et al. 1997).

Significant increase in mean diffusivity and significant decrease in FA have been demonstrated in the peritumoral region of both gliomas and metastatic tumors when compared with those of normal appearing white matter (Lu et al. 2003). Furthermore, the peritumoral mean diffusivity of metastatic lesions measured significantly greater than those of gliomas, whereas the FA values showed no discrepancy between tumor and metastasis, suggesting that the FA changes surrounding gliomas can be attributed to both increased water content and tumor infiltration (Lu et al. 2003).

Lu et al. 2004 have shown that FA-values and histograms of mean diffusivity in peritumoral areas could not be used to differentiate high grade from low-grade gliomas or meningiomas from intraaxial tumors. Other studies have demonstrated similar findings with a trend towards reduction of FA but not of mean diffusivity in the peritumoral edema of glioblastomas compared to meningioma (Tropine et al. 2004) and also alterations in FA in white matter in the affected as well as in the contralateral hemispheres in glioblastomas but not in metastases (Price et al. 2003). However, significant increase in mean diffusivity and significant decrease in FA have been demonstrated in the peritumoral region of both gliomas and metastatic tumors when compared with those of normal-appearing white matter (Lu et al. 2003). Other measurements such as Tumor Infiltration Index (TII) have recently been introduced to separate tumors with presumed purely vasogenic edema i.e., metastases and extra-axial lesions such as meningioma from those with tumor-infiltrated edema i.e.,

high and low-grade glial tumors. The mean TII were significantly higher in presumed tumor-infiltrated edema (Lu et al. 2004).

### Diffusion Imaging in Tumor Grading

The possibility of differentiating the type and the grade of a tumor has also been explored by the use of DWI and DTI, both in the adult as well as in the Pediatric populations. Several studies have shown that low-grade astrocytoma has higher ADC values, whereas high-grade malignant glioma has lower ADC values, findings reflecting more restricted diffusion with increasing tumor cellularity (Kono et al. 2001). Inoue et al. (2005) demonstrated significant differences in FA values in histologically proven high grade and low grade gliomas. They showed that the FA values were significantly lower in grade 1 gliomas tumor compared to grade 3 and 4 gliomas, and FA values in grade 2 gliomas were significantly lower than those found in grade 3 and 4 gliomas. They concluded that FA values can distinguish between high grade and low grade gliomas. However there is still a lot of controversy in the literature, and others have concluded that differentiation of tumors by the use of FA values, which are generally reduced in tumors suggesting structural disorder, does not add any additional information to the tissue differentiation (Sinha et al. 2002). Others indicate FA may help in the understanding of the effect of brain tumors on white matter fibers, which may be important in the pre-surgical planning (2000; Mori et al. 2002).

A possible explanation for the controversy regarding the value of FA measurements to grade tumors can be due to the normal variation of FA values depending on location in the brain (Pierpaoli et al. 1996).

This normal variation of FA values depending on the location in the brain can be exemplified by the more than twofold differences in FA between peripheral white matter such as neocortical association tracts and central commissural tracts such as splenium of the corpus callosum (Pierpaoli et al. 1996), which may reflect the results obtained. Tumor vascularity or microcirculation in the abnormal tissue may also affect the FA-values. Finally, the heterogeneity of the FA values within a tumor resulting in possible discrepancy between the placements of the ROI's which may or may not include areas of necrosis. As expected, the necrotic core of the high grade gliomas shows low FA values (Sinha et al. 2002).

Studies using more sophisticated methods for evaluation of tumors such as analysis of the role of different eigenvectors have demonstrated that the value of the major eigenvector of the diffusion reflecting the diffusivity in the longitudinal direction was significantly lower in white matter surrounding glioma than in white matter surrounding metastases, even when the anisotropy showed no difference. The latter suggests that more sophisticated approaches might yield more information than only mean diffusivity and anisotropy measurements.

### Diffusion Imaging in Pre-surgical Planning

The role of DTI in presurgical planning is not yet fully defined, and several technical problems remain to be solved before DTI can be considered a reliable method for presurgical planning. Much of the published data are from small number of patients or case reports. In these studies the dislocation or distortion of the white matter fiber tract by tumor is demonstrated by some form of tensor directional mapping with or without

additional fiber tracking (Mori et al. 2002; Witwer et al. 2002) (Figure 13.1). It is known that the neoplasm may alter the white matter in different ways. Depending on the way the fiber tracts are altered, we can expect them to exhibit normal diffusion anisotropy or even increased anisotropy due to compression of tracks, or a reduction of anisotropy toward becoming purely isotropic (Field et al. 2004). In a recent limited DTI study using FA-weighted, directionally encoded color maps, categorized on the basis of anisotropy and fiber direction or orientation, four major patterns of tumor altered white matter tracts were identified (Field et al. 2004). The four potential patterns of altered white matter fiber tract described are: deviated, edematous, infiltrated, and destroyed. These defined patterns may potentially be helpful in presurgical planning, to confirm an intact or disrupted fiber tract, to inform the surgeon as to the tracts location and/or displacement in relation to the tumor, and thereby potentially avoid damaging an intact tract during surgery.

### Diffusion Imaging in Treatment Follow-Up

In the treatment of patients with tumor it is crucial to obtain reliable information regarding tumor response to therapy. Recent data from both animal models and human studies suggest that diffusion imaging may be a sensitive tool in the evaluation of tumor response to therapy (Chenevert et al. 1997; Mardor et al. 2003) and be helpful in predicting chemosensitivity of glial tumors (Jager et al. 2005) as well as overall survival (Hamstra et al. 2008). Previous work by Chenevert et al. (2000) has demonstrated that DWI can provide early evidence of cancer treatment efficacy in an individual patient prior to completion of the therapeutic

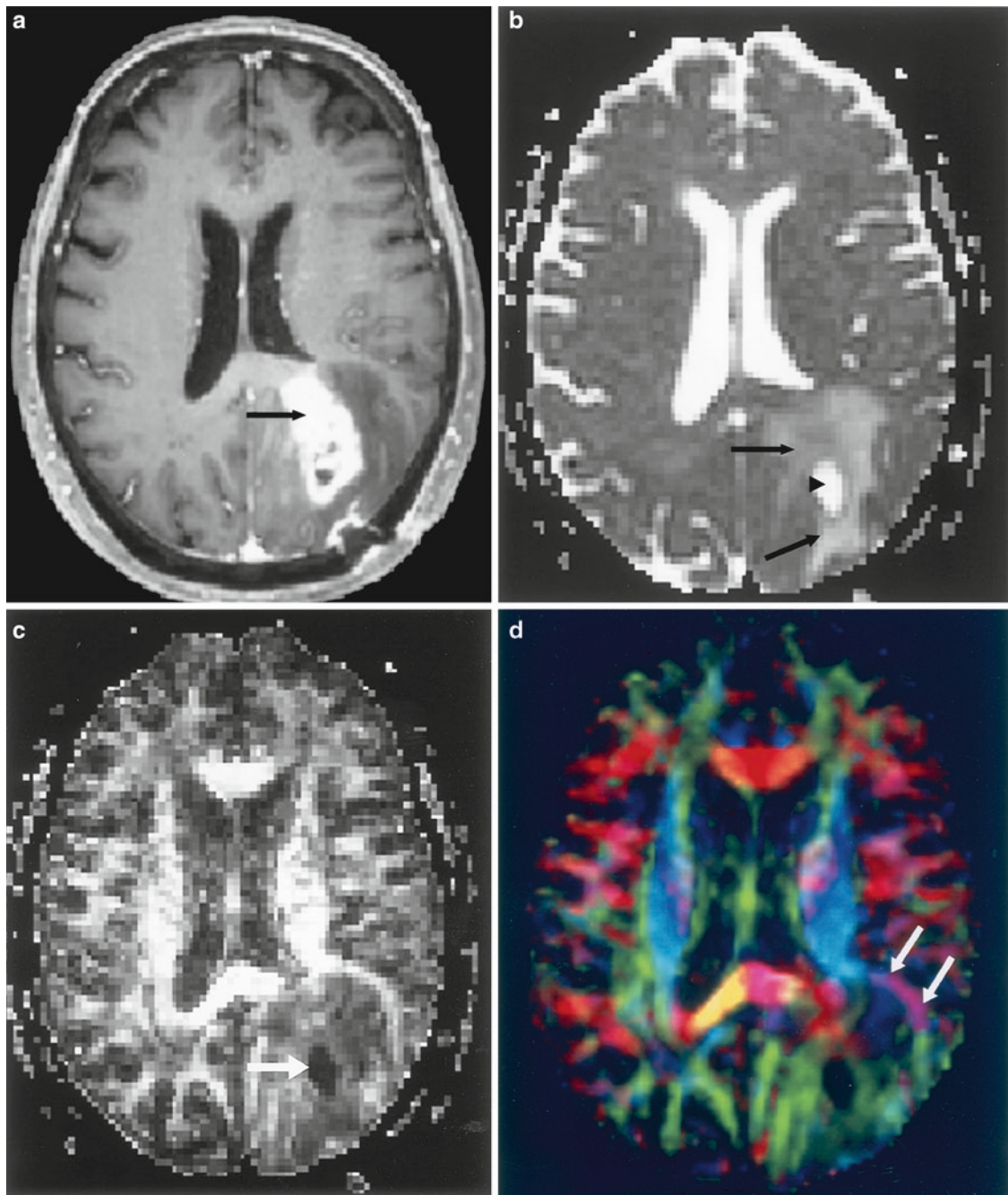


FIGURE 13.1. (a–d) MRI performed prior to treatment in a 62 year old female with biopsy proven glioblastoma in the left occipital lobe. (a) Postcontrast-enhanced axial T1-weighted images demonstrate a large heterogenous contrast enhancing mass in left occipital lobe with involvement of the splenium of the corpus callosum and effacement of the left atria (*black arrow*); (b) increased signal due to increase diffusivity is demonstrated on the ADC-maps (*black arrows*) with a focal area of even brighter signal representing a small area of necrosis within the tumor (*black arrowhead*); (c) a reduction of the fraction anisotropy can be seen as focal regions of decreased signal (*dark*) on the fraction anisotropy maps (FA-maps) (*black arrow*). (d) The adjacent white matter tracts are destroyed by the tumor as well as the appearance of displaced tracts in the anterior aspect of the tumor can be seen on the directional color encoded image (*small black arrows*) (\*Red = fibers in the *right to left* fiber direction, *green* = fibers running in the anterior posterior direction, and *blue* represents fibers running in the superior inferior direction)

regimen. They demonstrated that in the nonresponsive patients the diffusion values did not change, while they increased in patients with partial or full response, and concluded that diffusion values can be measured during treatment and appear to reflect dynamic therapeutic-induced changes or lack thereof in tissue cytoarchitecture. These data are supported by others demonstrating a significant difference in mean ADC between responders and nonresponders to therapy as well as linear correlation between the relative change in ADC and the normalized change in tumor volume (Mardor et al. 2003). Early increasing ADC values during therapy may relate to therapy-induced cell necrosis. The subsequent drop in ADC values within the tumor to pretreatment levels is thought to be an indicator of tumor regrowth. This hypothesis is supported by findings of differences in ADC values in recurrent gliomas compared with those obtained in patients with radiation necrosis. That study demonstrated lower ADC values in contrast enhancing parts of recurrent high-grade gliomas compared to those obtained in patients with radiation injury/necrosis (Hein et al. 2004). Also the combination of ADC-maps and relative cerebral blood volume measurements has been used to evaluate chemosensitivity: areas of the tumor with the lowest ADC values and highest rCBV demonstrated a significant volume reduction during treatment, whereas other components of the tumor demonstrated no change in volume (Jager et al. 2005).

#### Diffusion Imaging in Differentiation of Recurrent Tumor from Radiation Injury and Post-surgical Injury

Treatment with chemotherapy and radiation therapy for brain tumors can result in

white matter injury. Kitahara et al. (2005) showed that the mean FA value decreased and average of mean isotropic ADC value increased significantly in normal appearing white matter in patients treated with radiation compared to those found in normal white matter in control subjects. Long-term reduction in anisotropy in normal appearing white matter has also been demonstrated in children treated with combination therapy for medulloblastoma (Khong et al. 2003). It seems from these and other studies that diffusion anisotropy is highly sensitive to microstructural changes that might not have been seen on conventional imaging but that the pathological specificity is relatively low. Therefore, more sophisticated approaches will be required for tissue characterization using DTI. New enhancing lesions that arise on routine follow-up brain MR imaging at the site of a previously identified and treated primary brain neoplasm may also present a significant diagnostic dilemma. These lesions are typically subjected to radiation and/or chemotherapy and in most instances surgical resection. Many lesions do not have specific imaging characteristics that enable the neuroradiologist to discriminate tumor recurrence from the inflammatory or necrotic changes that result from treatment with radiation and/or chemotherapy. Both recurrent tumors and treatment-related changes (i.e., necrosis) typically demonstrate enhancement with gadolinium and are commonly surrounded by an area of increased T2 signal. However, recent reports have suggested that diffusion measurements can potentially provide important diagnostic information regarding newly enhancing lesions as well as on the surrounding areas of signal abnormality that may appear months to years after radiation therapy in patients previously treated for primary and metastatic brain tumors (Hein

et al. 2004). We found in a recent study of 19 patients who presented with a new area of contrast enhancement at or nearby the site of previously treated (surgery/biopsy and radiation therapy) brain neoplasm that the ADC values were significantly higher in patients with tumor recurrence (mean  $1.23 \times 10^{-3} \text{ mm}^2/\text{s}$ ) than those with treatment related changes (mean  $1.07 \times 10^{-3} \text{ mm}^2/\text{s}$ ). Fraction anisotropic (FA)-values were lower in both groups compared with FA-values in normal appearing frontal white matter but no statistical difference was seen in the FA values in the contrast-enhancing lesion between the two groups (Dong et al. 2004; Sundgren et al. 2006). Contradictions in literature exist regarding whether an increased or decreased ADC is to be expected in tumor or radiation injury/necrosis. In a recent study the recurrence group showed statistically lower mean ADC values (mean  $1.18 \times 10^{-3} \text{ mm}^2/\text{s}$ ) compared with the treatment-induced necrosis group (mean  $1.40 \times 10^{-3} \text{ mm}^2/\text{s}$ ) (Hein et al. 2004), while others have demonstrated increased ADC values in recurrent tumors (Le Bihan et al. 1993; Biousse et al. 2003).

Two other studies have shown that although the mean ADC values in areas of T2-prolongation surrounding the contrast-enhancing lesion differ compared to values obtained in normal brain tissue, no significant differences were demonstrated between patients with radiation injury and those with recurrent tumor (Hein et al. 2004; Sundgren et al. 2006). One of these studies demonstrated significantly higher ADC ratios (ADC in abnormal area/ADC in normal appearing brain tissue) in the edema in patients with radiation injury compared to those with tumor recurrence (Sundgren et al. 2006). More interestingly, the same study demonstrated that for the normal appearing white matter tract adjacent to the edema, both the

FA values and the FA ratios were significantly lower in patients with recurrent tumor compared to those with radiation injury. These findings may indicate that the DTI provide a helpful method in detecting occult white matter tract invasion in recurrent or primary brain tumors, and that the FA measurement and more advanced methods such as the different eigenvectors could be more sensitive than ADC values to demonstrate occult white matter changes. Noteworthy limitations for all these studies are the small number of patients and the lack of histological confirmation in all cases. There is certainly a need for further exploration in this field with larger studies, correlation with histological specimens, and correlation to long-term clinical outcome.

#### Pitfalls

One of the major pitfalls of DWI is related to the sensitivity of the technique to lesions containing high magnetic susceptibility such as blood products, calcium, metal, bone, and air. The susceptibility artifacts caused by ferromagnetic or paramagnetic material may result in signal changes on MR images that can be mistakenly interpreted as pathological processes or misdiagnosed as for example acute ischemia. Artifacts or pitfalls may also be due to properties of the subject imaged such as T2 effects as in “T2-shine through”. This problem can be reduced or resolved by using higher b-values and stronger gradients which will make it possible to record high b-value diffusion images with shorter TE, and thereby less T2-weighting (Koch and Norris 2005). However to reduce pitfalls, as mentioned already in the Introduction, the interpretation of diffusion-weighted imaging must be done in combination of reviewing the conventional anatomic MR images. Caution in



the interpretation should be made especially when evaluating images in the immediate postoperative state due to blood products and surgical metal.

### Future Applications

Physiology-based MRI methods such as DWI and DTI are rapidly becoming a part of the routine brain imaging protocol to improve diagnosis, characterization and grading of brain neoplasm, and in the management of patients with brain tumors. In the future these methods combined with other physiology-based methods, such as MR perfusion and/or magnetic resonance spectroscopy, will be combined with anatomical images to improve brain tumor diagnosis, biopsy guidance, for treatment and presurgical planning, and in the treatment follow-up of patients with brain tumors. In their current form, DWI and DTI yield remarkable insight into tissue/tumor cellularity and organization totally noninvasively. In the future, more sophisticated forms of diffusion-based image acquisition and analysis may increase the specificity of the method.

Recently, an alternate approach has been developed where regional changes in ADCs (both increasing and decreasing) can be quantified. When this approach was applied to a population of patients with a heterogeneous mix of primary brain tumors 3 weeks following the start of treatment, it was found to accurately predict radiographic response several months later (Moffat et al. 2005) and also differentiated overall survival (Hamstra et al. 2008). It is worth pointing out that this analytic approach is also based upon the volumetric change in the ADC. Further evaluation of this technique is warranted to determine if it may be useful in the individualization of treatment or evaluation of the regional therapeutic response.

New methods to perform diffusion-weighted images and real-time analysis of the tensor data are currently being developed, which will make these methods better, faster, and less affected by artifacts. In the future it might be possible to perform real-time intraoperative DTI to evaluate the white matter tracts during the surgical procedure, a protocol that might reduce the damage to the tracts and increase the neurosurgeons' ability to more aggressive surgery. A combined approach utilizing all available physiological MR techniques will increase our knowledge and be helpful in tissue characterization and tumor grading, in follow-up and adjustment of ongoing treatment, and increase our knowledge regarding what happens to radiated brain tissue, and hopefully be able to differentiate treatment related injuries from tumor recurrence.

*Acknowledgment.* This work, in part, was sponsored by NIH grant CA 85878.

### REFERENCES

- Bammer, R., Auer, M., Keeling, S.L., Augustin, M., Stables, L.A., Prokesch, R.W., Stollberger, R., Moseley, M.E., and Fazekas, F. (2002) Diffusion tensor imaging using single-shot SENSE-EPI. *Magn. Reson. Med.* 48(1): 128–136
- Basser, P.J., and Jones, D.K. (2002) Diffusion-tensor MRI: theory, experimental design and data analysis – a technical review. *NMR Biomed.* 15(7–8):456–467
- Bastin, M.E., Sinha, S., Whittle, I.R., and Wardlaw, J.M. (2002) Measurements of water diffusion and T1 values in peritumoural oedematous brain. *Neuroreport* 13(10):1335–1340
- Biousse, V., Newman, N.J., Hunter, S.B., and Hudgins, P.A. (2003) Diffusion weighted imaging in radiation necrosis. *J. Neurol. Neurosurg. Psychiatry* 74(3): 382–384
- Cha, S. (2005) Update on brain tumor imaging. *Curr. Neurol. Neurosci. Rep.* 5(3):169–177

- Chenevert, T.L., McKeever, P.E., and Ross, B.D. (1997) Monitoring early response of experimental brain tumors to therapy using diffusion magnetic resonance imaging. *Clin. Cancer Res.* 3(9): 1457–1466
- Chenevert, T.L., Stegman, L.D., Taylor, J.M., Robertson, P.L., Greenburg, H.S., Rehemtulla, A., Ross, B.D. (2000) Diffusion magnetic resonance imaging an early surrogate marker of therapeutic efficacy in brain tumors. *J Natl cancer Inst.* 92(24):2029–2036
- Dong, Q., Welsh, R.C., Chenevert, T.L., Carlos, R.C., Maly-Sundgren, P., Gomez-Hassan, D.M., Mukherji, S.K. (2004) Clinical applications of diffusion tensor imaging. *J Magn Reson Imaging.* 19(1):6–8
- Field, A.S., and Alexander, A.L. (2004) Diffusion tensor imaging in cerebral tumor diagnosis and therapy. *Top. Magn. Reson. Imaging* 15(5): 315–324
- Field, A.S., Alexander, A.L., Wu, Y.C., Hasan, K.M., Witwer, B., and Badie, B. (2004) Diffusion tensor eigenvector directional color imaging patterns in the evaluation of cerebral white matter tracts altered by tumor. *J. Magn. Reson. Imaging* 20(4):555–562
- Hamstra, D.A., Galban, C.J., Meyer, C.R., Johnson, T.D., Sundgren, P.C., Tsien, C., Lawrence, T.S., Junck, L., Ross, D.J., Rehemtulla, A., Ross, B.D., and Chenevert, T.L. (2008) Functional diffusion map as an early imaging biomarker for high-grade glioma: correlation with conventional radiologic response and overall survival. *J. Clin. Oncol.* 26(20):3387–3394
- Hein, P.A., Eskey, C.J., Dunn, J.F., and Hug, E.B. (2004) Diffusion-weighted imaging in the follow-up of treated high-grade gliomas: tumor recurrence versus radiation injury. *AJNR Am. J. Neuroradiol.* 25(2):201–209
- Inoue, T., Ogasawara, K., Beppu, T., Ogawa, A., Kabasawa, H. (2005) Diffusion tensor imaging for preoperative evaluation of tumor grade in gliomas. *Clin Neurol Neurosurg.* 107(3):174–180
- Jager, H.R., Waldman, A.D., Benton, C., Fox, N., and Rees, J. (2005) Differential chemosensitivity of tumor components in a malignant oligodendroglioma: assessment with diffusion-weighted, perfusion-weighted, and serial volumetric MR imaging. *AJNR Am. J. Neuroradiol.* 26(2):274–278
- Khong, P.L., Kwong, D.L., Chan, G.C., Sham, J.S., Chan, F.L., and Ooi, G.C. (2003) Diffusion-tensor imaging for the detection and quantification of treatment-induced white matter injury in children with medulloblastoma: a pilot study. *AJNR Am. J. Neuroradiol.* 24(4):734–740
- Kitahara, S., Nakasu, S., Murata, K., Sho, K., Ito, R. (2005) Evaluation of treatment-induced cerebral white matter injury by using diffusion-tensor MR imaging: initial experience. *AJNR Am. J. Neuroradiol.* 26(9):2200–2206
- Koch, M.A., and Norris, D.G. (2005) Artifacts and pitfalls in diffusion MR imaging: diffusion. In: *Clinical MR Neuroimaging*—Gillard J, Waldman A, Barker P, eds Cambridge: Cambridge University Press. 99–108
- Kono, K., Inoue, Y., Nakayama, K., Shakudo, M., Morino, M., Ohata, K., Wakasa, K., and Yamada, R. (2001) The role of diffusion-weighted imaging in patients with brain tumors. *AJNR Am. J. Neuroradiol.* 22(6):1081–1088
- Krabbe, K., Gideon, P., Wagn, P., Hansen, U., Thomsen, C., and Madsen, F. (1997) MR diffusion imaging of human intracranial tumours. *Neuroradiology* 39(7):483–489
- Le Bihan, D. (1991) Molecular diffusion nuclear magnetic resonance imaging. *Magn. Reson. Q.* 7(1):1–30
- Le Bihan, D. (1993) *Clinical perfusion and diffusion imaging.* Raven press, New York
- Le Bihan, D., Douek, P., Argyropoulou, M., Turner, R., Patronas, N., and Fulham, M. (1993) Diffusion and perfusion magnetic resonance imaging in brain tumors. *Top. Magn. Reson. Imaging* 5(1):25–31
- Le Bihan, D., Mangin, J.F., Poupon, C., Clark, C.A., Pappata, S., Molko, N., and Chabriat, H. (2001) Diffusion tensor imaging: concepts, applications. *J. Magn. Reson. Imaging* 13(4):534–546
- Lu, S., Ahn, D., Johnson, G., and Cha, S. (2003) Peritumoral diffusion tensor imaging of high-grade gliomas and metastatic brain tumors. *AJNR Am. J. Neuroradiol.* 24(5):937–941
- Lu, S., Ahn, D., Johnson, G., Law, M., Zagzag, D., and Grossman, R.I. (2004) Diffusion-tensor MR imaging of intracranial neoplasia and associated peritumoral edema: introduction of the tumor infiltration index. *Radiology* 232(1):221–228
- Mardor, Y., Pfeffer, R., Spiegelmann, R., Roth, Y., Maier, S.E., Nissim, O., Berger, R., Glicksman, A., Baram, J., Orenstein, A., Cohen, J.S., and Tichler, T. (2003) Early detection of response to radiation therapy in patients with brain malignancies

- using conventional and high b-value diffusion-weighted magnetic resonance imaging. *J. Clin. Oncol.* 21(6):1094–1100
- Moffat, B.A., Chenevert, T.L., Lawrence, T.S., Meyer, C.R., Johnson, T.D., Dong, Q., Tsien, C., Mukherji, S., Quint, D.J., Gebarski, S.S., Robertson, P.L., Junck, L.R., Rehemtulla, A., and Ross, B.D. (2005) Functional diffusion map: a noninvasive MRI biomarker for early stratification of clinical brain tumor response. *Proc. Natl. Acad. Sci. USA* 102(15):5524–5529
- Mori S, and van Zijl PC (2002) Fiber tracking: principles and strategies – a technical review. *NMR Biomed* 15(7–8):468–480
- Mori, S., Frederiksen, K., van Zijl, P.C., Stieltjes, B., Kraut, M.A., Solaiyappan, M., and Pomper, M.G. (2002) Brain white matter anatomy of tumor patients evaluated with diffusion tensor imaging. *Ann. Neurol.* 51(3):377–380
- Moseley, M.E., Kucharczyk, J., Mintorovitch, J., Cohen, Y., Kurhanewicz, J., Derugin, N., Asgari, H., and Norman, D. (1990) Diffusion-weighted MR imaging of acute stroke: correlation with T2-weighted and magnetic susceptibility-enhanced MR imaging in cats. *AJNR Am. J. Neuroradiol.* 11(3):423–429
- Mukherjee, P., Miller, J.H., Shimony, J.S., Conturo, T.E., Lee, B.C., Almlı, C.R., and McKinstry, R.C. (2001) Normal brain maturation during childhood: developmental trends characterized with diffusion-tensor MR imaging. *Radiology* 221(2):349–358
- Pajevic, S., and Pierpaoli, C. (1999) Color schemes to represent the orientation of anisotropic tissues from diffusion tensor data: application to white matter fiber tract mapping in the human brain. *Magn. Reson. Med.* 42(3):526–540
- Pfefferbaum, A., Sullivan, E.V., Hedehus, M., Lim, K.O., Adalsteinsson, E., and Moseley, M. (2000) Age-related decline in brain white matter anisotropy measured with spatially corrected echo-planar diffusion tensor imaging. *Magn. Reson. Med.* 44(2):259–268
- Pierpaoli, C., and Basser, P.J. (1996) Toward a quantitative assessment of diffusion anisotropy. *Magn. Reson. Med.* 36(6):893–906
- Pierpaoli, C., Jezzard, P., Basser, P.J., Barnett, A., and Di Chiro, G. (1996) Diffusion tensor MR imaging of the human brain. *Radiology* 201(3):637–648
- Pipe, J.G., Farthing, V.G., and Forbes, K.P. (2002) Multishot diffusion-weighted FSE using PROPELLER MRI. *Magn. Reson. Med.* 47(1):42–52
- Price, S.J., Burnet, N.G., Donovan, T., Green, H.A., Pena, A., Antoun, N.M., Pickard, J.D., Carpenter, T.A., and Gillard, J.H. (2003) Diffusion tensor imaging of brain tumours at 3T: a potential tool for assessing white matter tract invasion? *Clin. Radiol.* 58(6):455–462
- Provenzale, J.M., McGraw, P., Mhatre, P., Guo, A.C., and Delong, D. (2004) Peritumoral brain regions in gliomas and meningiomas: investigation with isotropic diffusion-weighted MR imaging and diffusion-tensor MR imaging. *Radiology* 232(2):451–460
- Sinha, S., Bastin, M.E., Whittle, I.R., and Wardlaw, J.M. (2002) Diffusion tensor MR imaging of high-grade cerebral gliomas. *AJNR Am. J. Neuroradiol.* 23(4):520–527
- Stadnik, T.W., Chaskis, C., Michotte, A., Shabana, W.M., van Rompaey, K., Luypaert, R., Budinsky, L., Jellus, V., and Osteaux, M. (2001) Diffusion-weighted MR imaging of intracerebral masses: comparison with conventional MR imaging and histologic findings. *AJNR Am. J. Neuroradiol.* 22(5):969–976
- Sundgren, P.C., Fan, X., Weybright, P., Welsh, R.C., Carlos, R.C., Petrou, M., McKeever, P.E., and Chenevert, T.L. (2006) Differentiation of recurrent brain tumor versus radiation injury using diffusion tensor imaging in patients with new contrast-enhancing lesions. *J. Magn. Reson. Imaging* 24(9):1131–1142
- Tropine, A., Vucurevic, G., Delani, P., Boor, S., Hopf, N., Bohl, J., and Stoeter, P. (2004) Contribution of diffusion tensor imaging to delineation of gliomas and glioblastomas. *J. Magn. Reson. Imaging* 20(6):905–912
- Turner, R., Le Bihan, D., Maier, J., Vavrek, R., Hedges, L.K., and Pekar, J. (1990) Echo-planar imaging of intravoxel incoherent motion. *Radiology* 177(2):407–414
- Witwer, B.P., Moftakhar, R., Hasan, K.M., Deshmukh, P., Haughton, V., Field, A., Arfanakis, K., Noyes, J., Moritz, C.H., Meyerand, M.E., Rowley, H.A., Alexander, A.L., and Badie, B. (2002) Diffusion-tensor imaging of white matter tracts in patients with cerebral neoplasm. *J. Neurosurg.* 97(3):568–575

# 14

## Brain Tumors: Planning and Monitoring Therapy with Positron Emission Tomography

D.J. Coope, K. Herholz, and P. Price

### INTRODUCTION

The term ‘brain tumor’ encompasses a broad spectrum of individual pathologies, affecting a heterogeneous patient population, with few clear etiological factors and widely varying prognostic implications. These tumors range from localized, potentially curable, benign lesions in childhood to rapidly progressive malignant disease with an increasing prevalence in an ageing population. Most primary brain tumors in adults are inherently infiltrating lesions, giving rise to progressive symptoms for the patient and adding to the difficulty of treating the condition without imposing permanent neurological deficits. Despite improvements in diagnostic techniques and potential therapies, outcomes for these patients have not improved substantially over recent years. In fact, the average “years of life lost” by a patient with a tumor of the central nervous system was more than that for any other cancer in one recent review (Burnet et al. 2005). This highlights the need to optimize current management as well as the necessity for further research and development.

Imaging of brain tumors provides challenges in terms of accurately delineating

the lesion and in attempting to maximize the prognostic information which can be derived from the scan data. These details are key to guiding further treatment and accurately informing the patient of their likely outcome. Making decisions as to whether the patient is likely to benefit from attempted surgical resection or whether they should be treated initially with radiotherapy or chemotherapy depend primarily upon the nature of the lesion and the extent to which it has infiltrated the surrounding brain tissue. High-grade primary brain tumors in particular are highly heterogeneous lesions and histopathological information derived from biopsies of the tumor may sample only a relatively small region. For patients with tumors in which only imaging-guided biopsies are practicable or desirable, and particularly in those for whom histological diagnosis is not possible, neuroimaging may present the only opportunity to derive diagnostic and prognostic information from the lesion as a whole. Tumors in pediatric patients present a particular problem with an increased proportion of mid-line and infra-tentorial lesions making surgery more challenging and the potential complications even more severe. Maximizing preoperative planning

is, therefore, of paramount importance in this patient group and positron emission tomography (PET) is likely to have a role to play.

## IMAGING BRAIN TUMORS WITH POSITRON EMISSION TOMOGRAPHY AND FDG

Positron emission tomography, incorporating a number of different radioisotope tracers, has been utilized at several stages in the management of brain tumors. As a molecular imaging technique, PET has the potential to add more data on the nature and behavior of a tumor than structural imaging techniques alone. Topics of ongoing interest include differentiating tumors of different grades by their metabolic characteristics and delineating tumor from normal brain by inherent characteristics such as increased amino acid uptake.

<sup>18</sup>F-fluoro-2-deoxyglucose (FDG) is the best established PET tracer and the compound most commonly used in current clinical PET applications. This imaging method has been applied to the study of physiological and pathological conditions affecting many organ systems, but the technique is based upon a model by Sokoloff et al. (1977) which was designed to measure cerebral glucose consumption. Fluorodeoxyglucose is taken up by normal brain tissue having been transported across the blood-brain barrier (BBB) by the same carrier protein as glucose. It is then phosphorylated by the enzyme hexokinase to <sup>18</sup>F-fluoro-2-deoxyglucose-6-phosphate at which point, unlike glucose-6-phosphate, it cannot be further metabolized and accumulates within the cell with only a small proportion being hydrolyzed back to FDG.

It is primarily this property of FDG that makes it an effective tracer for PET studies.

Brain tumors may show increased, equal or reduced levels of FDG uptake as compared to healthy brain tissue not least due to the high glucose consumption of normal grey matter. This lack of clear contrast between tumor and normal tissue has been a limiting factor for the use of FDG-PET in localizing brain tumors. The use of image coregistration may partially overcome this difficulty by allowing useful information to be extracted even in tumors with an FDG uptake very similar to that of the surrounding brain. Coregistration is the process by which the images produced from an investigation are reoriented to align them with another dataset which acts as a template. In the context of PET imaging of brain tumors, this usually refers to aligning a PET scan with a structural magnetic resonance (MR) scan so that both can be viewed together. This allows a structural abnormality visualized on the MR scan to be characterized with the corresponding PET uptake data even if the lesion cannot be readily identified on PET imaging alone. The same technique can also be used to combine the results of PET imaging with different tracers in the same individual or to overlay the results of activation studies onto the corresponding structural scans.

In gliomas, the most common primary brain tumors in adults, FDG uptake is greater in tumors of a higher histological grade. Semi-quantitative assessment of glucose metabolism can be calculated as a ratio of FDG uptake in tumor to contralateral cortex or white matter. Tumor metabolism exceeding 1.5-fold that of normal white matter (or 0.6-fold relative to normal grey matter) indicates a high-grade glioma.

This cut-off value has been shown to give 94% sensitivity and 77% specificity in gliomas (Delbeke et al. 1995). The prognostic value of this information in isolation, however, is limited by overlapping ranges of FDG uptake in tumors of different subtypes with similar radiological appearances. For example, oligodendrogliomas tend to show higher tumor metabolism than astrocytomas of the same grade. Thus, interpretation of FDG-PET is easier when the histological type is known, when the data can be interpreted in conjunction with other imaging modalities, or when assessing follow-up scans in a patient for whom a baseline scan exists.

The role of PET imaging with FDG in screening for metastases in general oncology is increasingly well established with most tumors being easily identified as hypermetabolic lesions. A number of common extracranial malignancies metastasize to the brain, making metastases the most common intra-cranial tumors in adults. Using PET as a screening tool in the brain, however, does not offer the same sensitivity as conventional imaging techniques. Metastases may be seen as regions of reduced or increased FDG uptake, depending upon the characteristics of the primary tumor, and may be difficult to differentiate from normal grey matter particularly in small tumors. The role of other PET tracers currently used for neuroimaging are not yet well established in metastatic disease. Most metastatic lesions retain the metabolic pathways of the primary tumor and as such may not take up tracers in the same way as primary brain tumors. Although perhaps precluding the use of a single tracer for all intracranial tumors, this may present an opportunity for development of tracers based upon metabolic pathways

that are uncommon in normal brain tissue to specifically identify metastatic tumors.

## AMINO ACID PET IN BRAIN TUMORS

Amino acid tracers have an advantage over FDG in that they may provide a higher tumor to normal brain ratio, facilitating more accurate delineation of tumor extent in primary brain tumors. However, the mechanism that connects tumorigenesis to the altered amino acid uptake demonstrated on imaging is incompletely understood, making interpretation of the images less straightforward. L-methyl-<sup>11</sup>C-methionine (MET) is the most widely used amino acid PET tracer in human brain tumors. In addition to PET studies, methionine with <sup>14</sup>C and <sup>3</sup>H radioisotope labels has been studied extensively in vitro and in animal studies, allowing for a more complete understanding of its uptake and metabolism within the brain.

Methionine is transported across the endothelial cells of cerebral capillaries by system L amino acid carrier proteins and its availability is an important factor for cellular function and proliferation. Tumor cell lines based upon common human cancers, including gliomas, have shown a particular sensitivity to restriction of dietary methionine which induces reduced proliferation rates and increases cellular vulnerability to cytotoxic agents (Poirson-Bichat et al. 2000). Disruption of the blood brain barrier, such as seen in cerebral ischemia, leads to a modest increase in local methionine uptake, but this is generally less than the rise seen in association with tumor tissue. The increased uptake of methionine seen in gliomas has

been demonstrated to reflect a functional increase in the system L transport system (Langen et al. 2000) but it does not correlate directly with rates of protein synthesis. The mechanism by which glioma cells influence the surrounding vasculature is not fully understood but it is likely to involve the altered expression of tyrosine kinase growth factors seen in these cells. Studies of tumor bearing rats have also demonstrated increased methionine uptake by viable cancer cells as compared to normal glial cells and other cellular components (Kubota et al. 1995). This specific cellular uptake in vitro correlates with cellular proliferation rates and may contribute to the image seen on MET-PET scans.

In vivo uptake of  $^{11}\text{C}$ -methionine on PET imaging has been shown to correlate with cellular proliferation (as determined by quantification of Ki-67 labelling index) (Chung et al. 2002) and to microvessel count (Kracht et al. 2003) in gliomas. Each of these are important prognostic factors and the identification of vascular proliferation may become increasingly valuable with the introduction of anti-angiogenic therapies. Methionine PET in clinical use has been demonstrated to be particularly valuable in delineating tumor extent. A threshold value can again be applied as a ratio of tumor to contra-lateral brain which gives a sensitivity of 76% and a specificity of 87% in distinguishing tumors from non-tumorous lesions (Herholz et al. 1998). Uptake is commonly increased in the metabolically active periphery of the tumor; areas of tumor infiltration may show even higher levels of methionine uptake than the tumor core itself (Kracht et al. 2004). This has the potential for use in planning both radiotherapy and surgical interventions, with very high sensitivity

and specificity, as discussed further in the next section.

Several groups have demonstrated the ability of MET-PET to distinguish between low and high-grade gliomas, with increased uptake in higher-grade lesions as is seen with FDG-PET. Correlation between tracer uptake and tumor grade in these scans is demonstrable but is far from perfect. This may reflect a weakness of the technique, but may also be contributed to by sampling error and inherent difficulties in histological differentiation of tumor grade; the current gold standard. It may be more useful to consider metabolic activity as quantified on PET imaging as an independent marker of tumor behavior rather than trying to fit the results obtained to a physiologically unrelated histopathological grading scheme.

Other amino acid tracers include O-(2-[ $^{18}\text{F}$ ]fluoroethyl)-L-tyrosine (FET) which is transported by the same carrier protein as methionine, although it is transported at a lower rate than alternately labelled amino acids. FET-PET demonstrates similar uptake to MET-PET in human brain tumors with data acquired over a longer period (Weber et al. 2000), but has the practical advantage of a longer half-life.  $^{18}\text{F}$ -fluorodopa also shows increased uptake in low-grade gliomas although its use around the basal ganglia is restricted by the high background dopa uptake in this region.  $^{18}\text{F}$ -fluorothymidine (FLT) has been developed as a marker of proliferative activity in extra-cranial tumors and exhibits better correlation with the Ki-67 index of proliferative activity in gliomas than FDG (Chen et al. 2005). It has been applied to staging for thoracic tumors where it has the advantage of good sensitivity in identifying brain metastases due

to the contrast between high uptake in the tumor versus very low uptake by healthy brain tissue.

## POSITRON EMISSION TOMOGRAPHY IMAGING IN LESS COMMON TUMOR TYPES

In addition to the substantial body of published research on the use of PET imaging in gliomas, FDG and MET-PET studies have been performed on several other intra-cranial tumors. Some of these results have been published as case reports which must be viewed with caution as there can be significant variability both between tumors of a given histological subtype and within an individual tumor. A number of larger case series have been published, typically from retrospective reviews, which are briefly outlined below.

Primary central nervous system lymphoma accounts for ~6% of intra-cranial neoplasms. However, the incidence is more than 3,000 times higher in patients with AIDS and, as a result of the increasing prevalence of HIV infection, the overall incidence has also increased in some populations. Fluorodeoxyglucose uptake in lymphomas is significantly increased over that for normal cortex (Roelcke and Leenders 1999). A valuable clinical application for FDG-PET in this patient group has been to the differentiation of lymphomas from non-neoplastic processes such as toxoplasmosis.

Primary brain tumors in children and young adults have also been characterized with PET imaging. These include ependymomas, which account for 6–12% of intracranial tumors in childhood and

which demonstrate low FDG uptake in accordance with their low-grade histology. Methionine uptake has been shown to be increased in a small series (O'Tuama et al. 1990) making it a potential tracer for delineating tumor extent. There are also case reports of the use of MET-PET in the imaging of spinal ependymomas where it was suggested to be useful in distinguishing between viable tumor and cystic areas (Sasajima et al. 1996). Medulloblastomas are invasive embryonal tumors that again present more commonly in children and young adults. These demonstrated very high FDG uptake, in a series of childhood posterior fossa tumors (Holthoff et al. 1993). Other primitive neuroectodermal tumors (PNETs) in the same series showed lower FDG uptake, but this was only a small sample of a histologically diverse group of tumors.

Neuronal and mixed neuronal-glial tumors include gangliocytomas, gangliogliomas, and central neurocytomas. These are typically low-grade tumors although gangliogliomas may have anaplastic or even rarely glioblastoma like changes amongst the glial component. Low-grade gangliogliomas show hypo- or isometabolism on FDG-PET and it seems likely that malignant progression will lead to an increase in FDG uptake in accordance with that seen in other high-grade glial tumors, although this has yet to be demonstrated in practice. Gangliogliomas may be difficult to differentiate from dysembryoplastic neuroepithelial tumors (DNETs) on conventional imaging but this distinction is significant. Both of these tumor types typically present with seizures but, as purely benign lesions, DNETs are amenable to curative surgical resection. Methionine PET has been demonstrated to have value



in this situation with lesions demonstrating increased methionine uptake being likely to represent gangliogliomas or low-grade gliomas rather than DNETs (Maehara et al. 2004).

Up to a quarter of intracranial tumors are made up of meningiomas which are neoplastic lesions of meningotheial cells that can show varying clinical characteristics depending on the histological subtype. This inconsistency, in addition to the variable vascularity of the tumors, may explain why some groups have found correlation between FDG uptake and proliferative rates in these tumors (Lippitz et al. 1996), whereas others have not (Iuchi et al. 1999). In terms of diagnosis of the tumor, the specific somatostatin analogue 1,4,7,10-tetraazacyclododecane-*N,N',N,N''*-tetraacetic-acid-D-Phe<sup>1</sup>-Tyr<sup>3</sup>-octreotide (DOTATOC) can be labelled with <sup>68</sup>gallium as a PET tracer which shows very low uptake in normal brain but high uptake in meningiomas (Henze et al. 2001). Other intracranial tumors include schwannomas which, as benign lesions of differentiated Schwann cells, show FDG uptake that is typically isointense to the surrounding tissue. Methionine uptake is sufficiently elevated to allow it to be used for the diagnosis of a proportion of acoustic neuromas although the sensitivity is poor at ~66% in one small series (Sakamoto et al. 2000).

These examples of different tumor types reflect the diversity of lesions that can be characterized with PET imaging. In most cases the trend towards higher uptake of FDG in higher-grade lesions is maintained although this cannot be assumed. A given FDG or amino acid uptake value for a space-occupying lesion may result from one of several different types of tumors

that display similar activity on PET imaging. Positron emission tomography therefore, may not be sufficient to provide a specific diagnosis when used in isolation. However, it is in the combination of the behavior of the tumor, as characterized by PET imaging, with findings on other imaging modalities and the clinical history that the most accurate diagnosis can be made prior to proceeding to a tissue diagnosis.

## DELINEATION OF TUMOR EXTENT FOR TREATMENT PLANNING

Following the initial diagnosis, accurately mapping the location, size and characteristics of a tumor is an important initial step in treatment planning. Primary brain tumors are heterogeneous lesions with several tumor compartments that differ with the nature and grade of the lesion. The core of the tumor is typically a hypercellular area in high-grade lesions which is highly metabolically active, and hence demonstrates high uptake of both FDG and amino acids. Conversely, low-grade gliomas may show only a slight increase in cell density, and amino acid uptake maybe less in the tumor core than in peripheral areas of tumor infiltration. Most gliomas demonstrate a zone of tumor infiltration which progresses preferentially along white matter tracts and which may be difficult to distinguish radiologically from peritumoral edema. Tumor cells can be found within the brain distant to the primary tumor, including spread to the contralateral hemisphere, although extracranial metastases of primary brain tumors are rare; medulloblastomas, anaplastic ependymomas and rarely glioblastoma multiforme

(GBM) may give rise to extracranial metastases as they progress. The pattern of invasion and progression in primary brain tumors is notably dissimilar to intracranial metastases, which typically have a reasonably well demarcated tumor margin with invasion along vascular structures and marked vasogenic edema.

The ability to accurately differentiate between tumor compartments is important in planning imaging guided interventions. Biopsy results provide the best prognostic information if they are obtained from the highest grade or “most malignant” area of the tumor. Both FDG and MET-PET scans have been incorporated into biopsy planning to optimize the selection of the region of interest to be sampled. Fluorodeoxyglucose PET scans were used to plan biopsies based on the principle that the area of tumor with the highest metabolic rate corresponds to the most malignant area. This has proven successful in increasing the proportion of diagnostic specimens obtained from stereotactic biopsies, but can be difficult to apply in low-grade tumors in which FDG uptake is typically low. As MET-PET shows higher sensitivity for tumor extent in low-grade tumors, it has been applied either in addition to FDG or in preference to it (Pirotte et al. 2004). When these two tracers are used together, the areas of maximal uptake correspond, suggesting that FDG usage to identify the most malignant area is not necessary if  $^{11}\text{C}$ -methionine is available.

The role for PET imaging in planning tumor resections is less clear than in biopsy planning, primarily because a consensus on surgical strategy is lacking even if optimal imaging can be provided. There are four broad aims to surgical intervention: to obtain a tissue diagnosis, to reduce

tumor load, to relieve mass effects, or to affect a cure. Noninvasive tumors such as pilocytic astrocytomas may be amenable to complete resection, but such lesions are rare in adults. The inherently infiltrative nature of most primary brain tumors would seem to make total cure by resection unlikely as tumor cells distant to the primary lesion will be missed. Possible advantages in operative strategies planned to reduce tumor load over simply obtaining a tissue diagnosis remain a subject for debate.

Incorporation of PET information into surgical planning has the potential to accurately identify and target the volume of active tumor, hence facilitating resection of the maximal volume of tumor. Unfortunately, the literature does not consistently show a survival advantage for patients who have undergone subtotal or near total resection over those who have had less extensive procedures. This may be due to patient selection in the case series presented, few of which are prospective, compounded by difficulties in comparing the extent of resection achieved between individual cases and between series (Keles et al. 2001). The proportion of the tumor resected during a surgical procedure has been typically determined by the impression of the operating surgeon in previous series. This is clearly difficult and depends heavily upon an estimation of the depth of any remaining tumor which may be impossible to measure directly. The use of early postoperative MR imaging has improved the objectivity of the assessment of tumor residual, but conventional imaging from this period remains difficult to interpret with tumor residual being potentially masked by changes resulting from the surgery itself. It may also be a

feature of the disease process that reducing tumor load does not slow progression in the tumor cells inevitably left behind and hence does not greatly impact upon survival.

Surgical procedures for the resection of brain tumors increasingly rely upon neuro-navigation techniques to aid in preoperative planning and to improve accuracy. This technology utilizes computerized tracking of surgical instruments which, after registration of the patient co-ordinates to the imaging data, allows for the location of an instrument in the operating room to be represented on the preoperative imaging. Methionine PET images have been integrated with MR scans and functional activation studies for use in multi-modal neuro-navigation techniques. Several steps exist in the technique at which errors can be introduced which limit its overall accuracy. Coregistration of PET and MR images followed by registration of this data to the patient co-ordinate system may introduce errors that can, to some extent, be ameliorated by technical improvements. There is also an inherent weakness of the technique which arises from shifts in the position of the brain in response to patient positioning, opening of the dura with drainage of CSF, brain retraction, and later edema. These effects can be minimized by an appropriate technique and the use of intraoperative imaging modalities, such as ultrasound or preferably MR, but cannot be completely removed. Despite this, studies have demonstrated the value of employing MET-PET data in delineating regions of viable tumor (Braun et al. 2002) which may allow the surgeon to be more selective in terms of targeting the tumor core. The results also suggest the possibility of identifying zones of tumor infiltration

which, although not an ideal surgical target, could then be specifically targeted by other treatment modalities such as radiotherapy (Figure 14.1).

The ability to identify tumor infiltration raises the question of whether resecting a brain which has been infiltrated by tumor, but which is nonetheless functionally active, will benefit the patient enough to compensate for any neurological deficit incurred. Minimizing residual tumor load may improve the likelihood of successful adjuvant therapy, but even with improved diagnostic imaging the likelihood of a microscopically complete resection of an infiltrating tumor is small. In this context, treatments that can be targeted to areas of infiltration without destroying functional tissue, such as radiotherapy, are more appropriate than surgery alone.

Planning procedures for radiotherapy have similar requirements for identification of tumor compartments and similar constraints on avoiding damage to surrounding structures as planning for interventional procedures. Radiotherapy is a routine part of the treatment of many intrinsic brain tumors and metastases, but the treatment regimens applied vary depending on the lesion and often upon the predicted life expectancy. In low-grade tumors with good life expectancy the potential complications of radiotherapy such as white matter lesions, cerebral atrophy, and radiation necrosis are limiting factors in the dose given and the amount of potentially normal tissue included in the radiotherapy field. For aggressive tumors, such as GBM, these complications, which typically have a significant delay in presentation from the time of treatment, may be a secondary concern to achieving maximal control of tumor progression. However, any

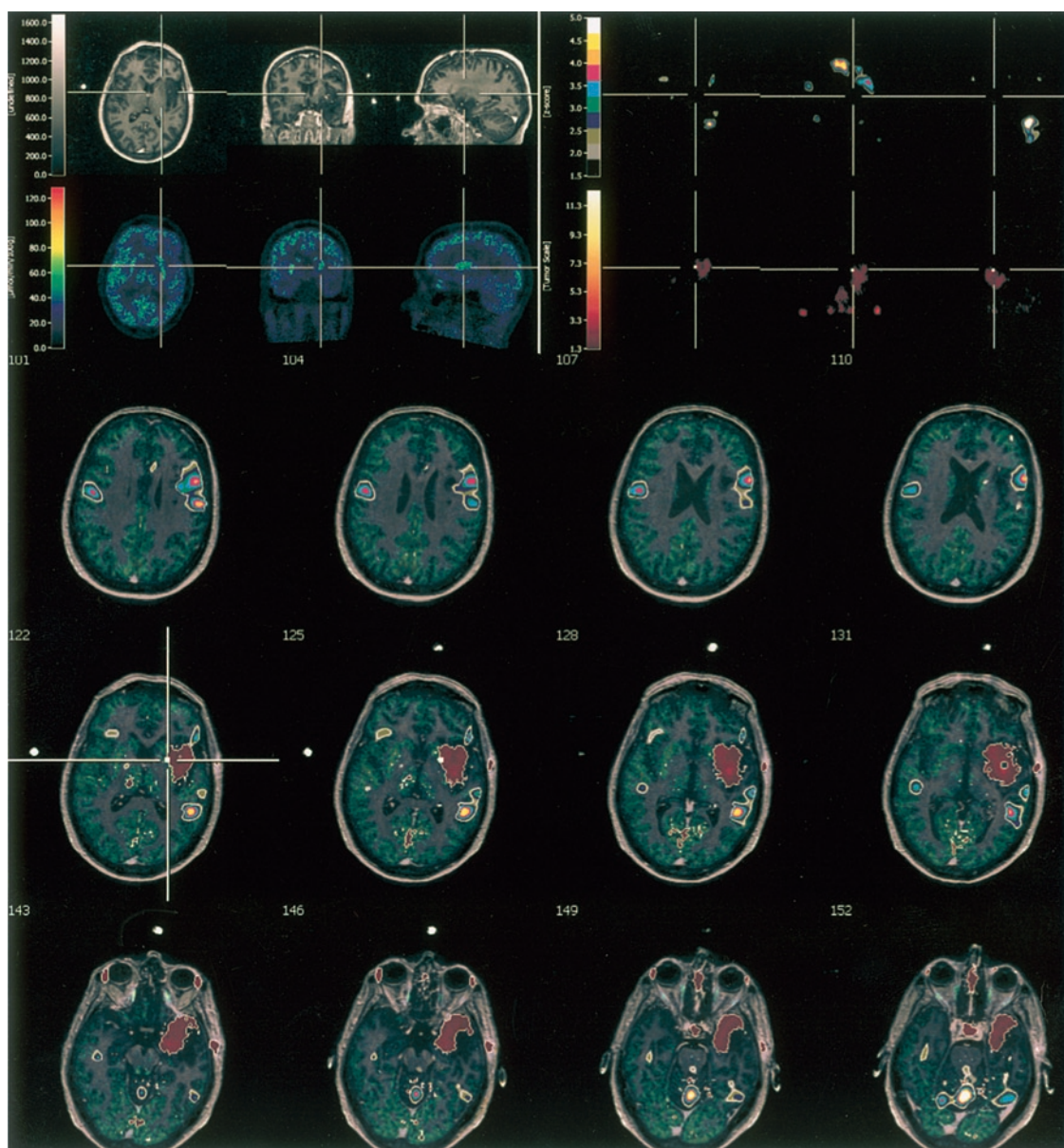


FIGURE 14.1. Multi-modal imaging of a low-grade glioma for surgical planning. A =  $T_1$  MRI; B =  $H_2^{15}$  O-PET activation study; C = FDG-PET; D = MET-PET with threshold set to display only high methionine uptake regions (including tumor); E = coregistered images of A–D (S. Vollmar, Max-Planck-Institute for Neurological Research, Cologne)

resultant loss of neurological or cognitive function will reduce the quality of life of the patient.

With current treatment strategies, recurrence of high-grade brain tumors is

inevitable, and in most, recurrence occurs within the field of previous radiotherapy. Attempts to improve outcome with higher radiation doses have met with mixed results. A recent analysis of outcomes in more

than 180 patients with high-grade gliomas revealed a significant improvement in 2-year survival rate and a median survival rate for patients who received conformal radiotherapy at 80–90y over those who received 60 Gy (Tanaka et al. 2005). These two groups, although well matched clinically, reflected changing practices at one unit over 23 years, and hence the improvements seen in the latter high-dose group may also reflect methodological improvements in radiotherapy planning and administration. The complications seen in this study occurred both more frequently and earlier in the high-dose radiotherapy group. This highlights the need for accurate diagnostic imaging to target therapy to those most likely to benefit from it.

Methionine PET has been used in radiotherapy planning to help refine the extent of the gross tumor volume (GTV, the extent of macroscopic tumor spread as delineated on planning neuroimaging), particularly in patients for whom this region is difficult to define on MR due to the presence of postoperative changes such as edema and necrosis. As the GTV will receive the maximum dose of radiation, it is vital that radiation is as accurate as possible to minimize central recurrence and to minimize the proportion of healthy brain exposed to the highest doses. Increased methionine uptake can be seen beyond the area of gadolinium enhancement and outside of areas of  $T_2$  hyperintensity on MR, suggesting the presence of a viable tumor mass not identified on MR. The area of increased methionine uptake may extend 25–45 mm beyond the core of gadolinium enhancement (Grosu et al. 2005), and as such, would be unlikely to be otherwise included in the planned volume of maximal radio-

therapy dose. Regions of enhancement on MR that did not show increased methionine uptake could similarly be identified, although the implication of this combination is less clear. Some areas will simply represent postoperative changes, but biopsies of peri-tumoral edema and necrosis have been frequently shown to contain viable tumor cells. This not only necessitates their inclusion in the radiotherapy target volume, but as regions with a high proportion of functional brain tissue; they could perhaps be spared from the highest doses applied to the tumor core. Multi-modal identification of tumor compartments with specific radiotherapy doses targeted to each may be the only effective way to maximize efficacy whilst minimizing side-effects. However, despite evidence of more precise targeting with incorporation of PET imaging, a survival advantage for the patient has yet to be demonstrated (Figure 14.2).

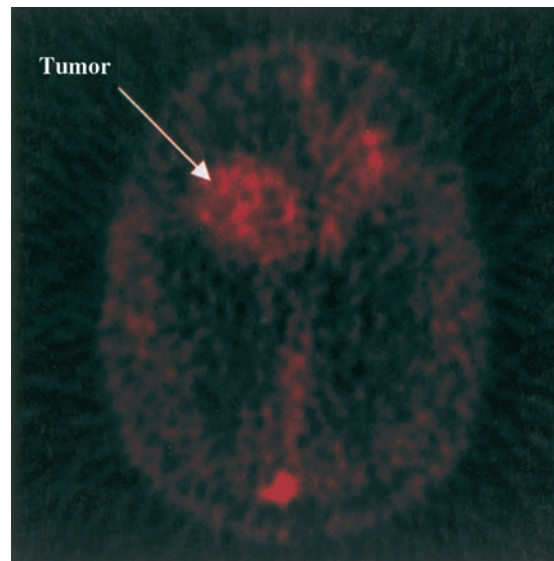


FIGURE 14.2. Increased uptake of <sup>11</sup>C labelled Temozolomide by tumor as compared to surrounding brain tissue (Saleem et al. 2003)

## MINIMIZING DAMAGE TO UNINVOLVED BRAIN STRUCTURES

Tumors that impinge upon “eloquent” areas of brain exacerbate difficulties in minimizing the sequelae to surgical interventions and radiotherapy. Low-grade gliomas in adults present a particular difficulty, as they preferentially arise from “secondary” functional areas, adjacent to the primary motor cortex or to regions of functional importance for speech production (Duffau and Capelle 2004). In children, infra-tentorial locations are more common and gliomas may arise in or adjacent to the brain stem. Patients suffering from these tumors typically present with seizures but many are neurologically intact and can reasonably expect a period of progression free survival without severe symptoms until the tumor progresses. Any intervention carries a risk of significant disability if these key structures are damaged. This may substantially reduce quality of life and may not lead to a significant improvement in overall survival.

Primary brain tumors may infiltrate healthy brain tissue leaving functional neuronal tissue within the volume of the tumor. Alternatively, the brain may exhibit plasticity in response to the functional deficit induced by the mass effect of the tumor, the reactionary immune response and any peritumoral edema. This may include the recruitment of neurons in neighboring anatomical locations with similar functional roles, recruitment of functionally related regions distant or contra-lateral to the tumor or even the recruitment of apparently functionally unrelated tissue to “take-over” the role of the involved area of brain. Rapidly progressing high-grade

tumors may infiltrate extensive areas of the brain which can still be demonstrated to be functionally important when attempts are made to resect the tumor (Ojemann et al. 1996). When planning diagnostic or therapeutic interventions, assumptions about the functional importance of a specific region of brain are often made based upon *a priori* knowledge of the functional organization of the brain. The varied responses in terms of functional reorganization that may be seen in the presence of a tumor highlight the hazards in such assumptions.

Two principle approaches exist to address the need to identify functionally important areas of brain with a view to predicting and preventing functional impairment as a result of interventions. The first of these approaches is preoperative coregistration of structural imaging with functional data in the form of functional MR imaging (fMRI), PET activation studies, electroencephalography (EEG), or magnetoencephalography (MEG). The second is neurophysiological mapping with preoperative transcranial magnetic stimulation (TMS) or intraoperative direct cortical stimulation or electrocorticography. Each of these techniques has both technical and practical advantages and disadvantages. Direct cortical mapping yields easy to interpret results with regions that elicit either a motor response or impairment of a desired function, which should be clearly protected during surgery. However, it may identify alternate pathways to those normally employed by the brain and the technique necessitates awake procedures that significantly increase the demands placed upon both the patient and the surgical team. It also cannot be applied to minimally invasive diagnostic procedures,

such as stereotactic biopsies, or for planning of radiotherapy or radiosurgery procedures. Navigated transcranial magnetic stimulation (nTMS) overcomes some of these shortfalls by extending the principles of cortical stimulation into a noninvasive technique. The motor cortex can be mapped using nTMS by recording neurophysiologically the response of individual muscles to transcranial stimulation of a cortical region. Whilst this recording is made, a neuro-navigation system is used to identify and record the region of cortex adjacent to the stimulating coil on an MR scan performed prior to the procedure (Krings et al. 2001). This technique is not currently widely available but is a safe, non-invasive alternative to the gold-standard of electrocorticography.

Noninvasive functional imaging allows incorporation of functional data into preoperative planning and may help to avoid unnecessarily extending the surgical procedure. It can be applied to radiotherapy and radiosurgery allowing key functional structures to be potentially excluded from planned fields of high radiation dose. Application of the results of functional neuroimaging is less straightforward than direct cortical mapping. These techniques attempt to record changes in the brain which temporally correlate with a specific activity or occur in response to a given stimulus. Recording the cortical activations that occur during an event may help to identify the pathways that are physiologically employed for that activity. Current techniques for imaging neuronal activation rely upon indirect measures of activity such as alterations in blood flow or local metabolic activity. This indirect measurement results in reductions of both temporal and spatial resolution as compared to

electrophysiological techniques. Examples exist of functionally important areas on preoperative imaging that were not confirmed on direct cortical stimulation and that were ultimately lesioned during the surgical procedure without the patient suffering from any overt deficits. This may be due to plasticity and redundancy within the neural network that is not apparent on activation studies or may reflect inaccuracies of the technique.

Functional MR imaging is more readily available and hence more widely used than other functional imaging modalities. It also currently has the largest evidence base for use in preoperative planning (Vlieger et al. 2004). Concerns have been raised with regard to the accuracy of the technique within and immediately adjacent to tumors, particularly with regards to gliomas. The BOLD (blood-oxygen-level-dependent) response on which the technique relies may be reduced in these areas as compared to contralateral tissue, possibly as a result of altered venous drainage or of deranged neuro-vascular coupling (Holodny et al. 2000). This may be of significance if it is to be applied to surgical planning although it has not been proven to be detrimental in clinical trials to date.

Positron emission tomography activation studies have been performed using  $H_2^{15}O$  which, as a metabolically inert freely diffusing tracer with a short half-life, can be used to measure regional cerebral blood flow with good spatial and temporal resolution. Accurate delineation of key motor areas has been shown in the presence of tumors, although as blood flow is measured, it may be influenced by the same neuro-vascular decoupling as is seen in fMRI. Delineation of language areas is technically more difficult than identifying the motor cortex

as the change in signal obtained is smaller. The short half-life of  $^{15}\text{O}$  labelled water (~2 min) allows for multiple stimulation paradigms to be performed in a single imaging session. With direct electrical cortical stimulation taken as the “gold standard”,  $\text{H}_2^{15}\text{O}$ -PET identifies cortical areas which produce speech disturbance when they are stimulated with 73% sensitivity and 81% specificity (Herholz et al. 1997).

FDG-PET activation studies can also be performed with simplified paradigms to allow for the reduced temporal resolution (20–30 min) achieved with the technique. The advantages of the technique are improved signal to noise ratio over fMRI or  $\text{H}_2^{15}\text{O}$ -PET and the ability to perform the activation paradigm before data acquisition commences, thus removing potential motion artefact (to which fMRI is particularly sensitive). Fluorodeoxyglucose motor activation studies in patients with tumors impinging upon the primary motor cortex have been shown to have 94% sensitivity and 95% specificity in identifying regions that evoke a corresponding motor response on electrical stimulation (Schreckenberger et al. 2001). Disadvantage of the technique mostly relate to the longer half-life of  $^{18}\text{F}$  which necessitates a gap of 2–4 h between resting and activation scans, thus allowing the activation seen in response to only a single task to be acquired in a session. This is partially compensated for by the metabolic data with regards to FDG uptake by the tumor that is obtained whilst the activation study is being performed.

Selection of the appropriate functional imaging modality for an individual patient is likely to depend heavily upon the circumstances unique to that case, as each technique has discrete advantages

and disadvantages. In terms of practical considerations, PET equipment is typically less noisy, less claustrophobic and less sensitive to motion artifact than fMRI which may have advantages for children or other patients with cognitive impairment resulting from their disease process. Functional MRI data, on the other hand, can be acquired at the same session as structural imaging, is typically a quicker overall process and avoids the small dose of radiation required for each PET scan. In addition to locating the cortical structures responsible for initiating a motor response or responding to a stimulus, identifying and protecting the tracts interconnecting these areas is essential to preserve function. Mapping of cortical tracts or “tractography” can be achieved using current clinical MR systems through diffusion tensor imaging (DTI). This technique can be combined with fMRI or PET activation data to aid with interpretation of the results, although this process may be more straightforward with fMRI data.

With current technology, it seems unlikely that any imaging modality will replace intraoperative cortical mapping for tumors involving “eloquent” areas of brain. Both PET and fMRI have a role in the preoperative planning of the surgical approach to be adopted and in highlighting the cortical areas that require intraoperative assessment of their functional status. It is likely to be through this combined approach, in addition to techniques such as tractography, that the safety of surgical procedures can be maximized. Perhaps of equal importance, PET data may be employed to isolate the group of patients for whom the risk of surgical intervention does not outweigh any potential benefits. This may require the combination of



activation studies to identify procedures with a high-risk of resulting in a functional deficit, with other PET data to characterize the nature of the tumor and the associated prognosis.

### MONITORING BRAIN TUMORS: WHEN IS THE BEST TIME TO INTERVENE?

The majority of low-grade tumors will progress over time and may infiltrate functionally important structures, making appropriate initial management of particular importance. Treating the lesion after it has progressed to involve other brain structures may be extremely difficult without causing irreparable damage. The side-effects of any potential treatment modality must also be considered, with the relevance of potential long-term complications depending upon the prognosis of the individual patient. Radiotherapy in particular carries a risk of significant side-effects which may occur several months or even years later, with cerebral necrosis being the most feared. Many of the factors involved in treatment planning relate back to making an accurate diagnosis, for which the benefits of PET have already been discussed. However, if the decision to delay initial treatment is made, monitoring of the tumor becomes of paramount importance to allow for timely intervention if there is evidence of progression. A similar situation exists after surgical resection of a tumor. Patients who fall into a good prognostic group may be spared the complications of immediate adjuvant therapy in favor of treatment on evidence of recurrence. The effective use of these delayed treatment strategies relies on effective

surveillance neuroimaging for which PET imaging is one useful modality.

The use of PET imaging in tumor surveillance has been limited, at least in part, by the combination of the need for repeated imaging of an individual, the cost, and the relative lack of availability of the technique. The design of clinical trials of disease surveillance with PET is also always constrained by concerns about the radiation doses involved in an application with unproven benefits. Fluorodeoxyglucose PET typically results in a whole-body equivalent radiation dose similar to that of a CT of the abdomen or pelvis. In terms of neuroimaging, this is significantly more than the radiation dose of a head CT, although the relevance of this in a patient population with a malignant disease process is less clear. The definition of tumor progression in brain tumors is not straightforward as it must incorporate an increase of tumor size, including infiltration of previously uninvolved tissue, and progression to a "more malignant" tumor type. As a functional imaging modality, PET has the capacity to image this change in the behavior of a tumor. Positron emission tomography is well suited to serial imaging of a tumor as prior knowledge of the tumor location maximizes the benefits of monitoring quantitative or semi-quantitative changes in tracer uptake in a specific region of interest. This also negates any difficulties in differentiating between tumor and normal brain for tracers such as FDG, although adequate sensitivity to identify new secondary lesions is a consideration for a potential surveillance modality.

Small studies of both FDG and methionine uptake in gliomas have shown increasing uptake in tumors that show evidence

of malignant progression at further surgery (Roelcke et al. 1999). This can be seen as changes within the volume of an individual tumor on serial imaging and could be used as an indication to initiate further treatment. Whether this would provide any improvement in survival has yet to be demonstrated but it may allow for treatment to be commenced before a tumor demonstrates a significant increase in volume on structural imaging. This would seem to be advantageous both in terms of maximizing the potential benefits from adjuvant therapies and from minimizing neurological impairment as a consequence of tumor expansion. Positron emission tomography performed on clinical or other radiological evidence of tumor progression has been used to specifically investigate the value of the technique in assessing disease progression. Similar elevation in the uptake of both methionine and FDG has been demonstrated in cases later proven to show histological progression. The rarity of longitudinal studies means that few of these patients would have had preoperative or postoperative PET imaging for comparison. However, the finding of high uptake in a patient with previous low-grade histology may be adequate to signify “malignant progression” of the tumor.

A particular difficulty in the surveillance of brain tumors is the differentiation between recurrent tumor and the sequelae of previous treatment. Radiation necrosis may occur months or even years after radiotherapy or radiosurgery and presents with symptoms such as seizures, focal neurological deficits, and features of raised intracranial pressure. These symptoms would be equally typical of tumor recurrence, with conventional imaging likely

to reveal an area of contrast enhancement and surrounding edema that may not help to distinguish between the two. Positron emission tomography has been used in this setting to identify possible recurrence of both primary and secondary brain tumors. Sensitivity of 75% and specificity of 81% has been suggested for FDG-PET in the diagnosis of tumor recurrence across a variety of tumor types within this group of patients (Chao et al. 2001). The sensitivity of the technique was also demonstrated to be further enhanced by coregistration of the images with MR data. Smaller studies with methionine uptake have shown similar or even better sensitivity but with increased uptake being less specific for tumor recurrence. The sensitivity of these investigations is of particular importance as patients with a negative result could potentially be spared further intervention. However, the evidence is presently lacking to justify not obtaining a histological diagnosis in a patient for whom there is a contrast MR scan that is suspicious of recurrence, even with a negative PET result, if there remains the possibility for further treatment.

## SELECTION OF TREATMENT MODALITIES

Comparison of the efficacy of different treatment regimens has proven difficult in brain tumors as different centers have substantially different approaches and uncertainties in preoperative diagnosis compound the difficulty in designing randomized trials. Positron emission tomography may have a role in predicting the response of a tumor to a specific treatment modality or chemotherapeutic agent. Methionine PET

imaging performed before and after radiotherapy in low-grade gliomas shows a larger drop in methionine uptake following radiotherapy in those patients who had higher uptake prior to treatment (Ribom et al. 2002). This variance may reflect differences in the radioresponsiveness of individual tumors but the clinical significance of the change seen on imaging has yet to be elucidated. Trials on low-grade gliomas have rarely been sub-divided as the small number of patients in any resulting groups risks further diluting the statistical significance of any results obtained. Patients with low methionine uptake form a potential sub-group with a better prognosis which can be identified by PET imaging. If it were to be demonstrated that this group also derived less benefit from radiotherapy, then there may be an argument to delay radiotherapy in this group, perhaps in favor of other adjuvant treatments to minimize the risk of long-term side-effects.

Chemotherapeutic agents show great potential for assessment with PET imaging as the drugs themselves and other compounds binding to the same targets can be radiolabelled for use as PET tracers. This has been used in drug development to further the understanding of the kinetics and metabolism of developmental compounds. It could also be applied clinically to monitor the uptake of a drug into a target area without the need, for example, of receptor profiling which requires a tissue specimen. A pertinent example of PET use in chemotherapy has been the application of PET methodologies to the study of the biodistribution and metabolism of Temozolomide in gliomas. Temozolomide is an alkylating agent which has been shown to provide a survival advantage in

glioblastomas and which shows promising results in other gliomas. A dual radiolabelling technique was applied to the study of the drug, with two different forms of the molecule being manufactured with  $^{11}\text{C}$  radiolabels substituted into different points on the molecule (Saleem et al. 2003). Comparative analysis of the tissue uptake of these markers and their loss into the blood as drug metabolites allowed the specific mechanism of action of Temozolomide to be modelled *in vivo*. The technique also allowed for the distribution of the drug within the tumor to be imaged, helping to confirm the potentially beneficial pharmacodynamic characteristics of the compound. This demonstrates the scope of the technique both in drug development and in the potential even for assessing the uptake and distribution of a compound within an individual tumor.

## ASSESSING RESPONSE TO TREATMENT AND PROGNOSIS

The initial response of a tumor to treatment may provide information on the success of the intervention, the sensitivity of the tumor and may refine the prognostic information available to the physician and the patient. This is a difficult period in which to obtain accurate diagnostic images as the effects of surgery or radiotherapy on disturbing the blood-brain barrier, inducing edema and activating cellular repair mechanisms make image interpretation more difficult. After surgical resection, assessment of the presence and volume of any tumor residual is a factor in considering the need for early adjuvant therapy. Contrast MR imaging in the first 48–72 h

postoperatively may give an indication of residual tumor volume, but this depends upon the patient being clinically fit to undergo the investigation in the early postoperative period. Beyond this time window it is very difficult to differentiate between residual tumor and postoperative changes on MR imaging alone.

If radiotherapy is to be considered, then not only must the presence of residual tumor be recognized but it must also be clearly delineated from the changes in and around the operative field to identify the target for radiotherapy planning. With its demonstrated sensitivity for identifying neoplastic tissue in the brain, MET-PET is a valuable imaging modality in this difficult group. Methionine uptake is only modestly increased in areas of blood-brain barrier breakdown as compared to the more marked increase in association with primary brain tumors and particularly with high-grade tumors. This allows areas of residual tumor to be more readily identified on MET-PET imaging and the technique has been applied effectively for radiotherapy planning in this patient group (Grosu et al. 2005). However, there will still be a small number of low-grade tumors with low methionine uptake that cannot be well visualized using MET-PET either preoperatively or postoperatively.

Assessing early response to radiotherapy suffers from similar difficulties to imaging after surgery, particularly due to edema induced by the treatment. Methionine PET has again been used, with reduced methionine uptake in the early post-radiotherapy period being associated with a better response to radiotherapy. In particular, a greater drop in uptake from initial diagnostic imaging to repeat imaging post-radiotherapy has been correlated with an

improved response to treatment. It is also advantageous to use MET-PET imaging in the post-treatment period, as this gives a baseline uptake value against which further PET imaging can be compared. A continued stable or decreasing level of methionine uptake during follow-up is a positive prognostic indicator for the patient in terms of both overall and disease free progression (Nuutinen et al. 2000).

FDG uptake following radiotherapy can add further prognostic information to that obtained with other modalities and tracers, although the pathophysiological mechanisms being imaged are less straightforward. For example, an increase in FDG uptake in PET imaging post-radiotherapy as compared to pretreatment is associated with improved outcome and longer survival in patients with high-grade gliomas (Spence et al. 2002). This effect has also been documented in intra-cerebral metastases and meningiomas. The reason for this rise in local metabolic activity is incompletely understood but is likely to result from a number of different processes. These may include the influx of metabolically active inflammatory cells, increased metabolic activity in surviving cells when the mass effect of the tumor is relieved and the cellular energy requirements of apoptosis.

Positron emission tomography studies can enhance the ability of the physician to assess the response of a tumor to a selected therapy early in the treatment course. This may provide the opportunity to alter the treatment plan in cases where the response is poor and an alternative treatment modality exists. There is also the possibility to add to the information available to the patient in terms of their likely prognosis which is important to both patients and carers.

Finally, uptake values during the initial response to treatment provide a baseline for further use of PET in follow-up and early identification of tumor progression as has previously been discussed in this chapter.

## THE FUTURE OF PET IMAGING IN BRAIN TUMORS

Future directions for PET imaging in brain tumors would seem to be split between extending the availability in clinical practice of existing PET techniques and introducing new tracers and methodologies to expand upon the clinical applications. In terms of technology, PET brain scanners in research units are already capable of 2 mm resolution which approaches the fundamental limit of the technique. Development of smaller, self-shielded cyclotrons and standard radio-chemical synthesis systems have allowed an increasing number of centers to produce and use tracers with short half-lives that cannot be transported between centers. This expansion would seem likely to continue although the cost of setting up a new unit remains extremely high. For the imaging of most primary brain tumors,  $^{11}\text{C}$ -methionine provides the best sensitivity and specificity of the currently available tracers although it belongs to the group of tracers that must be produced locally because of their short half-lives. The use of serial MET-PET for the diagnosis, monitoring and planning of treatment in brain tumors has thus far been limited but it has the potential for more extensive use in all of these situations. It is particularly useful in low-grade primary brain tumors which are difficult to distinguish from normal grey matter with other

techniques. An alternative for the future may be to develop further amino acid PET tracers labelled with radioisotopes with longer half-lives, making regionalized production and transport more practicable. As has been discussed,  $^{18}\text{F}$ -fluoroethyl-L-tyrosine and  $^{18}\text{F}$ -fluorodopa have already shown promising results. However, it would take time to reaccumulate the knowledge bank currently available for  $^{11}\text{C}$ -methionine with another tracer.

The expanding clinical use of image coregistration technology can partially overcome any lack of contrast between a tumor and the surrounding tissue by allowing a specific region of interest to be identified on structural imaging and then characterized on functional or molecular imaging. Current techniques have been demonstrated to be accurate and robust enough for clinical application with only modest requirements in terms of technology, time, and expertise. Methods for presenting the results of PET investigations to physicians and surgeons such that all of the information obtained is made available have scope for improvement in the future.

Development of new PET tracers presents wide-ranging opportunities to increase the usefulness of PET imaging in characterizing different physiological and disease processes. It is difficult to know which direction tracer development will take but recent areas of particular interest have included markers of tumor proliferation and of specific tumor processes. For example, FMAU (1-(2'-deoxy-2'-fluoro- $\beta$ -D-arabinofuranosyl)thymine) is a thymidine analogue which is incorporated into DNA and which can be labelled with  $^{11}\text{C}$  or  $^{18}\text{F}$  as a PET tracer. In a pilot study, FMAU showed low uptake in normal brain with increased uptake in intracerebral

metastases and recurrent gliomas (Sun et al. 2005). Interestingly, uptake was noted to be only slightly higher than that for normal brain in a metastasis which showed no evidence of progression in the subsequent year of follow-up. This suggests that the technique may have the capacity to distinguish actively proliferating tumor in the future.

Another example of a novel application of PET tracers is in the use of radiolabelled flumazenil to image  $\gamma$ -aminobutyric acid (GABA) type A-benzodiazepine receptors in dysembryoplastic neuroepithelial tumors (DNET). One peculiarity of this benign tumor is its propensity to act as an epileptogenic focus leading to seizures that are resistant to pharmaceutical treatment. Positron emission tomography reveals decreased flumazenil binding within the tumor which is presumed to represent a decrease in GABA<sub>A</sub>-benzodiazepine receptor density (Richardson et al. 2001). This may, at least in part, explain the tendency of these tumors to cause seizures and is an example of the use of PET to image the functional characteristics of a tumor. There is also value to this technique from the perspective of management of the tumor as characteristically low flumazenil uptake may help to confirm the MR diagnosis of DNET without the need for biopsy. In addition, imaging of altered GABA<sub>A</sub>-benzodiazepine receptor expression elsewhere in the brain may help to predict the likelihood of surgical resection improving seizure control.

The peripheral benzodiazepine binding site ligand PK11195 has been used in the study of inflammatory and neurodegenerative diseases. It can be labelled as a PET tracer with <sup>11</sup>C and shows relatively selective binding to activated microglia.

The role of this marker in neuro-oncology has yet to be fully elucidated but it provides an opportunity to image the innate response of the brain to the presence of a tumor. Changes in this response may provide evidence of tumor progression and infiltration before morphological changes become apparent on conventional imaging techniques.

Development of further tracers to demonstrate the presence or absence of targets for specific chemotherapeutic or immunological treatments also seems likely. Ultimately, it is this ability to develop tracers which are highly specific to the individual molecular characteristics of a tumor and to image them at good spatial resolutions that sets PET aside from other imaging modalities. The scope for further development would seem to be enormous although costs remain high, especially in terms of setting up new centers and developing new methodologies. Future developments may, therefore, be shaped as much by the political and financial climate as by the benefits and limitations of PET itself.

In conclusion, challenges remain in the diagnosis, treatment planning, and outcome monitoring of brain tumors that are peculiar to this group of diseases. Extensive research interest has begun to demonstrate the value of PET imaging in overcoming some of these problems but the introduction of these techniques into clinical practice has been restricted to specific centers. <sup>18</sup>F-fluorodeoxyglucose is likely to remain the most widely available PET tracer and despite being less suitable for screening techniques in the brain than elsewhere in the body it can provide highly useful information for characterizing brain tumors. On the other hand, amino acid tracers on the other hand are

ideally suited to imaging primary brain tumors, providing information on tumor infiltration and behavior that is difficult to obtain by any other means. Combining these techniques with current and future technologies for morphological imaging may be the best method to optimize the interventions presently available and to assess the effectiveness of novel therapies in an effort to improve the outlook for this group of patients.

## REFERENCES

- Braun, V., Dempf, S., Weller, R., Reske, S.N., Schachenmayr, W., and Richter, H.P. (2002) Cranial neuronavigation with direct integration of [11C] methionine positron emission tomography (PET) data – results of a pilot study in 32 surgical cases. *Acta Neurochir. (Wien)* 144:777–782
- Burnet, N.G., Jefferies, S.J., Benson, R.J., Hunt, D.P., and Treasure, F.P. (2005) Years of life lost (YLL) from cancer is an important measure of population burden – and should be considered when allocating research funds. *Br. J. Cancer* 92:241–245
- Chao, S.T., Suh, J.H., Raja, S., Lee, S.Y., and Barnett, G. (2001) The sensitivity and specificity of FDG PET in distinguishing recurrent brain tumor from radionecrosis in patients treated with stereotactic radiosurgery. *Int. J. Cancer* 96:191–197
- Chen, W., Cloughesy, T., Kamdar, N., Satyamurthy, N., Bergsneider, M., Liau, L., Mischel, P., Czernin, J., Phelps, M.E., and Silverman, D.H. (2005) Imaging proliferation in brain tumors with 18F-FLT PET: comparison with 18F-FDG. *J. Nucl. Med.* 46:945–952
- Chung, J.K., Kim, Y.K., Kim, S.K., Lee, Y.J., Paek, S., Yeo, J.S., Jeong, J.M., Lee, D.S., Jung, H.W., and Lee, M.C. (2002). Usefulness of 11C-methionine PET in the evaluation of brain lesions that are hypo- or isometabolic on 18F-FDG PET. *Eur. J. Nucl. Med. Mol. Imaging* 29:176–182
- Delbeke, D., Meyerowitz, C., Lapidus, R.L., Maciunas, R.J., Jennings, M.T., Moots, P.L., and Kessler, R.M. (1995) Optimal cutoff levels of F-18 fluorodeoxyglucose uptake in the differentiation of low-grade from high-grade brain tumors with PET. *Radiology* 195:47–52
- Duffau, H., and Capelle, L. (2004) Preferential brain locations of low-grade gliomas. *Cancer* 100:2622–2626
- Grosu, A.L., Weber, W.A., Riedel, E., Jeremic, B., Nieder, C., Franz, M., Gumprecht, H., Jaeger, R., Schwaiger, M., and Molls, M. (2005) L-(methyl-11C) methionine positron emission tomography for target delineation in resected high-grade gliomas before radiotherapy. *Int. J. Radiat. Oncol. Biol. Phys.* 63:64–74
- Henze, M., Schuhmacher, J., Hipp, P., Kowalski, J., Becker, D.W., Doll, J., Macke, H.R., Hofmann, M., Debus, J., and Haberkorn, U. (2001) PET imaging of somatostatin receptors using [68GA]DOTA-D-Phe1-Tyr3-octreotide: first results in patients with meningiomas. *J. Nucl. Med.* 42:1053–1056
- Herholz, K., Reulen, H.-J., von Stockhausen, H.-M., Thiel, A., Ilmberger, J., Kessler, J., Eisner, W., Yousry, T.A., and Heiss, W.D. (1997) Preoperative activation and intraoperative stimulation of language-related areas in patients with glioma. *Neurosurgery* 41:1253–1262
- Herholz, K., Holzer, T., Bauer, B., Schroder, R., Voges, J., Ernestus, R.I., Mendoza, G., Weber-Luxenburger, G., Lottgen, J., Thiel, A., Wienhard, K., and Heiss, W.D. (1998) 11C-methionine PET for differential diagnosis of low-grade gliomas. *Neurology* 50:1316–1322
- Holodny, A.I., Schulder, M., Liu, W.C., Wolko, J., Maldjian, J.A., and Kalnin, A.J. (2000) The effect of brain tumors on BOLD functional MR imaging activation in the adjacent motor cortex: implications for image-guided neurosurgery. *Am. J. Neurorad.* 21:1415–1422
- Holthoff, V.A., Herholz, K., Berthold, F., Widemann, B., Schroder, R., Neubauer, I., and Heiss, W.D. (1993) In vivo metabolism of childhood posterior fossa tumors and primitive neuroectodermal tumors before and after treatment. *Cancer* 72:1394–1403
- Iuchi, T., Iwadate, Y., Namba, H., Osato, K., Saeki, N., Yamaura, A., and Uchida, Y. (1999) Glucose and methionine uptake and proliferative activity in meningiomas. *Neurol. Res.* 21:640–644
- Keles, G.E., Lamborn, K.R., and Berger, M.S. (2001) Low-grade hemispheric gliomas in adults: a critical review of extent of resection as a factor influencing outcome. *J. Neurosurg.* 95:735–745

- Kracht, L.W., Friese, M., Herholz, K., Schroeder, R., Bauer, B., Jacobs, A., and Heiss, W.D. (2003) Methyl-[11C]-L-methionine uptake as measured by positron emission tomography correlates to microvessel density in patients with glioma. *Eur. J. Nucl. Med. Mol. Imaging* 30:868–873
- Kracht, L.W., Miletic, H., Busch, S., Jacobs, A.H., Voges, J., Hoevels, M., Klein, J.C., Herholz, K., and Heiss, W.-D. (2004) Delineation of brain tumor extent with [11C]L-methionine positron emission tomography: local comparison with stereotactic histopathology. *Clin. Cancer Res.* 10:7163–7170
- Krings, T., Foltys, H., Reinges, M.H., Kemeny, S., Rohde, V., Spetzger, U., Gilsbach, J.M., and Thron, A. (2001) Navigated transcranial magnetic stimulation for presurgical planning – correlation with functional MRI. *Minim. Invasive Neurosurg.* 44:234–239
- Kubota, R., Kubota, K., Yamada, S., Tada, M., Takahashi, T., Iwata, R., and Tamahashi, N. (1995) Methionine uptake by tumor tissue: a microautoradiographic comparison with FDG. *J. Nucl. Med.* 36:484–492
- Langen, K.J., Muhlensiepen, H., Holschbach, M., Hautzel, H., Jansen, P., and Coenen, H.H. (2000) Transport mechanisms of 3-[123I]iodo-alpha-methyl-L-tyrosine in a human glioma cell line: comparison with [3H]methyl-L-methionine. *J. Nucl. Med.* 41:1250–1255
- Lippitz, B., Cremerius, U., Mayfrank, L., Bertalanffy, H., Raoofi, R., Weis, J., Bocking, A., Bull, U., and Gilsbach, J.M. (1996) PET-study of intracranial meningiomas: correlation with histopathology, cellularity and proliferation rate. *Acta Neurochir. Suppl.* 65:108–111
- Maehara, T., Nariai, T., Arai, N., Kawai, K., Shimizu, H., Ishii, K., Ishiwata, K., and Ohno, K. (2004) Usefulness of [11C]methionine PET in the diagnosis of dysembryoplastic neuroepithelial tumor with temporal lobe epilepsy. *Epilepsia* 45:41–45
- Nuutinen, J., Sonninen, P., Lehtikoinen, P., Sutinen, E., Valavaara, R., Eronen, E., Norrgard, S., Kulmala, J., Teras, M., and Minn, H. (2000) Radiotherapy treatment planning and long-term follow-up with [11C]methionine PET in patients with low-grade astrocytoma. *Int. J. Radiat. Oncol. Biol. Phys.* 48:43–52
- Ojemann JG, Miller JW, and Silbergeld DL (1996) Preserved function in brain invaded by tumor. *Neurosurgery* 39:253–258
- O’Tuama, L.A., Phillips, P.C., Strauss, L.C., Carson, B.C., Uno, Y., Smith, Q.R., Dannals, R.F., Wilson, A.A., Ravert, H.T., Loats, S., Loats, H.A., LaFrance, N.D., and Wagner, H.N. Jr. (1990) Two-phase [11C]L-methionine PET in childhood brain tumors. *Pediatr. Neurol.* 6:163–170
- Pirotte, B., Goldman, S., Massager, N., David, P., Wikler, D., Vandesteene, A., Salmon, I., Brotchi, J., and Levivier, M. (2004) Comparison of 18F-FDG and 11C-methionine for PET-guided stereotactic brain biopsy of gliomas. *J. Nucl. Med.* 45:1293–1298
- Poirson-Bichat, F., Goncalves, R.A., Miccoli, L., Dutrillaux, B., and Poupon, M.F. (2000) Methionine depletion enhances the antitumoral efficacy of cytotoxic agents in drug-resistant human tumor xenografts. *Clin. Cancer Res.* 6:643–653
- Ribom, D., Engler, H., Blomquist, E., and Smits, A. (2002) Potential significance of [11C]-methionine PET as a marker for the radiosensitivity of low-grade gliomas. *Eur. J. Nucl. Med. Mol. Imaging* 29:632–640
- Richardson, M.P., Hammers, A., Brooks, D.J., and Duncan, J.S. (2001) Benzodiazepine-GABA(A) receptor binding is very low in dysembryoplastic neuroepithelial tumor: a PET study. *Epilepsia* 42:1327–1334
- Roelcke, U., and Leenders, K.L. (1999) Positron emission tomography in patients with primary CNS lymphomas. *J. Neurooncol.* 43:231–236
- Roelcke, U., von Ammon, K., Hausmann, O., Kaech, D.L., Vanloffeld, W., Landolt, H., Rem, J.A., Gratzl, O., Radu, E.W., and Leenders, K.L. (1999) Operated low grade astrocytomas: a long term PET study on the effect of radiotherapy. *J. Neurol. Neurosurg. Psychiatry* 66:644–647
- Sakamoto, H., Nakai, Y., Matsuda, M., Ohashi, Y., Tsuyuguchi, N., Kawabe, J., Okamura, T., and Ochi, H. (2000) Positron emission tomographic imaging of acoustic neuromas. *Acta Otolaryngol. Suppl.* 542:18–21
- Saleem, A., Brown, G.D., Brady, F., Aboagye, E.O., Osman, S., Luthra, S.K., Ranicar, A.S., Brock, C.S., Stevens, M.F., Newlands, E., Jones, T., and Price, P. (2003) Metabolic activation of temozolomide measured in vivo using positron emission tomography. *Cancer Res.* 63:2409–2415
- Sasajima, T., Mineura, K., Itoh, Y., Kowada, M., Hatazawa, J., Ogawa, T., and Uemura, K. (1996) Spinal cord ependymoma: a positron



- emission tomographic study with (11C-methyl)-L-methionine. *Neuroradiology* 38:53–55
- Schreckenberger, M., Spetzger, U., Sabri, O., Meyer, P.T., Zeggel, T., Zimny, M., Gilsbach, J., and Buell, U. (2001) Localisation of motor areas in brain tumor patients: a comparison of preoperative [18F]FDG-PET and intraoperative cortical electrostimulation. *Eur. J. Nucl. Med.* 28:1394–1403
- Sokoloff, L., Reivich, M., Kennedy, C., Des Rosiers, M.H., Patlak, C.S., Pettigrew, K.D., Sakurada, O., and Shinohara, M. (1977) The [14C]deoxyglucose method for the measurement of local cerebral glucose utilization: theory, procedure, and normal values in the conscious and anesthetized albino rat. *J. Neurochem.* 28:897–916
- Spence, A.M., Muzi, M., Graham, M.M., O'Sullivan, F., Link, J.M., Lewellen, T.K., Lewellen, B., Freeman, S.D., Mankoff, D.A., Eary, J.F., and Krohn, K.A. (2002) 2-[(18F)Fluoro-2-deoxyglucose and glucose uptake in malignant gliomas before and after radiotherapy: correlation with outcome. *Clin. Cancer Res.* 8:971–979
- Sun, H., Sloan, A., Mangner, T.J., Vaishampayan, U., Muzik, O., Collins, J.M., Douglas, K., and Shields, A.F. (2005) Imaging DNA synthesis with [18F]FMAU and positron emission tomography in patients with cancer. *Eur. J. Nucl. Med. Mol. Imaging* 32:15–22
- Tanaka, M., Ino, Y., Nakagawa, K., Tago, M., and Todo, T. (2005) High-dose conformal radiotherapy for supratentorial malignant glioma: a historical comparison. *Lancet Oncol.* 6:953–960
- Vlietger, E.J., Majoie, C.B., Leenstra, S., and Den Heeten, G.J. (2004) Functional magnetic resonance imaging for neurosurgical planning in neurooncology. *Eur. Radiol.* 14:1143–1153
- Weber, W.A., Wester, H.J., Grosu, A.L., Herz, M., Dzewas, B., Feldmann, H.J., Molls, M., Stocklin, G., and Schwaiger, M. (2000) O-(2-[18F]fluoroethyl)-L-tyrosine and L-[methyl-11C]methionine uptake in brain tumors: initial results of a comparative study. *Eur. J. Nucl. Med.* 27:542–549

# 15

## Clinical Evaluation of Primary Brain Tumor: O-(2-[<sup>18</sup>F]Fluorethyl)-L-Tyrosine Positron Emission Tomography

Matthias Weckesser and Karl-Josef Langen

### INTRODUCTION

Positron emission tomography (PET) has been used for more than 2 decades for the diagnostic evaluation of patients with brain tumors. The workhorse of PET, radiolabelled deoxyglucose (FDG), suffers limitations in the evaluation of brain tumors due to the high metabolic activity of normal gray matter. A brain tumor with a metabolic activity at the level of cortical glucose consumption or even slightly lower is suggestive of high grade malignancy. Positron emission tomography with FDG has therefore a limited role in the diagnosis and delineation of brain tumors (Figure 15.1). Radiolabeled amino acids have an established role in the diagnosis of brain tumors (Jager et al. 2001). The most common technique is PET using [<sup>11</sup>C] methionine (MET). As a natural amino acid, MET is taken up in neoplastic cells by specific amino acid transporters. It has been shown, that amino acid transport is upregulated in glioma cells. The tracer is also used for protein synthesis. This metabolic step, however, is not predominant for the accumulation of MET. For the majority of amino acids used for brain tumor imaging until now, the upregulation of amino

acid transporters in neoplastic cells is the key step of tracer accumulation. The distribution of MET has been shown to reflect tumor spread more accurately than morphological imaging techniques. Tumor to brain contrast of MET uptake is generally higher in grade III/IV gliomas than in low grade gliomas but a reliable prediction of tumor grade in individual cases is not possible. Positron emission tomography with MET has also been shown useful in monitoring of low grade gliomas. The labeling with short lived <sup>11</sup>C (half-life 20 min) is a major drawback of MET and precludes distribution of the tracer to PET centers without on site cyclotron.

Recently, O-(2-[<sup>18</sup>F]fluorethyl)-L-tyrosine (FET) has been introduced for the diagnosis of brain tumors (Wester et al. 1999; Hamacher and Coenen 2002). This agent has been shown to exhibit a similar pattern and intensity of accumulation as MET (Heiss et al. 1999; Weber et al. 2000). Experiments in animals and cell cultures have demonstrated that FET enters the cell by specific amino acid transport mechanisms but is not incorporated into proteins (Heiss et al. 1999; Langen et al. 2003). Owing to a slow blood clearance and to relatively stable tumor contrast, static

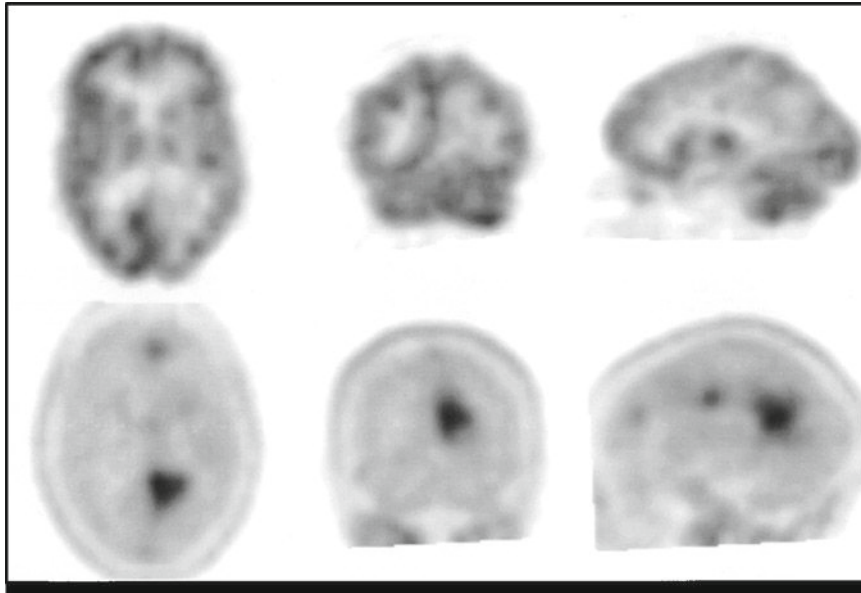


FIGURE 15.1. Comparison of glucose metabolism as measured by FDG-PET (*upper row*) and uptake of the amino acid FET (*lower row*) in a 72 year old female patient with glioblastoma. Apparent defect of FDG uptake e.g., in the left occipital cortex, but metabolic activity is higher than white matter activity. The distribution of FET clearly delineates the tumor and shows tumor growth along the corpus callosum, which is typical of glioblastoma (*left: axial slices, middle: coronal slices, right: sagittal slices*)

images from 20 to 40 min after injection have been recommended (Weber et al. 2000). The aim of the present overview is to describe the accumulation pattern and dynamics of FET in primary brain tumors, mainly in astrocytic gliomas, and to provide recommendations for image acquisition and interpretation.

### INTENSITY AND DYNAMICS OF O-(2-[<sup>18</sup>F]FLUORETHYL)- L-TYROSINE-UP TAKE

A comparative study on patients with brain tumors in whom both FET-PET and MET-PET was done first to describe uptake kinetics of FET (Weber et al. 2000). The study reports on imaging results in

16 patients. Three patients had radiation necrosis or postoperative changes. The 13 tumors formed a heterogeneous group of primary and recurrent parenchymal brain tumors and metastases. Overall the authors reported that FET uptake in tumors increased rapidly within the first 10 min and was more or less constant thereafter. Tumor to nontumor contrast as expressed by the ratio of tumor uptake versus normal brain uptake also showed a rapid increase within the first 10 min and slightly decreased thereafter. Because this heterogeneous group contained only one low grade tumor, a subgroup analysis was not performed. The main finding of this study was that MET and FET yield comparable results in terms of the intensity of tumor uptake with a correlation coefficient of 0.94. As a

consequence of the kinetic data, the authors recommended static imaging from 20 to 40 min after injection as imaging protocol for FET-PET. Recently, we analyzed FET uptake kinetics, in a series of primary brain lesions (Weckesser et al. 2005). Positron emission tomography data of FET uptake were analyzed in 44 patients with suspected brain tumors. Morphological imaging, mostly with magnetic resonance tomography (MRI), had previously been performed and had been suggestive of a brain tumor. Final diagnoses were high grade (WHO III° or IV°) brain tumors in 19 patients, low grade (WHO I° or II°) tumors in six patients, four lesions had a proven nonneoplastic origin, three patients had cerebral lymphomas three patients had other lesions and no final diagnosis was available in nine patients (probably a group with a high proportion of low grade gliomas or nonneoplastic lesions). Positron emission tomography was performed after overnight fasting. The injected dose was 2.5 MBq FET/kg bodyweight. Scanning was done in four consecutive 10 min frames, starting with injection. Each frame was reconstructed separately. In addition, raw data of frames 2–4 were added and were also reconstructed. These images were used for visual analysis. For the region of interest analysis, a polygonal reference region was drawn on normal brain tissue. A transaxial slice at the level of the semi-oval center was used for that purpose. The region comprised the contralateral hemisphere or, in case of midline tumors, the unaffected anterior or posterior half of the brain. Venous structures, which were clearly defined in the first frame, were not included. Next, the transaxial slice showing the highest tumor intensity was chosen

and an isocontour region around the tumor maximum was drawn using a cut-off three standard deviations above average activity in the reference region. Since mean and maximal uptake values were strongly correlated, only maximal uptake was used to calculate tumor to nontumor ratios ( $FET_{max}$ ). Blood activity within the venous sinus was also measured.

Mean FET uptake in the reference region increased by 21% from frame 1 to frame 2 and by 31% from frame 1 to frame 4. Maximal activity in the sinus decreased by 26% from frame 1 to frame 2 and by 37% from frame 1 to frame 4. Maximal activity in all visible lesions increased by 18% from frame 1 to frame 2 and was nearly constant thereafter (14% higher in frame 4 than in frame 1). O-(2-[<sup>18</sup>F]fluorethyl)-L-tyrosine uptake above cortical level was observed in 35/44 lesions. All histologically confirmed gliomas and all other malignant primary tumors showed increased FET uptake. When splitting the tumors in low (i.e., WHO I° and II°) and high grade tumors (i.e., WHO III° and IV°) a significant decrease of  $FET_{max}$  occurred in high grade lesions ( $3.2 \pm 0.9$  in frame 1 and  $2.7 \pm 0.8$  in frame 4), whereas an increase in  $FET_{max}$  over time was found in low grade tumors ( $2.0 \pm 1.3$  in frame 1 and  $2.4 \pm 1.4$  in frame 4).

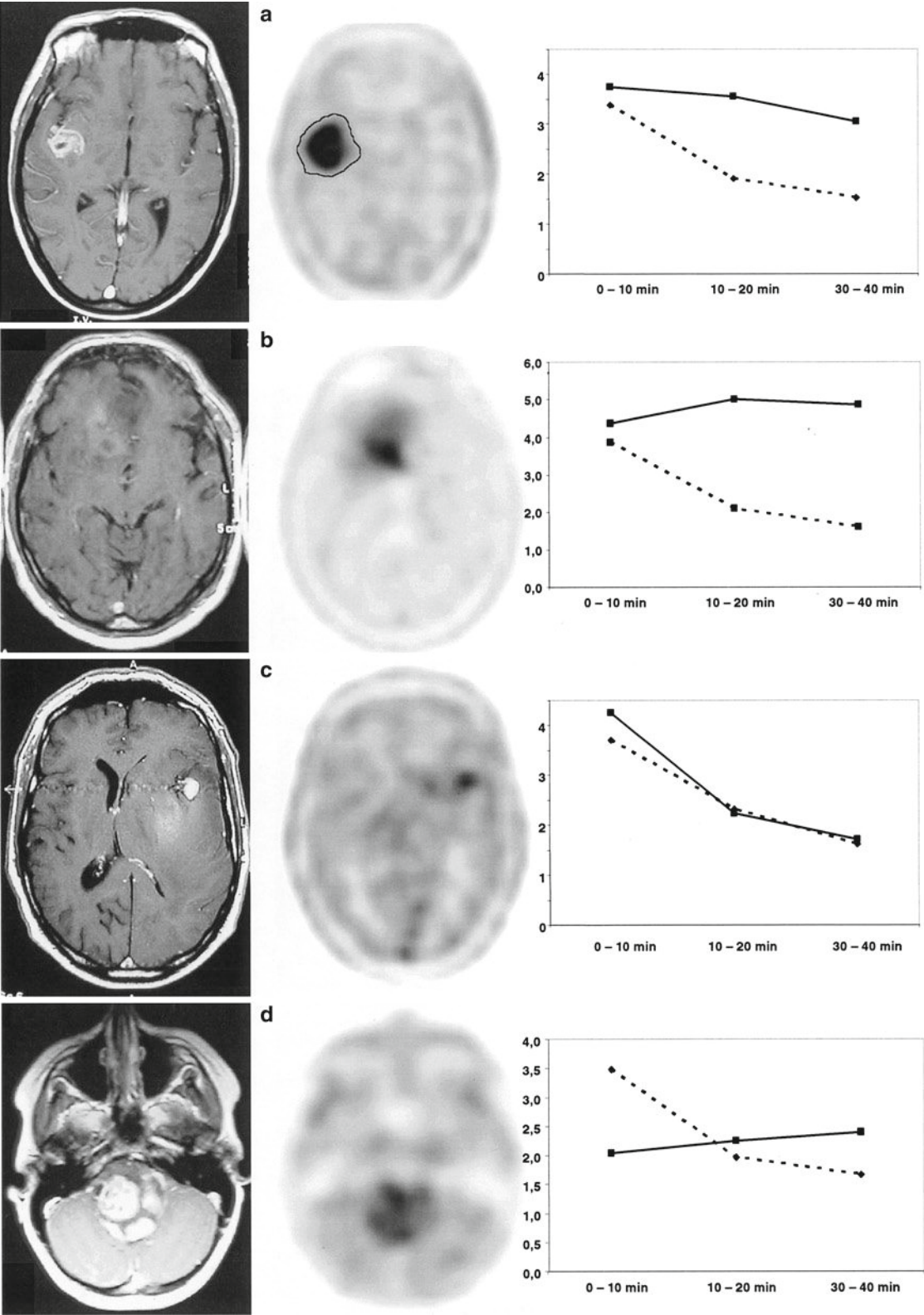
Figure 15.2 shows examples of different uptake patterns. Comparing high and low grade tumors, significant differences of  $FET_{max}$  were found in frame 1 ( $2.0 \pm 1.3$  in low grade tumors vs.  $3.2 \pm 0.9$  in high grade tumors;  $p < 0.05$ ) but not in frame 2 or 4. Restricting the analysis to tumors of astrocytic origin resulted in the same pattern. This observation indicates that there are differences in uptake kinetics depending

on the degree of malignancy. As a next step, the accuracy of FET uptake kinetics for tumor grading was assessed by calculating a retention index. A ratio of FET uptake in frame 4 to that in frame 1 was calculated for this purpose. This ratio was significantly higher in low grade tumors than in high grade tumors (ratio  $1.5 \pm 0.3$  in low grade and  $1.1 \pm 0.2$  in high grade tumors,  $p < 0.01$ ). This parameter resulted in a reasonable separation of high and low grade tumors. In astrocytic gliomas, only 3/16 high grade tumors had ratios above 1.33, whereas 4/5 low grade tumors surpassed this threshold. On ROC-analysis of grading astrocytic tumors, this ratio resulted in the largest area under the curve (0.9, 95% confidence interval: 0.76–1.0). Although grading was correct in 17/21 patients with astrocytic gliomas, the resulting accuracy is certainly not sufficient to replace histological confirmation. Furthermore, evaluation of contrast enhancement on MRI or CT was slightly superior in differentiating high and low grade astrocytomas (correct in 18/21 patients). Presence and kinetics of FET uptake however may aid to make clinical decisions in cases where no histological confirmation can be achieved.

The nonneoplastic lesions showed variable patterns. The aneurysm had a high

uptake in frame 1 ( $FET_{max}$  4.3) and showed a decrease to 2.2 and 1.7 in frames 2 and 4, respectively. Thus, activity was nearly identical to blood pool activity in the sinus of the same patient (sinus activity 3.7, 2.3, and 1.6 in frames 1, 2, and 4, respectively). Blood pool activity was therefore correctly identified (Figure 15.2c). Although a washout of activity was an indicator of malignancy, none of the neoplastic lesions of that series exhibited a comparable pattern. The diagnosis of an aneurysm could thus be confirmed by dynamic FET PET. Therefore a comparison of blood pool activity and tumor activity is mandatory to correctly identify blood pool activity. Meanwhile we have observed one case of a choroid papilloma, a tumor originating of the vascular structures of the choroid plexus, which showed a similar kinetic behavior. The patient with a hemorrhage had a constant moderate uptake ( $FET_{max}$  1.4, 1.5, and 1.5 in frame 1, 2, and 4, respectively). This patient was studied to assess a possible neoplastic origin of an acute hemorrhage. The uptake pattern might have falsely been interpreted as suggestive of low grade glioma, although these tumors do not tend to cause hemorrhage. The patient with an encephalitis showed considerable uptake ( $FET_{max}$  2.1, 2.0, 1.9 in frame 1, 2, and 4 respectively).

FIGURE 15.2. Examples of FET kinetics. *Left*: contrast enhanced T1 weighted MRI, *middle*: FET uptake from 10 to 40 min p.i., *right*: graph of  $FET_{max}$  in frame 1, 2, and 4. The corresponding blood/brain ratios of the same patients are shown as dotted lines. Glioblastoma: high uptake but decreasing  $FET_{max}$  over time, note the more pronounced decrease in blood activity (a); astrocytoma WHO II°: increasing  $FET_{max}$  over time (the tumor was not contrast enhanced, hyperintense regions were also present on nonenhanced images) (b); atypical giant aneurysm: initially high uptake decreasing parallel to venous blood activity. The summed image was suggestive of a neoplastic lesion, a correct diagnosis was obtained because the washout was considered atypical of a neoplasm (c); pilocytic astrocytoma WHO I° (patient 1): increasing uptake in a strongly contrast enhanced tumor (d) (From Weckesser et al. (2005). With kind permission of Springer Science and Business Media)



In the clinical setting, encephalitis was favored as diagnosis even before histological confirmation, both because of signs and symptoms of the patient and because the uptake area was strictly limited to the cortex. Nevertheless, a biopsy was taken to rule out diffuse gliomatosis. The negative cases comprised one teratoma, a benign tumor and one dysembryoplastic neuroepithelial tumor (DNT) WHO I°. One case of acute disseminated encephalomyelitis (ADEM) was negative as well. These inflammatory demyelinating lesions may mimic tumors on MRI. Meanwhile we have observed another patient with a lesion resulting from multiple sclerosis (MS), which showed a heterogeneous contrast enhancement on MRI. In that patient FET was completely negative as well, indicating that FET may serve as a tool to exclude a tumor in MS patients. In a recent series, however, a case of demyelination has been described with increased FET uptake (Floeth et al. 2006). In six negative cases no histological confirmation was obtained. These patients are likely to have either scars or low grade gliomas.

Blood activity was higher than average brain activity throughout the 40 min protocol with values decreasing over time (ratio of maximal blood to average brain activity  $3.3 \pm 0.6$  in frame 1,  $2.0 \pm 0.3$  in frame 2,  $1.6 \pm 0.2$  in frame 4). An advantage of dynamic acquisition is the delineation of the venous system on the early scan. Since blood activity is above mean brain activity even after 40 min, demarcation of tumors, which are situated adjacent to the sinus, may be facilitated when the distribution on early and late frames is taken into account. This advantage was particularly evident in the atypical giant aneurysm in the present series as discussed above.

## CORRELATION OF O-(2-[<sup>18</sup>F]FLUORETHYL)- L-TYROSINE-UP TAKE WITH MORPHOLOGICAL IMAGING

In the series of patients described so far, 15 tumors did not show any contrast enhancement (CE) on MRI and/or CT. Within this group, six patients showed no FET uptake (four with unknown histology, one DNT, one ADEM), whereas nine lesions showed constant uptake of FET ( $FET_{max} \sim 2.0$ ). Thus, a leakage of the blood brain barrier is not a prerequisite for increased FET uptake. This observation is in line with the results in other amino acids, which delineate viable tumor tissue regardless of disturbances of the blood brain barrier. All lesions with CE showed considerable FET uptake with  $FET_{max} \sim 3$ . There was no difference of FET uptake in patients with minor CE and major CE but there was a significant decrease of the tumor to brain ratio in contrast enhanced lesions ( $FET_{max}$  3.2 in frame 1 and 2.7 in frame 4).

Previous investigations suggest that FET passes the blood brain barrier mainly by facilitated transport via amino acid transport system L (Heiss et al. 1999; Langen et al. 2003). System L is a bidirectional transport system but there is little back diffusion of FET from normal brain tissue indicating trapping of the tracer or asymmetrical transport. Since FET is not incorporated into proteins, the mechanism of FET retention is probably caused by transport phenomena. High grade tumors are usually characterized by a break-down of the blood brain barrier as demonstrated by increased uptake of contrast media in the corresponding CT or

MRI scans. The disrupted blood brain barrier may allow an easier back diffusion especially of unbound tracer which may lead to a faster decrease of tracer concentration in the corresponding area when the tracer concentration in the plasma decreases. This hypothesis may explain the observation that a significant decrease of  $FET_{max}$  over time was observed in the group of tumors, which exhibited contrast enhancement in MRI and CT but not in those without leakage of the blood brain barrier. Nevertheless, exceptions from this pattern were found. Some contrast enhancing tumors showed increasing  $FET_{max}$  and some nonenhancing tumors exhibited decreasing  $FET_{max}$ . Thus, a disruption of the BBB may contribute to the observed phenomenon of decreasing  $FET_{max}$  but appears not to be its exclusive explanation.

Solitary ring enhanced brain lesions on CT or MRI may represent neoplastic and nonneoplastic conditions. In a series of 14 such patients, Floeth et al. (2006) evaluated FDG-PET and FET-PET in differentiating gliomas from nonneoplastic lesions. They found the highest FET uptake in 5/5 malignant gliomas but 3/9 benign lesions also showed uptake values indicative of a neoplastic lesion (two abscesses and one demyelinating lesion). It can be concluded that absence of FET uptake in ring enhanced brain lesions is highly suggestive of a nonneoplastic lesion as opposed to a glioma. Whether a solitary brain metastasis can be excluded by a negative FET-PET can not be concluded from that study, since no patients with metastases were included. Overall, the authors conclude that FET is not a substitute of histological sampling in this patient group.

## RECOMMENDATIONS FOR IMAGE ACQUISITION AND INTERPRETATION

As a result of the data discussed above, a dynamic acquisition protocol should be used for amino acid PET with FET. Using four time frames of 10 min each, an estimation of the uptake kinetics is possible with a simple process of analysis. The tracer is obviously accumulated in the majority of histologically confirmed gliomas. A maximal FET uptake ratio above 2.0 on images taken later than 30 min after injection is strongly suggestive of a neoplastic lesion but lower values do not exclude a tumor. Late static images do not allow predicting tumor grade reliably. This observation is in line with previous reports on amino acid imaging. If a lesion is not contrast enhanced on MRI or CT but accumulates FET with increasing contrast, a low grade glioma is the most likely diagnosis. If a tumor is contrast enhanced and shows intensive FET uptake, with a slightly decreasing contrast over time, a malignant tumor is likely. In the case of a major decrease in FET uptake over time, blood pool activity should be considered. A comparison of tumor uptake and uptake in the venous sinus may aid in detecting blood pool activity.

Tumor extent is accurately reflected by FET uptake between 15 and 40 min after injection. Pauleit et al. (2005) have shown that MRI is highly sensitive in delineating tumors but not very specific, when compared to stereotaxic biopsies (sensitivity 96%, specificity 53%). Taking FET uptake into account the accuracy for the presence of tumor tissue as opposed to peritumoral changes increased significantly



(sensitivity 93%, specificity 94%). It has to be kept in mind that FET-PET is not recommended as a substitute for MRI but as an additional tool.

## CLINICAL APPLICATION

Positron emission tomography using FET or other amino acid tracers should always be considered, when targeting tumor diagnosis or therapy. As amino acids delineate tumors most accurately, sampling errors may be avoided when using the metabolic information of amino acid uptake to target biopsy (Messing-Junger et al. 2002). Whether it is justified to abandon biopsy in incidental lesions which are metabolically inactive is still a matter of discussion and requires further studies. An example of targeted therapy is computer assisted surgery. This application of FET-PET, however, suffers from inaccuracies of image fusion, when the patients

are operated on in an upright position and after opening the skull. Radiotherapy planning is another promising application of amino acid imaging. With the introduction of PET-CT hybrid scanners, the accuracy of PET and CT fusion is beyond doubt. Especially in radiotherapy of recurrent disease or in adjuvant therapy, the differentiation of postoperative changes or scars may be facilitated by amino acid PET (Figure 15.3). However, further studies should be conducted to prove the benefit of this application for the patient. Although it is reasonable to use the most accurate method for tumor delineation for radiotherapy planning, the therapeutic benefit may be marginal owing to the poor prognosis of high grade gliomas. A restriction of the target volumes, however, may result in a lower toxicity of therapy.

Amino acid tracers have been shown to be useful in evaluating patients with gliomas.

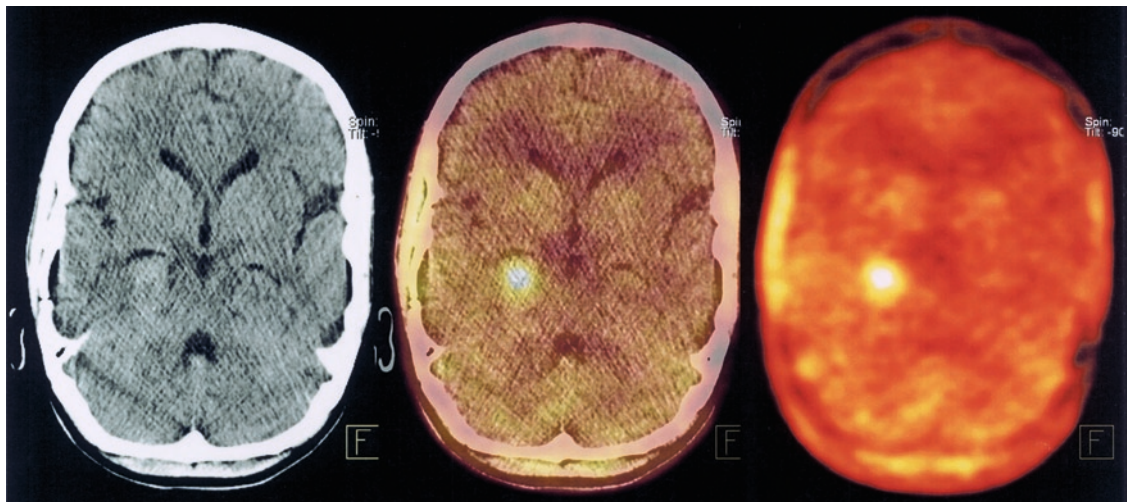


FIGURE 15.3. Twenty-five year old female patient with astrocytoma WHO II°. The FET PET-CT study was done 15 days after surgery. Patient positioning was done using a special flat bed and a thermoplastic head mask for reproducible positioning. Residual tumor is delineated by FET uptake (*right*), image fusion (*middle*) with the radiotherapy planning CT (*left*) allows for inclusion of the metabolic information in the definition of target volumes

mas after initial therapy. Experimental data suggest that differentiating post-therapeutic inflammatory changes (e.g., radionecrosis) from recurrent tumors is possible using FET (Rau et al. 2002; Spaeth et al. 2004). In a series of patients evaluated for the presence of recurrent tumors, Rachinger et al. 2005, showed a higher specificity of FET-PET (92.9%) as compared with MRI (50%), whereas sensitivity of the two procedures was comparable. Initial results indicate that FET PET may also be useful in monitoring therapy (Pöpperl et al. 2004), but further studies are needed to provide recommendations on the clinical use in this setting.

In conclusion, amino acid PET offers additional information to MRI in many clinical problems. With the increasing number of scanners, the availability of PET and PET-CT in patient care has improved considerably in the last years. In search of a fluorine-18 labeled amino acid, which can be used without on site cyclotron, FET has yielded promising experimental and clinical results. Positron emission tomography using FET has the potential to be introduced in routine clinical praxis in near future.

## REFERENCES

- Floeth, F.W., Pauleit, D., Sabel, M., Reifenberger, G., Stoffels, G., Stummer, W., Rommel, F., Hamacher, K., and Langen, K.J. (2006)  $^{18}\text{F}$ -FET PET differentiation of ring-enhancing brain lesions. *J. Nucl. Med.* 47:776–782
- Hamacher, K., and Coenen, H.H. (2002) Efficient routine production of the F-18-labelled amino acid O-(2-[ $^{18}\text{F}$ ]fluoroethyl)-L-tyrosine. *Appl. Radiat. Isotopes* 57:853–856
- Heiss, P., Mayer, S., Herz, M., Wester, H.J., Schwaiger, M., and Senekowitsch-Schmidtke, R. (1999) Investigation of transport mechanism and uptake kinetics of O-(2-[ $^{18}\text{F}$ ]fluoroethyl)-L-tyrosine *in vitro* and *in vivo*. *J. Nucl. Med.* 40:1367–1373
- Jager, P.L., Vaalburg, W., Pruijm, J., de Vries, E.G., Langen, K.J., and Piers, D.A. (2001) Radiolabeled amino acids: basic aspects and clinical applications in oncology. *J. Nucl. Med.* 42:432–445
- Langen, K.J., Jarosch, M., Muhlensiepen, H., Hamacher, K., Broer, S., Jansen, P., Zilles, K., and Coenen, H.H. (2003) Comparison of fluorotyrosines and methionine uptake in F98 rat gliomas. *Nucl. Med. Biol.* 30:501–508
- Messing-Junger, A.M., Floeth, F.W., Pauleit, D., Reifenberger, G., Willing, R., Gartner, J., Coenen, H.H., and Langen, K.J. (2002) Multimodal target point assessment for stereotactic biopsy in children with diffuse bithalamic astrocytomas. *Childs Nerv. Syst.* 18:445–449
- Pauleit, D., Floeth, F., Hamacher, K., Riemenschneider, M.J., Reifenberger, G., Muller, H.W., Zilles, K., Coenen, H.H., and Langen, K.J. (2005) O-(2-[ $^{18}\text{F}$ ]fluoroethyl)-L-tyrosine PET combined with MRI improves the diagnostic assessment of cerebral gliomas. *Brain* 128:678–687
- Pöpperl, G., Gotz, C., Rachinger, W., Gildehaus, F.J., Tonn, J.C., and Tatsch, K. (2004) Value of O-(2-[ $^{18}\text{F}$ ]fluoroethyl)-L-tyrosine PET for the diagnosis of recurrent glioma. *Eur. J. Nucl. Med. Mol. Imaging* 31:1464–1470
- Rachinger, W., Goetz, C., Pöpperl, G., Gildehaus, F.J., Kreth, F.W., Holtmannspotter, M., Herms, J., Koch, W., Tatsch, K., and Tonn, J.C. (2005) Positron emission tomography with O-(2-[ $^{18}\text{F}$ ]fluoroethyl)-L-tyrosine versus magnetic resonance imaging in the diagnosis of recurrent gliomas. *Neurosurgery* 57:505–511
- Rau, F.C., Weber, W.A., Wester, H.J., Herz, M., Becker, I., Kruger, A., Schwaiger, M., and Senekowitsch-Schmidtke, R. (2002) O-(2-[ $^{18}\text{F}$ ]Fluoroethyl)-L-tyrosine (FET): a tracer for differentiation of tumour from inflammation in murine lymph nodes. *Eur. J. Nucl. Med.* 29:1039–1046
- Spaeth, N., Wyss, M.T., Weber, B., Scheidegger, S., Lutz, A., Verwey, J., Radovanovic, I., Pahnke, J., Wild, D., Westera, G., Weishaupt, D., Hermann, D.M., Kaser-Hotz, B., Aguzzi, A., and Buck, A. (2004) Uptake of  $^{18}\text{F}$ -fluorocholine,  $^{18}\text{F}$ -fluoroethyl-L-tyrosine, and  $^{18}\text{F}$ -FDG in acute cerebral radiation injury in the rat: implications for separation of radiation necrosis from tumor recurrence. *J. Nucl. Med.* 45:1931–1938
- Weber, W.A., Wester, H.J., Grosu, A.L., Herz, M., Dzewas, B., Feldmann, H.J., Molls, M., Stöcklin, G., and Schwaiger, M. (2000) O-(2-[ $^{18}\text{F}$ ]fluoroethyl)-L-tyrosine and L-[methyl- $^{11}\text{C}$ ]methionine uptake

- in brain tumours: initial results of a comparative study. *Eur. J. Nucl. Med.* 27:542–549
- Weckesser, M., Langen, K.J., Rickert, C.H., Kloska, S., Straeter, R., Hamacher, K., Kurlmann, G., Wassmann, H., Coenen, H.H., and Schober, O. (2005) Initial experiences with O-(2-[18F]fluoroethyl)-L-tyrosine PET in the evaluation of primary brain tumors. *Eur. J. Nucl. Med. Mol. Imaging* 32:422–429
- Wester, H.J., Herz, M., Weber, W., Heiss, P., Senekowitsch-Schmidtke, R., Schwaiger, M., and Stöcklin, G. (1999) Synthesis and radiopharmacology of O-(2-[18F]fluoroethyl)-L-tyrosine for tumor imaging. *J. Nucl. Med.* 40:205–212

# 16

## Combined Use of [F-18] Fluorodeoxyglucose and [C-11] Methionine in 45 PET-Guided Stereotactic Brain Biopsies

Benoit Pirotte

### INTRODUCTION

Because brain tumors are histologically heterogeneous, computerized tomography (CT) or magnetic resonance (MR)-guided stereotactic brain biopsy do not always yield the actual diagnosis or grading (Black 1991; Chandrasoma et al. 1989; Choksey et al. 1989; Feiden et al. 1991). Positron emission tomography (PET) provides useful, independent and complementary metabolic information on brain tumors (Glantz et al. 1991b). We have previously developed a technique allowing the routine integration of PET data in the planning of stereotactic brain biopsy (Levivier et al. 1992, 1995; Pirotte et al. 2004). We originally used [F-18]-labeled fluorodeoxyglucose (FDG) as the radiotracer because of the large core of information on the use of this tracer in neurooncology. The selection of targets on stereotactic PET images with FDG (FDG-PET) allows to direct biopsies accurately in the abnormal metabolic foci of brain tumors (Levivier et al. 1992). These authors have shown that FDG-PET-guided stereotactic brain biopsy increases the diagnostic yield and the accuracy of the technique.

Experience with FDG-PET-guided biopsy has shown, however, some limitations.

Indeed, targeting may be difficult when there is no or minor FDG uptake, such as in low-grade tumors (Chung et al. 2002). Also, when a hypermetabolic lesion is in close relationship with the cortical or sub-cortical grey matter, tumor and normal FDG uptake are difficult to differentiate (Chung et al. 2002; Delbeke et al. 1995). Therefore, we tested [C-11]-labeled methionine (Met) as an alternative tracer for stereotactic PET guidance. As a first step toward the use of PET with Met (Met-PET) in stereotactic conditions, we used combined FDG- and Met-PET-guidance for stereotactic brain biopsy (Pirotte et al. 2004). The aim of the present study is to evaluate the relative contribution of Met and FDG in all patients that underwent PET-guided stereotactic brain biopsy with both tracers during this limited period of time.

### MATERIALS AND METHODS

#### Patient Selection

Since June 1991, we routinely perform PET-guided stereotactic brain biopsy in patients suspected of having a non-resectable brain tumor based on a preoperative neuroimaging work-up (Levivier et al. 1995).

Our current series comprises more than 250 cases. Between July 1992 and June 1997, 45 patients underwent biopsy guided by combined FDG-PET and Met-PET performed in stereotactic conditions. These patients presented a lesion that was in close relationship with the cortical or subcortical grey matter (including the basal ganglia and the brainstem), suggesting that FDG could be poorly contributive to target selection. There were 30 men and 15 women whose ages ranged between 2 and 87 years (mean 52.6 years). Forty-four patients were previously untreated and one presented with a recurrent lesion.

#### Stereotactic PET Data Acquisition

For data acquisition, the technique of combined stereotactic PET with Met and FDG was adapted from our previous experience with FDG-PET-guided stereotactic brain biopsy (Levivier et al. 1992, 1995). Placement of the stereotactic frame, data acquisition including stereotactic PET with Met and FDG as well as CT or MR, surgical planning and the biopsy procedure were performed the same day. All patients gave their informed consent, and the procedure was in accordance with the ethical guidelines of our institution.

After placement of the CT- and MR-compatible base ring (Fischer ZD-Neurosurgical Localizing Unit, Howmedica Leibinger, Freiburg, Germany), stereotactic CT or MR without and with intravenous contrast enhancement were obtained. For stereotactic PET, a clamp specifically designed to secure the head ring to the Siemens couch (Howmedica Leibinger, Freiburg, Germany) was used. In order to create a fiducials reference system compatible with PET, we have used the

commercial MR localizers with minor modifications as previously described (Figures 16.1a, c, and d) (Levivier et al. 1992). After the transmission scan, the patient was first injected intravenously with 10–15 mCi of Met. Images used for stereotactic calculation were acquired between 20 and 40 min after injection of the tracer. Eighty minutes after Met injection, the patient was injected with 6–9 mCi of FDG. Images used for stereotactic calculation were acquired between 40 and 60 min later. The PET camera used at the time of this study (CTI/Siemens 933/08/12 tomograph, Knoxville, Tennessee, USA) allowed simultaneous acquisition of 15 slices ~6.5 mm-thick, with a full width at half-maximum resolution of ~5 mm. The accuracy of target calculation is within PET camera resolution as previously described (Levivier et al. 1992). Briefly, as demonstrated in a study based on phantom, there is a tight correspondence between PET- and CT-located targets. With this camera, PET sections are of  $2.591 \times 2.591$  mm pixels and are 6.75 mm thick. Thus, the precision of the target definition corresponds to a volume of 45 mL (Levivier et al. 1992).

#### Analysis of Stereotactic PET Images and Target Definition

The surgical planning began with analysis of the PET images. Since this series represents an evaluation of Met-PET, we always started by an independent analysis of FDG-PET images, as based on our previous experience. Met-PET images were analyzed afterwards. Areas of abnormal metabolism used for target selection were either zones of FDG or Met uptake that were higher than the

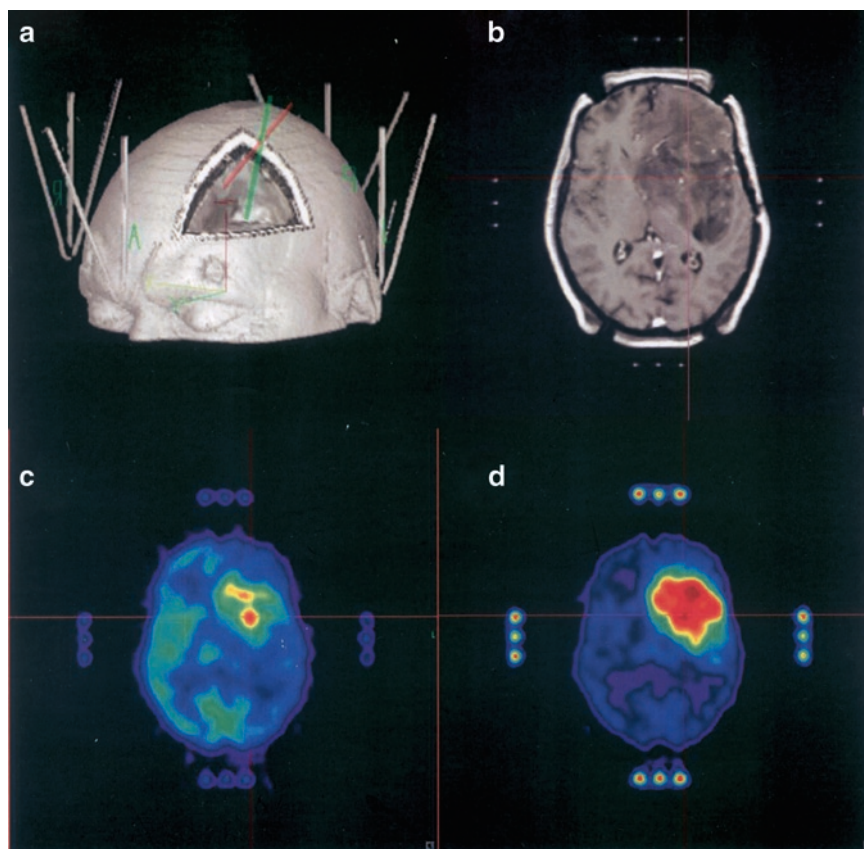


FIGURE 16.1. Stereotactic acquisition of MRI (a and b), FDG-PET (c) and Met-PET (d) images in an anaplastic oligoastrocytoma located in the right frontal area. The 3D surface reconstruction (a) shows the fiducials embedded into the localizers grooves which are filled up with radioactive  $^{18}\text{F}$ -fluoride sodium for allowing visualization on PET images (c and d). The extent of MET uptake was much larger than the extent of FDG uptake. There was a correspondence between the areas of highest tracer uptake on both PETs (c and d)

surrounding normal appearing brain tissue or foci of relative increase of FDG or Met uptake in a hypometabolic lesion. The tracer FDG was used for target selection when its uptake in the tumor was higher than, or distinguishable from the grey matter. Met was used for target selection when there was no FDG uptake or when FDG uptake was equivalent to that of the grey matter. If the PET images revealed areas of abnormal increased tracer uptake within the lesion's area, the plane that best displayed the abnormal FDG or Met uptake was selected and a

pixel located in the center of this zone was interactively pointed at on visual inspection. The coordinates of that pixel were calculated and set as a target for biopsy. When a target was selected on FDG-PET, it was then projected onto the corresponding Met-PET slice to analyze and compare the local uptake of both tracers in order to determine which tracer offers the best information. These targets were also projected onto the corresponding stereotactic CT or MR slice to control the reliability and the safety of the target selection and of the trajectory,

especially verifying that the PET-defined target remains within the lesion's boundaries.

Whenever possible, two targets were selected for biopsy, in order to sample different metabolic areas of the tumor. When the area of highest FDG uptake was smaller than the limits of the lesion visualized on the corresponding slice of Met-PET, another target was selected on the Met-PET, outside the area of increased FDG uptake. In patients where there was no obvious abnormal FDG or Met uptake that could be used to select a target for biopsy, surgery was planned using CT or MR data only.

### Data Analysis

In all patients, serial stereotactic biopsies were performed along each trajectory, following the Kelly's technique (Kelly et al. 1987). For all biopsy specimens, smear preparation and formalin-fixed samples were analyzed after appropriate staining (Kleihues et al. 1993; Levivier et al. 1995; Pirotte et al. 2004). For the present study, glial tumors were classified using a three-tier system: low-grade glioma (LGG), including astrocytoma, oligodendroglioma, giant cell astrocytoma and gangliocytoma; anaplastic astrocytoma (AA) and glioblastoma (GB). Non-glial tumors, whether neoplastic or not, were also included, as well as non-tumor lesions. For each patient, a histological diagnosis was established. Then, the pathological description obtained in each biopsy trajectory was recorded separately, regardless of the patient's final diagnosis. If non-tumor samples made of gliotic, reactional or necrotic tissue were found, they were classified as non-diagnostic trajectories.

In order to evaluate the role of Met-PET in target selection, we retrospectively clas-

sified biopsy trajectories in three groups, according to their metabolic characteristics: FDG-PET-guided trajectory, Met-PET-guided trajectory, or CT/MR-guided trajectory. For that purpose and since we found that all areas of increased FDG uptake were in areas of increased Met uptake, we first looked at whether Met uptake was increased [Met(+)] or not [Met(-)]. In Met(+) trajectories, we further looked at whether FDG-PET was used for the target selection. Indeed, as described above, FDG-PET images were used in priority for target selection either when they gave more information than Met-PET images or when both tracers were equivalent (FDG-PET-guided trajectory). On the other hand, when Met-PET data were superior to those of FDG-PET, Met-PET was used for target selection (Met-PET-guided trajectory). In Met(-) trajectories, target selection was based on CT or MR only (CT/MR-guided trajectory).

## RESULTS

Histological diagnosis was obtained in all patients. Diagnoses included 10 GB, 12 AA, 10 LGG (including 6 astrocytomas, 2 oligodendrogliomas, 1 giant cell astrocytoma and 1 gangliocytoma), 3 primary non-Hodgkin's lymphomas (PNHL), 3 metastases, 1 primitive neuroectodermal tumor (PNET), 1 ischemic lesion, 1 hematoma, 1 abscess, 2 progressive multifocal leucoencephalopathies (PML) and 1 post-radiation gliosis (PR) without tumor recurrence.

**Abnormal Met and FDG Uptakes.** All tumors (n = 39) had an area of abnormal Met uptake. Among them, 18 tumors were biopsied based on FDG-defined targets and the other 21 tumors based on

Met-defined targets. These 39 tumors may be divided in 3 groups according to their level of FDG uptake. When tumor FDG uptake was higher than in the grey matter ( $n = 18$ ), i.e., the tumor was clearly visible on FDG-PET, it was used for target selection. In this group we found 7 GB, 6 AA, 1 LGG, 2 PNHL and 2 metastases. When tumor FDG uptake was equivalent to that of the surrounding grey matter ( $n = 15$ ), a target could not easily be defined on FDG-PET, and therefore Met-PET was used for target selection. This was the case in 3 GB, 5 AA, 5 LGG, 1 PNHL, and 1 PNET. Finally, when no FDG uptake was found ( $n = 6$ ), targets were also selected on Met-PET as in 1 AA, 5 LGG and 1 metastasis (Figures 16.2 and 16.3). Thus, Met was the tracer used to define a target for biopsy in 21 of these 39 tumors (54%). The remaining six lesions were non-tumor

and had no Met uptake. They were biopsied on CT- or MR-defined targets.

**Lesions in the Cortical Grey Matter.** In this series, 25 lesions involved the cortical area. They were 21 tumors (6 GB, 8 AA, 1 PNHL and 6 LGG) and four non-tumor lesions. In the 21 tumors, Met was used for target selection in 15 (71%) while FDG only was used in six (4 GB, 1 AA and 1 LGG). The 15 cortical tumors biopsied on Met-PET included four lesions that were not enhanced on CT or MR (three LGG and one AA). The four non-tumor lesions had no Met uptake and biopsy was guided on CT- or MR-enhanced areas.

**Lesions in the Sub-Cortical Grey Matter.** The 20 other lesions were located in the sub-cortical grey matter. Thirteen were located in the basal ganglia and seven in the brainstem. There were 18 tumors and two non tumor lesions. In 11 of the tumors

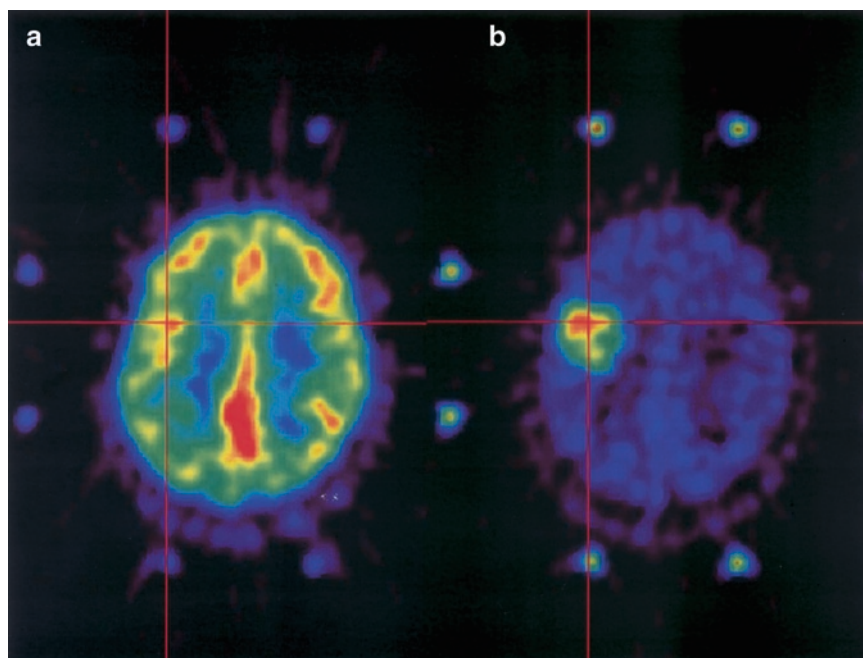


FIGURE 16.2. Stereotactic FDG-PET (a) and Met-PET (b) images in a glioblastoma located in the left fronto-rolandic cortical area. Tumor FDG uptake was equivalent to that of the surrounding grey matter and a target could not easily be defined on FDG-PET alone. Therefore, Met-PET was used for target selection



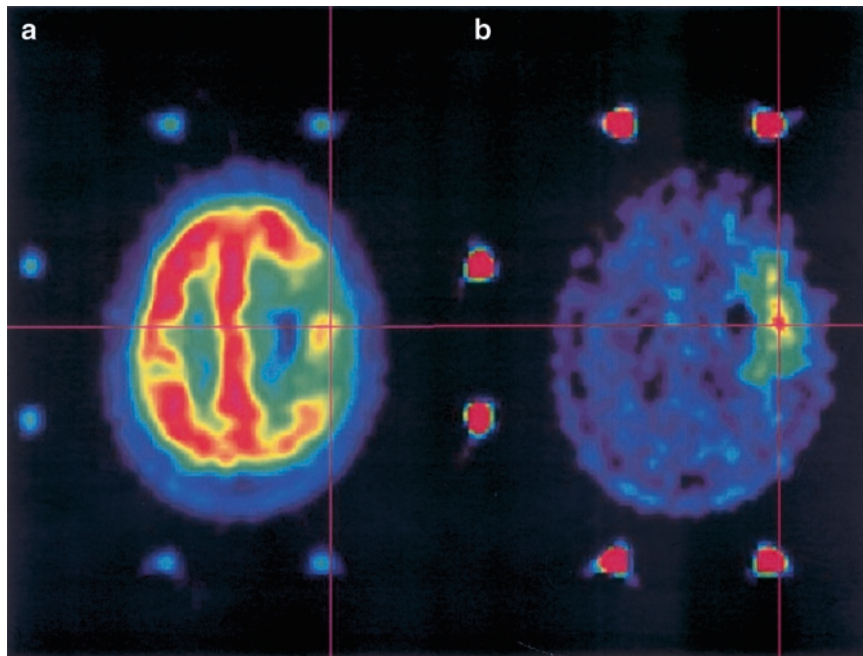


FIGURE 16.3. Stereotactic FDG-PET (a) and Met-PET (b) images in an anaplastic astrocytoma located in the right fronto-rolandic cortical area. Tumor FDG uptake was lower than that of the surrounding grey matter and a target could not be defined on FDG-PET. Therefore, Met-PET was used for target selection

(61%), FDG was used for target selection because its uptake was higher than in the grey matter. However, in two cases (one GB and one PNHL), a second trajectory was performed in an area of high Met uptake outside the limits of high FDG uptake and also yielded similar tumor tissue. In five other tumors (one GB, one PNHL, and one LGG), FDG uptake was equivalent to that of the grey matter and Met-PET was used to guide the biopsy. In the remaining four cases with no FDG uptake, one metastasis and one LGG were biopsied using target selection on Met-PET and the two others (two non-tumor lesions) had no Met uptake and were biopsied on CT- or MR-defined targets.

***Specific Contribution of Met-PET and FDG-PET.*** In order to evaluate the specific contribution of Met-PET, compared to FDG-PET, in target selection for biopsies,

we reviewed all tumors which had both FDG(+) and Met(+) areas, and in which two biopsy trajectories were performed. There were 14 gliomas (seven GB, six AA and one LGG). In all of them, this diagnosis was obtained in the trajectory targeting the area of highest FDG uptake which also corresponded to the area of highest Met uptake. The second trajectory was always performed in an area of Met uptake but outside the area of increased FDG uptake. In those trajectories, the same diagnosis was obtained in all cases. The diagnostic yield of the 97 stereotactic trajectories performed in the 45 patients (2.1 trajectories per patient) was studied according to their Met uptake. Seventy-three trajectories corresponded to an area of increased Met uptake. In the other 24 trajectories, there was no abnormal Met uptake and biopsy was based on CT- or MR-defined

targets. All the 73 Met+ trajectories yielded tumor tissue. When these trajectories are analyzed for their FDG uptake (superior or equivalent to that of grey matter, or absent), it reveals that Met was superior to FDG to differentiate tumor tissue from the surrounding brain. Consequently, Met was used more often than FDG to define target for biopsy (43 of the 73 trajectories, 59%). The 24 Met(-) trajectories yielded non-tumor tissue. Among them, there were ten non-diagnostic trajectories. All these non-diagnostic trajectories were obtained in patients where the diagnosis was always given in another trajectory that presented increased Met uptake. They included two GB, three AA, four LGG and one metastasis.

***Specificity and Sensitivity to Detect Tumor Tissue.*** Thus, in this series, Met-PET provided 100% sensitivity and 100% specificity. A comparative analysis between Met and FDG characteristics in each tumor trajectory showed a good correspondence between tumor grade or malignancy and the uptake of both tracers (Figure 16.1). Similarly, Met-PET and FDG-PET were concordant in non-tumor trajectories, as the uptake of both tracers was negative.

We analyzed and compared the specificity and sensitivity to detect tumor tissue of FDG-PET, MET-PET, and MRI in this series. For that purpose, we analyzed the diagnoses of 97 biopsy targets performed in these 45 patients and classified them according to the presence or the absence of tumor tissue; it is easy to calculate the rate of false positive (10%, 0% and 26.6% for FDG-PET, Met-PET and MRI respectively), false negative (18.5% and 0% for FDG-PET and Met-PET respectively), true positive ( $n = 55$ ,  $n = 73$  and  $n = 73$  for FDG-PET, Met-PET and MRI,

respectively) and true negative ( $n = 14$  and  $n = 24$  for FDG-PET and Met-PET respectively) results in each imaging modality. Sensitivity is measured by the number of false negative samples (tumor tissue in areas of negative signal on imaging). Specificity is measured by the number of false positive samples (non-tumor tissue in areas of positive signal). A chi-square statistical analysis showed that:

1. The specificity of Met-PET was significantly higher than that of FDG-PET and of MRI ( $p = 0.0009$  and  $p = 0.00002$ , respectively)
2. The sensitivity of Met-PET was significantly higher than that of FDG-PET ( $p = 0.00004$ )
3. The false positive rate of FDG-PET ( $10/97 = 10\%$ ) was half of the false positive rate of MRI ( $22/97 = 22.7\%$ )
4. The specificity of FDG-PET was, however, not significantly lower ( $p = 0.18$ ) than that of MRI
5. The reduction in the non-diagnostic sampling rate by the PET-guidance compared to the results by using MRI alone was very significant ( $p = 0.00001$ )
6. The sensitivity of FDG-PET was weak ( $18/97 = 18.5\%$  of false negative)

## DISCUSSION

### PET for the Guidance of Stereotactic Brain Biopsy

Brain tumors, especially gliomas, are characterized by geographic variations of their histological malignancy (Paulus and Peiffer 1989; Wong et al. 2002) that cannot be distinguished on conventional anatomic imaging such as MRI even with contrast injection (Patronas et al. 1983). Therefore CT- or MR-guided stereotactic

brain biopsy do not always yield the actual diagnosis or grading, since target selection may lead to significant sampling error and secondary potential understaging (Black 1991; Chandrasoma et al. 1989; Choksey et al. 1989; Feiden et al. 1991; Glantz et al. 1991a).

PET provides independent and complementary metabolic information on brain tumors (Glantz et al. 1991a; Wong et al. 2002). Literature has collected numerous data on PET in brain tumors, mainly with the tracer FDG. When combined with anatomical imaging techniques, FDG-PET can provide information regarding tumor grading (Goldman et al. 1996, 1997; Levivier et al. 1995; Pirotte et al. 2005), response to therapy (De Witte et al. 1998; Levivier et al. 1999) and prognosis (De Witte et al. 1996, 2000). In particular, early clinical studies had demonstrated that the glycolytic rate of brain tumors, as assessed by FDG uptake, is a more accurate reflection of tumor grade than contrast enhancement (Patronas et al. 1983).

To take advantage of these metabolic data in the management of brain tumors, we have previously developed a technique allowing the routine integration of PET data in the planning of stereotactic brain biopsy (Levivier et al. 1995). We originally used FDG because it was the most widely used radiotracer in brain tumors (Wong et al. 2002). The selection of targets on stereotactic FDG-PET-generated images allows to direct biopsies accurately in the abnormal metabolic foci of brain tumors (Levivier et al. 1995; Pirotte et al. 2003). We have shown that FDG-PET-guided stereotactic brain biopsy increases the diagnostic yield and the accuracy of the technique (Levivier et al. 1995, Massager et al. 2000; Pirotte et al. 2004). Moreover,

PET-guided stereotactic brain biopsy has allowed to accurately correlate metabolism and histology and to confirm further the correlation between PET tracers uptake and the tumor grade (Wong et al. 2002). Indeed, we have found with this method, a significant correlation between FDG uptake, as well as Met uptake, and the presence of anaplasia (Goldman et al. 1996, 1997), which supports the present observation of the good concordance between Met-PET and FDG-PET in biopsy trajectories. This study does not allow to answer specifically the question of the marginal utility of PET over just using CT or MRI. This has, however, been already addressed in previous work in which at least two trajectories were performed within the tumor boundaries in areas of different PET tracer uptake (Levivier et al. 1995; Massager et al. 2000). The same study could have also been prospectively conducted in this series. However, it would have required to design a more complex protocol comparing at least two PET+ trajectories with at least one PET- MR+ trajectory. This design did not appear to be ethically justified since this could have increased the risk of the procedure and the goal of the present study was different. However, the specificity of Met-PET was calculated as significantly higher than that of FDG-PET and of MRI which had a high false positive rate of (FDG-PET:  $10/97 = 10\%$ ; MRI:  $22/97 = 22.7\%$ ), the sensitivity of FDG-PET was weak and the specificity of FDG-PET was not significantly lower than that of MRI. Nevertheless, the reduction in the non-diagnostic sampling rate by the PET-guidance compared to the results by using MRI alone was very significant which suggests the marginal utility of PET over just using MRI guidance.

The increased use of PET guidance in neurosurgical procedures, such as neuro-navigation and radiosurgery (Levivier et al. 2002) in which the issue of tracer choice is crucial, prompted us to review in details this unique series with the use of two tracers in stereotactic conditions.

### Choice of Radiotracer

The type of information obtained with PET mostly depends on the radiotracer used. There has been numerous studies on the use of FDG for the management of brain tumors (Coleman et al. 1991; Delbeke et al. 1995; Derlon et al. 1997; De Witte et al. 1996, 2000; Glantz et al. 1991a, b; Wong et al. 2002). However, our experience with FDG-PET-guided biopsy has shown some limitations. Indeed, targeting may be difficult when there is no or minor FDG uptake, such as in low-grade tumors (Chung et al. 2002). Also, when a hypermetabolic lesion is in close relationship with the cortical or sub-cortical grey matter, tumor and normal FDG uptake are difficult to differentiate (Delbeke et al. 1995). The use of Met, a marker of amino acids uptake and protein synthesis, has also been validated in neurooncology (Chung et al. 2002; Derlon et al. 1997, 2000; Mineura et al. 1991; Kaschten et al. 1998). This PET tracer has several advantages: (1) it is considered as efficient and more suitable than FDG in delineating areas of tumor tissue (Derlon et al. 1997; Wienhard et al. 1991; Wong et al. 2002), (2) its uptake is reported as increased in low-grade glial tumors (Delbeke et al. 1995; Derlon et al. 1997; Derlon et al. 2000), (3) its uptake is low in the grey matter, and (4) the biological behavior of this tracer in neoplastic tissues shows that

its accumulation is representative of the active transport of amino acids. For all these reasons, we tested Met as an alternative tracer for stereotactic PET guidance. As a first step toward the use of stereotactic Met-PET in neurosurgery, we used combined FDG- and Met-PET-guidance for stereotactic brain biopsy during a limited period of time (Pirotte et al. 2004) which represents the materials of the current study.

### Accuracy of Stereotactic PET Coregistration

To accurately compare PET images obtained with different tracers or integrate PET images with other imaging modalities, visual correlation requires a procedure of electronic frame-based or frameless image coregistration. The criteria in the choice of one or the other approach will be a trade-off between accuracy and reliability against minimal invasiveness and clinical routine feasibility. This study, using frame-based high-precision PET-MR coregistration technique, represents therefore a unique opportunity to compare accurately both tracers. Indeed, for stereotactic PET, imaging fiducials system defining the stereotactic coordinate space of a frame attached to the patient is the most accurate and reliable way of registering PET images. The various technical challenges associated with PET acquisition had been addressed carefully, especially with phantom-based validation (Levivier et al. 1992, 2000; Pirotte et al. 2003). The recent developments of PET technology are improving the performance of neurosurgical PET guidance both in terms of resolution and sensitivity. New PET tomographs have increased number of

detectors which particularly enhance the axial resolution of the system. These new machines also allow tridimensional acquisition and storage of the data. For example, our newer camera, which is routinely used for PET-guided navigation and radiosurgery allows the simultaneous acquisition of 63 planes with a slice thickness of 2.4 mm.

### Comparison Between Met and FDG

Our results confirm our preliminary data showing that Met may be a good alternative to FDG for target selection in PET-guided stereotactic brain biopsy (Pirotte et al. 2004). With Met-PET guidance, histological diagnosis was obtained in all patients. The ten non-diagnostic samples were found exclusively in trajectories defined on CT or MR, in areas where there was no Met uptake. Because CT or MR were abnormal in those areas, one cannot rule out that biopsy guidance limited to CT/MR data in those ten patients would have jeopardized the final diagnosis. This high diagnostic value of Met-PET is also illustrated by the fact that, in this series of patients, all tumors presented with an area of increased Met uptake. Tumor detection by Met did not present false negative in this series.

Our experience with both tracers acquired and compared in stereotactic conditions shows that, in 21 of the 39 tumors, which were all located in grey matter areas, Met was the only tracer usable for target selection. This was the case in high-grade tumors where tumor and normal FDG uptake were difficult to differentiate as well as in low-grade tumors where there was no FDG uptake. Indeed, in nine LGG, the highest focus of Met uptake was used for target definition. In those LGG, Met was more

contributive than FDG because no FDG uptake was found. One could argue that Met uptake in LGG is not a constant finding (Derlon et al. 1997; De Witte et al. 2001). However, the chances to find an abnormal increased uptake of radiotracer remains higher with Met than with FDG (De Witte et al. 2001; Goldman et al. 1996, 1997).

When located in the cortex, we found that the majority of high grade tumors (19 out of 25) present limitations in target definition with FDG-PET. Met is therefore superior to FDG for target selection in enhanced or non-enhanced tumors located in the cortex. Interestingly, the four non tumor lesions in the cortical area indicate that absence of Met uptake could already have suggested, before the biopsy, a non tumor diagnosis. When the tumor was seated in the sub-cortical grey matter, FDG was more frequently useful for target selection (11 out of 20 cases). In the other nine, only Met showed abnormal uptake. All stereotactic biopsies performed in brainstem lesions yielded a diagnosis of tumor, as anticipated by a high uptake of Met. This further confirms that the integration of stereotactic PET, especially with Met, should allow to increase the diagnostic yield while reducing the number of trajectories, in highly functional brain areas (Massager et al. 2000).

The measurements of the specificity of Met-PET to detect tumor tissue showed the superiority of this tracer on FDG and MRI. The sensitivity of FDG-PET was weak and the specificity of FDG-PET was not significantly lower than that of MRI. The significant reduction in the non-diagnostic sampling rate by the FDG-PET-guidance compared to the results by using MRI alone (Levivier et al. 1995), remains compatible with a weak sensitivity and

specificity of this tracer because non-diagnostic samples represent false positive results in MRI but true negative results in FDG-PET. Unfortunately, the sensitivity of MRI to detect tumor tissue has not been studied here because no biopsy was made outside the tumor boundaries on MRI.

In all tumor locations, even those where FDG provide useful information, Met was easily used for target selection. Because Met uptake was increased in all tumors, whether benign or malignant, one can argue that Met-PET was not discriminant enough to direct the biopsy to the most malignant area of the tumor, as allowed by FDG-PET. Moreover, if Met-PET was the only tracer available, one cannot rule out that target selection could have been different (especially in those cases with high FDG uptake) and would not have been as accurate in all cases. Our comparison of the diagnostic yield of the two trajectories in gliomas illustrates the high reliability of Met-based targeting (Pirotte et al. 2004). Also, in all tumors, we found that areas of highest tracer uptake usually corresponded on equivalent FDG-PET and Met-PET images, at visual analysis. This is in accordance with our previous comparative study of Met and FDG uptake in biopsy samples has confirmed a significant correlation between the uptake of both tracers and the degree of anaplasia (Goldman et al. 1997). Thus, this relationship between the distribution of areas of highest uptake of both tracers is also found in this series, and we believe that Met is a good option for a single-tracer PET-guided stereotactic biopsy.

One of the limitations of using [11C]-labeled amino acids, such as Met, is their short half-life (20.3 min), and therefore the need of cyclotrons for in-

house tracer production, which highly increases the cost of the procedure. Therefore, further tests should be conducted with [18F]-labeled amino acids, such as [18F]-Tyrosine, in order to render this methodology accessible to centers without in-house tracer production. Indeed, the longer half life of [18F] (109.7 min) compared to [11C] may facilitate the application of PET targeting with amino acid PET tracers (Inoue et al. 1999; Weber et al. 2000; Wienhard et al. 1991).

In conclusion, multiple-tracer PET-guided stereotactic biopsy has offered a unique opportunity to accurately compare the characteristics of two tracers and accordingly, has contributed to a better understanding of the role of PET in neurooncology. The results of the current retrospective analysis confirm that Met can be used accurately as a radiotracer in routine image-guided neurosurgery of brain tumors. The higher sensitivity and specificity of Met uptake in brain tumors also shows that Met is a better choice than FDG for target selection in PET-guided stereotactic brain biopsy, because it avoids the risk of low or absent FDG uptake and offers equivalent possibility of target selection in areas of highest metabolic activity. Thus, Met also represents a better choice when PET-guidance is used in image-guided neurosurgical therapeutic modalities, such as tumor resection under neuronavigation (Levivier et al. 1999) and radiosurgery (Levivier et al. 2000).

## REFERENCES

- Black, P.M. (1991) Brain tumors (second of two parts). *N. Engl. J. Med.* 324:1555–1564
- Chandrasoma, P.T., Smith, M.M., and Apuzzo, M.L.J. (1989) Stereotactic biopsy in the diagnosis of brain masses: comparison of results of biopsy

- and resected surgical specimen. *Neurosurgery* 24:160–165
- Choksey, M.S., Valentine, A., Shawdon, H., Freer, C.E.R., and Lindsay, K.D. (1989) Computed tomography in the diagnosis of malignant brain tumours: do all patients require biopsy? *J. Neurol. Neurosurg. Psychiatry* 52:821–825
- Chung, J.K., Kim, Y.K., Kim, S.K., Lee, Y.J., Paek, S., Yeo, J.S., Jeong, J.M., Lee, D.S., Jung, H.W., and Lee, M.C. (2002) Usefulness of <sup>11</sup>C-methionine PET in the evaluation of brain lesions that are hypo- or isometabolic on <sup>18</sup>F-FDG-PET. *Eur. J. Nucl. Med. Mol. Imaging* 29:176–182
- Coleman, R.E., Hoffman, J.M., Hanson, M.W., Sostman, H.D., and Schold, S.C. (1991) Clinical application of PET for the evaluation of brain tumors. *J. Nucl. Med.* 32:616–622
- De Witte, O., Levivier, M., Violon, P., Salmon, I., Damhaut, P., Wikler, D. Jr., Hildebrand, J., Brotchi, J., and Goldman, S. (1996) Prognostic value of positron emission tomography with [<sup>18</sup>F]fluoro-2-deoxy-D-glucose in the low-grade glioma. *Neurosurgery* 39:470–476
- De Witte, O., Levivier, M., Violon, P., Brotchi, J., and Goldman, S. (1998) Quantitative imaging study of extent of surgical resection and prognosis of malignant astrocytomas. *Neurosurgery* 43:398–399
- De Witte, O., Lefranc, F., Levivier, M., Salmon, I., Brotchi, J., and Goldman, S. (2000) FDG-PET as a prognostic factor in high-grade astrocytoma. *J. Neurooncol.* 49:157–163
- De Witte, O., Goldberg, I., Wikler, D., Rorive, S., Damhaut, P., Monclus, M., Salmon, I., Brotchi, J., and Goldman, S. (2001) Positron emission tomography with injection of methionine as a prognostic factor in glioma. *J. Neurosurg.* 95:746–750
- Delbeke, D., Meyerowitz, C., Lapidus, R.L., Maciunas, R.J., Jennings, M.T., Moots, P.L., and Kessler, R.M. (1995) Optimal cutoff levels of F-18 fluorodeoxyglucose uptake in the differentiation of low-grade from high-grade brain tumors with PET. *Radiology* 195:47–52
- Derlon, J.M., Petit-Taboue, M.C., Chapon, F., Beaudouin, V., Noel, M.H., Creveuil, C., Courtheoux, P., and Houtteville, J.-P. (1997) The *in vivo* metabolic pattern of low-grade brain gliomas: a positron emission tomographic study using <sup>18</sup>F-fluorodeoxyglucose and <sup>11</sup>C-L-methylmethionine. *Neurosurgery* 40:276–288
- Derlon, J.M., Chapon, F., Noel, M.H., Khouri, S., Benali, K., Petit-Taboue, M.C., Houtteville, J.-P., Chajari, M.H., and Bouvard, G. (2000) Non-invasive grading of oligodendrogliomas: correlation between *in vivo* metabolic pattern and histopathology. *Eur. J. Nucl. Med.* 27:778–787
- Feiden, W., Steude, U., Bise, K., and Gündisch, O. (1991) Accuracy of stereotactic brain tumor biopsy: comparison of the histologic findings in biopsy cylinders and resected tumor tissue. *Neurosurg. Rev.* 14:51–56
- Glantz, M.J., Burger, P.C., Herndon, II J.E., Friedman, A.H., Cairncross, J.G., Vick, N.A., and Schold, Jr. S.C. (1991a) Influence of the type of surgery on the histological diagnosis in patients with anaplastic gliomas. *Neurology* 41:1741–1744
- Glantz, M.J., Hoffman, J.M., Coleman, R.E., Friedman, A.H., Hanson, M.W., Burger, P.C., Herndon, II J.E., Meisler, W.J., and Schold, Jr. S.C. (1991b) Identification of early recurrence of primary central nervous system tumors by [<sup>18</sup>F]fluorodeoxyglucose positron emission tomography. *Ann. Neurol.* 29:347–355
- Goldman, S., Levivier, M., Pirotte, B., Brucher, J.M., Wikler, D., Damhaut, P., Stanus, E., Brotchi, J., and Hildebrand, J. (1996) Regional glucose metabolism and histopathology of gliomas. A study based on positron emission tomography-guided stereotactic biopsy. *Cancer* 78:1098–1106
- Goldman, S., Levivier, M., Pirotte, B., Brucher, J.M., Wikler, D., Damhaut, P., Dethy, S., Brotchi, J., and Hildebrand, J. (1997) Regional methionine and glucose metabolism in gliomas: a comparative study on PET-guided stereotactic biopsy. *J. Nucl. Med.* 38:1–4
- Inoue, T., Shibasaki, T., Oriuchi, N., Aoyagi, K., Tomiyoshi, K., Amano, S., Mikuni, M., Ida, I., Aoki, J., and Endo, K. (1999) <sup>18</sup>F alpha-methyl tyrosine PET studies in patients with brain tumors. *J. Nucl. Med.* 40:399–405
- Kaschten, B., Stevenaert, A., Sadzot, B., Deprez, M., Degeldre, C., Del Fiore, G., Luxen, A., and Reznik, M. (1998) Preoperative evaluation of 54 gliomas by PET with fluorine- <sup>18</sup>-fluorodeoxyglucose and/or carbon-11-methionine. *J. Nucl. Med.* 39:778–785

- Kelly, P.J., Dumas-Duport, C., Kispert, D.B., Kall, B.A., Scheithauer, B.W., and Illig, J.J. (1987) Imaging-based stereotactic serial biopsies in untreated intracranial glial neoplasms. *J. Neurosurg.* 66:865–874
- Kleihues, P., Burger, P.C., and Scheithauer, B.W. (1993) The new WHO classification of brain tumors. *Brain Pathol.* 3:255–268
- Levivier, M., Goldman, S., Bidaut, L.M., Luxen, A., Stanus, E., Przedborski, S., Balériaux, D., Hildebrand, J., and Brotchi, J. (1992) Positron emission tomography-guided stereotactic brain biopsy. *Neurosurgery* 31:792–797
- Levivier, M., Goldman, S., Pirotte, B., Brucher, J.M., Balériaux, D., Luxen, A., Hildebrand, J., and Brotchi, J. (1995) Diagnostic yield of stereotactic brain biopsy guided by positron emission tomography with [<sup>18</sup>F]fluorodeoxyglucose. *J. Neurosurg.* 82:445–452
- Levivier, M., Wikler, D., Goldman, S., Pirotte, B., and Brotchi, J. (1999) Positron emission tomography in stereotactic conditions as a functional imaging technique for neurosurgical guidance. In: Alexander, III E.B., Maciunas, R.M. (eds) *Advanced neurosurgical navigation*. Thieme Medical Publishers, Inc., New York, pp 85–99
- Levivier, M., Wikler, D., Goldman, S., David, P., Metens, T., Massager, N., Gerosa, M., Devriendt, D., Desmedt, F., Simon, S., Van Houtte, P., and Brotchi, J. (2000) Integration of the metabolic data of positron emission tomography in the dosimetry planning of radiosurgery with the gamma knife: early experience with brain tumors. *J. Neurosurg.* 93:233–238
- Levivier, M., Wikler, D. Jr., Massager, N., David, P., Devriendt, D., Lorenzoni, J., Pirotte, B., Desmedt, F., Simon, S. Jr., Goldman, S., Van Houtte, P., and Brotchi, J. (2002) The integration of metabolic imaging in stereotactic procedures including radiosurgery: a review. *J. Neurosurg.* 97:542–550
- Massager, N., David, P., Goldman, S., Pirotte, B., Wikler, D., Salmon, I., Nagy, N., Brotchi, J., and Levivier, M. (2000) Combined MRI – and PET – guided stereotactic biopsy in brainstem mass lesions: diagnostic yield in a series of 30 patients. *J. Neurosurg.* 93:951–957
- Mineura, K., Sasajima, T., Kowada, M., Uesaka, Y., and Shishido, F. (1991) Innovative approach in the diagnosis of gliomatosis cerebri using carbon-11-L-methionine positron emission tomography. *J. Nucl. Med.* 32:726–728
- Patronas, N.J., Brooks, R.A., DeLaPaz, R.L., Smith, B.H., Kornblith, P.L., and Di Chiro, G. (1983) Glycolytic rate (PET) and contrast enhancement (CT) in human cerebral gliomas. *AJNR Am. J. Neuroradiol.* 4:533–535
- Paulus, W., and Peiffer, J. (1989) Intratumoral histologic heterogeneity of gliomas. A quantitative study. *Cancer* 64:442–447
- Pirotte, B., Goldman, S., Salzberg, S., Wikler, D., David, P., Vandesteene, A., Van Bogaert, P., Salmon, I., Brotchi, J., and Levivier, M. (2003) Combined positron emission tomography and magnetic resonance imaging for the planning of stereotactic brain biopsies in children: experience in 9 cases. *Pediatr. Neurosurg.* 38:146–155
- Pirotte, B., Goldman, S., Massager, N., David, P., Wikler, D., Vandesteene, A., Salmon, I., Brotchi, J., and Levivier, M. (2004) Comparison of 18F-FDG and 11C-methionine for PET-guided stereotactic brain biopsy of gliomas. *J. Nucl. Med.* 45:1293–8
- Pirotte, B., Goldman, S., Van Bogaert, P., David, P., Wikler, D., Rorive, S., Brotchi, J., and Levivier, M. (2005) Integration of [11C]methionine-positron emission tomographic and magnetic resonance imaging for image-guided surgical resection of infiltrative low-grade brain tumors in children. *Neurosurgery* 57:128–139
- Weber, W.A., Wester, H.J., Grosu, A.L., Herz, M., Dzewas, B., Feldmann, H.J., Molls, M., Stocklin, G., and Schwaiger, M. (2000) O-(2-[18F] fluoroethyl)-L-tyrosine and L-[methyl- 11C] methionine uptake in brain tumours: initial results of a comparative study. *Eur. J. Nucl. Med.* 27:542–549
- Wienhard, K., Herholz, K., Coenen, H.H., Rudolf, J., Kling, P., Stocklin, G., and Heiss, W.D. (1991) Increased amino acid transport into brain tumors measured by PET of L-(2- 18F) fluorotyrosine. *J. Nucl. Med.* 32:1338–1346
- Wong, T.Z., Van der Westhuizen, G.J., and Coleman, R.E. (2002) Positron emission tomography imaging of brain tumors. *Neuroimag. Clin. N. Am.* 12:615–626



*This page intentionally left blank*

# 17

## Hemorrhagic Brain Neoplasm – $^{99m}\text{Tc}$ -Methoxyisobutyl Isonitrile-Single Photon Emission Computed Tomography

Filippo F. Angileri, Fabio Minutoli, Domenico La Torre, and Sergio Baldari

### INTRODUCTION

Contrast-enhanced computed tomography (CT) or magnetic resonance imaging (MRI) are the first examinations usually performed in patients suspected of brain neoplasm. However, although these morphological imaging techniques are quite sensitive in identifying lesions and provide an accurate evaluation of their extension, they still remain unable to answer all questions that clinicians consider to be crucial for brain tumors management.  $^{99m}\text{Tc}$ -methoxyisobutylisonitrile-single photon emission computed tomography (SPECT) can answer many of these questions.

### RADIOPHARMACEUTICAL AND TECHNICAL ISSUES

Methoxyisobutylisonitrile (MIBI) is a technetium labeled compound introduced as an alternative to  $^{201}\text{Tl}$  for myocardial perfusion imaging. MIBI is provided in a kit vial containing a lyophilized mixture. It is labeled by adding an adequate amount of  $^{99m}\text{TcO}_4^-$  to the vial and warming the mixture in a bath of boiling water for 10 min. Labeling efficiency is  $>90\%$  and MIBI can

be used for 6 h after its constitution. MIBI is a lipophilic cation (net charge of  $1^+$ ) which, after cellular entry, is trapped inside the mitochondria of metabolically active cells in relationship to the negative potential of the inner mitochondrial membrane; its retention in the mitochondria is not organ specific and appears to be a mechanism common to most tissues. MIBI uptake seems to occur passively as shown by the poor correlation between cellular MIBI uptake and ATP depletion (Filippi et al. 2005). Because MIBI is accumulated by cells with high metabolic activity, it is very suitable to be used in oncology. Furthermore, because of its optimal physical characteristics, compared with  $^{201}\text{Tl}$ -SPECT,  $^{99m}\text{Tc}$ -MIBI-SPECT yields sharp and well-contrasted images with clearer delineation of the margin of the tumor. MIBI is almost totally excluded from normal brain accumulation by the blood-brain barrier (BBB), whereas it is strongly taken up by choroid plexus (this uptake cannot be inhibited by potassium perchlorate). This may be a disadvantage because of possible interference with lesions lying close to the ventricle, although it offers a useful landmark for lesion localization. The dual integrated imaging modality SPECT/CT could be of

value in obtaining a more precise anatomical localization (Townsend and Cherry 2001), allowing an easier distinction between disease and physiological uptake, thus, improving the diagnostic accuracy of SPECT findings.

In brain lesions, the initial distribution of  $^{99m}\text{Tc}$ -MIBI seems to reflect mainly BBB disruption. However, many different factors as the cationic charge and lipophilic properties of the radiopharmaceutical, the lesional vascular supply and the increased membrane potential, mitochondrial content, density and proliferation rate (MIBI uptake correlates with the proliferative activities of gliomas, estimated by quantification of Ki-67 antigen expression) of viable tumoral cells play an important role in tumors MIBI uptake (Baldari et al. 2002; Nagamachi et al. 2001).

In adults, SPECT images are acquired 10 min (early images) after i.v. injection of 740 MBq (20 mCi) of  $^{99m}\text{Tc}$ -MIBI. Often, images are acquired also 3 h (delayed images) after radiopharmaceutical administration. With a dual-headed gamma camera the following parameters can be used: circular orbit, high resolution collimators,  $128 \times 128$  matrix,  $360^\circ$  rotation,  $3^\circ$  step-and-shoot technique, acquisition time of 25 s per frame. The data are processed, after a ramp filtered back-projection and an attenuation correction, using a low-pass filter. The data are displayed in the transaxial, sagittal and coronal slices, followed by orbitomeatal line reorientation of the reconstructed volume.

$^{99m}\text{Tc}$ -MIBI-SPECT studies should be evaluated visually and semiquantitatively. In fact, although a qualitative analysis can be satisfactory (a study should be considered negative when absent or faint increased activity is seen, and positive

when there is clear increased tracer uptake compared to the contralateral side), MIBI tumor uptake is usually also evaluated semiquantitatively by determining MIBI index. It is defined as the ratio between tumor activity and counts measured in a normal structure. Various methods have been described to evaluate this parameter. In particular, different reconstruction filters and modalities of drawing tumor and control regions of interest (ROIs) have been proposed. In addition, different structures as cerebral cortex, pituitary gland, lung, skull, and choroid plexus have been used as control regions. In recent studies, MIBI index is determined as the ratio between tumor activity and counts in a mirrored region in an uninvolved cerebral area (early ratio (ER)): after spatial localization of the lesion, using morphological imaging as a guide, a round shaped ROI should be drawn encompassing the maximum uptake area in the lesional region; MIBI index is obtained as the ratio of counts in the "lesion ROI" to the counts in its contralateral homologous "mirror image". If the control ROI is close to the scalp or the choroid plexus or a midline located lesion is revealed, the control ROI should be drawn on an uninvolved cerebral parenchymal area. In addition, the delayed ratio (DR) (i.e., the ratio between tumor activity and counts in the control area after a few hours; generally 3 h) and the retention index (RI) (i.e., the ratio between delayed ratio and early ratio) can be determined (Baldari et al. 2002).

Because MIBI index values consistently change using different methods for images acquisition and reconstruction and for semiquantitative analysis, it is important that each Center always use the same procedure. Moreover, it is very important

to encircle within the tumor ROI only the hottest part of the tumor in order to assess the degree of MIBI uptake in the region of the tumor with the most probability of malignancy. On the other hand encircling the entire tumor could be preferable in monitoring therapy effects.

Recently, a new lipophilic complex known as tetrofosmin (1,2-bis [bis (2-ethoxyethyl) phosphino] ethane) has been developed for myocardial perfusional scintigraphy. Its mechanism of accumulation is similar to that of MIBI, thus representing a potential substitute for imaging of various tumors, including cerebral neoplasms. To date only few studies of cerebral lesions with tetrofosmin exist. Like MIBI, tetrofosmin is almost excluded from cerebral parenchyma by BBB and it is strongly accumulated by choroid plexus. With respect to MIBI, it has the technical advantage of an easier labeling with technetium, because it is not necessary to heat the radiopharmaceutical (Filippi et al. 2005).

### $^{99m}\text{Tc}$ -MIBI-SPECT IN BRAIN TUMORS EVALUATION

Functional imaging is widely applied in diagnosis and follow-up of brain tumors. Because MIBI uptake is related not only to BBB disruption, as contrast enhancement on CT and MR scans, but also to the tumoral metabolic activity,  $^{99m}\text{Tc}$ -MIBI-SPECT assists tumor grading evaluation, biopsy localization, and therapy monitoring, and permits differentiation of tumor recurrence from radiation necrosis.  $^{99m}\text{Tc}$ -MIBI-SPECT shows 67% sensitivity and 100% specificity in detecting intracranial tumors, especially gliomas (O'Tuama et al. 1993). Lesions localization is very impor-

tant because lesions are more easily detected in the fronto-parietal area than in the temporal lobes or in the posterior fossa, because of the presence of high non-specific uptake. Furthermore, very small lesions cannot be detected because of the limited resolving power of the SPECT technique.

It has been demonstrated that MIBI uptake is independent of the extent of the tumor as determined by morphological imaging; on the other hand, a trend between MIBI uptake and the grade of the glioma has been found (Bagni et al. 1995). MIBI uptake is higher in high grade gliomas, in glioblastoma multiforme, lymphoma and metastases; however, its uptake is not limited to malignant brain tumors but can also be seen in ipervascular benign tumors such as meningiomas and neurilemmomas. Low grade brain tumors show low or no uptake of MIBI. In such cases, positron emission tomography (PET) using  $^{11}\text{C}$ -methionine (accumulated in neoplastic lesion and not in normal parenchyma) should be used for imaging; low grade tumors, infact, may be overlooked by  $^{18}\text{F}$ -FDG-PET because of a low target to background uptake ratio due to the physiological uptake of FDG by normal brain tissue. However, PET is presently not widely available, because it is characterized by high cost, and because of the short physical half life of  $^{11}\text{C}$ , a cyclotron should be locally available. SPECT, on the other hand, is less expensive and largely available.

A variable MIBI uptake pattern may be determined by inhomogeneity of cellular distribution (e.g., presence of cystic areas in the tumor) and/or the presence of regressive phenomena as occurs in glioblastoma. Small alterations to the BBB, as demonstrable by the lack of contrast enhancement

on CT scan or MR imaging, can be responsible for low MIBI accumulation also in tumors with high cellular density and lack of regressive phenomena (Bagni et al. 1995). For the same reason, in the case of gliomas, MIBI does not accumulate in tumor cells that extensively invades into the brain adjacent to the contrast enhanced lesion.

$^{99m}\text{Tc}$ -MIBI-SPECT is helpful in the differential diagnosis of brain lesion in patients affected by AIDS. In such cases CT or MR imaging are not able to discriminate between lymphoma and several different non neoplastic lesions (mainly toxoplasmosis or tuberculomas).  $^{99m}\text{Tc}$ -MIBI-SPECT has 100% sensitivity and 69% specificity in revealing lymphoma; false-positive studies are frequently caused by toxoplasmosis healing after medical treatment (Naddaf et al. 1998). Due to the capability to reveal the most metabolically active area of brain lesions (i.e., the probably most malignant part of the lesion),  $^{99m}\text{Tc}$ -MIBI-SPECT can be used as a guide for biopsies. Furthermore, the degree of MIBI uptake is a reliable indicator of the tumor aggressiveness, permitting prognostic evaluations. The degree of MIBI uptake, in fact, inversely correlates with the patient survival rate.  $^{99m}\text{Tc}$ -MIBI-SPECT is predictive of patients survival also after treatment. Using  $^{99m}\text{Tc}$ -MIBI-SPECT within 10 days after radiation therapy, it is possible to detect tumor presence better than CT and to determine the “metabolic tumor volume”, which represents a reliable prognostic factor. Moreover, measuring “tumour bulk” by  $^{99m}\text{Tc}$ -MIBI-SPECT can provide a useful index of viable tumor size in evaluating early tumor response and during ongoing chemotherapy (Beauchesne et al. 2004).

Predicting tumor response to chemotherapy is a very interesting field in which  $^{99m}\text{Tc}$ -MIBI-SPECT seems to be effective, because of the close relationship between efflux of MIBI from tumoral cells and MDR-1 gene expression. MDR-1 is a gene located on chromosome 7 codifying for Pgp, a 170 Kda plasma-membrane glycoprotein, observed in capillary endothelial cells of normal brains and in several human tumors. Pgp acts as an energy dependent efflux pump for several antineoplastic agents, resulting in multidrug resistance. Because MIBI is also effluxed from tumoral cells by Pgp, it has been concluded that MIBI wash-out could reflect the presence of Pgp.

$^{99m}\text{Tc}$ -MIBI-SPECT has been proposed for evaluation of multidrug resistance phenotype in brain tumors by determining tumoral RI (Yokogami et al. 1998). However, the RI of MIBI is significantly lower than that of  $^{201}\text{Tl}$  (not a substrate for Pgp) in metastatic brain tumors, but not in malignant gliomas, so Pgp seems not to be the main cause of chemoresistance in these primary brain tumors.

In brain tumors follow-up, it is often impossible to separate, clinically or by CT or standard MR imaging, recurrent tumor from radiotherapy- or chemotherapy-induced brain damage. Although presently PET with  $^{18}\text{F}$ -FDG represents the standard of reference in this field,  $^{99m}\text{Tc}$ -MIBI-SPECT is characterized by high sensitivity, specificity, accuracy, and very high positive predictive value (PPV) (98%), and appears to have complementary roles in the assessment of tumor activity and the decision of an inevitable biopsy site.  $^{99m}\text{Tc}$ -MIBI-SPECT imaging shows accumulation in malignant tumor and lack of radiotracer accumulation despite contrast enhance-

ment on CT or MR imaging in radiation necrosis. In a recent study (Jeune et al. 2005), 81 patients treated for brain gliomas underwent 201 <sup>99m</sup>Tc-MIBI-SPECT examinations. Authors reported 91% and 89% sensitivity, 100% and 83% specificity and 95% and 87% accuracy for tumor recurrence of low and high grade glioma, respectively. <sup>99m</sup>Tc-MIBI-SPECT allowed the diagnosis of anaplastic progression of low grade gliomas sometimes earlier than clinical or MR imaging signs. False-positive cases (3/81 patients) were due to an inflammatory reaction after radiosurgery in two patients and remained with no explanation in one patient. False-negative cases (5/81 patients) occurred in patients with deep periventricular lesion (n = 1), temporal tumors (n = 2) or lesions with no contrast enhancement on MR imaging (n = 2). <sup>99m</sup>Tc-MIBI-SPECT is better than CT or MR imaging, except a low, negative predictive value (NPV); this limitation can be withdrawn by coupling SPECT and CT results. The combined test have 100% sensitivity, 75% specificity, 96% accuracy, 96% PPV, and 100% NPV (Maffioli et al. 1996).

### <sup>99m</sup>Tc-MIBI-SPECT IN HEMORRHAGIC BRAIN NEOPLASM

During daily clinical practice, it is important to remember that a neoplasm can be hidden behind an intraparenchymal brain hemorrhage (ICH). In fact, ~7% of ICHs are due to an underlying neoplasm. On the other hand, some hemorrhagic non-neoplastic lesions may mimic neoplastic lesions. Five to 10% of all brain tumors develop hemorrhage of some type because of fast-growing and high vascularization with an

irregular and fragile vascular architecture. Bleeding is the first clinical sign of neoplastic disease in 9–58% of patients harboring hemorrhagic neoplasms. Both metastatic tumors and primary brain tumors may cause intracranial hemorrhage. Metastatic lesions, including melanoma, bronchogenic carcinoma, choriocarcinoma, and hypernephroma are known to carry a high risk of hemorrhage. Of the primary brain tumors, glioblastoma appears to be the most common source of ICH. Oligodendrogliomas also have a predilection for hemorrhage and do so more frequently than astrocytomas. Ependymomas and medulloblastomas also have been associated with ICH. Benign extraaxial tumors rarely hemorrhage. In this group, pituitary adenomas and meningiomas are the lesions most likely to develop this complication.

The tumoral origin of cerebral hematoma is not always correctly diagnosed by CT and MR imaging even after intravenous contrast medium administration. The high density of blood on CT and the varied appearance of hemoglobin products on MR imaging may obscure the presence of an underlying neoplasm (Chan and Peh 1999). In addition, lesion enhancement may be indistinguishable from contiguous hemorrhagic areas of intrinsically high density or increased signal intensity (Gaul et al. 1996; Hanna et al. 1991). Moreover, on neuro-radiologic imaging, the diagnosis of neoplasm-related hemorrhage is frequently based on evolution patterns, being delayed hematoma evolution, persistent edema, and diminished, irregular, or absent hemosiderin deposition signs of neoplastic ICH. Thus, a complex diagnostic protocol is frequently needed and a significantly delayed diagnosis can occur (Minutoli et al. 2003).

Positron emission tomography (PET) scanning with  $^{18}\text{F}$ -FDG and  $^{11}\text{C}$ -methionine have been proposed as diagnostic tools for the differential diagnosis of ICH but results in clinical series were not conclusive. Dethy et al. (1994) concluded that PET studies with these tracers were not helpful in distinguishing neoplastic and non-neoplastic intracerebral hemorrhage. Other authors suggested that  $^{11}\text{C}$ -methionine-PET could distinguish neoplastic from non-neoplastic hematomas on the basis of differences in lesion extent compared with CT or MR imaging findings. Disadvantages of this method could be the high cost of the examinations and the poor availability of PET scanners (Ogawa et al. 1995).

We performed  $^{99\text{m}}\text{Tc}$ -MIBI-SPECT on patients suspected of harboring a neoplastic bleeding according to standard clinical and neuroradiologic criteria. As mentioned above,  $^{99\text{m}}\text{Tc}$ -MIBI has been used as an imaging SPECT agent for various neoplasms, including brain tumors. High-grade astrocytomas, glioblastomas multiforme, metastases, intracranial meningiomas, and neurilemmomas show high  $^{99\text{m}}\text{Tc}$ -MIBI uptake. On the other hand, non-neoplastic lesions show no or low  $^{99\text{m}}\text{Tc}$ -MIBI accumulation. These characteristics make  $^{99\text{m}}\text{Tc}$ -MIBI-SPECT an ideal tool to study atypical ICHs of suspected neoplastic etiology. In a recent study, we evaluated 29 patients harboring an acute onset of clinical deterioration caused by ICH (Minutoli et al 2003). Patients were enrolled according to the following inclusion criteria: (1) nontraumatic acute onset of neurologic deterioration occurred; (2) a ICH was demonstrated by emergency CT scan; (3) clinical data (young age, negative medical history for arterial hypertension, diabetes, drug abuse, and anticoagulant or antiplatelet medica-

tion therapy) or findings on emergency CT scan (atypical location, irregular shape, disproportional large edema) could be compatible with a neoplastic hemorrhage; (4) the patient did not have any known brain neoplasm; (5) a single lesion was evident on brain CT scan; and (6) emergent craniotomy was not required. Patients with pituitary, pure subarachnoid, and pure intraventricular hemorrhage were excluded. All patients in that study underwent  $^{99\text{m}}\text{Tc}$ -MIBI-SPECT within 48 h from the clinical onset. Independently from  $^{99\text{m}}\text{Tc}$ -MIBI-SPECT findings, patients underwent a neuroradiologic protocol constituted by an early standard MR examination and one or more additional MR examinations if required by non-definitive diagnosis. Other neuroradiologic examinations such as digital subtraction angiography or enhanced CT scan were obtained if needed. Patients were followed-up until a definitive diagnosis was obtained. Images were acquired 10 min (early images) and 3 h (delayed images) after intravenous injection of 740 MBq (20 mCi) of  $^{99\text{m}}\text{Tc}$ -MIBI. Visual and semiquantitative analysis were performed.

Among 29 patients studied, in 19 cases (65.5%) a non-neoplastic hemorrhage was diagnosed, and in ten cases (34.5%) a neoplastic etiology was demonstrated. Visual analysis of early images showed no focal increased tracer uptake in all non-neoplastic hemorrhages (Figure 17.1), whereas it showed a focal increased tracer uptake in all neoplastic lesions (Figure 17.2). Sensitivity, specificity, accuracy, PPV, and NPV in revealing neoplasm-related ICH by means of  $^{99\text{m}}\text{Tc}$ -MIBI-SPECT were 100%. The semiquantitative analysis showed a wide cutoff in the ER between neoplastic hemorrhages and non-neoplastic hemorrhages; however, it was of no help

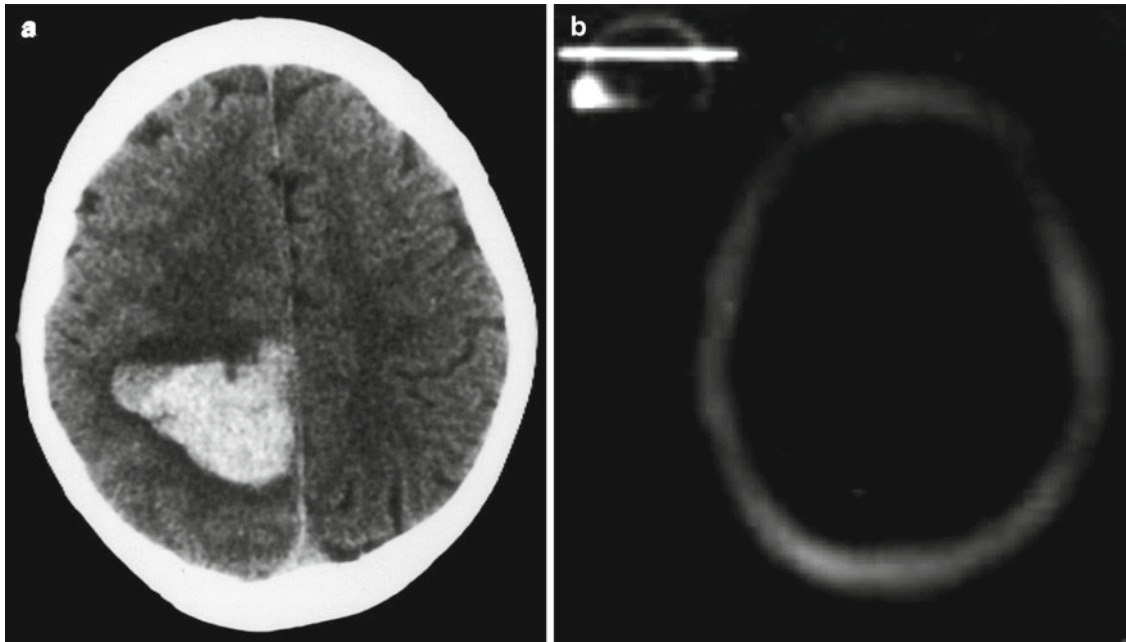


FIGURE 17.1. **(a)** Emergency CT scan in a patient with sudden onset of headache and mild left hemiparesis, showing an atypically located brain hematoma in a 42-year old male patient. **(b)**  $^{99m}\text{Tc}$ -MIBI SPECT, obtained within 2 days from the symptoms onset, shows no areas of pathological MIBI accumulation. The lesion was thought to be a benign hematoma. Two years follow-up confirmed this hypothesis

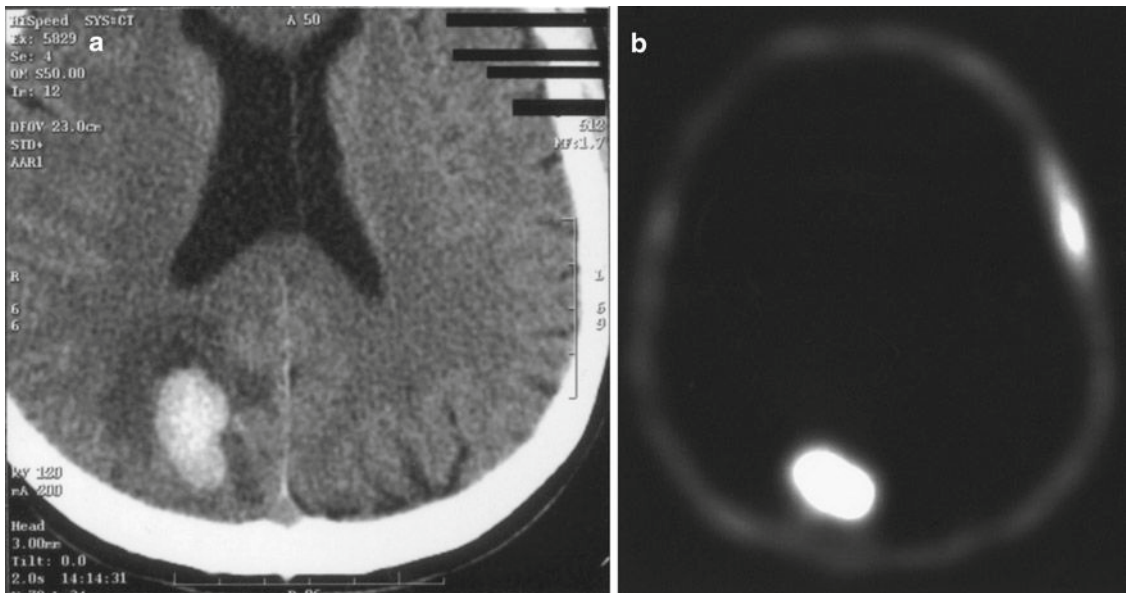


FIGURE 17.2. **(a)** Emergency CT scan obtained after sudden onset of drowsiness and left hemiparesis, showing a brain hematoma atypically located in the right parieto-occipital region in a 56 year-old male patient without vascular risk factors. The lesion is surrounded by moderate edema. **(b)** On  $^{99m}\text{Tc}$ -MIBI SPECT, obtained 24 h after CT scan, the lesion shows very high MIBI uptake. After MR imaging, that was not conclusive nor for malignant etiology or for benign hematoma, the patient underwent surgery and pathological analysis of the excised lesion revealed hemorrhagic glioblastoma multiforme



in the discrimination of neoplastic ICHs, because visible lesions on early images were neoplastic and invisible ones were non-neoplastic. Thus, we believe that visual analysis of early SPECT images alone can be satisfactory in the evaluation of suspected neoplastic hemorrhagic lesions.

It can be hypothesized that  $^{99m}\text{Tc}$ -MIBI accumulation in neoplastic ICH correlates to the pre-existing BBB disruption and the presence of metabolically active neoplastic cells, whereas in non-neoplastic hematomas the absence of metabolically active cells in acute phase are responsible for the lack of  $^{99m}\text{Tc}$ -MIBI accumulation independently by the BBB integrity. The major limitation of the study was the lack of ICHs related to low grade gliomas. It is well known that such lesions do not show  $^{99m}\text{Tc}$ -MIBI uptake, thus this feature can lead to a potential false-negative. Moreover, in our experience  $^{99m}\text{Tc}$ -MIBI-SPECT is not able to distinguish between different etiologies in the non-neoplastic ICH group. Nevertheless,  $^{99m}\text{Tc}$ -MIBI-SPECT appears as a reliable tool in the early differential diagnosis of ICH, suspected of neoplastic etiology.

Because ICH may reach clinical attention or may undergo  $^{99m}\text{Tc}$ -MIBI-SPECT in the subacute phase and the neuropathologic features of ICH significantly change over time, we decided to investigate the appearance of non-neoplastic ICH on early and delayed  $^{99m}\text{Tc}$ -MIBI-SPECT examinations and to determine how the timing of the examination can affect the reliability of  $^{99m}\text{Tc}$ -MIBI-SPECT in differentiating neoplastic from non-neoplastic ICH (Minutoli et al. 2005).

Enzmann et al. (1981) categorized, in a canine model, the evolution of intracerebral hemorrhage into four stages: acute, subacute, capsule, and organization. In the acute stage (days 1–3), only mild

perivascular inflammatory reaction and a narrow zone of neuron death may occur. In the subacute stage (days 4–8), inflammation peaks, foamy macrophages and fibroblasts appear peripherally, and reactive astrocytes appear in the surrounding brain. During the capsule stage (days 9–13), macrophages and fibroblasts increase and vascular proliferation begins to encroach on the hematoma from the periphery. At the same time, inflammation regresses and reactive astrocytosis becomes pronounced. The formation of a dense capsule at the edge of the hematoma and a less organized collagen proliferation in the center of the hematoma occurs in the organization stage (days 13 and on).

Patient harboring non traumatic (typical and atypical) ICH were consecutively enrolled and randomly divided into four groups. Patients in the first group underwent  $^{99m}\text{Tc}$ -MIBI-SPECT 2 days after the onset of clinical symptoms. Patients in the second, third, and fourth groups underwent  $^{99m}\text{Tc}$ -MIBI-SPECT 5, 10, and 30 days, respectively, after the clinical onset. Furthermore, patients in the first group underwent a second  $^{99m}\text{Tc}$ -MIBI-SPECT examination 30 days after the neurological deterioration onset. Both visual and semi-quantitative analysis were conducted for each  $^{99m}\text{Tc}$ -MIBI-SPECT in all patients. The neuroradiologic and clinical follow-up of these patients was the same as in the previous study and was independent from the  $^{99m}\text{Tc}$ -MIBI-SPECT results. At the end of the study two patients were excluded because a neoplastic ICH was diagnosed and the analysis was limited to 30 patients. Visual analysis showed no focal increased tracer uptake (0% positive findings) in group 1 (day 2). In group 2 (day 5), visual analysis showed increased tracer uptake in 14% (1/7) of the patients. In group 3 (day

10), visual analysis showed increased tracer uptake in 62.5% (5/8) of the patients (Figure 17.3). In group 4 (day 30), visual analysis showed increased tracer uptake in 71% (5/7) of the patients.

MIBI indexes of non-neoplastic ICHs ranged from 0.95 to 1.1 (mean,  $1.03 \pm 0.06$ ) in group 1, from 0.96 to 1.7 (mean,  $1.14 \pm 0.26$ ) in group 2, from 1 to 1.9 (mean,  $1.39 \pm 0.35$ ) in group 3, and from 1.08 to 2.3 (mean,  $1.64 \pm 0.45$ ) in group 4. All patients in group 1, who showed no focal increased radiotracer uptake at 2 days after the onset of clinical symptoms, showed significant  $^{99m}\text{Tc}$ -MIBI accumulation when studied at 30 days after the neurological deterioration onset. This study shows that the reliability of  $^{99m}\text{Tc}$ -MIBI-SPECT in revealing neoplastic ICH significantly decreases as the time between bleeding and examination

increases. These data demonstrate that neuropathologic changes that occur over time in non-neoplastic brain hematoma influence radiotracer accumulation on  $^{99m}\text{Tc}$ -MIBI-SPECT. Thus, non-neoplastic ICH showing no early  $^{99m}\text{Tc}$ -MIBI uptake after clinical onset may change its behavior later. This concept is particularly supported by our results in patients who underwent two different SPECT examinations, at 2 days and at 30 days, because no reasonable hypothesis other than the timing of the examination could explain the difference in the appearance of non-neoplastic ICH in these examinations.

On  $^{99m}\text{Tc}$ -MIBI-SPECT examinations with positive findings, many non-neoplastic hematomas showed a ring-like pattern of accumulation (Figure 17.3). This pattern, even if not specific for non-neoplastic ICH,

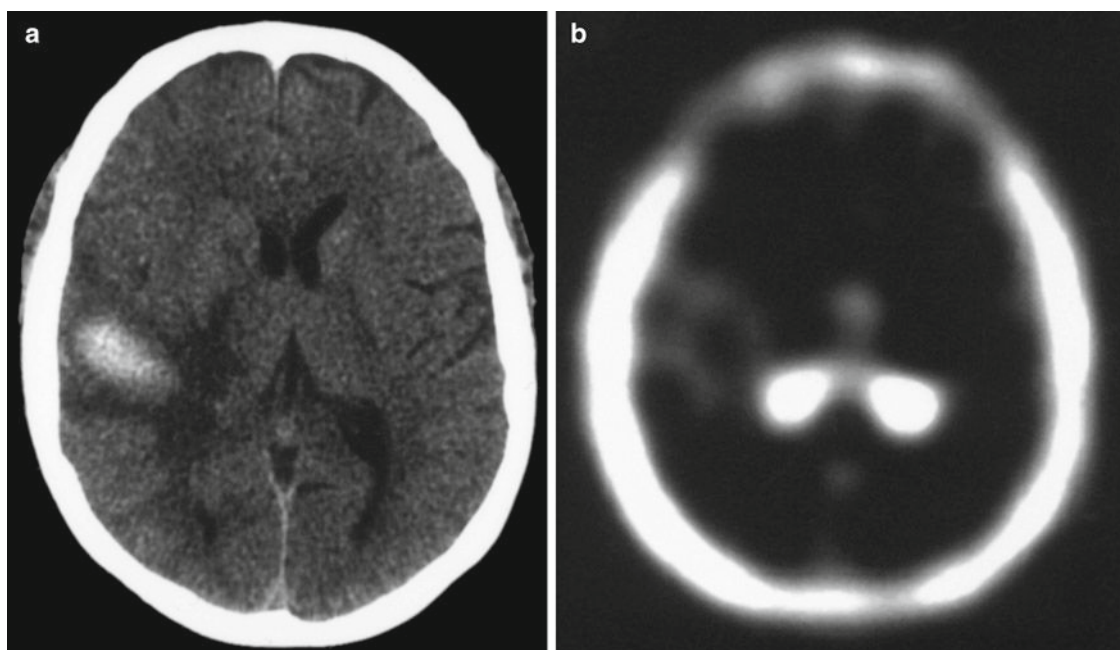


FIGURE 17.3. (a) CT scan obtained 9 days after onset of headache not responsive to standard therapy and progressively worsening, shows an atypically located brain hematoma in the right temporal region in a 52 year-old female patient without vascular risk factors. The lesion is surrounded by moderate edema. (b)  $^{99m}\text{Tc}$ -MIBI SPECT, obtained 10 days after symptoms onset, reveals a ring-like MIBI accumulation in the lesional area. One year follow-up suggests the diagnosis of benign brain hematoma

could be explained by peripheral accumulation of metabolically active cells. Ring-like radiotracer accumulation in brain hematomas is not completely surprising because it has been previously reported in a few patients imaged with  $^{201}\text{Tl}$  (Kinuya et al 2002) or  $^{11}\text{C}$ -methionine (Dethy et al. 1994; Ogawa et al. 1995), and is similar to the ring enhancement that can be seen on CT scans.

It is suggested that  $^{99\text{m}}\text{Tc}$ -MIBI-SPECT, together with neuroradiologic imaging, can play a role in the early non invasive diagnostic work-up of hemorrhagic brain lesions, allowing a clear differentiation between neoplastic and non-neoplastic ICHs. The reliability of this examination decreases over time and non-neoplastic ICH, showing no  $^{99\text{m}}\text{Tc}$ -MIBI uptake within 2 days, can accumulate  $^{99\text{m}}\text{Tc}$ -MIBI on more delayed imaging. Thus,  $^{99\text{m}}\text{Tc}$ -MIBI-SPECT can clearly differentiate between neoplastic and non-neoplastic ICH only in the acute phase. Our findings suggest that the examination should be performed early after symptoms onset and certainly within 5 days.

## REFERENCES

- Bagni, B., Pinna, L., Tamarozzi, R., Cattaruzzi, E., Marzola, M.C., Bagni, I., Ceruti, S., Valentini, A., Zanasi, A., Mavilla, L., Guerra, P.U., and Merli, A.G. (1995) SPET imaging of intracranial tumours with  $^{99\text{Tc}}\text{m}$ -sestamibi. *Nucl. Med. Commun.* 16:258–264
- Baldari, S., Restifo Pecorella, G., Cosentino, S., and Minutoli, F. (2002) Investigation of brain tumors with  $^{99\text{m}}\text{Tc}$ -MIBI SPET. *Q. J. Nucl. Med.* 46:336–345
- Beauchesne, P., Pedoux, R., Boniol, M., and Soler, C. (2004)  $^{99\text{m}}\text{Tc}$ -sestamibi brain SPECT after chemoradiotherapy is prognostic of survival in patients with high-grade glioma. *J. Nucl. Med.* 3:409–413
- Chan, J.H., and Peh, W.C. (1999) Methemoglobin suppression in T2-weighted pulse sequences: an adjunctive technique in MR imaging of hemorrhagic tumors. *Am. J. Roentgenol.* 173:13–14
- Dethy, S., Goldman, S., Blečić, S., Luxen, A., Levivier, M., and Hildebrand, J. (1994) Carbon-11-methionine and fluorine-18-FDG PET study in brain hematoma. *J. Nucl. Med.* 35:1162–1166
- Enzmann, D.R., Britt, R.H., Lyons, B.E., Buxton, J.L., and Wilson, D.A. (1981) Natural history of experimental intracerebral hemorrhage: sonography, computed tomography and neuropathology. *Am. J. Neuroradiol.* 2:517–526
- Filippi, L., Santoni, R., Manni, C., Danieli, R., Floris, R., and Schillaci, O. (2005) Imaging primary brain tumors by single-photon emission computerized tomography (SPECT) with technetium-99m sestamibi (MIBI) and tetrafosmin. *Curr. Med. Imag. Rev.* 1:61–66
- Gaul, H.P., Wallace, C.J., and Crawley, A.P. (1996) Reverse enhancement of hemorrhagic brain lesions on postcontrast MR: detection with digital image subtraction. *Am. J. Neuroradiol.* 17:1675–1680
- Hanna, S.L., Langston, J.W., and Gronemeyer, S.A. (1991) Value of subtraction images in the detection of hemorrhagic brain lesions on contrast-enhanced MR images. *Am. J. Neuroradiol.* 12:681–685
- Jeune, F.P., Dubois, F., Blond, S., and Steinling, M. (2005) Sestamibi technetium-99m brain single-photon emission computed tomography to identify recurrent glioma in adults: 201 studies. *J. Neurooncol.* 29:1–7
- Kinuya, K., Ohashi, M., Itoh, S., Yamamoto, K., Sakai, S., Kakuda, K., Nobata, K., Kato, N., Terahara, S., and Taki, S. (2002) Differential diagnosis in patients with ring-like thallium-201 uptake in brain SPECT. *Ann. Nucl. Med.* 16:417–421
- Maffioli, L., Gasparini, M., Chiti, A., Gramaglia, A., Mogioj, V., Pozzi, A., and Bombardieri, E. (1996) Clinical role of technetium-99m sestamibi single-photon emission tomography in evaluating pretreated patients with brain tumours. *Eur. J. Nucl. Med.* 23:308–311
- Minutoli, F., Angileri, F.F., Cosentino, S., Restifo-Pecorella, G., Cardali, S., de Divitiis, O., Germanò, A., and Baldari, S. (2003)  $^{99\text{m}}\text{Tc}$ -MIBI SPECT in distinguishing neoplastic from nonneoplastic intracerebral hematoma. *J. Nucl. Med.* 44:1566–1573
- Minutoli, F., Angileri, F.F., Conti, A., Herberg, A., Aricò, D., Baldari, S., Cardali, S., de Divitiis, O.,

- Germanò, A., and Baldari, S. (2005) Timing of examination affects reliability of <sup>99m</sup>Tc-methoxyisobutylisonitrile SPECT in distinguishing neoplastic from nonneoplastic brain hematomas. *J. Nucl. Med.* 46:574–579
- Naddaf, S.Y., Akisik, M.F., Aziz, M., Omar, W.S., Hirschfeld, A., Masdeu, J., Donnenfeld, H., and Abdel-Dayem, H.M. (1998) Comparison between <sup>201</sup>Tl-chloride and <sup>99m</sup>Tc(m)-sestamibi SPET brain imaging for differentiating intracranial lymphoma from non-malignant lesions in AIDS patients. *Nucl. Med. Commun.* 19:47–53
- Nagamachi, S., Jinnouchi, S., Nabeshima, K., Nishii, R., Flores, L. 2nd, Kodama, T., Kawai, K., Tamura, S., Yokogami, K., Samejima, T., and Wakisaka, S. (2001) The correlation between <sup>99m</sup>Tc-MIBI uptake and MIB-1 as a nuclear proliferation marker in glioma – a comparative study with <sup>201</sup>Tl. *Neuroradiology* 43:1023–1030
- O’Tuama, L.A., Treves, S.T., Larar, J.N., Packard, A.B., Kwan, A.J., Barnes, P.D., Scott, R.M., Black, P.M., Madsen, J.R., Goumnerova, L.C., Sallan, S.E., and Tarbell, N.J. (1993) Thallium-201 versus technetium-99m-MIBI SPECT in evaluation of childhood brain tumours: a within-subject comparison. *J. Nucl. Med.* 34:1045–1051
- Ogawa, T., Hatazawa, J., Inugami, A., Murakami, M., Fujita, H., Shimosegawa, E., Noguchi, K., Okudera, T., Kanno, I., and Uemura, K. (1995) Carbon-11-methionine PET evaluation of intracerebral hematoma: distinguishing neoplastic from non-neoplastic hematoma. *J. Nucl. Med.* 36:2175–2179
- Townsend, D.W., and Cherry, S.R. (2001) Combining anatomy and function: the path to true image fusion. *Eur. Radiol.* 11:1968–1974
- Yokogami, K., Kawano, H., Moriyama, T., Uehara, H., Sameshima, T., Oku, T., Goya, T., Wakisaka, S., Nagamachi, S., Jinnouchi, S., and Tamura, S. (1998) Application of SPET using technetium-99m sestamibi in brain tumours and comparison with expression of the MDR-1 gene: is possible to predict the response to chemotherapy in patients with gliomas by means of <sup>99m</sup>Tc-sestamibi SPET? *Eur. J. Nucl. Med.* 25:401–409

*This page intentionally left blank*

# 18

## Brain Tumor Imaging Using p-[<sup>123</sup>I]Iodo-L-Phenylalanine and SPECT

Dirk Hellwig

### INTRODUCTION

Patient care in neurooncology is mainly based on computed tomography (CT) and nuclear magnetic resonance (NMR) imaging as standard imaging modalities (DeAngelis 2001). Even if these methods are broadly used, there are diagnostic difficulties in the characterization of brain lesions, the definition of tumor extent, the evaluation of the response to therapy, and the detection of tumor progression or recurrence. Radioactive amino acids show an increased uptake into glioma and were introduced to overcome the diagnostic difficulties in brain tumor imaging. Their capability for the visualization of brain tumors is based on their property of accumulation even in low-grade gliomas, without disruption of the blood-brain barrier. This property is valuable in the characterization of cerebral lesions with inconclusive anatomical imaging (Vander Borgh et al. 2006).

For cancer imaging with radioactive amino acids, positron emission tomography (PET) using <sup>11</sup>C-methionine (MET) is mainly used. The short physical half-life of 20 min for carbon-11 limits the use of MET-PET in medical centers equipped with an on-site cyclotron and a PET

scanner. The current development of <sup>18</sup>F-labelled amino acids, especially O-(2-<sup>18</sup>F-fluoroethyl)-L-tyrosine (FET) has shown encouraging results in clinical investigations (Pauleit et al. 2005). Perhaps the clinical use of FET-PET might be possible with a satellite concept supplying the radiopharmaceutical from a central cyclotron unit to peripheral PET imaging sites, but currently FET lacks the necessary approval by legal authorities.

Amino acids labelled with <sup>123</sup>I (physical half-life ~ 13 h) are intended for use with SPECT. The imaging equipment for SPECT and the radiation protection shielding for <sup>123</sup>I are less costly than that for PET imaging. Each department of nuclear medicine possesses a SPECT system, so that a more wide spread use of radioactive amino acids for brain tumor imaging seems possible. L-3-[<sup>123</sup>I]-iodo- $\alpha$ -methyl tyrosine (IMT) was the first radioiodinated amino acid introduced for brain tumor imaging in 1989 and has been used continuously for this purpose. The clinical applications of IMT are well documented in several clinical studies, namely the delineation of the tumor and its infiltration into adjacent brain structures, the differentiation of glioma and non neoplastic

tumors in patients with inconclusive anatomical imaging, non-invasive grading of gliomas, therapy monitoring, and detection of tumor recurrence or progression (Vander Borgh et al. 2006).

IMT shows a characteristic kinetic in primary brain tumors. After intravenous application, IMT is rapidly taken up into glioma. The uptake reaches a maximum of ~10–15 min post-injection with a subsequent washout. So, tumor visualization by IMT-SPECT is limited to the first 45 min after injection. Because blood pool activity is also changing during that time, artefacts may occur during SPECT imaging, because the technique assumes constant tracer concentrations during the acquisition.

To overcome this disadvantage, new radioiodinated amino acids with high affinity for brain tumors were developed. Among these, p-[<sup>123</sup>I]iodo-L-phenylalanine (IPA) shows a tumor uptake comparable to that of IMT. However, its persistent retention in glioma cells may represent a major advantage compared with the radiopharmaceuticals currently available for SPECT tumor imaging. This was demonstrated in preclinical studies (Samnick et al. 2000, 2001) as well as in a pilot study in humans (Samnick et al. 2002). In cell experiments, IMT and IPA showed a rapid uptake into human glioblastoma cells. The uptake of IMT initially exceeds that of IPA and reaches a plateau, whereas with time an increasing uptake of IPA can be observed.

Based on these early results, a first clinical investigation in a larger patient series was performed. The aims of that study were to validate IPA uptake into human brain lesions by SPECT in patients with indeterminate brain lesions or with suspected recurrence or progression of brain tumors, and to evaluate its potential to dif-

ferentiate gliomas and non neoplastic brain lesions. The results of that study were reported in a clinical article (Hellwig et al. 2005). To our knowledge, this subject has not been published elsewhere. In the meantime, the experience with brain tumor imaging using IPA increased in our institution with incrementing patient numbers, mainly confirming the initial results. Below the imaging method and its results in a larger patient cohort are detailed.

## IMAGING METHOD

### Preparation of <sup>123</sup>I-IPA

IPA can be prepared and formulated as reported previously (Samnick et al. 2001, 2002). Sodium [<sup>123</sup>I]iodide for radiolabelling was obtained in the highest obtainable radiochemical purity from Zyklotron AG (Karlsruhe, Germany). A mixture of sodium [<sup>123</sup>I]iodide (500–1,000 MBq in 20–50 µL 0.01N NaOH) and 5 µL aqueous Na<sub>2</sub>S<sub>2</sub>O<sub>5</sub> (4.0 mg Na<sub>2</sub>S<sub>2</sub>O<sub>5</sub>/mL) was evaporated to dryness by passing a stream of nitrogen through a reaction vessel at 100°C, followed by addition of 100 µL of p-bromo-L-phenylalanine hydrochloride (0.25 mg/mL 0.1N H<sub>3</sub>PO<sub>4</sub>), 10 µL aqueous L-ascorbic acid (10 mg/mL) and 5 µL aqueous Cu(I) sulfate (0.10 mol/L). The reaction vessel was heated for 60 min at 160°C in a Heating Module (Pierce) and then cooled, and the mixture was diluted with 150 µL of EtOH. The radioiodinated product was separated from unreacted starting materials, and radioactive impurities by high performance liquid chromatography (HPLC) purification. HPLC was performed on a Hewlett Packard HPLC system consisting of a binary

gradient pump (HP 1100), a Valco 6-port valve with 250- $\mu$ l loop, a variable-wavelength detector (HP 1100) with a UV detection at 254 nm and a sodium iodide scintillation detector (Berthold, Wildbad, Germany), using reversed-phased RP-C<sub>18</sub> column (250  $\times$  4 mm, Nucleosile, Latak) and water/ethanol/acetic acid (89:10:1) as eluent system at 1.1 mL/min. <sup>123</sup>I-IPA (retention time 19.2 min) was obtained in  $88 \pm 5\%$  radiochemical yield. The product fraction was collected in a sterile tube, buffered with 0.6M PP (pH 7.0; Braun) and diluted with water (aq. ad inj.; Braun) to yield an isotonic and injectable radiopharmaceutical after sterile filtration through a 0.22- $\mu$ m sterile membrane (Millex GS, Millipore) in evacuated sterile tubes.

#### Patient Preparation and Administration of <sup>123</sup>I-IPA

Patients should be instructed to fast overnight before an IPA injection. Iodine uptake by the thyroid needs to be blocked to reduce the radiation dose. The recommendation in Germany (area with iodine deficiency) is an oral medication with 900 mg sodium perchlorate (Irenat®, Bayer, Germany), starting on the morning of the examination and lasting for 3 days. A typical activity dose of 250 MBq IPA is recommended. The intravenous administration of the new radiopharmaceutical was well tolerated by all patients. Adverse events were not observed.

#### SPECT Acquisition

The SPECT imaging should start at 30 min, 3 h and, in selected cases, up to 24 h post-injection. In clinical studies, the acquisitions were performed with a triple-

head gamma camera (MultiSPECT 3, Siemens, Erlangen, Germany). The camera was equipped with a low-energy high-resolution collimator using a 20% energy window centered on the 159-keV photopeak of <sup>123</sup>I. System resolution for <sup>123</sup>I was 7.5 mm full-width at half-maximum (FWHM) at 10 cm distance. During a 360° rotation, 120 projections were recorded into a 128  $\times$  128 matrix, corresponding to a pixel size of 3.56 mm. To avoid motion artefacts, a semicircular headholder was attached to the patient's head. Transaxial tomograms were reconstructed using iterative image reconstruction with six subsets and four iterations. The modelling of the system resolution and a first-order attenuation correction according to the method of Chang were included in reconstruction. Post-processing included 3D filtering with a Butterworth filter of fourth order and a cut-off frequency of 1.0 cycles/cm. The in-plane resolution of the reconstructed images was 10 mm FWHM.

Because the image quality of the SPECT images is important for the subsequent registration process, any movement artefact needs to be avoided. We checked every SPECT scan in a cine view mode of the raw data for movements and compensated for it by motion correction tools provided by the image analysis software.

#### Correlative Nuclear Magnetic Resonance Imaging

In our experience, an NMR imaging of the brain is needed for adequate interpretation of IPA-SPECT images. At least a T2 weighted or FLAIR image must be available in digital form for image registration and for reliable scan interpretation. For study reasons, NMR imaging of the brain



was performed in all patients using a 1.5-T scanner (Sonata, Siemens, Erlangen, Germany) or a 1.0-T scanner (Expert, Siemens, Erlangen, Germany). Axial images covering the whole brain with a plane separation of <6 mm were acquired with the fluid attenuated inversion recovery (FLAIR) sequence as well as with T1-weighted contrast-enhanced (T1CE) images.

### Coregistration of SPECT and NMR Images

Image fusion of the NMR images and the corresponding SPECT slices was performed on a HERMES work station (Hermes Medical Solutions, Stockholm, Sweden). During the registration processing, prefiltered NMR images were used with an isotropic 3D Butterworth filter of fifth order, with a cut-off frequency of 1.5 cycles/cm for resolution adaptation of the SPECT images. Supervised automated registration was performed by maximization of mutual information. After the automated registration step, the prefiltering of the NMR image data set was undone.

In our experience, most cases need human interaction after the automated registration process. To check the orientation of NMR and SPECT images, the simultaneous display is important. Misrotations in the transverse plane should be corrected first. A basal slice can be used to adjust blood pool activity in the nasal mucosa in the IPA-SPECT and the corresponding anatomical structures within the nose. Another anatomical structure to be used for transversal alignment is the superior sagittal sinus vein. It can be identified in the IPA-SPECT images due to increased blood pool activity. To register misrotations in the sagittal plane, the nose and the

root of the nose are helpful, as well as the confluens venosum. The eyes can be recognized as areas of low IPA accumulation. In the sagittal plane, this structure together with the shape of the skull, can be used for correction of misrotations in this direction. In a view with frontal slicing, a plane through the eyes can be used for adjustment of coronal misrotations. Once the rotational errors are corrected, the translational positioning is usually rapidly performed. The accuracy of the image registration process was reported to show a translation error of <2.5 mm (mean 1.3 mm) and a misrotation of <1.5° (Hellwig et al. 2005).

### Qualitative Interpretation and Quantitative Image Analysis

Visual interpretation of the IPA-SPECT images should be performed simultaneously with the NMR images after image fusion, especially if there is apparently no increased uptake of IPA. By no means, a negative IPA finding may be reported without image fusion. Because IPA shows an extendedly increased blood pool activity, lesions next to larger blood vessels must be interpreted carefully. The anatomical information needed is obtained from overlaid NMR images.

For the quantitative analysis in our studies, the brain lesions were delineated in the FLAIR images to define a volume of interest (VOI). The same VOI was used for quantification of the early and delayed SPECT studies. A reference region was defined containing normal supratentorial brain tissue without any sign of abnormalities in current NMR images. This region usually encompassed the contralateral structures covered by the VOI mirrored at

the interhemispheric fissure. The maximum count rate in the lesion VOI and the mean count rate in the reference VOI were used to calculate tumor to normal brain ratios (TBR).

## RESULTS OF BRAIN TUMOR IMAGING USING <sup>123</sup>I-IPA

### Initial Evaluation of Suspected Brain Tumors

Whereas the publication on the clinical validation of IPA-SPECT comprised the results in 24 patients at first presentation of a suspected glioma (Hellwig et al. 2005), the current experience in a total of 66 cases is reported here.

We studied 27 men and 37 women aged  $53 \pm 14$  years for the initial evaluation of a suspected glioma. The mean tumor diameter as determined by NMR imaging with the FLAIR sequence was  $4.1 \pm 1.8$  cm. In 30 cases, the T1CE images showed a contrast-enhancing area with a mean diameter of  $2.4 \pm 1.4$  cm. The final diagnosis of a primary brain tumor was established in 50 subjects with 28 low-grade (one WHO grade I, 27 WHO grade II) and 22 high-grade tumors (one WHO grade III, 21 WHO grade IV). Brain metastases originating from lung cancer were present in three cases. Non neoplastic brain lesions were identified in 13 cases with inflammatory and gliotic lesions ( $n = 9$ ), brain dysplasias ( $n = 3$ ) or epidermoid cyst ( $n = 1$ ), which showed contrast enhancement on NMR imaging in four cases. The final diagnosis was verified by stereotactic biopsy ( $n = 34$ ), open resection ( $n = 22$ ), extracranial biopsy ( $n = 1$ ), autopsy ( $n = 1$ ) or serial imaging ( $n = 8$ ).

Figure 18.1 presents an example of a patient with increased uptake of IPA into a high-grade glioma. In this case, some interesting properties of IPA are illustrated. IPA accumulates in brain tumors and shows an increased uptake even into a low-grade glioma. In this patient, the IPA concentration rose especially in the tumor areas without contrast enhancement in the NMR images, suggesting low-grade parts of the glioma. So, in this case, we have a true positive finding with the confirmation *in vivo* that IPA is retained in gliomas.

The findings in a patient with a non neoplastic brain lesion are shown in Figure 18.2. No increased IPA uptake was found in non neoplastic lesions. This case demonstrates the importance of anatomical coregistration and image fusion with NMR images. The blood pool activity in the adjacent parasellar veins and cavernous sinus must not be interpreted as an increased IPA uptake in cerebral structures.

In our series, the IPA-SPECT images in cases of indeterminate brain lesions were interpreted with high concordance by different observers based on visual analysis ( $\kappa = 0.90$ ,  $p < 0.001$ ). Ten false negative findings occurred, mostly in patients with low-grade gliomas, especially in cases with gliomatosis cerebri or patients with tumors exhibiting low cellular density. Similar to the initial results of the published interim analysis (Hellwig et al. 2005) no false-positive findings occurred in the extended patient series. The diagnostic test performance parameters were 80% sensitivity (95% confidence interval [95%CI]: 68–92%), 100% specificity (95%CI: 87–100%), 84% accuracy (95%CI: 74–94%), 100% positive predictive value (95%CI: 95–100%), and 57% negative predictive value (95%CI: 30–84%).

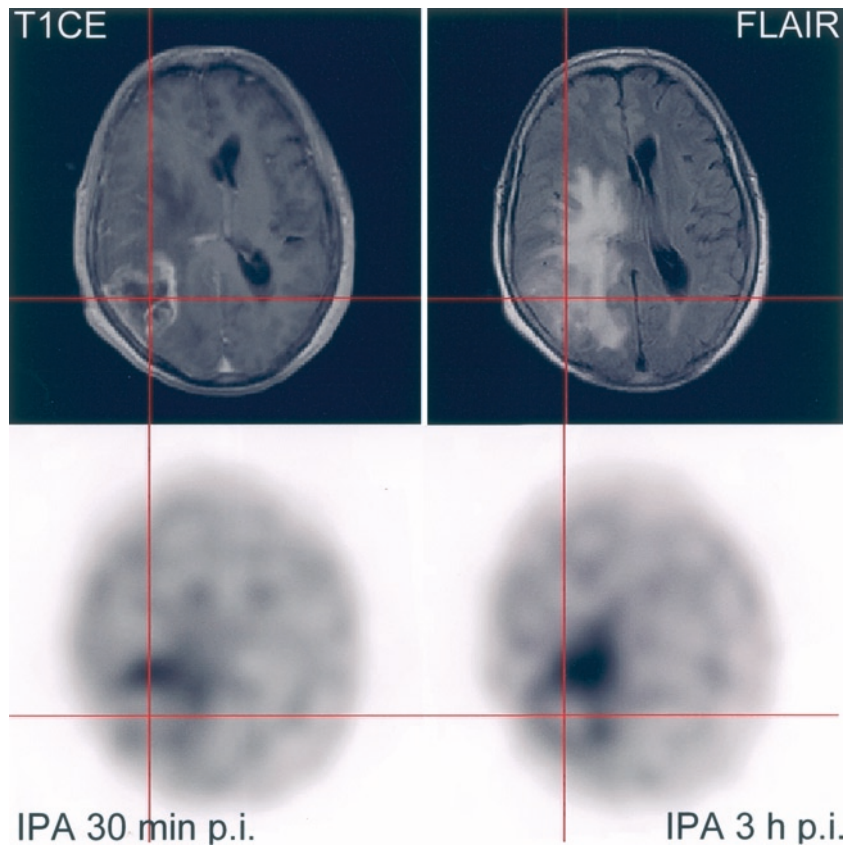


FIGURE 18.1. MRI scans (T1CE and FLAIR) as well as early and delayed IPA-SPECT in a 63 year old female with initial diagnosis of glioblastoma. Note the increasing uptake in the central tumour areas with hyperintensity in FLAIR images without contrast enhancement in T1CE indicating an intact blood-brain-barrier in that area

Quantitative results for patient groups with non neoplastic lesions and different subgroups of malignant brain tumors were similar to that reported in the initial publications. The maximum IPA uptake in primary brain tumors at 30 min and 3 h p.i., was higher than that in non neoplastic brain lesions (30 min p.i.:  $1.69 \pm 0.35$  versus  $1.21 \pm 0.14$ ; 3 h p.i.:  $1.68 \pm 0.42$  versus  $1.19 \pm 0.13$ ,  $p < 0.01$ ).

Contrary to the results in the initial, smaller first patient cohort study (15 patients with glioma), in the subsequent larger patient group with 50 glioma a sig-

nificant difference was observed in the IPA uptake between low-grade and high-grade tumors at 30 min and 3 h p.i. (30 min p.i.:  $1.59 \pm 0.29$  versus  $1.83 \pm 0.38$ ; 3 h p.i.:  $1.53 \pm 0.31$  versus  $1.87 \pm 0.47$ ,  $p = 0.020$ ). The tumoral uptake of IPA was not influenced by the histopathological type of glioma (astrocytoma, oligodendroglioma or oligoastrocytoma), as shown by a multivariate analysis. All brain metastases were contrast enhanced on the T1CE images. Their IPA uptake did not significantly differ from that of non neoplastic lesions.

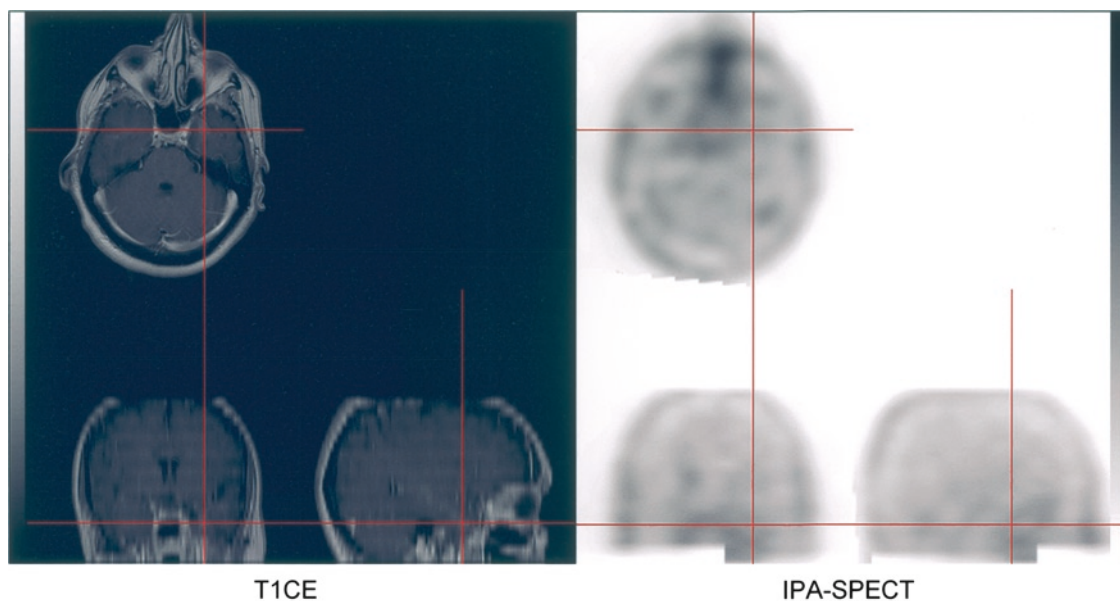


FIGURE 18.2. True negative IPA-SPECT in left mesiotemporal cortical dysplasia. IPA-SPECT showed no increased uptake

#### Evaluation of Suspected Recurrence or Progression

Currently, our experience with patients with recurrent brain tumors is based on results in a population of 33 patients (18 men, 15 women, aged  $45 \pm 12$  years), whereas our initial evaluation included the findings in 21 cases. The final diagnosis was established by biopsy (stereotactic biopsy:  $n = 11$ ; open resection:  $n = 6$ ) or serial imaging ( $n = 16$ ). Persistent or progressive brain tumors were present in 31 cases, comprising four low-grade (all WHO grade II) and 26 high-grade recurrences (WHO grade III:  $n = 12$ , WHO grade IV:  $n = 14$ ). In one single case with previous diagnosis of low-grade glioma, no definite assignment to low or high-grade glioma was possible from the material obtained for confirmation of recurrence. Two non neoplastic necrotic lesions were found in two patients after effective treatment of a glioma. On NMR, these lesions

appeared hyperintense on T2-weighted images without contrast enhancement.

Visual interpretation of IPA-SPECT images in patients with suspected progression and upgrading of a previously treated glioma resulted in highly concordant results ( $\kappa = 0.764$ ,  $p < 0.001$ ). The recurrences and progressions were detected with high sensitivity, but three false negative findings occurred in a WHO grade II and in two WHO grade III tumors. The specificity was high because no false-positive findings occurred. The diagnostic test performance parameters were as follows: 90% sensitivity (95%CI: 79–100%), 100% specificity (95%CI: 37–100%), 91% accuracy (95%CI: 81–100%), 100% positive predictive value (95%CI: 94–100%), and 40% negative predictive value (95%CI: 30–84%). In the quantitative analysis, there was no difference in the IPA uptake of primarily diagnosed gliomas and recurrent brain tumors (30 min p.i.:  $1.67 \pm 0.36$

versus  $1.82 \pm 0.42$ ,  $p = 0.143$ ; 3 h p.i.:  $1.66 \pm 0.41$  versus  $1.78 \pm 0.38$ ,  $p = 0.147$ ).

#### Quantitative Criteria for the Evaluation of Brain Lesions by IPA-SPECT

To derive a quantitative threshold of the IPA accumulation measured as TBR for the differentiation of non neoplastic and neoplastic lesions, an ROC curve was constructed from comparison of the TBR on early SPECT imaging, with the final diagnosis in all patients (initial evaluation or diagnosis of recurrence). The area under the ROC curve was 0.903 (95%CI 0.841–0.965), indicating a high accuracy of this diagnostic test. The shoulder of the curve corresponds to a threshold TBR of 1.30 and confirms the value obtained in the interims analysis (Hellwig et al. 2005). Using this cut-off, the resulting diagnostic test performance parameters were of 85% sensitivity (95%CI: 77–94%), of 80% specificity (95%CI: 57–100%), of 84% accuracy (95%CI: 77–92%), 96% positive predictive value (95%CI: 91–100%), and negative predictive value of 50% (95%CI: 22–78%).

#### Comparison of $^{123}\text{I}$ -IPA and $^{123}\text{I}$ -IMT

Data on repeated SPECT examinations using the radiolabelled amino acids  $^{123}\text{I}$ -IPA and  $^{123}\text{I}$ -IMT in the same patients within 10 days are available (Hellwig et al. 2008b). This intraindividual comparison demonstrated that tumoral uptake of IPA and IMT is strongly correlated within the first hour after injection. The initial contrast of the IMT accumulation exceeds that of IPA, especially in low-grade glioma. This observation explains why the threshold for the differentiation of glioma and non neoplastic lesions is lower for IPA

than IMT (1.30 versus 1.43). Figure 18.3 shows the findings in a patient with the diagnosis of a low-grade glioma. The early IMT-SPECT image shows a clear delineation of the tumor, whereas the initial IPA contrast is clearly lower than that of IMT. The delayed SPECT acquisitions at 3 h post-injection demonstrate the tumoral wash-out of IMT despite a persistent accumulation of IPA in the glioma without evidence of a disruption of the blood-brain barrier (no contrast enhancement in NMR images). Apparently, IPA and IMT differ in their kinetics.

#### Dosimetry of $^{123}\text{I}$ -IPA

The whole body kinetics of IPA is mainly characterized by an early phase of rapid blood clearance, followed by a longer retention in the blood volume and then by renal elimination without any metabolism. The average effective dose caused by the injection of  $^{123}\text{I}$ -IPA was estimated from a dosimetry study in humans with 14.6  $\mu\text{Sv}/\text{MBq}$ . The resulting effective dose for a typical activity of 250 MBq  $^{123}\text{I}$ -IPA is 3.6 mSv (Hellwig et al. 2008a).

## DISCUSSION

p-[ $^{123}\text{I}$ ]iodo-L-phenylalanine (IPA) is a new radioiodinated amino acid with a similar uptake, but longer intracellular retention compared with IMT. In laboratory studies, the feasibility of using IPA-SPECT for brain tumor imaging was demonstrated (Samnick et al. 2000, 2001, 2002). IPA-SPECT was validated in a prospective clinical investigation with a larger patient series with indeterminate brain lesions according to current standards of neuroimaging (Hellwig et al. 2005). No

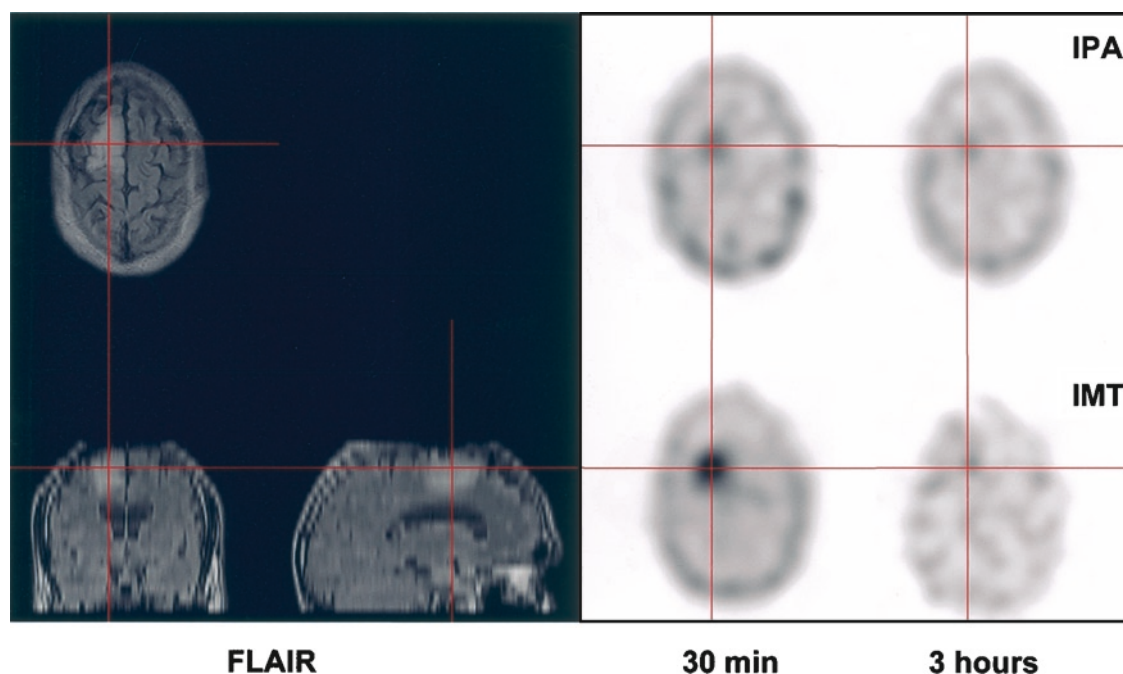


FIGURE 18.3. Intraindividual comparison of <sup>123</sup>I-IPA and <sup>123</sup>I-IPA in a patient with a low-grade glioma (oligoastrocytoma, WHO grade II) using early and delayed SPECT imaging. IMT-SPECT shows intense initial uptake with rapid wash-out, whereas IPA-SPECT demonstrates a lower but persistent retention in the brain tumour. No disruption of the blood-brain barrier was visible in NMR images after injection of contrast agent (not shown)

adverse events were observed after application of <sup>123</sup>I-IPA. Thus, IPA-SPECT can be considered a safe procedure.

It was shown *in vivo* that IPA uptake does not depend on a disruption of the human blood-brain barrier. Because IPA is a molecule that does not easily cross lipid membranes, there must be a carrier-mediated transport system into tumor cells. As previously shown by means of cell experiments, this transport system involves the L and ASC transport system (Samnick et al. 2000), which is also responsible for the tumor uptake of <sup>123</sup>I-IMT, <sup>11</sup>C-MET, and <sup>18</sup>F-FET (Langen et al. 2004). Because IPA accumulates even in tumors without contrast enhancement in T1CE images, IPA differs from non-specific tracers that

visualize the breakdown of the blood-brain barrier only. Thus, IPA tumor uptake is, at least in part, specific.

As suggested by the intraindividual comparison of IPA-SPECT and IMT-SPECT, the clinical experience with IMT-SPECT can be used as a basis for clinical interpretation of IPA-SPECT studies in patients with a brain tumor. The high kappa values for the visual interpretation of IPA-SPECT at initial diagnosis or suspected recurrence of brain tumors indicate a close agreement between different observers.

SPECT imaging has a clearly lower spatial resolution than on NMR imaging. Therefore, image fusion is helpful for precise interpretation of SPECT imaging results. For the best anatomical alignment

of IPA-SPECT and NMR images, the use of a supervised automated image fusion algorithm in all patients is recommended. Standardized NMR imaging was performed at our institution in all patients.

A prolonged retention of IPA in low-grade glioma and high-grade glioma can be observed. The underlying mechanisms remain unclear. A small fraction of up to 10% of IPA radioactivity, however, may enter protein synthesis or intracellular metabolism as suggested by cell experiments (Samnick et al. 2001). One potential mechanism contributing to the prolonged retention of IPA in primary brain tumors might be a continuous input from the plasma, as suggested by the observed blood pool activity on delayed imaging, and by the analysis of blood samples (Samnick et al. 2002). This theory is supported by the fact that no radiolabelled metabolites of IPA were identified in the plasma or urine in rodents or in humans (Samnick et al. 2000, 2002, 2004). Thus, the blood pool signal in the vessels is most likely caused by IPA and not by radioactive metabolites.

Tumor grading is important for the selection of the therapeutic strategy for gliomas (DeAngelis 2001). IPA-SPECT allows the visualization of low-grade as well as high-grade gliomas, and IPA uptake shows a significant difference between low-grade and high-grade tumors. Thus, IPA-SPECT might permit brain tumor grading. Controversial results were reported for the non-invasive grading using IMT-SPECT. Some publications on IMT have reported a significant difference in the IMT uptake of low-grade and high-grade gliomas, and concluded that SPECT with IMT allows non-invasive grading of gliomas (Vander Borgh et al. 2006).

Brain metastases showed no increased IPA uptake. As far as a possible comparison is concerned, given the limited number of patients, this corresponds to the results of IMT-SPECT (Matheja et al. 2000). IMT accumulations were observed in brain metastases; however, a case of a small cell lung cancer metastasis without IMT uptake was also reported.

Using ROC analysis, a cut-off value of 1.30 for the IPA uptake to differentiate gliomas and non neoplastic lesions was determined. The diagnostic performance of prospective visual analysis (80% sensitivity, 100% specificity), as well as the accuracy resulting from ROC analysis (cut-off 1.30, sensitivity 85%, specificity 80%) are comparable with the results of IMT-SPECT obtained in retrospective studies. Even if IMT is the recommended  $^{123}\text{I}$ -labelled amino acid for SPECT imaging of brain tumors (Vander Borgh et al. 2006), there are no prospective studies performed using IMT-SPECT in the evaluation of indeterminate brain lesions at first presentations. This indication can be covered by IPA-SPECT as proven by a prospective trial.

One potential drawback of IPA-SPECT imaging of brain tumors is the limited sensitivity in low-grade gliomas. One of five low-grade gliomas was not detected by IPA-SPECT. Thus, a negative IPA-SPECT cannot exclude the presence of viable glioma (negative predictive value 57% and 40% for evaluation at first presentation and suspected recurrence, respectively). Even if there are no laboratory data on IPA uptake in non neoplastic brain lesions, our recent investigation on IPA in experimental pancreatic tumors and inflammation models in rodents indicates that IPA shows only moderately increased uptake in acute

or chronic inflammation (Samnick et al. 2004). Similar observation for IPA in inflammation have been reported (Lahoutte et al. 2003). This might explain the high specificity of IPA-SPECT. The fact that no false-positive findings occurred with careful image analysis using image fusion techniques, implicates a very high positive predictive value. If IPA-SPECT gives a positive result, the patient is suffering from a primary brain tumor.

## POTENTIAL ADVANCEMENTS

Prospective investigations in vivo confirmed the properties of IPA anticipated on the basis of preclinical studies and human feasibility studies. IPA is a safe radiopharmaceutical for the characterization of brain lesions and visualization of gliomas. The application of the typical radioactivity of 250 MBq <sup>123</sup>I-IPA for a SPECT examination results in an effective dose of 3.6 mSv, well acceptable for a diagnostic procedure in oncology imaging. IPA shows a specific, pertinent uptake even in low-grade tumors without disruption of the blood-brain barrier, but no increased uptake in non neoplastic brain lesions. An intraindividual comparison of IPA-SPECT and IMT-SPECT showed a lower accumulation of IPA in brain tumors than in IMT. IPA-SPECT was validated for the differentiation of indeterminate brain lesions at first presentation in a prospective clinical trial.

The indication “evaluation of indeterminate brain lesions at first presentation” might be covered by IPA-SPECT in upcoming recommendations of brain tumor imaging using labelled amino acid analogues. The current guideline only contains the following indications: detection of viable

tumor tissue, tumor delineation, selection of the best biopsy site, non-invasive tumor grading and therapy planning (Vander Borght et al. 2006).

The presented data obtained in diagnostic studies on IPA-SPECT imaging demonstrated in vivo the persistent accumulation of IPA in brain tumors, especially the low-grade parts of the tumor. Studies in glioma cell cultures and in vivo experiments in rodents proved the concept of radionuclide therapy of glioma by <sup>131</sup>I-IPA (Romeike et al. 2004). The persistence of IPA accumulations in gliomas may be used for a new approach to treat primary brain tumors by internal radionuclide therapy in humans.

This contribution was possible due to my colleagues being committed to our projects, to whom I am thankful, especially to Professor Dr. S. Samnick, Dr. B. Romeike, and Dr. R. Ketter. This work was supported by the “Deutsche Krebshilfe” by Grant 70-3024-He-1.

## REFERENCES

- DeAngelis, L.M. (2001) Brain tumors. *N. Engl. J. Med.* 344:114–123
- Hellwig, D., Ketter, R., Romeike, B.F., Sell, N., Schaefer, A., Moringlane, J.R., Kirsch, C.M., and Samnick, S. (2005) Validation of brain tumour imaging with p-[<sup>123</sup>I]iodo-L-phenylalanine and SPECT. *Eur. J. Nucl. Med. Mol. Imaging* 32:1041–1049
- Hellwig, D., Gouverneur, E., Schaefer, A., Raedle, J., Menges, M., Kirsch, C.M., and Samnick, S. (2008a) Para-[<sup>123</sup>I]iodo-L-phenylalanine in patients with pancreatic adenocarcinoma: tumour uptake, whole-body kinetics, dosimetry. *Nuklearmedizin* 47:220–224
- Hellwig, D., Romeike, B.F., Ketter, R., Moringlane, J.R., Kirsch, C.M., and Samnick, S. (2008b) Intra-individual comparison of p-[<sup>123</sup>I]-iodo-L-phenylalanine and L-3-[<sup>123</sup>I]-iodo-alpha-methyltyrosine for SPECT imaging of gliomas. *Eur. J. Nucl. Med. Mol. Imaging* 35:24–31



- Lahoutte, T., Mertens, J., Caveliers, V., Franken, P.R., Everaert, H., and Bossuyt, A. (2003) Comparative biodistribution of iodinated amino acids in rats: selection of the optimal analog for oncologic imaging outside the brain. *J. Nucl. Med.* 44:1489–1494
- Langen, K.J., and Broer, S. (2004) Molecular transport mechanisms of radiolabeled amino acids for PET and SPECT. *J. Nucl. Med.* 45:1435–1436
- Matheja, P., Rickert, C., Weckesser, M., Palkovic, S., Lottgen, J., Riemann, B., Kopka, K., Kuwert, T., Wassmann, H., Paulus, W., and Schober, O. (2000) Sequential scintigraphic strategy for the differentiation of brain tumours. *Eur. J. Nucl. Med.* 27:550–558
- Pauleit, D., Floeth, F., Hamacher, K., Riemenschneider, M.J., Reifenberger, G., Müller, H.W., Zilles, K., Coenen, H.H., and Langen, K.J. (2005) O-(2-[<sup>18</sup>F]fluoroethyl)-L-tyrosine PET combined with MRI improves the diagnostic assessment of cerebral gliomas. *Brain* 128:678–687
- Romeike, B.F., Hellwig, D., Heimann, A., Kempfski, O., Feiden, W., Kirsch, C.M., and Samnick, S. (2004) Action and efficacy of p-[<sup>131</sup>I]iodo-L-phenylalanine on primary human glioma cell cultures and rats with C6-gliomas. *Anticancer Res.* 24:3971–3976
- Samnick, S., Richter, S., Romeike, B.F., Heimann, A., Feiden, W., Kempfski, O., and Kirsch, C.M. (2000) Investigation of iodine-123-labelled amino acid derivatives for imaging cerebral gliomas: uptake in human glioma cells and evaluation in stereotactically implanted C6 glioma rats. *Eur. J. Nucl. Med.* 27:1543–1551
- Samnick, S., Schaefer, A., Siebert, S., Richter, S., Vollmar, B., and Kirsch, C.M. (2001) Preparation and investigation of tumor affinity, uptake kinetic and transport mechanism of iodine-123-labelled amino acid derivatives in human pancreatic carcinoma and glioblastoma cells. *Nucl. Med. Biol.* 28:13–23
- Samnick, S., Hellwig, D., Bader, J.B., Romeike, B.F., Moringlane, J.R., Feiden, W., and Kirsch, C.M. (2002) Initial evaluation of the feasibility of single photon emission tomography with p-[<sup>123</sup>I]iodo-L-phenylalanine for routine brain tumour imaging. *Nucl. Med. Commun.* 23:121–130
- Samnick, S., Romeike, B.F., Kubuschok, B., Hellwig, D., Amon, M., Feiden, W., Menger, M.D., and Kirsch, C.M. (2004) p-[<sup>123</sup>I]iodo-L-phenylalanine for detection of pancreatic cancer: basic investigations of the uptake characteristics in primary human pancreatic tumour cells and evaluation in in vivo models of human pancreatic adenocarcinoma. *Eur. J. Nucl. Med. Mol. Imaging* 31:532–541
- Vander Borcht, T., Asenbaum, S., Bartenstein, P., Halldin, C., Kapucu, O., Van Laere, K., Varrone, A., and Tatsch, K. (2006) EANM procedure guidelines for brain tumour imaging using labelled amino acid analogues. *Eur. J. Nucl. Med. Mol. Imaging* 33:1374–1380

# 19

## Diagnosis and Staging of Brain Tumours: Magnetic Resonance Single Voxel Spectra

Margarida Julià-Sapé, Carles Majós, and Carles Arús

### SINGLE VOXEL MAGNETIC RESONANCE SPECTROSCOPY

Where does the information given by a single voxel MR spectrum come from? The spectroscopic variant of magnetic resonance, magnetic resonance spectroscopy (MRS) allows detection and identification of a wide repertoire of molecules in solutions present in cells and tissues in the millimolar range. It has the advantage of being a non-invasive technique. The  $^1\text{H}$  isotope of hydrogen, with almost 100% natural abundance, is the most frequently studied nucleus in the clinical setting, and the technique is normally referred to as proton magnetic resonance spectroscopy or  $^1\text{H}$ -MRS. Other nuclei, such as  $^{31}\text{P}$  and  $^{13}\text{C}$ , can also be detected for studying tissue energetics or metabolic pathways, respectively. This chapter will focus on proton MR spectroscopy.

In the presence of a magnetic field, protons precess at a certain frequency called *Larmor frequency*, resulting in net magnetization. However, protons in different molecules experience slightly different magnetizations and frequencies of precession depending on the surrounding

molecular environment (chemical shielding), which is helpful for identifying different metabolites. In this way, the precession frequency will be characteristic of each chemical group in a given molecule and the changes in electronic shielding of the nucleus of interest. As a result, magnetic resonance gives the possibility of simultaneously detecting several chemical compounds present in a given sample (Figure 19.1). The precession frequency of protons is normally given in adimensional units of parts per million (ppm) instead of in Hz. It is obtained from the calculation of the chemical shift of the resonance of interest with respect to a reference resonance. The ppm scale does not depend on the magnetic field strength. Presently, most clinical scanners have a magnetic field of 1.5 T, but 3T machines are becoming increasingly popular. This chapter will focus on Single Voxel spectroscopy at 1.5 T.

There is a variety of methods for obtaining the MRS signal, and key for that is to accurately localize the volume of tissue we plan to measure. Broadly, these methods can be divided into single volume (voxel) (SV) and multi-voxel techniques (MV). This chapter will focus on SV  $^1\text{H}$ -MRS. In SV  $^1\text{H}$ -MRS, a spectrum is acquired from a small volume

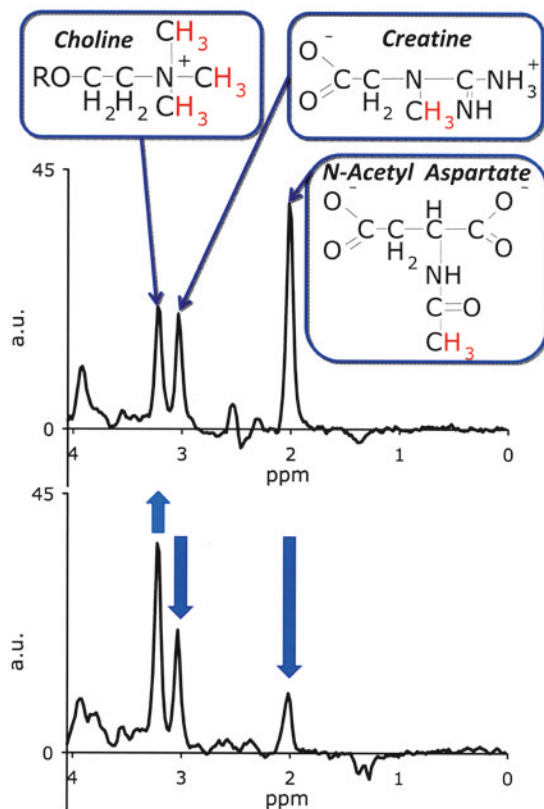


FIGURE 19.1. *Top*: Spectrum (mean from 15 cases at long TE, 135–136 ms) from normal volunteers. Resonating protons from choline-containing compounds, creatine and phosphocreatine and N-acetyl aspartate are marked in red and arrows point to the corresponding peaks. *Bottom*: Spectrum (mean from 20 cases at long TE, 135–136 ms) from Astrocytoma WHO II cases. Note the increase in choline-containing compounds and the decrease in both creatine and phosphocreatine and N-acetyl aspartate (*blue thick arrows*). Note the appearance of the inverted lactate doublet centered at 1.33 ppm

of tissue defined by the intersection of three orthogonal planes. Two approaches are generally used in clinical practice: the stimulated echo acquisition mode (STEAM) or the point resolved spectroscopy (PRESS). The PRESS sequence has double signal-to-noise than STEAM and is, therefore, preferable for most applications.

It should be reminded that after the radio frequency pulses have been applied, the

nuclei start to relax. This process in resonance is described by the time constants T1 (spin-lattice relaxation time constant) and T2 (spin-spin relaxation time constant), which are tissue dependent and will have influence in certain metabolic signals.

Other acquisition parameters apart from the magnetic field strength have an influence as well in the signals of metabolites we detect in a SV  $^1\text{H}$ -MRS. Echo time (TE), usually measured in milliseconds (ms) is perhaps the parameter with a most dramatic influence on the spectra obtained.

Acquisitions at long TE (TE > 45 ms) provide spectra with less baseline distortion, although a lower number of metabolites is observed, especially those with a short T2 relaxation time (i.e., lipids, macromolecules) that give less or no signal at longer TEs, or others for which phase modulation may obscure their detection at intermediate or long TE (i.e., myo-Inositol, mI).

Once an MR spectrum has been obtained it has to be processed and analyzed, which usually requires assigning the contribution of a biochemical substance to each of the peaks or signals observed in the spectrum, i.e., peak identification. This is usually performed using readily available chemical shift information from high-resolution MR spectroscopy (performed at high field intensities with model solutions and biopsies or extracts) and from phantoms (model solutions placed in the same 1.5 T magnets used for in-vivo studies).

## WHAT DOES SINGLE VOXEL MRS TELL US ABOUT A BRAIN TUMOR?

As Danielsen and Ross (1999) point out, a spectrum can be simplistically described as *a curve, or graph, with peaks* (Figure 19.1).

On the X axis the resonance frequency of the different metabolites detected is plotted, usually in parts per million (ppm). On the Y axis the peak heights are proportional to the relative intensity of the signal produced by the concentration of these metabolites and the number of magnetically equivalent protons in each chemical group of interest, such as the three protons in the methyl ( $\text{CH}_3$ ) resonance of alanine (ALA). At the same concentrations, peaks from metabolites with low cellular mobility will have lower heights and larger linewidths (amplitudes) due to their shorter T2 values.

Metabolites detected in brain tumors mainly do not differ qualitatively from those detected in normal brain (there is no single MRS biomarker peak for tumor, or for a specific brain tumor type), and the important information to take into account is the distribution of peaks and their relative heights (increase or decrease) with respect to normal brain and to other tumor types or diseases. This is what the expression spectral pattern refers to:  $^1\text{H}$ -MRS provides us with a biochemical fingerprint of the tissue studied. Scientifically, it may be interesting to unequivocally associate one pattern to a certain tumor type, grade or stage (Negendank 1992). Clinically, the analytical task to be performed by the radiologist will consist in qualitatively and quantitatively associating one individual graph with peaks from an individual patient to a given biochemical fingerprint and, therefore, to a certain disease, tumor type, grade or stage.

## INFORMATION PROVIDED BY A SINGLE VOXEL MR SPECTRUM

An exhaustive summary of the most important metabolites that can be identified in

the normal or pathological human brain follows:

The methyl ( $\text{CH}_3$ ) of lactate (LAC) gives a doublet signal centered at 1.33 ppm which is inverted at TE 135–144 ms with STEAM or PRESS sequences due to J-coupling phase modulation. The doublet is upright at short TE (20–35 ms) or at longer TE (272–288 ms). The  $\text{CH}_3$  of alanine (ALA) is another doublet centered at 1.47 ppm. It is also inverted at long TE (135–144 ms) and upright at short TE (20–35 ms) or at longer TE (272–288 ms). The  $\text{CH}_3$  of fatty acids and the  $(\text{CH}_2)_n$  of fatty acids, usually contained in triglycerides, give peaks at 0.9 and 1.3 ppm. These are referred to as NMR-visible mobile lipids (LIP), which are more intense at short TE sequences due to their short T2. The  $\text{CH}_3$  group of N-acetyl groups, at 2.02 ppm. This signal is basically contributed by N-acetyl aspartate (NAA) in contralateral or peritumoral brain, although it can also have contributions from other N-acetylated substances, as in cystic tumors (Candiota et al. 2004). The methylene ( $\text{CH}_2$ ) group of NAA appears centered at 2.61 ppm.

Glutamine (GLN) and glutamate (GLU) are commonly referred to as GLX. Their  $\beta$ - $\text{CH}_2$  and  $\gamma$ - $\text{CH}_2$  produce several peaks in the 2.0–2.46 ppm range and the  $\alpha$ -CH group does so in the 3.6–3.8 ppm range.

The  $\text{CH}_3$  of creatine (CRE) and phosphocreatine, usually referred as total CRE give one strong signal at 3.03 ppm. Their  $\text{CH}_2$  resonates at 3.93 ppm. CRE at 3.03 ppm is considered to have the lowest variability in comparison to other resonances, and is commonly used as internal reference when reporting relative concentrations of other brain metabolites. Gamma-aminobutyric acid (GABA) shows peaks at 1.9 ppm ( $\beta$ - $\text{CH}_2$ ), 2.3 ppm ( $\alpha$ - $\text{CH}_2$ ), and 3.00 ppm ( $\gamma$ - $\text{CH}_2$ ), but the latter is usually masked by

the CRE peak at 3.03 ppm. It is scarcely visible with MRS at 1.5 T and dedicated acquisition sequences should be applied to detect it. The nine protons in the  $(\text{CH}_3)_3$  group of choline (CHO) and other choline-containing compounds such as phosphocholine and glycerophosphocholine give a signal centered at 3.21 ppm.

Taurine (TAU) has two  $\text{CH}_2$  groups that give two triplets at 3.25 and 3.42 ppm. However, at 1.5 T these resonances overlap with CHO, myo-inositol and glucose.

The C1–C6 protons of glucose (GLUC) give peaks in the 3.43–3.80 ppm range, but signals at 1.5 T are usually low and difficult to distinguish from noise. Two  $\text{CH}_2$  protons of glycine (GLY) and the CH protons on C1, C3, C4 and C6 of myo-inositol (mI) co-resonate at 3.55. There is another mI resonance at 4.06 ppm. It is possible to distinguish GLY from mI at 3.55 ppm by recording two SV spectra, one at short and the other one at long TE (for example, 30 and 136 ms), as the mI signal is detected at short TEs, but is significantly reduced at longer TEs such as 136 ms (Barba et al. 2001).

## METHODS

### How to Perform a Single Voxel Magnetic Resonance Spectroscopy Study When a Brain Tumor Is Suspected

The main technical goal of a SV MRS study is to obtain a spectrum of the best quality, which includes the part of the tumor that provides the most relevant information.

The first decision to be taken therefore is to choose between the solid-proliferative part of the tumor or the necrotic-cystic one. Most protocols do prefer to study the first one as it is considered the

most metabolically active component of the tumor, and therefore should contain the most characteristic information. According to this, the voxel or Volume of Interest (VOI) should be preferentially chosen after having performed the MRI exam, preferably with contrast administration. Conversely, when the MRS exam is aimed to differentiate between abscess and necrotic tumor, the cystic-necrotic component should be studied in order to detect if bacterial metabolic products have been secreted to the cyst.

Another situation is when the VOI cannot be positioned in the solid component because the lesion is a cystic tumor and the solid component is too small to yield a good signal. In these cases MRS must be performed in the cystic component, under the knowledge that the spectrum should not be compared to those obtained from the solid parts of the tumor. Spectroscopy of cystic components has proven useful for the diagnosis of hemangioblastoma (Candiota et al. 2004) and for differentiating between high-grade and low-grade tumors.

Another decision to be taken is regarding VOI size. The most common is  $(2 \times 2 \times 2)$   $\text{cm}^3$ . VOIs of a larger size would provide a higher signal-to-noise ratio (SNR) but most probably with some worsening in field homogeneity especially in case of heterogeneous tumors. In this respect, it has to be considered that enlarging the voxel from  $(2 \times 2 \times 2)$   $\text{cm}^3$  to  $(2.5 \times 2.5 \times 2.5)$   $\text{cm}^3$  would provide an increase of approximately twice in the SNR, while this increase would be approximately 3.4 for a voxel of  $(3 \times 3 \times 3)$   $\text{cm}^3$ . On the other hand, smaller voxels, such as  $(1.5 \times 1.5 \times 1.5)$   $\text{cm}^3$  could enable to study a more selective component of the tumor (the most enhancing area, for example), at the cost of a lower SNR.

A general rule in this respect would be that the VOI should be as small as necessary and as large as possible. When a reduction in the size of the VOI is considered, it is advisable to increase the SNR by increasing the number of accumulated transients. It should be taken into account that the increase in the SNR is not linear: an increase of 2 in the number of accumulated scans would produce an increase of only 1.4-fold in the SNR. Then, a compromise solution has to be accepted by considering the improvement in the SNR required and the possibility of the study to be influenced by patient motion due to an extended data acquisition period. In addition, it should be taken into account that areas of susceptibility artifacts, such as the skull base or its vicinity, should be avoided, whenever possible. For this, it is advisable that VOI size and position are decided by an experienced radiologist with some training in MRS, who is as well used to evaluating brain tumors.

#### Acquisition Parameters for Single Voxel Magnetic Resonance Spectroscopy

It is advisable to perform the MRS acquisition using parameters that are widely accepted and used in the MR community, in order to later be able to compare results with literature or for being able to share results with other hospitals or clinical centers. As a guide, parameters originally used by a multicentre project called INTERPRET ([http://azizu.uab.es/INTERPRET/mrs\\_data/mrs\\_data.html](http://azizu.uab.es/INTERPRET/mrs_data/mrs_data.html)) (Tate et al. 2006) are listed below, which have been adopted by other multicentre initiatives (<http://www.etumour.net>). INTERPRET generated a validated database of spectra from 304

patients and normal volunteers that is also available to clinical centers worldwide (Julià-Sapé et al. 2006b), therefore, it is interesting to use acquisition parameters that will allow comparison to a carefully checked set of patients with different brain tumor types.

RF coils: Use the standard head coil for send and receive, or body coil for exciting and head coil (standard CP or multi-array) for receiving; Magnetic field, 1.5 T; VOI size, between  $(1.5 \times 1.5 \times 1.5)$  and  $(2 \times 2 \times 2)$  cm<sup>3</sup>.

1. Short echo time PRESS acquisition: TE (30–32) ms; TR (1,600–2,000) ms; Number of acquisitions, no water suppression (8–16); Number of acquisitions, suppressed water, (128–192); Dummy scans, 4.
2. Short echo time STEAM acquisition (this is an alternative to protocol 1 above). TE (20–32) ms, TR (1,600–2,000) ms; Number of acquisitions, no water suppression (8–32); Number of acquisitions, suppressed water, 256; Dummy scans, 4.
3. Long echo time PRESS acquisition: TE (135–144) ms; TR (1,600–2,000) ms; Number of acquisitions, no water suppression (8–16); Number of acquisitions, suppressed water (128–192); Dummy scans, 4.

#### Reporting on a Single Voxel Magnetic Resonance Spectroscopy Study

The first task when analyzing an MR spectrum for its use in the clinical diagnosis or staging of brain tumors is to qualitatively evaluate it (Danielsen and Ross 1999). We will refer to this as performing a structured description of the SV study, and should comprise the following: Acquisition

parameters that have an influence on the spectral pattern. Ideally, the values of the following parameters should be included in the report:

Study number and date; Magnetic field (in Tesla); Scanner model and manufacturer; VOI size (expressed as  $n \times n \times n$  for each of the three orientations of the plane, in mm or cm). Sequence (PRESS or STEAM), TE, recycling time (TR) (both in milliseconds), number of acquisitions for the suppressed and the unsuppressed water spectra. Number of points in the MRS file and sweep width in Hz. Sweep width tells us the range of frequencies covered by the acquisition and allow calculating the spectral resolution (data points/ppm).

Measures of acquisition quality. These should at least include SNR (van der Graaf et al. 2008) and width of the water peak in the acquisition without water suppression, such as in Kreis 2004.

The structured description of the spectrum, which should first, identify the peaks (assign them to known metabolites) and second, describe the relationships between one another, in such a way that a colleague could mentally picture the spectrum without needing to see it. MR spectra are read from right to left, then peaks should be described from 0 (right) usually up to 4.5 ppm, as this is the most informative region in human brain tumor MRS. For describing the relationships between peaks, it is useful to use CRE as reference and for instance report about NAA:CRE or CHO:CRE ratios such as 1:1, or 2:1, etc.

The following important features should be evaluated, and they are summarized in Figure 19.2. The first step should be to visually identify which is the peak with the highest signal intensity. This will indicate whether we are in front of a cyst, a necrotic

lesion, a highly proliferating tissue or one that has suffered damage or inflammation, as will be accounted next.

1. Are there LIP signals at 0.9 and 1.3 ppm? If so, indicate at which TEs they are visible. If they are the most prominent peaks of the spectrum at both short and long TE, this is indicative of necrosis, and therefore of a WHO grade IV (mostly glioblastomas, metastases). If the LIP pattern is only found at short TE, it cannot be concluded that there is clear necrotic pattern, but presence of mobile lipids instead, which may be seen in perfectly viable cells. Interestingly, *Toxoplasma Gondii* abscesses can also present with a typical necrotic pattern (Chinn et al. 1995) and consequently the rest of clinical signs and the full MR study should be taken into account when discarding or suggesting this diagnosis on the basis of the SV MRS study.
2. Presence/absence of LAC resonance. An inverted LAC doublet at long TE is one of the landmarks of glial tumors of low and intermediate grade (WHO grades II–III). This resonance can also be detected in medulloblastomas in adults. When the LAC peak is the most prominent resonance in the spectrum, we must consider whether it is a cystic liquid from a malignant (WHO grade IV) tumor (Candiota et al. 2004). Furthermore, certain non-tumoral processes like the acute phase of ictus and certain multiple sclerosis plaque stages may show increased LAC as well. If the LAC resonance at long TE is accompanied by other inverted peaks in the 0–1.4 ppm region, we will consider a bacterial abscess (Rémy et al. 1995).

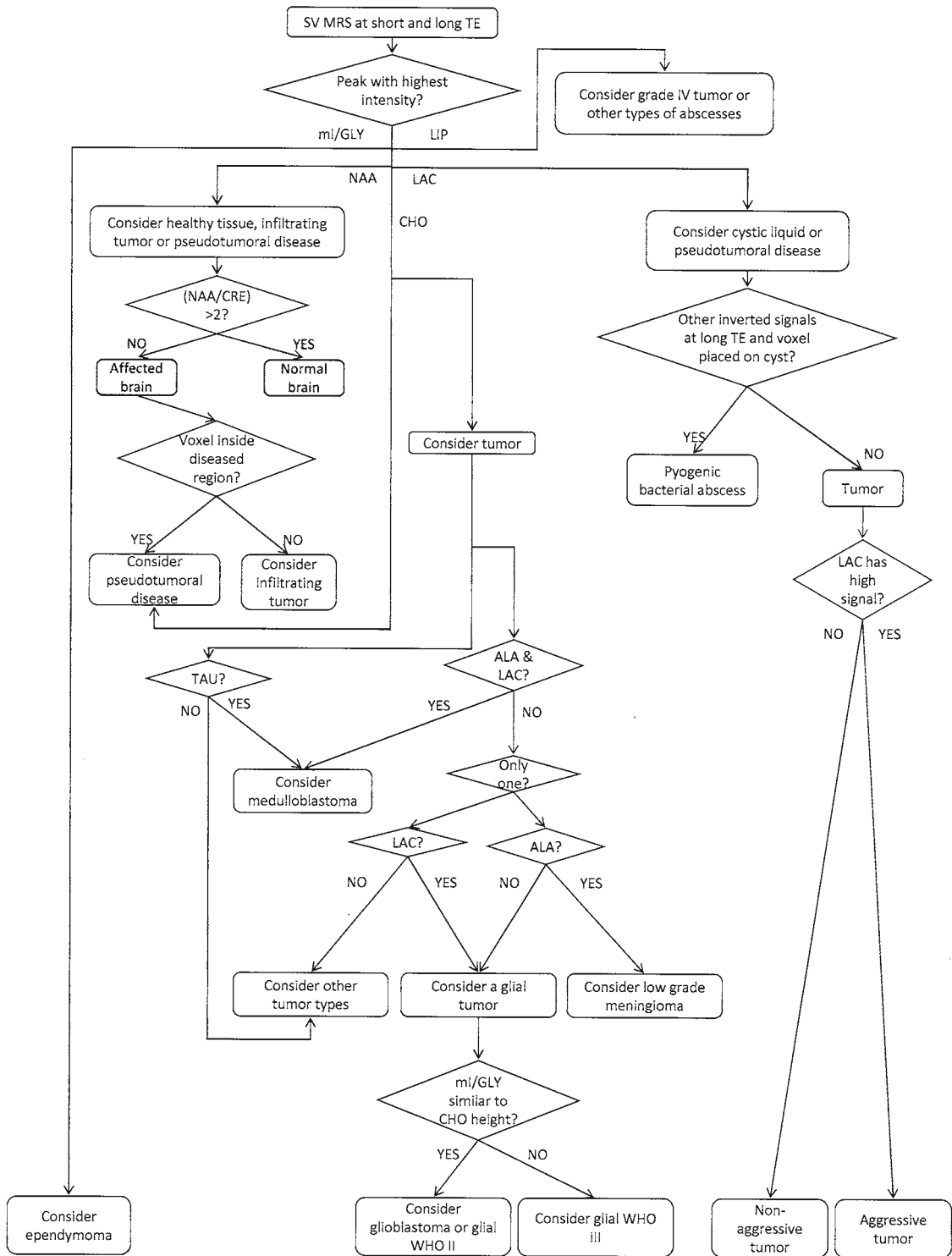


FIGURE 19.2. Flow diagram for reporting on a SV MRS study



3. Presence/absence of ALA resonance. At long TE, the inverted ALA resonance is a hallmark of low and intermediate meningioma (WHO grades I–II) grades. It can also be found in medulloblastomas of adults, which frequently present with LAC and ALA resonances.
4. NAA resonance at 2.01 ppm. Which is the ratio with respect to CRE? In normal brain tissue, the NAA peak should be the one with the highest intensity, approximately double of that of CRE and CHO. In general, NAA decreases in any situation that causes a decrease or malfunction in neurons, be it a tumor, or a pseudotumoral mass such as those of multiple sclerosis or infarcted volumes. In tumors, the degree of NAA decrease correlates with increasing malignancy. It has to be noted that this assertion does not stand for the case of low-grade meningiomas, which do not display NAA resonance as the tumor cells that compose them arise from meningeal precursors.
5. Which is the CHO/CRE ratio? In general, CHO will be increased and the rise will be directly proportional to proliferation rate in neuroepithelial tumors (Herminghaus et al. 2002). CHO will also be increased in inflammatory conditions, such as reactive gliosis or multiple sclerosis lesions. CHO is also increased in low and intermediate grade meningiomas (WHO grades I–II). The CHO/CRE ratio in glial tumors increases with grade from WHO II to III, but this feature is difficult to evaluate visually and for this discrimination it is preferable to use a quantitative method.
6. Presence/absence of TAU resonance. One can find relatively intense TAU resonances in medulloblastomas (Kovanlikaya et al. 2005), being in the latter a helpful hint for differentiation from astrocytomas.
7. Presence/absence of mI/GLY and its variation in relative intensity with respect to the CRE signal, when TE is changed. Glial tumors of low and intermediate grade (WHO grade II–III) show mI/GLY signals, these being frequently one of the most prominent signals in the spectrum. There are certain glioblastomas that do not display a necrotic profile upon SV MRS (Martínez-Bisbal et al. 2004) and also show a high mI/GLY signal. Other glial tumors also present with high mI/GLY signals, such as ependymomas (Panigrahi et al. 2006). Therefore, if the MRI study and the rest of the spectral pattern bears characteristics of a glial tumor, the mI/GLY resonance would enhance the certainty of such an orientation. Furthermore, the mI resonance allows to differentiate low-grade meningiomas from hemangiopericytomas (Barba et al. 2001). Meningioma and hemangiopericytoma spectra are indistinguishable except for the resonance at 3.55 ppm that drastically decreases at long TE in hemangiopericytomas. This is a useful differentiation, as meningiomas and hemangiopericytomas are difficult to distinguish from one another by MRI alone (Julià-Sapé et al. 2006a).
8. Presence/absence of any other signal of interest that is found, indicating at which TE is observed. A useful reference to put names on resonances is provided by Govindaraju et al. (2000). However, the radiologist should be careful in the discovery of potential signals, and only those that are clearly distinguishable from the noise (SNR higher than 5–10) should be taken into account. In addition, artifacts near the water region due to poor field homogeneity could lead to incorrect assignments.

The report should contain as well a brief conclusion about the observations and if considered necessary, a spectroscopic orientation of the type or grade of the tumor. The key concepts to be included in the conclusion are therefore if the abnormal brain mass is a tumor or an abscess or perhaps a pseudotumoral mass (infarct, multiple sclerosis) should be considered. If the mass appears to have a clear tumoral pattern upon the spectroscopic examination, then it is advisable to include a suggested type of tumor. It has to be reminded here that MRS is not yet a substitute to histopathological examination. Therefore, the emphasis should be put first, in the broad tumor origin, i.e., is it a glial tumor, is it a meningeal tumor?, and second in its grade. The WHO grade IV of malignancy can easily be assigned (with the exceptions already mentioned) upon visual examination of the spectrum, when the necrotic LIP pattern is identified. However, in low and intermediate grades (WHO I–III), a quantitative analysis with a well characterized cohort of patients would be needed to support such an orientation. Finally, the description should be accompanied by the images of the spectra (ideally both at short and at long TE) processed, for example with jMRUI (Naressi et al. 2001) or the scanner's software. A good ppm range for displaying the spectra is between 0 and 4.5 ppm. In case that a signal of interest appears outside this range, an additional view in the 0–10 ppm range should be added. This can happen when there is presence of vinyl ML protons of necrotic tumors at ca. 5.3 ppm or protons from phenylalanine (Martínez-Pérez et al. 1997). It can be a good option to accompany the report with mean spectra from the suggested pathologies from a local database or from available literature.

### Quantifying a Magnetic Resonance Spectroscopy Study: Processing a Single Voxel Magnetic Resonance Spectrum

In order to perform statistics or intra-center comparisons on patient cohorts, it is necessary to choose a set of processing parameters and to process all spectra in the same way. There are several software packages for processing MRS data. Many radiologists use scanner-proprietary software, such as SAGE (General Electric), or PRIDE (Philips). There are also other programs for general use with data from many scanners, and the most popular are jMRUI (Naressi et al. 2001) and LC model (Provencher 2001). jMRUI is free to non-profit institutions while LC model requires a license. If spectra from several machines are to be compared, it is necessary to adjust the number of points and the frequency range between manufacturers. This is provided by the INTERPRET software (Tate et al. 2006), that uses a canonical format of 512 points in the  $[-2.7, 7.1]$  ppm region. Except in those centers where two scanners from different manufacturers are available, in the day-to-day patient management it is frequently sufficient to choose a processing software to process patient data to be compared probably with reference ratio values or mean spectra from patient series at the same institution. The commonest choice is to use the same processing software available in the scanner console. In centers with interest in further analysis of the MRS data, then a package that allows more sophisticated manipulations on spectra like the above mentioned jMRUI or LC model should be available.

The basic manipulations to be performed on a spectrum are the following: The spectral signal is in fact a recording of the signal

current intensity against time, in the time domain, and is commonly known as the free induction decay (FID). This signal has to be transformed in another type of signal, in the frequency domain, in order to be able to identify the resonating molecules. This is achieved by a mathematical transformation called fast Fourier transform (FFT). The frequency signal that is obtained after the FFT is known as the MR spectrum (Figure 19.1). The spectrum will consist of a large signal from water and several small signals from the metabolites that are in solution. Therefore, additional data processing is needed in order to remove the residual water signal and to isolate the signals from metabolites, and several methods exist for that (In't Zandt et al. 2001). After FFT, subtraction of the water signal, phase correction, baseline correction and additional phasing – if needed – are usually performed. If signals are being quantitated, a variety of methods also exist, such as those available in LCmodel or AMARES and QUEST, which are included in the jMRUI package (<http://www.mrui.uab.es/mrui/>).

## QUANTIFYING AN MRS STUDY: RATIO-BASED DETERMINATIONS

As it has been mentioned earlier, an MR spectrum can be simplistically described as a graph with some peaks, scaled in arbitrary units. These units are relative, and cannot be directly used for comparing among cases, especially among different clinical centers. For this, it is necessary to obtain absolute values, by metabolite quantization, or by normalizing the values for example, to a reference. Metabolite quantization should in theory be the most

robust approach (Opstad et al. 2008). Nevertheless, the methods suggested above (jMRUI or LCmodel-based) are time-consuming and difficult to implement in a real clinical environment. They also usually rely on accepting certain prior knowledge published about T1 and T2 of the resonances of interest in the tissue, which could be uncertain or variable. Several methods have been suggested for normalizing the spectra, but the simplest and probably the most commonly used is to calculate ratios between resonances. The main advantage of ratios relies on their simplicity. Nowadays, most MR manufacturers automatically provide these ratio values integrated in their scanner software (Figure 19.3) without the need of any additional data manipulation. Furthermore, the simplicity of the method reduces the chance of unwanted operator bias. Several ratios can be calculated in a spectrum. As total CRE has been considered the less variable compound in brain and brain masses, most ratios include CRE in the denominator.

The CHO resonance in vivo originates mostly from intermediates of phospholipid metabolism, which closely correlate with changes in the structure and function of cell membranes. Usually, increased CHO can be seen in processes with elevated cell-membrane turnover, such as in highly proliferating tumors, and the degree of increase in this ratio will correlate with the degree of cell-membrane turnover (Herminghaus, et al. 2002). Accordingly, the CHO/CR ratio has been suggested as a normalized value to evaluate neuroepithelial tumor proliferation stage.

NAA is predominantly found in neurons and consequently, reduction in the NAA signal has been considered to be caused by neuron destruction or displacement.

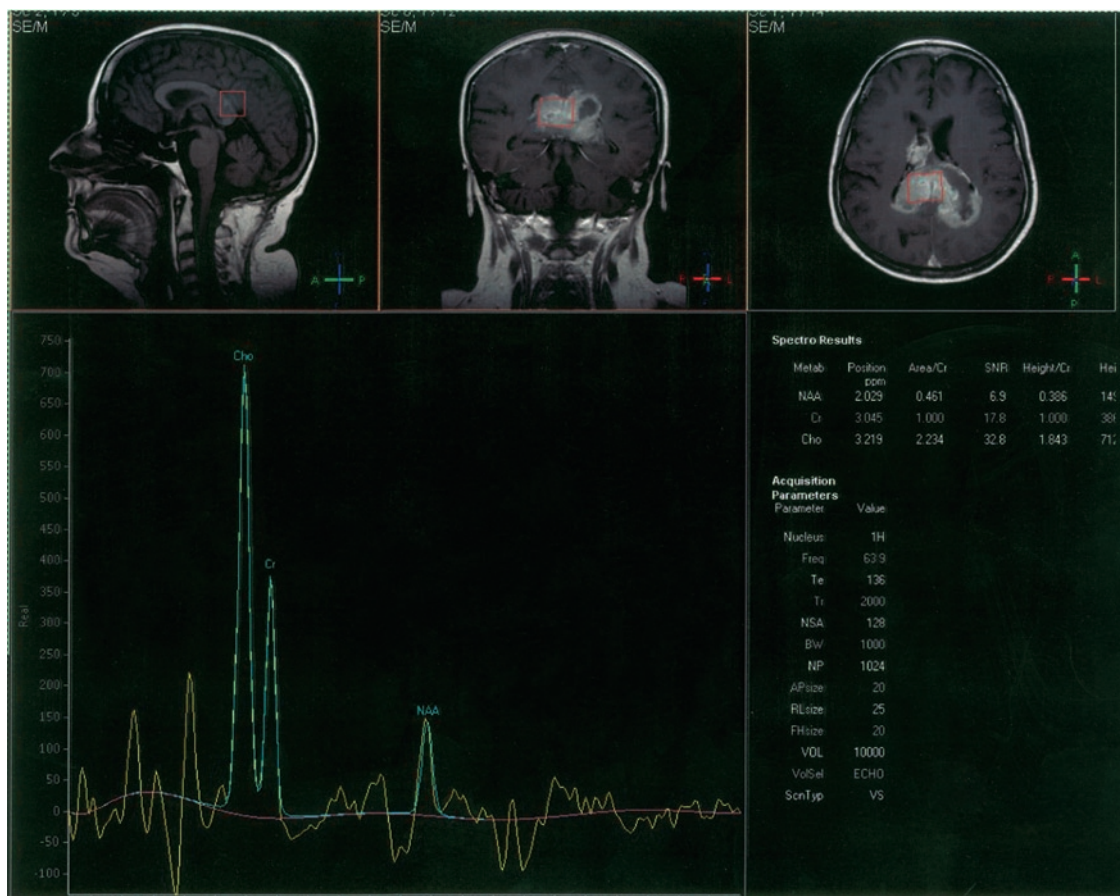


FIGURE 19.3. Typical screen from a scanner console (Philips). *Top, from right to left*, sagittal, coronal and axial images with the VOI marked in red color. *Bottom left*, spectrum at long TE with NAA, CRE (Cr, in the image) and CHO (Cho, in the image). *Bottom right*, several figures of interest are given, such as the integrated area or the height of these peaks with respect to CRE or the SNR, as well as acquisition parameters. Spectro results displays the position in ppm, area/Cr (peak area relative to CRE area), SNR, height/Cr (peak height relative to CRE height) and height for the following metabolites: NAA, CRE and CHO. In addition, the Acquisition Parameters section gives several parameters from the study as well as their value. In this example: Nucleus, <sup>1</sup>H; Frequency, 63.9; TE, 136; TR, 2000; NSA, 128; BW, 1000; NP, 1024; AP size, 20; RL size, 25; FH size, 25; VOL, 10000; VolSel, ECHO; ScnTyp: VS

Then, the NAA/CR ratio has been used as a marker of neuronal integrity.

Furthermore, any peak intensity ratio may also be considered and the result can constitute a normalized value which may be used to compare among different cases. For example, the CHO/NAA ratio could be used to highlight proliferation rate changes and neuronal destruction in a sole ratio.

Additionally, ratios from other metabolites could provide additional information, such as mI/CRE for assessing glial proliferation, or the GLX/CRE as meningioma marker.

A large number of studies have evaluated brain tumors with metabolite ratios. An in depth report of their results is out of the scope of this chapter, nevertheless, some relevant aspects to be taken into

account when evaluating an MR spectrum can be summarized:

1. There is a positive correlation between CHO/CRE and tumoral WHO grade in gliomas. An increased value in the CHO/CRE ratio correlates with proliferation rate (Herminghaus et al. 2002), and as a consequence, with the WHO grade in glial tumors. This correlation is linear when comparing between low-grade (WHO grade II) and anaplastic astrocytomas (WHO grade III), but is variable in glioblastomas. Some authors have shown CHO to be higher in glioblastomas than in anaplastic astrocytomas (Herminghaus et al. 2002), while others have described CHO/CRE to be lower in glioblastomas (Dowling et al. 2001). These differences could be caused by varying proportions of necrotic versus proliferative cellular regions in the VOI. Accordingly, discrepancies between studies may be due to both the relationship between solid proliferative and necrotic areas in the tumors, as well as to the VOI position.
2. In a recent study comparing glial tumors without necrosis and pseudotumoral lesions, the increased mI/NAA ratio at short TE was found to be the most useful classifier with 82% accuracy in the classification of low-grade glial tumors (Majós et al. 2008).

## QUANTIFYING AN MRS STUDY: CLASSIFIERS AND DECISION-SUPPORT SYSTEMS

Up to now in this chapter, it has been shown that there is no distinct marker resonance that appears, disappears, increases

or decreases in a fully specific way in certain tumors or pseudotumor types. On the contrary, several peaks change their intensities simultaneously, and behave as continuous variables, i.e. the signal is numerically measurable. For this reason, statistical techniques based in multivariate analysis have been traditionally employed in the area since 1992 (Negendank 1992; Tate et al. 1998, 2006). However, despite the ample literature on the matter (whose review is out of the scope of this chapter) none of the automated classifiers described in the literature is widely available and easily usable or reproducible by non-mathematical experts. This fact set a common ground for developing an automated system in 2000, the already mentioned INTERPRET ([http://azizu.uab.es/INTERPRET/int\\_Disc\\_Proto.shtml](http://azizu.uab.es/INTERPRET/int_Disc_Proto.shtml)), to help clinicians to easily type and grade brain tumors with the help of MRS in a push button way (no tedious processing or quantification steps). The system is nowadays still available (<http://gabrmn.uab.es/dss>, Figure 19.4) and has been reported to be easy to use and useful for the discrimination of brain tumor types ([http://rsna2005.rsna.org/rsna2005/V2005/conference/event\\_display.cfm?em\\_id=4407124](http://rsna2005.rsna.org/rsna2005/V2005/conference/event_display.cfm?em_id=4407124)).

## WHEN THERE IS AN INDICATION FOR A SV MRS EXAM

Three situations can be considered for its indication in suspected brain tumors: Discrimination between tumor and pseudotumoral lesion; Tumor classification; Follow-up of brain tumors after treatment.

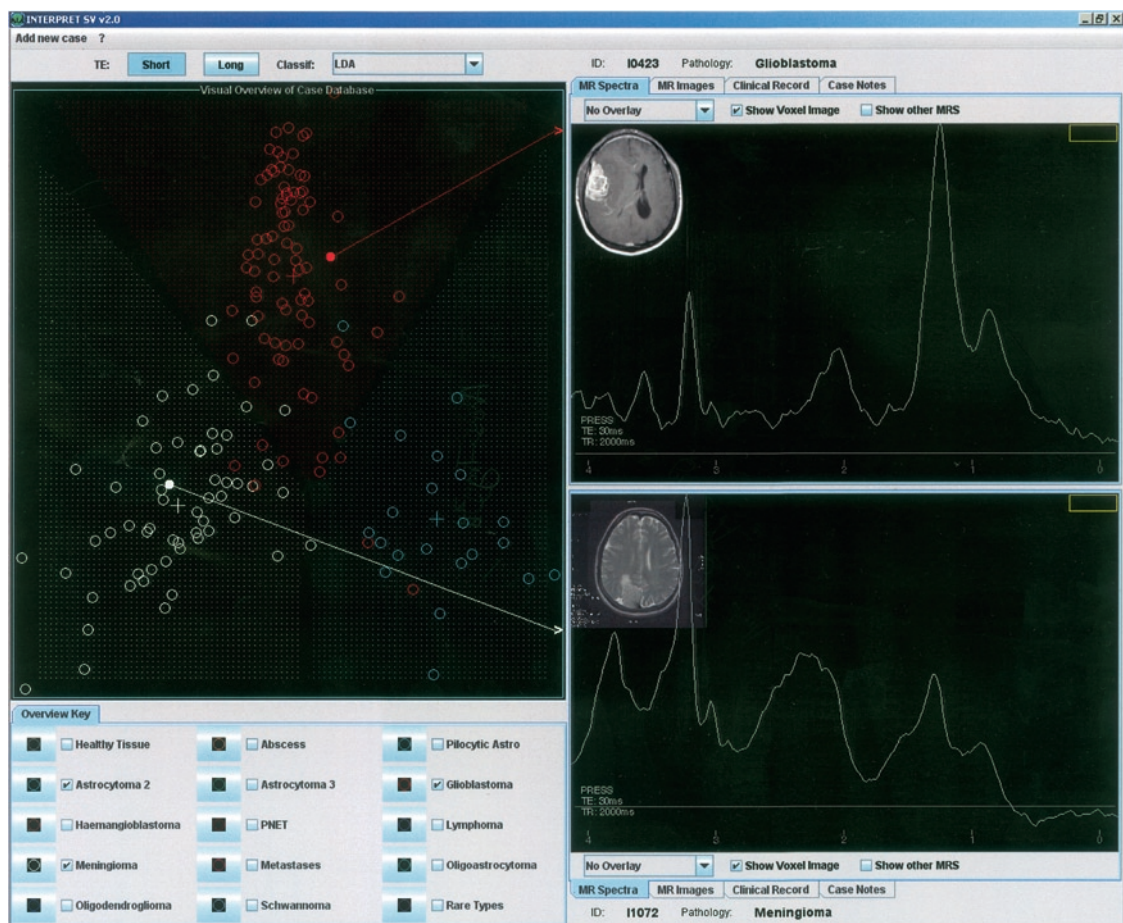


FIGURE 19.4. The INTERPRET decision-support system. The *left overview* displays the cases in the database, with different colors depending on the type of tumor. The *top and bottom right overviews* allow display, analysis and comparison of two spectra

### Discrimination Between Tumor and Pseudotumoral Lesion

Depending on the radiological solid or necrotic aspect of the mass, two situations may be encountered. When the lesion is solid, the main diagnoses include tumors without necrosis and pseudotumoral demyelinating disease. Some ischemic lesions with atypical clinical and radiological aspect can also mimic a solid pseudotumoral mass. Finally, in certain cases for which pathologic examination is absent or indeterminate, the lesion spontaneously regresses upon follow-up, and

only an unspecific diagnosis of “benign pseudotumoral lesion” can be established. MR spectroscopy may help differentiating between tumor and pseudotumor in these situations, on the basis of higher CHO levels, as well as low NAA (Saindane et al. 2002) in tumors. These spectroscopic changes may be attributed to a larger membrane turnover in proliferating cells and decrease of neuron content caused by tumor infiltration. In a recent study (Majós et al. 2008), it was found that the CHO/NAA ratio provided the highest discriminative performance between tumor and

pseudotumor at long TE (TE, 136 ms). This ratio therefore can gauge the level of membrane turnover and neuron loss in a sole parameter, and provides an accuracy of 79% when differentiating between tumor and pseudotumor in an independent test set. In the same work, it was also found that the best discrimination between tumor and pseudotumor at short TE (TE, 30 ms) was provided by the mI/NAA ratio (accuracy 82%), by means of a relative evaluation of glial proliferative status versus neuron loss.

When a necrotic mass has thin regular walls, especially if some degree of hyperintensity is found on diffusion weighted images (DWI), a pyogenic abscess has to be considered. In this respect, it has to be taken into account that not all lesions with apparent diffusion coefficient (ADC) reduction correspond to abscess. Necrotic tumors with hemorrhage or large extracellular protein content can occasionally show this feature. This is the reason why DWI has low specificity and high sensitivity for the diagnosis of abscess. The opposite happens with MRS, which is highly specific, but with low sensitivity. Metabolism largely varies between human tumors and bacteria, and these differences can be non-invasively detected by MRS (Rémy et al. 1995; Martínez-Pérez et al. 1997; Saindane et al. 2002). Then, the combination of DWI and MRS may provide the highest diagnostic performance. Nowadays, the suspicion of brain abscess can be considered the only indication for emergency MRS, because patient management largely depends of this diagnosis (urgent stereotactic drainage of brain abscess versus elective surgery for brain tumors), and MRS should be performed before starting treatments

that could mask bacterial metabolism (Burtscher and Holtas 1999).

### Tumor Classification

Most extra-axial lesions can be diagnosed by MRI, such as meningioma or schwannoma without the need of performing an MRS exam (Julià-Sapé et al. 2006a). On the other hand, most intra-axial brain tumors can be classified as glial tumors by MRI. Nevertheless, there are some cases in which the differentiation between intra or extra-parenchymatous tumor is not as evident. In these cases, an MRS exam showing a typical aspect of meningioma may be of help for suggesting to the surgeon an extra-axial nature of the mass (Majós et al. 2003). MRS can also be helpful in suggesting a particular diagnosis in other situations. An example could be posterior fossa tumors in children (Wang et al. 1995) in which the possibility of ependymoma, medulloblastoma or pilocytic astrocytoma would stand up for a different patient management. When a diagnosis of glial tumor is put forward, MRS can be useful in suggesting an oligodendroglial component that could indicate a higher sensitivity to chemotherapy and maybe an alternative chemotherapeutic protocol. Proton MRS can also be helpful in adjusting the WHO grade of a glial tumor. The classical concept by imaging is that a glial tumor that enhances after contrast would be high grade because there is hematoencephalic barrier damage, while a non-enhancing tumor would be low-grade. Nowadays, it is well known that some exceptions to this rule exist, and that up to 37% of non-enhancing tumors may be WHO grade III or IV and up to 10% of WHO grade III astrocytomas may be non-enhancing tumors (Scott et al. 2002). Then, MRS could provide a metabolic insight into the tumor that can

be of help for its grading into the WHO scale. According to all these arguments, MRS can be of help in most brain masses, including some cases in which MR imaging alone could seem effective enough *ab initio*. As a consequence, our advice would be to include MRS in the study of all brain masses suggestive of brain tumor.

### Follow-Up of Brain-Tumors After Treatment

MRS may play a role in the follow-up of brain tumors after treatment. Whereas multivoxel MRS has been shown to be of prognostic value (Oh et al. 2004), SV MRS has been found to be useful in radiation necrosis assessment. In two different studies, Weybright et al (2005) and Zeng et al. (2007) found that the criterion if CHO/CRE ratio higher than 1.8 or CHO/NAA higher than 1.8, then tumor recurrence (1.71 as threshold in the study of Zeng et al.) was able to differentiate between radiation necrosis and tumor recurrence with an accuracy higher than 95%. However, it has yet to be shown whether the metabolic differences between tumor infiltration and post-treatment changes can produce spectroscopic differences applicable in the differentiation between tumor progression and pseudoprogression (Brandsma et al. 2008).

In conclusion, SV <sup>1</sup>H-MRS is a simple, quick and powerful technique that gives information about the metabolic state of a tissue. In brain tumors, it can be used as a confirmatory technique together with the rest of the MR study to aid in characterization of the abnormal brain mass. This chapter has given a set of guidelines that allow a radiologist to indicate MRS in the adequate clinical circumstances and

to analyze the resulting data. It is possible now to distinguish among the most important types of brain tumors: meningiomas, glial tumors and those that have reached the WHO grade IV. In addition, further analyses on the MRS can also be performed for refined characterization of the masses, with the help of the analytical tools here outlined.

*Acknowledgements.* MJS and CA acknowledge funding from eTUMOUR (FP6-2002-LIFESCIHEALTH-503094) and HealthAgents (FP6-2005-IST-027213). CA acknowledges funding from MCYT SAF 2002-0440, SAF 2005-03650 and SAF 2008-03323. MJS, CM and CA are also funded by the CIBER of Bioengineering, Biomaterials and Nanomedicine, an initiative of the Instituto de Salud Carlos III (ISCIII) of Spain.

### REFERENCES

- Barba, I., Moreno, A., Martínez-Pérez, I., Tate, AR., Cabañas, M.E., Baquero, M., Capdevila, A., and Arús, C. (2001) Magnetic resonance spectroscopy of brain hemangiopericytomas: high myoinositol concentrations and discrimination from meningiomas. *J. Neurosurg.* 94(1):55–60
- Brandsma, D., Stalpers, L., Taal, W., Sminia, P., and van den Bent, M.J. (2008) Clinical features, mechanisms, and management of pseudoprogression in malignant gliomas. *Lancet Oncol.* 9:453–461
- Burtscher, I.M., and Holtas, S. (1999) In vivo proton MR spectroscopy of untreated and treated brain abscess. *AJNR Am. J. Neuroradiol.* 20:1049–1053
- Candiota, A.P., Majós, C., Bassols, A., Cabanas, M.E., Acebes, J.J., Quintero, M.R., and Arus, C. (2004) Assignment of the 2.03 ppm resonance in in vivo <sup>1</sup>H MRS of human brain tumour cystic fluid: contribution of macromolecules. *Magn Reson Mater Phy* 17:36–46
- Chinn, R.J., Wilkinson, I.D., Hall-Craggs, M.A., Paley, M.N., Miller, R.F., Kendall, B.E., Newman,



- S.P., and Harrison, M.J. (1995) Toxoplasmosis and primary central nervous system lymphoma in HIV infection: diagnosis with MR spectroscopy. *Radiology* 197(3):649–654
- Danielsen, E.R., Ross, B. (1999) Magnetic resonance spectroscopy diagnosis of neurological diseases. Marcel Dekker, New York
- Dowling, C., Bollen, A.W., Noworolski, S.M., McDermott, M.W., Barbaro, N.M., Day, M.R., Henry, R.G., Chang, S.M., Dillon, W.P., Nelson, S.J., and Vigneron, D.B. (2001) Preoperative proton MR spectroscopy imaging of brain tumors: correlation with histopathologic analysis of resection specimens. *AJNR Am. J. Neuroradiol.* 22:604–612
- Govindaraju, V., Young, K., and Maudsley, A.A. (2000) Proton NMR chemical shifts and coupling constants for brain metabolites. *NMR Biomed.* 13(3):129–153
- Herminghaus, S., Pilatus, U., Moller-Hartmann, W., Raab, P., Lanfermann, H., Schlote, W., and Zanella, F.E. (2002) Increased choline levels coincide with enhanced proliferative activity of human neuroepithelial brain tumors. *NMR Biomed.* 15:385–392
- In 't Zandt, H., van Der Graaf, M., and Heerschap, A. (2001) Common processing of in vivo MR spectra. *NMR Biomed.* 14(4):224–232
- Julià-Sapé, M., Acosta, D., Majós, C., Moreno-Torres, A., Wesseling, P., Acebes, J.J., Griffiths, J.R., and Arús, C. (2006a) Comparison between neuroimaging classifications and histopathological diagnoses using an international multicenter brain tumor magnetic resonance imaging database. *J. Neurosurg.* 105(1):6–14
- Julià-Sapé, M., Acosta, D., Mier, M., Arús, C., and Watson, D. (2006b) INTERPRET consortium. A multi-centre, web-accessible and quality control-checked database of in vivo MR spectra of brain tumour patients. *Magn Reson Mater Phy* 19(1):22–33
- Kovanlikaya, A., Panigrahy, A., Krieger, M.D., Gonzalez-Gomez, I., Ghugre, N., McComb, J.G., Gilles, F.H., Nelson, M.D., and Blüml, S. (2005) Untreated pediatric primitive neuroectodermal tumor in vivo: quantitation of taurine with MR spectroscopy. *Radiology* 236:1020–1025
- Kreis, R. (2004) Issues of spectral quality in clinical 1H-magnetic resonance spectroscopy and a gallery of artifacts. *NMR Biomed.* 17(6):361–381
- Majós, C., Aguilera, C., Alonso, J., Julià-Sapé, M., Castañer, M., Sánchez, J.J., Samitier, A., León, A., Rovira, A., and Arús, C. (2009) Proton MR spectroscopy improves discrimination between tumor and pseudotumoral lesion in solid brain masses. *AJNR Am. J. Neuroradiol.* 30(3): 544–551 (published on-line)
- Majós, C., Alonso, J., Aguilera, C., Serrallonga, M., Coll, S., Acebes, J.J., Arús, C., and Gili, J. (2003) Utility of proton MR spectroscopy in the diagnosis of radiologically atypical intracranial meningiomas. *Neuroradiology* 45:129–136
- Martinez-Bisbal MC, Marti-Bonmati L, Piquer J, Revert A, Ferrer P, Llacer JL, Piotto M, Assemat O, Celda B. (2004) 1H and 13C HR-MAS spectroscopy of intact biopsy samples ex vivo and in vivo 1H MRS study of human high grade gliomas. *NMR Biomed* 17:191–205
- Martínez-Pérez, I., Moreno, A., Alonso, J., Aguas, J., Conesa, G., Capdevila, A., and Arús, C. (1997) Diagnosis of brain abscess by magnetic resonance spectroscopy. Report of two cases. *J. Neurosurg.* 86(4):708–713
- Naressi, A., Couturier, C., Devos, J.M., Janssen, M., Mangeat, C., de Beer, R., and Graveron-Demilly, D. (2001) Java-based graphical user interface for the MRUI quantitation package. *Magn Reson Mater Phy* 12:141–152
- Negendank, W. (1992) Studies of human tumors by MRS: a review. *NMR Biomed.* 5(5):303–324
- Oh, J., Henry, R.G., Pirzkall, A., Lu, Y., Li, X., Catalaa, I., Chang, S., Dillon WP, Nelson SJ. (2004) Survival analysis in patients with glioblastoma multiforme: predictive value of choline-to-N-acetylaspartate index, apparent diffusion coefficient, and relative cerebral blood volume. *J Magn Reson Imaging* 19:546–554
- Opstad, K.S., Bell, B.A., Griffiths, J.R., and Howe, F.A. (2008) Toward accurate quantification of metabolites, lipids, and macromolecules in HRMAS spectra of human brain tumor biopsies using LCModel. *Magn. Reson. Med.* 60(5):1237–1242
- Panigrahy, A., Krieger, M.D., Gonzalez-Gomez, I., Liu, X., McComb, J.G., Finlay, J.L., Nelson, M.D., Jr., Gilles, F.H., Blüml, S. (2006) Quantitative short echo time 1H-MR spectroscopy of untreated pediatric brain tumors: preoperative diagnosis and characterization. *AJNR Am J Neuroradiol* 27:560–572

- Provencher, S.W. (2001) Automatic quantitation of localized in vivo <sup>1</sup>H spectra with LCModel. *NMR Biomed.* 14(4):260–264
- Rémy, C., Grand, S., Lai, E.S., Belle, V., Hoffmann, D., Berger, F., Estève, F., Ziegler, A., Le Bas, J.F., Benabid, A.L., Décorps, M., and Segebarth, M. (1995) <sup>1</sup>H MRS of human brain abscesses in vivo and in vitro. *Magn. Reson. Med.* 34(4):508–514
- Saindane, A.M., Cha, S., Law, M., Xue, X., Knopp, E.A., and Zagzag, D. (2002) Proton MR Spectroscopy of tumefactive demyelinating lesions. *AJNR Am. J. Neuroradiol.* 23: 1378–1386
- Scott, J.N., Brasher, P.M.A., Sevick, R.J., Rewcastle, N.B., and Forsyth, P.A. (2002) How often are nonenhancing supratentorial gliomas malignant? A population study. *Neurology* 59:947–949
- Tate, A.R., Griffiths, J.R., Martínez-Pérez, I., Moreno, A., Barba, I., Cabañas, M.E., Watson, D., Alonso, J., Bartumeus, F., Isamat, F., Ferrer, I., Vila, F., Ferrer, E., Capdevila, A., and Arús, C. (1998) Towards a method for automated classification of <sup>1</sup>H MRS spectra from brain tumours. *NMR Biomed.* 11(4–5):177–191
- Tate, A.R., Underwood, J., Acosta, D.M., Julià-Sapé, M., Majós, C., Moreno-Torres, A., Howe, F.A., van der Graaf, M., Lefournier, V., Murphy, M.M., Loosemore, A., Ladroue, C., Wesseling, P., Luc Bosson, J., Cabañas, M.E., Simonetti, A.W., Gajewicz, W., Calvar, J., Capdevila, A., Wilkins, P.R., Bell, B.A., Rémy, C., Heerschap, A., Watson, D., Griffiths, J.R., and Arús, C. (2006) Development of a decision support system for diagnosis and grading of brain tumours using in vivo magnetic resonance single voxel spectra. *NMR Biomed.* 19(4):411–434
- van der Graaf, M., Julià-Sapé, M., Howe, F.A., Ziegler, A., Majós, C., Moreno-Torres, A., Rijpkema, M., Acosta, D., Opstad, K.S., van der Meulen, Y.M., Arús, C., and Heerschap, A. (2008) MRS quality assessment in a multicentre study on MRS-based classification of brain tumours. *NMR Biomed.* 21(2):148–158
- Wang, Z., Sutton, L.N., Cnaan, A., Haselgrove, J.C., Rorke, L.B., Zhao, H., Bilaniuk, L.T., and Zimmerman, R.A. (1995) Proton magnetic resonance spectroscopy of pediatric cerebellar tumors. *AJNR Am. J. Neuroradiol.* 16:1821–1833
- Weybright, P., Sundgren, P.C., Maly, P., Hassan, D.G., Nan, B., Rohrer, S., and Junck, L. (2005) Differentiation between brain tumor recurrence and radiation injury using MR spectroscopy. *AJR Am. J. Roentgenol.* 185:1471–1476
- Zeng, Q.S., Li, C.F., Zhang, K., Liu, H., Kang, X.S., and Zhen, J.H. (2007) Multivoxel 3D proton MR spectroscopy in the distinction of recurrent glioma from radiation injury. *J. Neurooncol.* 84:63–69

*This page intentionally left blank*

# 20

## Parallel Magnetic Resonance Imaging Acquisition and Reconstruction: Application to Functional and Spectroscopic Imaging in Human Brain

Fa-Hsuan Lin and Shang-Yueh Tsai

### INTRODUCTION

Magnetic resonance imaging (MRI) has contributed significantly to modern cancer diagnosis and treatment planning because of its noninvasive nature, versatile image contrast, and high spatiotemporal resolution. For decades, the quest for higher sensitivity and greater spatial and/or temporal resolution has been approached by means of increasing major field strengths, enhancing gradient performance, and improving radio frequency (RF) technology. In this chapter, we present recent MRI advances that use an RF coil array to achieve “parallel” data acquisition for higher spatiotemporal resolution.

In the context of cancer imaging, parallel MRI has immediate potential application to two long-standing challenges. First, in interventional MRI increased performance of real-time imaging is generally dependent on high spatiotemporal resolution. Second, magnetic resonance spectroscopic imaging (MRSI) has been widely utilized for diagnosis and quantification of cancer. However, given that 2D or 3D imaging of MRS data has been hampered by lengthy data encoding time, it has been rendered less clinically feasible. With the aid of

parallel MRI, the challenges of achieving high spatiotemporal resolution and data encoding time can be mitigated.

In the following sections, we will present the theory of parallel MRI data acquisition and associated reconstruction algorithms, followed by examples of applications of parallel MRI for functional MRI and MRS. Although we focus on the applications of parallel MRI for brain imaging, the general concept of parallel MRI can be adaptively extended to other organs and systems with appropriate modifications to the data acquisition system and image reconstruction algorithm.

### PRINCIPLES OF PARALLEL MRI

Parallel MRI is a recent advance in MRI technology that utilizes simultaneous data acquisitions from multiple RF coil receivers to improve the spatiotemporal resolution of imaging. The advantage of high signal-to-noise ratio (SNR) in phased array (Roemer et al. 1990), along with reduced k-space sampling schemes (Carlson and Minemura 1993) forms the core of parallel MRI. The idea of utilizing spatially varying sensitivity from different channels of

an RF array to reduce imaging encoding time was initially implemented in different imaging approaches (Hutchinson and Raff 1988; Carlson and Minemura 1993; Ra and Rim 1993). Currently, there exist two major commercially available implementations of parallel MRI: the image space sensitivity encoding (SENSE) approach (Pruessmann et al. 1999), and the k-space spatial harmonics (SMASH) approach (Sodickson and Manning 1997), along with its derivative, generalized autocalibrating partial parallel acquisition (GRAPPA) (Griswold et al. 2002). Implementation of parallel MRI requires data from multiple RF coil receivers, each of which observes the spatial distribution of the imaged object's spin density modulated by the coil sensitivity profile of the individual RF coil. The reduced k-space sampling in classical Fourier imaging produces aliased images in individual receivers. Given the coil sensitivity profiles from the RF array, we can unfold these aliased images.

Parallel MRI techniques can reduce scan time and thereby improve temporal resolution. Alternatively, parallel MRI can be used to increase the spatial resolution of an image within the same amount of acquisition time (Weiger et al. 2000). Additional benefits of the parallel MRI technique include lowered susceptibility artifact due to reduced read-out duration, decreased geometrical distortion due to increased phase-encoding bandwidth (Bammer et al. 2001; Schmidt et al. 2005), and lower echo-planar imaging (EPI) acoustic noise due to reduced gradient switching (de Zwart et al. 2002c).

A major price for the above-mentioned advantages is decreased image SNR. The reduction in SNR arises from two sources: reduced number of data samples, and

reconstruction instability due to correlations in spatial information, as determined by the geometrical arrangement of the array coil. The first of these disadvantages is an inevitable result of reducing the number of samples. The second disadvantage might be addressed by optimizing coil geometry (de Zwart et al. 2002a) or by improving the stability of the reconstruction algorithm (Lin et al. 2004). Increased noise originating from correlated spatial information from the array elements can be estimated from the array geometry and quantified by the geometric factor map (g-factor map) (Pruessmann et al. 1999).

In practice, parallel MRI can be divided into two parts: data acquisition and image reconstruction. In data acquisition, the goal is to optimize the k-space traversing trajectory in order to achieve desired spatiotemporal resolution. In image reconstruction, the goal is to utilize the information available in an RF array to reconstruct high spatiotemporal resolution images with minimal aliasing artifact resulting from the Nyquist sampling theorem.

## PARALLEL MRI ACQUISITIONS

The time required to traverse the k-space is closely related to total data acquisition time in traditional MRI. The purpose of parallel MRI is to avoid "full" sampling of the k-space by skipping certain data collection points. The skipped k-space data produce aliased images, as predicted by the Nyquist sampling theorem. Using information from all channels in the RF coil array, the skipped data can be numerically interpolated from sampled data to restore full field-of-view (FOV) images without aliasing artifacts. Typically, in rectilinear Cartesian

coordinates, parallel MRI skips data in the phase-encoding direction; skipping data in the frequency-encoding direction saves little data acquisition time because the duration of the frequency-encoding gradient is the same regardless of whether sampling is full or skipped. Parallel MRI acquisition with skipped phase encoding data can reduce data acquisition time and thus improve temporal resolution. The benefit of skipping data collection in the phase encoding direction can also be translated to higher bandwidth and less geometrical distortion (Bammer et al. 2001; Schmidt et al. 2005).

In rectilinear Cartesian coordinates, implementing parallel MRI acquisition can be easily achieved by increasing the step size in the phase-encoding direction. The EPI trajectory is therefore similar to that of segmented EPI (McKinnon 1993). Reconstruction of individual EPI segments from all array elements renders itself as parallel MRI. When using non-Cartesian sampling such as spiral imaging, parallel MRI acquisition can be implemented by reducing the number of spiral arms to cover the k-space. These 2D sampling trajectories can be extended to 3D, which has two phase-encoding directions in Cartesian sampling. Parallel MRI can reduce sampling in both phase-encoding directions by using complimentary information from array elements to reconstruct images without aliasing artifacts (Weiger et al. 2002a). Optimization of data acquisition schemes in parallel MRI can also be combined with RF modulation to control spatial aliasing in accelerated acquisition, and thereby improve reconstruction quality (Breuer et al. 2005a).

The capability for improving temporal resolution makes parallel MRI an appealing

data acquisition approach. When applied to dynamic scans, where imaging planes or volumes are repeated, parallel MRI data acquisition can be further optimized by taking both k-space and time domain into consideration. For example, TSENSE (Kellman et al. 2001) utilizes interleaved segmented EPI acquisition, each segment of which can later be reconstructed from an aliased image to a full-FOV image. This approach can be further combined with a time-domain filtering method, such as UNFOLD (Madore et al. 1999), to further improve the temporal resolution of dynamic scanning (Tsao et al. 2003). Similar to TSENSE, which uses SENSE as the reconstruction kernel, the same time-interleaved k-space sampling was used in the implementation of TGRAPPA, which uses GRAPPA as the reconstruction kernel (Breuer et al. 2005b).

In parallel MRI, sensitivity maps for all channels in the coil array critically determine the quality of the reconstructed image. Traditionally, a separate scan is required to estimate coil maps (Pruessmann et al. 1999). Because coil maps vary smoothly over the FOV in most cases, low spatial resolution scans usually are adequate to serve this purpose. Low spatial resolution in coil sensitivity maps inspired the integration of data collection for coil map estimation into the accelerated parallel MRI acquisition; accelerated scanning is achieved by skipping data with high spatial frequency while at the same time maintaining full sampling around the center of the k-space for coil map estimation. This method is called “auto-calibration” because in single acquisition such data potentially contain both coil map information and the image to be reconstructed. And it was used in SMASH (Jakob et al. 1998),

SENSE (Madore 2004), and GRAPPA implementations (Griswold et al. 2002). Different from rectilinear Cartesian trajectory sampling, non-Cartesian sampling using a spiral trajectory is intrinsically self-calibrated. This means that the dense sampling around the center of k-space in spiral trajectory can be used as the coil sensitivity maps required in parallel MRI reconstruction. Methods have been proposed to utilize the more densely sampled central part of the k-space to extract coil maps for improved reconstructions (Yeh et al. 2005a; Heberlein and Hu 2006).

## PARALLEL MRI RECONSTRUCTIONS

The goal of reconstructing parallel MRI data is to remove aliasing artifacts using coil sensitivity information and observations from multiple channels in a coil array. Currently, there are two prevailing major variants of reconstruction algorithms: the k-space-based SMASH/GRAPPA method (Sodickson and Manning 1997; Griswold et al. 2002) and the image domain SENSE method (Pruessmann et al. 1999). In practice, image reconstruction can be divided into three stages: The first stage is preparation of parallel MRI reconstruction, which includes quantification of array coil performance, coil map estimation, and pre-processing of accelerated data. The second stage is reconstruction of the full-FOV image from under-sampled k-space data. The third stage is combination of reconstructed images for final presentation.

In the first stage, it is typically desirable to quantify the correlation between channels in an RF coil array. Correlated information between array channels causes redundant observations from different channels. And

it may thus degrade the quality of reconstructed image, because of insufficient independent information to remove aliasing. Correlations between channels in an array may be due to imperfection of coil fabrication, such as common mode signal or electromagnetic coupling. Typically, we can quantify the correlation among channels of an RF coil array by the noise covariance matrix, which can be estimated experimentally by turning off RF excitation while turning on data acquisition for a period of time (Pruessmann et al. 1999). The noise covariance matrix can thus be calculated using the time series from all channels, and its structure indicates the correlation between channels. Ideally, we expect minimal correlation among channels, corresponding to a noise covariance matrix with minimal off-diagonal entries. A large off-diagonal entry implies that information between two channels is highly correlated, and thus the information from these two corresponding channels may be redundant. Given a quantitative noise covariance matrix, we can “whiten” the parallel MRI acquisition to balance the independent information between channels in a coil array.

The other essential part of preparing parallel MRI data reconstruction is coil sensitivity map estimation. Using a separate sensitivity map scan, we may apply either local polynomial fitting (Pruessmann et al. 1999) or novel wavelet filtering (Lin et al. 2003) to estimate coil maps. However, estimation of coil maps can be avoided if the *in vivo* sensitivity method is employed (Sodickson 2000). Unlike traditional SENSE/SMASH reconstructions, the *in vivo* sensitivity method estimates the ratio of the spin density in the accelerated scan over that in the full-FOV reference scan. Restoration of the final

reconstructed image from the estimated full-FOV spin density ratio requires a multiplication operation. The estimated spin density ratio must multiply the coil sensitivity maps, which are full-FOV reference images themselves, to obtain coil-by-coil reconstructed images. The benefit of the in vivo sensitivity is that it requires no coil sensitivity map estimation; thus making it possible to avoid errors associated with misspecification of coil maps. However, ill conditioning at pixels, where the ratio between accelerated and unaccelerated scans is not defined, also limits the ability of the in vivo sensitivity method. Similarly, GRAPPA reconstruction (Griswold et al. 2002) also does not require explicit coil map estimation. In GRAPPA, coil map information is embedded in auto-calibration scans (ACS), which are usually k-space samples around the center of the k-space satisfying the Nyquist sampling theorem. The purpose of ACS is to sample some k-space data, which would be avoided in the accelerated scan, in order to estimate the parallel MRI reconstruction coefficients. This auto-calibration technique has also been employed in spiral trajectory MRI (Yeh et al. 2005b).

The core of parallel MRI employs under-sampled data from multiple channels in an RF coil array and coil map information to restore full-FOV images. Usually, due to the computational efficiency of an analytical solution, such restoration is done by linear (weighted) least square fitting (Sodickson and Manning 1997; Pruessmann et al. 1999). Mathematically, the least square fitting solution corresponds to an optimization problem with a cost function defined as the L-2 norm of the model error, the discrepancy between actually observed accelerated data and model-predicted data, for all channels in a

coil array. To further improve the stability of parallel MRI reconstructions, Tikhonov regularization framework (Tikhonov and Arsenin 1977) has recently shown to be effective for incorporating spatial prior in the cost function to reduce noise amplification arising from the “unfolding” process of aliased matrix (Lin et al. 2004). Given appropriate regularization parameters, prior regularized parallel MRI reconstructions show improved stability in both structural and functional MRI (Lin et al. 2004, 2005).

Typically with Cartesian sampling, parallel MRI data reconstruction can be separated into many small linear systems, each of which consists of aliasing pixels in the final reconstructed image. Such reconstruction is possible because the point-spread function derived from the k-space sampling pattern separates the reconstruction into many decoupled linear systems. However, for non-Cartesian sampling methods, such as spiral imaging, we cannot separate reconstruction into many smaller linear systems. Instead, we must directly solve a huge linear equation of size  $n^2$ -by- $n^2$ , where  $n^2$  is the number of voxels in the whole 2D image. An iterative solver using a Conjugated-Gradient (CG) algorithm has been proposed to address this issue (Pruessmann et al. 2001).

Finally, reconstruction of parallel MRI may involve strategies to combine the estimated spin distribution from all channels in the array. Using SENSE reconstruction, this process is implicitly implemented during image reconstruction using coil sensitivity as the weighting function to produce a final composite image. In SMASH/GRAPPA imaging, alternatives to combining different channels in the array after parallel MRI reconstruction have been proposed, including direct averaging,



matched filter combination, and sum-of-squares combination (McKenzie et al. 2001; Griswold et al. 2002).

## MATHEMATICAL FORMULATION

Formation of aliased images from multiple receivers in parallel MRI can be formulated as a linear operation to “fold” the full-FOV spin density images (Sodickson and McKenzie 2001).

$$\bar{y} = A\bar{x} \quad (20.1)$$

Here  $\bar{y}$  is the vector formed from the pixel intensities recorded by each receiver (folded image) and  $\bar{x}$  is the vector formed from the full FOV image. The encoding matrix  $A$  consists of the product of the aliasing operation due to k-space data sub-sampling and modulation of coil-specific sensitivity over the image. The goal of image reconstruction is to solve for  $\bar{x}$  given our knowledge of  $A$  derived from understanding the folding process and an estimate of the coil sensitivity maps. Whereas Eq. 20.1 is expressed in the image domain SENSE approach (Pruessmann et al. 1999), similar linear relationships are formed in the k-space-based SMASH (Sodickson and Manning 1997) method. Furthermore, the same basic formulation is used in either the in vivo sensitivity method (Sodickson 2000), or the conventional SENSE/SMASH methods requiring coil sensitivity estimation. In general, Eq. 20.1 is an over-determined linear system, i.e., the number of array coils, which is the row dimension of  $\bar{y}$ , exceeds the number of pixels that folds into the measured pixel; the row dimension of  $\bar{x}$ .

To solve for  $\bar{x}$  (the full FOV image), the over-determined matrix is inverted utilizing least-square estimation (Pruessmann et al. 1999).

$$\begin{aligned} \bar{x} &= U\bar{y} \\ &= (A^H\Psi^{-1}A)^{-1}A^H\Psi^{-1}\bar{y} \end{aligned} \quad (20.2)$$

where the  $H$  superscript denotes the transposed complex conjugate and  $\Psi$  is the receiver noise covariance (Pruessmann et al. 1999). When  $\Psi$  is positive semi-definite, the eigen decomposition of the receiver noise covariance ( $\Lambda$  and  $V$ ) leads to the unfolding matrix,  $U$ , using the whitened aliasing operator  $\tilde{A}$  and the whitened observation  $\tilde{y}$ . Whitening of the aliasing operator will be used in the regularization formulation introduced in the next section.

$$\begin{aligned} \Psi &= V\Lambda V^H \\ \tilde{A} &\equiv \Lambda^{-1/2}V^H A \\ \tilde{y} &\equiv \Lambda^{-1/2}V^H \bar{y} \\ \bar{x} &= U\tilde{y} \\ &= (\tilde{A}^H\tilde{A})^{-1}\tilde{A}^H\tilde{y} \end{aligned} \quad (20.3)$$

Whitening incorporates the receiver noise covariance matrix implicitly allowing optimal SNR reconstruction within the regularization formulation. The noise sensitivity of the parallel imaging reconstruction is thus quantified by amplification of the noise power that results from the array geometry. This g-factor is thus written (Pruessmann et al. 1999)

$$\begin{aligned} g_{\rho\rho} &= \frac{\sqrt{X_{\rho\rho}^{\text{parallel imaging}}}}{\sqrt{R}\sqrt{X_{\rho\rho}^{\text{full}}}} \\ &= \sqrt{[(\tilde{A}^H\tilde{A})^{-1}]_{\rho\rho}(\tilde{A}^H\tilde{A})_{\rho\rho}} \end{aligned} \quad (20.4)$$

The subscript  $\rho$  indicates the voxels to be “unfolded” in the full FOV image, and  $\mathbf{X}$  denotes the covariance of the reconstruction image vector  $\bar{\mathbf{x}}$ . Here  $R$  denotes the factor by which the number of samples is reduced (the acceleration rate).

Tikhonov regularization (Tikhonov and Arsenin 1977) provides a framework to stabilize the solution of an ill-conditioned linear equation. Using Tikhonov regularization, the solution of Eq. 20.1 can be written as

$$\bar{\mathbf{x}}^\lambda = \arg \min_{\bar{\mathbf{x}}} \left\{ \left\| \tilde{\mathbf{A}}\bar{\mathbf{x}} - \tilde{\mathbf{y}} \right\|_2 + \lambda^2 \left\| L(\bar{\mathbf{x}} - \bar{\mathbf{x}}^0) \right\|_2 \right\} \quad (20.5)$$

Here  $\lambda^2$  is the regularization parameter.  $L$  is a positive semi-definite linear transformation,  $\bar{\mathbf{x}}^0$  denotes the prior information about the solution  $\bar{\mathbf{x}}$ , and  $\|\cdot\|_2$  represents the L-2 norm. The second term in Eq. 20.5, defined as the prior error, is the deviation of the solution image from the prior knowledge. The first term, defined as the model error, represents the deviation of the observed aliased image from the model observation, which is a folded version solution image. The regularization parameter determines the relative weights with which these two estimates of error combine to form a cost function.

Consider the extreme case when  $\lambda^2$  is zero and we attempt to minimize only the first term – a calculation that is equivalent to solving the original equation,  $\bar{\mathbf{y}} = \mathbf{A}\bar{\mathbf{x}}$ , without conditioning (conventional SENSE reconstruction). On the other extreme, when  $\lambda^2$  is large, the solution will duplicate of the prior information  $\bar{\mathbf{x}}^0$ . Thus, the regularization parameter  $\lambda^2$  quantifies the trade-off between model error and prior error. An appropriate chosen  $\lambda^2$

(regularization) decreases the otherwise complete dependency on the whitened model ( $\tilde{\mathbf{A}}$ ) and the whitened observation ( $\tilde{\mathbf{y}}$ ), to constrain the solution to within a reasonable “distance” from the prior knowledge ( $\bar{\mathbf{x}}^0$ ). Thus regularization increases the influence of prior knowledge full FOV image information during parallel MRI reconstruction.

Given the regularization parameter  $\lambda^2$  and defining  $L$  as an identity matrix, the solution of Eq. 20.4 is written (Hansen 1998):

$$\bar{\mathbf{x}}^\lambda = \sum_{j=1}^n \left( f_j \frac{\bar{\mathbf{u}}_j^H \tilde{\mathbf{y}}}{s_{jj}} + (1 - f_j) \bar{\mathbf{v}}_j^H \bar{\mathbf{x}}^0 \right) \bar{\mathbf{v}}_j \quad (20.6)$$

$$f_j = \frac{s_{jj}^2}{s_{jj}^2 + \lambda^2} \equiv \begin{cases} 1, S_{jj} \gg \lambda \\ s_{jj}^2 / \lambda^2, S_{jj} \ll \lambda \end{cases}$$

Here  $\bar{\mathbf{u}}_j$ ,  $\bar{\mathbf{v}}_j$ , and  $s_{jj}$  are the left singular vector, right singular vector and singular value of  $\mathbf{A}$ , respectively, generated by singular value decomposition (SVD); singular values and vectors are indexed by  $j$ . This calculation leads to the following matrix representations:

$$\bar{\mathbf{x}}^\lambda = \mathbf{V}\mathbf{\Gamma}\mathbf{U}^H \tilde{\mathbf{y}} + \mathbf{V}\mathbf{\Phi}\mathbf{V}^H \bar{\mathbf{x}}^0$$

$$\text{VAR}(\bar{\mathbf{x}}^\lambda) = \mathbf{V}\mathbf{\Gamma}^2\mathbf{V}^H$$

$$\Gamma_{ii} = \frac{f_i}{s_{ii}} = \frac{s_{ii}}{s_{ii}^2 + \lambda^2} \quad (20.7)$$

$$\Phi_{ii} = 1 - f_i = \frac{\lambda^2}{s_{ii}^2 + \lambda^2}$$

Using regularization and Eq. 20.4, the ratio of the noise levels between the regularized parallel MRI reconstruction and the original full FOV image normalized by the factor of acceleration yields the local geometry factor for noise amplification.

$$g_{\rho\rho} = \sqrt{[(VT^2V^H)]_{\rho\rho}[(VS^2V^H)]_{\rho\rho}} \quad (20.8)$$

Inside the square root of Eq. 20.8, the first square bracket term denotes the variance of unfolding using regularization from Eq. 20.7; the second square bracket term denotes the variance of the full FOV reference image.

## APPLICATION – SENSE HUMAN BRAIN FUNCTIONAL MAGNETIC RESONANCE IMAGING

Applications of parallel MRI acquisition protocols for fMRI experiments have been reported by different groups, which used either the PRESTO sequence (Golay et al. 2000) or the gradient-echo EPI sequence (de Zwart et al. 2002b; Weiger et al. 2002b; Preibisch et al. 2003). The rationale for using parallel MRI is that fMRI data acquisition protocol focuses on enhancement of spatiotemporal resolution due to reduced k-space traversing time. At high field ( $\geq 3T$ ) scanners,  $T2^*$  relaxation time of human gray matter may be less than 30 ms in areas that exhibit pronounced field inhomogeneities (Barth et al. 1999). Traditionally such a short  $T2^*$  made single-shot EPI intractable for sufficient spatiotemporal resolution because the data acquisition time was insufficient to traverse the entire k-space. With parallel imaging, the time needed to traverse the k-space is reduced by means of mathematically “unfolding” the aliased images from individual receivers in the array. Reduced k-space traversing time also benefits the reduction of susceptibility artifacts and

geometrical distortion originating from local magnetic field inhomogeneity. This is because the shortened readout time for data acquisition contributes to reduced local spin dephasing within individual voxels and produces higher bandwidth in the phase-encoding direction. Another significance of utilizing SENSE as the fMRI data acquisition protocol at high fields includes lowered acoustic noise owing to gradient switching for complete k-space trajectory traversing (de Zwart et al. 2002c).

Echo-planar imaging (EPI) is the most popular functional MRI acquisition protocol for capturing  $T2^*$ -weighted image contrast derived from intrinsic hemoglobin, which can infer local neural activity. Here we demonstrate the effect of reduced EPI distortion with GRAPPA-reconstructed EPI on a 3T scanner (Siemens Medical Solution, Erlangen, Germany) equipped with an eight-channel head phased array coil (Figure 20.1). The imaging parameters are: FOV = 200 mm, TR/TE = 2,000/30 ms, Flip angle =  $90^\circ$ , slice thickness = 3 mm, bandwidth = 1,440 Hz. Note that image distortion around the frontal and temporal lobes was improved using GRAPPA imaging. Regularization can also suppress noise at the center of the reconstructed image, compared to unregularized reconstruction in the same acceleration rate.

To further demonstrate how EPI with regularized parallel MRI reconstruction can be applied to human brain fMRI experiments, we collected a set of blocked-design visual fMRI data from a 3T scanner equipped with an eight-channel phased array coil. And subsequently SENSE reconstructions were performed. We recruited one healthy subject for the study after receiving approval from the Institutional Review Board and obtaining the subject’s

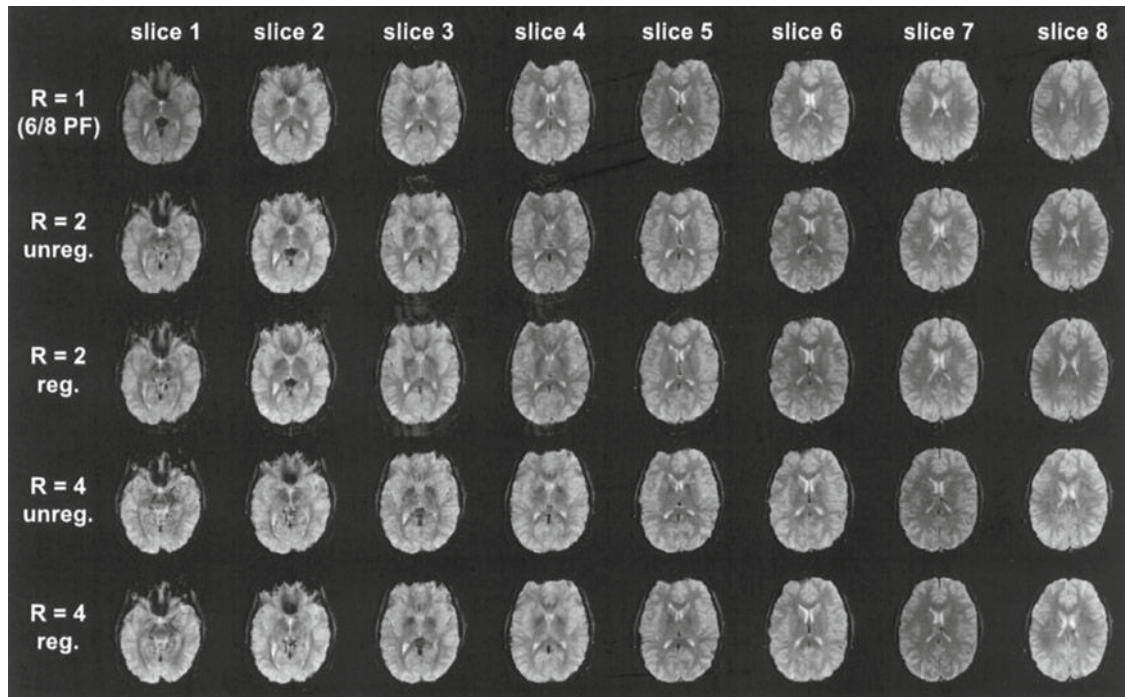


FIGURE 20.1. Compared to non-accelerated reconstruction ( $R = 1$ ) with 6/8 partial Fourier (PF) sampling, GRAPPA EPI reconstructions at 2X ( $R = 2$ ) and 4X ( $R = 4$ ) accelerations show decreased distortion around the temporal and frontal lobes, where susceptibility and  $B_0$  inhomogeneity is strong. At the same acceleration rate, regularized (reg.) reconstructions show less noise amplification than unregularized (unreg.) reconstructions, particularly around the center of the brain

informed consent. A checkerboard visual stimulus, designed to display either continuous flashing checkerboards at 4 Hz (the “on” condition), or fixation (the “off” condition), was presented to the subject. Three “off” conditions and two “on” conditions of seconds each were alternately presented, starting with the “off” condition. We used a 2D EPI sequence with the parameters: TR = 2,000 ms, TE = 50 ms, flip angle =  $90^\circ$ , slice thickness = 5 mm with 0.5 mm gap, 14 slices, FOV =  $200 \times 200$  mm, image matrix =  $128 \times 128$  for image acquisition. We collected three-segment EPI data (20 volumes in composition reconstruction, with eight “on” and 12 “off” conditions; ten dummy scans)

and four-segment EPI data (15 volumes in composition reconstruction with six “on” and nine “off” conditions; ten dummy scans). Phase encoding was in the anterior-posterior direction. We used the in vivo sensitivity method to reconstruct accelerated images and thus avoid misestimating the coil sensitivity maps. We also acquired the full FOV spatial prior required for regularized reconstruction by temporal collapsing EPI segments using interleaved segmented EPI (Lin et al. 2005). Figure 20.2a shows the  $t$  statistics maps of the 3T visual fMRI experiment using SENSE EPI both with and without regularization at three- and four-fold accelerations. At three-fold SENSE acceleration,

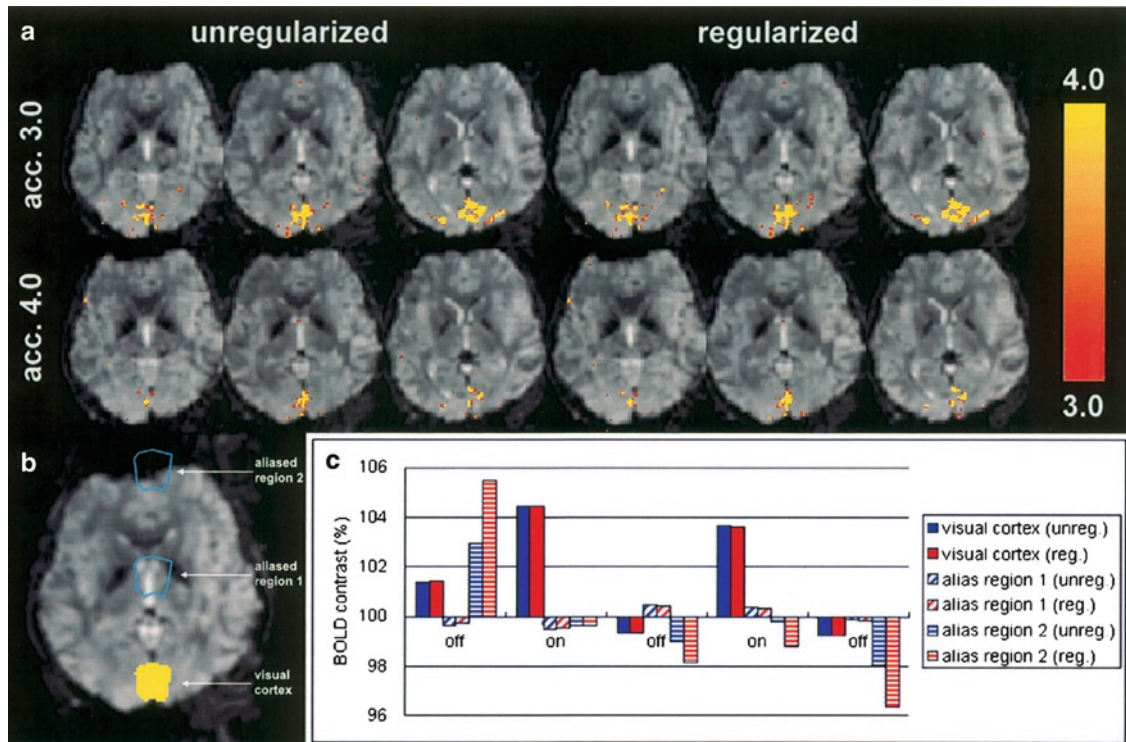


FIGURE 20.2. (a) The  $t$  statistics maps calculated from 3X and 4X SENSE reconstructions. (b) EPI image depicting the three aliased regions with 3X acceleration. One of the aliased regions, highlighted in yellow, is the visual cortex. (c) The time courses of the three aliased regions. Note that only the time course from the visual cortex corresponded well to the stimulus paradigm

regularized reconstructions yielded larger activated functional areas than unregularized reconstructions around the occipital lobe (regularized: 2,327 mm<sup>2</sup>; unregularized: 2,139 mm<sup>2</sup>). A similar increase in sensitivity by regularization was also observed in the four-fold SENSE acceleration (regularized: 896 mm<sup>2</sup>; unregularized: 735 mm<sup>2</sup>).

Figure 20.2b shows the three regions aliased with three-fold acceleration. One of the aliased regions shown here is visual cortex region, highlighted in yellow. The corresponding time courses of all three aliased regions are depicted in Figure 20.2c. Note that only the activated visual cortex region exhibited a time course that matched to the stimulus paradigm. The

other two aliased regions showed either low BOLD contrasts in all conditions or a time course mismatched to the stimulus paradigm. We have previously reported more detailed Monte Carlo simulations on the improvement of the stability of SENSE EPI reconstructions (Lin et al. 2005).

Here we demonstrated the benefits of parallel MRI to reduce distortion artifact. Spatial prior can also be incorporated to regularize reconstructions for suppression of noise levels introduced in parallel MRI reconstructions during dynamic fMRI scan. Further improvement of parallel MRI reconstruction can potentially be accomplished by using a large- $N$  coil array and optimizing the k-space trajectory for accelerated scans.

## APPLICATION – SENSE PROTON SPECTROSCOPIC IMAGING

In vivo magnetic resonance spectroscopy (MRS) and magnetic resonance spectroscopic imaging (MRSI) have been used for almost 3 decades to measure possible prognostic or diagnostic markers in living tissue (Gillies and Morse 2005). The former has been suggested as a clinical tool for cancer in various regions of the body (Belouche-Babari et al. 2005) and is a primary focus for applications in brain cancer (Preul et al. 1996). The major goals of MRS studies for applications in cancer diagnosis and treatment planning are to identify types and grades of cerebral neoplasm (Del Sole et al. 2001). Because MRS is sensitive to alterations in the chemical signals of various metabolites including choline (Cho), creatine (Cr), lactate, myoinositol, and N-acetyl-aspartate (NAA), MRS technology can help clinicians evaluate brain tumors and neoplasm metabolic states. The most frequently observed biomarkers of brain tumors include decreases in choline and lactate and increases in NAA. Magnetic resonance spectroscopic imaging (MRSI) techniques allow metabolic “images” to be obtained throughout the volume of interest with a single measurement (Brown et al. 1982), but are often limited by long echo times to reduce contamination from overwhelming peripheral lipids. Short-TE MRSI techniques are feasible and allow additional measurements of lipid signals in brain tumors. Measuring these signals is significant because their levels are indicative of macrophage activity in necrosis. Although identification of a tumor mass and assessment of its size and vasculature are best achieved with MRI,

MRSI can provide additional biochemical information that can be crucial for tumor classification, differential diagnosis and follow-up (Preul et al. 1998). The ability to display the metabolite distribution as a map is therefore very important and useful in clinical settings (Preul et al. 1998).

Magnetic resonance spectroscopic imaging (MRSI) measures spatially encoded time-domain signals from free-induction decay (FID), stimulated echoes, or spin echoes using gradient phase encoding to resolve the two- or three-dimensional spatial distribution of spectroscopic information that originated from different locations within the field-of-view (FOV). Data acquisition time grows in proportion to the spatial encoding specified in the imaging protocol. For example, in 2D proton MRSI with  $32 \times 32$  imaging matrix and  $TR = 2$  s, encoding time is  $>30$  min.

Several methods have been proposed to speed up conventional MRSI: Reduced k-space encoding techniques such as circular k-space sampling (Maudsley et al. 1994), variable repetition times for different phase encoding steps (Kuhn et al. 1996), and individually phase-encoded multi-echo techniques (Duyn et al. 1993) offer moderate acceleration of conventional phase encoding. Implementation of echo-time-encoded high-speed imaging methods is straightforward (Haase 1990), but achieving high spectral resolution at large spectral width is still time-consuming. Furthermore, short echo times are not feasible, and sensitivity is usually lower than with conventional techniques (Pohmann et al. 1997).

Even with above-mentioned efforts to accelerate MRSI, three-dimensional spatial encoding is still not clinically feasible. Data quality during such long data acquisition

times can be seriously degraded by head motion and scanner instability. Motion artifact is especially problematic with respect to tremors associated with neural degenerative diseases such as Alzheimer's, and dynamic metabolic imaging, which requires repeated measurements to provide time-resolved information, is limited to rather coarse temporal resolution.

Much faster spatial-spectral encoding can be achieved using either echo-planar (Posse et al. 1994) or spiral read-out methods (Adalsteinsson et al. 1998). Using echo-planar readout, proton-echo-planar-spectroscopic-imaging (Pepsi) can accelerate encoding times in human brain by more than an order of magnitude and has been developed for clinical MR scanners to measure two-dimensional metabolite distributions at short TE in just 1 min (minimum acquisition time for a  $32 \times 32$  matrix is 64 s with TR = 2 s) (Posse et al. 1995), and three-dimensional metabolite distributions in just a few minutes (Posse et al. 1994). Proton-echo-planar-spectroscopic-imaging (PEPSI) has also been employed for time-resolved metabolic imaging to map dynamically changing lactate concentrations during respiratory and metabolic challenges (Posse et al. 1997) and to characterize metabolic dysfunction during sodium-lactate infusion in patients with panic disorder (Dager et al. 1999).

Here we present the combination of PEPSI and parallel MRI, specifically SENSE reconstruction, to further accelerate data acquisition in high-speed spectroscopic imaging. The major motivation of this approach is to tradeoff SNR for rapid spatial encoding and reduced motion sensitivity during long data acquisition times. In vivo human subject experiments were performed under the supervision of

the Institutional Review Board, and with subjects' informed consent. PEPSI (Posse et al. 1995) was performed on healthy volunteers, using a 3T scanner (Trio, SIEMENS Medical Solution, Erlangen, Germany) equipped with an eight-channel surface array coil that covers the whole brain circumferentially by eight surface coils. This procedure includes water suppression by chemical shift selective saturation (CHESS) sequence (Haase et al. 1985), complete eight-slice outer volume suppression along the perimeter of the brain, spin-echo excitation, and fast spatial-spectral encoding of the half-echo using an EPI read-out gradient train along the x-axis (Posse et al. 1995). Data were acquired at 2.5 KHz per data point, using online regridding to account for ramp sampling (O'Sullivan 1985), and 1,024 gradient inversions. Reconstructed spectral width after even/odd echo editing was 1,080 Hz. Additional phase encoding along the Y-axis was applied to obtain 2D spatial encoding. SENSE for spatiotemporal acceleration, spatial phase encoding along the Y-axis was skipped by sampling one k-space line in a block of two, three, or four consecutive k-space lines in the phase encoding direction to achieve 2X, 3X, and 4X acceleration, respectively. Both non-water-suppressed (NWS) and water-suppressed (WS) PEPSI data were collected. Non-water suppressed data were collected without spatial presaturation and used for automatic phase and frequency shift correction. Proton-Echo-Planar-Spectroscopic Imaging (PEPSI) data were acquired from a para-axial slice at the upper edge of the ventricles with TR of 2 s and short TE of 15 ms using a  $32 \times 32$  spatial matrix with FOV of 220 mm; slice thickness was 15 mm. Such data were collected with eight

averages, among which single average data were also extracted to test whether SNR was sufficient for SENSE acceleration. The acquisition times for single-average and eight-average data were 64 and 512 s, respectively, without SENSE acceleration.

Reconstructed PEPSI data with eight averages were reconstructed with LCMoDel fitting. Water-suppressed data were acquired with 8.5, 4.25, 2.8 and 2.1 min acquisition times for fully sampled, 2X, 3X, and 4X SENSE, respectively. The three major metabolite peaks representing Cho, Cre, and NAA were also observed in unaccelerated scans and 2X, 3X, and 4X accelerated data with similar width and shape (not shown here). The shape of the baseline in all reconstructed data was mostly similar. The Cho, Cre, and NAA metabolite maps are shown in Figure 20.3 (top panel). The maps of fully sampled and 2X SENSE accelerated data are very similar. Signal-to-noise constraints in the 3X and 4X SENSE results failed to preserve the homogenous metabolite distribution in brain parenchyma regions seen in the fully sampled data.

A single signal average was extracted from the same data set with eight averages to evaluate the effect of SNR loss on SENSE acceleration quality. The Cho, Cre, NAA metabolite maps are shown in Figure 20.3 (bottom panel). Single-average, fully sampled data generated homogeneous maps. With only slight degradation, using 2X SENSE, which corresponds to 32 s data acquisition time, the metabolite maps were still comparable to the unaccelerated maps. 3X and 4X SENSE acceleration with 22 s and 16 s data acquisition times generated more noisy metabolite maps in brain paren-

chyma, indicating insufficient SNR for SENSE acceleration in both cases.

We have demonstrated the feasibility of using SENSE reconstruction to accelerate high-speed gradient-encoded MRSI data acquisition, which was achieved by trading off image SNR for faster data acquisition time. The reduced SNR results from decimated data samples and reconstruction-associated noise amplification. We have shown that at high field ( $\geq 3T$ ) the combination of PEPSI with SENSE can further reduce the intrinsic single-average 64 s data acquisition time for a  $32 \times 32$  matrix to 32 s (2X SENSE) with little degradation of metabolite information. With even higher field strength and improved RF coil arrays, we anticipate that SENSE-accelerated metabolite mapping with scan times on the order of a few seconds will become feasible. Another appropriate application of single-average SENSE PEPSI is the context of transient high SNR, such as in hyperpolarized  $^{13}C$  experiments (Golman et al. 2003). At lower field ( $\leq 1.5 T$ ), averaging was necessary to maintain SNR, and the chief advantage of the SENSE PEPSI imaging technique is thus reduced motion sensitivity associated with shortened acquisition time for a single average. Reduced motion sensitivity is particularly advantageous in clinical studies of patients with movement disorders. The overall SNR can be maintained with averaging, provided that the g-factor does not deviate too far from 1.0 using a dedicated array coil design and optimal coil placement.

Sensitivity-encoding (SENSE) acceleration is particularly important to reducing long scan times in 3D spatial encoding, which is currently under development in our laboratory. As mentioned above,



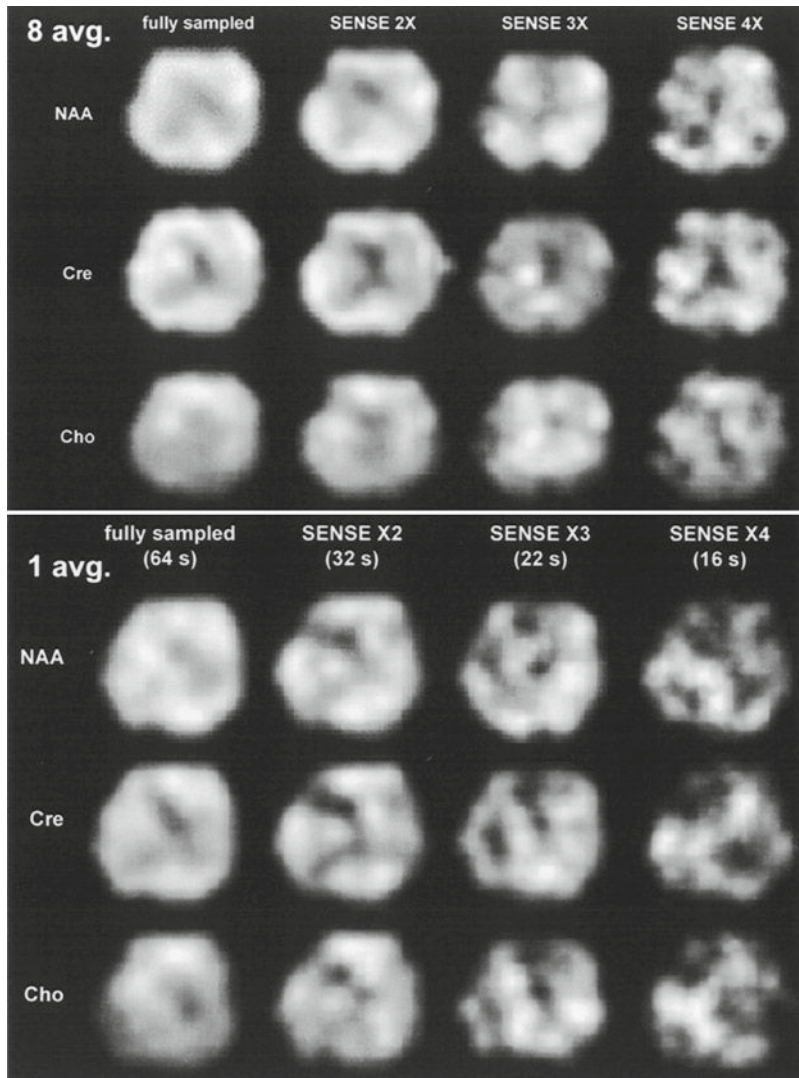


FIGURE 20.3. NAA, creatine (Cre), and choline (Cho) metabolite maps measured in a para-axial slice at the upper edge of the ventricles from full sampled data and 2X, 3X, 4X SENSE acceleration at 3 T with eight averages (*top* panel) and single average (*bottom* panel) after LCMoel quantification. Acquisition times for eight-average data were 8.5, 4.25, 2.8 and 2.1 min, respectively; for single-average data, 64, 32, 21 and 16 s, respectively

one-dimensional SENSE acceleration can be utilized to accelerate the slow spatial phase encoding in a 2D PEPSI experiment. Further acceleration can be achieved using two-dimensional SENSE in 3D PEPSI experiments, where two orthogonal spatial phase encoding gradients are used. The SENSE PEPSI imaging tech-

nique presented can also be generalized to other echo-planar-based read-out methods, such as echo-shifted EPI (Guimaraes et al. 1999) or spiral (Adalsteinsson et al. 1998) MRSI. In those methods, oscillating read-out gradients are used to encode 2D spatial information in a single shot. In that regard, direct application of 2D SENSE would be

feasible. In fact, the cylindrically symmetric layout of the currently available head RF array coil encourages use of 2D SENSE to minimize the g-factor. As we noted earlier, in the future a large- $N$  coil array may further increase the acceleration rate for high spatiotemporal resolution, with acceptable reconstructed spatio-spectral MRSI data.

In conclusion, in this chapter, we presented the principle of parallel MRI with a brief review of recent advances in data acquisition and image reconstruction strategies. We also presented mathematical formulation of image reconstruction. We demonstrated examples of parallel MRI using SENSE reconstructions in EPI and brain fMRI to reduce geometrical distortion. In particular, we showed that with good prior knowledge about the image to be reconstructed, sensitivity-encoded echo-planer imaging (SENSE EPI) can be further stabilized to improve sensitivity and specificity in dynamic scanning. For spectroscopic imaging, we showed that MRSI experiments at high field ( $\geq 3T$ ) may utilize parallel MRI to reduce imaging acquisition times with tolerable SNR reduction using single average PEPSI sequence, while low field ( $\leq 1.5T$ ) may still use SENSE to reduce motion sensitivity and acquire multiple averages to maintain overall SNR. In conclusion, improvement of spatiotemporal resolution by parallel MRI can benefit static, dynamic, and metabolic MR imaging for cancer diagnosis and management.

*Acknowledgements.* We thank Dr. Stefan Posse and Dr. Larry Wald for their helpful comments. We also thank Nichole Eusemann for her help with the text. This

work was supported by National Institutes of Health Grants R01 HD040712, R01 NS037462, P41 RR14075, R01 DA14178-01 and the Mental Illness and Neuroscience Discovery Institute (MIND).

## REFERENCES

- Adalsteinsson, E., Irarrazabal, P., Topp, S., Meyer, C., Macovski, A., and Spielman, D. M. (1998) Volumetric spectroscopic imaging with spiral-based k-space trajectories. *Magn. Reson. Med.* 39:889–898
- Bammer, R., Keeling, S. L., Augustin, M., Pruessmann, K. P., Wolf, R., Stollberger, R., Hartung, H. P., and Fazekas, F. (2001) Improved diffusion-weighted single-shot echo-planar imaging (EPI) in stroke using sensitivity encoding (SENSE). *Magn. Reson. Med.* 46:548–554
- Barth, M., Metzler, A., Klarhofer, M., Roll, S., Moser, E., and Leibfritz, D. (1999) Functional MRI of the human motor cortex using single-shot, multiple gradient-echo spiral imaging. *Magn. Reson. Imaging* 17:1239–1243
- Belouche-Babari, M., Jackson, L.E., Al-Saffar, N.M., Workman, P., Leach, M.O., and Ronen, S.M. (2005) Magnetic resonance spectroscopy monitoring of mitogen-activated protein kinase signaling inhibition. *Cancer Res.* 65:3356–3363
- Breuer, F.A., Blaimer, M., Heidemann, R.M., Mueller, M.F., Griswold, M.A., and Jakob, P.M. (2005a) Controlled aliasing in parallel imaging results in higher acceleration (CAIPIRINHA) for multi-slice imaging. *Magn. Reson. Med.* 53:684–691
- Breuer, F.A., Kellman, P., Griswold, M.A., and Jakob, P.M. (2005b) Dynamic autocalibrated parallel imaging using temporal GRAPPA (TGRAPPA). *Magn. Reson. Med.* 53:981–985
- Brown, T.R., Kincaid, B.M., and Ugurbil, K. (1982) NMR chemical shift imaging in three dimensions. *Proc. Natl. Acad. Sci. USA* 79:3523–3526
- Carlson, J.W., and Minemura, T. (1993) Imaging time reduction through multiple receiver coil data acquisition and image reconstruction. *Magn. Reson. Med.* 29:681–687
- Dager, S.R., Friedman, S.D., Heide, A., Layton, M.E., Richards, T., Artru, A., Strauss, W., Hayes, C., and Posse, S. (1999) Two-dimensional

- proton echo-planar spectroscopic imaging of brain metabolic changes during lactate-induced panic. *Arch. Gen. Psychiatry* 56:70–77
- de Zwart, J.A., Ledden, P.J., Kellman, P., van Gelderen, P., and Duyn, J.H. (2002a) Design of a SENSE-optimized high-sensitivity MRI receive coil for brain imaging. *Magn. Reson. Med.* 47:1218–1227
- de Zwart, J.A., van Gelderen, P., Kellman, P., and Duyn, J.H. (2002b) Application of sensitivity-encoded echo-planar imaging for blood oxygen level-dependent functional brain imaging. *Magn. Reson. Med.* 48:1011–1020
- de Zwart, J.A., van Gelderen, P., Kellman, P., and Duyn, J.H. (2002c) Reduction of gradient acoustic noise in MRI using SENSE-EPI. *Neuroimage* 16:1151–1155
- Del Sole, A., Falini, A., Ravasi, L., Ottobri, L., De Marchis, D., Bombardieri, E., and Lucignani, G. (2001) Anatomical and biochemical investigation of primary brain tumours. *Eur. J. Nucl. Med* 28:1851–1872
- Duyn, J.H., Gillen, J., Sobering, G., van Zijl, P.C., and Moonen, C.T. (1993) Multisection proton MR spectroscopic imaging of the brain. *Radiology* 188:277–282
- Gillies, R.J., and Morse, D.L. (2005) In vivo magnetic resonance spectroscopy in cancer. *Annu. Rev. Biomed. Eng.* 7:287–326
- Golay, X., Pruessmann, K.P., Weiger, M., Crelier, G.R., Folkers, P.J., Kollias, S.S., and Boesiger, P. (2000) PRESTO-SENSE: an ultrafast whole-brain fMRI technique. *Magn. Reson. Med.* 43:779–786
- Golman, K., Ardenkjaer-Larsen, J.H., Petersson, J.S., Mansson, S., and Leunbach, I. (2003) Molecular imaging with endogenous substances. *Proc. Natl. Acad. Sci. USA* 100:10435–10439
- Griswold, M.A., Jakob, P.M., Heidemann, R.M., Nittka, M., Jellus, V., Wang, J., Kiefer, B., and Haase, A. (2002) Generalized autocalibrating partially parallel acquisitions (GRAPPA). *Magn. Reson. Med.* 47:1202–1210
- Guimaraes, A.R., Baker, J.R., Jenkins, B.G., Lee, P.L., Weisskoff, R.M., Rosen, B.R., and Gonzalez, R.G. (1999) Echoplanar chemical shift imaging. *Magn. Reson. Med.* 41:877–882
- Haase, A. (1990) Snapshot FLASH MRI. Applications to T1, T2, and chemical-shift imaging. *Magn. Reson. Med.* 13:77–89
- Haase, A., Frahm, J., Hanicke, W., and Matthaei, D. (1985) 1H NMR chemical shift selective (CHESS) imaging. *Phys. Med. Biol.* 30:341–344
- Hansen, P.C. (1998) Rank-deficient and discrete ill-posed problems: numerical aspects of linear inversion. SIAM, Philadelphia, PA
- Heberlein, K., and Hu, X. (2006) Auto-calibrated parallel spiral imaging. *Magn. Reson. Med.* 55:619–625
- Hutchinson, M., and Raff, U. (1988) Fast MRI data acquisition using multiple detectors. *Magn. Reson. Med.* 6:87–91
- Jakob, P.M., Griswold, M.A., Edelman, R.R., and Sodickson, D.K. (1998) AUTO-SMASH: a self-calibrating technique for SMASH imaging. Simultaneous acquisition of spatial harmonics. *Magma* 7:42–54
- Kellman, P., Epstein, F.H., and McVeigh, E.R. (2001) Adaptive sensitivity encoding incorporating temporal filtering (TSENSE). *Magn. Reson. Med.* 45:846–852
- Kuhn, B., Dreher, W., Norris, D.G., and Leibfritz, D. (1996) Fast proton spectroscopic imaging employing k-space weighting achieved by variable repetition times. *Magn. Reson. Med.* 35:457–464
- Lin, F.H., Chen, Y.J., Belliveau, J.W., and Wald, L.L. (2003) A wavelet-based approximation of surface coil sensitivity profiles for correction of image intensity inhomogeneity and parallel imaging reconstruction. *Hum. Brain Mapp.* 19:96–111
- Lin, F.H., Kwong, K.K., Belliveau, J.W., and Wald, L.L. (2004) Parallel imaging reconstruction using automatic regularization. *Magn. Reson. Med.* 51:559–567
- Lin, F.H., Huang, T.Y., Chen, N.K., Wang, F.N., Stufflebeam, S.M., Belliveau, J.W., Wald, L.L., and Kwong, K.K. (2005) Functional MRI using regularized parallel imaging acquisition. *Magn. Reson. Med.* 54:343–353
- Madore, B. (2004) UNFOLD-SENSE: a parallel MRI method with self-calibration and artifact suppression. *Magn. Reson. Med.* 52:310–320
- Madore, B., Glover, G.H., and Pelc, N.J. (1999) Unaliasing by fourier-encoding the overlaps using the temporal dimension (UNFOLD), applied to cardiac imaging and fMRI. *Magn. Reson. Med.* 42:813–828

- Maudsley, A.A., Matson, G.B., Hugg, J.W., and Weiner, M.W. (1994) Reduced phase encoding in spectroscopic imaging. *Magn. Reson. Med.* 31:645–651
- McKenzie, C.A., Ohliger, M.A., Yeh, E.N., Price, M.D., and Sodickson, D.K. (2001) Coil-by-coil image reconstruction with SMASH. *Magn. Reson. Med.* 46:619–623
- McKinnon, G.C. (1993) Ultrafast interleaved gradient-echo-planar imaging on a standard scanner. *Magn. Reson. Med.* 30:609–616
- O'Sullivan, J. (1985) A fast sinc function gridding algorithm for Fourier inversion in computer tomography. *IEEE Trans. Med. Imaging MI-4*:200–207
- Pohmann, R., von Kienlin, M., and Haase, A. (1997) Theoretical evaluation and comparison of fast chemical shift imaging methods. *J. Magn. Reson.* 129:145–160
- Posse, S., DeCarli, C., and Le Bihan, D. (1994) Three-dimensional echo-planar MR spectroscopic imaging at short echo times in the human brain. *Radiology* 192:733–738
- Posse, S., Tedeschi, G., Risinger, R., Ogg, R., and Le Bihan, D. (1995) High speed 1H spectroscopic imaging in human brain by echo planar spatial-spectral encoding. *Magn. Reson. Med.* 33:34–40
- Posse, S., Dager, S.R., Richards, T.L., Yuan, C., Ogg, R., Artru, A.A., Muller-Gartner, H. W., and Hayes, C. (1997) In vivo measurement of regional brain metabolic response to hyperventilation using magnetic resonance: proton echo planar spectroscopic imaging (PEPSI). *Magn. Reson. Med.* 37:858–865
- Preibisch, C., Pilatus, U., Bunke, J., Hoogenraad, F., Zanella, F., and Lanfermann, H. (2003) Functional MRI using sensitivity-encoded echo planar imaging (SENSE-EPI). *Neuroimage* 19:412–421
- Preul, M.C., Caramanos, Z., Collins, D.L., Villemure, J.G., Leblanc, R., Olivier, A., Pokrupa, R., and Arnold, D.L. (1996) Accurate, noninvasive diagnosis of human brain tumors by using proton magnetic resonance spectroscopy. *Nat. Med.* 2:323–325
- Preul, M.C., Caramanos, Z., Leblanc, R., Villemure, J.G., and Arnold, D.L. (1998) Using pattern analysis of in vivo proton MRSI data to improve the diagnosis and surgical management of patients with brain tumors. *NMR Biomed.* 11:192–200
- Pruessmann, K.P., Weiger, M., Scheidegger, M.B., and Boesiger, P. (1999) SENSE: sensitivity encoding for fast MRI. *Magn. Reson. Med.* 42:952–962
- Pruessmann, K.P., Weiger, M., Bornert, P., and Boesiger, P. (2001) Advances in sensitivity encoding with arbitrary k-space trajectories. *Magn. Reson. Med.* 46:638–651
- Ra, J.B., and Rim, C.Y. (1993) Fast imaging using subencoding data sets from multiple detectors. *Magn. Reson. Med.* 30:142–145
- Roemer, P.B., Edelstein, W.A., Hayes, C.E., Souza, S.P., and Mueller, O.M. (1990) The NMR phased array. *Magn. Reson. Med.* 16:192–225
- Schmidt, C.F., Degonda, N., Luechinger, R., Henke, K., and Boesiger, P. (2005) Sensitivity-encoded (SENSE) echo planar fMRI at 3T in the medial temporal lobe. *Neuroimage* 25:625–641
- Sodickson, D.K. (2000) Tailored SMASH image reconstructions for robust in vivo parallel MR imaging. *Magn. Reson. Med.* 44:243–251
- Sodickson, D.K., and Manning, W.J. (1997) Simultaneous acquisition of spatial harmonics (SMASH): fast imaging with radiofrequency coil arrays. *Magn. Reson. Med.* 38:591–603
- Sodickson, D.K., and McKenzie, C.A. (2001) A generalized approach to parallel magnetic resonance imaging. *Med. Phys.* 28:1629–1643
- Tikhonov, A.N., and Arsenin, V.I. (1977) Solutions of ill-posed problems. Winston, Washington, DC and New York; distributed solely by Halsted Press
- Tsao, J., Boesiger, P., and Pruessmann, K.P. (2003) k-t BLAST and k-t SENSE: dynamic MRI with high frame rate exploiting spatiotemporal correlations. *Magn. Reson. Med.* 50:1031–1042
- Weiger, M., Pruessmann, K.P., Kassner, A., Roditi, G., Lawton, T., Reid, A., and Boesiger, P. (2000) Contrast-enhanced 3D MRA using SENSE. *J. Magn. Reson. Imaging* 12:671–677
- Weiger, M., Pruessmann, K.P., and Boesiger, P. (2002a) 2D SENSE for faster 3D MRI. *Magma* 14:10–19
- Weiger, M., Pruessmann, K.P., Osterbauer, R., Bornert, P., Boesiger, P., and Jezzard, P. (2002b) Sensitivity-encoded single-shot spiral imaging for reduced susceptibility artifacts in BOLD fMRI. *Magn. Reson. Med.* 48:860–866
- Yeh, E.N., McKenzie, C.A., Ohliger, M.A., and Sodickson, D.K. (2005a) Parallel magnetic

- resonance imaging with adaptive radius in k-space (PARS): constrained image reconstruction using k-space locality in radiofrequency coil encoded data. *Magn. Reson. Med.* 53:1383–1392
- Yeh, E.N., Stuber, M., McKenzie, C.A., Botnar, R.M., Leiner, T., Ohliger, M.A., Grant, A.K., Willig-Onwuachi, J.D., and Sodickson, D.K. (2005b) Inherently self-calibrating non-Cartesian parallel imaging. *Magn. Reson. Med.* 54:1–8

# 21

## Intra-axial Brain Tumors: Diagnostic Magnetic Resonance Imaging

Elias R. Melhem and Riyadh N. Alokaili

### INTRODUCTION

During the last century, central nervous system (CNS) imaging has witnessed a revolution with advances that have impacted all aspects of neuroscience practice in general and the management of intra-axial brain tumors in particular. In the pre-twentieth century era neurologists and neurosurgeons developed elaborate and sophisticated bedside examination techniques to gain insight into the calvarium. At the end of the nineteenth century and in the early twentieth century X-ray machines were developed and the ability to look through the opaque skull was a welcomed development by means of pneumoencephalography and later with cerebral angiography. In the 1970s, the way clinical neuroscience disciplines were practiced dramatically changed with the advent of X-ray computed tomography. Then in the 1980s, magnetic resonance imaging (MRI) was introduced. In the last 3 decades MRI became the imaging modality of choice for non-emergent neurological conditions, such as imaging of intra-axial brain masses, due to many advances including exquisite tissue contrast resolution and multi-planar capabilities.

Subsequent developments of additional nonanatomical MRI methods provided molecular, physiological, and metabolic information regarding the CNS. These advanced MRI techniques include perfusion imaging, diffusion weighted imaging, diffusion tensor imaging, magnetic resonance spectroscopy (MRS), blood oxygen level dependant (BOLD) imaging, and molecular imaging.

The role of MRI in the workup of intra-axial brain tumors can be broadly divided into tumor diagnosis and classification, treatment planning, and post-treatment surveillance. This chapter focuses on the diagnostic role of the most commonly used conventional anatomical and advanced MRI techniques, such as perfusion imaging, diffusion weighted imaging, and proton magnetic resonance spectroscopy (PMRS), in the management of common intra-axial brain tumors.

### CLASSIFICATION AND OVERVIEW OF CENTRAL NERVOUS SYSTEM TUMORS

CNS tumors can be divided broadly into neoplastic and non-neoplastic masses or mass-like lesions. Non-neoplastic conditions

that can be mistaken for intra-axial brain neoplasms include: tumefactive demyelinating lesions, encephalitis, abscesses (Figure 21.1), and hamartomas of tuberous sclerosis, mass-like cortical dysplasias, hematomas, and acute and subacute infarcts. Furthermore, neoplasms can also be broadly divided into metastasis and primary neoplasms. Several cell types give rise to primary CNS neoplasms; however, neoplasms of glial (Figure 21.2) and lymphocytic cell origins are responsible for the overwhelming majority of primary intra-axial brain neoplasms with those of glial cell origin being much more common.

## INTRA-AXIAL TUMOR IMAGING PROTOCOL

MRI protocols for brain tumors vary depending on the type of medical institution and the availability of equipment and expertise. It is beyond the scope of this chapter to outline the specifics of the various protocols. Instead, we will outline a few general imaging protocol principles that ought to be seriously considered by medical institutions interested in providing comprehensive care for patients with brain tumors.

Different imaging modalities used in brain tumor protocols, such as X-ray computed tomography, single photon emission tomography (SPECT), positron emission tomography (PET), or MRI have advantages and disadvantages. Hence, these modalities are not necessarily exclusionary but often complement one another, especially in complicated cases. In this

chapter however, we will emphasize MRI, which is the best single imaging modality in the evaluation of intraaxial tumors because of its multi-planar capability, lack of ionizing radiation, and versatility in contrast resolution. This reflects various aspects of tissue characteristics including water diffusivity, metabolic concentration, and hemoglobin saturation.

The basic MRI protocol should include fluid attenuated inversion recovery (FLAIR), T1, and T2 sequences. These sequences provide essential anatomical information such as location and size of the tumor as well as its relationship to eloquent structures. With respect to imaging planes, no protocol should be limited to a single plane and three orthogonal planes are preferred. Due to their ease and speed of acquisition, diffusion weighted images have become part of the basic protocol for imaging of brain tumors.

Gadolinium based contrast enhanced images are also an essential component of the basic MRI protocol. Enhancement indicates disruption of the blood brain barrier. The general purpose that contrast serves is to discriminate typically non-enhancing low-grade neoplasms, cortical dysplasia, and encephalitis from typically enhancing abscesses, lymphomas, tumefactive demyelinating lesions, high-grade primary and metastatic brain neoplasms. Although contrast enhancement alone is not highly specific for brain tumor characterization, it has been shown to improve lesion detection and differentiation (Runge et al. 2001). In addition to the essential minimum protocol described above, many academic and tertiary

---

bright on the axial diffusion weighted image (c), dark on the apparent diffusion coefficient map (d). On spectroscopy (e) there is an elevated amino acid signal (at 0.9 ppm), elevated Lac signal (at 1.33 ppm), elevated alanine signal (at 1.47 ppm), elevated acetate signal (at 1.92 ppm), absent NAA signal (at 2.02 ppm), absent Cr signal (at 3.0 ppm), and absent Cho signal (at 3.2 ppm)

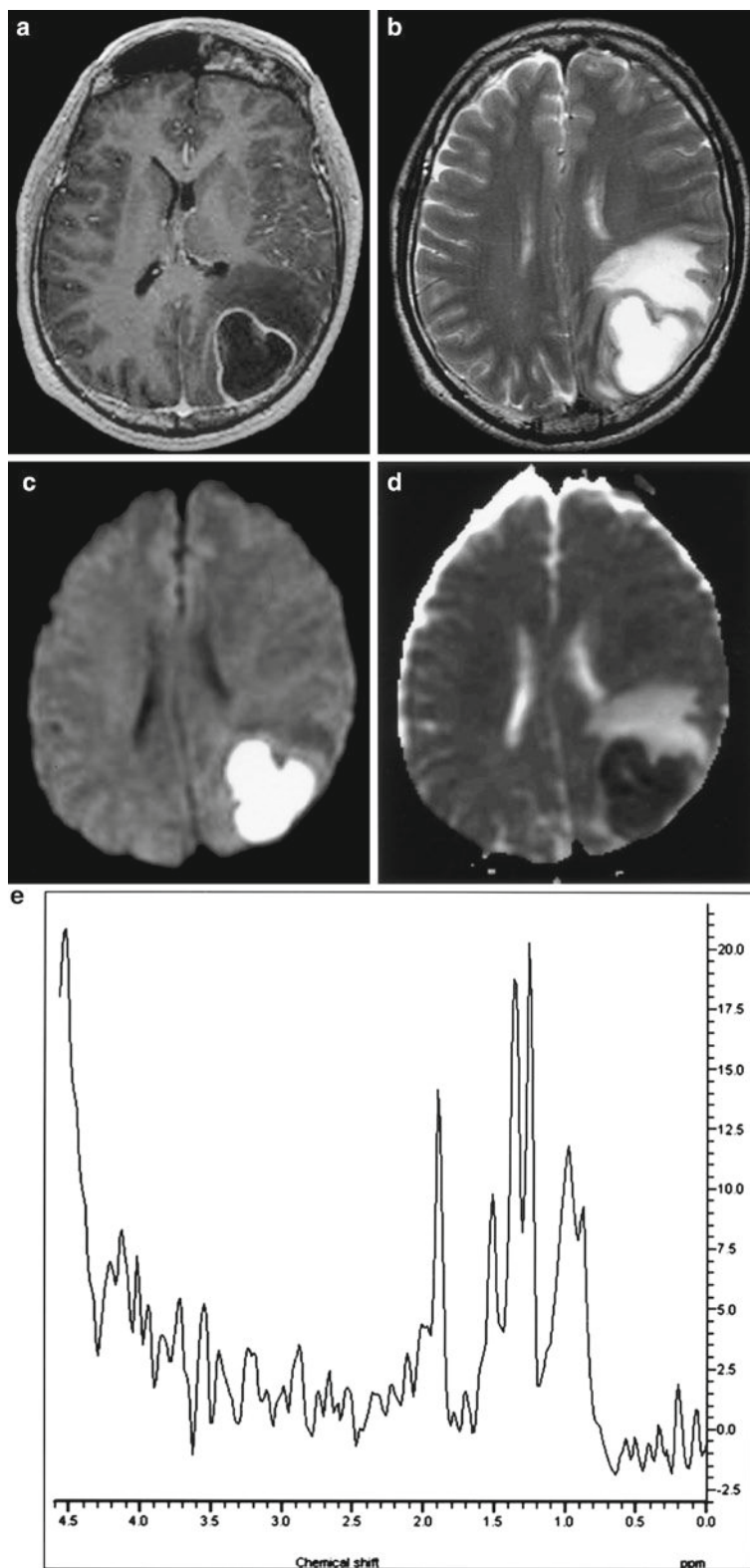


FIGURE 21.1. Left occipitoparietal pyogenic abscess. The lesion appears dark with a thin rim of enhancement on the axial post-contrast T1 image (a), bright with a dark rim on the axial T2 image (b), lightbulb



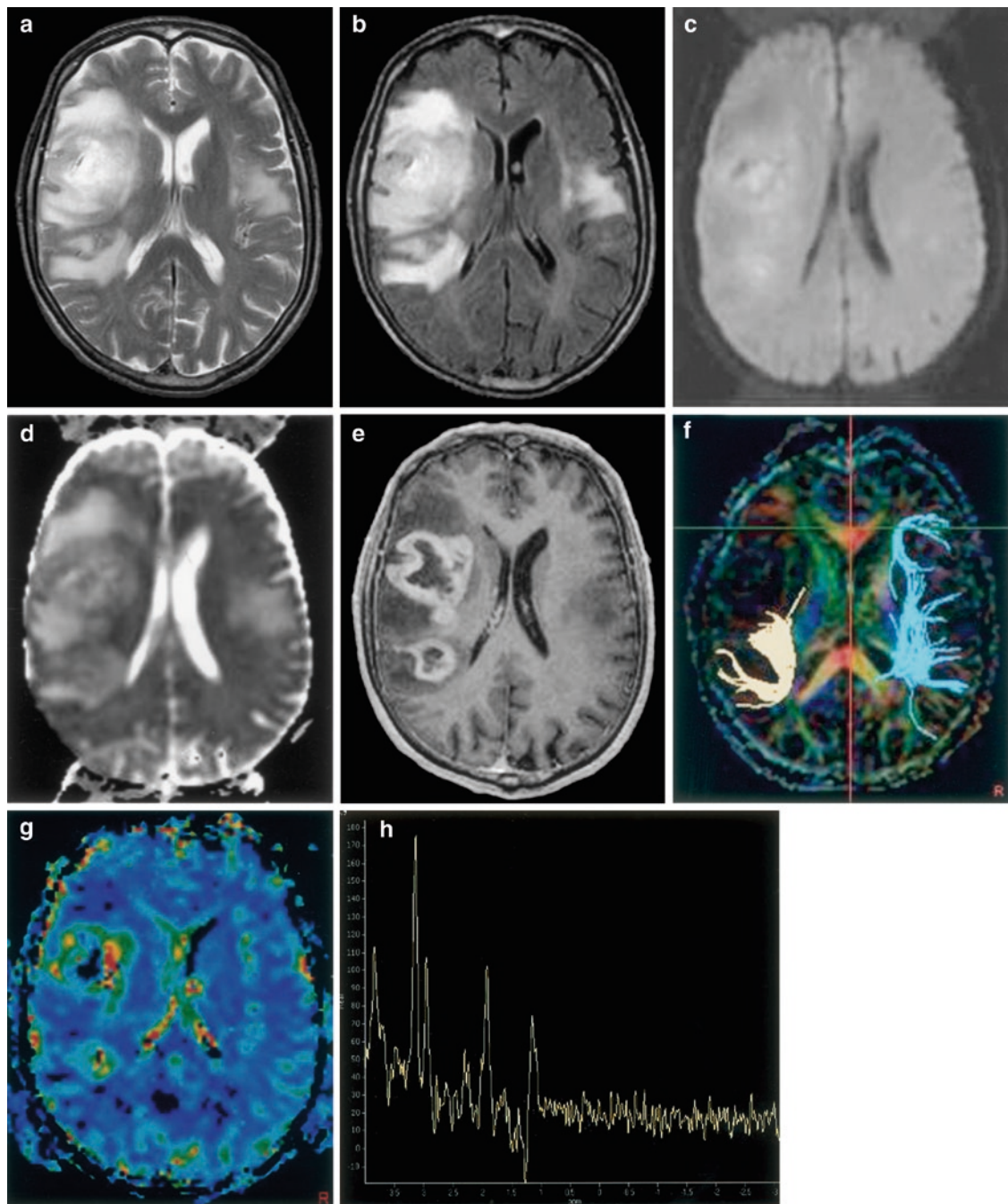


FIGURE 21.2. Glioblastoma multiforme. The lesion appears bright on the axial T2 image (a) and bright on the axial fluid attenuated inversion recovery image (b) with areas of bright signal on the axial diffusion weighted image (c) and corresponding dark signal on the apparent diffusion coefficient map (d) consistent with restricted diffusion. Multi-focal thick rim enhancement is seen on the axial post-contrast T1 image (e). The fiber tractography image (f) shows interruption of the right hemispheric associated white matter fibers (normal uninterrupted associated fibers are seen on the contra-lateral side). The axial negative integral perfusion map (g) shows markedly elevated perfusion. On the spectroscopic tracing at a TE of 288 ms, there is elevated Lac signal (at 1.33 ppm), decreased NAA signal (at 2.02 ppm), and marked elevation of the Cho signal (at 3.2 ppm). A synchronous non-enhancing mass is also seen on the contra-lateral side

care centers have elaborate brain tumor protocols that include many other sophisticated and exciting MRI techniques that are outlined next. Some protocols include a high-resolution anatomical often post-contrast sequence that can be loaded onto one of many commonly used surgical navigation systems which have become standard in many neurosurgical operating theaters.

Brain tumor imaging protocols may include PMRS. When PMRS is performed, it is beneficial to combine single-voxel and multi-voxel spectroscopy at least at a long TE (time to echo) of ~270 ms, but preferably also at short and intermediate TEs. From a practical standpoint, we encourage the adoption of one PMRS method in clinical practice in order to enhance familiarity and optimize utility. Perfusion magnetic resonance and diffusion tensor imaging are increasingly being added to brain tumor imaging protocols.

Functional BOLD MRI is not a routine part of tumor imaging protocols; however, it is often performed as a separate imaging session for patients with masses that are close to eloquent cortex (such as motor, sensory, or language). As mentioned above in regard to the anatomical navigation sequence, nearly any imaging sequence can be loaded onto the surgical navigation systems, where it is possible to superimpose physiologic, metabolic, white matter tracts, and cortical functional maps on anatomical images by merging and coregistering algorithms.

## DIFFUSION IMAGING

The random microscopic movement of water and molecules of similar size in tissues is what is meant by molecular diffusion. This motion is often referred to as Brownian motion and is caused

by the thermal energy harbored by these molecules. With MRI, random movement of water molecules from one voxel (an imaging volume element on a regular grid in three dimensional space) to adjacent ones, which changes the gradient the molecules experience, causes spin dephasing and resultant signal loss. The signal loss on routine MRI sequences caused by the diffusion phenomenon is minor and barely perceptible. On the other hand, diffusion weighted imaging is specifically designed to detect this phenomenon by applying an additional pair of strong pulsed magnetic gradients during imaging, known as bipolar gradients. Diffusion imaging therefore provides insight into the freedom of movement of water molecules in biological tissue with higher signal on diffusion weighted imaging indicating decreased motion, often referred to as restricted diffusion. To avoid misinterpretation of the signal modulation on diffusion weighted images, it is routine to calculate apparent diffusion coefficient maps from diffusion weighted imaging. On these maps, a lower apparent diffusion coefficient value corresponds to restricted diffusion. In clinical practice, diffusion weighted imaging is extremely sensitive for the demonstration of acute brain infarct because of the decrease of the diffusivity of water molecules in cytotoxic edema. However, the diffusivity of water molecules in brain tissue may be decreased due to several other factors, including high cellular density (Lai et al. 2002) and pus (Figures 21.1c and d).

## DIFFUSION TENSOR IMAGING

On apparent diffusion coefficient maps, the random movement of water is assigned a numerical value with no information on

the direction of movement. Free water movement is expected to be equal in all directions and is described as an isotropic movement; however, in biological tissues water movement is hindered by barriers due to the presence of cellular structures and the interstitial supporting framework. Hence, water movement in biological tissues may not be equal in all directions, an observation typical for well structured tissues such as white matter tracts and muscle, and often referred to as diffusion anisotropy. Water movement tends to be greater parallel versus perpendicular to the direction of the white matter tracts. Simplistically, diffusion tensor imaging is a more accurate representation of diffusion where diffusion is illustrated as a vector with a magnitude and direction. Diffusion tensor imaging has many potential advantages in clinical practice over standard diffusion weighted imaging, such as more reliable mapping of the extent of the tumors. Diffusion tensor imaging may also help illustrate the relationship of white matter tracts to tumors, and may show if these fiber tracts are disrupted or displaced (Figure 21.2) (Helton et al. 2006).

## PERFUSION MAGNETIC RESONANCE IMAGING

A variety of imaging modalities are capable of performing perfusion imaging by observing how a tracer in blood flows through the capillary bed using time-intensity or time-concentration curves, and then applying modified tracer kinetic equations. For MRI, one can use gadolinium-based contrast agents as tracers, a technique called dynamic susceptibility

contrast imaging. Alternatively, perfusion magnetic resonance imaging (PMRI) can be performed with spin labeling where there is no need for an extrinsic tracer, such as gadolinium-based contrast agents; instead, electromagnetically labeled blood water is used as a freely diffusible intrinsic tracer. An additional advantage of this technique is the ability to repeat perfusion imaging several times in one session as the electromagnetic label is nontoxic, and has a short half-life. A major drawback of this technique is the lower signal-to-noise ratio. Despite this last disadvantage, spin labeling may become the standard PMRI technique.

Perfusion imaging provides information regarding the hemodynamics of brain tumor microcirculation and, in an indirect manner tumor angiogenesis. On perfusion imaging, primary high-grade neoplasms (Figure 21.2g) and metastases are expected to have elevated relative tumor blood volume compared to tumefactive demyelinating lesions, abscesses, and low-grade neoplasms, most likely due to differences in angiogenesis.

## PROTON MAGNETIC RESONANCE SPECTROSCOPY

PMRS provides the ability to non-invasively generate biochemical profile characteristics of the normal brain and brain neoplasms in vivo. Through careful analysis of spectra, one can obtain information regarding neuronal viability, cell membrane integrity, or cellular bioenergetics.

Several brain metabolites can be separated based on differences in resonance

frequency using PMRS. Metabolites that are identified on PMRS and commonly used in clinical assessment of the brain include: (1) N-acetyl aspartate (NAA), that comprises a majority of the resonances at 2.01 ppm, is synthesized almost exclusively in the mitochondria of the neurons, and hence is a marker of neuronal density and function; (2) creatine and creatine phosphate (Cr), with resonances at 3.02 ppm, are involved in the regulation of cellular energetics. In general, Cr is used as an internal reference against which other metabolites are compared; (3) phosphocholine and glycerophosphocholine (Cho), with resonances at 3.21 ppm, are markers of membrane biochemistry. Cho is a sensitive but not very specific marker, which can be elevated in a multitude of conditions that cause myelin breakdown or cellular proliferation; (4) myoinositol (mI), with resonance at 3.50 ppm, is involved in the regulation of intracellular sodium content and glial activation. Again not a very specific metabolite that increases in regions of gliosis and astrocytic activation; (5) lactate (Lac), with a doublet at 1.30 ppm, is a marker of anaerobic metabolism, which can be elevated in conditions that cause brain hypoxia and necrosis. (Negendank et al. 1996; Tien et al. 1996). A recent systemic review by Hollingworth et al. (2006) concluded that PMRS is promising in the characterization of brain tumors, where typically the spectrum will demonstrate elevated Cho and reduce NAA peaks (Figure 21.2h).

There are several ways of performing PMRS. For instance, tracings can be obtained from a single voxel or from multiple voxels within a two-dimensional slice. Additionally, most commercial MR

scanners generate qualitative spectra and some are capable of generating semiquantitative spectra from which concentrations of brain metabolites can be estimated. Despite the several recent encouraging reports on quantitative PMRS (Panigrahy et al. 2006), in most institutions radiologists continue to interpret spectral tracings by comparing ratios of metabolic peak heights or the areas under the peaks.

## BASICS OF CENTRAL NERVOUS SYSTEM TUMOR IMAGE INTERPRETATION

It is important to follow the basics of CNS image interpretation in order to reduce the chance of erroneous classification of brain lesions and to diminish potential adverse effects on patient care. The first basic question to ask is whether the brain lesion is a mass. To be a mass the lesion must displace adjacent structures. Admittedly, with small lesions this elementary question may not be answerable and caregivers often resort to follow-up imaging. Next in line is the question of whether a lesion is inside the substance of the brain (intra-axial) or outside (extra-axial). The importance of the location of the lesion cannot be over-emphasized as the differential diagnosis of masses in these two compartments is considerably different. The rule of thumb in answering this question, is that masses expand the space they live in and compress adjacent structures. For example, an extra-axial mass is expected to cause compression of brain tissue with thinning and crowding of the cortical gyri, whereas an intra-axial mass is expected to cause expansion of brain tissue and thickening

of cortical gyri. Once the two basic criteria are met, one can properly label a lesion as an intra-axial mass and move on to analyzing the signal characteristics of the lesion on MRI.

## GENERAL CONVENTIONAL MAGNETIC RESONANCE IMAGING APPEARANCE OF INTRA-AXIAL TUMORS

Besides having the features of an intra-axial mass, these masses typically are expected to appear dark on T1-weighted images and bright on fluid attenuated inversion recovery and T2-weighted images compared to normal brain tissue. This, however, is not universal as increased tumor cellularity, presence of hemorrhage, or calcification can cause the lesion to be dark on fluid attenuated inversion recovery and T2-weighted images. On the other hand, lesions with subacute hemorrhagic components and/or melanin typically appear bright on T1-weighted images. Hence, signal characteristics on T1-weighted, T2-weighted, and fluid attenuated inversion recovery images may provide valuable information regarding the cellularity and contents of brain tumors, but are usually insufficient to allow accurate diagnosis.

Presence or absence of enhancement of intra-axial tumors following intravenous contrast administration, which depends on whether there is breakdown of the blood brain barrier or not, further helps in their characterization. In general, enhancement tends to be associated with masses that rapidly evolve, and, therefore, overwhelm the repair process of the blood brain barrier. This is typically observed with metastasis, high grade malignant gliomas

(Figure 21.2e), lymphomas, abscesses (Figure 21.1a), and tumefactive demyelinating lesions.

## APPEARANCE OF SPECIFIC INTRA-AXIAL BRAIN TUMORS ON ADVANCED MAGNETIC RESONANCE IMAGING

In the following sections we have concentrated on the most commonly used advanced MRI methods: perfusion MRI, diffusion weighted imaging and PMRS for the most common intra-axial brain tumors.

### Primary (Non-lymphomatous) Neoplasms

These can be broadly divided into low-grade (WHO grades I and II) and high grade (WHO grades III and IV) neoplasms. Although low and high grade neoplasms generally differ in their time of presentation, symptoms, and imaging features, the definitive distinction is based on microscopic findings where high-grade gliomas have relatively more cellular atypia, nuclear pleomorphism, neoangiogenesis, and necrosis. Typical distinguishing features on PMRS (Figure 21.2h) are elevated lipid signal (at 0.9 and 1.3 ppm) and elevated lactate (Lac) signal (at 1.33 ppm), which favor high grade neoplasms, and elevated myoinositol (mI) signal (at 3.55 ppm), which favor low-grade neoplasms, including Gliomatosis Cerebri (Howe et al. 2003; Law et al. 2003).

Tracings of PMRS should never be interpreted in isolation, as there are no precise peak ratios that clearly distinguish neoplasm from non-neoplastic conditions even with 3T scanners (Kim et al. 2006).

PMRS results, such as those published by Butzen et al. (2000), report a sensitivity of 79% and a specificity of 77% with a Cho/ NAA ratio of >1 as an indicator of a neoplastic process. Butzen et al. (2000) also report a sensitivity of 87% and a specificity of 85% by using a logistical regression model with ten input PMRS variables. A meta-analysis by failed to show a reliable spectroscopic feature that separates non-neoplastic from neoplastic conditions; however, this meta-analysis suggested that a Cho/NAA cutoff ratio of 2.2 offers the best accuracy in distinguishing high-grade neoplasms from low-grade neoplasms and non-neoplastic conditions.

On diffusion weighted imaging, primary neoplasms have variable apparent diffusion coefficients with most showing facilitated diffusion but some exhibiting restricted diffusion. Apparent diffusion coefficient is inversely proportional to neoplasm cellularity presumably due to heterogeneity and tortuosity of the interstitial space that limits water movement. The apparent diffusion coefficient value of high-grade gliomas is typically lower than that of low-grade gliomas (Yang et al. 2002). However, overlap exists making apparent diffusion coefficient measurements alone insufficient for determining the grade of a neoplasm (Lam et al. 2002).

With PMRI, one can generate several parameters related to tumor neovascularity. For instance, the relative tumor blood volume parameter provides a surrogate marker for the degree of neoplastic angiogenesis, which tends to increase with the grade of the neoplasm (Figure 21.2g). Additionally, neoplasm induced angiogenesis results in structurally abnormal vessels with increased permeability parameters on PMRI. Several studies have

shown that the grade of the neoplasm correlates with the relative tumor blood volume. A relative tumor blood volume ratio of 1.75 has been suggested as a cutoff threshold distinguishing high- from low-grade neoplasm (Law et al. 2003), where relative tumor blood volume is measured as a ratio of the maximal tumor blood volume to a region of interest in normal white matter. An important exception is low-grade glial neoplasms with oligodendroglial features, which may have markedly elevated relative tumor blood volume (Lev et al. 2004). This has been observed, in particular, with low-grade oligodendrogliomas and oligoastrocytomas with chromosome 1p deletion (Whitmore et al. 2007).

#### Secondary Neoplasms (Metastases)

Typical PMRS features include elevated lipid signal (at 0.9 and 1.3 ppm), elevated Lac signal (at 1.33 ppm), reduced or absent NAA signal (at 2.02 ppm), and an elevated Cho signal (at 3.2 ppm). Distinguishing metastases from high-grade primary neoplasm with spectroscopic analysis of the enhancing portion of the tumor is unreliable even though it has been shown by some to be possible by looking for higher degrees of lipid signal in metastases (Howe et al. 2003). On the other hand, because primary neoplasms have the propensity to infiltrate surrounding brain tissue, analysis of areas outside the enhancing portion of the mass was shown to be more promising (Burtscher et al. 2000; Law et al. 2002). Various metabolite signal ratios have been suggested for this purpose. In one study, a Cho/ NAA ratio of greater than one had an accuracy of 100% (Burtscher et al. 2000).

Typically, metastatic lesions have elevated apparent diffusion coefficient measurements; however, apparent diffusion coefficient map values of metastatic lesions are variable and overlap with those of primary neoplasms (Hartmann et al. 2003). Recently, it has been shown that because of neoplastic infiltration in primary neoplasms the apparent diffusion coefficient values obtained from peritumoral hyperintensity are lower in primary neoplasms compared to metastatic disease (Lu et al. 2003).

Metastatic lesions are expected to have elevated relative tumor blood volume. As explained above for primary neoplasms, the ability to induce angiogenesis is crucial for metastatic lesion growth. Perfusion parameters of metastatic lesions tend to overlap with high-grade neoplasm probably because of similarity in the degree of angiogenesis. One possible distinguishing feature is lower relative tumor blood volume measurements outside the enhancing portion of the metastatic lesion compared to that of the more infiltrative primary neoplasms (Law et al. 2002; Camacho et al. 2003).

### Lymphoma

Typical PMRS features resemble other high grade neoplasms and include elevated lipid signal (at 0.9 and 1.3 ppm), elevated Lac signal (at 1.33 ppm), reduced NAA signal (at 2.02 ppm), and elevated Cho signal (at 3.2 ppm). PMRS of lymphoma in AIDS patients demonstrates mild to moderately increased Lac and lipids along with a prominent Cho peak, decreased NAA, Cr, and mI signals (Chang et al. 1995; Simone et al. 1998). This pattern can help in differentiation from toxoplasmosis, which typically has elevated Lac and lipid but absence of the other metabolites on PMRS (Chinn et al. 1995).

High cellularity and large nuclear to cytoplasmic ratio in lymphoma is thought to be the cause of low apparent diffusion coefficient values in this type of neoplasm. This can help differentiate lymphoma from toxoplasmosis, which typically has significantly greater apparent diffusion coefficient values than lymphoma lesions (Camacho et al. 2003). A low apparent diffusion coefficient value would also favor lymphoma over glial neoplasms.

Differentiation of lymphoma from primary high-grade glial neoplasms is feasible with PMRI because lymphoma tends to have lower relative tumor blood volume (Cha et al. 2002; Sugahara et al. 1999; Hartmann et al. 2003) and the intensity time curves for lymphoma tend to significantly undershoot below the baseline (Hartmann et al. 2003). However, lymphoma tends to show higher relative tumor blood volume compared to toxoplasmosis (Ernst et al. 1998).

### Tumefactive Demyelinating Lesions

Multiple sclerosis is an idiopathic demyelinating disease that results in episodes of neurological deficits that are separated in time and brain lesions that are separated in space. On occasion this disease may present as an acute monophasic syndromes such as Marburg variant of multiple sclerosis, Baló's concentric sclerosis, and other focal tumefactive demyelinating lesions that may simulate brain neoplasms. Distinction of these rare demyelinating processes early in the course of the disease process has prognostic and treatment implications.

Typical PMRS features include reduced NAA signal (at 2.02 ppm) and elevated Cho signal (at 3.2 ppm), especially with acute lesions. Fulminant tumefactive

demyelinating lesions may show high Cho and low NAA signals as well as presence of Lac (Bitsch et al. 1999). It is often difficult to distinguish tumefactive demyelinating lesions from neoplastic lesions on PMRS (Bitsch et al. 1999). In multiple sclerosis, the spectroscopic abnormalities are not limited to the visible lesions on conventional T2-weighted and fluid attenuated inversion recover imaging, as normal appearing white matter can have reduced NAA compared to normal controls. In early stages an increase in the ml peak may be more apparent than decrease in NAA peak on spectra of normal appearing white matter

Acute lesions may show crescent or concentric areas of reduced apparent diffusion coefficient values on diffusion weighted imaging. Chronic lesions have elevated apparent diffusion coefficient values (Bernarding et al. 2002).

Bernarding et al. (2002) have also shown that perfusion imaging of tumefactive demyelinating lesions typically shows relative tumor blood volume values that are lower than normal brain. Perfusion imaging can aid in distinguishing tumefactive demyelinating lesions from high-grade primary neoplasms and metastatic lesions, which tend to have higher relative tumor blood volume (Cha et al. 2002).

### Brain Abscess

Occasionally, brain abscesses can be confused with neoplasm. These masses are more common in immune compromised patients. Predisposing factors in immunocompetent individuals include ear and sinus infections, distant foci of infection such as a pyogenic lung infection, and presence of pulmonary arteriovenous fistulas. Typical PMRS features (Figure 21.1e) include

elevated amino acid (at 0.9 ppm), Lac (at 1.33 ppm), alanine (at 1.47 ppm), acetate (at 1.92 ppm), pyruvate (at 2.37 ppm), and succinate (at 2.40 ppm) signals, as well as absent NAA (at 2.02 ppm), Cr (at 3.0 ppm), and Cho (at 3.2 ppm) signals.

Abscesses, therefore, have a distinct spectroscopic pattern that allows differentiation from other entities. For instance, elevation of the Cho peak and absence of signal from a variety of amino acids, acetate, and succinate are features that would favor a neoplastic process, whereas the presence and elevation of alanine, acetate, pyruvate, and succinate, favor abscesses. Additionally, PMRS can hint to the type of bacterium causing the abscess. For instance, abscesses caused by anaerobic bacteria tend to have elevated acetate and succinate peaks, whereas absence of acetate and succinate peaks are more likely with obligate aerobes or facultative anaerobes. Tuberculous abscesses usually have high lipid and Lac peaks. In contradistinction to pyogenic abscesses amino acids (leucine, isoleucine, and valine), succinate, acetate, and alanine signals are absent.

Apparent diffusion coefficient maps are of great value in distinguishing neoplasms, which often have facilitated diffusion, from abscesses, which classically have markedly restricted diffusion in their necrotic portions (Figure 21.1c and d). However, there are reports of some exceptions. Furthermore, the walls of necrotic or cystic tumors have been shown to have lower apparent diffusion coefficient values than that of an abscess (Chan et al. 2002). On perfusion MRI, there is lower relative tumor blood volume in the capsule of an abscess compared to the wall of necrotic or cystic neoplasms (Chan et al. 2002).



## Encephalitis

In encephalitis, typical PMRS features include elevated Lac (at 1.33 ppm), Cho (at 3.2 ppm), and mI (at 3.55 ppm) signals and reduced NAA (at 2.02 ppm) signal. Encephalitis can resemble low-grade gliomas on spectroscopy with a reduction of the NAA peak and elevation of the Cho and mI peaks. A Lac peak is inconsistent and cannot always be relied upon to distinguish encephalitis from low-grade gliomas. Following the early acute phase of encephalitis, there is a gradual return to a normal pattern on PMRS in approximately a year (Takanashi et al. 1997).

Encephalitis typically has low apparent diffusion coefficient values. However, this is not as consistent as reduction in apparent diffusion coefficient values obtained from acutely infarcted brain tissue (Tsuchiya et al. 1999). Diffusion weighted imaging carries prognostic information as fulminant cases more often cause diffusion restriction than milder ones.

A case-report by Nonaka et al. (2004) on computed tomography perfusion suggested elevated perfusion in the acute phase. In nuclear medicine imaging, there is normal to elevated perfusion in the early phase followed by abnormal reduction in the chronic phase (Launes et al. 1988). To our knowledge, findings on perfusion MRI in acute herpetic and non-herpetic encephalitis have not been reported in the medical literature.

## APPROACH TO AN UNKNOWN INTRA-AXIAL BRAIN TUMOR

Although there is a wealth of literature on the subject of advanced MRI of intra-axial brain tumors, very little research has been

published on how these various techniques can be integrated into a comprehensive approach for these tumors. The majority of publications on advanced MRI of intra-axial brain tumors has focused on the value of a single imaging technique in answering a binary question such as if the neoplasm is secondary or primary? However, a few researchers have shown that combining techniques can provide more reliable differentiation. To date, the most ambitious attempt to develop a strategy that integrates multiple techniques was published by. This group proposed a strategy where an unknown intra-axial brain tumor is analyzed by answering a series of simple imaging questions, which yield a specific diagnosis or a limited differential (Figure 21.3). This group has methodically shown that their strategy markedly increases the diagnostic specificity of intra-axial brain tumors. Readers who are interested in the details of this strategy can refer to the original publication as it is beyond the scope of this chapter. This group's encouraging initial experience has paved the way for a prospective study at the same center and has encouraged others to develop similar schemes that integrate techniques to improve accuracy instead of focusing only on isolated imaging technique and on narrow clinical questions.

## LIMITATIONS AND FUTURE DIRECTION

As is the case with conventional MRI, advanced techniques may be less reliable near locations with an intrinsic large magnetic gradient, as this results in susceptibility artifacts. For example, the analysis of small masses near the base of the skull or masses containing large amounts of blood

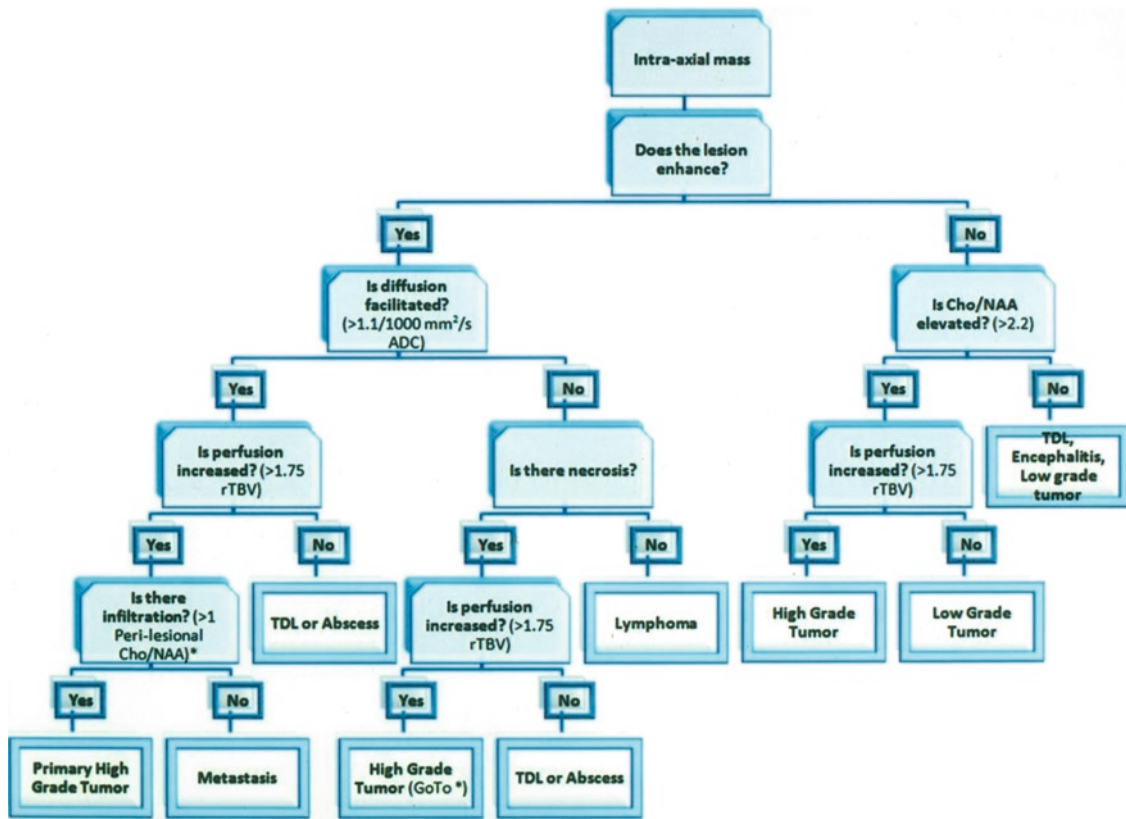


FIGURE 21.3. A practical magnetic resonance imaging based diagnostic algorithm for unknown intra-axial brain mass classification. This algorithm is composed of a series of nodes or questions that would suggest a diagnosis if the paths are followed to the bottom. Cho: Choline, NAA: N-acetylaspartate, ADC: Apparent diffusion coefficient, rTBV: relative tumor blood volume, TDL: Tumefactive demyelinating lesion

or calcium may be inaccurate. An additional limitation is that advanced imaging findings might be altered in patients who have undergone prior treatment, be it surgical intervention or medicinal (e.g., steroid therapy). Caution needs to be exercised in the pediatric age group as some pediatric brain neoplasms do not follow the general patterns described in this chapter. For instance pilocytic astrocytomas typically have elevated relative tumor blood volume despite being low grade (WHO I).

Conventional and advanced MRI stand to gain greatly with the wider spread use of higher field magnets. For example,

compared to 1.5 T, 3 T scanners can enhance the quality of both conventional and advanced methods by improving signal-to-noise ratio, which in turn can be traded for better spatial and temporal resolution. Scanning at high fields has a significant positive impact on motion sensitive and low signal intensity imaging sequences such as diffusion-weighted imaging. Dynamic susceptibility contrast perfusion imaging also benefits from the increased magnetic susceptibility effects at 3 T and arterial spin labeling perfusion imaging benefits from T1 prolongation of blood at 3 T. PMRS will also benefit from

the improved spectral and spatial resolution at high fields. In addition to proton based MRS, phosphorous and sodium based spectroscopy may play an increasingly important role in clinical practice in the near future. For instance, it is known that neoplastic cells have elevated intracellular sodium and therefore sodium MRS has the potential for better mapping the extent of neoplasms and distinguishing edema for neoplastic infiltration.

Quantitative PMRS will most likely become the default magnetic resonance spectroscopic analysis technique. Early published experience with this technique suggests an advantage over the conventional qualitative approaches. Tremendous work is going into developing a variety of new contrast agents. For instance, the use of iron-based contrast agents, which have a much longer half life in the tumor bed than gadolinium-based contrast agents, has been quite beneficial for intraoperative MRI where these agents are given only once prior to surgery in order to help differentiate disruption of the blood brain barrier due to brain tumor from disruption caused by surgery. For a comprehensive discussion of the use of various contrast agents in cancer imaging, the reader is referred to recent publications (Hayat 2008). Another area of great potential is nanotechnology where work is being done on linking contrast agents such as gadolinium on to nano-probes that will target specific healthy or pathologic cell lines.

In conclusion, intra-axial brain tumors are often a diagnostic challenge on imaging. Familiarity with the imaging characteristics of common intra-axial masses on conventional and advanced MRI has been shown to substantially improve the accuracy of interpretation and analysis of

such masses, especially when conventional and advanced imaging information is judiciously integrated.

## REFERENCES

- Bernarding, J., Braun, J., and Koennecke, H.C. (2002) Diffusion- and perfusion-weighted MR imaging in a patient with acute demyelinating encephalomyelitis (ADEM). *J. Magn. Reson. Imaging* 15:96–100
- Bitsch, A., Bruhn, H., Vougioukas, V., Stringaris, A., Lassmann, H., Frahm, J., and Brück, W. (1999) Inflammatory CNS demyelination: histopathologic correlation with in vivo quantitative proton MR spectroscopy. *Am. J. Neuroradiol.* 20:1619–1627
- Burtscher, I.M., Skagerberg, G., Geijer, B., Englund, E., Stahlberg, F., and Holtas, S. (2000) Proton MR spectroscopy and preoperative diagnostic accuracy: an evaluation of intracranial mass lesions characterized by stereotactic biopsy findings. *Am. J. Neuroradiol.* 21:84–93
- Butzen, J., Prost, R., Chetty, V., Donahue, K., Neppl, R., Bowen, W., Li, S.J., Haughton, V., Mark, L., Kim, T., Mueller, W., Meyer, G., Krouwer, H., and Rand, S. (2000) Discrimination between neoplastic and nonneoplastic brain lesions by use of proton MR spectroscopy: the limits of accuracy with a logistic regression model. *Am. J. Neuroradiol.* 21:1213–1219
- Camacho, D.L.A., Smith, J.K., and Castillo, M. (2003) Differentiation of toxoplasmosis and lymphoma in AIDS patients by using apparent diffusion coefficients. *Am. J. Neuroradiol.* 24:633–637
- Cha, S., Knopp, E.A., Johnson, G., Wetzel, S.G., Litt, A.W., and Zagzag, D. (2002) Intracranial mass lesions: dynamic contrast-enhanced susceptibility-weighted echo-planar perfusion MR imaging. *Radiology* 223:11–29
- Chan, J.H., Tsui, E.Y., Chau, L.F., Chow, K.Y., Chan, M.S., Yuen, M.K., Chan, T.L., Cheng, W.K., and Wong, K.P. (2002) Discrimination of an infected brain tumor from a cerebral abscess by combined MR perfusion and diffusion imaging. *Comput. Med. Imaging Graph* 26:19–23
- Chang, L., Miller, B.L., McBride, D., Cornford, M., Oropilla, G., Buchthal, S., Chiang, F., Aronow, H., Beck, C.K., and Ernst, T. (1995) Brain-

- lesions in patients with Aids - H-1 MR spectroscopy. *Radiology* 197:525-531
- Chinn, R.J., Wilkinson, I.D., Hall-Craggs, M.A., Paley, M.N., Miller, R.F., Kendall, B.E., Newman, S.P., and Harrison, M.J. (1995) Toxoplasmosis and primary Central-Nervous-System lymphoma in Hiv-infection - diagnosis with MR spectroscopy. *Radiology* 197:649-654
- Ernst, T.M., Chang, L., Witt, M.D., Aronow, H.A., Cornford, M.E., Walot, I., and Goldberg, M.A. (1998) Cerebral toxoplasmosis and lymphoma in AIDS: perfusion MR imaging experience in 13 patients. *Radiology* 208:663-669
- Hartmann, M., Heiland, S., Harting, I., Tronnier, V.M., Sommer, C., Ludwig, R., and Sartor, K. (2003) Distinguishing of primary cerebral lymphoma from high-grade glioma with perfusion-weighted magnetic resonance imaging. *Neurosci. Lett.* 338:119-122
- Hayat, M.A. (ed) (2008) Cancer imaging, Volumes 1 and 2. San Diego, CA/London: Elsevier/Academic
- Helton, K.J., Phillips, N.S., Khan, R.B., Boop, F.A., Sanford, R.A., Zou, P., Li, C.S., Langston, J.W., and Ogg, R.J. (2006) Diffusion tensor imaging of tract involvement in children with pontine tumors. *Am. J. Neuroradiol.* 27:786-93
- Hollingsworth, W., Medina, L.S., Lenkinski, R.E., Shibata, D.K., Bernal, B., Zurakowski, D., Comstock, B., and Jarvik, J.G. (2006) A systematic literature review of magnetic resonance spectroscopy for the characterization of brain tumors. *Am. J. Neuroradiol.* 27:1404-1411
- Howe, F.A., Barton, S.J., Cudlip, S.A., Stubbs, M., Saunders, D.E., Murphy, M., Wilkins, P., Opstad, K.S., Doyle, V.L., McLean, M.A., Bell, B.A., and Griffiths, J.R. (2003) Metabolic profiles of human brain tumors using quantitative in vivo H-1 magnetic resonance spectroscopy. *Magn. Reson. Med.* 49:223-232
- Kim, J.H., Chang, K.H., Na, D.G., Song, I.C., Kwon, B.J., Han, M.H., and Kim, K. (2006) 3T 1H-MR Spectroscopy in grading of cerebral gliomas: comparison of short and intermediate echo time sequences. *Am. J. Neuroradiol.* 27:1412-1418
- Lai, P.H., Ho, J.T., Chen, W.L., Hsu, S.S., Wang, J.S., Pan, H.B., and Yang, C.F. (2002) Brain abscess and necrotic brain tumor: discrimination with proton MR spectroscopy and diffusion-weighted imaging. *Am. J. Neuroradiol.* 23:1369-1377
- Lam, W.W.M., Poon, W.S., and Metreweli, C. (2002) Diffusion MR imaging in glioma: does it have any role in the pre-operation determination of grading of glioma? *Clin. Radiol.* 57:219-225
- Launes, J., Lindroth, L., Liewendahl, K., Nikkinen, P., Brownell, A.L., and Iivanainen, M. (1988) Diagnosis of acute herpes-simplex encephalitis by brain perfusion single photon-emission computed-tomography. *Lancet* 1(8596):1188-1191
- Law, M., Cha, S., Knopp, E.A., Johnson, G., Arnett, J., and Litt, A.W. (2002) High-grade gliomas and solitary metastases: differentiation by using perfusion and proton spectroscopic MR imaging. *Radiology* 222:715-721
- Law, M., Yang, S., Wang, H., Babb, J.S., Johnson, G., Cha, S., Knopp, E.A., and Zagzag, D. (2003) Glioma grading: sensitivity, specificity, and predictive values of perfusion MR imaging and proton MR spectroscopic imaging compared with conventional MR imaging. *Am. J. Neuroradiol.* 24:1989-1998
- Lev, M.H., Ozsunar, Y., Henson, J.W., Rasheed, A.A., Barest, G.D., Harsh, G.R. 4th, Fitzek, M.M., Chiocca, E.A., Rabinov, J.D., Csavoy, A.N., Rosen, B.R., Hochberg, F.H., Schaefer, P.W., and Gonzalez, R.G. (2004) Glial tumor grading and outcome prediction using dynamic spin-echo MR susceptibility mapping compared with conventional contrast-enhanced MR: confounding effect of elevated rCBV of oligodendrogliomas. *Am. J. Neuroradiol.* 25:214-221
- Lu, S., Ahn, D., Johnson, G., and Cha, S. (2003) Peritumoral diffusion tensor imaging of high-grade gliomas and metastatic brain tumors. *Am. J. Neuroradiol.* 24:937-941
- Negendank, W.G., Sauter, R., Brown, T.R., Evelhoch, J.L., Falini, A., Gotsis, E.D., Heerschap, A., Kamada, K., Lee, B.C.P., Mengeot, M.M., Moser, E.C., Padavic-Shaller, K.A., Sanders, J.A., Spraggins, T.A., Stillman, A.E., Terwey, B., Vogl, T.J., Wicklow, K., and Zimmerman, R.A. (1996) Proton magnetic resonance spectroscopy in patients with glial tumors: a multicenter study. *J. Neurosurg.* 84:449-458
- Nonaka, M., Ariyoshi, N., Shonai, T., Kashiwagi, M., Imai, T., Chiba, S., and Matsumoto, H. (2004) CT perfusion abnormalities in a case of

- non-herpetic acute limbic encephalitis. *Rinsho Shinkeigaku* 44:537–540
- Panigrahy, A., Krieger, M.D., Gonzalez-Gomez, I., Liu, X., McComb, J.G., Finlay, J.L., Nelson, M.D. Jr, Gilles, F.H., and Blüml, S. (2006) Quantitative short echo time 1H-MR spectroscopy of untreated pediatric brain tumors: preoperative diagnosis and characterization. *Am. J. Neuroradiol.* 27:560–72
- Runge, V.M., Muroff, L.R., and Jinkins, J.R. (2001) Central nervous system: review of clinical use of contrast media. *Top. Magn. Reson. Imaging* 12:231–263
- Simone, I.L., Federico, F., Tortorella, C., Andreula, C.F., Zimatore, G.B., Giannini, P., Angarano, G., Lucivero, V., Picciola, P., Carrara, D., Bellacosa, A., and Livrea, P. (1998) Localised H-1-MR spectroscopy for metabolic characterisation of diffuse and focal brain lesions in patients infected with HIV. *J. Neurol. Neurosurg. Psychiatry* 64:516–523
- Sugahara, T., Korogi, Y., Shigematsu, Y., Liang, L., Yoshizumi, K., Kitajima, M., and Takahashi, M. (1999) Value of dynamic susceptibility contrast magnetic resonance imaging in the evaluation of intracranial tumors. *Top. Magn. Reson. Imaging* 10:114–124
- Takanashi, J., Sugita, K., Ishii, M., Aoyagi, M., and Niimi, H. (1997) Longitudinal MR imaging and proton MR spectroscopy in herpes simplex encephalitis. *J. Neurol. Sci.* 149:99–102
- Tien, R.D., Lai, P.H., Smith, J.S., and Lazeyras, F. (1996) Single-voxel proton brain spectroscopy exam (PROBE/SV) in patients with primary brain tumors. *Am. J. Roentgenol.* 167: 201–209
- Tsuchiya, K., Katase, S., Yoshino, A., and Hachiya, J. (1999) Diffusion-weighted MR imaging of encephalitis. *Am. J. Roentgenol.* 173:1097–1099
- Whitmore, R.G., Krejza, J., Kapoor, G.S., Huse, J., Woo, J.H., Bloom, S., Lopinto, J., Wolf, R.L., Judy, K., Rosenfeld, M.R., Biegel, J.A., Melhem, E.R., and O'Rourke, D.M. (2007) Prediction of oligodendroglial tumor subtype and grade using perfusion weighted magnetic resonance imaging. *J. Neurosurg.* 107:600–609
- Yang, D., Korogi, Y., Sugahara, T., Kitajima, M., Shigematsu, Y., Liang, L., Ushio, Y., and Takahashi, M. (2002) Cerebral gliomas: prospective comparison of multivoxel 2D chemical-shift imaging proton MR spectroscopy, echoplanar perfusion and diffusion-weighted MRI. *Neuroradiology* 44:656–666

# 22

## Brain Tumors: Apparent Diffusion Coefficient at Magnetic Resonance Imaging

Fumiyuki Yamasaki, Kazuhiko Sugiyama, and Kaoru Kurisu

### INTRODUCTION

Diffusion-weighted magnetic resonance imaging (MRI) provides information on water mobility or diffusion within tissues by allowing visualization of the Brownian motion in those tissues. Also called diffusion-weighted imaging (DWI), this technique involves the use of phase-defocusing and phase-refocusing gradients to evaluate the rates of microscopic water diffusion within tissues, which allows visualization and characterization of biological tissues at a microscopic level *in vivo*. In living tissues, many factors influence water diffusion, including physical restrictions (cellular compartmentalization, cell type and number, cell membrane density, and macromolecule size and type), physicochemical properties of tissue (viscosity and temperature), and perfusion. In the human brain, water diffusion is a three-dimensional process that is not truly random because the motion of water is influenced by cell membranes, myelin sheaths, white matter fiber tracts, and protein molecules. The use of DWI has been explored as a means of visualizing and characterizing morphologic features such as edema, necrosis, and histopathologic characteristics of tumors and

tumor-like lesions by measuring differences in the apparent diffusion coefficient (ADC) caused by changes in water proton mobility (Tien et al. 1994). In biological tissues, variations in ADC are thought to result from changes in the balance between intracellular and extracellular water and differences in the structure of the two compartments (Hsu et al. 1996). In normal brain tissue, 20% of the aqueous fraction is distributed in the extracellular space, and 80% is in the intracellular space. The ADC within cells is lower than that in the extracellular space because of the presence of intracellular barriers such as organelles, membranes, and macromolecules (Hsu et al. 1996).

### DIFFUSION-WEIGHTED IMAGING AND T2 SHINE-THROUGH

Because DWI includes contributions from changes in T2, spin density, and ADC and thus does not provide “pure” maps of ADC, DW images should be interpreted in parallel with images obtained with other sequences, such as T2-weighted images and ADC maps. In DWI, signal intensity

inversely correlates with ADC and directly with T2 values and proton density. T2 shine-through effects occasionally produce high signal intensity on DWI, which can complicate evaluation of tissue characteristics with DWI. However, ADC maps are easily generated from DWI by using software available on most MRI systems. The ADC maps have several advantages, including the ability to distinguish T2 shine-through effects or artifacts from the true ADC in an area of interest. They also allow quantitative and reproducible assessments of diffusion changes, not only in areas exhibiting signal abnormality on conventional MR images but also in areas of normal signal, which could allow histologic changes to be detected earlier than on conventional images.

## DIFFUSION-WEIGHTED IMAGING SEQUENCES

The most widely used method for acquiring DW images is single-shot echo-planar imaging (EPI), because it is fast, efficient, and relatively insensitive to macroscopic motion as well as being widely available on most clinical MRI scanners. Drawbacks to EPI-based DWI include its susceptibility to artifacts from off-resonance effects and its low spatial resolution. Alternative scanning approaches include multiple-shot techniques, such as multi-shot EPI with navigator echo correction or diffusion-weighted Periodically Rotated Overlapping Parallel Lines with Enhanced Reconstruction (PROPELLER), and parallel imaging methods such as SENSitivity Encoding (SENSE). These DWI methods were described in a recent review (Bammer 2003). Diffusion tensor imaging (DTI) is also becoming more widespread as a means of visualizing the

location and orientation of white matter tracts; DTI requires data from at least six independent spatial directions of DWI. Two independent parameters can be derived from DTI – mean diffusivity (akin to ADC) and fractional anisotropy. Finally, DTI can also be used for tractography, which illustrates white-matter connectivity.

## CELLULARITY AND APPARENT DIFFUSION COEFFICIENT

The ADC is strongly affected by microscopic biological structures such as the number, type, and spatial arrangement of cells. These structures create barriers to the free diffusion of water. Therefore, changes in ADC may reflect changes occurring within and between cells more directly than other forms of imaging. The cellularity of tumors, defined as the number of cells in a given area of tumor tissue, seems to correlate inversely with ADC in gliomas, meningiomas, pediatric brain tumors (including embryonal tumors), malignant lymphomas, and human melanoma xenografts, as determined by automated quantitative evaluation of cell blocks (Sugahara et al. 1999; Gupta et al. 1999; Kono et al. 2001; Guo et al. 2002; Gauvain et al. 2001). Although the presence of cystic or necrotic changes in high-grade tumors can confound the inverse relationship between ADC and cellularity (Gupta et al. 1999), evaluating ADC during MRI of brain tumors would be useful to refine diagnoses because cellularity is an important histologic determinant (e.g., malignant grade of glioma). Cellularity of tumors is an important factor that influences microscopic water diffusion in tumors, because it determines the ratio of extracellular to intracellular space in a given area of

the tissue. Therefore, an increase in cellularity, which would decrease the fraction of extracellular space, would also likely result in more restricted water diffusion.

The nuclear/cytoplasmic ratio, which is known to influence tumor grade, may also influence ADC values (Kono et al. 2001). Some studies have suggested that intranuclear ADC is higher than cytoplasmic ADC (Hsu et al. 1996), which implies that tumors with a high nuclear/cytoplasmic ratio would have a higher (rather than a lower) ADC. However, assessment of ADC in tumors with high nuclear/cytoplasmic ratios actually showed *lower* ADC values, probably because diffusion in single cells may not adequately reflect diffusion in a multicellular environment. The ADC of tissues can be affected by diffusion outside the cell as well as that inside the cell. Tumors that have a high nuclear/cytoplasmic ratio also tend to have a relatively small amount of extracellular matrix because of an increased number of cells per tissue area. The amount of extracellular matrix is probably more important than the minor difference in diffusivity between the nucleus and cytoplasm (Guo et al. 2002). Therefore, cellularity, not nuclear/cytoplasmic ratio, seems to be the more important determinant of ADC in tumors.

## CLINICAL APPLICATION OF APPARENT DIFFUSION COEFFICIENT IN BRAIN TUMOR ASSESSMENTS

The most common use of DWI and ADC for tumor imaging in routine clinical practice has been to distinguish tumors from non-neoplastic masses that may appear similar on conventional imaging, such as necrotic

tumor versus brain abscess, epidermoid tumor versus arachnoid cyst, or lymphoma versus toxoplasmosis (Ebisu et al. 1996; Okamoto et al. 2000; Camacho et al. 2003). Cerebrovascular, demyelinating, inflammatory, infectious, and other types of diseases can also mimic brain tumors on MRI. Brain tumors can usually be distinguished from nonneoplastic masses on the basis of clinical and radiologic characteristics. However, nonneoplastic diseases can follow an atypical clinical course or show radiologic findings resembling those of brain tumors. The information gained from DWI and ADC could be invaluable for distinguishing brain tumors from other diseases, a critical issue in neuroradiology given the need to avoid invasive procedures (e.g., surgical biopsy) in making a diagnosis.

The use of ADC has also been explored for estimating tumor histology and grade (Sugahara et al. 1999; Stadnik et al. 2001). Although ADC is thought to reflect cellularity, recent reports have shown no significant differences in ADC among the three most common types of intracranial neoplasms: gliomas, metastatic lesions, and meningiomas (Kono et al. 2001; Yamasaki et al. 2005). However, it would be too hasty to conclude that ADC is not useful for distinguishing among various types of brain tumors. Some tumors, especially those of the same World Health Organization (WHO) grade, can be difficult to diagnose with conventional imaging; ADC could be useful for distinguishing among diagnostic candidates suggested by conventional MRI.

The ADC has also been used to distinguish peritumoral edema from tumor infiltration (Kono et al. 2001; Lu et al. 2004), to monitor early responses to treatment (Chenevert et al. 2000), to distinguish tumor recurrence from radiation necrosis (Hein et al. 2004), to quantify white-



matter injury related to tumor therapy, and to distinguish postoperative injury from tumor recurrence (Smith et al. 2005). Aspects of these applications are discussed briefly in the paragraphs that follow.

## TUMOR GRADE AND APPARENT DIFFUSION COEFFICIENT

Exact depiction, diagnosis, and grading of brain tumors are essential for planning treatments. Although conventional MRI can characterize the location and extent of some brain tumors, it is sometimes insufficient for distinguishing between tumor types or for assigning a tumor grade. The sensitivity of conventional MRI for determining the grade of gliomas, for example, ranges from 55% to 83%. Some high-grade tumors demonstrate minimal edema with no significant enhancement, necrosis, or mass effect; and some low-grade tumors show strong enhancement, central necrosis, mass effect, and peritumoral edema. The enhancement is thought to result mainly from disruption of the blood–brain barrier rather than from vascular proliferation within the tumor, and the enhanced areas may not always reflect the most malignant part of the tumor. In previous neuro-oncology studies in which ADC was used to determine tumor grade in gliomas, the mean ADC for high-grade tumors ranged from  $0.82 \times 10^{-3}$  to  $1.4 \times 10^{-3}$  mm<sup>2</sup>/s, and the mean ADC for low-grade tumors ranged from  $0.96 \times 10^{-3}$  to  $2.7 \times 10^{-3}$  mm<sup>2</sup>/s (Kono et al. 2001; Bulakbasi et al. 2004). Although previous studies have shown a wide range of tumoral ADC values, ADCs in high-grade gliomas generally are higher than those in low-grade gliomas, and significant

negative correlations have been found between ADC and astrocytic tumors of WHO grades 2–4. Notably, we previously showed the accuracy of ADC alone for the differential diagnosis of low-grade versus high-grade gliomas to be 84% (Yamasaki et al. 2005). Moreover, the accuracy of differential diagnosis between low-grade and high-grade malignant tumors can be increased from 70% to 80% to more than 90% by adding ADC to conventional MRI (Bulakbasi et al. 2004). Large prospective studies will be necessary to confirm the utility of adding ADC to conventional MRI for distinguishing among glioma grades.

## DIFFERENTIATION OF BRAIN TUMORS AND APPARENT DIFFUSION COEFFICIENT

### Astrocytomas, Oligodendrogliomas, and Ependymomas

The ability to distinguish between oligodendroglial and astrocytic brain tumors is clinically relevant because oligodendroglial tumors are more sensitive to adjuvant therapy. Identifying the pathologic subtype of gliomas of the same grade (e.g., astrocytomas, oligodendrogliomas, ependymomas, and others) presents more of a challenge than does grading gliomas; indeed, distinguishing astrocytomas from oligodendrogliomas in tumors of the same grade may not be possible (Bulakbasi et al. 2004; Yamasaki et al. 2005).

Astrocytomas are the most common form of glioma. Documented differences in ADC between low-grade and high-grade gliomas in general may be due to differences in ADC between low-grade versus high-grade astrocytomas in particular. The potential usefulness of ADC measurements for distin-

guishing between grade 2 oligodendroglial tumors and grade 3 oligodendrogliomas, between grade 2 and grade 3 ependymal tumors, between grade 2 astrocytic tumors and grade 2 ependymal tumors, and between grade 3 astrocytic tumors and grade 3 ependymal tumors needs further study.

### Dysembryoplastic Neuroepithelial Tumors

Among the dysembryoplastic neuroepithelial tumors (DNTs), the ADC values are highest for benign brain tumors (Yamasaki et al. 2005). Typically, DNTs develop in the temporal or frontal supratentorial cortex and, less often, in the caudate nucleus, cerebellum, third ventricles and pons, and septum pellucidum. The preoperative diagnosis of DNT is important because aggressive surgical treatments like those given for glioma are not necessary for DNT; however, DNTs tend to exhibit only nonspecific features on conventional MRI and computed tomography (CT). We previously found that the ADC of DNTs was higher than that of

astrocytic grade 2 tumors (accuracy, 100%) and other glioneuronal tumors (Yamasaki et al. 2005). Preoperative ADC measurements may facilitate a differential diagnosis of DNT; MR spectroscopy may be also helpful for identifying DNTs because DNTs tend to show normal spectra.

### Medulloblastomas, Primitive Neuroectodermal Tumors, and Ependymomas

The ADC values for embryonal tumors such as medulloblastomas, primitive neuroectodermal tumors (PNETs), or atypical teratoid/rhabdoid tumors, all of which tend to develop in childhood, are lower than those of ependymomas (Gauvain et al. 2001; Yamasaki et al. 2005), which may reflect the high cellularity of embryonal tumors (the so-called ‘blue tumors’). Preoperative measurement of the ADCs of fourth-ventricle tumors may facilitate the differential diagnosis between ependymomas and medulloblastomas (Figure 22.1a and b).

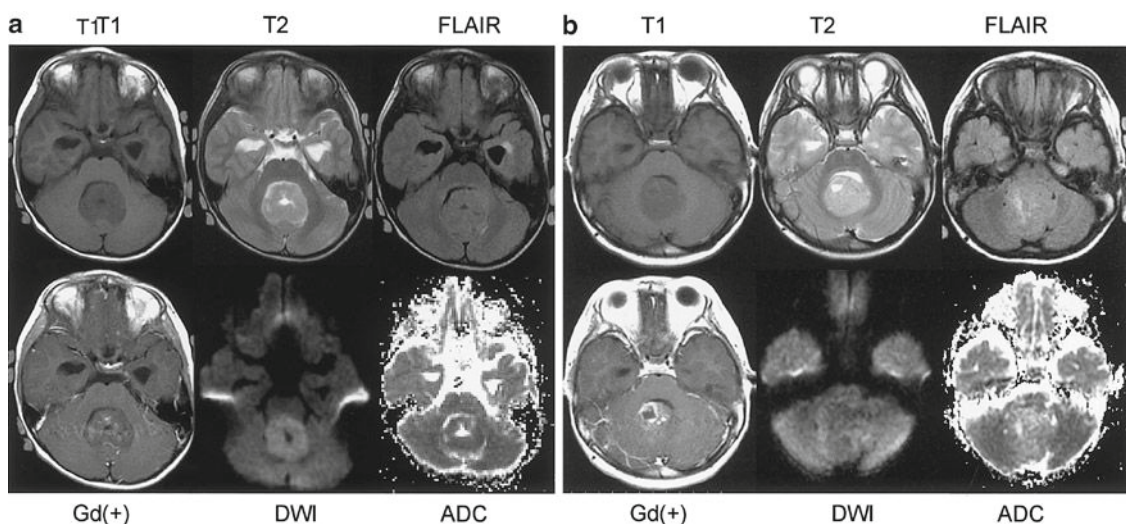


FIGURE 22.1. Images of fourth ventricle tumors. (a) Medulloblastoma in a 5-year-old boy. Mean ADC is  $0.692 \times 10^{-3} \text{ mm}^2/\text{s}$ . (b) Ependymoma in a 4-year-old girl. Mean ADC is  $1.112 \times 10^{-3} \text{ mm}^2/\text{s}$

### Central Neurocytomas and Subependymomas

Several types of tumors can develop in the lateral ventricles, and the diagnosis of some of these tumors can be deduced from the patient's age or sex or the anatomic location of the tumor (e.g. meningiomas at the trigon in females), but are difficult to diagnose in others. Preoperative measurements of the ADC may be useful for distinguishing central neurocytomas, which have low ADCs, from subependymomas, which have high ADCs (Yamasaki et al. 2005) (Figure 22.2a and b). These preliminary findings need to be replicated in larger studies that include cases of aggressive subependymoma.

### Hemangioblastomas and Other Posterior Cranial Fossa Tumors

Hemangioblastomas have been reported as having higher ADCs than do other posterior cranial fossa tumors. Hemangioblastomas are characterized by the presence of a network of capillary-like channels, separated

by trabeculae or islands of stromal cells. However, this finding is not specific, as it appears in highly vascular tumors as well (e.g., angiomatous meningioma, renal cell carcinoma) (Filippi et al. 2001). Therefore, further studies are necessary to confirm the possible value of ADC for distinguishing hemangioblastomas from other types of tumors.

### Glioblastomas, Metastatic Tumors, and Malignant Lymphomas

Preoperative ADC assessment may also be helpful in the differential diagnosis of malignant lymphoma. Previous studies found that ADCs in malignant lymphomas were lower than ADCs in high-grade astrocytomas (Guo et al. 2002) or in glioblastomas and metastatic tumors (Yamasaki et al. 2005), presumably because of the higher cellularity of malignant lymphoma (Guo et al. 2002). The ability to distinguish malignant lymphoma from glioblastomas and metastatic tumors is clinically relevant because malignant lymphomas usually respond to adjuvant therapy, making complete surgical

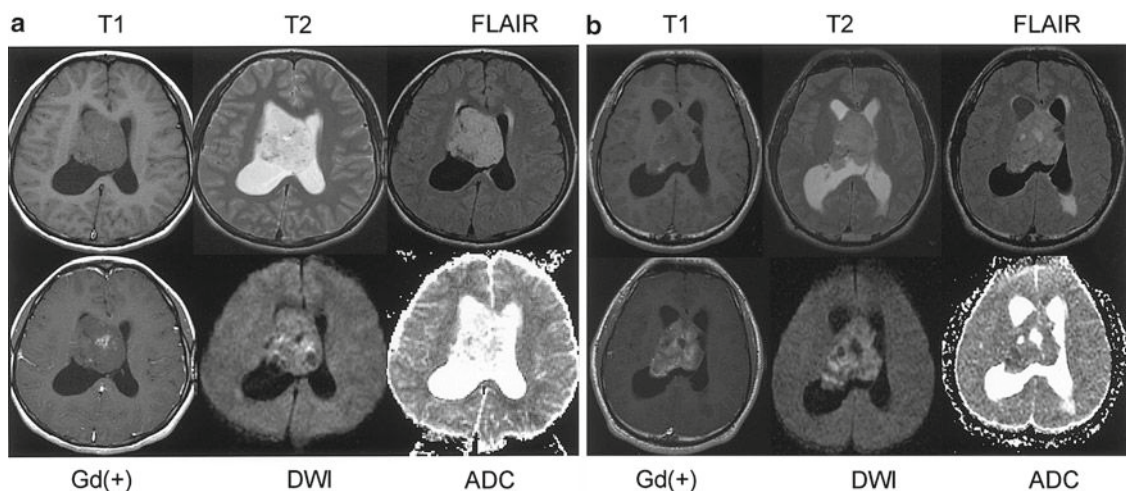


FIGURE 22.2. Images of lateral ventricle tumors. (a) Subependymoma in a 20-year-old woman. Mean ADC is  $1.516 \times 10^{-3} \text{ mm}^2/\text{s}$ . (b) Central neurocytoma in a 29-year-old man. Mean ADC is  $0.704 \times 10^{-3} \text{ mm}^2/\text{s}$

removal of the mass less critical; by contrast, every effort should be made to resect the entire tumor mass for glioblastomas and metastatic tumors if possible. The ADC values for extracranial malignant lymphoma have also been reported as being lower than ADCs for other types of tumors at the same anatomic site, and these results further suggest that the ADC for malignant lymphomas may be lower than the ADC for some metastatic tumors.

Gliomas and metastases from other primary tumors are the most common brain tumors. One group found that ADC values could distinguish glioblastomas from metastatic tumors, being higher for the glioblastomas (Krabbe et al. 1997), but other groups found no difference in ADC between these types of tumors (Kono et al. 2001; Yamasaki et al. 2005). However, none of the studies done to date has attempted to analyze metastatic tumors according to their origin or histologic type. Presumably, the range of ADC values would be different for metastatic lesions from different primary tumors of different histologic types.

Some have reported that the edema surrounding metastatic lesions in the brain was associated with a significantly higher ADC than that for high-grade glial tumors, whereas others found no difference in ADC values for peritumoral edema or tumor (Krabbe et al. 1997; Bulakbasi et al. 2004). This discrepancy may reflect the grouping together of grade 3 and grade 4 gliomas. The edema associated with grade 3 tumors is usually less extensive than that associated with grade 4 tumors, and this difference may confound the ADC results. Also, the edema associated with metastatic tumors is affected by the histology of the primary tumor. Further studies with large numbers of samples will be necessary to examine the

effects of histologic subtype and malignant tumor grade on ADC measurements.

### Histologic Subtyping of Meningiomas and Schwannomas

Preoperative measurement of ADCs was not indicative of the histologic subtype of meningiomas in two studies (Kono et al. 2001; Yamasaki et al. 2005), but in another, atypical (WHO grade 2) and anaplastic (WHO grade 3) meningiomas had lower ADCs than did benign meningioma subtypes (Filippi et al. 2001). Although the more malignant subtypes may have lower ADCs, some benign meningiomas also had low ADCs, suggesting that the ADC would not be particularly helpful for discriminating benign from malignant subtypes of meningiomas (Yamasaki et al. 2005). Additional studies with large numbers of patients would be needed to draw definitive conclusions.

We previously found that ADCs for schwannomas were higher than those of meningiomas (Yamasaki et al. 2005). Histologically, schwannomas comprise Antoni type A and type B neurinomas, and their higher ADC may reflect the lower cell density of the Antoni type B neurinomas. Preoperative ADC measurement of tumors at the cerebellopontine angle and the middle cranial fossa may be useful for distinguishing meningiomas from schwannomas; however, additional studies are needed.

### Pituitary and Parasellar Tumors and Others

Many types of tumors can develop in the sellar/parasellar region, including pituitary adenomas, craniopharyngiomas, germ cell tumors, and meningiomas, and making

a preoperative differential diagnosis from imaging findings can be difficult. For example, craniopharyngioma may be difficult to distinguish from pituitary adenomas because the squamous-papillary type of craniopharyngioma may contain only solid components, whereas pituitary adenomas may be complicated by cystic formation. Sellar meningiomas can also be hard to distinguish from pituitary adenomas. We found that the ADC values for craniopharyngioma were higher than those for pituitary adenoma and possibly higher than those for meningioma and germ cell tumors (Yamasaki et al. 2005). However, ADC measurements were not useful for distinguishing among pituitary adenomas, meningiomas, and germ cell tumors (Yamasaki et al. 2005).

Pituitary apoplexy and pituitary abscess have been reported to show high signal intensity on DWI and low ADC, but these findings need to be replicated in a larger study.

The ADC for epidermoid tumors was reported to be lower than that for chordomas. Compared with the ADC of normal brain, the ADC of epidermoids was either the same or somewhat higher, and the ADC for chordomas was much higher (Yamasaki et al. 2005). The measurement of ADC may aid in distinguishing between epidermoid tumors and chordomas.

In summary, ADC measurements may be most useful for improving the accuracy of diagnosis after conventional MRI. An automated diagnostic system based on age, sex, location of tumor, information from conventional MRI (T1, T2, FLAIR, enhancement pattern), and ADC would be highly desirable. MR spectroscopy, perfusion studies, and positron emission tomography (PET) could be helpful for

grading the malignancy of a tumor. The availability of such parameters from MR spectroscopy, perfusion studies and PET scans would make an auto-diagnostic system a more powerful tool.

## VISUALIZING TUMOR INFILTRATION

Another potential application of ADC in tumor diagnosis is to demonstrate the boundary between tumor tissue and peritumoral areas, especially in gliomas. The peritumoral abnormal high signal intensity on T2-weighted images can reflect vasogenic edema, the tumoral infiltration, or both, and these possibilities cannot be distinguished by conventional MRI. The ability to reliably and noninvasively distinguish between tumor tissue and adjacent edematous and gliotic peritumoral brain tissue would be extremely relevant clinically for planning surgical resections, targeted biopsies, and radiation therapy for cerebral gliomas. Several studies have suggested that ADC measurements may be useful for discriminating edema from tumor (Sinha et al. 2002; Tien et al. 1994; Krabbe et al. 1997; Lu et al. 2004), but there is also much evidence to the contrary (Stadnik et al. 2001; Kono et al. 2001; Provenzale et al. 2004; Pauleit et al. 2004). The methods as well the results of these studies have varied considerably, which complicates the ability to reach firm conclusions. Contrast-enhanced T1-weighted images have been proposed as the most valuable predictor of the presence of tumor tissue (Pauleit et al. 2004), and one of these groups found that the accuracy of conventional MRI for distinguishing tumor tissue from peritumoral brain tissue was

not improved by the addition of ADC or lesion-to-brain ratios of various sequences used (Pauleit et al. 2004). The presence of intratumoral vasogenic edema in high-grade brain tumors complicates the distinction on ADC maps between contiguous areas of tumor and edema versus areas of only edema (Kono et al. 2001). Evidence discussed in the section on limitations of ADC later in this chapter and the fact that edema can have many causes suggest that ADC is not particularly useful for detecting peritumoral neoplastic cell infiltration in gliomas. In other words, ADC would not be any more useful than conventional MRI for delineating the border between tumor and normal brain. Future studies should include not only ADC but also measures of fractional anisotropy and tractography from DTI to delineate the border between tumor and peritumor areas, because infiltration occurs within and along white matter tracts.

## DISTINGUISHING TUMOR RECURRENCE FROM RADIATION NECROSIS

Malignant brain tumors are almost invariably treated with surgery followed by radiation therapy and chemotherapy, and considerable numbers of patients develop enhancing lesions at or near the postoperative tumor beds after adjuvant therapy. Enhancement on MRI can reflect breakdown of the blood–brain barrier, which can result from either tumor recurrence or radiation- or chemotherapy-induced endothelial damage of cerebral vessels and glial damage. Recurrent tumors and treatment-induced necrosis (particularly from radiation) may share similar imaging

characters, although the management strategy and outcome are obviously different. Therefore, distinguishing between radiation necrosis and recurrent tumor has significant therapeutic implications. Recently, MR spectroscopy, PET, single-photon emission computed tomography, and dynamic susceptibility contrast-enhanced MRI have been assessed to distinguish recurrent disease from nonneoplastic tissue necrosis. However, currently biopsy or resection is the only definitive means of distinguishing between recurrent tumors and radiation necrosis. The problem is made more complex by the frequent coexistence of recurrent neoplasm and necrosis; indeed, surgical studies indicate that pure necrosis or pure recurrence are rare. Further, it is difficult, if not impossible, to predict whether tumor spots within necrotic tissue will die or survive. Biopsy is often deemed necessary, and the results of pathologic examination can run counter to the diagnosis suggested by the imaging tests.

The measurement of ADC may be helpful for distinguishing radiation necrosis from tumor recurrence. An early hypothesis was that recurrent tumors would show high perfusion and that radiation damage would show low perfusion and decreased diffusion (Le Bihan et al. 1993). Some case reports have found lower ADC values in radiation necrosis than in recurrent tumor (Le Bihan et al. 1993), but other larger studies showed exactly the opposite result, where ADC was higher in radiation necrosis ( $1.40\text{--}1.68 \times 10^{-3} \text{ mm}^2/\text{s}$ ) than in recurrent tumor ( $1.18\text{--}1.37 \times 10^{-3} \text{ mm}^2/\text{s}$ ) or in mixed recurrence plus necrosis ( $1.42 \times 10^{-3} \text{ mm}^2/\text{s}$ ) (Hein et al. 2004; Asao et al. 2005; Rock et al. 2004). Evidence in support of ADC being higher for radiation necrosis than for tumor comes from several

sources, including gamma knife irradiation in animal models and temporal lobe necrosis after radiation therapy for nasopharyngeal carcinomas in humans. In necrotic tissues, the extracellular volume fraction is augmented because of the breakdown of cell membranes. Because the ADC for the extracellular compartment is larger than that for the intracellular compartment, the ADC for necrotic tissues might be expected to be higher than the ADC for tumor (Rock et al. 2004). Another study found that radiation necrosis was characterized by significantly higher maximum ADC values and heterogeneity on DWI, including spotty, marked hypointensity on DWI (meaning high ADC), relative to recurrent tumor (Asao et al. 2005).

Some of the discrepancies in ADC values for radiation necrosis may also come from differences in the timing of the imaging studies. Acute radiation necrosis might be expected to show low ADC, given the high viscosity and presence of inflammatory cells, particularly polymorphonuclear leukocytes, in purulent fluid, all of which may restrict water diffusion. Vascular change, an important feature of radiation necrosis, usually progresses slowly but can occasionally cause acute localized necrosis (infarctions) from occlusion of blood vessels, which would be reflected as a decrease in ADC. The most important message from these findings is that recurrent tumors rarely, if ever, show high ADC values or show an increase during the follow-up period.

Clinically, periodic measurements of ADC during the follow-up period may be also helpful and could provide important clues to distinguish lesions with mixed tumor plus necrosis from those with tumor progression or pure necrosis. If enhancing lesions reflected nonviable tissue or radia-

tion necrosis, then the ADC values would not decrease over time with corticosteroid treatment. On the other hand, if enhancing lesions represented viable tissue, the cellularity of the lesion would increase over time as the tumor grows, which would result in progressive decreases in ADC. Monitoring T2-high lesions surrounding the tumor bed after total resection followed by adjuvant therapy would also be useful; a change in the ADC of such a lesion, especially a decrease, could be an early sign of recurrence.

## MONITORING TREATMENT EFFECTS

ADC can also be used during follow-up to monitor the effects of adjuvant therapy. Noninvasive means of assessing the efficacy of anticancer treatment is important for improving the therapeutic window; early detection of recurrence would be invaluable for deciding whether current treatment should be continued or not. Cellularity is probably the most important factor that would influence ADC after therapy; theoretically, changes in tumor water diffusion that occur after successful treatment would reflect decreased cellularity owing to cell death. Cells sensitive to therapy could undergo necrosis or mitotic catastrophe initiated by a transient increase in cell-membrane permeability (cell swelling), which would manifest as a decreased ADC relatively soon after therapy is begun. Focal ischemic hypoxia caused by reduction in tumor blood flow also could result in cell swelling. These processes eventually can progress to cell lysis and necrosis, which would increase the ADC via a decrease in viable cell density (Moffat et al. 2005).

Cells can also undergo apoptosis involving cell shrinkage and blebbing followed by phagocytosis, which would increase the ADC. Meanwhile, necrotic or cystic regions of a tumor can undergo displacement of water as cells move into the region, resulting in a decrease in ADC. If cells were resistant to therapy, the ADC would not change. If cells were viable and cell density increased, that would eventually lead to a decrease in ADC.

Several *in vivo* studies have been done to investigate whether an increase in ADC could serve as an early marker of response to a variety of therapies, including chemotherapy or gene therapy in an orthotopic glioma model derived from implanted rat 9L glioma cells; ganciclovir and thymidine kinase gene therapy in another rat glioma model involving BT4C cells; therapy with tumor necrosis factor-related apoptosis-inducing ligand or paclitaxel in nude mice implanted with MCF-7 breast cancer cells; and therapy with cyclophosphamide in murine RIF-1 radiation-induced fibrosarcomas (Chenevert et al. 2000). In these studies, the ADC was found to increase after effective treatments, and the change in ADC preceded any change in tumor size. Tumor regrowth (i.e., treatment failure) was indicated by a subsequent fall in ADC within the tumor to pretreatment levels.

In the clinical setting, some preliminary work suggests that ADC measurements may also be effective for monitoring treatment effects in human brain tumors (Chenevert et al. 2000). However, heterogeneity among tumors and their response to therapeutic interventions make drawing firm conclusions difficult at this time. Use of a functional diffusion map may overcome this issue (Moffat et al. 2005), but this method requires extra steps and is time-consuming.

Attempts to test the efficacy of ADC for monitoring treatment effects should consider the type of cell death resulting from the treatment, because apoptosis will produce an increase in ADC and necrosis will appear as a temporary decrease in ADC. In one study, vascular-targeted therapy led to a decrease followed by an increase in ADC (Thoeny et al. 2005). Another point to consider is the optimal time at which to decide whether a treatment is effective or not. For example, conventional radiotherapy is typically delivered in fractions, and late effects of such therapy would be reflected in vascular changes. Another possibly confounding factor is the use of steroids, which significantly reduce the ADC in edematous brain and tumor. These points and others must be addressed before ADC can be used to monitor treatment effects in a clinical setting.

## DISTINGUISHING TUMOR RECURRENCE FROM RESECTION INJURY

Abnormalities in and around the resection cavity on DWI have been observed after surgery for infiltrating glioma. Areas of reduced diffusion on DWI, particularly in combination with an ADC of less than  $0.5 \times 10^{-3} \text{ mm}^2/\text{s}$ , immediately after surgery have in some cases demonstrated enhancement on follow-up imaging that eventually resembled encephalomalacia on long-term follow-up. Such enhancement could be misinterpreted as the reappearance of tumor and treatment failure. To distinguish this enhancement from tumor recurrence, it is essential to perform DWI immediately after surgery and MRI immediately before the initiation of radiotherapy to monitor disease progression (Smith et al. 2005).



## DISTINGUISHING BRAIN ABSCESSSES FROM CYSTIC OR NECROTIC MALIGNANT TUMORS

Pyogenic, tuberculous, and fungal brain abscesses tend to appear hyperintense on DWI and have a low ADC, whereas cystic or necrotic lesions tend to appear hypointense on DWI and have a high ADC (Ebisu et al. 1996). The ADC seems to be inversely proportional to protein concentration, and the restriction of water diffusion in brain abscesses may be due to mucoid proteins in the highly viscous pus and restriction of the microscopic movement of water molecules by bacteria, inflammatory cells, necrotic cellular

debris as well as exuded plasma. Water molecules in the abscess also can connect to the carboxy-, hydroxy- and amino groups on these macromolecules.

Although the ability of DWI and the ADC to distinguish brain abscesses from cystic brain tumors has been statistically confirmed, this picture can be complicated by the presence of hemorrhage or a proteinaceous component, which may appear as an area of heterogeneous or bright signal. Indeed, the appearance of high signal intensity on DW images and low ADC values has also been reported for metastatic tumors, glioblastomas, and a fibrillary low-grade astrocytoma (Park et al. 2000), thus complicating the usefulness of these signs for diagnosing an abscess (Figure 22.3a and b).

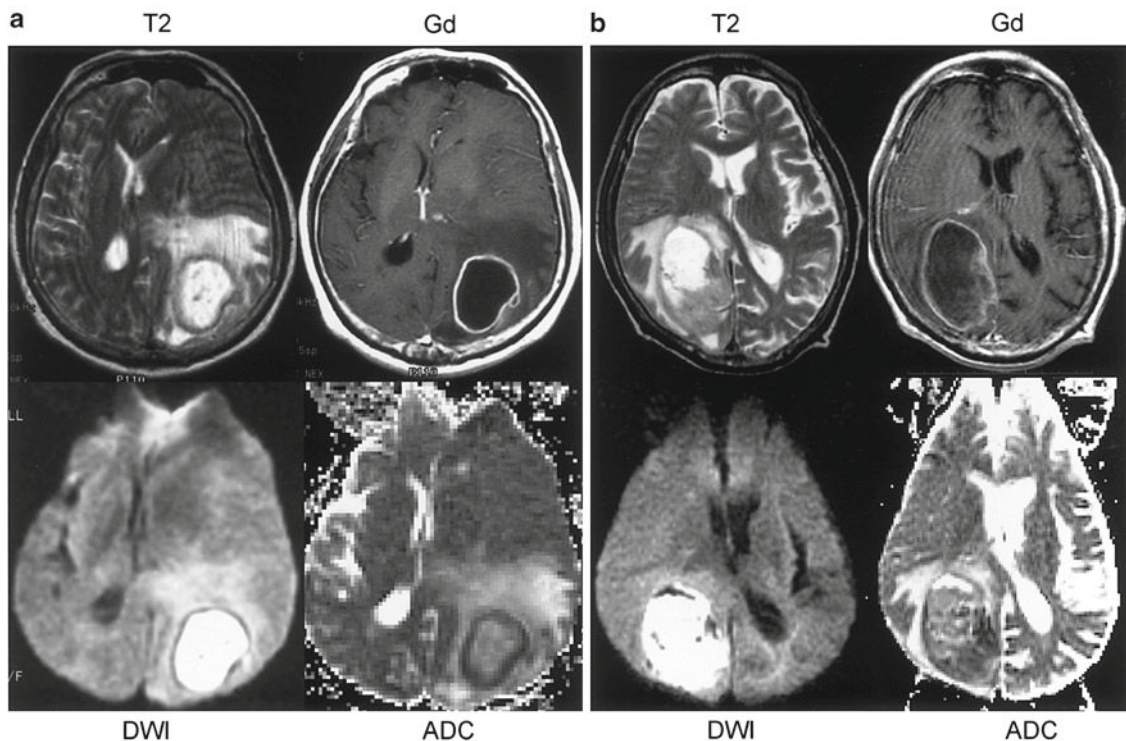


FIGURE 22.3. Images of ring-enhancing lesions. (a) Pyogenic abscess in a 64-year-old woman. Mean ADC of central lesion is  $1.097 \times 10^{-3} \text{ mm}^2/\text{s}$ . (b) Metastatic tumor in a 72-year-old man. Mean ADC of central lesion is  $1.062 \times 10^{-3} \text{ mm}^2/\text{s}$

Restricted diffusion in tumors may be explained by one of several proposed mechanisms, including intracellular edema of the ischemic core, complete liquefaction necrosis, or early necrosis. High signal intensity on DWI and low ADC values in tumors could come from the viscous mucin content of the lesion, and necrotic contents of the tumor could resemble pus (Park et al. 2000). Although no abscess has yet been reported as having low DWI signal intensity and high ADC, lesions that show hyperintensity on DWI and a low ADC should be subjected to additional imaging to distinguish abscesses from non-abscess lesions. Magnetic resonance spectroscopy has been claimed to show a specific pattern in untreated pyogenic brain abscesses; however, this technique has limitations when the lesion is close to or at the skull base, where susceptibility effects reduce the quality of the spectra, and it is available at only a few hospitals. Further, others have found that tuberculous abscesses did not show a multi-amino-acid peak pattern and thus could not be distinguished from cystic tumors (Gupta et al. 2001). The lower magnetic-transfer ratio of the wall in tuberculous abscesses may help to distinguish them from pyogenic abscesses (Gupta et al. 2001), but it is not clear whether the magnetic-transfer ratio could help in distinguishing tuberculous abscesses from cystic tumors.

#### Distinguishing Toxoplasma Abscesses and Malignant Lymphoma in AIDS

Toxoplasmosis and lymphoma, the two most common opportunistic neoplasms and infections that cause CNS lesions in patients with acquired immune deficiency syndrome (AIDS), often show similar characteristics on conventional CT and MRI. In the non-AIDS population, primary brain

lymphoma shows a solid pattern of contrast enhancement on CT and MRI, and subependymal spread of lymphoma encasing the ventricles is highly characteristic when present. However, in patients with AIDS, lymphoma is associated with Epstein-Barr virus infection and often is multicentric, grows rapidly, and shows necrosis of central areas due to thrombosis and deterioration of the vessels in the oldest parts of the lesions. Therefore, on MRI, lymphoma appears as nonspecific ring enhancement. Toxoplasmosis in patients with AIDS also appears as ring enhancement. Moreover, toxoplasmosis and lymphoma can occur in isolation or simultaneously. The few studies done to date with DWI for these conditions suggest that toxoplasmosis was associated with a high ADC and lymphoma with a low ADC (Camacho et al. 2003). However, the numbers of patients in these studies were small, and some overlap in ADC existed between some of the toxoplasmosis lesions and some of malignant lymphoma lesions. Replication of these findings in a larger study is needed. Further, the differential diagnosis of lymphoma should also include other AIDS-associated focal brain lesions such as cryptococcosis, progressive multifocal leukoencephalopathy (due to infection with the JC polyomavirus), tuberculoma, syphilitic gumma, bacterial abscesses, lymphoid granulomatosis, and focal encephalitic cytomegalovirus. Future prospective studies using ADC or other neuroradiologic parameters to distinguish among these AIDS-associated conditions would be greatly desirable.

#### Study Limitations: Variations in Apparent Diffusion Coefficient Measurements, Selection of Regions of Interest

Attention to the methods used to generate ADC values is important, as the ability

to generalize findings between studies is limited by inconsistencies in methodology (Sinha et al. 2002). An approach that is standardized yet can be customized to meet specific individual needs is essential if ADC values are to be used in the diagnosis of brain tumors. Differences in the hardware or pulse sequences used for diffusion image acquisition, application of motion suppression techniques, number of applied diffusion sensitizing gradients, contributions from bulk capillary flow or active transport mechanisms, posttreatment effects, sampling bias, and the effect of partial volume (e.g., intratumoral cyst, hemorrhage, adjacent nontumoral tissues) can all affect ADC measurements. Differences in post-processing techniques and analysis of regions of interest (ROIs) are especially likely to result in variations in ADC measurements and for apparently contradictory results among studies. The ROIs should be placed centrally within the area of tumor to avoid partial volume effects with cystic, necrotic, hemorrhagic regions, or adjacent nontumoral tissues that might influence ADC. However, structural heterogeneity, such as the presence of micronecrosis, microcysts, and microhemorrhages in brain tumors, could also contribute variation and bias in locating the ROI. The size of the ROI can also affect ADC values, and no consensus has been reached about whether to use mean ADC, minimum ADC, or maximum ADC. However, the minimum ADC or maximum ADC values can be influenced by the presence of microcystic, micro-necrotic, or microhemorrhagic lesions, partial volume effects, and the size and location of the ROI. Future studies are necessary to clarify this point.

Some authors have recommended using an ADC ratio for standardization purposes

in which the ADC of a tumor would be compared with the ADC of a contralateral normal white matter region (Ulug et al. 1997; Guo et al. 2002), thereby reducing the variations between reported values that come from using different parameters for DWI (Ulug et al. 1997; Guo et al. 2002). The legitimacy of such a ratio will depend on whether the ADC is affected by aging, with some reporting no change with age, others reporting that ADC changes with age (Rovaris et al. 2003), and others reporting that ADC is relatively constant between and within individuals, except for children and young adults, and does not vary with sex. Future studies are necessary to determine whether using the original ADC or an ADC ratio of tumor to contralateral white matter would be the better approach.

Moreover, diffusion may not be equal in all directions in the presence of white matter (Ulug et al. 1997). Some studies evaluated gradients in only one axis, typically in the cephalocaudal direction (Tien et al. 1994; Krabbe et al. 1997; Stadnik et al. 2001); however, calculating ADC in one direction may mask the accurate assessment of anisotropy. Therefore, gradients should be studied in three orthogonal planes to avoid contrast from diffusion anisotropy (Ulug et al. 1997).

Several investigators have chosen to compare the ADC values in various types of tumor rather than evaluating the diffusion properties characteristic of a single disease (Krabbe et al. 1997; Kono et al. 2001; Stadnik et al. 2001). Caution must be used, however, when combining tumors of different grades, especially grade 3 and grade 4 gliomas, in a single study, as this may overshadow potential differences among tissues. The intervention performed

before MRI is also relevant, and the effects of surgery and adjuvant therapy on ADC should be clarified. Use of steroids, often a first step in therapy for brain tumors, could affect the ADC of tumor and edematous tissue. However, the nature of the contrast medium used during MRI does not seem to affect ADC values.

## FUTURE DIRECTIONS

Use of high-field MR systems will increase the spatial resolution and accuracy of ADC. Moreover, several useful indices of diffusion can be derived from the advanced MR technique DTI, a more sophisticated form of DWI that allows assessment of directionality as well as the magnitude of water diffusion. The first diffusion-tensor MRI metric is mean diffusivity, which like ADC is a measure of magnitude. The second metric is the fractional anisotropy, which is a measure of the directionality of molecular motion; in the brain, this parameter may reflect white matter integrity. The combination of ADC (mean diffusivity) and fractional anisotropy is expected to increase the accuracy of diagnosis of brain tumors.

Another possible way of improving the sensitivity of DWMRI for detecting early responses to treatment is to manipulate the diffusion-sensitizing coefficient of the DWI pulse sequence,  $b$  (Mardor et al. 2003). A  $b$  value of  $1,000 \text{ s/mm}^2$  has long been thought to be sufficient for visualizing changes in high- and low-mobility water populations, and most institution that use DWI have used this  $b$  value. At this  $b$  value, diffusion within brain tissue was considered to be mono-exponential. However, increasing the  $b$  value up to  $4,000 \text{ s/mm}^2$  revealed a bi-exponential

response (Niendorf et al. 1996). In other words, fast diffusion and slow diffusion components exist, and these diffusions are not equal to each other, fast diffusion being proportional to extracellular diffusion and slow diffusion proportional to intracellular diffusion (Niendorf et al. 1996). The fast component dominates at relatively low  $b$  values ( $<1,000 \text{ s/mm}^2$ ) and thus ADC measurements obtained at these values primarily reflect fast diffusion, especially when the data are fitted to a mono-exponential curve (DeLano et al. 2000). At higher  $b$  values, signal intensity is contributed largely by the slower component of diffusion. Consequently, as  $b$  values increase beyond  $1,000 \text{ s/mm}^2$ , the signal intensity in the trace images transitions from a fast to a slow weighting. As a result, as  $b$  values increase, the ADC for white matter becomes progressively lower than the ADC for gray matter (DeLano et al. 2000). Therefore, ADC dependence on  $b$  value must be considered in interpreting quantitative measurements. Future studies are necessary to define the role of ADC obtained from DWI with high  $b$  values for the evaluation of brain tumors.

In conclusion, ADC measurements have many practical advantages for the non-invasive diagnosis of brain tumors. The measurement of ADC is part of standard neuroimaging procedures at many institutions and thus would incur no additional costs. With use of fast imaging sequences (echo-planar imaging) and with ADC calculating software integrated in the workstation, DWI is not time-consuming. Its spatial resolution is sufficient to demarcate lesions and is superior to that of PET, SPECT, and MR spectroscopy. The ADC can also provide valuable information about cellularity. Having information on

ranges of ADC values in individual diseases would help in the differential diagnosis not only of brain tumors but also of other central nervous diseases. Follow-up examinations with periodic measurements of ADC may also help in the differential diagnosis. Establishment of standardized methods for measuring ADC will enhance the capabilities of this potentially powerful diagnostic tool.

*Acknowledgments.* We thank Christine F. Wogan, for editorial review. We also thank Junko Takaba, for contributions to the collection of imaging data from our patients and for helpful discussions. Thanks are due to Yoshinori Kajiwara, and Tomohide Akimitsu, for helpful discussions.

## REFERENCES

- Asao, C., Korogi, Y., Kitajima, M., Hirai, T., Baba, Y., Makino, K., Kochi, M., Morishita, S., and Yamashita, Y. (2005) Diffusion-weighted imaging of radiation-induced brain injury for differentiation from tumor recurrence. *Am. J. Neuroradiol.* 26:1455–1460
- Bammer, R. (2003) Basic principles of diffusion-weighted imaging. *Eur. J. Radiol.* 45:169–184
- Bulakbasi, N., Guvenc, I., Onguru, O., Erdogan, E., Tayfun, C., and Ucoz, T. (2004) The added value of the apparent diffusion coefficient calculation to magnetic resonance imaging in the differentiation and grading of malignant brain tumors. *J. Comput. Assist. Tomogr.* 28:735–746
- Camacho, D.L., Smith, J.K., and Castillo, M. (2003) Differentiation of toxoplasmosis and lymphoma in AIDS patients by using apparent diffusion coefficients. *Am. J. Neuroradiol.* 24:633–637
- Chenevert, T.L., Stegman, L.D., Taylor, J.M., Robertson, P.L., Greenberg, H.S., Rehemtulla, A., and Ross, B.D. (2000) Diffusion magnetic resonance imaging: an early surrogate marker of therapeutic efficacy in brain tumors. *J. Natl. Cancer Inst.* 92:2029–2036
- DeLano, M.C., Cooper, T.G., Siebert, J.E., Potchen, M.J., and Kuppusamy, K. (2000) High-b-value diffusion-weighted MR imaging of adult brain: image contrast and apparent diffusion coefficient map features. *Am. J. Neuroradiol.* 21:1830–1836
- Ebisu, T., Tanaka, C., Umeda, M., Kitamura, M., Naruse, S., Higuchi, T., Ueda, S., and Sato, H. (1996) Discrimination of brain abscess from necrotic or cystic tumors by diffusion-weighted echo planar imaging. *Magn. Reson. Imaging* 14: 1113–1116
- Filippi, C.G., Edgar, M.A., Ulug, A.M., Prowda, J.C., Heier, L.A., and Zimmerman, R.D. (2001) Appearance of meningiomas on diffusion-weighted images: correlating diffusion constants with histopathologic findings. *Am. J. Neuroradiol.* 22:65–72
- Gauvain, K.M., McKinstry, R.C., Mukherjee, P., Perry, A., Neil, J.J., Kaufman, B.A., and Hayashi, R.J. (2001) Evaluating pediatric brain tumor cellularity with diffusion-tensor imaging. *Am. J. Roentgenol.* 177:449–454
- Guo, A.C., Cummings, T.J., Dash, R.C., and Provenzale, J.M. (2002) Lymphomas and high-grade astrocytomas: comparison of water diffusibility and histologic characteristics. *Radiology* 224:177–183
- Gupta, R.K., Sinha, U., Cloughesy, T.F., and Alger, J.R. (1999) Inverse correlation between choline magnetic resonance spectroscopy signal intensity and the apparent diffusion coefficient in human glioma. *Magn. Reson. Med.* 41:2–7
- Gupta, R.K., Vatsal, D.K., Husain, N., Chawla, S., Prasad, K.N., Roy, R., Kumar, R., Jha, D., and Husain, M. (2001) Differentiation of tuberculous from pyogenic brain abscesses with in vivo proton MR spectroscopy and magnetization transfer MR imaging. *Am. J. Neuroradiol.* 22:1503–1509
- Hein, P.A., Eskey, C.J., Dunn, J.F., and Hug, E.B. (2004) Diffusion-weighted Imaging in the follow-up of treated high-grade gliomas: tumor recurrence versus radiation injury. *Am. J. Neuroradiol.* 25:201–209
- Hsu, E.W., Aiken, N.R., and Blackband, S.J. (1996) Nuclear magnetic resonance microscopy of single neurons under hypotonic perturbation. *Am. J. Physiol.* 271:C1895–C1900
- Kono, K., Inoue, Y., Nakayama, K., Shakudo, M., Morino, M., Ohata, K., Wakasa, K., and

- Yamada, R. (2001) The role of diffusion-weighted imaging in patients with brain tumors. *Am. J. Neuroradiol.* 22:1081–1088
- Krabbe, K., Gideon, P., Wagn, P., Hansen, U., Thomsen, C., and Madsen, F. (1997) MR diffusion imaging of human intracranial tumours. *Neuroradiology* 39:483–489
- Le Bihan, D., Douek, P., and Argyropoulou, M. (1993) Diffusion and perfusion magnetic resonance imaging in brain tumors. *Top. Magn. Reson. Imaging* 5:25–31
- Lu, S., Ahn, D., Johnson, G., Law, M., Zagzag, D., and Grossman, R.I. (2004) Diffusion-tensor MR imaging of intracranial neoplasia and associated peritumoral edema: introduction of the tumor infiltration index. *Radiology* 232:221–228
- Mardor, Y., Pfeffer, R., Spiegelmann, R., Roth, Y., Maier, S.E., Nissim, O., Berger, R., Glicksman, A., Baram, J., Orenstein, A., Cohen, J.S., and Tichler, T. (2003) Early detection of response to radiation therapy in patients with brain malignancies using conventional and high b-value diffusion-weighted magnetic resonance imaging. *J. Clin. Oncol.* 21:1094–1100
- Moffat, B.A., Chenevert, T.L., Lawrence, T.S., Meyer, C.R., Johnson, T.D., Dong, Q., Tsien, C., Mukherji, S., Quint, D.J., Gebarski, S.S., Robertson, P.L., Junck, L.R., Rehemtulla, A., and Ross, B.D. (2005) Functional diffusion map: a noninvasive MRI biomarker for early stratification of clinical brain tumor response. *Proc. Natl. Acad. Sci. USA* 102:5524–5529
- Niendorf, T., Dijkhuizen, R.M., Norris, D.G., van Lookeren Campagne, M., and Nicolay, K. (1996) Biexponential diffusion attenuation in various states of brain tissue: implications for diffusion-weighted imaging. *Magn. Reson. Med.* 36:847–857
- Okamoto, K., Ito, J., Ishikawa, K., Sakai, K., and Tokiguchi, S. (2000) Diffusion-weighted echo-planar MR imaging in differential diagnosis of brain tumors and tumor-like conditions. *Eur. Radiol.* 10:1342–1350
- Park, S.H., Chang, K.H., Song, I.C., Kim, Y.J., Kim, S.H., and Han, M.H. (2000) Diffusion-weighted MRI in cystic or necrotic intracranial lesions. *Neuroradiology* 42:716–721
- Pauleit, D., Langen, K.J., Floeth, F., Hautzel, H., Riemenschneider, M.J., Reifenberger, G., Shah, N.J., and Muller, H.W. (2004) Can the apparent diffusion coefficient be used as a noninvasive parameter to distinguish tumor tissue from peritumoral tissue in cerebral gliomas? *J. Magn. Reson. Imaging* 20:758–764
- Provenzale, J.M., McGraw, P., Mhatre, P., Guo, A.C., and Delong, D. (2004) Peritumoral brain regions in gliomas and meningiomas: investigation with isotropic diffusion-weighted MR imaging and diffusion-tensor MR imaging. *Radiology* 232:451–460
- Rock, J.P., Scarpace, L., Hearshen, D., Gutierrez, J., Fisher, J.L., Rosenblum, M., and Mikkelsen, T. (2004) Associations among magnetic resonance spectroscopy, apparent diffusion coefficients, and image-guided histopathology with special attention to radiation necrosis. *Neurosurgery* 54:1111–1117
- Rovaris, M., Iannucci, G., Cercignani, M., Sormani, M.P., De Stefano, N., Gerevini, S., Comi, G., and Filippi, M. (2003) Age-related changes in conventional, magnetization transfer, and diffusion-tensor MR imaging findings: study with whole-brain tissue histogram analysis. *Radiology* 227:731–738
- Sinha, S., Bastin, M.E., Whittle, I.R., and Wardlaw, J.M. (2002) Diffusion tensor MR imaging of high-grade cerebral gliomas. *Am. J. Neuroradiol.* 23:520–527
- Smith, J.S., Cha, S., Mayo, M.C., McDermott, M.W., Parsa, A.T., Chang, S.M., Dillon, W.P., and Berger, M.S. (2005) Serial diffusion-weighted magnetic resonance imaging in cases of glioma: distinguishing tumor recurrence from postresection injury. *J. Neurosurg.* 103:428–438
- Stadnik, T.W., Chaskis, C., Michotte, A., Shabana, W.M., van Rompaey, K., Luypaert, R., Budinsky, L., Jellus, V., and Osteaux, M. (2001) Diffusion-weighted MR imaging of intracerebral masses: comparison with conventional MR imaging and histologic findings. *Am. J. Neuroradiol.* 22: 969–976
- Sugahara, T., Korogi, Y., Kochi, M., Ikushima, I., Shigematu, Y., Hirai, T., Okuda, T., Liang, L., Ge, Y., Komohara, Y., Ushio, Y., and Takahashi, M. (1999) Usefulness of diffusion-weighted MRI with echo-planar technique in the evaluation of cellularity in gliomas. *J. Magn. Reson. Imaging* 9:53–60
- Thoeny, H.C., De Keyser, F., Chen, F., Ni, Y., Landuyt, W., Verbeken, E.K., Bosmans, H., Marchal, G., and Hermans, R. (2005) Diffusion-weighted MR imaging in monitoring the effect of

- a vascular targeting agent on rhabdomyosarcoma in rats. *Radiology* 234:756–764
- Tien, R., Felsberg, G., Friedman, H., Brown, M., and Mac-Fall, J. (1994) MR imaging of high-grade cerebral gliomas: value of diffusion-weighted echoplanar pulse sequences. *Am. J. Roentgenol.* 162:671–677
- Ulug, A.M., Beauchamp, N. Jr., Bryan, R.N., and van Zijl, P.C. (1997) Absolute quantitation of diffusion constants in human stroke. *Stroke* 28: 483–490
- Yamasaki, F., Kurisu, K., Satoh, K., Arita, K., Sugiyama, K., Ohtaki, M., Takaba, J., Tominaga, A., Hanaya, R., Yoshioka, H., Hama, S., Ito, Y., Kajiwara, Y., Yahara, K., Saito, T., and Thohar, M.A. (2005) Apparent diffusion coefficient of human brain tumors at MR imaging. *Radiology* 235:985–991

# 23

## Magnetic Resonance Imaging of Brain Tumors Using Iron Oxide Nanoparticles

Matthew A. Hunt and Edward A. Neuwelt

### INTRODUCTION

Magnetic resonance (MR) imaging is the standard tool used in the diagnosis and treatment of brain tumors. Magnetic resonance imaging relies on various imaging sequences, as well as administration of contrast agents to delineate tumor and tumor-infiltrated brain tissue from normal brain tissue. Due to its ability to rapidly cross blood–brain barrier (BBB) defects, gadolinium is the standard contrast agent used, and generally provides clear delineation of areas of vascular permeability and BBB defects. Other contrast agents with differing biologic properties may provide additional information or functionality and complement the use of gadolinium-enhanced MR imaging.

### BIOLOGIC AND MOLECULAR CHARACTERISTICS

Superparamagnetic iron oxide (SPIO) particles, such as ferumoxides (Feridex IV<sup>®</sup>, Berlex, Inc., Wayne, NJ), ultrasmall superparamagnetic iron oxide (USPIO) nanoparticles, such as ferumoxtran-10 (Combidex<sup>®</sup>, Advanced Magnetics, Inc.,

Cambridge, MA), and ferumoxytol (Feraheme<sup>®</sup>, Advanced Magnetics, Inc., Cambridge, MA), have unique properties that are useful for MR imaging. The superparamagnetic nature of the particles' iron oxide core makes them visible on MR images. These particles are composed of an iron oxide core coated with either dextran (ferumoxides and ferumoxtran-10) or a semi-synthetic carbohydrate (ferumoxytol). Ferumoxides particles are 120–180 nm in diameter, and ferumoxtran-10 and ferumoxytol particles are 20–50 nm in diameter (Jung and Jacobs 1995). USPIO particles are ~100 times larger than gadolinium chelates. Particle size and coating properties affect how the particle behaves in vivo. A complete coating coupled with a small diameter helps to slow opsonization and endocytosis, and leads to a longer plasma half-life (Raynal et al. 2004). Conversely, large and incompletely coated SPIO particles (ferumoxides) are rapidly taken up by cells of the reticuloendothelial system and sequestered in the body's lymphoid tissue. This property is useful in imaging of other organs in systemic cancers, but currently has no application for brain tumors (Harisinghani et al. 2003; Jaffer and Weissleder 2005; Keller et al. 2004).



USPIO particles differ in many ways when compared to gadolinium: (1) USPIO particle uptake is intracellular, gadolinium is not. (2) Gadolinium is small and rapidly crosses defects in the BBB into the extracellular space and is visible on MR sequences performed shortly after administration. (3) USPIO particles require longer time periods to exit the bloodstream to be visible on MR sequences even where the BBB is defective. Although the enhancement takes longer to appear, it persists because particles are trapped intracellularly. (4) Repeated imaging with a single administration of the agent is possible (Hunt et al. 2005; Neuwelt et al. 2004, 2007; Varallyay et al. 2002). (5) USPIO particle circulating plasma half-life is longer than that of gadolinium. This difference may increase the sensitivity for subtle defects in the BBB caused by tumors (Murillo et al. 2005; Varallyay et al. 2002).

In central nervous system (CNS) tumors, those without a reactive/inflammatory component cannot be well visualized using USPIO particles (Varallyay et al. 2002). Tumors such as meningiomas and pituitary adenomas, unless they have a significant reactive component, do not enhance well with ferumoxtran-10 or ferumoxytol. In tumors that do have a reactive/inflammatory component, more commonly found in gliomas, lymphomas, and some metastases, USPIO particles are taken up mostly by reactive cells at the periphery of the tumor (Neuwelt et al. 2004; Taschner et al. 2005). One of the advantages of these particles over gadolinium is that, not only can they be visualized on MR images, but they can also be detected using histochemistry and electron microscopy on pathologic specimens as shown in Figure 23.1c and d (Neuwelt et al. 2004; Neuwelt et al. 1994). This property confirms that the patho-

logic specimen originated from an area of enhancement on MR imaging. The iron particles are located intracellularly in reactive cells such as astrocytes or mononuclear cells (Hunt et al. 2005; Neuwelt et al. 2004; Varallyay et al. 2002).

## IMAGING CHARACTERISTICS

When utilized as contrast agents for MR imaging, USPIO particles exhibit unique signal properties. On T2 sequences, particles cause increasing signal loss with increasing concentration. This phenomenon appears as a dark signal on MR images. Usually there is significant susceptibility artifact or ‘blooming’ of this signal on T2\* or gradient echo (GRE) images, which makes interpretation of true particle volume difficult but does allow detection of small particle concentrations possible. T1 properties of USPIO particles differ from T2 properties. MR image signal increases with increasing concentration to a point at which the signal begins to decline. Image appearance of gadolinium and ferumoxtran-10 using different MR sequences are illustrated in Figures 23.2 and 23.3. T1 sequences usually provide better anatomic imaging interpretation and the observed enhancement is similar to that observed with gadolinium.

## EXPERIMENTAL STUDIES

SPIO and USPIO particles have been used in experimental brain tumor models to help delineate the radiological and pathological characteristics of these agents (Moore et al. 2000; Muldoon et al. 2005; Zimmer et al. 1997). Moore

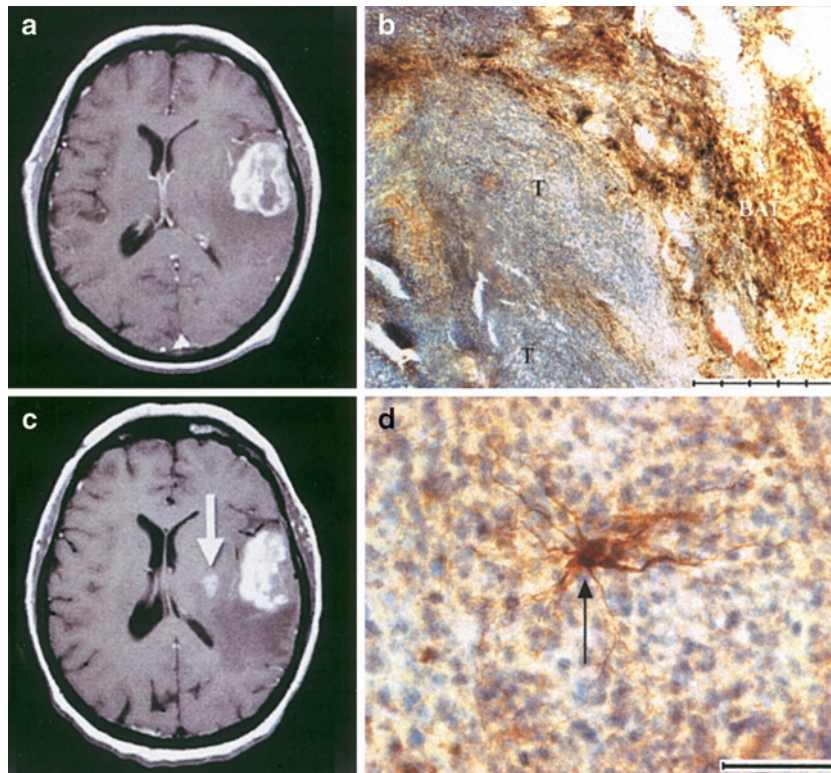


FIGURE 23.1. Patient with glioblastoma. (a) T1-weighted image with gadolinium. (b) T1-weighted image with ferumoxtran-10. Note additional lesion observed, marked with arrow. (c) Pathologic specimen showing iron staining. T = tumor BAT = brain around tumor. (d) Cell staining for iron, possibly astrocytic in origin (Used with permission from Neuwelt et al. 2004, Blackwell Publishing)

et al. (2000), using a non-clinical formulation (MION-46), demonstrated that uptake was predominantly by tumor and peritumoral macrophages. Muldoon et al. (2005) showed that MION-46, ferumoxides, ferumoxtran-10, and ferumoxitol were non-toxic to rat brain parenchyma. This group of investigators confirmed that iron seemed to be limited mostly to reactive cells at the tumor margins. Comparable to human studies, they reported that tumor type strongly influenced the amount of enhancement observed with these agents.

Other iron oxide particles are available for use in nonhuman experimental models, such as CLIO-Cy5.5, an iron oxide

particle conjugated to a fluorochrome and allows for both MR and optical imaging of the same particle (Bremer et al. 2003; Denis et al. 2004; Kircher et al. 2003). Iron oxide particles have also been conjugated to monoclonal antibodies for non-invasive diagnostic purposes in an animal model (Remsen et al. 1996). Recent studies using ferumoxides have begun to explore cellular labeling with MR imaging techniques. Using protamine and ferumoxides, cells can be loaded with SPIO particles and imaged using MR (Arbab et al. 2004). This technique may offer further insights into brain tumors and other diseases of the CNS that involve cellular trafficking. It may

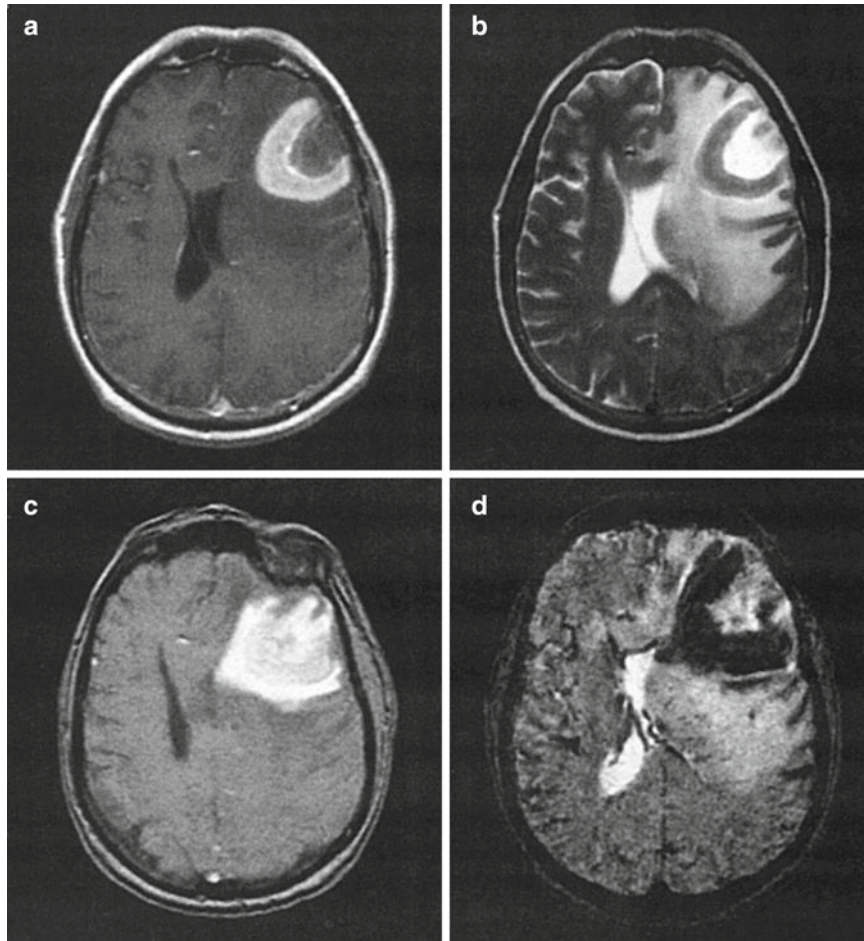


FIGURE 23.2. Representative images using ferumoxtran-10 in a patient with CNS lymphoma. (a) T1-weighted image with gadolinium (b) T1-weighted image 1 day after ferumoxtran-10 administration. (c) T2-weighted image prior to ferumoxtran-10 administration. (d) T2 GRE image 1 day after ferumoxtran-10 administration

also provide a method for tracking cells implanted into the CNS.

## HUMAN IMAGING

Properties unique to ferumoxtran-10 and ferumoxytol complement traditional gadolinium-based MR imaging. The signal characteristics of lesions observed on MR imaging using these agents can be similar to gadolinium on T1 sequences

and show increased signal intensity in areas of enhancement (Enochs et al. 1999; Hunt et al. 2005; Murillo et al. 2005; Taschner et al. 2005; Varallyay et al. 2002). However, these agents are also visible using T2 sequences, especially T2\* or GRE sequences, showing signal dropout. Unfortunately, T2 sequences are often degraded by a susceptibility artifact or 'blooming' which degrades the image's anatomic information. For this reason, T1 sequences are favored for anatomic

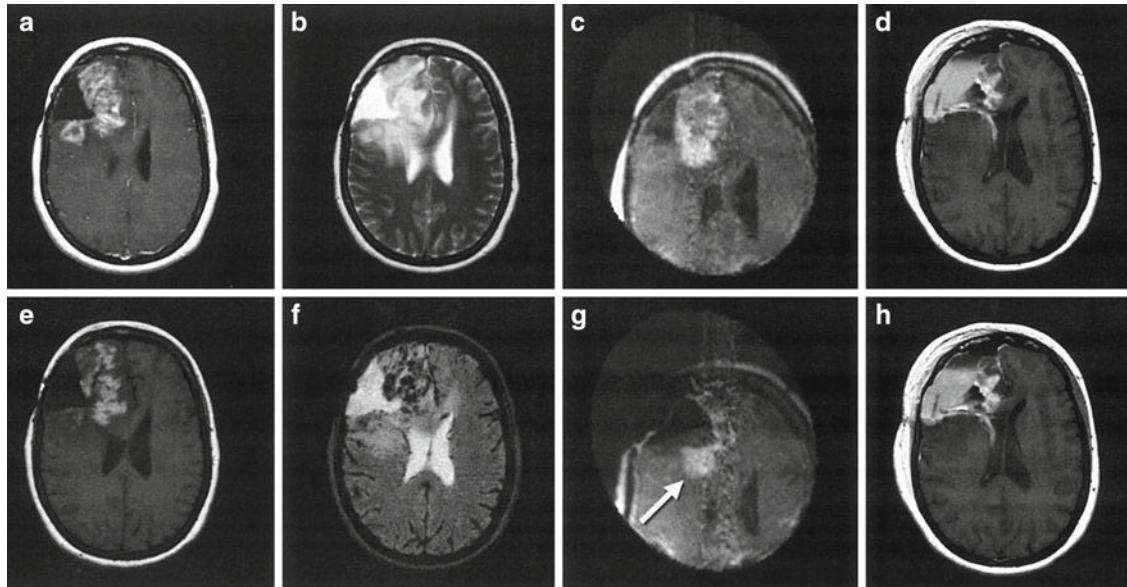


FIGURE 23.3. MR Images from a patient with glioblastoma including pre-, intra-, and postoperative images. (a) T1-weighted with gadolinium. (b) T1-weighted after ferumoxtran-10. (c) T2-weighted. (d) T2 GRE images after ferumoxtran-10. (e) Intraoperative MR image prior to surgery after ferumoxtran-10. (f) Intraoperative MR image during surgery after a partial resection. Residual lesion noted with arrow. (g) Postoperative T1-weighted images without gadolinium. (h) Postoperative T1-weighted images with gadolinium. Note the increased T1 signal in the resection cavity and from intraventricular hemorrhage

interpretation of the enhancement. To avoid anaphylactoid reactions care must be taken during ferumoxtran-10 administration, which must be slow. Ferumoxytol may be administered as a bolus, and is now approved for use by the FDA. Following administration of USPIO particles, a delay is necessary before imaging. Lesions are generally not visible for 6 h, with enhancement intensity greatest at ~24 h post administration (Enochs et al. 1999; Neuwelt et al. 2004, 2007). Enhancement persists and can be observed for up to 1 week post administration. When used in conjunction with intraoperative MR imaging at low field strength and with postoperative MR imaging, these agents provide the unique ability to reimagine lesions without further contrast agent administration (Hunt et al. 2005; Neuwelt et al. 2004).

USPIO particles highlight inflammatory cells in areas where the BBB is defective, although the defect may be minimal. In 2002, Varallyay et al. (2002) reported that while ferumoxtran-10 enhancement was comparable to gadolinium enhancement, it exhibited a more variable intensity. Additionally, tumors that did not have a significant inflammatory component did not show significant enhancement with ferumoxtran-10. The nature of the relationship between inflammation and imaging with iron oxide particles has also been examined. In a case series of 55 patients with a combination of glial and non-glial tumor etiologies, Murillo et al. (2005) concluded that the most consistent indicator for enhancement with USPIO particles was the presence of inflammatory cells with a defective BBB. They also concluded that in

tumors with an inflammatory component, much smaller BBB defects can sometimes be observed than with gadolinium. Lesions that may not be visible with gadolinium may be visible with ferumoxtran-10 as is shown in Figure 23.1a and b (Murillo et al. 2005; Neuwelt et al. 2004). However, prior therapy including radiation and/or chemotherapy may influence the appearance of lesions on MR images (Murillo et al. 2005; Taschner et al. 2005).

## INTRAOPERATIVE MAGNETIC RESONANCE IMAGING

Intraoperative MR (IMR) imaging is a relatively new application of MR technology. Over the last 10 years, IMR imaging has become increasingly widely available, although generally found only in academic neurosurgical institutions. These systems vary in configuration and strength (0.1–3 T) of the magnetic field, but all provide a means to provide updated MR images while maintaining the patient in the operative environment. The goals of utilization of IMR imaging are to improve tumor resection and patient outcomes (Wirtz et al. 2000). The rationale behind administration of these agents with IMR imaging is to avoid the pitfalls of repeated gadolinium enhancement during surgery (Knauth et al. 1999, 2001a, b). In an animal study, gadolinium caused intense enhancement in the surgically disrupted brain, while USPIO particles did not cause enhancement (Knauth et al. 2001a). USPIO particles may be administered prior to surgery using IMR imaging, and can be used to delineate the tumors intraoperatively (Hunt et al. 2005). USPIO particles need to be administered at least 6–8 h prior to surgery, and optimally

the day prior. As mentioned above, tumors without an inflammatory component such as meningiomas and pituitary adenomas, which generally do not show enhancement with USPIO particles, are not suitable for this application. However, gliomas with any degree of inflammatory component, i.e., anaplastic lesions, can be imaged. Most modern IMR imaging systems incorporate neuronavigation, and intraoperatively obtained images may be used to determine factors such as the size and location of craniotomy and the extent of resection. After initial imaging and image-guided resection, repeated imaging may be obtained to determine the true extent of resection and to minimize the confounding factors of brain shift and blood-products. Figure 23.3 shows pre-, intra-, and post-operative imaging in a patient with glioblastoma and also illustrates how postoperative imaging can be confounded by blood products in the resection cavity.

## FUTURE DIRECTIONS

The newest USPIO, ferumoxytol, may provide new insights into the response to treatment of brain tumors using dynamic MR imaging. Ferumoxytol may be administered as an intravenous bolus, which allows for MR perfusion studies. In areas of leaky BBB, gadolinium rapidly leaves the vascular compartment, possibly confounding MR perfusion measurements. Ferumoxytol, which remains in the vascular compartment longer, does not confound these measurements (Neuwelt et al. 2007). Whether perfusion measurements provide an early indicator of tumor response prior to changes in tumor size remains unknown. Cellular labeling using a mixture of ferumoxides

and protamine may also allow tracking of cells as they enter the CNS.

In conclusion, use of iron-based magnetic imaging contrast agents complements the use of traditional gadolinium-based contrast agents. USPIO particles have unique biologic properties, and these properties may provide an advantage when attempting to determine subtle BBB defects and in delineating peritumoral inflammation. Additionally, persistent enhancement after administration makes these agents suitable for repeated imaging before, after, and during operative interventions. These particles may provide for cellular imaging within the brain, as well as early measures of tumor response (Arbab et al. 2007; Cao et al. 2006).

## REFERENCES

- Arbab, A.S., Yocum, G.T., Kalish, H., Jordan, E.K., Anderson, S.A., Khakoo, A.Y., Read, E.J., and Frank, J.A. (2004) Efficient magnetic cell labeling with protamine sulfate complexed to ferumoxides for cellular MRI. *Blood* 104:1217–1223
- Arbab, A.S., Rad, A.M., Iskander, A.S., Jafari-Khouzani, K., Brown, S.L., Churchman, J.L., Ding, G., Jiang, Q., Frank, J.A., Soltanian-Zadeh, H., and Peck, D.J. (2007) Magnetically-labeled sensitized splenocytes to identify glioma by MRI: a preliminary study. *Magn. Reson. Med.* 58:519–526
- Bremer, C., Mustafa, M., Bogdanov, A., Jr., Ntziachristos, V., Petrovsky, A., and Weissleder, R. (2003) Steady-state blood volume measurements in experimental tumors with different angiogenic burdens a study in mice. *Radiology* 226:214–220
- Cao, Y., Tsien, C.I., Nagesh, V., Junck, L., Ten Haken, R., Ross, B.D., Chenevert, T.L., and Lawrence, T.S. (2006) Survival prediction in high-grade gliomas by MRI perfusion before and during early stage of RT. *Int. J. Radiat. Oncol. Biol. Phys.* 64:876–885
- Denis, M.C., Mahmood, U., Benoist, C., Mathis, D., and Weissleder, R. (2004) Imaging inflammation of the pancreatic islets in type 1 diabetes. *Proc. Natl. Acad. Sci. USA* 101:12634–12639
- Enochs, W.S., Harsh, G., Hochberg, F., and Weissleder, R. (1999) Improved delineation of human brain tumors on MR images using a long-circulating, superparamagnetic iron oxide agent. *J. Magn. Reson. Imaging* 9:228–232
- Harisinghani, M.G., Barentsz, J., Hahn, P.F., Deserno, W.M., Tabatabaei, S., van de Kaa, C.H., de la Rosette, J., and Weissleder, R. (2003) Noninvasive detection of clinically occult lymph-node metastases in prostate cancer. *N. Engl. J. Med.* 348:2491–2499
- Hunt, M.A., Bago, A.G., and Neuwelt, E.A. (2005) Single-dose contrast agent for intraoperative MR imaging of intrinsic brain tumors by using ferumoxtran-10. *AJNR Am. J. Neuroradiol.* 26:1084–1088
- Jaffer, F.A., and Weissleder, R. (2005) Molecular imaging in the clinical arena. *JAMA* 293:855–862
- Jung, C.W., and Jacobs, P. (1995) Physical and chemical properties of superparamagnetic iron oxide MR contrast agents: ferumoxides, ferumoxtran, ferumoxsil. *Magn. Reson. Imaging* 13:661–674
- Keller, T.M., Michel, S.C.A., Frohlich, J., Fink, D., Caduff, R., Marincek, B., and Kubik-Huch, R.A. (2004) USPIO-enhanced MRI for preoperative staging of gynecological pelvic tumors: preliminary results. *Eur. Radiol.* 14:937–944
- Kircher, M.F., Mahmood, U., King, R.S., Weissleder, R., and Josephson, L. (2003) A multimodal nanoparticle for preoperative magnetic resonance imaging and intraoperative optical brain tumor delineation. *Cancer Res.* 63:8122–8125
- Knauth, M., Aras, N., Wirtz, C.R., Dorfler, A., Engelhorn, T., and Sartor, K. (1999) Surgically induced intracranial contrast enhancement: potential source of diagnostic error in intraoperative MR imaging. *AJNR Am. J. Neuroradiol.* 20:1547–1553
- Knauth, M., Egelhof, T., Roth, S.U., Wirtz, C.R., and Sartor, K. (2001a) Monocrystalline iron oxide nanoparticles: possible solution to the problem of surgically induced intracranial contrast enhancement in intraoperative MR imaging. *AJNR Am. J. Neuroradiol.* 22:99–102
- Knauth, M., Wirtz, C.R., Aras, N., and Sartor, K. (2001b) Low-field interventional MRI in

- neurosurgery: finding the right dose of contrast medium. *Neuroradiology* 43:254–258
- Landry, R., Jacobs, P.M., Davis, R., Shenouda, M., and Bolton, W.K. (2005) Pharmacokinetic study of ferumoxytol: a new iron replacement therapy in normal subjects and hemodialysis patients. *Am. J. Nephrol.* 25:400–410
- Moore, A., Marecos, E., Bogdanov, A., Jr., and Weissleder, R. (2000) Tumoral distribution of long-circulating dextran-coated iron oxide nanoparticles in a rodent model. *Radiology* 214:568–574
- Muldoon, L.L., Sandor, M., Pinkston, K.E., and Neuwelt, E.A. (2005) Imaging, distribution, and toxicity of superparamagnetic iron oxide magnetic resonance nanoparticles in the rat brain and intracerebral tumor. *Neurosurgery* 57:785–796
- Murillo, T.P., Sandquist, C., Jacobs, P.M., Nesbit, G., Manninger, S., and Neuwelt, E.A. (2005) Imaging brain tumors with ferumoxtran-10, a nanoparticle magnetic resonance contrast agent. *Therapy* 2:871–882
- Neuwelt, E.A., Weissleder, R., Nilaver, G., Kroll, R.A., Roman-Goldstein, S., Szumowski, J., Pagel, M.A., Jones, R. S., Remsen, L.G., McCormick, C.I., Shannon, E.M., and Muldoon, L.L. (1994) Delivery of virus-sized iron oxide particles to rodent CNS neurons. *Neurosurgery* 34:777–784
- Neuwelt, E.A., Varallyay, P., Bago, A.G., Muldoon, L.L., Nesbit, G., and Nixon, R. (2004) Imaging of iron oxide nanoparticles by MR and light microscopy in patients with malignant brain tumours. *Neuropathol. Appl. Neurobiol.* 30:456–471
- Neuwelt, E.A., Varallyay, C.G., Manninger, S., Solymosi, D., Haluska, M., Hunt, M.A., Nesbit, G., Stevens, A., Jerosch-Herold, M., Jacobs, P.M., and Hoffman, J.M. (2007) The potential of ferumoxytol nanoparticle magnetic resonance imaging, perfusion, and angiography in central nervous system malignancy: a pilot study. *Neurosurgery* 60:601–611; discussion 611–602
- Raynal, I., Prigent, P., Peyramaure, S., Najid, A., Rebuzzi, C., and Corot, C. (2004) Macrophage endocytosis of superparamagnetic iron oxide nanoparticles: mechanisms and comparison of ferumoxides and ferumoxtran-10. *Invest. Radiol.* 39:56–63
- Remsen, L.G., McCormick, C.I., Roman-Goldstein, S., Nilaver, G., Weissleder, R., Bogdanov, A., Hellstrom, I., Kroll, R.A., and Neuwelt, E.A. (1996) MR of carcinoma-specific monoclonal antibody conjugated to monocrySTALLINE iron oxide nanoparticles: the potential for noninvasive diagnosis. *AJNR Am. J. Neuroradiol.* 17:411–418
- Taschner, C.A., Wetzel, S.G., Tolnay, M., Froehlich, J., Merlo, A., and Radue, E.W. (2005) Characteristics of ultrasmall superparamagnetic iron oxides in patients with brain tumors. *AJR Am. J. Roentgenol.* 185:1477–1486
- Varallyay, P., Nesbit, G., Muldoon, L.L., Nixon, R.R., Delashaw, J., Cohen, J.I., Petrillo, A., Rink, D., and Neuwelt, E.A. (2002) Comparison of two superparamagnetic viral-sized iron oxide particles ferumoxides and ferumoxtran-10 with a gadolinium chelate in imaging intracranial tumors. *AJNR Am. J. Neuroradiol.* 23:510–519
- Wirtz, C.R., Knauth, M., Staubert, A., Bonsanto, M.M., Sartor, K., Kunze, S., and Tronnier, V.M. (2000) Clinical evaluation and follow-up results for intraoperative magnetic resonance imaging in neurosurgery. *Neurosurgery* 46:1112–1120; discussion 1120–1112
- Zimmer, C., Wright, S.C., Jr., Engelhardt, R.T., Johnson, G.A., Kramm, C., Breakefield, X.O., and Weissleder, R. (1997) Tumor cell endocytosis imaging facilitates delineation of the glioma–brain interface. *Exp. Neurol.* 143:61–69

# 24

## Metastatic Solitary Malignant Brain Tumor: Magnetic Resonance Imaging

Nail Bulakbasi and Murat Kocaoglu

### INTRODUCTION

Brain metastases are secondary deposits of cancer cells that have spread to the brain from primary tumors in other organs. It is a very common and devastating clinical problem for both cancer patients and treating physicians. Although the cancer database showed that the metastatic brain tumor is the second most common adult brain tumor following gliomas, the exact incidence of brain metastasis is underestimated, and in fact it is more likely than double of primary brain tumors (Gavrilovic and Posner 2005). The incidence of brain metastasis has increased during the last two decades, due to improvement in survival of cancer patients particularly in those whose systemic tumors have responded to chemotherapy and due to significant advances in tumor diagnosis. The incidence varies not only with the primary tumor type, but also with its stage when diagnosed and with the treatment applied. Sex or race predilection usually follows that of the primary tumor and the incidence is usually increased by age. Autopsy studies showed that 24% of cancer patients had intracranial metastasis. Of these ~20% are in the dura, ~15% are in the brain, ~8%

are in the leptomeninges, and in ~10% the brain is the only site of intracranial metastases (Posner and Chernik 1978)

The lung (45–50%), breast (15%), melanoma (10–15%), gastrointestinal/genitourinary (10–15%) cancers are the most common primary tumors metastasize to the brain (Schouten et al. 2002). Less common causes of brain metastases are prostate and thyroid cancers, sarcomas, lymphoma/leukemia, germ cell tumors of testis, and gestational trophoblastic tumors (Gavrilovic and Posner 2005). The incidence of metastases to brain within the first year of diagnosis is ~91% in lung cancer, ~50% in melanoma and renal cancer, ~40% in colorectal cancer, and ~19% in breast cancer (Schouten et al. 2002).

Solitary brain metastases are ~39–53% of all brain metastases (Posner and Chernik 1978). The distribution of the sources of solitary brain metastasis is slightly different from multiple ones. The primary site of most solitary brain metastases (70%) remains unknown. In others, common causes are gastrointestinal (67%), genito-urinary (60%), gynecological (54%), melanoma (48%), breast (48%), lung (45%), and other miscellaneous (66%) cancers (Nussbaum et al. 1996).



The most common primary tumors associated with hematogeneous dural metastases are breast, lung and prostate cancers, melanoma, neuroblastoma, lymphoma and leukemia. Dural metastases may usually occur as an extension of tumor to the dura from the adjacent calvarial metastases. Contrary to dural metastases, leptomeningeal involvement occurs by hematogeneous spread from extracranial malignancies or by cerebrospinal fluid seeding of primary brain neoplasm such as anaplastic astrocytoma, glioblastoma multiforme, ependymoma, or medulloblastoma.

Existence of brain metastases plays an important role in the management of cancer patients and can directly affect their morbidity and mortality. Thus, brain metastases present a therapeutic challenge for the treating physician and a psychologically and physically devastating experience for the patient. The prognosis of a cancer patient usually becomes worst when a brain metastasis has developed. The median survival rate is several months and the percentage of 2-year survival is in single digits. Of particular significance, imaging of patients with a surgically treated solitary brain metastasis, shows an approximately doubled rate of survival after 1 year. The 1- and 2-year actual local control rates for brain metastases are 69% and 46%, respectively (Chang et al. 2003). Prompt diagnosis is particularly important for an appropriate treatment, which may result in remission of brain symptoms and may improve the quality of the patient's life.

Brain metastases may be the first sign of cancer disease in 45% of patients and the prognosis of patients with this presentation is better than that of patients with brain metastasis in general (Nguyen et al. 1998). Although lung cancer and melanoma

metastasis usually remain silent, approximately two thirds of brain metastases are symptomatic at some point. The primary sources of the symptoms are the mass effect of the lesion causing an increase in intracranial pressure, headache, nausea, vomiting, vertigo, confusion, lethargy and intracranial herniation, and local irritation and/or destruction of neurons resulting in motor deficits, visual field defects, aphasia, new-onset seizures, ataxia, and other focal neurological signs or symptoms. Furthermore systemic cancer and its treatment can cause cerebrovascular complications including intratumoral hemorrhage, tumoral invasion of arterial or venous sinuses, and tumor emboli; coagulative conditions involving disseminated intravascular coagulation, thrombocytopenia, nonbacterial thrombotic endocarditis, and cerebral intravascular coagulation; infectious events such as septic infarction from fungal or bacterial sepsis and infectious vasculitis manifest in immunocompromised cancer patients through malignancy, or cancer therapy (Katz and Segal 2005). Small tumor emboli can often cause stroke-like symptoms, which usually resolve after breaking up of the emboli. Cranial nerve palsy is a sign of meningeal involvement. The type and the onset of the symptoms are subject to change due to location, size, and the degree of the mass effect of lesion.

There are two hypotheses to explain the primary distribution of brain metastases (Gavrilovic and Posner 2005). First is the "mechanical hypothesis" proposed by Ewing (1940), which suggests that the usual distribution of brain metastases is similar to that of cerebral blood flow, and they occur ~80–85% in the cerebrum, ~10–15% in the cerebellum and ~3–5%

in the brain stem. Second is the “seed and soil” hypothesis proposed by Paget (1889), which assumes that genetic changes in some cancer cells, such as melanoma, allow them to locate a more favorable biochemical environment to proliferate. Fidler et al. (1999) have developed different melanoma clones, which involve preferentially different specific areas of brain such as parenchyma, meninges, and ventricles separately. Several important molecules that are responsible for invasion, proliferation, metastatic cell signaling, and angiogenesis of metastatic cancer cells, have been identified; examples are E-cadherin, catenins, neurotrophins, plasminogen activators and inhibitors, and matrix metalloproteases (Nathoo et al. 2005). Weiss (1992) suggests that the distribution of brain metastases can be explained by blood flow alone in 66% of cases but not so in the remaining patients. These findings propose that both hypotheses play an important role in the distribution of brain metastases.

Metastatic spread of primary tumor to the brain is a complex series of steps and requires genetically suited cancer cells, mediated by molecular mechanisms (Gavrilovic and Posner 2005). In summary, on the primary site, cancer cells need some transformation steps including genetic change, growth, angiogenesis, and invasion. Subsequently, they have to be transported to the brain, including intravasation into the capillary bed or lymph vessels, reach to circulation, escape from immune response and shear forces; arrest in lung, liver or vertebral bodies depending on whether the venous drainage is into vena cava, portal vein or Batson venous plexus; reenter into arterial circulation by growing into the lung and invade pulmo-

nary venous circulation, or pass through the capillary bed, or cross from a patent foramen ovale; and then arrest in the cerebral capillary bed, which usually occurs at the gray-white matter junction and in the watershed areas of brain similar to cerebral emboli; extravasate across the capillary membrane into the brain parenchyma; finally dormancy or grow in brain parenchyma (Gavrilovic and Posner 2005). Blood-brain-barrier does not hinder tumor cell extravasation, and furthermore it provides a shelter to those cells against many water-soluble chemotherapeutic agents and also macromolecules such as antibodies (Gavrilovic and Posner 2005). This protection is the major cause of late solitary metastases following total eradication of primary tumor and is responsible for the dormancy of metastatic cells, in which a balance is established between proliferation and apoptosis of cancer cells, such that metastasis remains at microscopic level (Gavrilovic and Posner 2005). For these reasons prophylactic whole brain radiation therapy is recommended to reduce the incidence of brain metastases especially in patients with small-cell lung cancer.

Surgical excision followed by adjuvant whole-brain radiotherapy is the choice of treatment of solitary brain metastases in a carefully selected patient group to prolong the median survival and to improve or stabilize their performance status. However, it is relatively unnecessary in the presence of either systemic disease or substantial neurological deficit (Korinith et al. 2002). Radiosurgery is also another effective and noninvasive option to treat surgically inaccessible lesions or up to six metastases. Chang et al. (2003) found that, for lesions of 1 cm ( $0.5 \text{ cm}^3$ ) or less, the corresponding local control rates are

86% and 78%, respectively, which is significantly higher than the corresponding rates of 56% and 24%, respectively, for lesions larger than 1 cm ( $0.5 \text{ cm}^3$ ) ( $p = 0.0016$ ). Furthermore, they recommend a close observation for the ambiguous suspected brain metastasis up to a diameter of 1 cm.

## SCREENING AND INITIAL EVALUATION

In patients with known primary cancer, brain imaging is required and also cost-effective when neurological signs and symptoms develop, except in patients with lung cancer and melanoma, which can cause frequent silent brain metastases. A brain imaging for screening purpose should be performed periodically in patients with lung cancer and melanoma, despite good neurological status. Computed tomography (CT) is more widely used because of its easy accessibility and low cost, but magnetic resonance (MR) imaging is the modality of choice for screening and initial staging of cancer patients with suspicious brain metastases, because it is more sensitive and specific than CT in determining the existence, location, and number of metastases. Contrast-enhanced MR imaging detects two or three times as many lesions as contrast-enhanced CT, especially the lesions less than 5 mm in diameter. In addition, ~20% of patients with solitary metastatic lesions on computed tomography show multiple lesions on MR imaging.

The use of magnetization transfer with single-dose gadolinium administration can improve sensitivity of MR imaging roughly equivalent to triple-dose, post-contrast, spin-echo imaging, in detecting lesions

and lesion conspicuity (Thng et al. 1999). Limited brain MR imaging (only T1- and contrast-enhanced T1-weighted images) appears to be a useful, and cost-effective method to screen for brain metastases at the time of initial staging, and it may facilitate timely treatment of cancer patients and improve their survival and quality of life (Kim et al. 2005). Detection of single metastasis is crucial for diagnosis and possible surgical management, and directly affects the mortality and morbidity of cancer patients. If no definitive diagnosis can be established for a solitary brain lesion, then a biopsy and/or surgical removal is recommended in patients with good systemic performance status.

## IMAGING PROTOCOL

Brain MR imaging protocol for cancer patients with brain metastases is subject to change due to many factors, such as clinical status of the patient, emergency conditions, capability of MR imaging systems, preferences of the user or the requirements of surgical stereotaxic systems. Patient-based modifications can be made in protocol during examination. In patients with poor clinical status or loss of consciousness, fast sequences and single-voxel MR spectroscopy techniques can be preferred for initial examination, and complete imaging examination can be delayed until patient reaches a more appropriate clinical status.

Classical spin echo (SE) or turbo (fast) SE (TSE) sequences can be selected for conventional brain MR imaging due to performance of MR imaging systems or the habits of the user. Typical parameters of brain tumor imaging at 1.5 T MR imaging system for initial diagnostic work-up are

TABLE 24.1. A typical brain tumor imaging protocol including manufacturer specific parameters at 1.5 T

Sequence	TR (ms)	TE (ms)	FA/TI	Acq/NEX	Thickness (mm)	Slice number	Matrix		FOV (mm)	Acq Time (min)
							Scan	Recon		
Localizer	15	5,2	20	1	10	3	256	256	250	0,17
T1 SE	S (584)	15	69	2	5	22	176	256	230	3,11
FLAIR	8000	100	90/2,000	2	5	22	176	256	230	4,00
T2 TSE	S (4471)	100	90	3	5	22	224	512	230	2,05
Dual Echo PD/T2*	S (2,296)	20/90	90	1	5	22	176	256	230	6,16
DWI/ADC	S (4213)	91	90	1	5	22	112	128	230	0,29
DTI	4000	95	NA	4	5	20	128	128	230	1,56
DSC MRI (FE-EPI)	S (627)	30	40	50	3 to 7	10-15	128	128	230	1,37
Post Gd T1 SE	S (212)	15	69	2	3 to 7	10-15	256	256	230	2,21
Post Gd MT T1 SE	S (890)	15	69	2	5	22	176	256	230	3,21
3D T1 FFE	25	4,6	30	1	0.8	160	256	256	230	6,58
fMRI (FE-EPI)	3000	50	90	1	4	16	64	64	230	4,09
MR spectroscopic imaging (Multivoxel)										
2D TSI	2,000	136	90	2	10	1	32	32	250	8,45
2D TSI	2,000	31	90	2	10	1	32	32	250	8,56

TR: time of repetition, TE: time of echo, FA: flip angle, TI: time of inversion, Acq: acquisition, NEX: number of excitation, Recon: reconstruction, SE: spin echo, FLAIR: fluid attenuated inversion recovery, TSE: turbo spin echo, PD: proton density, DWI: diffusion-weighted imaging, ADC: apparent diffusion calculation, DTI: diffusion tensor imaging (12 directions), DSC: dynamic susceptibility imaging, FE: field (gradient) echo, EPI: echo-planar imaging, Gd: gadolinium (typically 0.1–0.2 mm/kg), MT: magnetization transfer, FFE: fast field (gradient) echo reconstructed in the axial, coronal and sagittal planes, TSI: turbo spectroscopic imaging

shown in Table 24.1. The choice of plains for each sequence is subject to change due to user preference or location of tumor. Typically sagittal T1-weighted SE, axial fluid attenuated inversion recovery (FLAIR), axial and coronal T2-weighted TSE images preferentially with fat saturation, are obtained for routine brain examination. Dual T2-weighted SE imaging (T2 and proton density images) with larger field of view can be required for some surgical stereotaxic frames, and can be replaced by FLAIR. Single dose (0.1 mg/kg gadolinium or equivalent) contrast-enhanced SE sequence with magnetization transfer is usually adequate and more cost effective than triple-dose applications (Thng et al. 1999). Instead of obtaining post-contrast images in two (axial, coronal) or three (additional sagittal) different orthogonal planes, a single 3D volume imaging with subsequent multiplanar

reformations should be preferred because it usually takes less time with adequate resolution. Additionally, it also allows for 3D surface rendering reformations and provides base images for stereotaxic coordinating systems and image fusion studies. Contrast-enhanced FLAIR images can improve the lesion conspicuity especially the ones located in cortical, subcortical, ventricular, or leptomeningeal areas (Ercan et al. 2004).

Faster echo-planar sequences are preferred for diffusion-weighted imaging. They are typically acquired using at least three b values of 0, 500, and 1,000 s/mm<sup>2</sup> applied in the phase (P), measurement (M), and slice selection (S) directions for the evaluation of either intra-tumoral changes especially in cystic metastasis and ischemic changes due to tumor thrombosis. Antero-posterior fold-over direction is used for transverse orientation to keep distortion artifacts symmetric

over the left and right hemispheres of the brain. Cardiac triggering is not usually required. Automatic shimming and spectral saturation inversion recovery are added to remove the high water/fat shift. Half-scan can be used to compensate the flow-related local phase errors by reducing time of echo (TE). Post-processing of isotropic diffusion-weighted images from three different main directions is obtained from the formula of  $DWI = (|P| \cdot |M| \cdot |S|)^{1/3}$ . The apparent diffusion coefficient (ADC) calculation is based on the formula:  $S_{(b)}/S_{(b=0)} = \exp(-b \text{ value} \times ADC)$  in which  $S_{(b)}$  is signal intensity with the diffusion gradient,  $S_{(b=0)}$  is signal intensity without the diffusion gradient,  $b$  value is attenuation factor (in  $s/mm^2$ ), and ADC is the apparent diffusion coefficient (in  $mm^2/s$ ) (Bulakbasi et al. 2004). The ADC maps are calculated on a pixel-by-pixel basis.

Diffusion tensor imaging is a relatively new technique compared with MR spectroscopy, diffusion-weighted imaging, and perfusion imaging, and widely utilized for research purposes, rather than for routine clinical imaging. Applications of diffusion tensor imaging have used everything from simple, unidirectional ADC measurements, to full-tensor acquisitions processed with sophisticated tractography techniques. For diffusion tensor imaging, at least 12 or more directions are usually necessary for an adequate diffusion tensor process and for the evaluation of white matter tract invasion/displacement (Field and Alexander 2004). Diffusion anisotropy is easily understood as the degree to which diffusivity is directionally dependent or, in tensor terms, the extent to which the tensor ellipsoid shape deviates from that of a sphere (Field and Alexander 2004). Mathematically, anisotropy is the

degree to which the three tensor eigenvalues differ from one another. Any of several anisotropy metrics may be used to quantify this difference, such as fractional anisotropy (FA), lattice index, mean diffusivity (MD), relative anisotropy, volume ratio, and tumor infiltration index (Lu et al. 2003, 2004; Field and Alexander 2004; ).

Contrast-enhanced gradient echo T2\*-weighted echo planar dynamic susceptibility contrast (DSC) weighted perfusion imaging based on the kinetic principles for non-diffusible exogenous tracer is usually sufficient for the evaluation of perfusion characteristics of brain metastases (Rosen et al. 1990). It is widely used in a clinical setting due to its relatively short imaging time and the wide availability of image-processing tools. High flow (5–7 mL/s) injection of contrast material (0.1–0.2 mg/kg gadolinium or equivalent) by automatic power injector is crucial for adequate perfusion imaging. Gradient-echo sequences are much more sensitive than SE sequences for the detection of differences in local magnetic susceptibility between vessels and the surrounding tissue, during the first pass of gadolinium chalets (Cha 2004). However, gradient-echo sequences are more prone to magnetic susceptibility artifacts than SE sequences. To overcome these artifacts slice thickness can be reduced or SE sequences may be preferred for imaging lesions near brain–bone–air interfaces such as the temporal lobes or posterior fossa.

Echo planar technique, which allows obtaining a series of images acquired at intervals of ~1 s, are fast enough to provide robust measurements of cerebral blood volume (CBV). Among post-processed perfusion parameters, CBV values of obtained from tumoral and peritumoral areas are the most important parameters for differential

diagnosis of solitary brain metastasis from primary brain neoplasm (Bulakbasi et al. 2005). The raw data are usually processed during the first pass of the bolus of paramagnetic contrast material, the signal intensity in T2\*-weighted sequence decreases, whereas the signal intensity partially restores directly after the passage. The relative measure of contrast agent concentration can be calculated from signal-intensity changes over time on kinetic principles for non-diffusible tracers by using the following relationship:  $\Delta R2^*(t) = -k/TE \ln[S(t)/S(0)]$ , where TE is the echo-time, k is an unknown proportionality constant, S(t) is the signal intensity at time t, and S(0) is the pre-contrast signal intensity (Rosen et al. 1990). The contribution of tracer leakage or recirculation, due to disruption of blood–brain barrier in tumoral tissue, can be minimized by using a mathematical model, fitting gamma variate function to the measured  $\Delta R2^*$  curve (Rosen et al. 1990). The area under this curve is proportional to the CBV (Rosen et al. 1990). Fitting algorithm, which approximates the curve that would have been obtained without recirculation or leakage, is also unstable and can cause wide variations in the results. To eliminate this instability, CBV values are expressed to the measurement relative to a standard reference, usually contralateral white matter, which refers as relative CBV (rCBV) (Bulakbasi et al. 2005).

Magnetic resonance spectroscopy can be performed by using single or multi-voxel techniques and using different sequences such as stimulated-echo acquisition mode (STEAM) or point-resolved excitation spin-echo (PRESS) (Bulakbasi 2004). A volume selective 3D or 2D (depending on lesion size) chemical shift imaging (CSI) with high matrix ( $16 \times 16$  or  $32 \times 32$ ), has to be

the choice technique for MR spectroscopy in tumor diagnosis because simultaneous acquisition of spectra can be obtained from multiple regions, and the quantification and metabolite maps can be created from MR spectroscopy data (Bulakbasi 2004). By the CSI technique, 1–2 cc nominal voxel size and a 0.5 cc resolution limit can be obtained in 1.5 T, and up to 0.4 and 0.094 cc in a 3 T static magnet systems, which causes a linear loss in signal to noise ratio between 44% and 60% due to the decreasing line-width (Gruber et al. 2003). Although CSI has a low resolution, it can be compensated by the increase of signal to noise ratio, which improves the spectral resolution and provides better separation of metabolite signal.

Magnetic resonance spectra can be obtained by using long (270 ms), intermediate (135 or 144 ms) or short (30 or 40 ms) TE according to T2 resonance of the desired metabolite. While intermediate or long TE values allow us to measure the major metabolites with long T2 resonance such as n-acetyl aspartate (NAA), choline (Cho), creatine and phosphocreatine (Cr) and lactate, short TE technique allows us to measure the metabolites with short T2 resonance such as lipid, alanine, glutamine and glutamate complex, glucose, myoinositol, and other amino acids (Bulakbasi 2004). Intermediate TE values are crucial for tumor diagnosis, with a preferential addition of short TE values, if applicable. To prevent strong contribution to the spectra from subcutaneous fat signals, the volume of interest is completely enclosed within the brain and positioned at the center of the phase-encoded field of view, and up to eight outer volume saturation slabs can be placed over the skull. Performing spectroscopy on all patients following contrast can

minimize inter-patient and intra-patient variability with minimal effect of contrast on metabolite ratios and peak areas, as it also allows us to determine metabolite changes within areas of enhancement, necrosis and infiltrating tumor or edema (Law 2004).

Processing steps, such as time domain apodization, Fourier transformation and reconstruction of spatial dependence of data, are usually applied to the MR spectroscopy data. Quantification is essential in MR spectroscopy diagnosis. Different metabolite levels and ratios, such as NAA/Cho, NAA/Cr, Cho/Cr, Lip/Cr, and Lac/Cr, can be obtained. Especially, relative metabolite levels, expressed as a percentage of tumor/normal brain metabolite proportions, are very useful for the comparison of the MR spectra, obtained by different scan parameters or at different magnetic fields (Bulakbasi et al. 2003). It also allows us to make the statistical analysis and comparison of MR spectra of different tumor types. Metabolic maps are displayed in a pseudo anatomic format, rather than a spectrum, and provide the information in a more familiar way to radiologist and clinicians. Metabolic map imaging represents the distribution of particular species such as NAA, Cho, Cr, and different ratio combinations. Images appear blurry due to low concentration of protons of desired species compared with water protons, but high-resolution techniques can improve the image quality (Bulakbasi 2004).

Functional MR imaging is a promising method to evaluate the relationship of a tumor with important functional areas of brain. It is very informative in preoperative treatment planning of cancer patients, and allows maximum tumor resection, while preserving important brain functions, and also

shortens the operation time under anesthesia. It provides a valuable information tool for neurosurgeons in deciding operation type (a resection, a stereotaxic biopsy, or not to operate at all) and the selection of tumor approach during surgery. The basic outline for performing a functional MR imaging study is as follows: (1) acquisition of the functional MR imaging data, including paradigm selection and patient preparation, (2) acquisition of high-resolution anatomic data, (3) analysis of the functional MR imaging data, (4) co-registration of the functional MR imaging data to the high-resolution anatomic data, (5) downloading of the co-registered data into the neurosurgical navigational computer (Bogomolny et al. 2004). The selection of paradigms (motor, memory, or language) performed during the functional MR imaging study is subject to change due to location of the tumor and the parts of the brain involved.

## IMAGING PROPERTIES OF SOLITARY BRAIN METASTASIS

Brain metastases are typically seen as multiple contrast-enhanced lesions with prominent vasogenic edema and mass effect. This is also true for solitary metastasis. A lesion has a variable intensity on MR images depending on many factors such as nature (solid, semisolid, partly, or totally cystic), location of the lesion, amount of necrosis, degree of cellularity and vascularity, and existence of hemorrhage, mucin, or calcification. Classical MR signal intensity characteristics of metastasis are usually not diagnostic. It is typically isointense to mildly hypointense on T1-weighted images and hyperintense on T2-weighted and FLAIR

images. The degree of hyperintensity on T2-weighted images is usually increased by the degree of cystic/necrotic components. However, signal characteristics of some metastases have some clues regarding the origin of the lesion. Metastatic mucinous adenocarcinoma and hemorrhagic metastases show a decrease on T2 signal due to slowing of rotational and translational proton motion caused by increased protein content of mucin and chronic blood breakdown products, respectively (Atlas et al. 2002). Melanoma metastases are typically hyperintense on T1-weighted images and isointense to cortex on T2-weighted images according to free radical content of melanin (Atlas et al. 2002). Gradient echo images can also improve the lesion detection in patients with melanoma metastases, which demonstrate prominent loss on T2\* signal due to susceptibility effect of melanin (Atlas et al. 2002).

An extensive surrounding edema, which is usually not proportional to tumor size, is a typical finding of metastasis, but it may also be seen in an abscess or in primary gliomas (Figure 24.1a). Surrounding vasogenic edema is usually homogeneous and indistinguishable from metastatic focus until contrast administration. Edema is relatively hypointense to cortex on T1-weighted images and hyperintense on T2-weighted and FLAIR images. It extensively scatters along the white matter tracts and ends with finger-like boundaries made by unaffected subcortical fibers, causing digit-like appearance (Figure 24.1a). Unlike infiltrative glial tumors, the edema of metastasis neither involves the cortex nor crosses the corpus callosum (Atlas et al. 2002). Contrary to parenchymal metastasis, the cortical metastasis usually does not have a prominent surrounding

edema and is easily missed on pre-contrast T1- and T2-weighted images (Atlas et al. 2002). The amount of edema is gradually decreased following a steroid regimen, because it usually modifies some intrinsic characteristic of the tumor, e.g., endothelial “pores” or “fenestations”, thereby restoring a normal restriction to diffusion across the endothelium and re-balancing the vascular hydrostatic pressure force against the oncotic and osmotic pressures, as well as restoring trans-membrane homeostasis (Andersen and Jensen 1998).

Hemorrhage is present in ~3–14% of metastases, and is most likely seen in metastases from melanoma, choriocarcinoma, renal, thyroid, lung, and breast cancers. However, bronchogenic metastases are the most common source of hemorrhagic lesions because of their higher incidence. Although hemorrhage more frequently occurs in metastases than in gliomas, it is not specific for metastases, and is seen in up to 3% of gliomas (Nussbaum et al. 1996). Hemorrhagic metastases have different signal intensities on T1- and T2-weighted images due to the stage of hemorrhage. Unless it is metastatic melanoma, a bright signal on T1-weighted images suggests a hemorrhagic or calcified metastasis.

Solid, nodular, or irregular ring patterns of enhancement are seen in metastatic focus due to absent or deficient blood–tumor barriers in the vascular endothelium of the involved capillaries (Figure 24.1b). A non-enhancing lesion is less likely to be a metastasis. Contrast-enhanced MR imaging with magnetization contrast is the best method for detection of additional lesions and meningeal tumor seeding (Thng et al. 1999). Detection of additional lesions is very important when considering surgical



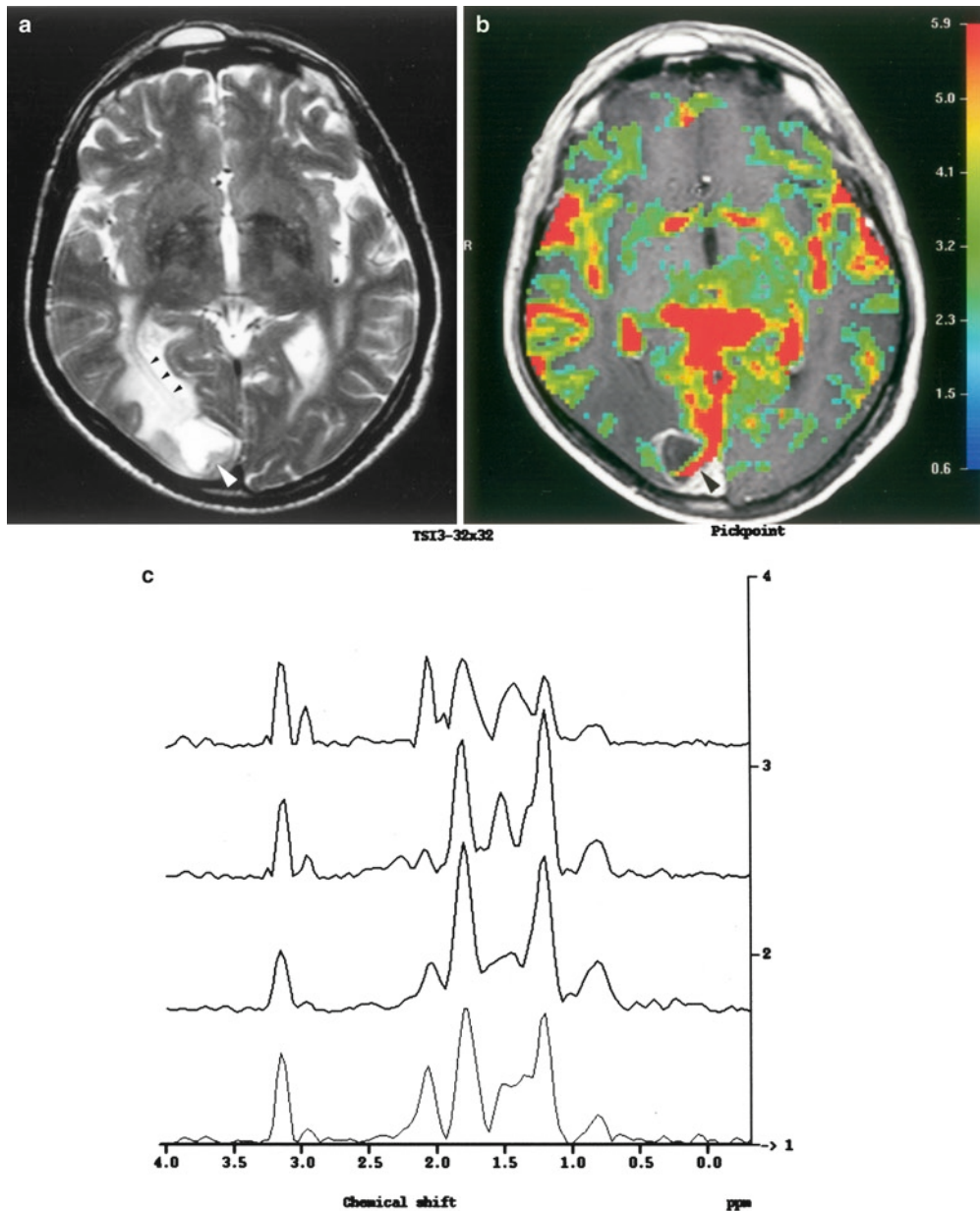


FIGURE 24.1. Fifty-seven years-old male with solitary metastasis from lung cancer has progressive visual disturbance. (a) T2-weighted axial image shows partly solid (*white arrowhead*) partly cystic lesion located at the subcortical white matter of right occipital lobe. Extensive peritumoral edema surrounding optic tract (*black arrowheads*) is very typical for metastasis and ends with finger-like boundaries made by unaffected subcortical fibers, causing digit-like appearance. (b) Axial DSC-weighted perfusion image overlaid onto contrast-enhanced T1-weighted image shows increased perfusion with high rCBV value in the solid part of tumor (*black arrowhead*), which can be consistent with both glioma and metastasis, but not with abscess. On the other hand, low peritumoral perfusion values compared to normal white matter helps to differentiate metastasis from glioma. (c) MR spectra obtained with intermediate TE (135 ms) from different parts of tumor, demonstrate high Cho/Cr ratios with low or absent NAA, which is consistent with high grade malignant tumor. High lipid peaks suggest a metastasis

treatment of a solitary metastasis. On the other hand, metastases can demonstrate heterogeneous enhancement patterns and time of onset during the examination. As a general rule, the immediate post-contrast scan is probably the most practical method for detecting metastases, given that the radiologist will typically obtain only one post-contrast scan (Atlas et al. 2002). Dural and leptomeningeal metastases are best shown on post-contrast T1-weighted and FLAIR studies, as local or diffuse thickening and enhancement of meninges (Ercan et al. 2004). Leptomeningeal metastases presents with increased enhancement in the subarachnoid spaces of the cortical sulci, the fissures, and the cisterns. A small solitary nodular enhancing lesion can also develop in the subarachnoid spaces, which may invaginate within the adjacent brain parenchyma and may mimic cortical metastases. Multi-planar post-contrast T1-weighted images and 3D surface rendering techniques are required for differential diagnosis.

The contrast between high-grade gliomas and metastases is generally lower on diffusion-weighted images and ADC maps, compared to conventional MR imaging, and it is not useful in their differentiation (Bulakbasi et al. 2004; Kitis et al. 2005). On the other hand, in patients with ring-enhancing cerebral mass lesion, restricted diffusion might be characteristic, but is not pathognomonic, for abscess in the early capsule formation stage. Low ADC values may also be found both in brain metastases, due to intracellular edema in the viable tumor cells during the development of early tumor necrosis without prominent liquefaction, and in glial tumors due to cystic/necrotic changes or high cellularity (Hartmann et al. 2001). Furthermore, in the peritumoral areas of untreated high-grade

gliomas and metastases, the mean ADC values were higher in metastases than in high-grade gliomas due to higher amounts of pure surrounding vasogenic edema of metastases, than in those of gliomas in which a combination of tumoral infiltration and edema is present together (Krabbe et al. 1997). T2 values are more useful than ADC for characterizing contrast enhancing tumor and immediate-edema regions. T2 relaxation times are significantly lower in contrast-enhancing tumor regions and are significantly higher in immediate-edema regions for patients with meningiomas or metastases, compared with those for gliomas (Oh et al. 2005).

Solitary metastasis typically demonstrates variable elevations of Cho, to values comparable with anaplastic astrocytomas, and strongly elevated lipids and/or lactate peaks (Figure 24.1c). An increased Lip/Cr ratio is more prominent in metastasis than in primary glial tumors, which is helpful to distinguish them from high-grade astrocytomas. Moreover, absence of lipid may exclude metastasis (Bulakbasi et al. 2003). The secondary deposits of cancer cells originating from other parts of the body do not contain neuroglial components. Therefore, NAA is low or absent in metastases but it is usually seen in MR spectra owing to contamination of normal brain tissue in imaging voxel. Creatin value is also low in metastasis. The major diagnostic MR spectroscopy criterion of metastasis is the lack of tumoral markers in the peritumoral area because metastasis is not infiltrative in nature unlike primary glial tumors. This information is not available from the single-voxel MR spectroscopy spectra and it requires a multi-voxel technique. On the other hand, MR spectroscopy has some limitations in

lesions close to the cranial vault, where susceptibility effects and lipid contamination reduce the quality of spectra.

In the absence of neuroglial elements, tumor capillaries of brain metastasis are not similar to those of the brain but of the originating organ of cancer. Metastases have newly formed capillaries with fenestrated membranes, open endothelial junctions, and maldeveloped blood-brain-barrier, so they are leaky (Cha 2004). The peritumoral capillaries have three times as many endothelial surface-connected vesicles, a markedly thicker basal lamina, and significantly reduced extension of pericytic and glial investments (Bertossi et al. 1997). The absent or deficient of blood-brain-barrier causes an intense leakage of contrast material in the early bolus phase on DSC-weighted perfusion imaging, similar to choroid plexus tumors and meningiomas.

The tumoral rCBV values of metastases can change due to degree of vascularity of primary neoplasm (Kremer et al. 2003; Bulakbasi et al. 2005). Metastases from melanoma and renal cell cancer have higher tumoral rCBV values than high-grade gliomas and lung cancer metastases (Kremer et al. 2003). Similar to MR spectroscopy findings, peritumoral rCBV measurements are more effective than tumoral rCBV values in differentiating solitary metastasis from primary glioma (Law et al. 2002; Bulakbasi et al. 2005). Peritumoral rCBV values of metastasis, in which the peritumoral region contains pure vasogenic edema, are significantly lower than those of gliomas with edema and tumoral tissue infiltrating along proliferated vascular channels (Figure 24.1b). Although the rCBV measurement obtained before treatment is not useful to predict the treatment outcome, it is more sensitive and specific

for the prediction of treatment outcome at the 6-week follow-up than the tumor volume change alone (Essig et al. 2003). A steroid regiment does not significantly affect tumor blood flow, but may subtly increase perfusion in the edematous brain by reducing peritumoral water content and local tissue pressure (Bastin et al. 2006).

Diffusion tensor imaging properties of metastasis are also originating from the non-infiltrative nature of the lesion. The major eigenvalue of the diffusion tensor (reflecting mean diffusivity in the longitudinal direction) is significantly lower in the white matter surrounding high-grade gliomas than those surrounding metastases, even when the anisotropy showed no difference (Jellison et al. 2004). Decreased FA and increased MD with normal location and direction in peritumoral regions reflect increased extracellular water (vasogenic edema) due to the leaky capillaries (Jellison et al. 2004). These findings indicate that bland (tumor-free) edema increases inter-fiber distances without substantially altering fiber directions, such that, anisotropy is reduced without significant changes in hue on directionally encoded color maps (Field et al. 2004).

Displacement but not invasion or destruction of white-matter fibers is another finding suggestive of metastasis. Although there is no significant FA difference between the hyperintense regions surrounding metastases and gliomas on T2-weighted images, the peritumoral MD of metastatic lesions measured significantly greater than that of gliomas (Lu et al. 2003). Furthermore, this FA difference becomes apparent only when tumor FA values are expressed as a differential from values “expected” in bland edema, which are the product of a linear regression of FA onto ADC for a series of

bland edema cases. The difference between “expected” and observed FA is named as the “tumor infiltration index,” and this index was higher (i.e., FA lower than expected) in active tumor tissue (Lu et al. 2004).

Although diffusion tensor imaging is a very promising technique to show the interaction between a tumor and adjacent white matter tracts, lack of direct histological correlation between FA maps and the status of white matter tracts near brain tumors in the literature is the major drawback of this technique. On the other hand, diffusion tensor tractography maps of desired white matter tracts (especially corticospinal tract) overlaid onto high-resolution anatomic images are quite useful for preoperative planning and intra-operative guidance of tumor resection to avoid undesired motor deficits. This information particularly can be doubled when the colored 3D MR tractography images are fused or combined with the functional MR imaging data obtained from different tasks. The relationship of tumor with either motor or association areas of cortex showed by functional MR imaging, or white matter tracts originating from these motor areas, showed by MR tractography technique can clearly be demonstrated by the functional MR imaging-tractography combination or by the evaluation of data obtained by these two techniques combined.

## DIFFERENTIAL DIAGNOSIS OF SOLITARY BRAIN METASTASIS

The major diagnostic problem of solitary metastasis is its differential diagnosis. Although there are some clues in classical

MR imaging findings, the conventional contrast enhanced MR images are usually insufficient to differentiate solitary metastasis from primary glioma, abscess, hemorrhage, and ischemic or demyelinating lesions. Presently, more advanced MR techniques can be used for specific diagnosis.

The imaging appearance of dural-based metastases may mimic meningiomas in conventional MR imaging. Enhancement of adjacent meninges is considered as typical for meningiomas as it is in meningeal metastases. The rCBV mapping can provide additional information by demonstrating a low rCBV, which may suggest the diagnosis of metastasis, with the exception of Merkel carcinoma metastasis of the skin, which showed an elevated rCBV, not different from that of meningiomas (Kremer et al. 2004).

Although dural or leptomeningeal thickening and enhancement due to metastatic involvement are more irregular and local than the changes due to chronic meningitis or intracranial hypotension, it is not always easy to differentiate them from each other. Clinical findings and patient history are crucial for specific diagnosis. Nontumoral leptomeningeal enhancement may also occur following irradiation, prior extra-axial hemorrhage, or below a craniotomy site. Magnetic resonance spectroscopy or DSC-weighted perfusion imaging are insufficient to differentiate leptomeningeal carcinomatosis from other etiologies because of their low spatial resolution. Magnetic resonance spectra are usually inefficient due to fat contamination from subgaleal fatty tissue, and perfusion increases due to the meningeal metastatic involvement adjacent to the cortex which is usually hidden by the high perfusion characteristics of normal cerebral cortex.

Solitary ring-enhancing lesion may resemble benign conditions, such as abscess, resolving hematoma, acute or subacute infarcts and demyelination, as well as malignant ones such as metastasis or glioma. Although malignant lesions tend to demonstrate thick, irregular, or nodular enhancement, as opposed to the regular, thin, even and smooth enhancing wall of the benign conditions, this not the case all the time.

An abscess has a markedly low signal of capsule on T2-weighted images, which also occurs in some cases with metastases. Furthermore, another typical finding of an abscess, is that the capsule on the ventricular side is thinner than the one on the cortical side, which is not always recognizable in every abscess. Diffusion-weighted imaging is quite useful to differentiate brain abscess from cystic metastasis (Nadal Desbarats et al. 2003). An abscess in the early capsule formation stage shows prominent restricted diffusion on ADC maps, and some necrotic metastasis or primary tumors may also have low ADC values due to restricted motion of free water protons in pus or necrotic area (Hartmann et al. 2001). Furthermore, DSC-weighted perfusion imaging may also allow the differentiation of pyogenic brain abscess from cystic brain tumors, making it a strong additional imaging modality in the early diagnosis of these two entities. While the capsular portions of abscesses are hypovascular, causing a marked decrease in rCBV ratios, the peripheral portions of malignant cystic tumors, gliomas, and metastasis, have higher vascularization and higher rCBV ratios than those of abscesses (Erdogan et al. 2005). Kadota et al. (2001), suggest that the presence of acetate and succinate peaks on MR spectroscopy are indicators of inflammation and may exclude

existence of tumor tissue. For these reasons, all MR imaging findings have to be evaluated together for final diagnosis. In some cases, a biopsy is still required.

Especially on routine MR examinations of older patients with some kind of neurological sign or symptom, the imaging features of small high-signal lesions on T2-weighted images with restricted diffusion may resemble either small acute/subacute stage infarcts or metastases. In equivocal cases, contrast administration may be helpful for differential diagnosis, but enhancing patterns and locations of both lesions can be similar; both can be multiple. In solitary lesions, diffusion-weighted imaging, MR spectroscopy, and DSC-weighted perfusion imaging should be performed for exact diagnosis. Especially in the acute stage, infarcts show prominent restricted diffusion due to cytotoxic edema as a result of acute energy failure (Pierpaoli et al. 1993). Although some cystic metastasis may show some diffusion restriction, this is very unusual for solitary solid metastasis resembling acute infarcts. Lack of tumoral MR spectroscopy markers and low rCBV values also represent ischemic changes.

A solitary tumefactive demyelinating lesion is occasionally rare and can show ring-enhancement and resemble metastasis. Histopathologically, demyelinating lesions consist of perivascular inflammatory infiltration and demyelination, and hypervascularity is uncommon. Absence of prominent peripheral edema is an important clue for differential diagnosis. However, in patients with impaired immune response, edema around metastasis may not be as expected. Low Cho/Cr ratio on MR spectra, mild elevation of rCBV, and characteristic intralesional venous enhancement without

marked hypervascularity, are quite helpful in differentiating it from the tumoral process (Cha 2006). Single photon emission computed tomography is more useful than MR imaging in differential in the diagnosis of solitary demyelinating lesion and metastasis (Terada and Kamata 2003).

Resolving hematomas may mimic cystic/necrotic metastasis, but previous history and characteristic signal changes of evolving hematoma due to different oxygenation states of hemoglobin and lyses of initially intact red-blood cell membranes usually allow a definitive differential diagnosis. On the other hand, hemorrhagic metastasis with prominent edema may resemble hematomas. Contrary to hematomas, hemorrhagic metastasis do not have an irregular hypointense rim due to chronic iron deposition. Furthermore, heterogeneous metastasis has usually had a non-hemorrhagic enhancing solid component with a high rCBV value and persistent surrounding edema (Atlas et al. 2002). Gradient echo T2\*-weighted images are also more useful in detecting additional hemorrhagic lesions than SE images (Atlas et al. 2002).

The major differential diagnosis of supratentorial, solitary, solid enhancing lesion in adults includes primary glioma (usually grade 3 or 4) versus solitary metastasis, in the absence of a history of prior irradiation. The infratentorial solitary enhancing metastatic lesion should be differentiated from heman-gioblastoma and lymphoma. Absence of a blood-brain-barrier in metastases and disruption of blood-brain-barrier in high-grade gliomas and other primary brain tumors leads to massive enhancement in both tumor groups with prominent peritumoral edema. Because of the destructive nature and high vascularity of these lesions, and the similarity between MR spectroscopy and perfusion

parameters obtained from enhanced portions of tumors, the two are not easily distinguishable. On the other hand, the infiltrative nature of primary gliomas helps to differentiate them from non-infiltrative solitary metastasis. Higher peritumoral Cho/Cr ratios and rCBV values, indicating existence of tumor cells, help to differentiate infiltrative gliomas from metastasis (Law et al. 2002; Bulakbasi et al. 2005). Furthermore, the mean peritumoral ADC value of metastasis is higher than that of gliomas on images obtained at high-field magnets due to increased water diffusivity of pure surrounding vasogenic edema in metastasis, than found in gliomas with intervening tumor cells. When interpreted in concert with pre- and post-contrast T1-weighted images, FLAIR may be useful in differentiating a glioma from metastasis in patients with a solitary enhancing cerebral lesion. Involvement of the adjacent cortex with FLAIR signal intensity abnormality without gadolinium enhancement is very specific (91%) but not sensitive (44%) for glioma (Tang et al. 2006).

Primary cerebral lymphoma can mimic gliomas, metastases, or even infection on MR images. Differential diagnosis of lymphomas is critical because it requires different treatment options and surgery is relatively contraindicated and may result in increased patient morbidity and mortality. Dynamic susceptibility contrast-weighted perfusion MR images are less effective than diffusion-weighted imaging because lymphomas show elevated rCBV similar to metastases, but not to the same degree as in glioblastoma (Cha 2006). However, lymphomas tend to show lower ADC values than others due to high cellularity of the tumor (Kitis et al. 2005).

A Hemangioblastoma is usually located in the posterior fossa and is associated with

von Hippel–Lindau syndrome. It tends to be multiple, and history of von Hippel–Lindau syndrome usually suggests the diagnosis of hemangioblastoma. A tumor can be pure cystic, pure solid, or partially cystic with intramural solid nodule, usually peripheral in location. It is avidly enhanced and show tubular signal void striations due to enlarged feeding arteries. The hypervascular nature of hemangioblastoma causes higher rCBV value than that of both gliomas and metastasis (Cho et al. 2002).

In the follow-up of treatment, ischemic changes occurring during surgery or radiotherapy can mimic tumor recurrence. Smith et al. (2005) showed that areas with restricted diffusion after glioma surgery demonstrated contrast enhancement on a follow-up study and may simulate the appearance of recurrent tumor. These areas of enhancement invariably evolved into encephalomalacia or gliotic cavity on long-term follow-up studies, as one would expect in a region of permanent brain injury (Smith et al. 2005). Early postoperative diffusion-weighted imaging is quite useful to detect these post-surgical ischemic changes and to help differentiate them from tumor recurrence in follow-up examinations.

## FUTURE TRENDS AND CONCLUSION

The tremendous opportunities and amazing progress during the last few decades in biomedicine, molecular biology, chemistry, physics, engineering, informatics and nanotechnology make a spectacular contribution to medicine as well as imaging. The concept of “personalization of the diagnosis and the treatment” has become very popular in research during the last decade

(Li et al. 2004). The major component of this “personalized diagnosis” is molecular imaging, which is defined as the characterization of measurement of a biologic process in living animals, model systems and humans, at cellular and molecular levels by using remote imaging detectors (Luker and Piwnica-Worms 2001). In connection with this concept, the role of neuroimaging in patients with brain tumors has changed from anatomical and morphological evaluation, to the analysis of functional, hemodynamic, metabolic, cellular, and cytoarchitectural alterations. This remarkable progress has provided an opportunity to detect physiological changes in compartmental kinetics, cellular metabolism, and hemodynamics of brain tumors (Cha 2006). Furthermore, the widespread usage of these sophisticated techniques has allowed neuroradiologists to take a more active role, not only in diagnosis, but also in preoperative planning, treatment follow-up, and assessment of the prognosis of brain tumors.

Nanotechnology applications of cellular and molecular imaging targeted at differentiation of tumor, neural lesions, and necrosis from healthy brain tissue; methods of imaging delivery contrast and therapeutic agents across the blood–brain-barrier to endothelial targets; and new iron oxide-based nanoparticle contrast agents for MR imaging, open new insights in imaging and therapy of brain tumors (Li et al. 2004). These results suggest that this remarkable progress in imaging, with the improvements in nanomedicine, allows us to design multidisciplinary, more sophisticated clinical trials for both diagnosis and treatment of brain metastasis.

In conclusion, although the diagnosis of solitary brain tumors is still somewhat problematic, usage of physiologic

MR imaging techniques such as diffusion-weighted and tensor imaging, proton MR spectroscopy, and DSC-weighted perfusion and functional MR imaging, as part of a routine protocol of brain tumor imaging, provides valuable information to overcome the diagnostic hindrance and to increase effectiveness in therapy monitoring. Assessment of imaging findings with associated clinical signs and symptoms is crucial in making a specific diagnosis. Widespread applications of these sophisticated MR imaging techniques allow collection of more accurate clinical and imaging data. Combination of this enormous experience with impending technologies will certainly improve the diagnostic ability of MR imaging in the near future.

## REFERENCES

- Andersen, C., and Jensen, F.T. (1998) Differences in blood-tumour-barrier leakage of human intracranial tumours: quantitative monitoring of vasogenic oedema and its response to glucocorticoid treatment. *Acta Neurochir. (Wien)* 140:919-924
- Atlas, S.W., Lavi E., and Fisher P.G. (2002) Intraaxial brain tumors. In: Atlas, S.W. (Ed). MRI of the brain and spine, 3rd edn, vol 1. Lippincott Williams & Wilkins, Philadelphia, PA, pp. 565-693
- Bastin, M.E., Carpenter, T.K., Armitage, P.A., Sinha, S., Wardlaw, J.M., and Whittle, I.R. (2006) Effects of dexamethasone on cerebral perfusion and water diffusion in patients with high-grade glioma. *AJNR Am. J. Neuroradiol.* 27:402-408
- Bertossi, M., Virgintino, D., Maiorano, E., Occhiogrosso, M., and Roncali, L. (1997) Ultrastructural and morphometric investigation of human brain capillaries in normal and peritumoral tissues. *Ultrastruct. Pathol.* 21:41-49
- Bogomolny, D.L., Petrovich, N.M., Hou, B.L., Peck, K.K., Kim, M.J., and Holodny, A.I. (2004) Functional MRI in the brain tumor patient. *Top. Magn. Reson. Imaging* 15:325-335
- Bulakbasi, N. (2004) Clinical applications of proton MR spectroscopy in the diagnosis of brain tumours. *Spectroscopy-An. Int. J.* 18:143-153
- Bulakbasi, N., Kocaoglu, M., Ors, F., Tayfun, C., and Ucoz, T. (2003) Combination of single-voxel proton MR spectroscopy and apparent diffusion coefficient calculation in the evaluation of common brain tumors. *AJNR Am. J. Neuroradiol.* 24:225-233
- Bulakbasi, N., Guvenc, I., Onguru, O., Erdogan, E., Tayfun, C., and Ucoz, T. (2004) The added value of the apparent diffusion coefficient calculation to magnetic resonance imaging in the differentiation and grading of malignant brain tumors. *J. Comput. Assist. Tomogr.* 28:735-746
- Bulakbasi, N., Kocaoglu, M., Farzaliyev, A., Tayfun, C., Ucoz, T., and Somuncu, I. (2005) Assessment of diagnostic accuracy of perfusion MR imaging in primary and metastatic solitary malignant brain tumors. *AJNR Am. J. Neuroradiol.* 26:2187-2199
- Cha, S. (2004) Perfusion MR imaging of brain tumors. *Top. Magn. Reson. Imaging* 15:279-289
- Cha, S. (2006) Update on brain tumor imaging: from anatomy to physiology. *AJNR Am. J. Neuroradiol.* 27:475-487
- Chang, E.L., Hassenbusch, S.J.3rd., Shiu, A.S., Lang, F.F., Allen, P.K., Sawaya, R., and Maor, M.H. (2003) The role of tumor size in the radiosurgical management of patients with ambiguous brain metastases. *Neurosurgery* 53:272-280; discussion: 280-281
- Cho, S.K., Na, D.G., Ryoo, J.W., Roh, H.G., Moon, C.H., Byun, H.S., and Kim, J.H. 2002. Perfusion MR imaging: clinical utility for the differential diagnosis of various brain tumors. *Korean J. Radiol.* 3:171-179
- Ercan, N., Gultekin, S., Celik, H., Tali, T.E., Oner, Y.A., and Erbas, G. (2004) Diagnostic value of contrast-enhanced fluid-attenuated inversion recovery MR imaging of intracranial metastases. *AJNR Am. J. Neuroradiol.* 25:761-765
- Erdogan, C., Hakyemez, B., Yildirim, N., and Parlak, M. (2005) Brain abscess and cystic brain tumor: discrimination with dynamic susceptibility contrast perfusion-weighted MRI. *J. Comput. Assist. Tomogr.* 29: 663-667
- Essig, M., Waschkies, M., Wenz, F., Debus, J., Hentrich, H.R., and Knopp, M.V. (2003) Assessment of brain metastases with dynamic



- susceptibility-weighted contrast-enhanced MR imaging: initial results. *Radiology* 228:193–199
- Ewing, J. (1940) Metastasis. In: Ewing, J. (ed) Neoplastic diseases: a treatise on tumors. W.B. Saunders, Philadelphia, PA, pp. 62–74
- Fidler, I.J., Schackert, G., Zhang, R.D., Radinsky, R., and Fujimaki, T. (1999) The biology of melanoma brain metastasis. *Cancer Metastasis Rev.* 18:387–400
- Field, A.S., Alexander, A.L., Wu, Y.C., Hasan, K.M., Witwer, B., Badie, B. (2004) Diffusion tensor eigenvector directional color imaging patterns in the evaluation of cerebral white matter tracts altered by tumor. *J. Magn. Reson. Imaging.* 20:555–562
- Field, A.S., and Alexander, A.L. (2004) Diffusion tensor imaging in cerebral tumor diagnosis and therapy. *Top. Magn. Reson. Imaging* 15:315–324
- Gavrilovic, I.T., and Posner, J.B. (2005) Brain metastases: epidemiology and pathophysiology. *J. Neurooncol.* 75:5–14
- Gruber, S., Mlynarik, V., and Moser, E. (2003) High resolution 3D proton spectroscopic imaging of the human brain in 3T: SNR issues and application for anatomy-matched voxel sizes. *Mag. Reson. Med.* 49:299–306
- Hartmann, M., Jansen, O., Heiland, S., Sommer, C., Munkel, K., and Sartor, K. (2001) Restricted diffusion within ring enhancement is not pathognomonic for brain abscess. *AJNR Am. J. Neuroradiol.* 22:1738–1742
- Jellison, B.J., Field, A.S., Medow, J., Lazar, M., Salamat, M.S., and Alexander, A.L. (2004) Diffusion tensor imaging of cerebral white matter: a pictorial review of physics, fiber tract anatomy, and tumor imaging patterns. *AJNR Am. J. Neuroradiol.* 25:356–369
- Kadota, O., Kohno, K., Ohue, S., Kumon, Y., Sakaki, S., Kikuchi, K., and Miki, H. (2001) Discrimination of brain abscess and cystic tumor by in vivo proton magnetic resonance spectroscopy. *Neurol. Med. Chir. (Tokyo).* 41:121–126
- Katz, J.M., and Segal, A.Z. (2005) Incidence and etiology of cerebrovascular disease in patients with malignancy. *Curr. Atheroscler Rep.* 7:280–288
- Kim, S.Y., Kim, J.S., Park, H.S., Cho, M.J., Kim, J.O., Kim, J.W., Song, C.J., Lim, S.P., and Jung, S.S. (2005) Screening of brain metastasis with limited magnetic resonance imaging (MRI): clinical implications of using limited brain MRI during initial staging for non-small cell lung cancer patients. *J. Korean Med. Sci.* 20:121–126
- Kitis, O., Altay, H., Calli, C., Yuntun, N., Akalin, T., and Yurtseven, T. (2005) Minimum apparent diffusion coefficients in the evaluation of brain tumors. *Eur. J. Radiol.* 55:393–400
- Korinth, M.C., Delonge, C., Hutter, B.O., and Gilsbach, J.M. (2002) Prognostic factors for patients with microsurgically resected brain metastases. *Onkologie* 25:420–425
- Krabbe, K., Gideon, P., Wagn, P., Hansen, U., Thomsen, C., and Madsen, F. (1997) MR diffusion imaging of human intracranial tumours. *Neuroradiology* 39:483–489
- Kremer, S., Grand, S., Berger, F., Hoffmann, D., Pasquier, B., Remy, C., Benabid, A.L., and Bas, J.F. (2003) Dynamic contrast-enhanced MRI: differentiating melanoma and renal carcinoma metastases from high-grade astrocytomas and other metastases. *Neuroradiology* 45:44–49
- Kremer, S., Grand, S., Remy, C., Pasquier, B., Benabid, A.L., Bracard, S., and Le Bas, J.F. (2004) Contribution of dynamic contrast MR imaging to the differentiation between dural metastasis and meningioma. *Neuroradiology* 46:642–648
- Law, M. (2004) MR spectroscopy of brain tumors. *Top. Magn. Reson. Imaging* 15:291–313
- Law, M., Cha, S., Knopp, E.A., Johnson, G., Arnett, J., and Litt, A.W. (2002) High-grade gliomas and solitary metastases: differentiation by using perfusion and proton spectroscopic MR imaging. *Radiology* 222:715–721
- Li, K.C., Pandit, S.D., Guccione, S., and Bednarski, M.D. (2004) Molecular imaging applications in nanomedicine. *Biomed. Microdevices* 6: 113–116
- Lu, S., Ahn, D., Johnson, G., and Cha, S. (2003) Peritumoral diffusion tensor imaging of high-grade gliomas and metastatic brain tumors. *AJNR Am. J. Neuroradiol.* 24:937–941
- Lu, S., Ahn, D., Johnson, G., Law, M., Zagzag, D., and Grossman, R.I. (2004) Diffusion-tensor MR imaging of intracranial neoplasia and associated peritumoral edema: introduction of the tumor infiltration index. *Radiology* 232:221–228
- Luker, G.D., and Pivnicka-Worms, D. (2001) Molecular imaging in vivo with PET and SPECT. *Acad. Radiol.* 8:4–14

- Nadal Desbarats, L., Herlidou, S., de Marco, G., Gondry-Jouet, C., Le Gars, D., Deramond, H., and Idy-Peretti, I. (2003) Differential MRI diagnosis between brain abscesses and necrotic or cystic brain tumors using the apparent diffusion coefficient and normalized diffusion-weighted images. *Magn. Reson. Imaging* 21:645–650
- Nathoo, N., Chahlavi, A., Barnett, G.H., and Toms, S.A. (2005) Pathobiology of brain metastases. *J. Clin. Pathol.* 58:237–342
- Nguyen, L.N., Maor, M.H., and Oswald, M.J. (1998) Brain metastases as the only manifestation of an undetected primary tumor. *Cancer* 83: 2181–2184
- Nussbaum, E.S., Djalilian, H.R., Cho, K.H., and Hall, W.A. (1996) Brain metastases. Histology, multiplicity, surgery, and survival. *Cancer* 78: 1781–1788
- Oh, J., Cha, S., Aiken, A.H., Han, E.T., Crane, J.C., Stainsby, J.A., Wright, G.A., Dillon, W.P., and Nelson, S.J. (2005) Quantitative apparent diffusion coefficients and T2 relaxation times in characterizing contrast enhancing brain tumors and regions of peritumoral edema. *J. Magn. Reson. Imaging* 21:701–708
- Paget, S. (1889) The distribution of secondary growths in cancer of the breast. *Lancet* i: 571–573
- Pierpaoli, C., Righini, A., Linfante, I., Tao-Cheng, J.H., Alger, J.R., and Di Chiro, G. (1993) Histopathologic correlates of abnormal water diffusion in cerebral ischemia: diffusion-weighted MR imaging and light and electron microscopic study. *Radiology* 189:439–448
- Posner, J.B., and Chernik, N.L. (1978) Intracranial metastases from systemic cancer. *Adv. Neurol.* 19:579–592
- Rosen, B.R., Belliveau, J.W., Vevea, J.M., and Brady, T.J. (1990) Perfusion imaging with NMR contrast agents. *Magn. Reson. Med.* 14:249–265
- Schouten, L.J., Rutten, J., Huvencers, H.A., and Twijnstra, A. (2002) Incidence of brain metastases in a cohort of patients with carcinoma of the breast, colon, kidney, and lung and melanoma. *Cancer* 94:2698–2705
- Smith, J.S., Cha, S., Mayo, M.C., McDermott, M.W., Parsa, A.T., Chang, S.M., Dillon, W.P., and Berger, M.S. (2005) Serial diffusion-weighted magnetic resonance imaging in cases of glioma: distinguishing tumor recurrence from postresection injury. *J. Neurosurg.* 103:428–438
- Tang, Y.M., Ngai, S., and Stuckey, S. (2006) The solitary enhancing cerebral lesion: can FLAIR aid the differentiation between glioma and metastasis? *AJNR Am. J. Neuroradiol.* 27:609–611
- Terada, H., and Kamata, N. (2003) Contribution of the combination of (201)Tl SPECT and (99m)TcO(4)(-) SPECT to the differential diagnosis of brain tumors and tumor-like lesions. A preliminary report. *J. Neuroradiol.* 30:91–94
- Thng, C.H., Tay, K.H., Chan, L.L., Lim, E.H., Khoo, B.K., Huin, E.L., and Tan, K.P. (1999) Magnetic resonance imaging of brain metastases: magnetisation transfer or triple dose gadolinium? *Ann. Acad. Med. Singapore* 28:529–533
- Weiss, L. (1992) Comments on hematogenous metastatic patterns in humans as revealed by autopsy. *Clin. Exp.* 10:191–199

*This page intentionally left blank*

# 25

## Brain Tumor Resection: Intra-operative Ultrasound Imaging

Christof Renner

### INTRODUCTION

Surgery of brain tumors is still a challenge, because undoubtedly the extent of tumor resection correlates strongly with the survival time or progressive free interval, respectively. Because neurosurgeons view alone can make mistake (Albert et al. 1994), the success of a brain tumor operation depends on additional supporting tools for detection of suspected masses to optimize the extent of tumor removal. Therefore, besides the pre-operative diagnostic imaging, intra-operative imaging tools are of special importance.

During the last several decades enormous advantages in micro-neurosurgical techniques and the development of navigational systems have improved the intra-operative safety, but the extent of tumor removal still requires improvement. The main problem is the lack of a suitable real-time imaging system taking into consideration the anatomical brain and tumor deformations, which is also known as tissue shifting. The tissue shifting arises at the beginning of the operation after craniotomy with bone flap removal and dura opening secondary to the effects of

gravity, loss of cerebrospinal fluid, and elevated intra-parenchymal pressure (e.g., perifocal edema). During the progress of operation the shifting itself is changed because of increasing loss of cerebrospinal fluid and increasing tumor removal leading to a displacement of parenchyma into the defect of craniotomy.

Since the first ultrasound experiments in the 1950s (French et al. 1951) the intra-operative ultrasound (IOUS) evolved to a serious alternative to other intra-operative imaging systems such as frame-based navigation or intra-operative magnetic resonance imaging. With increasing technical improvement during the last two decades IOUS became a reliable real-time imaging system, which is able to visualize tumor and normal tissue shifting during the operation with an acceptable accuracy. Simultaneously, real-time orientation to anatomical adjacent landmarks is possible, allowing the identification of high risk regions and reducing procedure related morbidity. Furthermore, the handling is easy, safe, and repeated applications are possible at any time. Compared with frame-based navigation and intra-operative MRI, the ultrasound machine is of low cost.

Thus, many reports have been published about the application of IOUS in surgical neurology during the last 20 years.

## GENERAL PRINCIPLES

To take the best advantage of the IOUS the neurosurgeon should be aware of its technical abilities and the principles of diagnostic procedure. With this knowledge it is possible to optimize the quality and interpretation of ultrasound imaging to obtain comprehensive information regarding the suspected tissue, its extension, and relationship to surrounding structures.

### Transducers (Arrays)

The ultrasound imaging is based on the fact that any vibrating source placed in contact with a medium produces a sound wave of

vibrating particles. In modern ultrasound machines the waves are originated from a vibrating synthetic piezoelectric crystal. This crystal generates a focused ultrasonic pulse that goes through the human brain tissue in a well defined direction. A part of this pulse is absorbed (known as attenuation) and a part is transmitted through the tissue according to the tissue's unique acoustic properties. When the pulse reaches a point where tissues of different acoustic properties interface, a portion of the transmitted pulse is reflected. The reflected signal returns to the transducer and mechanically distorts the same piezoelectric crystal inducing a small voltage in the crystal. The amplitude and the time of flight of the reflected signal is then recorded and analyzed by a computer. Depending on the arrangement of these crystals, three different transducer types (arrays) are distinguished (Figure 25.1). Because the most linear arrays require a large surface contact, they are

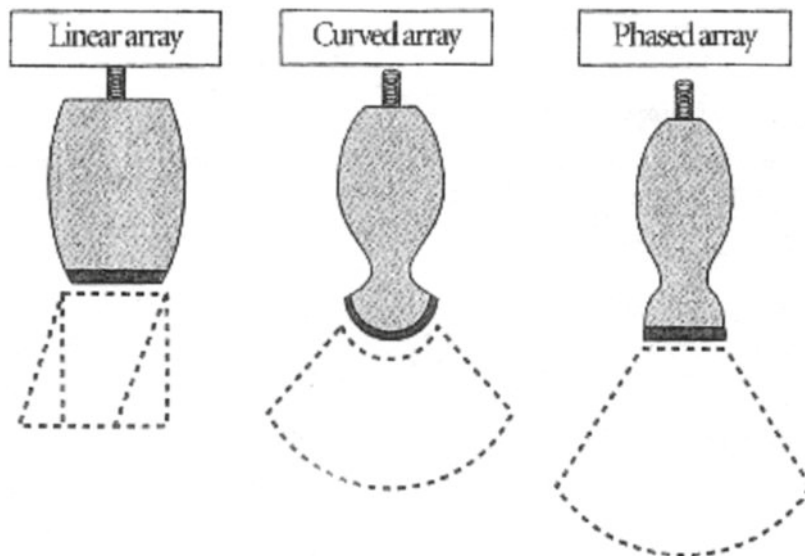


FIGURE 25.1. Different types of sound transducers; Linear array transducer: the piezoelectric crystals are arranged at full length and the surface contact is plane; Curved array transducer: the surface contact is convex with a radiate image sector, artefacts can happen because of an incomplete contact; Phased array transducer: the surface contact is plane and artefacts by incomplete contact are not very likely, the image sector is radial because of serial impulses to the crystals

not suitable for neurosurgical procedures as the craniotomies are too small for these. Therefore, curved or phased arrays are usual in neurosurgery and a frequency of 5–8 MHz has proved to be suitable.

### Modes of Imaging

The reflected echo signals can be processed into several different formats for display. One can distinguish between the following modes

#### *B-Mode (Brightness-Mode)*

By insonating adjacent segments of tissue with multiple crystals located within the transducer, a two-dimensional grey scale display of the insonated tissue is obtained.

#### *C-Mode (Color-Mode)*

Combination of real-time B-Mode grey-scale with color encoding Doppler flow information representing blood flow and blood vessels respectively; the color assigned to the frequency data depends on the magnitude and direction of flow, with hue (red vs. blue) depicting the direction of flow; the hue's saturation denotes the magnitude of the frequency shift and the brightness (luminosity) demonstrates the variance in mean flow (e.g., turbulence).

#### *D-Mode (Doppler-Mode)*

Velocity of blood flow is determined by controlling the angle of insonation, the insonating frequency, and the known speed of sound through the insonated tissue.

#### *Power-Mode*

The power spectrum of the Doppler signal; the reflected signal is separated in its numerous single-frequency components and the relative contribution of each single-frequency component to the origi-

nal signal is then visually displayed. The Power-Mode allows distinguishing various flow characteristics, which exist in normal and pathological vessels. Thus it is more sensitive than C-Mode.

#### *Color-Duplex-Mode*

Simultaneous combination of B-, C- and D-Modes.

### Image-Characteristics

The demarcation of a lesion depends on its contrast to the surrounding structures.

The contrast is caused by the different echoic pattern of the lesion compared to the surrounding tissue. The echoic pattern is a scale of the brightness and determined by the sound reflections. Following echoic patterns are distinguishable:

- Anechoic: lacking reflections of the interesting tissue lead to a black area (e.g., ventricles, cystic lesions without containing corpuscles)
- Poor (hypo-)echoic: few reflections lead to slightly grey findings such as the sub-cortical tissue
- Moderate or strong echoic: frequent reflections lead to stronger brightness of the lesion (e.g., most brain tumors in different grades or fresh blood)
- Hyperechoic: the interesting tissue shows a very strong brightness because of nearly complete reflection seen in the case of calcifications (e.g., in oligodendrogliomas) or in the case of bone

Characteristic echoic patterns of typical tumors are shown in Figure 25.2a–c.

### Resolution

Generally the resolution of ultrasound imaging depends on three factors. Selection of image field, frequency, and focussing

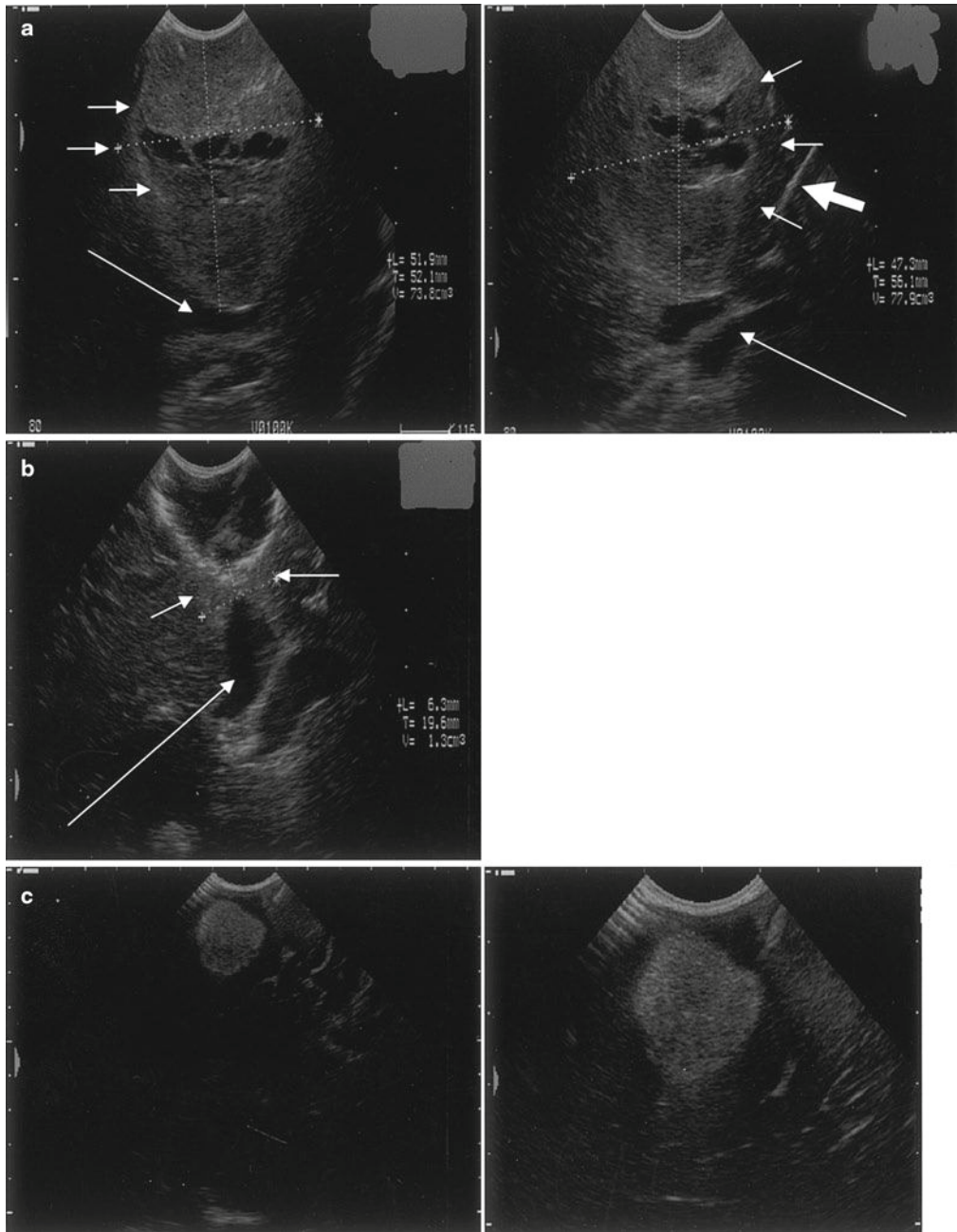


FIGURE 25.2. (a) A right frontal located glioblastoma multiforme in two different planes of insonation; the small *arrows* show the relatively sharp defined margine zone of this tumor. Compared with the surrounding tissue the echogenicity of this tumor ranges from moderate hyperechoic to anechoic in the center as a result of central cysts. Both anterior horns of lateral ventricles are compressed (*long arrows*). On the right picture the thick arrow points out the shifted interhemispheric fissure. (b) As a result of relief due to tumor removal the anterior horns get their normal extend (*long arrow*). Because of infiltration of the internal capsule and the corpus callosum a small rest of tumor was left (*small arrows*). (c) Left picture shows a typical ultrasound feature of a metastasis during the first screening with a selected large image field. Compared to the surrounding tissue the tumor has a well defined and strong elevated homogeneous echoic pattern. Picture on the right shows the same tumor with a higher resolution due to selection of a lower image field

make possible a resolution of 1 mm and below with modern ultrasound machines. The image field corresponds to the selected depth of the screened area. In strong connection with the selected image field the sound frequency is chosen. One has to note that high frequency sound has more attenuation compared with low frequency sound. Thus, subcortical lesions can be insonated at frequency of 7–8 MHz, providing a high-resolution image in this region of interest. Deeper lesions require a lower frequency transducer ( $\approx 5$  MHz) because attenuation is less for lower frequency sound. An additional increase of resolution can be obtained by focussing, meaning an eligible region of interest with best resolution.

### PRINCIPLES OF INTRA-OPERATIVE ULTRASOUND EXAMINATION

In addition to the above mentioned technical adjustments (e.g., the selection of the right transducer) some patient related principles need to be observed. First, the neurosurgeon should be aware of the correct patient positioning. The craniotomy should be the highest point avoiding the subsequent loss of fluid out of the resection cavity. During the operation it is necessary to repeatedly fill up the cavity with saline solution to have an acoustic coupling, guaranteeing a correct insonation of the regions of interest. Most sound transducers require a sterile covering. Before the transducer head is inserted into the bag, enough ultrasound jelly has to be placed on it. Because air-bubbles cause sound shadows and consequently disturbances of insonation result, air-bubbles in the jelly as well as irrigation with hydrogen peroxide solution must be avoided, at least as long as the ultrasound is being applied.

After craniotomy and before dura opening, the first B-Mode ultrasound screening should be performed. Thereby the brain is insonated over the whole length and breadth of the craniotomy, which means that the transducer is continuously moved in two planes that are perpendicular to each other (axial and coronal or coronal and sagittal). Then, the first localization of the lesion and orientation to surrounding landmarks (e.g., ventricles, vessels, bony structures or falx) are made in correspondence to the preoperative MRI. After dura opening and further tissue shifting, this procedure should be repeated, and the image is optimized by the adaptation of different adjustments mentioned above. In the next step, the most gentle and safest approach to the tumor is chosen, which means a trans-sulcal, trans-fissural, or trans-cortical approach.

During the tumor removal the ultrasound is used repeatedly to define the extent of resection. For this it is necessary to fill up the resection cavity with saline solution to have an acoustic coupling, and it must be free of blood or air-bubbles to avoid sound disturbances. Furthermore, the margins of the resection cavity should be insonated by several different planes to detect tumor residues. The resection is completed when no more tumor is detectable under the microscopic and ultrasound examination, unless the infiltration of functional brain areas prevent further resection.

### EFFICACY OF INTRA-OPERATIVE ULTRASOUND

Although the literature of the past 20 years abounds with novel uses of intra-operative ultrasonography, formal studies to determine the efficacy of this technology are rare.



A possible reason is that efficacy and benefit of IOUS must be seen in context with several aspects of brain tumor surgery. Two main aspects are emphasized. First, because of its real-time imaging, the tissue shifting can be compensated, allowing a comprehensive intra-operative navigation with reference to both the tumor itself and adjacent structures (e.g., vessels). Undoubtedly, this fact increases the intra-operative safety making possible a more gentle preparation. Second, in dependence of accurate tumor visualization by IOUS, an ultrasound guided tumor resection is possible. Indeed this question is controversial (van Velthoven 2003; Reinacher and van Velthoven 2003; Woydt et al. 1996) and studies about it are rare (Chacko et al. 2003; Hammoud et al. 1996; LeRoux et al. 1994). In accordance with our own experience (Renner et al. 2005), the accurate visualization or tumor echogenicity respectively is correlated to tumor type and size.

As a rule, metastases are well encapsulated tissue formations that generate a homogeneous clear elevated echoic pattern with good differentiation to surrounding structures. An image guided complete tumor resection here is almost possible (Figure 25.3a–d). In contrast to the more uniform appearance of metastases, high-grade gliomas often generate inhomogeneous echoic pictures corresponding to their inhomogeneous histomorphologic patterns. The ultrasonographic picture can vary between anechoic and hyperechoic areas depending on the presence of intratumorous cysts, bleeding, and portions of different malignancy. In particular, this makes more difficult the differentiation between the tumor margin zone, the tumor infiltrating zone, and the edematous normal brain. In some cases this poorly defined margin

zone is the reason for radiographic tumor residues (Figures 25.4a–d and 25.5a–d). Reliable sonographic criteria for an exact definition of margin or infiltrating zones do not yet exist (van Velthoven 2003). In the case of recurrent and preradiated gliomas the difficulties to identify margin zones are reinforced. These tumors can show portions of an isoechoic pattern, so that in general it can be difficult to differentiate the whole tumor masses. Low-grade gliomas imply a similar problem. These tumors show a minor and almost more homogeneous echogenicity than high-grade gliomas. Especially, the differentiation of these tumors from surrounding brain edema represents a challenge with regard to complete tumor resection. Even MRI-slices imply an inaccuracy regarding that problem.

Another term for an accurate tumor description by IOUS is the volumetric determination of tumor. The volumetric accuracy depends on two factors. In addition to the tumor type as expression of its differentiation from surrounding tissue, the tumor diameter represents a crucial factor. With increasing diameter the volumetric accuracy decreases. The main reason for that is the technical disability of ultrasound machines for exact determination of the 3D tumor volume. Until now the calculation is based on ellipsoid or cubic geometric formulas, which insufficiently represent the most 3D tumor figures. Metastases are an exception, where even large tumors allow a high accuracy in volumetric determination. An explanation for it lies on the one hand in the mostly well ultrasonographic differentiation of these tumors and on the other hand, most metastases are well encapsulated objects, which come close to the underlying geometric figures on which the calculation is based.

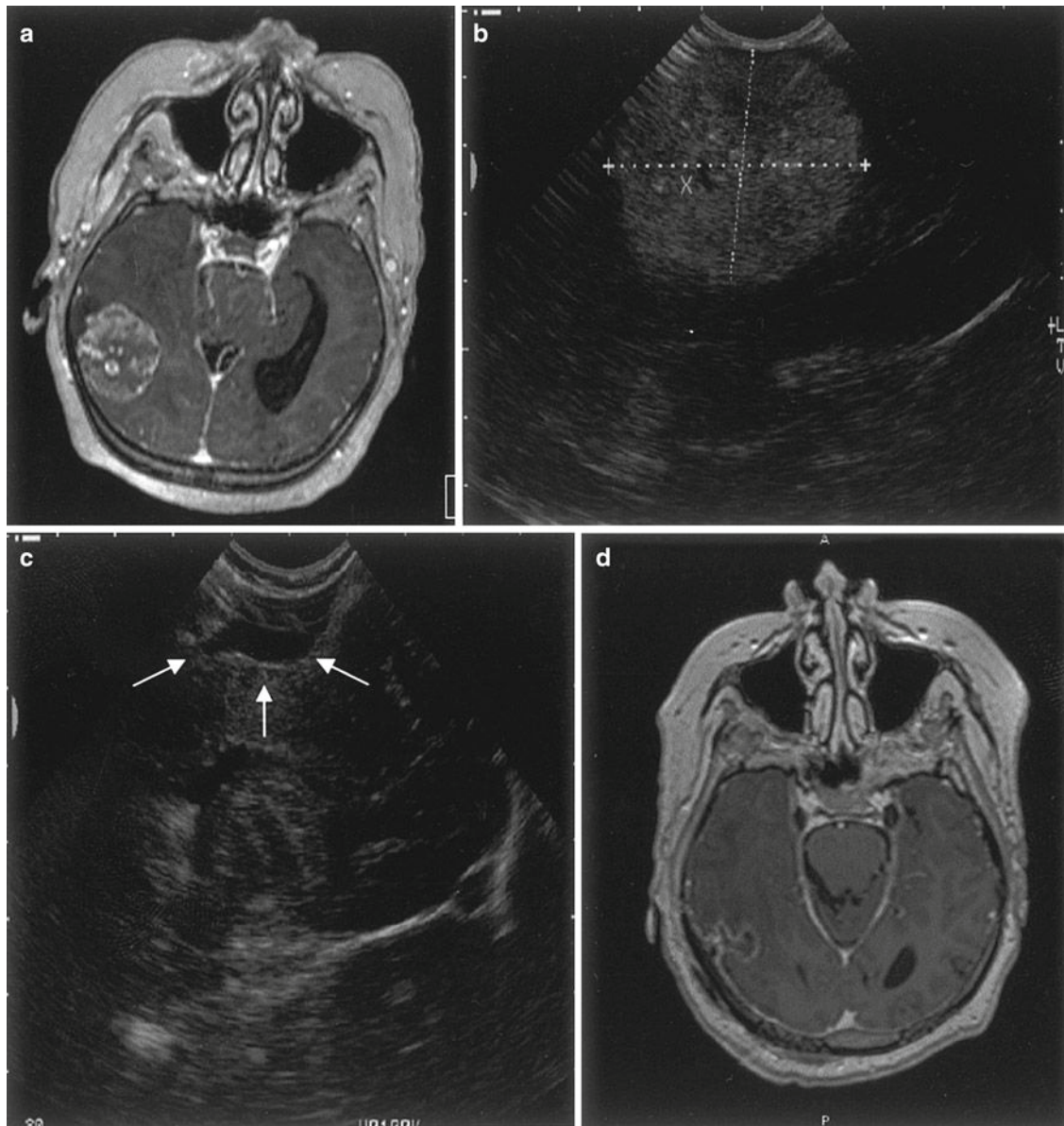


FIGURE 25.3. The sequence of images represents the good result of intra-operative ultrasound guided surgery in case of a right temporal metastasis. **(a)** Preoperative MRI with contrast medium; **(b)** intra-operative ultrasound before resection with the well defined tumor; **(c)** resection control after complete tumor removal, the arrows point out the rim of the resection cavity; **(d)** postoperative MRI with contrast medium showing no residual tumor masses

Compared with another intra-operative imaging technique such as frame-based neuronavigation, a higher extent of tumor resection is obtained with IOUS (Renner et al. 2005; Wirtz et al. 2000). The reason

for it seems to be disregarding the tissue shifting in neuronavigation as a real-time effect. The consequence is that the surgery is reduced to subjective criteria determined by the neurosurgeon. Using the

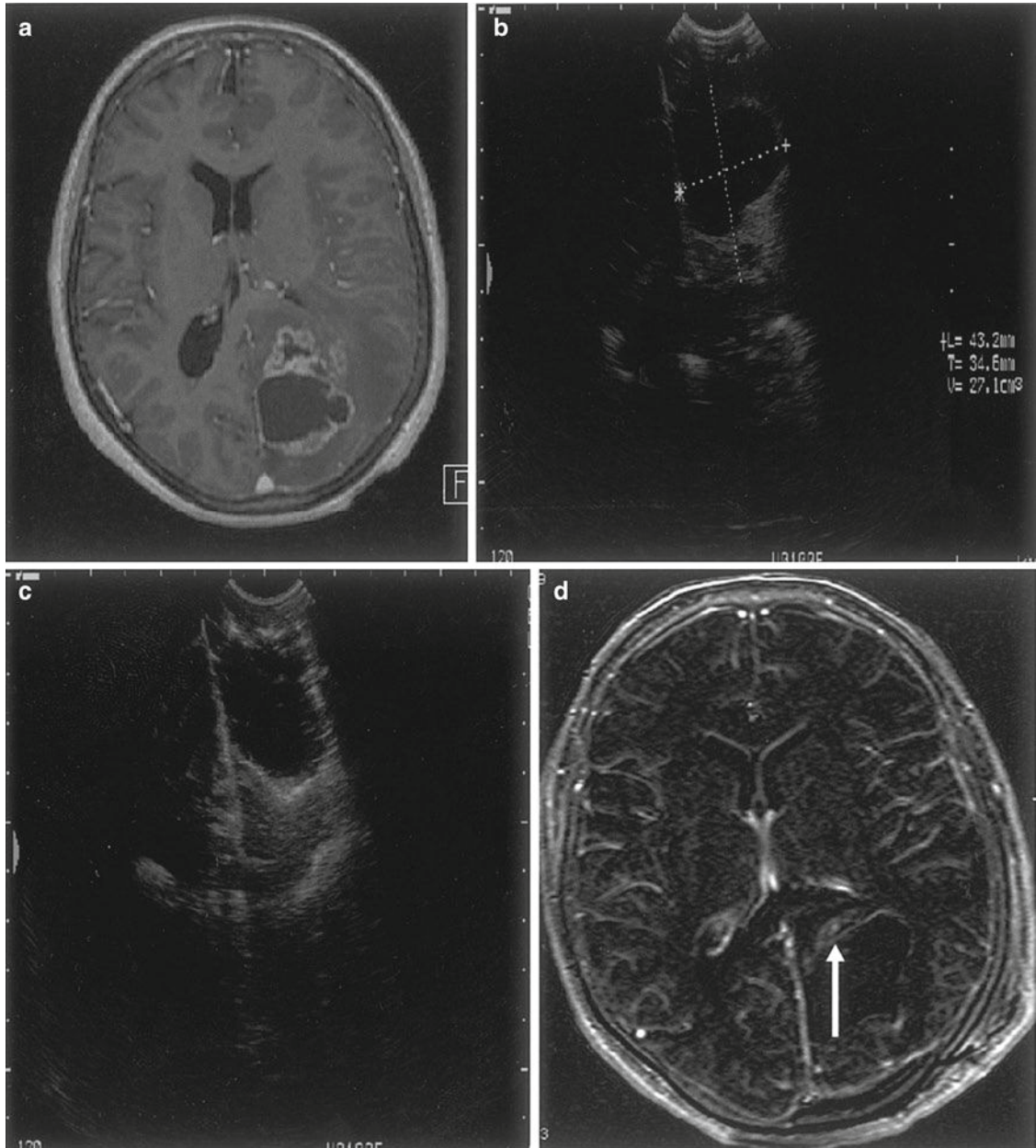


FIGURE 25.4. This sequence of images represents the operative result with a glioblastoma multiforme in the left occipital lobe. Corresponding to the inhomogeneous histological pattern, seen in the preoperative MRI (a), the echogenicity ranges from anechoic (tumor cyst) to moderate hyperechoic (necrosis, solid tumor) and in particular the tumor margin zone is not well defined (b). The resection control by ultrasound (c) shows no definitive tumor rest. In contrast to (c) the postoperative MRI (subtraction of T1-sequences with and without contrast medium = (d)) demonstrates a small tumor suspected area depicted by the white arrow

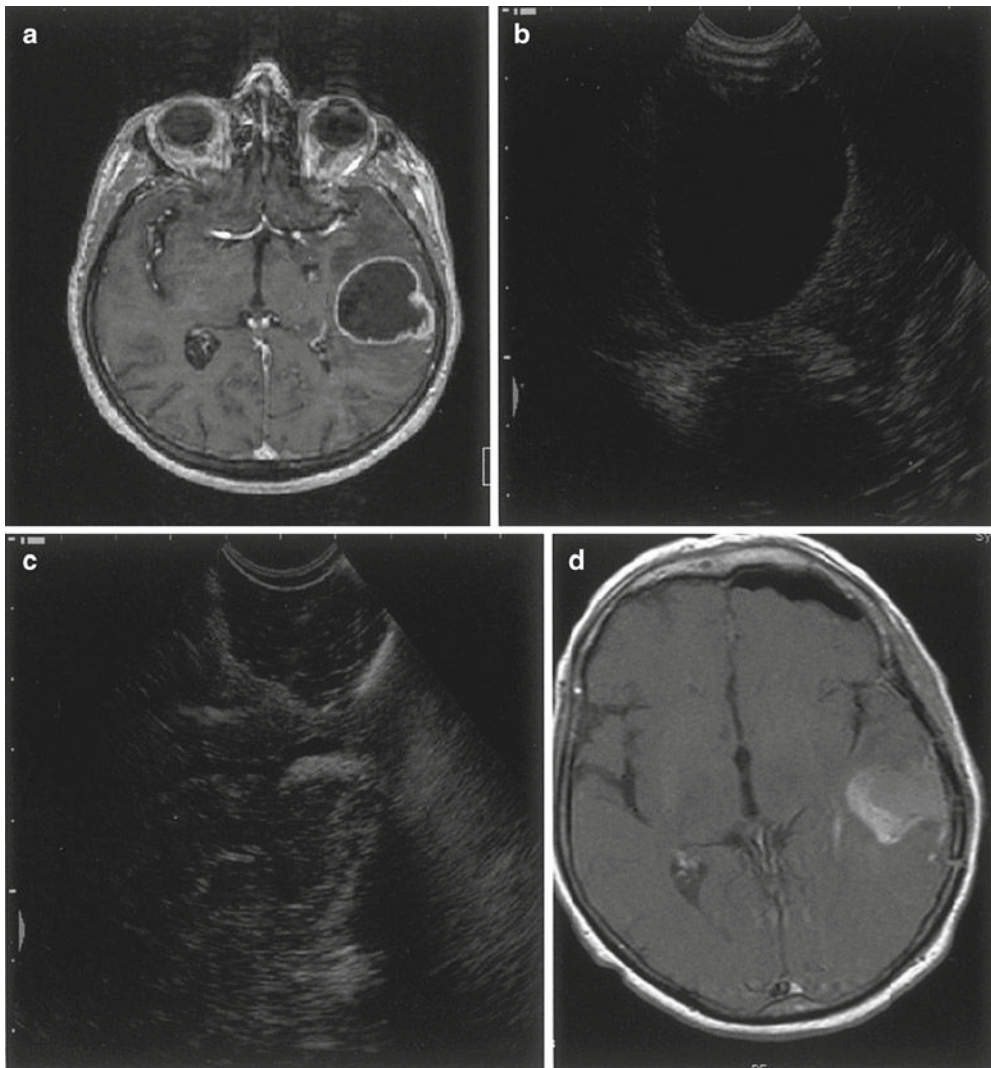


FIGURE 25.5. Pictures demonstrate the radiographic complete resection of a cystic left temporal glioblastoma multiforme. Preoperative MRI (a), intra-operative ultrasound (b) with a sonographic relatively sharp defined cystic wall, sonographic resection control (c) and postoperative MRI with contrast medium without tumor suspected masses (d)

IOUS, the tissue shifting is compensated and areas with good tumor echogenicity can be identified region by region, leading to a greater extent of resection. In the case of intra-operative MRI the IOUS is of inferior value, but even in this case some

restrictions must be imposed. The success of intra-operative MRI depends on the used field-strength. Most of the groups are reporting about their experiences with low-field systems (Schulder et al. 2001; Schneider et al. 2001), and the achieved

extent of resection is comparable with that of IOUS in some cases. Not comparable are the results with intra-operative high-field strength MRI. Only very few groups (Nimsky et al. 2004) have experience with it. They could demonstrate a radiological complete resection in all cases where a complete tumor removal was intended. However, this should be the result at least theoretically, if an intra-operative system is used, which represents the highest accuracy in brain tumor description.

## CONCLUSION

Intra-operative ultrasound is an imaging system that is easy to handle, repeatedly applicable and inexpensive in comparison to other intra-operative imaging systems in neurosurgery. Because of its real-time imaging the ultrasonography is able to compensate the tissue shifting (which is inherent in neurosurgical operations), contributing to a safe and gentle dissection. Related to visualization of tumor masses the reliability of IOUS depends on tumor type and size. It is more beneficial to use IOUS for the resection of metastases and some high-grade gliomas. Compared with other intra-operative imaging methods the percentage of intended complete tumor removal by IOUS lies between neuronavigation and intra-operative MRI assisted surgery. Thus, IOUS is a valuable adjunct in brain tumor surgery. New techniques such as 3D-ultrasound or the use of suitable contrast-enhancing agents are currently objects of experimental and first clinical (Lindner et al. 2005) studies, but not yet in routinely use. Contrast-enhancing agents are discussed in detail in these volumes.

## REFERENCES

- Albert, F.K., Forsting, M., Sartor, K., Adams, H.P., and Kunze, S. (1994) Early postoperative magnetic resonance imaging after resection of malignant glioma: objective evaluation of residual tumor and its influence on regrowth and prognosis. *Neurosurgery* 34:45–61
- Chacko, A.G., Kumar, N.K.S., Chacko, G., Athyal, R., and Rajshekhar, V. (2003) Intraoperative ultrasound in determining the extent of resection of parenchymal brain tumors – a comparative study with computed tomography and histopathology. *Acta Neurochir.* 145:743–748
- French, L.A., Wild, J.J., and Neal, D. (1951) The experimental application of ultrasonics to the localization of brain tumors. *J. Neurosurg.* 8:198–203
- Hammoud, M.A., Ligon, B.L., elSouki, R., Shi, W.M., Schomer, D.R., and Sawaya, R. (1996) Use of intraoperative ultrasound for localizing tumors and determining the extent of resection: a comparative study with magnetic resonance imaging. *J. Neurosurg.* 84:737–741
- LeRoux, P.D., Winter, T.C., and Berger, M.S. (1994) A comparison between preoperative magnetic resonance and intraoperative ultrasound tumor volumes and margins. *J. Clin. Ultrasound* 22:29–36
- Lindner, D., Trantakis, C., Arnold, S., Schmidtgen, A., Schneider, J., and Meixensberger, J. (2005) Neuronavigation based on intraoperative 3D-ultrasound during tumor resection. Computer assisted radiology and surgery proceedings of the 19<sup>th</sup> international congress and exhibition. Elsevier B.V., Berlin, pp. 815–820
- Nimsky, C., Gansland, O., von Keller, B., and Fahlbusch, R. (2004) Intraoperative high-field-strength MR Imaging: implementation and experience in 200 patients. *Radiology* 233:67–78
- Reinacher, P.C., and van Velthoven, V. (2003). Intraoperative ultrasound imaging: practical applicability as real-time navigation system. *Acta Neurochir. Suppl.* 85:89–93
- Renner, C., Lindner, D., Schneider, J.P., and Meixensberger, J. (2005) Evaluation of intraoperative ultrasound in brain tumor resection: a prospective study. *Neurol. Res.* 27:351–357
- Schneider, J.P., Schultz, T., Schmidt, F., and Kahn, T. (2001) Gross total surgery of supratentorial

- low-grade gliomas under intraoperative MR guidance. *Am. J. Neuroradiol.* 22:89–98
- Schulder, M., Liang, D., and Carmel, P. (2001) Cranial surgery navigation aided by a compact intraoperative magnetic resonance imager. *J. Neurosurg.* 94:936–945
- van Velthoven, V. (2003) Intraoperative ultrasound imaging: comparison of pathomorphological findings in US versus CT, MRI and intraoperative findings. *Acta Neurochir. Suppl.* 85:95–99
- Wirtz, C.R., Albert, F.K., Schwaderer, C.H., and Kunze, S. (2000) The benefit of neuronavigation for neurosurgery analyzed by its impact on glioblastoma surgery. *Neurol. Res.* 22:354–360
- Woydt, M., Krone, A., Becker, G., Schmidt, K., Roggendorf, W., and Roosen, K. (1996) Correlation of intraoperative ultrasound with histopathological findings after tumour resection in supratentorial gliomas. *Acta Neurochir. (Wien)* 138:1391–1398

*This page intentionally left blank*

# 26

## Primary Central Nervous System Lymphomas: Salvage Treatment

Michele Reni, Elena Mazza, and Andrés J.M. Ferreri

### INTRODUCTION

Primary central nervous system lymphoma (PCNSL) is a rare subtype of extranodal non-Hodgkin lymphoma (NHL) that arises from the brain parenchyma, eyes, cerebrospinal fluid, meninges or spinal cord without evidence of systemic spread. It has had an increase during last 3 decades, accounting for ~3% of all CNS malignancies in the United States from 1998 to 2002.

Due to the growing interest over the past 2 decades in PCNSL, more information is now available on optimal primary treatment, which has yielded a significant impact on survival.

The most important finding in PCNSL treatment has been that high-dose methotrexate (MTX  $\geq 1\text{g/m}^2$ ) – based chemotherapy regimens improve survival compared to historical controls treated with RT alone (Ferreri et al. 2003). Hence, there is general consensus that high-dose methotrexate is the cornerstone of the initial treatment of PCNSL (Reni et al. 1997; Ferreri et al. 2000, 2002; Reni and Ferreri 2004). The attempts to improve survival with combinations of HD-MTX and other chemotherapeutic agents have not con-

vincingly been shown to be superior to HD-MTX alone (Ferreri et al. 2002, 2003). While two retrospective analyses have suggested that the addition of high-dose cytarabine to HD-MTX might be an independent positive prognostic factor for improved survival (Ferreri et al. 2002; Reni et al. 2001), these observations seem to be confirmed in a phase II randomized trial, in which the addition of araC to MTX resulted in significantly better outcome and acceptable toxicity (Ferreri et al. 2009).

However, for most patients, this remains an incurable malignancy. Despite the high complete remission rate achieved with first-line therapy, 10–35% of PCNSL are treatment refractory and relapse after first-line therapy occur in ~35–60% of cases. Brain recurrence is the predominant cause of failure, as it is responsible for progressive neurological deficits and poor quality of life. Prognosis for both recurrent and progressive PCNSL is poor, with a survival after progression of 2–5 months without further treatment (Jahnke et al. 2006; Reni et al. 1999). Relapse of extraneural NHL had been considered fatal, until the advent of high-dose chemotherapy followed by



autologous or allogenic bone marrow or peripheral blood stem cell transplantation. However, only a subset of relapsed patients can be selected for such life-threatening treatment. Most patients undergo standard salvage chemotherapy, achieving an intriguing overall response rate of 45–85%, with 20–45% of complete responses, a median survival of 8–14 months and a 3-year survival rate of 20–30% (Rodriguez et al. 1995; Velasquez et al. 1994). Unlike extra-neural NHL, the impact of salvage therapy on survival and quality of life has rarely been addressed. Given the chemosensitivity and radiosensitivity of this disease, second-line treatment has also been considered and administered in recurrent and refractory PCNSL by numerous authors. In fact, Reni et al. (1999) and Jahnke et al. (2006) demonstrated that salvage therapy consistently prolonged survival in PCNSL from 1 to 2 months for untreated patients to 8–14 months. Due to the rarity of PCNSL, which has hampered prospective trials, there is no standardized approach for refractory or relapsed PCNSL.

In this chapter the major methodological caveats related to the design and conduction of studies focused on salvage therapies and the information available on prognostic factors and therapeutic outcome are reviewed and analyzed in order to provide therapeutic recommendations for the management of failed PCNSL patients.

## DIAGNOSTIC WORK UP AT RELAPSE

In order to choose the most adequate treatment plan for patients at relapse, a complete restaging of the extent of CNS, leptomeningeal and systemic disease is needed.

Systemic failure from PCNSL occurs in 7–15% of cases (Jahnke et al. 2006). Jahnke et al. (2006) observed that patients with systemic failure have a significantly longer survival (13.5 versus 4.5 months;  $p = 0.035$ ) than patients with isolated CNS failure, and should not be included in the series which assess the treatment outcome in patients affected by PCNSL recurrence. Therefore, restaging procedures must include: evaluation of the CSF, Gadolinium-enhanced MRI of the brain; ophthalmologic examination, computed tomography (CT) of the chest, abdomen, and pelvis and bone marrow biopsy to properly assess disease extension and to rule out the presence of extraneural dissemination. Gadolinium-enhanced MRI of the spine is not a routine procedure, but should be done if spinal cord or leptomeningeal spread are suspected.

## PROGNOSTIC FACTORS

In a series investigating the upfront management of PCNSL, the differences in outcome observed among various treatment options were attributed to an inhomogeneous distribution of prognostic indicators rather than the real efficacy of therapeutic strategies (Ferreri et al. 2003). The combination of two to five independent factors (including age, PS, LDH serum level, CSF protein concentration, involvement of deep structures of the brain and extent of disease) resulted in the formulation of different prognostic scores significantly associated with survival of PCNSL at the time of diagnosis (Ferreri et al. 2003; Abrey et al. 2006; Bessell et al. 2004). The International Extranodal Lymphoma Study Group scoring system (IELGS) revealed a 2-year overall survival (OS) of 85%, 57%,

and 24%, respectively, for patients who had zero to one, two to three, and four to five adverse factors. Limited and incomplete data are available for PCNSL at the time of failure. Patients with time to failure longer than 12 months had better survival than those with early relapse (10 versus 4 months;  $p = 0.005$ ; Reni et al. 1999). Similarly, patients with good performance status survived significantly longer than those with poor performance status ( $p = 0.004$ , Jahnke et al. 2006)

Finally, the type of failure may influence the outcome since patients with refractory disease had a significantly shorter median survival when compared to those who had recurrent disease (3 versus 5 months;  $p = 0.002$  in univariate analysis; Reni et al. 1999). However, this result could be biased due to the prevalence of untreated patients in the group with progressive disease (46 out of 53), while 52 out of 120 relapsed patients were retreated. Alternatively, multivariate analysis did not show any difference in relative risk between recurrent and progressive disease. Thus, the independent prognostic value of type of relapse remains uncertain and warrants further analysis. Unlike PCNSL at first diagnosis, age at time of failure does not independently predict the outcome and other parameters were unassessed. These findings cannot be considered conclusive and further research to better clarify this issue appears necessary.

## METHODOLOGICAL ISSUES

The prospective evaluation of novel agents against PCNSL is particularly useful, considering the limited results achieved with current first-line therapy. Salvage therapy, apart from improving survival and quality

of life, is also useful for testing new agents in PCNSL. The addition of other cytostatics to HD-MTX has been, until now, empirically based on the most extensively used agents in extracerebral NHL lymphomas, and single-agent prospective evaluation is very limited. Most cytostatics that did not cross the blood-brain barrier (BBB), such as alkylators and anthracyclines, produced disappointing results. In contrast, some drugs that permeate the barrier, like HD cytarabine, thiotepa, procarbazine, and nitrosoureas, that were used sporadically or within a number of polichemotherapy regimens (mainly in combination with HD-MTX) did not produce a clear survival benefit, as they increased morbidity and mortality. These drugs are known to produce relevant neurotoxicity, in elderly patients who represent about half of the PCNSL population, or when associated with radiotherapy. Therefore, prospective trials on relapsed or refractory PCNSL patients constitute the main strategy to carefully evaluate the therapeutic activity and toxicity of novel drugs. These trials will identify agents with limited neurotoxicity that are safe in elderly patients and able to cross the integral BBB, which could be associated with HD-MTX, or used as salvage therapy. Thus, these trials are of crucial relevance because they contribute a more complete definition of the optimal treatment schedule for both the first- and the second-line therapy.

To date, there are few studies reporting results of salvage therapy, while there is an increasing number of trials on new drugs in first-line treatment with high failure rates, ranging between 40% and 70%. Explanations can be ascribed to the rarity of the disease and to the severe impairment of performance status and neurological

deterioration due to the aggressiveness of the disease that makes it difficult to enroll patients in prospective trials. Recent trials of recurrent PCNSL treated with single-agent temozolomide (Reni et al. 2004, 2007) or topotecan (Fischer et al 2006; Hottinger et al. 2007) showed the feasibility of prospective assessment of drug activity in this rare disease and provided relevant information to improve PCNSL therapeutic management. In addition, other prospective experiences are currently ongoing (Altman et al. 2008; Kiewe et al. 2006; Iwamoto et al. 2007) and will hopefully contribute further reliable data when completed. On the other hand, most of the currently available information on salvage treatment of PCNSL is obtained from small retrospective series of patients who sometimes were included in the analysis in spite of heterogeneous treatment in terms of drugs, dose, and schedule, or inadequate restaging at recurrence, or known concurrent or prior systemic disease. The presence of systemic failure has prognostic relevance (Jahnke et al. 2006). Furthermore, primary and secondary CNS lymphomas have different clinical behavior and prognosis. Therefore, both patients with systemic failure from prior PCNSL and those with CNS failure from prior systemic NHL should be excluded from trials on salvage treatment in order to avoid unreliable conclusions (Ferreri et al. 1996).

Comparison of results across series is problematic due to dissimilar prognostic profiles of included patients. As reported above, limited information is available on which prognostic factors are relevant for PCNSL at time of failure. Apparent differences in terms of outcome across series, may be related to selection bias in terms of patients characteristics such as age, performance status, and other unknown variables rather than

to treatment itself. In the analysis of trial results, previously administered treatment has to be taken into account as well. Disease-related variables, like type of failure (recurrent or progressive) and time to prior failure may strongly influence outcome as well. In fact, reported results were consistently better in series in which patients with chemorefractory disease constituted less than 10% of cases (Plotkin et al. 2004; Enting et al. 2004). Furthermore, prior treatment should be taken into account when interpreting salvage therapy series. The number of prior chemotherapy lines and prior radiotherapy may affect chemosensitivity of the disease and lead to under- or overestimation of drug activity. Additionally, the role of further treatments after failure of the experimental drug or combination may be relevant. This is suggested by series with a substantial difference between progression-free survival and overall survival (Fischer et al. 2006; Enting et al. 2004). A clear impact on overall survival is yielded by radiotherapy, which is among the most active therapies against PCNSL. Finally, the median follow-up of patients alive at the time of publication is often too short, which generates unreliable actuarial data. Moreover, deferred updates of promising preliminary results are rarely published. All of these methodological caveats should be considered in order to avoid unduly, premature enthusiasm regarding novel drugs and combinations in the absence of well-conducted prospective trials.

## WHOLE-BRAIN RADIOTHERAPY

Due to well-known radiosensitivity of systemic NHL, radiotherapy is among the most active and effective therapeutic tools

against PCNSL. This is confirmed by the observation that upfront irradiation after induction chemotherapy increased the rate of complete remissions from 33–58% to 69–87%. Amongst patients who did not achieve a complete response to upfront chemotherapy, were those who had a disease with partial chemo-resistance. Radiotherapy yielded a complete remission in 66% of cases and a partial response in 12% (Reni et al. 2001). In a large review of patients receiving salvage treatment, median survival was 10 months in those who received chemotherapy alone and 16.5 months ( $p = 0.03$ ) in those who received radiotherapy associated or not to chemotherapy (Reni et al. 1999). Of note, about two-thirds of the latter patients were previously irradiated. Deferring radiotherapy in case of complete response to initial chemotherapy, particularly for older patients is a matter of debate, because of concerns regarding the risk of neurotoxicity (Reni et al. 2004). Remarkable response rates of 60–79%, including 37–60% of complete responses, median survival of 10.9–19 months and 1-year OS of 49–54% were reported (Nguyen et al. 2005; Herrlinger et al. 2005; Hottinger et al. 2007). However, the possibility that the risk of neurotoxicity after salvage radiotherapy in these patients could be greater than with radiotherapy given immediately after chemotherapy should be taken into account. In fact, at the time of failure patients would be older, will have a poorer performance status and a larger tumor burden, which would require higher doses and larger volumes for the tumor bed boost. Consistently with this hypothesis, Nguyen et al. (2005) and Herrlinger et al. (2005) reported rates of 15–58% of late neurotoxicity or leukoencephalopathy with salvage radiotherapy in PCNSL

patients who relapsed after single-agent HD-MTX, whereas lower rates of 8–13% were observed by Glass et al. (1994) and O'Brien et al. (2000) if radiotherapy was delivered immediately after the primary chemotherapy. On the other hand, similar neurotoxicity rates were reported for salvage radiotherapy with respect to upfront consolidation radiotherapy after HD-MTX-base combination chemotherapy (29% versus 15–32%, Hottinger et al. 2007). Apart from the possible underestimation of the true risk for patients treated at failure due to the shorter follow-up time (Gavrilovic 2006), these figures at least suggest that the deferral of irradiation does not offer any advantage in terms of the reduction of risk of side effects, as postulated. Furthermore, 12–14% of patients were unable to receive salvage radiotherapy at time of failure and 10% died during irradiation due to rapid progressive disease (Nguyen et al. 2005; Reni et al. 2001; Pels et al. 2003). This implies that about one out of every four patients was deprived of one amongst the most effective therapies for his/her, disease while his/her potential risk of developing neurotoxicity remained unchanged or was increased.

In summary, in PCNSL patients who experience relapse after upfront chemotherapy alone, salvage radiotherapy may represent a treatment option. Due the heterogeneity of radiotherapy parameters (fraction, volume and dose) used in reported series, it is not possible to draw conclusions about optimal treatment. The use of salvage chemotherapy without radiation therapy in patients with PCNSL who relapsed after primary HD-MTX-based chemotherapy should be considered as an experimental approach because available data suggest inferior efficacy.

## CHEMOTHERAPY

There are few agents with activity in PCNSL confirmed by well-designed prospective trials. Outcome of salvage chemotherapy in a large review (Reni et al. 1999) was likely underestimated due to the inclusion, in a retreated group, of patients receiving ineffective chemotherapy regimens. In fact, most active agents used for extracerebral non-Hodgkin lymphomas which were administered at time of failure, do not penetrate the blood-brain barrier at the sufficient concentration needed to be effective against PCNSL. Furthermore, agents that do penetrate the CNS have generally not been very effective, or have caused unacceptable toxicities (Ferreri et al. 2003; Reni et al. 2004). Due to the many different types of first- and second-line treatment employed in the published series, no conclusion could be drawn concerning optimal schedule. However, a few recommendations for ordinary clinical practice may be provided.

### Single Agent Chemotherapy

Single agent temozolomide and topotecan were prospectively assessed as salvage treatment in PCNSL failure (Reni et al. 2004, 2007; Fischer et al. 2006; Voloschin et al. 2008).

A phase II trial addressed activity of temozolomide, an oral second-generation alkylating agent used in the treatment of gliomas that is able to effectively penetrate the BBB passing into the cerebrospinal fluid, in 36 immunocompetent heavily-pretreated patients with recurrent primary brain lymphomas. The patients were previously treated with high-dose MTX-containing chemotherapy and/or radiotherapy in 86%. Of note, 17% of

patients received >3 prior chemotherapy lines. Median age was 60 years, 28% of patients had ECOG PS < 2. Refractory disease was present in 22% of cases, recurrent disease in 78%, median prior PFS was 19 months. Temozolomide was administered at 150 mg/m<sup>2</sup>/day, for 5 days every 4 weeks. Grade 3–4 toxicity was mild, including 6% of patients experiencing neutropenia and 3% each thrombocytopenia and vomiting. Nine complete responses (25%) and two partial responses (6%) were observed, median PFS was 2.8 months, median OS 4.0 months and 1-year OS 31% (Reni et al. 2007).

Topotecan, a topoisomerase I inhibitor with good CSF penetration and documented efficacy in patients with relapsed systemic non-Hodgkin's lymphoma, achieved an encouraging outcome as well with acceptable toxicity in two recent prospective trials (Fischer et al. 2006; Voloschin et al. 2008).

Fischer et al. (2006) treated 27 patients with relapsed (48%) or refractory (52%) PCNSL with topotecan at 1.5 mg/m<sup>2</sup> for 5 days every 3 weeks. All patients had previously received HD-MTX-containing chemotherapy and, in about half of cases, whole brain radiotherapy. Six patients (22%) received three or more prior chemotherapy lines and median prior PFS was 6 months. Median age was 51 years and 60% of patients had ECOG PS < 2. At time of failure, two patients had systemic disease and one patient had isolated ocular disease. Grade 3–4 leukopenia was reported in 26% of cases, neutropenic infection in 11%, thrombocytopenia in 11%, pneumonia, anemia, herpes stomatitis, paralytic ileus in 4% each. A complete response was yielded in 19% of cases and a partial response in 14%. Median PFS was 2.0 months, median

survival was 8.4 months and 1-year OS was 39%.

More recently, Voloschin et al. (2008) reported a further small prospective experience on 15 patients with relapsed or refractory PCNSL, treated with topotecan at 1.5 mg/m<sup>2</sup> for 5 days every 3 weeks. Median age was 56 years. All patients had previously received HD-MTX based chemotherapy and only one patient was previously irradiated. ECOG PS, prior PFS and type of failure were not reported. Complete response rate was 20% and partial response rate was 20%. Grade 3–4 neutropenia was 30%, thrombocytopenia was 20%. Median PFS was 2 months, median survival 31 months and 1-year OS 67%.

A new agent under investigation is pemetrexed, a novel multitargeted antifolate, with a broader spectrum of activity than methotrexate, since pemetrexed inhibits at least three enzymes (thymidylate synthase, dihydrofolate reductase and glycinamide ribonucleotide formyltransferase) involved in folate metabolism and DNA synthesis and is able to cross the blood brain barrier. Preliminary data of a phase II trial on eight patients with relapsed PCNSL treated with pemetrexed at 900 mg/m<sup>2</sup>/day i.v. every 3 weeks was reported by Altman et al. (2008). Median age was 62 years. Karnofsky PS was >60, five patients had previously received one chemotherapy regimen, two patients had been treated with two and one patient with four lines of chemotherapy. Previous median time to progression, type of prior treatment and number of patients that had previously received radiotherapy were not reported. Three patients had complete remissions (3, 5, 11+ months) and one partial remission (5+ mo.); three patients are still alive (4+, 8+, 11+ months), two died because

of sepsis after seven and three doses, and three deaths were due to progressive disease after two, three and six cycles of pemetrexed.

Grade 3–4 neutropenia and grade 4 thrombocytopenia was observed in five and four patients respectively, while three patients experienced grade 3 infection. This early experience suggests promising activity of pemetrexed in PCNSL, but more mature and complete data on toxicity and activity are needed.

In summary, temozolomide and topotecan are excellent candidate agents for salvage treatment for PCNSL at failure due to favorable toxicity profile, even in heavily pretreated, elderly or poor performance status patients. Pemetrexed is a promising drug, but more consistent and mature data are expected.

#### Retreatment with Methotrexate

Re-treatment with HD-MTX has been retrospectively studied in a highly selected multicenter study of 22 patients who relapsed after initially achieving a complete response to HD-MTX monotherapy. One patient had isolated ocular failure. Median time to relapse after upfront therapy was 24.4 months and only 14% of patients had received prior irradiation. MTX dose was heterogeneous ranging from 3 to 8 g/m<sup>2</sup> and one patient received stereotactic irradiation as well. In this analysis an overall response rate of 91%, an overall survival of 26 months and a 1-year OS of 70% was reported (Plotkin et al 2004). However, these encouraging results on this highly selected group of patients are difficult to compare to those from other series due to the very strict eligibility criteria and to the lack of data

about a key prognostic factor like performance status. Moreover, the increased risk of nephrotoxicity and of neurotoxicity exclude patients with renal insufficiency or previously treated with WBI, respectively.

In summary, strictly selected patients who have previously shown response to prior HD-MTX-based chemotherapy may find benefit with a second course of MTX-based treatment.

### Combination Chemotherapy

Several different combination regimens have been administered to patients with PCNSL failure, but reported series are retrospective, heterogeneous both in terms of upfront and salvage therapy, and with limited sample size, typically including less than ten patients each. Only two retrospective series included more than ten patients (Arellano-Rodrigo et al. 2003; Tyson et al. 2003). A combination of i.v. etoposide 100 mg/m<sup>2</sup> day 1–3, ifosfamide 1,000 mg/m<sup>2</sup> day 1–5, and cytarabine 2,000 mg/m<sup>2</sup>/12 h day 1, every 4 weeks was administered to 16 patients (Arellano-Rodrigo et al. 2003) with a median age of 54 years and a ECOG PS < 2 in 37% of cases. Six patients received intrathecal methotrexate as well. Patients were not restaged at time of recurrence. All patients had received previous radiotherapy and CHOD/BVAM regimen, with cyclophosphamide, doxorubicin, vincristine, dexamethasone (CHOD)/carmustine, vincristine, cytarabine and methotrexate (BVAM), median prior PFS was 19 months, refractory disease was present in 6% of cases and recurrent disease in 94%. Grade 3–4 treatment-related toxicity was relevant with 69% of neutropenia, 50% of thrombocytopenia, sepsis or pneumonia in 31% of cases and one case of severe

encephalopathy. Complete response rate was 37%, no partial response was observed, median PFS was 4 months, median OS 6 months and 1-year OS 41%. Thirty-seven patients with a median age of 57 years and a ECOG PS < 2 in 76% of cases who had failed upfront therapy with methotrexate-based intra-arterial therapy were treated with salvage carboplatin-based intra-arterial therapy with osmotic blood-brain barrier disruption (Tyson et al. 2003). Salvage treatment was heterogeneous, including one patient receiving intra-arterial carboplatin at 400 mg/m<sup>2</sup> alone, 16 patients treated with the addition of i.v. etoposide at 400 mg/m<sup>2</sup> and 20 patients treated with further addition of cyclophosphamide at 660 mg/m<sup>2</sup> as well. Prior radiotherapy was administered to 24% of patients and prior median PFS was 6.7 months. No restaging at time of failure was performed. Grade 3–4 treatment-related toxicity consisted of 22% neutropenia, 19% thrombocytopenia, 8% anemia, seizures and sepsis, 5% deep venous thrombosis and febrile neutropenia, 3% each hip fracture, aphasia, infarct, pulmonary embolism and pulmonary edema. Complete response rate was 24%, partial response rate was 11%, median PFS was 3 months, median OS 6.8 months and 1-year OS 25%.

Herrlinger et al. (2000) reported an 86% overall response rate and overall survival >16 months after the combination of procarbazine, lomustine, and vincristine (PCV). However, this study included only seven patients and PCV was associated with a high myelotoxicity rate, especially for patients pretreated with high-dose MTX. A second series of seven patients treated with PCV at salvage was more recently reported by the same institution (Herrlinger et al. 2005) with less enthusiastic results: response rate in this case was

28% and median survival 12 months. These two reports confirm that series with limited sample size generate unreliable data.

CHOP regimen at recurrence obtained poor results (Ruhstaller et al. 2000), confirming previous observations that also showed inefficacy of this regimen as first-line therapy (O'Brien et al. 2000).

HD-cytarabine has also been administered at failure after HD-MTX. At MSKCC (Abrey et al. 1998), eight cases failed after HD-MTX and RT and were treated with HD-cytarabine, alone or in combination with other cytostatics. This resulted in a further CR in three patients and a PR in two patients with a significant improvement of median survival after relapse (16 months) with respect to four patients receiving CHOP at failure (4 months) and to six untreated patients (2 months).

## MONOCLONAL ANTIBODIES

The role of monoclonal antibodies in PCNSL is controversial because of their high molecular weight which may be an obstacle to the access into the CNS through the blood-brain barrier. High doses of rituximab, an anti-CD20 monoclonal antibody largely used in patients with different B-cell lymphoma categories, achieves a cerebrospinal fluid concentration  $\leq 1.7\%$  of serum level after intravenous infusion (Ruhstaller et al. 2000).

The impact of the combination of temozolomide and rituximab, administered as a 1-week-on 1-week-off schedule was focused on a small, retrospective and biased series of patients with relapsed (93%) or refractory (7%) PCNSL (Enting et al. 2004). Median age was 69 years and 67% of patients had ECOG PS < 2.

Median prior PFS after HD-MTX containing upfront chemotherapy was 9 months. No restaging at time of failure was performed and one patient had prior systemic disease. Heterogeneous drug dose and schedule were administered, including 33% of patients treated with intrathecal methotrexate as well. This combination was associated with a mild toxicity mainly consisting of 27% grade 3–4 thrombocytopenia and 7% grade 3–4 neutropenia. A 53% response rate, a median survival of 10.5 months and a 1-year OS of 58% was observed. The median progression-free survival obtained with this combination is similar to that reported with the conventional temozolomide monotherapy (2.2 versus 2.8 months); therefore, no apparent benefit seems to be suggested either from the addition of rituximab or from the dose intensification of temozolomide with 1-week-on 1-week-off schedule.

Ibritumomab tiuxetan is a murine anti-CD20 monoclonal antibody (ibritumomab) conjugated to a linker-chelator (tiuxetan), which allows the incorporation of radioisotopes for both imaging studies and radioimmunotherapy. Ibritumomab tiuxetan can be chelated to Yttrium-90 (90Y), a  $\beta$ -emitter of ionizing radiation, which may deliver therapeutic radiation to tumor sites selectively without significantly affecting normal brain.

Preliminary results of a phase II study with a single administration of Y-90 anti-CD20 antibody ibritumomab tiuxetan in seven patients with relapsed/resistant PCNSL were reported (Kiewe et al. 2006). Treatment included rituximab 250 mg/m<sup>2</sup> on day-7 and day 0, followed by Y-90-ibritumomab tiuxetan 15 MBq/kg i.v. Data on patients age, ECOG PS, prior PFS and radiotherapy were not reported. Four responses were observed. Grade 3/5 toxicity consisted of leucopenia



(n = 6), pneumonia (n = 2) with one fatal outcome, and thrombocytopenia (n = 6).

Another similar anecdotal experience on six patients relapsed/refractory PCNSL treated with Y-90 anti-CD20 antibody ibritumomab tiuxetan at a dose of 0.3 to 0.4 mCi/kg of <sup>90</sup>Y, after two infusions of rituximab at 250 mg/m<sup>2</sup> on day-7 and day-0, was reported (Iwamoto et al. 2007). Median age was 60 years and median Karnofsky performance status 70. Patients previously treated with radiotherapy and with more than two prior chemotherapy regimens were excluded.

Two patients had a partial response, one patient had stable disease, and three patients had progressive disease within 1 month from treatment start. Median progression-free survival time was less than 7 weeks and median survival was 14.3 weeks. Grade 4 neutropenia and thrombocytopenia was observed in 17% and 33% of cases respectively. In summary, currently available data on monoclonal antibodies associated or not with radioisotopes do not appear encouraging.

## HIGH-DOSE CHEMOTHERAPY AND AUTOLOGOUS STEM-CELL RESCUE

In order to increase the drug delivery to the CNS across the BBB, the use of intensive chemotherapy followed by hematopoietic stem-cell rescue has been introduced in PCNSL, based on its efficacy in recurrent systemic NHL. Therefore, high-dose chemotherapy supported by autologous peripheral-blood stem-cell transplantation as salvage treatment has been suggested as a main strategy to intensify chemotherapy, to increase CNS drugs bioavailability, and to overcome chemo-resistance mechanisms (Soussain et al. 2001, 2008). In a first pro-

spective pilot trial, Soussain et al. (2001) demonstrated the feasibility and reported promising results of intensive chemotherapy with busulfan, cyclophosphamide and thiotepa in 22 patients affected by relapsed or refractory brain (n = 8), intraocular (n = 11) or leptomeningeal (n = 3) lymphoma. Patients had a median age of 52 years (27–64), while no data on PS were available. This pilot study achieved complete response rate of 72%, 1-year overall survival of 37.5% after a follow-up of 41 months. Nevertheless, these encouraging therapeutic results were associated with relevant morbidity, since all the patients experienced grade 4 neutropenia and thrombocytopenia, 86% of cases also had infectious complications, 32% neurotoxicity and mortality rate was 36%. Moreover, these promising results might be due to the less aggressive behavior shown by intraocular lymphoma, present in 50% of patients. Interestingly, outcome was better in patients with relapse limited to the eyes with respect to patients with a more common brain intraparenchymal relapse who conversely had a very short survival. Any attempt to estimate the efficacy of this approach in patients with isolated refractory or recurrent intraocular lymphoma is troublesome considering that this is a very uncommon condition, whose natural behavior remains to be defined. More recently, the same group of investigators published the final results of a prospective phase II multicenter study (Soussain et al. 2008) with the same strategy in 43 patients, mostly with brain intraparenchymal failure: 36 had brain parenchymal involvement, associated with IOL in four cases and with CSF infiltration in three cases; five patients had isolated IOL; one patient had isolated CSF infiltration and

one patient had concomitant IOL and CSF infiltration. After a median follow up of 36 months a complete response rate of 56% was obtained, with median survival of 18 months, 2-years overall and progression free survival of 45% and 43% respectively. Treatment-related mortality was 14%, due to septic shock in two cases and mesenteric necrosis in one, during salvage treatment with high-dose cytarabine and etoposide. While these results may appear promising, they should be compared to those obtained in a similarly selected population treated with conventional chemotherapy or radiotherapy; for instance, median survival in relapsing patients with a performance status ECOG score of 0 or 1 treated with temozolomide was 17.4 months (Reni et al. 2007), and the 1-year OS in patients <60 year old treated with radiotherapy alone was 67% (Nguyen et al. 2005).

Currently, high-dose chemotherapy supported by autologous peripheral-blood stem-cell transplantation is being addressed both as first-line and salvage therapy in PCNSL patients. Preliminary results clearly indicate that this strategy is feasible in these patients, but its role in PCNSL management remains to be defined considering that the worldwide experience is still limited, and further studies are necessary in order to identify the optimal induction and myeloablative regimens.

## INTRATHECAL CHEMOTHERAPY

Subarachnoid space and eyes are considered as “sanctuaries” for conventional chemotherapy, and they can be infiltrated by PCNSL in some cases (Ferreri et al. 2002). Some authors suggested the upfront

addition of intrathecal chemotherapy for meningeal treatment, when CSF cytology is positive, even though systemic HD-MTX should be able to eradicate neoplastic cells from CSF (Shapiro et al. 1975). Intrathecal or intraventricular route by an Ommaya’s reservoir can be used to deliver MTX, cytarabine, and steroids. However, with this approach Ferreri et al. (2002) observed increased risks of neurotoxicity and chemical meningitis. Efficacy of intrathecal chemotherapy in PCNSL patients is not yet well recognized and proven.

Leptomeningeal relapse occurs in 5–7% of PCNSL, and is almost always associated with brain recurrence. Information on intrathecal treatment is sparse and does not allow us to draw any conclusion regarding its impact on disease control and OS. Recently, the results of a phase I study of intraventricular administration of rituximab in patients with recurrent CNS and intraocular lymphoma was published by Rubenstein et al. (2007). This study proved the feasibility of intrathecal rituximab at a maximum tolerated dose of 25 mg in patients with CD20+ lymphomatous meningitis. Six cytologic responses (complete in four patients) were reported among the 10 patients included and two patients with intraocular lymphoma. Clinical improvement and objective response were observed in one patient with brain parenchymal disease. However, survival of these patients was short (median 22 weeks, range 1.1–134) due to parenchymal progressive disease, suggesting that intrathecal rituximab as exclusive treatment yields only a palliative role in the management of patients with CNS lymphomas and that the addition of systemic chemotherapy is necessary. Thus, further phase I studies addressing

the maximum tolerated dose of intrathecal rituximab in combination with other drugs are needed. Even though the potential benefit of intrathecal chemotherapy may be hardly extrapolated in the case of leptomeningeal relapse and concurrent brain recurrence, with the latter being the main prognostic variable influencing survival results in PCNSL (Ferreri et al. 2002).

## CONCLUSIONS

Despite recent progress, results following treatment for PCNSL patients remain disappointing. Salvage therapy appears to be a worthwhile treatment in these patients in view of its positive effect on survival and potential improvement in neurological symptoms and quality of life. As salvage therapy may have a relevant impact on survival, the description of treatment administered after failure in studies assessing drug efficacy in PCNSL seems requisite to avoid interpretation bias overestimating first-line treatment effect. Trials prospectively testing single agents in patients with relapsed or refractory disease represent an effective model for a quick identification of new promising drugs that can subsequently be incorporated into first-line treatment of PCNSL. Recent experience (Reni et al. 2004, 2007; Fischer et al. 2006; Voloschin et al. 2008) showed that such trials are feasible in spite of the rarity of this disease. The inclusion of relapsing or progressive PCNSL patients in well-designed salvage treatment prospective clinical trials for testing therapeutic agents should be strongly encouraged.

Definitive conclusion concerning the optimal salvage schedule could not be drawn due to the heterogeneity of the

salvage treatment employed and limited knowledge of main prognostic factors in PCNSL at the time of failure. In addition, interpretation of data in reported series is difficult because of selection bias and the limits of comparison of results across different series. Nevertheless, on the basis of data derived from reviews, retrospective and prospective series, some therapeutic guidelines can be suggested.

Radiotherapy is amongst the best options for unirradiated patients and retreatment with high-dose methotrexate (HD-MTX) can be suggested to well selected relapsing patients who experienced a prolonged lymphoma remission after first-line chemotherapy containing HD-MTX. Salvage monochemotherapy with temozolomide or topotecan in patients previously managed with a radiotherapy-containing approach is supported by prospective trials, while combination chemotherapy requires further investigation. High-dose chemotherapy supported by stem cell autotransplant and intrathecal chemotherapy in meningeal failure needs to be further investigated in prospective trials.

Salvage therapy improves survival in patients with failed PCNSL. The inclusion of patients with relapsed/refractory PCNSL in prospective trials addressing new active drugs or combinations is troublesome but should be strongly encouraged. In ordinary clinical practice, salvage strategy should be recommended on the basis of previous treatments, response duration, site and extent of disease, prognostic factors, and patient's clinical conditions. Radiotherapy appears to be the best option for unirradiated patients. Re-treatment with HD-MTX may be an option in patients who relapse after prolonged initial complete response to this agent and who did not receive prior

radiotherapy. The use of temozolomide or topotecan in monochemotherapy in PCNSL patients who experience relapse after a radiotherapy-containing approach is supported by prospective trials, while the use of combination chemotherapy warrants further investigation. High-dose chemotherapy supported by stem cell autotransplant and the use of intrathecal chemotherapy in patients with meningeal failure remain promising approaches to be further addressed in prospective trials.

## REFERENCES

- Abrey, L.E., Deangelis, L.M., and Yahalom, J. (1998) Long-term survival in primary CNS lymphoma. *J. Clin. Oncol.* 16:859–863
- Abrey, L.E., Ben-Porat, L., Panageas, K.S., Yahalom, J., Berkey, B., Curran, W., Schultz, C., Leibel, S., Nelson, D., Mehta, M., and DeAngelis, L.M. (2006) Primary central nervous system lymphoma: the Memorial Sloan-Kettering Cancer Center prognostic model. *J. Clin. Oncol.* 24:5711–5715
- Altman, J.K., Tellez, C., Chandler, J., Levy, R.M., Getch, C., Cohn, R., Gallot, L., Marymont, M., Grimm, S.A., and Raizer, J.J. (2008) Phase II trial of recurrent primary CNS lymphoma (PCNSL) treated with pemetrexed. 44th ASCO Annual Meeting Proceedings [Abstract]. *J. Clin. Oncol.* 26:2075
- Arellano-Rodrigo, E., Lopez-Guillermo, A., Bessell, E.M., Nomdedeu, B., Montserrat, E., and Graus, F. (2003) Salvage treatment with etoposide (VP-16), ifosfamide and cytarabine (Ara-C) for patients with recurrent primary central nervous system lymphoma. *Eur. J. Hematol.* 70:219–224
- Bessell, E.M., Graus, F., Lopez-Guillermo, A., Lewis, S.A., Villa, S., Verger E., and Petit, J. (2004) Primary non-Hodgkin's lymphoma of the CNS treated with CHOD/BVAM or BVAM chemotherapy before radiotherapy: long-term survival and prognostic factors. *Int. J. Radiat. Oncol. Biol. Phys.* 59:501–508
- Enting, R.H., Demopoulos, A., DeAngelis, L.M., and Abrey, L. (2004) Salvage therapy for primary CNS lymphoma with a combination of rituximab and temozolomide. *Neurology* 63:901–903
- Ferreri, A.J., Reni, M., Foppoli, M., Martelli, M., Pangalis, G.A., Frezzato, M., Cabras, M.G., Fabbri, A., Corazzelli, G., Ilariucci, F., Rossi, G., Soffiotti, R., Stelitano, C., Vallisa, D., Zaja, F., Zoppegno, L., Aondio, G.M., Avvisati, G., Balzarotti, M., Brandes, A.A., Fajardo, J., Gomez, H., Guarini, A., Pinotti, G., Rigacci, L., Uhlmann, C., Picozzi, P., Vezzulli, P., Ponzoni, M., Zucca, E., Calligaris-Cappio, F., Cavalli, F. International Extranodal Lymphoma Study Group (IELSG) (2009). High-dose cytarabine plus high-dose methotrexate versus high-dose methotrexate alone in patients with primary CNS lymphoma: a randomised phase 2 trial. *Lancet* 374: 1512–1520
- Ferreri, A.J., Reni, M., Zoldan, M.C., Terreni, M.R., and Villa, E. (1996) Importance of complete staging in non-Hodgkin's lymphoma presenting as a cerebral mass lesion. *Cancer* 77:827–833
- Ferreri, A.J.M., Reni, M., and Villa, E. (2000) Therapeutic management of primary central nervous system lymphoma: lessons from prospective trials. *Ann. Oncol.* 11:927–937
- Ferreri, A.J.M., Reni, M., Pasini, F., Calderoni, A., Tirelli, U., Pivnik, A., Aondio, G.M., Ferrarese, F., Gomez, H., Ponzoni, M., Borisch, B., Berger, F., Chassagne, C., Iuzzolino, P., Carbone, A., Weis, J., Pedrinis, E., Motta, T., Jouvet, A., Barbui, T., Cavalli, F., and Blay, J.Y. (2002) A multicenter study of treatment of primary CNS lymphoma for the International Extranodal Lymphoma Study Group. *Neurology* 58:1513–1520
- Ferreri, A.J.M., Blay, J.Y., Reni, M., Pasini, F., Spina, M., Ambrosetti, A., Calderoni, A., Rossi, A., Vavassori, V., Conconi, A., Devizzi, L., Berger, F., Ponzoni, M., Borisch, B., Tinguely, M., Cerati, M., Milani, M., Orvieto, E., Sanchez, J., Chevreau, C., Dell'Oro, S., Zucca, E., and Cavalli, F. (2003) Prognostic scoring system for primary CNS lymphomas: the International Extranodal Lymphoma Study Group experience. *J. Clin. Oncol.* 21:266–272
- Fischer, L., Thiel, E., Klasen, H.A., Birkmann, J., Jahnke, K., Martus, P., and Korfel, A. (2006) Prospective trial on topotecan salvage therapy in primary CNS lymphoma. *Ann. Oncol.* 17: 1141–1145
- Gavrilovic, I.T., Hormigo, A., Yahalom, J., DeAngelis, L.M., and Abrey, L.E. (2006)

- Long-term follow-up of high-dose methotrexate-based therapy with and without whole brain irradiation for newly diagnosed primary CNS lymphoma. *J. Clin. Oncol.* 24:4570–4574
- Glass, J., Gruber, M.L., Cher, L., and Hochberg, F.H. (1994) Preirradiation MTX chemotherapy of primary central nervous system lymphoma: long term outcome. *J. Neurosurg.* 81:188–195
- Herrlinger, U., Brugger, W., Bamberg, M., Küker, W., Dichgans, J., and Weller, M. (2000) PCV salvage chemotherapy for recurrent primary CNS lymphoma. *Neurology* 54:1707–1708
- Herrlinger, U., Küker, W., Uhl, M., Blaicher, H.P., Karnath, H.O., Kanz, L., Bamberg, M., and Weller, M. (2005) NOA-03 Trial of high-dose MTX in primary central nervous system lymphoma: final report. *Ann. Neurol.* 57:843–847
- Hottinger, A.F., DeAngelis, L.M., Yahalom, J., and Abrey, L.E. (2007) Salvage whole brain radiotherapy for recurrent or refractory primary CNS lymphoma. *Neurology* 69:1178–1182
- Iwamoto, F.M., Schwartz, J., Pandit-Taskar, N., Peak, S., Divgi, C.R., Zelenetz, A.D., Humm, J., and Abrey, L.E. (2007) Study of radiolabeled indium-111 and yttrium-90 ibritumomab tiuxetan in primary central nervous system lymphoma. *Cancer* 110:2528–2534
- Jahnke, K., Thiel, E., Martus, P., Herrlinger, U., Weller, M., Fischer, L., and Korfel, A. German Primary Central Nervous System Lymphoma Study Group (2006) Relapse of primary central nervous system lymphoma: clinical features, outcome and prognostic factors. *J. Neurooncol.* 80:159–165
- Kiewe, P., Korfel, A., Maza, S., Jahnke, K., Munz, D.L., and Thiel, E. (2006) Penetration of Yttrium-90-labeled ibritumomab tiuxetan (Zevalin™) into primary CNS lymphoma. 2006 ASH Annual Meeting Abstracts [Abstract] 108:2724
- Nguyen, P.L., Chakravarti, A., Finkelstein, D.M., Hochberg, F., Batchelor, T.T., and Loeffler, J.S. (2005) Results of whole brain radiation as salvage of MTX failure for immunocompetent patients with primary central nervous system lymphoma. *J. Clin. Oncol.* 23:1507–1513
- O'Brien, P., Roos, D., Pratt, G., Liew, K., Barton, M., Poulsen, M., Olver, I., and Trotter, G. (2000) Phase II multicentre study of brief single-agent MTX followed by irradiation in primary CNS lymphoma. *J. Clin. Oncol.* 18:519–526
- Pels, H., Schmidt-Wolf, I.G., Glasmacher, A., Schulz, H., Engert, A., Diehl, V., Zellner, A., Schackert, G., Reichmann, H., Kroschinsky, F., Vogt-Schaden, M., Egerer, G., Bode, U., Schaller, C., Deckert, M., Fimmers, R., Helmstaedter, C., Atasoy, A., Klockgether, T., and Schlegel, U. (2003) Primary central nervous system lymphoma: results of a pilot and phase II study of systemic and intraventricular chemotherapy with deferred radiotherapy. *J. Clin. Oncol.* 21:4471–4473
- Plotkin, S.R., Betensky, R.H., Hochberg, F.H., Grossman, S.A., Lesser, G.J., Nabors, L.B., Chon, B., and Batchelor, T.T. (2004) Treatment of relapsed PCNSL with high-dose methotrexate. *Clin. Cancer Res.* 10:5643–5646
- Reni, M., and Ferreri, A.J.M. (2004) Is withdrawal of consolidation radiotherapy an evidence-based strategy in primary central nervous system lymphomas? *J. Clin. Oncol.* 22:1165–1167
- Reni, M., Ferreri, A.J.M., Garancini, M.P., and Villa, E. (1997) Therapeutic management of primary central nervous system lymphoma in immunocompetent patients: Results of a critical review of the literature. *Ann. Oncol.* 8:227–234
- Reni, M., Ferreri, A.J.M., and Villa, E. (1999) Second-line treatment for primary central nervous system lymphoma. *Br. J. Cancer* 79:530–534
- Reni, M., Ferreri, A.J.M., Guha-Thakurta, N., Blay, J.Y., Dell'Oro, S., Biron, P., and Hochberg, F.H. (2001) The clinical relevance of consolidation radiotherapy and other main therapeutic issues in primary central nervous system lymphomas treated with upfront high-dose methotrexate. *Int. J. Radiat. Oncol. Biol. Phys.* 51:419–425
- Reni, M., Mason, W., Zaja, F., Perry, J., Franceschi, E., Bernardi, D., Dell'Oro, S., Stelitano, C., Candela, M., Abbadessa, A., Pace, A., Bordonaro, R., Latte, G., Villa, E., and Ferreri, A.J.M. (2004) Salvage chemotherapy with temozolomide in primary CNS lymphomas: preliminary results of a phase II trial. *Eur. J. Cancer* 40:1682–1688
- Reni, M., Zaja, F., Mason, W., Perry, J., Mazza, E., Spina, M., Bordonaro, R., Ilariucci, F., Faedi, M., Corazzelli, G., Manno, P., Franceschi, E., Pace, A., Candela, M., Abbadessa, A., Stelitano, C., Latte, G., and Ferreri, A.J.M. (2007) Temozolomide as salvage treatment in primary brain lymphomas. *Br. J. Cancer* 96:864–867
- Rodriguez, M.A., Cabanillas, F.C., Hagemester, F.B., McLaughlin, P., Romaguera, J., Swan, F., and

- Velasquez, W.S. (1995) A phase II trial of mesna/ ifosfamide, mitoxantrone and etoposide for refractory lymphomas. *Ann. Oncol.* 6:609–611
- Rubenstein, J.L., Fridlyand, J., Abrey, L., Shen, A., Karch, J., Wang, E., Issa, S., Damon, L., Prados, M., McDermott, M., O'Brien, J., Haqq, C., and Shuman, M. (2007) Phase I study of intraventricular administration of rituximab in patients with recurrent CNS and intraocular lymphoma. *J. Clin. Oncol.* 25:1350–1356
- Ruhstaller, T.W., Amsler, U., and Cerny, T. (2000) Rituximab: active treatment of central nervous system involvement by non-Hodgkin's lymphoma? *Ann. Oncol.* 11:374–375
- Shapiro, W.R., Young DF, Mehta BM. (1975) Methotrexate: distribution in cerebrospinal fluid after intravenous, ventricular and lumbar injections. *N Engl J Med* 293: 161–166
- Soussain, C., Suzan, F., Hoang-Xuan, K., Casanovas, O., Dupriez, B., Taksin, A.L., Souleau, B., Kolb, B., Jaccard, A., Zini, J.M., Choquet, S., Witz, F., Janvier, M., and Leblond, V. (2001) Results of intensive chemotherapy followed by hematopoietic stem-cell rescue in 22 patients with refractory or recurrent primary CNS lymphoma or intraocular lymphoma. *J. Clin. Oncol.* 19:742–749
- Soussain, C., Hoang-Xuan, K., Taillandier, L., Fourme, E., Choquet, S., Witz, F., Casanovas, O., Dupriez, B., Souleau, B., Taksin, A.L., Gisselbrecht, C., Jaccard, A., Omuro, A., Sanson, M., Janvier, M., Kolb, B., Zini, J.M., and Leblond, V. (2008) Intensive chemotherapy followed by hematopoietic stem-cell rescue for refractory and recurrent primary CNS and intraocular lymphoma: Société Française de Greffe de Moëlle Osseuse-Thérapie Cellulaire. *J. Clin. Oncol.* 26:2512–2518
- Tyson, R. M., Siegal, T., Doolittle, N.D., Lacy, C., Kraemer, D.F., and Neutwelt, E.A. (2003) Current status and future of relapsed primary central nervous system lymphoma (PCNSL). *Leuk. Lymphoma* 44:627–633
- Velasquez, W.S., McLaughlin, P., Tucker, S., Hagemester, F.B., Swan, F., Rodriguez, M.A., Romaguera, J., Rubenstein, E., and Cabanillas, F. (1994) ESHAP Ð an effective chemotherapy regimen in refractory and relapsing lymphoma: a 4-year follow-up study. *J. Clin. Oncol.* 12:1169–1176
- Voloschin, A.D., Betensky, R., Wen, P.Y., Hochberg, F., and Batchelor, T. (2008) Topotecan as salvage therapy for relapsed or refractory primary central nervous system lymphoma. *J. Neurooncol.* 86:211–215

*This page intentionally left blank*

# Central Nervous System Atypical Teratoid/ Rhabdoid Tumors: Role of Insulin-Like Growth Factor I Receptor

Michael A. Grotzer, Tarek Shalaby, and Alexandre Arcaro

## INSULIN-LIKE GROWTH FACTOR-I RECEPTOR

The insulin-like growth factor (IGF) system is composed of three ligands: IGF-I, IGF-II, and insulin. IGF-I and IGF-II are found in the circulation complexed to a family of binding proteins, called IGF-binding proteins (IGFBP), which serve to regulate bioavailability of these ligands in the tissues. The insulin-like growth factor-I receptor (IGF-IR) is a membrane-bound heterotetrameric receptor composed of two extracellular ligand-binding  $\alpha$ -subunits and two transmembrane  $\beta$ -subunits possessing intrinsic protein tyrosine kinase activity. The IGF-IR has high affinity for both IGF-I and IGF-II. The binding of IGF-I and/or IGF-II to the IGF-IR results in activation of its intrinsic tyrosine kinase with subsequent activation of the phosphoinositide 3-kinase (PI3K)-Akt-Bad cascade thereby protecting the cells from undergoing apoptosis (Datta et al. 1997; Dudek et al. 1997). Activation of the IGF-IR also suppresses pro-apoptotic pathways such as the JNK pathway (Okubo et al. 1998). Experiments using dominant nega-

tive mutants of IGF-IR, antibodies to IGF-IR, or antisense strategies directed against IGF-IR mRNA have shown that decreased or aberrant receptor expression is associated with a reversal of the transformed phenotype, induction of apoptosis, and a decrease in cellular radioresistance and chemoresistance (Benini et al. 2001; Scotlandi et al. 2002; Surmacz 2003; Turner et al. 1997). Hence, the IGF-IR has qualified as a molecular target for the development of novel anti-cancer therapies in selected tumor types.

### Role in CNS Atypical Teratoid/Rhabdoid Tumor

Central nervous system (CNS) atypical teratoid/rhabdoid tumor (AT/RT) is a highly malignant embryonal tumor in young children. CNS AT/RT is characterized by the presence of rhabdoid cells, with or without fields resembling classical primitive neuroectodermal tumor, epithelial tissue, and neoplastic mesenchyme (Rorke et al. 1996). The unique clinical, biological and histological features of this tumor have been defined over the past



decade (Biegel et al. 2002; Judkins et al. 2004). It is similar to the renal malignant rhabdoid tumor of infancy in its aggressiveness, in some histological features and in the loss of function of hSNF5/INI1, a candidate tumor suppressor gene on chromosome 22. Experience to date indicates that infants and children with CNS AT/RT respond very poorly to chemotherapy and radiotherapy (Bambakidis et al. 2002; Burger et al. 1998; Hilden et al. 2004; Tekautz et al. 2005). More recently, aggressive therapy, including high-dose chemotherapy with stem cell rescue and intrathecal chemotherapy, has prolonged the natural history in a subset of children (Hilden et al. 2004). However, the prognosis for children presenting with CNS AT/RT before the age of 3 years is still dismal (Hilden et al. 2004; Tekautz et al. 2005).

Ogino et al. (1999), analyzed two primary AT/RT by immunohistochemistry and demonstrated strong positivity for the IGF-IR and one of its ligands (IGF-II). In our own study, we found high IGF-IR expression in AT/RT tumors and cell lines (D'Cunja et al. 2007). Moreover, we found IGF-I and IGF-II mRNA in the BT-16 CNS AT/RT cell line and IGF-II mRNA in BT-12 CNS AT/RT cells. Autophosphorylated IGF-IR was detected in both cell lines, supporting the hypothesis that autocrine/paracrine stimulation of cell growth by the IGF-IR may be involved in AT/RT pathogenesis. It is conceivable that highly expressed activated IGF-IR in CNS AT/RT is involved in resistance to apoptosis. In agreement with this hypothesis is our finding that primary CNS AT/RT has a relatively high proliferation index, but only a low apoptotic index (D'Cunja et al. 2007).

## ANALYTICAL METHODS

### Immunohistochemistry

#### Materials

1. Xylene, methanol, EtOH 100%.
2. Phosphate buffered saline (PBS): 8 g NaCl, 0.2 g KCl, 1.44 g Na<sub>2</sub>HPO<sub>4</sub>, 0.24 g KH<sub>2</sub>PO<sub>4</sub>, 800 mL dH<sub>2</sub>O (pH 7.4), dH<sub>2</sub>O up to 1 L, autoclave.
3. Citrate buffer (10 mM citric acid): citric acid (anhydrous) 1.92 g. Distilled water 1,000 mL. Mix to dissolve. Adjust pH to 6.0.
4. DAB: 5 mL dH<sub>2</sub>O, two drops stock buffer, four drops stock DAB, two drops H<sub>2</sub>O<sub>2</sub> (hydrogen peroxide), filter and add DAB to 200 mL PBS.
5. Endogenous peroxidase quenching buffer: 200 mL PBS, 50 mL 30% H<sub>2</sub>O<sub>2</sub>, mix and use immediately.
6. Horse serum.
7. Primary antibodies: mouse monoclonal anti-GFAP, anti-EMA, smooth muscle alpha-actin, anti-human INI1 (BAF47), anti-human Phosphotyrosine-specific antibody (PY99) and Rabbit polyclonal anti-human IGF-IR $\beta$ .
8. Secondary antibodies: Goat anti-mouse IgG, Goat anti-rabbit biotinylated antibody.
9. IGF-IR $\beta$ -blocking peptide for negative control.

#### Methods

1. Deparaffinize (xylene) and rehydrate (dH<sub>2</sub>O) sections.
2. Immerse in 0.5% v/v hydrogen peroxide/methanol for 10 min.
3. Add citrate buffer – cover slides and microwave for 5 min.
4. Wash the tissue sections in two changes of dH<sub>2</sub>O (2  $\times$  5 min).

5. Immerse slides in PBS 2 × 5 min.
6. Cover sections with blocking solution: 0.1 M Tris and 2% horse serum.
7. Remove the blocking solution.
8. Add primary antiserum diluted in blocking solution and incubate overnight at 4°C.
9. Wash in PBS for 3 × 5 min.
10. Incubate sections with biotinylated secondary antibody diluted in blocking reagent; incubate for 30 min at 25°C.
11. Wash in PBS for 3 × 5 min.
12. Incubate sections with ABCComplex/HRP for 30 min at 25°C.
13. Wash in PBS buffer for 3 × 5 min.
14. Develop with diaminobenzidine tetrahydrochloride (DAB).
15. Rinse slides in running tap water.
16. Counterstain, dehydrate, clear, and mount sections.

### Immunoprecipitation

#### Materials

1. NP-40 Cell Lysis buffer: 50 mM Tris-HCl (pH 8.0), 150 mM NaCl, 1% (w/v) NP-40.
2. Protease Inhibitor Cocktail (100X): PMSF, 5 mg (50 µg/mL), Aprotinin, 100 µg (1 µg/mL), Leupeptin, 100 µg (1 µg/mL), Pepstatin, 100 µg (1 µg/mL), 100% Ethanol bring up to 1 mL.
3. SDS-PAGE sample buffer 2X: 3.55 mL dH<sub>2</sub>O, 1.25 mL 0.5 M Tris-HCl, pH 6, 8, 2.5 mL Glycerol, 2.0 mL 10% (w/v) SDS, 0.2 mL 0.5% (w/v) Bromophenol blue. Total volume is 9.5 mL. Add 50 µL of β-mercaptoethanol to 950 µL of sample buffer before use.

#### Method

1. Harvest 10<sup>7</sup> cells, wash with PBS and spin at 400 × g for 10 min.
2. Resuspend the cell pellet in 1 mL of cold lysis buffer (final concentration of 10<sup>7</sup> cells/mL).
3. Place the tube on ice for 30 min, with occasional mixing.
4. Spin cell lysate at 10,000 × g for 15 min at 4°C.
5. Carefully collect supernatant, without disturbing the pellet and transfer to a clean tube.
6. To preclear cell lysate, transfer 50 µL of the Protein A-Sepharose bead slurry to an Eppendorf tube and add 450 µL cold Lysis Buffer.
7. Spin at 10,000 × g for 30 s and remove the Lysis Buffer and resuspend the beads in 50 µL of cold Lysis Buffer.
8. Add this 50 µL of prepared Protein A slurry to 500 µL of Cell Lysate and incubate on ice for 30–60 min.
9. Spin at 10,000 × g for 10 min at 4°C and transfer the supernatant to a fresh Eppendorf tube.
10. For immunoprecipitation add 5–10 µg of IGF-IRβ antibody to the Eppendorf tube containing the cold precleared lysate.
11. Incubate at 4°C for 1 h.
12. Add 50 µL of washed Protein A slurry in prechilled Lysis Buffer and incubate for 1 h. at 4°C on a rocking platform or a rotator.
13. Spin the Eppendorf tube at 10,000 × g for 30 s at 4°C and remove supernatant and wash the beads three to five times with 500 µL of Lysis Buffer.
14. After the last wash, aspirate supernatant and add 50 µL of 1X Laemmli SDS-PAGE sample buffer to bead pellet.

15. Vortex and heat to 90–100°C for 10 min.
16. Spin at 10,000 × *g* for 5 min, collect supernatant and load onto the gel.
17. Proceed to Western blotting.

## Western Blotting

### Materials

1. SDS-PAGE Sample Buffer 2X: 3.55 mL dH<sub>2</sub>O, 1.25 mL 0.5 M Tris-HCl, pH 6.8, 2.5 mL Glycerol, 2.0 mL 10% (w/v) SDS, 0.2 mL 0.5% (w/v) Bromophenol blue. Total volume is 9.5 mL. Add 50 μL of β-mercaptoethanol to 950 μL of sample buffer before use.
2. SDS-PAGE Running Buffer 10X: 30.3 g Tris base, 144.0 g glycine, 10.0 g SDS. Dissolve in dH<sub>2</sub>O and fill to 1 L.
3. SDS-PAGE Transfer Buffer: 25 mM Tris-Base, 192 mM glycine, 20% Methanol (pH 8.3). For 1 L of buffer mix 3.03 g of Tris-Base, 14.4 g of glycine and 200 mL of methanol; Bring to 1 L with dH<sub>2</sub>O.
4. TBS 10X: 24.23 g Trizma HCl, 80.06 g NaCl Mix in 800 mL ultra pure water. Adjust pH to 7.6 with pure HCl. Top up to 1 L.
5. TBST for 1 l: 100 mL of TBS 10x + 900 mL ultra pure water + 1 mL Tween 20.
6. Lysis buffer: HEPES pH 7.6: 25 mM; Triton X-100: 0.1%; NaCl: 300 mM; β-glycerophosphate: 20 mM; MgCl<sub>2</sub>: 1.5 mM; EDTA: 0.2 mM; DTT: 2 M; sodium orthovanadate: 0.2 mM; sodium fluoride: 10 mM; benzamide: 1 mM; leupeptin: 2 μg/mL; aprotinin: 4 μg/mL and PMSF: 500 μM. Immediately before use add 10 mM dithiothreitol or beta-mercaptoethanol and protease inhibitors mixture.

7. Rabbit polyclonal primary, antibody against human IGF-IRβ (Santa Cruz Biotechnology, Santa Cruz, CA).
8. Mouse monoclonal anti-β-actin antibody against human beta-actin (Abcam Ltd., Cambridge, UK).
9. HRP-conjugated goat anti-rabbit secondary antibody (Santa Cruz Biotechnology, Santa Cruz, CA)
10. HRP-conjugated goat anti-mouse secondary antibody (Santa Cruz Biotechnology, Santa Cruz, CA)

### Method

1. Harvest, wash, and resuspend the cell pellet in 1 mL of cold lysis buffer.
2. Place the tube on ice for 30 min, with occasional mixing.
3. Spin cell lysate at 10,000 × *g* for 15 min at 4°C.
4. Carefully collect supernatant and transfer to a clean tube.
5. Add appropriate amount of sample buffer to sample lysis.
6. Heat to 95°C for 5 min.
7. Load in the gel and electrophorese proteins for the appropriate time (until the blue marker goes to the end of the gel).
8. Transfer proteins to nitrocellulose membrane.
9. Block membrane with 5% (w/v) non-fat dry milk in PBS for 1–3 h shaking at room temperature.
10. Incubate membrane with primary IGF-IRβ polyclonal antibody, 1:1,000 dilution overnight at 4°C on a shaker.
11. Wash the blot 3× with 1× PBS and then wash three times (10 min with 1× PBS + 0.1% Tween).
12. Incubate with HRP-conjugated anti-rabbit secondary antibody, diluted 1:10,000 for 1 h at room temperature.

13. Wash for 30 min with agitation in wash buffer (PBS with 0.1% Tween 20), changing the wash buffer every 5 min.
14. Place the blot in a plastic bag containing the ECL development working solution (0.125 mL/cm<sup>2</sup>) for 1–5 min.
15. Remove the blot from the bag and place it between two pieces of transparency film.
16. Expose to X-ray film or any sensitive screen.

### Quantitative RT-PCR

#### Materials

1. RNeasy kit (Qiagen) containing RNeasy spin column, RPE Buffer, RW1 Buffer.
2. 70% EtOH.
3. Sterile 15 mL conical tubes.
4. Buffer RLN: 50 mM Tris·Cl, pH 8.0, 140 mM NaCl, 1.5 mM MgCl<sub>2</sub>, 0.5% (v/v) Nonidet P-40 (1.06 g/mL), just before use, add 1,000 U/mL RNase inhibitor and 1 mM DTT.
5. SuperScript First-Strand Synthesis System kit (Invitrogen, AG Basel Switzerland) containing: 10X RT Buffer, MgCl<sub>2</sub> (25 mM), dNTP Mixture, Random Hexamer (50 μM), RNase Inhibitor (20 U/μL), Reverse Transcriptase (50 U/μL), RNase free Water (1,000 μL)
6. Primers and probes to target and the internal standard (housekeeping) genes were obtained from Applied Biosystems: IGF-IR Forward 5'-GTGAAAGTGACGTCCTGCA TTTC-3' Reverse 5'-CCTTGTAGTAAA CCGTGAAGCTGA-3', Probe 5'-CACC ACCACGTCGAAGAATCGCATC-3', 18S rRNA Forward 5'-AGTCCCTGCCC TTTGTACACA-3', Reverse 5'-GAT

CCGAGGGCCTCACTAAAC-3'  
Probe 5'-CGCCCGTCGCTACTACCG  
ATTGG-3'.

7. Taqman 2 X TaqMan Universal PCR Master Mix kit (Applied Biosystems, Rotkreuz, Switzerland) containing: AmpliTaq Gold DNA Polymerase, AmpErase UNG, dNTPs with dUTP, Passive Reference, and optimized buffer components (Applied Biosystems).
8. MicroAmp Optical 96-well Reaction Plate (Applied Biosystems).
9. Optical Caps (8 Caps/Strip) or Adhesive Covers (Applied Biosystems).
10. RNase and DNase Free Water.

#### Methods

1. Harvest, pellet 1 × 10<sup>7</sup> cells.
2. Lyse the cells in 175 μL of precooled (4°C) Buffer RLN.
3. Incubate on ice for 5 min.
4. Centrifuge the lysate at 4°C for 2 min at 300 × g and transfer the supernatant to a new centrifuge tube.
5. Add 600 μL Buffer RLT to the supernatant. Mix well by vigorously vortexing.
6. Add 430 μL ethanol (100%) to the homogenized lysate, and mix well.
7. Transfer up to 700 μL of the sample, including any precipitate that may have formed, to an RNeasy spin column placed in a 2 mL collection tube and centrifuge for 15 s at 8,000 × g.
8. Add 700 μL Buffer RW1 to the RNeasy spin column and centrifuge for 15 s at 8,000 × g.
9. Add 500 μL Buffer RPE to the RNeasy spin column and centrifuge for 15 s at 8,000 × g.
10. Place the RNeasy spin column in a new 1.5 mL collection tube and add 30–50 μL RNase-free water directly

- to the spin column membrane and centrifuge for 1 min at  $8,000 \times g$  to elute the RNA.
11. Quantify RNA using Nanodrop.
  12. Prepare the following RNA/primer mixture in each tube: total RNA 5 mg, random hexamers (50 ng/mL) 3 mL, 10 mM dNTP mix 1 mL, DEPC H<sub>2</sub>O up to 10 mL.
  13. Incubate the samples at 65°C for 5 min and then on ice for at least 1 min.
  14. Prepare reaction master mixture. For each reaction: 10× RT buffer 2 mL + 25 mM MgCl<sub>2</sub> 4 mL + 0.1 M DTT 2 mL + RNAaseOUT1 mL.
  15. Add the reaction mixture to the RNA/primer mixture, mix briefly, and then place at room temperature for 2 min.
  16. Add 1 mL (50 units) of SuperScript II RT to each tube, mix and incubate at 25°C for 10 min.
  17. Incubate the tubes at 42°C for 50 min, heat inactivate at 70°C for 15 min, and then chill on ice.
  18. Add 1 mL RNase H and incubate at 37°C for 20 min.
  19. Store the first strand cDNA at -20°C until use for real-time PCR.
  20. Prepare a mastermix of the reaction mix so that there is enough for all samples to be investigated: TaqMan Universal PCR Master Mix (2X) 25 μL, Forward primer 5 μL (100 nM), Reverse primer 5 μL (100 nM) TaqMan probe 5 μL (250 nM), DNA sample 5 μL (100 ng) Water 5 μL Total 50 μL.
  21. Add 50 μL of reaction mix above to each well in a 96-well plate.
  22. Subject plate to the following thermal cycling conditions cycling on the ABI Prism 7700 sequence detector: 50°C/2 min, 95°C/10 min (95°C/15s Denature Anneal and 60°C/1 min-Extend) for 40 cycles.
  23. Following amplification, record CT values for target gene and internal standard.

## Cell Viability

### Materials

1. Antisense phosphorothioate oligonucleotides directed against IGF-IR and controls (Biagnostik)
2. Doxorubicin (Sigma-Aldrich GmbH Basel)
3. Cisplatin (Sigma-Aldrich GmbH Basel)
4. Trypsin solutions for splitting cells (GIBCO, Invitrogen, AG Basel Switzerland)
5. DMEM (Supplier) with 10% fetal bovine serum (FBS), L-glutamine, and antibiotics
6. Colorimetric 3-(4,5-dimethylthiazol-2-yl)-5-(3-carboxymethoxyphenyl)-2-(4-sulfophenyl)-2H-tetrazolium, inner salt (MTS) assay kit (Promega) containing: 20 mL MTS Solution and 1 mL PMS Solution
7. Hemocytometer (with Trypan Blue Assay)

### Methods

1. Treat cells ( $3.0 \times 10^3$  cells/well in 90 μL medium) with 2 μM IGF-IR antisense oligonucleotides or controls for 0, 8, 12, 24, 48, 72, and 96 h.
2. Add 10 μL MTS assay reagent (Promega) to each well and incubate for 2 h. Use plate reader at OD 490 to obtain results.
3. For chemotherapeutic drug experiment: treat cancer cells with either antisense or controls for 48 h.

4. Trypsinize and resuspend the treated cells in complete DMEM and count on hemocytometer.
5. Set up 96-well microtiter plate, by adding 50  $\mu$ L containing equal cell numbers of the antisense or control treated cancer cells to each well.
6. Set up either doxorubicin or cisplatin drug dilution microtiter plate.
7. Add 40  $\mu$ L from each well of the doxorubicin, or cisplatin dilution plate to the corresponding wells on the cell plates and incubate plates for 2 days.
8. Add 10  $\mu$ L MTS assay reagent (Promega) to each well and incubate for 2 h. Use plate reader at OD 490 to attain results.
4. Repeat microplate centrifugation (200  $\times$  g) (10 min, room temperature).
5. Transfer aliquot of supernatant (lysate) to streptavidin-coated microplate.
6. Incubate supernatant with immunoreagent (containing anti-histone and anti-DNA) (2 h, room temperature).
7. Wash microplate wells three times with incubation buffer at room temperature.
8. Add substrate solution to wells and incubate (approx. 15 min, room temperature).
9. Measure absorbance at 405 nm.

#### EVALUATION OF IGF-I/-II/ IGF-IR IN CNS AT/RT

#### Detection of Apoptosis

##### *Material*

1. Cell Death Detection ELISA Kit (Roche) containing anti-histone antibody (clone H11-4), biotin-labeled, Anti-DNA antibody (clone M-CA-33), peroxidase-conjugated, DNA-histone complex (positive control), Incubation buffer, ready-to-use, Lysis buffer, ready-to-use, Substrate buffer, ready-to-use, ABTS substrate tablets, Microplate modules (12  $\times$  8 wells) and Adhesive plate cover.

##### *Methods*

1. Treat cancer cells with 2  $\mu$ M IGF-IR antisense in the well of a microplate (0, 24, 48, 72 and 96 h/ 37°C).
2. Centrifuge microplate (200  $\times$  g) and remove supernatant (10 min, room temperature).
3. Incubate treated cells with lysis buffer (30 min, room temperature).

To study the expression of the IGF-IR in primary CNS AT/RT, perform immunohistochemistry on formalin-fixed, paraffin-embedded tumor sections and observe the slides under light microscope. Western blotting using frozen tumor samples reveals IGF-IR over-expression in CNS AT/RT compared to near-normal brain samples and high IGF-IR expression in CNS AT/RT compared to medulloblastoma and pediatric glial CNS tumors. By using Western blotting, autophosphorylation studies and RT-PCR for IGF-I and IGF-II, high levels of autophosphorylated IGF-IR and expression of IGF-I and IGF-II mRNA could be detected in CNS AT/RT cells indicating a possible autocrine/paracrine loop. In BT-12 AT/RT cells, IGF-IR protein expression was lower when compared to BT-16 cells, and no IGF-I, but IGF-II was detectable. In BT-12 cells, the IGF-IR was also found to be autophosphorylated, but to a lesser extent than in BT-16 cells (D'Cunja et al. 2007).

## DOWN-REGULATION OF IGF-IR

Antisense phosphorothioate oligonucleotides directed against the IGF-IR and control scrambled IGF-IR oligonucleotides with the similar base composition but a randomized sequence as a control (Biognostik; Göttingen, Germany) can be used to further study the IGF-IR. Plate exponentially growing BT-12 and BT-16 human CNS AT/RT cells in 16-well plastic chamber slides ( $2 \times 10^3$  cells/well), and add 2  $\mu$ M fluorescein-labeled phosphorothioate oligonucleotides directly into the wells. Fix the cells after 8, 12, 24, and 48 h with  $-20^\circ\text{C}$  methanol and seal the slides with mounting medium. Visualize the uptake and distribution by fluorescence microscopy. To determine the percentage of uptake, FITC-labeled cells are counted and related to the total number of cells as previously described (Axel et al. 2000). A maximal uptake of 70–80% can be reached with a concentration of 2  $\mu$ M oligonucleotide after 12 h treatment.

After treating BT-12 and BT-16 human CNS AT/RT cells for 48 h with IGF-IR antisense oligonucleotides (2  $\mu$ M) the mean IGF-IR mRNA expression level was reduced to 51% (61%) compared to untreated cells and to 59% (75%) compared to control cells treated with scrambled oligonucleotides. In IGF-IR antisense oligonucleotide-treated BT-12 (BT-16) cells, the mean IGF-IR protein expression level was reduced to 39% (47%) compared to untreated cells and to 53% (51%) compared to control cells treated with scrambled oligonucleotides (D'Cunja et al. 2007)

Treatment of BT-12 and BT-16 human CNS AT/RT cells with IGF-IR antisense oligonucleotides (2  $\mu$ M) resulted in a sig-

nificant time-dependent decrease in cellular proliferation and in an increase in apoptotic cell death when compared to untreated and scrambled oligonucleotide-treated cells, as determined by MTS assay and by Cell Death ELISA (D'Cunja et al. 2007). Interestingly, IGF-IR down-regulation by antisense oligonucleotides resulted in significant increases of chemosensitivity of BT-12 and BT-16 cells to doxorubicin and cisplatin (D'Cunja et al. 2007).

In conclusion, our findings indicate that AT/RT express high levels of IGF-IR which may be activated through an auto-crine/paracrine IGF-I/IGF-II/IGF-IR loop, contributing to the aggressiveness and therapy-resistance of this particular pediatric brain tumor. Our results demonstrate that CNS AT/RT cell growth can be inhibited by treatment with IGF-IR antisense oligonucleotides. Moreover, we were able to demonstrate that antisense-mediated down-regulation of IGF-IR results in sensitization to doxorubicin and cisplatin. These results raise the possibility that curability of selected AT/RT tumors may be improved by pharmaceutical strategies directed against the IGF-IR. The *in vivo* effects of IGF-IR inhibition, and whether inhibition also influences the response of AT/RT cells to radiation therapy, are questions that remain to be answered.

## THERAPEUTIC SIGNIFICANCE OF IGF-IR IN CNS AT/RT

Recent studies have demonstrated that the concept of IGF-IR targeting is an approach for growth control in specific tumor cells and for the development of novel anti-cancer therapies (reviewed in Adachi et al. 2004; Wang and Sun, 2002). Several strategies

have been employed in different tumor cell lines to block either IGF-IR function or expression, both *in vitro* and *in vivo*. These included either inhibitors of ligand binding; e.g., peptide, small-molecule competitive binding antagonists and anti-receptor antibodies or the use of inhibitors of IGF-IR expression; such as small interfering RNA (siRNA) and antisense.

As is true in the case of impressive progress achieved with strategies targeting the epidermal growth factor receptor family in epithelial tumors (Scaltriti and Baselga 2006), the IGF-IR tyrosine kinase represents an attractive target for cancer therapy. However, the high degree of homology with the insulin receptor (IR) and the functional interplay between the IGF-IR and the IR represent a particular challenge for the development of targeted therapy. There is evidence for stimulation via both IGF-IR and IR receptors in cancer (Sachdev and Yee 2007), which indicates that both inhibitors with or without strong selectivity for the IGF-IR TK activity could be beneficial depending on the context. Because of the wide distribution of the IGF-IR and IR in normal tissues, a range of toxicities can be expected, but the existence of human populations with low levels of IGF-I (Laron 1984) or no IGF-I (Rosenbloom et al. 1990) indicates that anti-IGF-IR therapy may be tolerated reasonably well (Sachdev and Yee 2007).

A number of anti-IGF-IR agents are in preclinical and clinical development, mainly small-molecule inhibitors and monoclonal antibodies against IGF-IR. Two specific small molecule inhibitors have been recently developed, NVP-AEW541 (Garcia-Echeverria et al. 2004) and NVP-ADW-742 (Mitsiades et al. 2004), which are selective for the IGF-IR kinase activity

in cellular assays. Both agents inhibited tumor cell growth in a wide range of cancer types. At least in an *in vivo* mouse tumor model, NVP-AEW541 did not have short term detrimental side effects on the glucose/insulin metabolism (Garcia-Echeverria et al. 2004). Induction of diabetes remains a major concern to take into account for the translation into clinical trials. Other dual-specificity inhibitors are emerging for preclinical evaluation (Wittman et al. 2007). A number of monoclonal antibodies reagents are in development (Sachdev and Yee 2007). For example, a fully human anti-IGF-IR monoclonal antibody A12 was shown to inhibit IGF-IR phosphorylation and xenograft tumor growth effectively (Allen et al. 2007). However, the antibody-mediated cytotoxicity on normal cells expressing the receptor needs to be further investigated. Among other tissues expressing the IGF-IR, the central nervous system is of particular concern. IGF-I has been shown to be a survival factor in neurons, and the therapeutic benefit of IGF-I in the treatment of amyotrophic lateral sclerosis is currently under investigation (Sachdev and Yee 2007). Data from preclinical studies and ongoing early clinical phase studies with IGF-IR inhibitors will contribute in clarifying this issue.

Because the IGF-IR resides upstream of important prosurvival and antiapoptotic pathways, combinatorial strategies using IGF-IR inhibitors to augment the tumor response to conventional anticancer therapy could be of particular interest. As shown recently, NVP-AEW541 induced apoptosis in acute myeloid leukemia cells and sensitized leukemic blasts to etoposide (Doepfner et al. 2007; Tazzari et al. 2007). The combination of anti-IGF-IR A12 antibodies with radiation significantly



enhanced antitumor efficacy compared with either treatment modality alone (Allen et al. 2007). Furthermore, a combination of strategies against different receptor tyrosine kinases (RTKs) could improve efficacy, as exemplified by very effective combination trials targeting the epidermal growth factor receptor (EGFR) pathway (Scaltriti and Baselga 2006).

In order to prepare clinical translation for the treatment of pediatric CNS tumors, a more systematic evaluation using pre-clinical models will be required for a number of reasons. As we learned from the adult trials investigating new agents to target the EGFR family, selection of patients with EGFR-dependent tumors was important to assess efficacy (Scaltriti and Baselga 2006). Given the widespread expression of the IGF-IR, it is critical to be in a position to select patients that have an IGF-I pathway-dependent tumor. Furthermore, constitutive activation of downstream signaling nodes of the IGF pathway, such as PI 3-Kinase and the Akt pathway constitute the basis for resistance to IGF-IR inhibitors. Collectively, these aspects underscore the need for strong preclinical data for defined pediatric cancer entities and the requirement to establish biomarkers that are representative of the targeted pathway. Given the concerns of toxicity with long term treatment, identification of surrogate markers to monitor the biologic response to short term treatment would also be important.

Due to the small number of patients with pediatric CNS tumors eligible for experimental therapy, international collaboration is essential to further develop prioritized agents beyond phase I and II. Such initiatives from academic and

governmental institutions include the Innovative Therapies for Children with Cancer European Consortium (ITCC), the Children's Oncology Group (COG) Phase I Consortium and the North American Cancer Therapy Evaluation Program (CTEP-NCI).

## REFERENCES

- Adachi, Y., Lee, C.T., and Carbone, D.P. (2004) Genetic blockade of the insulin-like growth factor 1 receptor for human malignancy. *Novartis Found. Symp.* 262:177–189; 190–192; 265–268
- Allen, G.W., Saba, C., Armstrong, E.A., Huang, S.M., Benavente, S., Ludwig, D.L., Hicklin, D.J., and Harari, P.M. (2007) Insulin-like growth factor-I receptor signaling blockade combined with radiation. *Cancer Res.* 67:1155–1162
- Axel, D.I., Spyridopoulos, I., Riessen, R., Runge, H., Viebahn, R., and Karsch, K.R. (2000) Toxicity, uptake kinetics and efficacy of new transfection reagents: increase of oligonucleotide uptake. *J. Vasc. Res.* 37:221–234; 303–304
- Bambakidis, N.C., Robinson, S., Cohen, M., and Cohen, A.R. (2002) Atypical teratoid/rhabdoid tumors of the central nervous system. clinical, radiographic and pathologic features. *Pediatr. Neurosurg.* 37:64–70
- Benini, S., Manara, M.C., Baldini, N., Cerisano, V., Massimo, S., Mercuri, M., Lollini, P.L., Nanni, P., Picci, P., and Scotlandi, K. (2001) Inhibition of insulin-like growth factor I receptor increases the antitumor activity of doxorubicin and vincristine against Ewing's sarcoma cells. *Clin. Cancer Res.* 7:1790–1797
- Biegel, J.A., Tan, L., Zhang, F., Wainwright, L., Russo, P., and Rorke, L.B. (2002) Alterations of the hSNF5/INI1 gene in central nervous system atypical teratoid/rhabdoid tumors and renal and extrarenal rhabdoid tumors. *Clin. Cancer Res.* 8:3461–3467
- Burger, P.C., Yu, I.T., Tihan, T., Friedman, H.S., Strother, D.R., Kepner, J.L., Duffner, P.K., Kun, L.E., and Perlman, E.J. (1998) Atypical teratoid/rhabdoid tumor of the central nervous system: a highly malignant tumor of infancy and childhood

- frequently mistaken for medulloblastoma: a Pediatric Oncology Group Study. *Am. J. Surg. Pathol.* 22:1083–1092
- Datta, S.R., Dudek, H., Tao, X., Masters, S., Fu, H., Gotoh, Y., and Greenberg, M.E. (1997) Akt phosphorylation of BAD couples survival signals to the cell-intrinsic death machinery. *Cell* 91:231–241
- D'Cunja, J., Shalaby, T., Rivera, P., von Buren, A., Patti, R., Heppner, F. L., Arcaro, A., Rorke-Adams, L. B., Phillips, P. C., and Grotzer, M. A. (2007) Antisense treatment of IGF-IR induces apoptosis and enhances chemosensitivity in central nervous system atypical teratoid/rhabdoid tumours cells. *Eur. J. Cancer* 43:1581–1589
- Doepfner, K. T., Spertini, O., and Arcaro, A. (2007) Autocrine insulin-like growth factor-I signaling promotes growth and survival of human acute myeloid leukemia cells via the phosphoinositide 3-kinase/Akt pathway. *Leukemia* 21:1921–1930
- Dudek, H., Datta, S.R., Franke, T.F., Birnbaum, M.J., Yao, R., Cooper, G.M., Segal, R.A., Kaplan, D.R., and Greenberg, M.E. (1997) Regulation of neuronal survival by the serine-threonine protein kinase Akt. *Science* 275:661–665
- Garcia-Echeverria, C., Pearson, M.A., Marti, A., Meyer, T., Mestan, J., Zimmermann, J., Gao, J., Brueggen, J., Capraro, H.G., Cozens, R., Evans, D.B., Fabbro, D., Furet, P., Porta, D.G., Liebetanz, J., Martiny-Baron, G., Ruetz, S., and Hofmann, F. (2004) In vivo antitumor activity of NVP-AEW541-A novel, potent, and selective inhibitor of the IGF-IR kinase. *Cancer Cell* 5:231–239
- Hilden, J.M., Meerbaum, S., Burger, P., Finlay, J., Janss, A., Scheithauer, B.W., Walter, A.W., Rorke, L.B., and Biegel, J.A. (2004) Central nervous system atypical teratoid/rhabdoid tumor: results of therapy in children enrolled in a registry. *J. Clin. Oncol.* 22:2877–2884
- Judkins, A.R., Mauger, J., Ht, A., Rorke, L.B., and Biegel, J.A. (2004) Immunohistochemical analysis of hSNF5/INI1 in pediatric CNS neoplasms. *Am. J. Surg. Pathol.* 28:644–650
- Laron, Z. (1984) Laron-type dwarfism (hereditary somatomedin deficiency): a review. *Ergeb. Med. Kinderheilkd* 51:117–150
- Mitsiades, C.S., Mitsiades, N.S., McMullan, C.J., Poulaki, V., Shringarpure, R., Akiyama, M., Hideshima, T., Chauhan, D., Joseph, M., Libermann, T.A., Garcia-Echeverria, C., Pearson, M.A., Hofmann, F., Anderson, K.C., and Kung, A.L. (2004) Inhibition of the insulin-like growth factor receptor-1 tyrosine kinase activity as a therapeutic strategy for multiple myeloma, other hematologic malignancies, and solid tumors. *Cancer Cell* 5:221–230
- Ogino, S., Cohen, M.L., and Abdul-Karim, F.W. (1999) Atypical teratoid/rhabdoid tumor of the CNS: cytopathology and immunohistochemistry of insulin-like growth factor-II, insulin-like growth factor receptor type 1, cathepsin D, and Ki-67. *Mod. Pathol.* 12:379–385
- Okubo, Y., Blakesley, V.A., Stannard, B., Gutkind, S., and Le Roith, D. (1998) Insulin-like growth factor-I inhibits the stress-activated protein kinase/c-Jun N-terminal kinase. *J. Biol. Chem.* 273:25961–25966
- Rorke, L.B., Packer, R.J., and Biegel, J.A. (1996) Central nervous system atypical teratoid/rhabdoid tumors of infancy and childhood: definition of an entity. *J. Neurosurg.* 85:56–65
- Rosenbloom, A.L., Guevara Aguirre, J., Rosenfeld, R.G., and Fielder, P.J. (1990) The little women of Loja – growth hormone-receptor deficiency in an inbred population of southern Ecuador. *N. Engl. J. Med.* 323:1367–1374
- Sachdev, D., and Yee, D. (2007) Disrupting insulin-like growth factor signaling as a potential cancer therapy. *Mol. Cancer Ther.* 6:1–12
- Scaltriti, M., and Baselga, J. (2006) The epidermal growth factor receptor pathway: a model for targeted therapy. *Clin. Cancer Res.* 12:5268–5272
- Scotlandi, K., Avnet, S., Benini, S., Manara, M.C., Serra, M., Cerisano, V., Perdichizzi, S., Lollini, P.L., De Giovanni, C., Landuzzi, L., and Picci, P. (2002) Expression of an IGF-I receptor dominant negative mutant induces apoptosis, inhibits tumorigenesis and enhances chemosensitivity in Ewing's sarcoma cells. *Int. J. Cancer* 101:11–16
- Surmacz, E. (2003) Growth factor receptors as therapeutic targets: strategies to inhibit the insulin-like growth factor I receptor. *Oncogene* 22:6589–6597
- Tazzari, P.L., Tabellini, G., Bortul, R., Papa, V., Evangelisti, C., Grafone, T., Martinelli, G., McCubrey, J.A., and Martelli, A.M. (2007) The insulin-like growth factor-I receptor kinase

- inhibitor NVP-AEW541 induces apoptosis in acute myeloid leukemia cells exhibiting autocrine insulin-like growth factor-I secretion. *Leukemia* 21:886–896
- Tekautz, T.M., Fuller, C.E., Blaney, S., Fouladi, M., Broniscer, A., Merchant, T.E., Krasin, M., Dalton, J., Hale, G., Kun, L.E., Wallace, D., Gilbertson, R.J., and Gajjar, A. (2005) Atypical teratoid/rhabdoid tumors (ATRT): improved survival in children 3 years of age and older with radiation therapy and high-dose alkylator-based chemotherapy. *J. Clin. Oncol.* 23:1491–1499
- Turner, B.C., Haffty, B.G., Narayanan, L., Yuan, J., Havre, P.A., Gumbs, A.A., Kaplan, L., Burgaud, J.L., Carter, D., Baserga, R., and Glazer, P.M. (1997) Insulin-like growth factor-I receptor overexpression mediates cellular radioreistance and local breast cancer recurrence after lumpectomy and radiation. *Cancer Res.* 57:3079–3083
- Wang, Y., and Sun, Y. (2002) Insulin-like growth factor receptor-1 as an anti-cancer target: blocking transformation and inducing apoptosis. *Curr. Cancer Drug Targets* 2:191–207
- Wittman, M.D., Balasubramanian, B., Stoffan, K., Velaparthi, U., Liu, P., Krishnanathan, S., Carboni, J., Li, A., Greer, A., Attar, R., Gottardis, M., Chang, C., Jacobson, B., Sun, Y., Hansel, S., Zoeckler, M., and Vyas, D.M. (2007) Novel 1H-(benzimidazol-2-yl)-1H-pyridin-2-one inhibitors of insulin-like growth factor I (IGF-1R) kinase. *Bioorg. Med. Chem. Lett.* 17:974–977

# 28

## Central Nervous System Rosai–Dorfman Disease

Osama Raslan, Leena M. Ketonen, Gregory N. Fuller, and Dawid Schellingerhout

### INTRODUCTION, EPIDEMIOLOGY AND ETIOLOGY

In 1969, Rosai and Dorfman described the triad of massive cervical lymphadenopathy, expanded lymph node sinuses and characteristic histiocytes showing “emperipolesis” as a new, rare, idiopathic, nonneoplastic, lymphoproliferative disorder known as Rosai Dorfman Disease (RDD) or ‘sinus histiocytosis with massive lymphadenopathy (SHML) (Rosai and Dorfman 1969). Since then, over 750 cases have been reported in the literature (Hargett and Bassett 2005). Typically, RDD is characterized by bilateral painless cervical lymphadenopathy with fever, leukocytosis, increased erythrocyte sedimentation rate and hypergammaglobulinaemia (Chopra et al. 2006). However, in approximately 40% of cases, extranodal lesions in the skin, upper respiratory tract, orbit, testicle, soft tissue, kidney, thyroid, small bowel, breast, and bone can be found (Ruggiero et al. 2006).

CNS involvement is rare (<5%), with 75% of cases involving the brain and 25% involving the spinal canal. Involvement

of the CNS without concurrent nodal involvement is even rarer (Raslan et al. 2008). The etiology of RDD remains unknown and has been debated in the literature since recognition of the disease in 1969. Rosai and Dorfman (1969) postulated the expression of an abnormal immunologic response or an infectious factor. Becroft et al. (1973) demonstrated a defect in cellular immunity.

Epstein-Barr virus and human herpes virus 6 have been proposed as the infectious agent, and recently other diseases have been implicated, including varicella zoster virus, cytomegalovirus, Brucella, and Klebsiella (Moore et al. 2008). Mehraein et al. (2006) reported four cases of RDD, in which Parvovirus B19 infection was present in the RDD tissue. It has also been postulated that the development of RDD may be driven by dysregulated cytokine expression (Moore et al. 2008). Kismet et al. (2005) reported RDD in three children of one family. A familial incidence was also presented in two pairs of identical twins, and two sets of siblings developing RDD within a few years of each other (Foucar et al. 1990). Welbeck (2000) reported on two Ghanian brothers

who developed the disease, providing further evidence of a genetic link in RDD.

Patients with intracranial involvement of RDD differ from those with the classic manifestations of the disease: their age at onset is older than that of patients with nodal-based RDD (37.5 years compared with 20.6 years) (Kattner et al. 2000). However, the sex distribution is similar in the two forms, 1.5:1 (male to female) in isolated intracranial disease and 1.4:1 in the systemic variety (Gupta et al. 2006). Cases in African-Americans, Black Caribbeans and West-Africans are more frequent (43.6%) (Azoulay et al. 2004).

### INTRACRANIAL RDD: CLINICAL AND IMAGING FINDINGS AND DIFFERENTIAL DIAGNOSIS

Intracranial RDD typically presents as either a single or multiple dural-based extraaxial foci that may either assume a circumscribed, tumor-like configuration or grow as a diffuse plaque without noticeable mass effect (Figure 28.1). Both are readily confused with meningioma owing to their imaging qualities (Graggena et al. 2006). RDD has also been mistaken for subdural hematoma (Kumar et al. 2008). Depending on lesion size and the site(s) of involvement, RDD may or may not be clinically symptomatic. Signs and symptoms may include headaches, seizures, cranial nerve defects, hemiparesis, dysphasia or neglect (Geara et al. 2004).

Location can include the convexity, parasagittal region, cavernous sinus, and petroclival region (Kattner et al. 2000). Less than ten cases of suprasellar involvement have been reported (Wan et al. 2008). Two cases of primary intraparenchymatous

RDD are on record, one arising in the right frontal lobe of a 45-year-old woman (Natarajan et al. 2000), and one in the thoracic spinal cord (T4-5) of a 35-year-old man (Osenbach 1996). In 2003, a third case was reported by Juri et al. (2003). In addition, one rare instance of secondary brain invasion by RDD in the context of fatal systemic disease has been described (Foucar et al. 1990). Toh et al. (2005) recently described two cases of locally aggressive RDD causing dural sinus invasion.

On MRI, RDD lesions usually exhibit homogenous isointense signal intensity to gray matter on T1- and T2- weighted images, subtle hyperintensity on the fluid-attenuated inversion recovery images, and avid contrast uptake. Diffusion-weighted images (DW), apparent diffusion coefficient (ADC) values, and the exponential diffusion coefficient, are all isointense to gray matter. Depending on the size of the lesion, perilesional brain edema and mass effect may also be evident. An enhancing dural tail may be present (Raslan et al. 2008). Reports of CT findings of disease of the central nervous system have described dural-based masses that may be hyperattenuating, demonstrate enhancement, and be associated with bone erosion (Woodcock et al. 1999). Angiographically, the lesions have been described as being of variable vascularity (Konishi et al. 2003). The radiological differential diagnosis of intracranial RDD includes meningioma, Langerhans cell histiocytosis (LCH), lymphoproliferative disorders, plasma cell granuloma, granulomatous diseases (Geara et al. 2004), and, when multiple, neurofibromatosis. When it appears as a thin layer of extensive growth along, on, or in the dura, RDD should be differentiated from en plaque and malignant

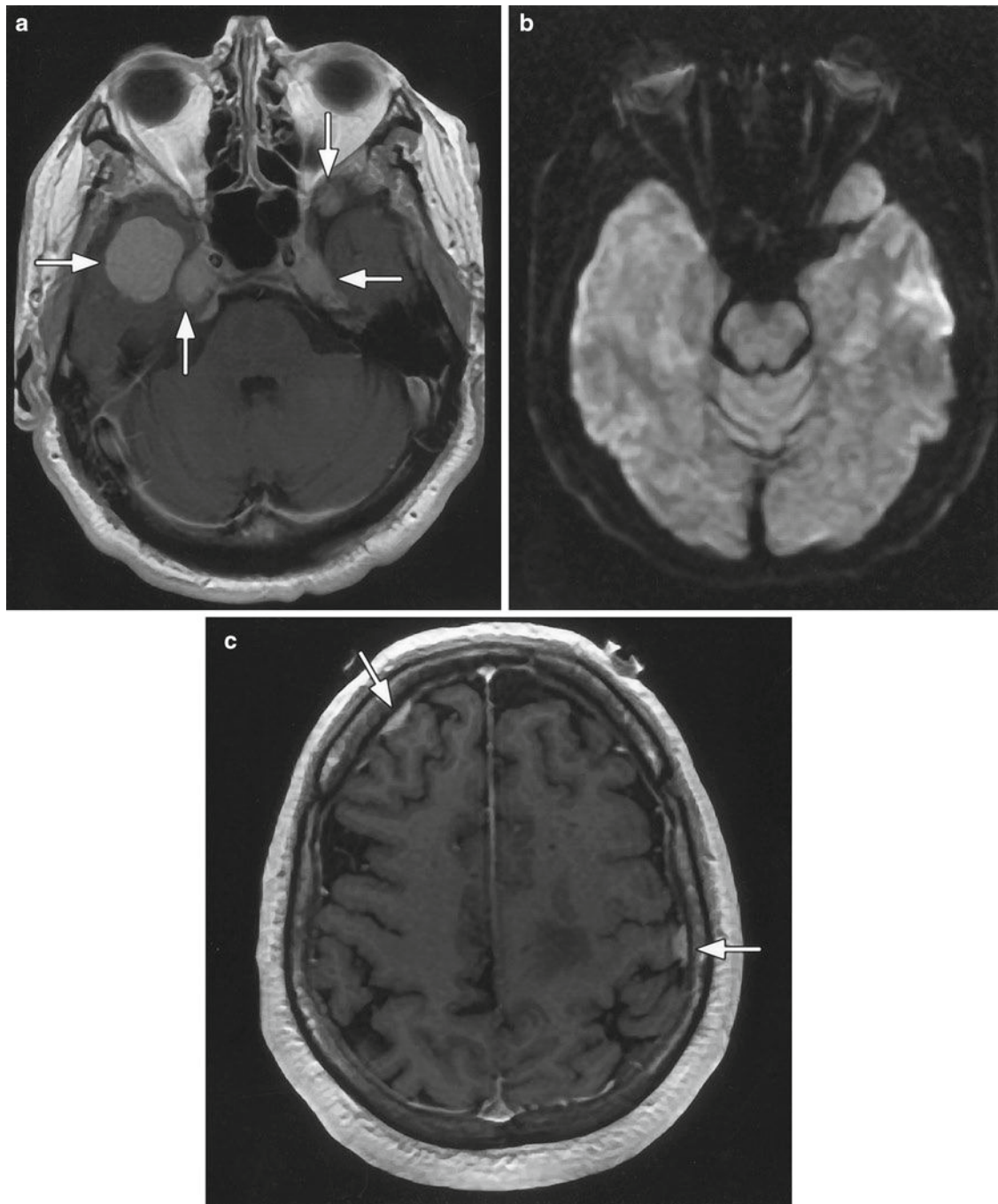


FIGURE 28.1. (a) Axial postcontrast T1 weighted image demonstrates multiple homogeneously enhancing dural based and paracavernous lesions (*arrows*). (b) Axial diffusion weighted image shows that the right temporal lobe lesion is isointense to the gray matter. (c) Axial postcontrast image shows plaque-like dural thickening (*arrows*). Fig. 1a and 1b is adapted from Raslan O, et al. *Journal of Clinical Oncology*, Vol 26, No 18 (June 20), 2008: pp. 3087–3089. Reprinted with permission © 2008 American Society of Clinical Oncology. All rights reserved

meningioma, melanoma, metastatic carcinoma, and infectious diseases (e.g., tuberculosis) (Konishi et al. 2003).

Although RDD is commonly identical to meningioma on CT, MRI, and even by gross examination at surgery, possible differentiating features include that unlike meningiomas, these tumors usually occur in males and may infiltrate the brain parenchyma (Geara et al. 2004). On T2-weighted MR images, meningiomas show low-to-high signal intensity, the variation due to a reflection of histologic subtype. In contrast, RDD shows rather low signal intensity. Meningiomas are frequently associated with hyperostosis, a feature that – to the best of our knowledge, has not been described with intracranial RDD. On angiograms, meningiomas are commonly seen as hypervascular lesions. In contrast, the results are variable for RDD. Konishi et al. (2003) described left frontal lobe RDD that derived its blood supply from the frontopolar artery. In contrast, meningiomas are largely fed by branches of the external carotid artery, and this can be a helpful feature in differentiating RDD from meningiomas. However, the feeding artery of intracranial RDD is generally thought to correspond with its location. Most benign meningiomas are isointense on DW images and ADC maps. In one study by Filippi et al. (2001), only 23% of benign meningiomas were slightly hyperintense (3 of 13). On average, these meningiomas had an elevation in the ADC value (Stadnik et al. 2003). On a microscopic level, however, the histopathologic features of meningioma and RDD are generally quite distinctive and can usually be easily distinguished on routine H&E-stained tissue section examination (Kattner et al. 2000).

The radiological differential diagnosis of suprasellar RDD includes suprasellar germinoma, granulomatous disease, other histiocytoses (LCH and hemophagocytic lymphohistiocytosis), and metastasis. Germinoma in the suprasellar region occurs with equal frequency in male patients and female patients, and is typically an infiltrating mass that is isointense to gray matter on T1-weighted images and hyperintense on T2-weighted images. Homogeneous enhancement is typical. Histologically, biphasic populations of very large germinoma cells with large nuclei are identified, with a surrounding population of small reactive lymphocytes (Woodcock et al. 1999).

LCH has variable manifestations in the CNS that range from localized enhancing masses to lytic osseous lesions. Whereas some histologic features are shared between LCH and RDD, there are several histological distinguishing features (Woodcock et al. 1999). Lymphoproliferative disorders frequently exhibit erythrophagocytosis rather than lymphohistiocytosis. Furthermore, aggressive lymphoproliferative disorders will show frank malignant cytological features on microscopic examination (Kattner et al. 2000). Granulomatous diseases (tuberculosis and sarcoidosis) are distinguished histologically by the presence of granulomas with or without caseation and organisms (Woodcock et al. 1999).

## SPINAL RDD: CLINICAL AND IMAGING FINDINGS AND DIFFERENTIAL DIAGNOSIS

There are 12 reported cases of spinal RDD. Eleven patients had an extramedullary tumor, which was epidural in seven

patients and intradural in four patients. Only two cases were associated with bone marrow involvement (Oner et al. 2007; Raslan et al. 2008). The cases of epidural and intradural spinal cord involvement have presented with spastic paraparesis or paraplegia secondary to cord compression (Hargett and Bassett 2005).

On imaging, the extramedullary tumors demonstrated a hypointense T1 and T2 WI, with homogeneous enhancement in the post-gadolinium study (Bhandari et al. 2006), while bone marrow involvement showed heterogeneous and decreased signal intensity on all series, with patchy enhancement following contrast injection (Figure 28.2). Diffusion weighted imaging showed mild heterogeneous signal over the vertebrae, whereas corresponding ADC maps revealed increased signal intensities (Oner et al. 2007). In our cases, the marrow signal showed high T2 signal

intensity in the fat suppressed image with avid enhancement.

MRI has limited value in differentiating between cellular bone marrow infiltration and benign bone marrow edema caused by inflammatory or infectious processes. In this setting, the DWI is a promising technology for outlining the undergoing process. Cellular bone marrow infiltration resulting from metastases or primary tumors has been reported to have lower ADC values compared to benign bone marrow edema resulting from infectious processes and compression fractures (Oner et al. 2007). Discovery of symptomatic spinal lesions after resection of an intracranial lesion have been reported. Based on the collective experience, it is our recommendation that meticulous spinal screening should be performed as a part of the diagnostic work-up for intracranial RDD (Raslan et al. 2008).

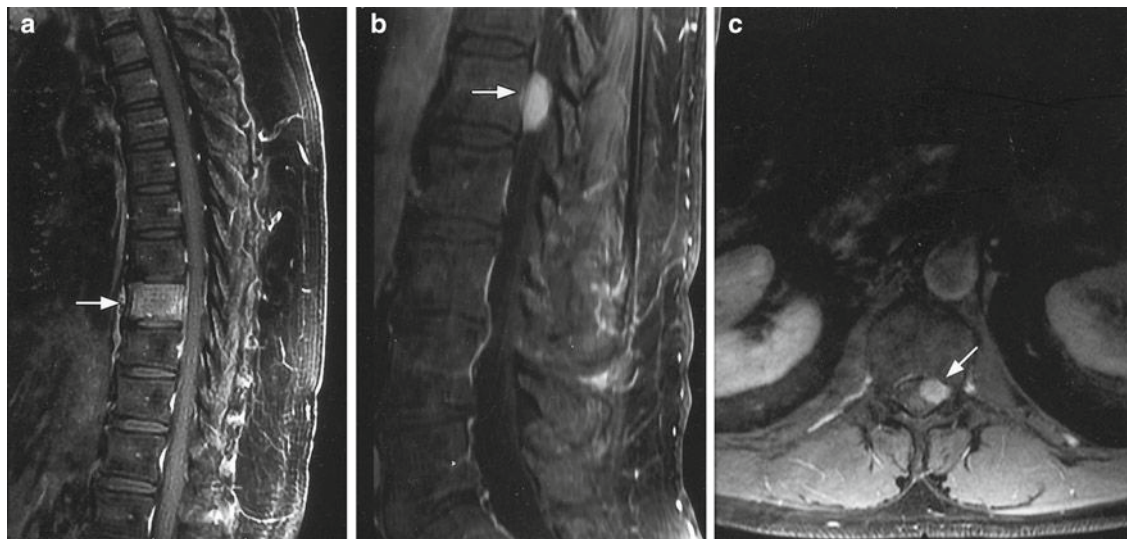


FIGURE 28.2. (a) Vertebral body marrow enhancement (*arrow*) is seen in sagittal postcontrast T1 weighted, fat suppressed image. (b) Sagittal and axial (c) postcontrast images demonstrate an intradural extramedullary enhancing mass in the spinal canal at L1 level (*arrow*). Fig. 1b is adapted from Raslan O, et al. *Journal of Clinical Oncology*, Vol 26, No 18 (June 20), 2008: pp. 3087–3089. Reprinted with permission © 2008 American Society of Clinical Oncology. All rights reserved



## HISTOPATHOLOGICAL AND DEFINITIVE DIAGNOSIS

Central nervous system RDD is definitively diagnosed by histology or cytology. Typical cytopathologic features of RDD include characteristic large polyclonal histiocytes with abundant pale, eosinophilic cytoplasm containing well-preserved phagocytosed lymphocytes (emperipolesis) and occasional plasma cells and granulocytes in a background of dense lymphoplasmacytic infiltrate. On immunohistochemistry, the histiocytes stain for S100 protein, CD68, and a-1 anti-chymotrypsin, and are negative for CD1a and lysozyme (Figure 28.3). The differential diagnosis on microscopic grounds should rule out disorders such as dermatofibroma, xanthoma, and Tangier disease, and other histiocytic disorders such

as histiocytosis X, reticulohistiocytoma, juvenile xanthogranuloma, leprosy, and Hodgkin disease (Ruggiero et al. 2006).

## CLINICAL COURSE AND TREATMENT

The clinical course of this disease is quite unpredictable, with periodic exacerbations and remissions of symptoms (Ocheni et al. 2007). Extra-nodal cases carry a poorer prognosis (Geara et al. 2004). The course of intracranial RDD is generally considered benign, although three deaths have been reported. The first occurred in a patient with coexisting systemic disease, and the second in an 89-year-old man 11 years after presentation with sellar disease, and in whom the cause of death

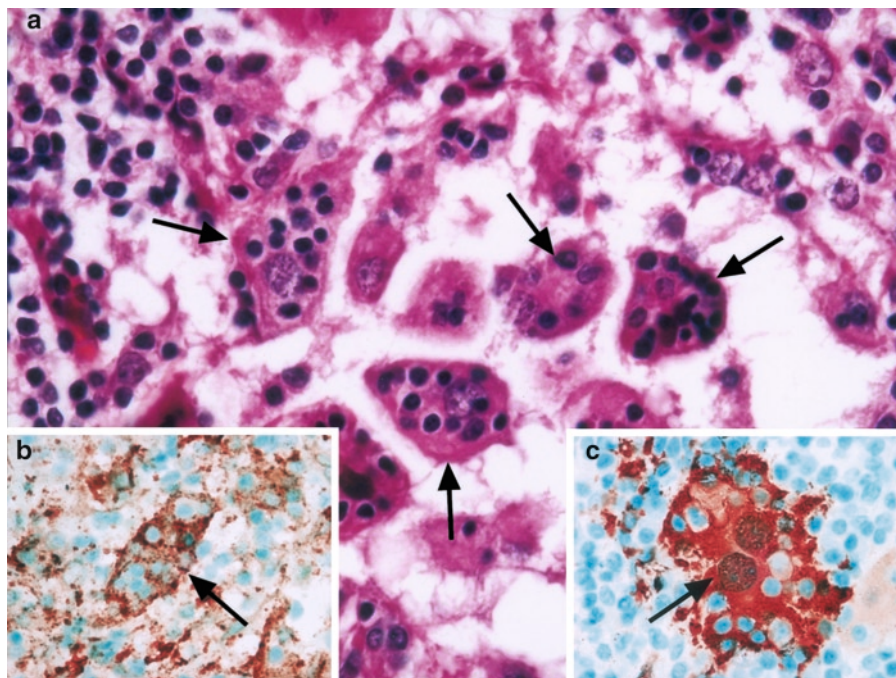


FIGURE 28.3. (a) The characteristic histopathologic hallmark of RDD is the presence of large histiocytes (arrows in (a)) that display numerous engulfed lymphocytes, a phenomenon that is called emperipolesis. RDD histiocytes are strongly immunopositive for both CD68 (arrow in (b)) and S-100 protein (arrow in (c))

is unknown. The third patient's death occurred 5 days after subtotal resection of falx deposits. Spontaneous regression in systemic RDD has been observed; however, to our knowledge there have been no reports of this occurring in the isolated intracranial form (Gupta et al. 2006). The reported mortality rate of RDD is 7%, with many patients who have a fatal outcome having concomitant immune dysfunction (Wang et al. 2001). RDD has been associated with various neoplasms, such as lymphoma and melanoma, and with LCH (Sachdev and Shyama 2008).

Ratzinger et al. (2003), have implied that there may exist a cause and effect aspect between RDD and cancer, and suggested four possibilities. RDD could develop within the immunological response to a malignant neoplasia. Alternatively, RDD, generally considered a disease of acquired immune dysregulation, could possibly encourage the development of malignancies in an immunosuppressed environment. Furthermore, one could imagine that immunosuppression of any origin could encourage the development of both RDD and a malignant process. Finally, the synchronous appearance of both diseases could happen by chance (Ratzinger et al. 2003).

As a result of uncertain etiology, various treatment approaches to RDD have been advocated. These include acyclovir, antibiotics, alpha-interferon, radiotherapy and several combinations of antineoplastic agents, such as cyclophosphamide, vinblastin, mercaptopurines, etoposide, methotrexate and corticosteroids. Some have suggested aggressive surgery, while others have suggested that patients should be offered no treatment at all (Komp 1990; Pulsoni et al. 2002; Ocheni et al. 2007).

In a recent literature review, Pulsoni et al. (2002), found spontaneous remission in 80% of cases that had not received any therapy. The highest rate of complete remission (near 90%) has been achieved through surgery. The benefit of radiotherapy alone seems rather limited (30%), while chemotherapy is in general ineffective. Among patients with primary intracranial RDD, up to 20% experience recurrent disease, the likelihood of relapse being influenced by the treatment modality chosen, and in particular by the extent of surgical resection (Graggena et al. 2006).

## REFERENCES

- Azoulay, R., Brisse, H., Fréneaux, P., Ferey, S., Kalifa, G., and Adamsbaum, C. (2004) Lacrimal location of sinus histiocytosis (Destombes–Rosai–Dorfman Disease). *AJNR Am. J. Neuroradiol.* 25:498–500
- Becroft, D., Dix, M., and Gillman, J. (1973) Benign sinus histiocytosis with massive lymphadenopathy transient immunological defects in a child with mediastinal involvement. *J. Clin. Pathol.* 26:403–469
- Bhandari, A., Patel, P.R., and Patel, M.P. (2006) Extranodal Rosai–Dorfman disease with multiple spinal lesions: a rare presentation. *Surg. Neurol.* 65:308–311
- Chopra, D., Svensson, W.E., Forouhi, P., and Poole, S. (2006) A rare case of extranodal Rosai–Dorfman disease. *Br. J. Radiol.* 79:e117–e119
- Filippi, C.G., Edgar, M.A., Uluğ, A.M., Prowda, J.C., Heier, L.A., and Zimmerman, R.D. (2001) Appearance of meningiomas on diffusion-weighted images: correlating diffusion constants with histopathologic findings. *AJNR Am. J. Neuroradiol.* 22:65–72
- Foucar, E., Rosai, J., and Dorfman, R. (1990) Sinus histiocytosis with massive lymphadenopathy (Rosai–Dorfman disease): review of the entity. *Semin. Diagn. Pathol.* 7:19–73
- Geara, A.R., Ayoubi, M.A., Achram, M.C., and Chamseddine, N.M. (2004) Rosai–Dorfman disease mimicking neurofibromatosis: case

- presentation and review of the literature. *Clin. Radiol.* 59:625–630
- Graggena, W.J.Z., Sturzeneggera, M., Mariania, L., Keseruea, B., Kappelerb, A., and Vajtai, I. (2006) Isolated Rosai–Dorfman disease of intracranial meninges. *Pathol. Res. Pract.* 202:165–170
- Gupta, D.K., Suri, A., Mahapatra, A.K., Mehta, V.S., Garg, A., Sarkar, C., and Ahmad, F.U. (2006) Intracranial Rosai–Dorfman disease in a child mimicking bilateral giant petroclival meningiomas: a case report and review of literature. *Childs Nerv. Syst.* 22:1194–1200
- Hargett, C., and Bassett, T. (2005) Atypical presentation of sinus histiocytosis with massive lymphadenopathy as an epidural spinal cord tumor: a case presentation and literature review. *J. Spinal Disord. Tech.* 18:193–196
- Jurić, G., Jakić-Razumović, J., Rotim, K., and Zarković, K. (2003) Extranodal sinus histiocytosis (Rosai–Dorfman disease) of the brain parenchyma. *Acta Neurochir. (Wien)* 145:145–149
- Kattner, K.A., Stroink, A.R., Roth, T.C., and Lee, J.M. (2000) Rosai–Dorfman disease mimicking parasagittal meningioma: case presentation and review of literature. *Surg. Neurol.* 53:452–457
- Kismet, E., Lu, V.K., Atay, A.A., Rkaya, S., and Tuncer, K. (2005) Sinus histiocytosis with massive lymphadenopathy in three brothers. *Pediat. Int.* 47:473–476
- Komp, D.M. (1990) The treatment of sinus histiocytosis with massive lymphadenopathy (Rosai–Dorfman disease). *Semin. Diagn. Pathol.* 7:83–86
- Konishi, E., Ibayashi, N., Yamamoto, S., and Scheithauer, B.W. (2003) Isolated intracranial Rosai–Dorfman Disease (sinus histiocytosis with massive lymphadenopathy). *AJNR Am. J. Neuroradiol.* 24:515–518
- Kumar, K.K., Menon, G., Nair, S., and Radhakrishnan, V.V. (2008) Rosai–Dorfman disease mimicking chronic subdural hematoma. *J. Clin. Neurosci.* Sept 26 [Epub ahead of print]
- Mehraein, Y., Wagner, M., Remberger, K., Fuzesi, L., Middel, P., Kaptur, S., Schmitt, K., and Meese, E. (2006) Parvovirus B19 detected in Rosai–Dorfman disease in nodal and extranodal manifestations. *J. Clin. Pathol.* 59:1320–1326
- Moore, J.C., Zhao, X., and Nelson, E.L. (2008) Concomitant sinus histiocytosis with massive lymphadenopathy (Rosai–Dorfman Disease) and diffuse large B-cell lymphoma: a case report. *J. Med. Case Rep.* 2:70
- Natarajan, S., Post, K.D., Strauchen, J., and Morgello, S. (2000) Primary intracerebral Rosai–Dorfman disease: a case report. *J. Neurooncol.* 47:73–77
- Ocheni, S., Ibegbulam, O.G., Okafor, O.C., Raveenthiran, V., and Nzegwu, M.A. (2007) Usefulness of oral corticosteroid in Rosai–Dorfman disease. *Eur. J. Cancer Care* 16:286–288
- Oner, A. Y., Akpek, S., and Tali, T. (2007) Rosai–Dorfman Disease with epidural and spinal bone marrow involvement: magnetic resonance imaging and diffusion-weighted imaging Features. *Acta Radiol.* 48:331–334
- Osenbach, R.K. (1996) Isolated extranodal sinus histiocytosis presenting as an intramedullary spinal cord tumor with paraplegia. *J. Neurosurg.* 85:692–696
- Pulsoni, A., Anghel, G., Falcucci, P., Matera, R., Pescarmona, E., Ribersani, M., Villiva, N., and Mandelli, F. (2002) Treatment of sinus histiocytosis with massive lymphadenopathy (Rosai–Dorfman disease): report of a case and literature review. *Am. J. Hematol.* 69:67–71
- Raslan, O., Ketonen, L.M., Fuller, G.N., and Schellingerhout, D. (2008) Intracranial Rosai–Dorfman disease with relapsing spinal lesions. *J. Clin. Oncol.* 26:3087–3089
- Ratzinger, G., Zelger, B.G., and Zelger, B. (2003) Is there a true association between Rosai–Dorfman disease and malignancy? *Br. J. Dermatol.* 149:1085
- Rosai, J., and Dorfman, R.F. (1969) Sinus histiocytosis with massive lymphadenopathy: a newly recognized benign clinicopathological entity. *Arch. Pathol.* 87:63–70
- Ruggiero, A., Attina, G., Maurizi, P., Mule, A., Tarquini, E., Barone, G., Lazzareschi, I., and Riccardi, R. (2006) Rosai–Dorfman Disease: two case reports and diagnostic role of fine-needle aspiration cytology. *J. Pediatr. Hematol. Oncol.* 28:103–106
- Sachdev, R., and Shyama, J. (2008) Co-existent Langerhans cell histiocytosis and Rosai–Dorfman disease: a diagnostic rarity. *Cytopathology* 19:55–58
- Stadnik, T.W., Demaerel, P., Luypaert, R.R., Chaskis, C., Van Rompaey, K.L., Michotte, A., and Osteaux, M.J. (2003) Imaging tutorial: differential

- diagnosis of bright lesions on diffusion-weighted MR Images. *Radiographics* 23:7e
- Toh, C.H., Chen, Y.L., Wong, H.F., Wei K.C., Ng, S.H., and Wan, Y.L. (2005) Rosai–Dorfman disease with dural sinus invasion: report of two cases. *J. Neurosurg.* 102:550–554
- Wan, S., Teng, X., Zhan, R., Yu, J., Gu, J., and Zhang, K. (2008) Isolated intracranial Rosai–Dorfman disease mimicking suprasellar meningioma: case report with review of the literature. *J. Int. Med. Res.* 36:1134–1139
- Wang, E., Anzai, Y., Paulino, A., and Wong, J. (2001) Rosai–Dorfman disease presenting with isolated bilateral orbital masses: report of two cases. *AJNR Am. J. Neuroradiol.* 22:1386–1388
- Welbeck, J.E. (2000) Sinus histiocytosis and massive lymphadenopathy in two Ghanian brothers. *Trop. Doct.* 30:182–183
- Woodcock, Jr., R.J., Mandell, J.W., and Lipper, M.H. (1999) Sinus Histiocytosis (Rosai–Dorfman Disease) of the suprasellar region: MR imaging findings—a case report. *Radiology* 213: 808–810

*This page intentionally left blank*

# Index

- AA. *See* Anaplastic astrocytomas
- Abscess  
ADC and, 240, 273, 290–293  
DWI for, 318  
metastases and, 318  
PMRS and, 273  
pyogenic  
DWI and, 240  
MRI of, 265  
rCBV and, 318
- Acetate, abscess and, 273
- Acquired immune deficiency syndrome (AIDS)  
ADC and, 291  
lymphoma and, 161, 272, 291  
MIBI-SPECT for, 206  
toxoplasmosis and, 291
- ACS. *See* Auto-calibration scans
- Acute disseminated encephalomyelitis (ADEM), 184
- Acyclovir, 371
- ADC. *See* Apparent diffusion coefficient
- ADEM. *See* Acute disseminated encephalomyelitis
- Adenosine triphosphate (ATP), 9  
MIBI and, 203
- Affymetrix gene expression  
microarrays, 21, 25
- AIDS. *See* Acquired immune deficiency syndrome
- ALA. *See* Alanine
- Alanine (ALA), 229, 233  
abscess and, 273
- Alpha-interferon, 371
- Alzheimer's disease, 256
- AMARES, 236
- Amide proton transfer (APT), 121–127  
of experimental tumor models,  
123–125  
MRI and, 125–127
- Amino acid tracers. *See* Radiolabeled amino acid tracers
- Anaplastic astrocytomas (AA), 192  
radiolabeled amino acid tracers for, 10
- Anaplastic ependymoma  
IHC for, 36  
metastases with, 162–163
- Anaplastic medulloblastoma, 5
- Anaplastic meningiomas, EMA and, 44
- Angiocentric glioma, 3–4
- Angiogenesis, VEGF-A and, 111–113
- Angiostatin, 102
- Antiangiogenic therapy  
BBB and, 116  
for gliomas, 109–117  
preclinical use of, 114  
vessel normalization and, 114
- Antibiotics, 371
- Antigen retrieval (AR), 46–47
- Anti-vascular therapy, 97–106
- Apoptosis, AT/RT and, 359
- Apparent diffusion coefficient (ADC), 134, 146,  
152, 279–294  
abscess and, 240, 273, 290–293  
AIDS and, 291  
cellularity and, 280–281  
central neurocytomas and, 284  
clinical application of, 281–282  
DNET and, 283  
encephalitis and, 274

- ependymoma and, 283
- GB and, 284–285
- for grey matter, 293
- HB and, 284
- lymphoma and, 284–285
- MB and, 283
- MD and, 293
- metastases and, 284–285
- MRI and, 279–294
- parasellar tumors and, 285–286
- pituitary tumors and, 285–286
- PNETs and, 283
- posterior cranial fossa
  - tumors and, 284
- radiation necrosis and, 287–288
- RDD and, 366
- recurrence and, 287–288, 289
- regional quantification of, 154
- resection injury and, 289
- ROI and, 148, 291–293
- schwannomas and, 285
- subependymomas and, 284
- treatment monitoring and,
  - 288–289
- tumor differentiation and, 282–286
- for tumor grading, 281, 282
- for tumor infiltration, 286–287
- APT. *See* Amide proton transfer
- AQP1, 54, 56–58
- AQP4, 54–55, 58–60
- AQP9, 55–56, 61–62
- AQPs. *See* Aquaporins
- Aquaglyceroporins, 53
- Aquaporins (AQPs), 53–62
  - BBB and, 54
  - distribution in tumors, 56–62
  - function of, 54–56
  - SAH and, 54
- AR. *See* Antigen retrieval
- ASCL1, 28
- Asn-Pro-Ala (NPA), 53
- Astrocytomas, 1. *See also specific types*
  - IHC for, 35
  - tumor grading for, 45
- ATP. *See* Adenosine triphosphate
- AT/RT. *See* Atypical teratoid rhabdoid tumor
- Atypical teratoid rhabdoid tumor (AT/RT)
  - apoptosis and, 359
  - in children, 43–44
  - IGF-IR and, 353–362
  - IHC for, 40–41, 354–355
  - immunoprecipitation for,
    - 355–366
  - QRT-PCR for, 357–358
  - Western blotting for, 356–357
- Auto-calibration, 247
- Auto-calibration scans (ACS),
  - GRAPPA and, 249
- Autologous stem cells, for PCNSL, 346–347
- Avastin. *See* Bevacizumab
- AZD2171. *See* Cedilanib
- BAF47, 40–41
- BAI-1, 65
- Basic fibroblast growth factor (bFGF)
  - bevacizumab and, 100
  - endostatin and, 102
- BBB. *See* Blood-brain barrier
- Bcl-2, 44
- BED. *See* Biological equivalent dose
- Benzodiazepine, 12, 175
- Ber-EP4, 44
- Beta-tubulin, 36
- Bevacizumab (Avastin), 99
  - CPT-11 with, 115
  - for GBM, 115
  - sorafenib and, 101
  - toxicities with, 100
- bFGF. *See* Basic fibroblast growth factor
- Biological equivalent dose (BED), 87
- Blood-brain barrier (BBB)
  - antiangiogenic therapy and, 116
  - AQP4 and, 60
  - AQPs and, 54
  - FDG and, 9, 158
  - FET and, 185
  - Gd and, 297, 302
  - gliomas and, 106, 110–111
  - HD-MTX and, 33
  - ICH and, 210
  - metastases and, 316
  - methionine and, 159
  - MIBI and, 203–204, 205–206, 210
  - monoclonal antibodies and, 345
  - radiotherapy and, 172
  - surgery and, 172
  - USPIO and, 288–298, 301–302, 303
  - vessel normalization and, 114
- Blood-oxygen level dependant (BOLD), 168, 254,
  - 263, 267

- BM. *See* Bone marrow  
B-mode. *See* Brightness mode  
BOLD. *See* Blood-oxygen level dependant  
Bone marrow (BM), EPC and, 104  
BrainLab, 22  
BRB-ArrayTools, 26  
Breast cancer, metastases and, 305  
Brightness mode (B-mode),  
for IOUS, 327  
Bronchogenic carcinoma  
ICH and, 207  
metastases and, 313  
Brucella, 365  
BT4C, 289  
BT-12, 360  
BT-16, 360  
BVAM. *See* Carmustine, vincristine,  
cytarabine, methotrexate
- C6 gliomas, 137–139  
cAMP. *See* Cyclic AMP  
Carmustine, vincristine, cytarabine,  
methotrexate (BVAM), 344  
Cartesian coordinates, 246–247  
Caspase, survivin and, 103  
Catenins, 307  
Cathepsin-L, endostatin and, 102  
Cavernous angioma, PGNT and, 2  
CD10, 42  
CD15, 44  
CD20, 345  
CD30, 40  
CD34  
meningiomas and, 38  
SFT and, 44  
CD36, TSP-1 and, 100  
CD44RI, 65  
CD68, RDD and, 370  
CD99, 36  
SFT and, 44  
CD117, 40  
cDNA, stereotactic biopsy and, 25, 28  
CE. *See* Contrast enhancement  
CEA, 44  
CED. *See* Convection-enhanced drug delivery  
Cedilanib (AZD2171), 115  
Cellularity, ADC and, 280–281  
Central neurocytomas, ADC and, 284  
C-erbB2, 65  
Cerebellar vermis, RGNT and, 3  
Cerebral blood volume (CBV), 310–311. *See also*  
Relative cerebral blood volume  
Cerebral hemispheres, PGNT in, 2  
CEST. *See* Chemical exchange-dependent saturation  
transfer  
CG. *See* Conjugated-Gradient algorithm  
CH<sub>3</sub>. *See* Methyl  
Chemical exchange-dependent saturation transfer  
(CEST), 122–123  
Chemical shift imaging (CSI), 311  
Chemical shift selective saturation (CHESS), 256  
Chemotherapy. *See also specific agents*  
FDG and, 11  
high-dose, for PCNSL, 346–347  
intrathecal, 347–348  
MIBI-SPECT and, 206  
for PCNSL, 342–345  
PET and, 172  
white matter and, 152  
CHESS. *See* Chemical shift selective saturation  
Children  
AT/RT in, 43–44  
MBEN in, 5  
methionine and, 161  
PET for, 161  
Children's Oncology Group (COG), 362  
CHO. *See* Choline  
CHOD. *See* Cyclophosphamide, doxorubicin,  
vincristine, dexamethasone  
Choline (CHO), 230, 233  
abscess and, 273  
CRE and, 236, 238, 241  
encephalitis and, 274  
metastases and, 315  
MRS and, 255  
NAA and, 241  
PMRS and, 269  
TE and, 311  
CHOP, 345  
Choriocarcinoma, ICH and, 207  
Choroid plexus carcinoma (CPC), AT/RT and, 41  
Choroid plexus papilloma (CPP), IHC for, 36  
Chromogranin A  
AT/RT and, 40  
EVN and, 37  
Cilengitide, 102  
Cisplatin, 360  
sorafenib and, 101  
CK. *See* Cytokeratin



- CK20, 44  
 C-kit, 39–40  
 Claudin-1, meningiomas and, 38–39  
 CLIO-Cy5.5, 299  
 C-mode. *See* Color-mode  
 COG. *See* Children's Oncology Group  
 Color-duplex-mode, for IOUS, 327  
 Color-mode (C-mode), for IOUS, 327  
 Computed tomography (CT)  
   extraventricular neurocytoma and, 2  
   FDG and, 16  
   FET and, 184–185  
   MB and, 4–5  
   MBEN and, 5  
   for metastases, 308  
   MIBI and, 206  
   PET and, 186  
   radiolabeled amino acid tracers and, 10  
   for RDD, 368  
   SPECT and, 15  
 Computer assisted surgery, FET-PET and, 186  
 Conjugated-Gradient algorithm (CG), 249  
 Contrast enhancement (CE), 184  
   FLAIR and, 308  
 Convection-enhanced drug delivery (CED), 27  
 Corpus callosum, PGNT and, 2  
 Corticosteroids, 115  
   for RDD, 371  
 CPC. *See* Choroid plexus carcinoma  
 CPP. *See* Choroid plexus papilloma  
 CPs. *See* Craniopharyngiomas  
 CPT-11. *See* Irinotecan  
 Cranial nerve palsy, 306  
 Craniopharyngiomas (CPs), 39  
 CRE. *See* Creatine  
 Creatine (CRE), 229–230, 233  
   CHO and, 236, 238, 241  
   GLX and, 237  
   MRS and, 255  
   PMRS and, 269  
   TE and, 311  
 cRNA, stereotactic biopsy and, 25, 28  
 CSI. *See* Chemical shift imaging  
 CT. *See* Computed tomography  
 Cyclic AMP (cAMP), PDE4 and, 71–80  
 Cyclophosphamide, for RDD, 371  
 Cyclophosphamide, doxorubicin, vincristine,  
   dexamethasone (CHOD), 344  
 Cytarabine, 344  
   high-dose, 345  
 Cytokeratin (CK)  
   AT/RT and, 40  
   CPP and, 36  
   ependymal tumors and, 36  
   meningiomas and, 38  
   metastatic small cell carcinoma and, 43  
   RCCs and, 42  
 Cytokines, 98  
 Cytomegalovirus, 365  
 DAB. *See* Diaminobenzidine tetrahydrochloride  
 DCC, 65  
 DEC FA. *See* Directionally-encoded FA maps  
 Delayed ratio (DR), 204  
 Dementia, FDG for, 9–10  
 Demyelinating lesions, 272–273, 318–319  
 Deparaffinize, 354  
 Dermatofibroma, 370  
 Desmin, AT/RT and, 40  
 Diabetes  
   FDG and, 11  
   STZ and, 56  
 Diaminobenzidine tetrahydrochloride (DAB), 355  
 Diffuse astrocytoma, reactive gliosis and, 42  
 Diffusion tensor imaging (DTI), 131–142,  
   145–154, 267–268, 280, 310  
   to differentiate recurrence from  
     post-surgery injury, 152–153  
   FA and, 146–147  
   for gliomas, 137–140  
   for 9L gliosarcoma, 136–137  
   for metastases, 316  
   in pre-surgical planning, 150  
   RA and, 146–147  
   tractography and, 169  
   in treatment follow-up, 150–152  
   for tumor grading, 149–150  
   VR and, 147  
   xenografts and, 140  
 Diffusion-weighted (DW)  
   EPI and, 280  
   RDD and, 366  
 Diffusion-weighted MRI (DWI), 131, 145–154,  
   267. *See also* Apparent diffusion  
   coefficient  
   for abscess, 318  
   to differentiate recurrence from post-surgery  
     injury, 152–153  
   encephalitis and, 274  
   EPI and, 308

- MRS and, 240
  - pitfalls of, 153
  - in pre-surgical planning, 150
  - pyogenic abscess and, 240
  - in treatment follow-up, 150–152
  - for tumor grading, 149–150
- Dihydrofolate reductase, 343
- Directionally-encoded FA maps (DEC FA), 147
- D-mode. *See* Doppler-mode
- DNA, QRT-PCR for, 29, 66
- DNET. *See* Dysembryoplastic neuroepithelial tumor
- Docetaxel, Sorafenib and, 101
- Doppler-mode (D-mode), for IOUS, 327
- Dosimetry
  - hypofractionation and, 91–92
  - of IPA, 222
  - isodose line and, 90
  - late *versus* early effects, 87–90
  - past experience and, 86–87
  - radiosurgery and, 86–91
  - for radiotherapy, 12–13
- DOTATOC. *See* 1,4,7,10-tetraazacyclododecane-*N,N',N',N'*-tetraacetic-acid-D-Phe<sup>1</sup>-Tyr<sup>3</sup>-octreotide
- Doxorubicin, 360
  - sorafenib and, 101
- DR. *See* Delayed ratio
- DSC. *See* Dynamic susceptibility contrast
- DTI. *See* Diffusion tensor imaging
- Dural-based tumors, 44
- DW. *See* Diffusion-weighted
- DWI. *See* Diffusion-weighted MRI
- Dynamic susceptibility contrast (DSC), 310
- Dysembryoplastic neuroepithelial tumor (DNET), 42–43, 184
  - ADC and, 283
  - GABA and, 175
  - GG and, 161
  - methionine and, 161–162
- E74-like factor 3 (ELF3), 66, 67
- Early ratio (ER), 204
- EC. *See* Extracellular
- E-cadherin, 307
- Echo-planar imaging (EPI), 135, 146, 246, 247, 252–253
  - DW and, 280
  - DWI and, 308
  - GRAPPA and, 252
  - SENSE and, 252–254, 258–259
- Echo time (TE), 228, 309
  - LAC and, 232
  - MRS and, 311
  - PRESS and, 231
  - pseudotumor and, 240
  - SNR and, 233
  - STEAM and, 231
- ECM. *See* Extracellular matrix
- EDTA, 47
- EEG. *See* Electroencephalography
- EGCG. *See* (-)-epigallocatechin gallate
- EGFR. *See* Epidermal growth factor receptor
- Elastase, endostatin and, 102
- Electroencephalography (EEG), 167
- ELF3. *See* E74-like factor 3
- EMA. *See* Epithelial membrane antigen
- Embryonal tumors, 4–5
- Encephalitis
  - FET and, 183–184
  - PMRS and, 274
- Endoplasmic reticulum (ER), 103
- Endostatin, 102
- Endothelial cells, adhesion and migration of, 102–104
- Endothelial progenitor cells (EPC), BM and, 104
- Endothelin-1 (Et-1), 98
- Enzo BioArray High Yield RNA Transcript Labeling Kit, 25
- EPC. *See* Endothelial progenitor cells
- Ependymal tumors, WHO classification of, 36
- Ependymoma
  - ADC and, 283
  - anaplastic
    - IHC for, 36
    - metastases with, 162–163
  - IHC for, 36
  - spinal, MET-PET for, 161
- EPI. *See* Echo-planar imaging
- Epidermal growth factor receptor (EGFR), 21–22, 65, 67, 68, 101
  - gliomas and, 110
  - IGF-IR and, 362
  - TKIs and, 112
- (-)-epigallocatechin gallate (EGCG), 103
- Epilepsy, FDG for, 9–10

- Epithelial membrane antigen (EMA), 36  
 anaplastic meningiomas and, 44  
 AT/RT and, 40  
 CPP and, 36  
 for meningiomas, 38  
 RCCs and, 42
- Epstein-Barr virus, 365
- ER. *See* Early ratio; Endoplasmic reticulum;  
 Estrogen receptor
- ERBB2. *See* Erythroblastic leukemia viral  
 oncogene homolog 2
- Erythroblastic leukemia viral oncogene homolog 2  
 (ERBB2), 67, 68
- Erythrophagocytosis, 368
- Estrogen receptor (ER), meningiomas and, 38
- Et-1. *See* Endothelin-1
- Etoposide, 344  
 for RDD, 371
- European Association of Nuclear  
 Medicine, 9–18
- EVN. *See* Extraventricular neurocytoma
- Extracellular (EC), 67–68
- Extracellular matrix (ECM), 97–98
- Extraventricular neurocytoma (EVN), 2–3  
 IHC for, 37
- F98, Gliomas, 139–140
- FA. *See* Fractional anisotropy
- FACT. *See* Fiber Assignment by Continuous  
 Tracking
- FasL, TSP-1 and, 100
- Fast Fourier transform (FFT), 236
- FDG. *See* [<sup>18</sup>F]Fluoro-2-deoxyglucose
- FDOPA, 18
- Ferumoxides, 299, 302–303
- Ferumoxtran-10, 298, 299, 300
- Ferumoxytol, 298
- FET. *See* O-(2-[<sup>18</sup>F]fluoroethyl)-L-tyrosine
- FFT. *See* Fast Fourier transform
- FGF. *See* Fibroblast growth factor
- Fiber Assignment by Continuous  
 Tracking (FACT), 141
- Fibroblast growth factor (FGF), 115
- FID. *See* Free induction decay
- Field-of-view (FOV), 246, 248–249  
 k-space and, 248  
 MRSI and, 255
- FLAIR. *See* Fluid-attenuated inversion  
 recovery
- FLT. *See* <sup>18</sup>F-fluorodopa
- Fluid-attenuated inversion recovery (FLAIR),  
 121, 127  
 CE and, 308  
 of GBM, 266  
 for gliomas, 319  
 IPA-SPECT and, 217–218  
 MRI and, 264  
 SE and, 308
- [<sup>18</sup>F]Fluoro-2-deoxyglucose (FDG), 9–10  
 abnormal uptakes of, 192–193  
 BBB and, 9, 158  
 chemotherapy and, 11  
 CT and, 16  
 diabetes and, 11  
 dosage for, 12  
 glucose and, 158  
 lymphoma and, 161  
 MB and, 161  
 metastases and, 159  
 MRI and, 16  
 patient preparation for, 11–12  
 PET with, 13–15, 158–159  
 for GG, 161  
 glucose and, 11  
 for ICH, 208  
 SNR and, 169
- PNETs and, 161  
 quantification for, 16  
 radiation dosimetry of, 12–13  
 radiotherapy and, 11, 173  
 rCMRGI and, 16  
 sedation and, 12  
 stereotactic biopsy with, 189–199  
 sub-cortical grey matter and, 193–194  
 for tumor grading, 162–163
- 1-(2'-deoxy-2'-fluoro-β-arabinofuranosyl)thymine  
 (FMAU), 174–175
- <sup>18</sup>F-fluorodopa (FLT), 160
- O-(2-[<sup>18</sup>F]fluoroethyl)-L-tyrosine (FET), 9  
 BBB and, 185  
 CT and, 184–185  
 encephalitis and, 183–184  
 MET and, 180–181  
 MRI and, 184–185  
 PET with, 13–15, 160, 179–187, 215  
 clinical application of, 186–187  
 computer assisted surgery and, 186  
 radiation dosimetry of, 12–13  
 ROC and, 182  
 uptake kinetics of, 180–184

- Fluorouracil, sorafenib and, 101  
FMAU. *See* 1-(2'-deoxy-2'-fluoro- $\beta$ -arabinofuranosyl)thymine  
fMRI. *See* Functional MRI  
Formalin-fixed paraffin-embedded tissue, IHC for, 46–49  
FOV. *See* Field-of-view  
Fractional anisotropy (FA), 134, 136–137, 149, 310  
DTI and, 146–147  
metastases and, 316–317  
ROI and, 150  
Free induction decay (FID), 236  
MRSI and, 255  
Functional MRI (fMRI), 167, 168  
parallel MRI and, 252–254  
PET and, 169  
  
GABA. *See* Gamma-aminobutyric acid  
GAC1. *See* Glioma amplified on chromosome 1  
Gadolinium (Gd), 121  
BBB and, 297, 302  
MRI and, 264, 338  
USPIO and, 298  
Gadolinium diethylenetriaminepenta-acetic acid (Gd-DTPA), 110  
Gamma-aminobutyric acid (GABA), 175, 229  
Ganglioglioma (GG)  
DNETs and, 161  
FDG-PET for, 161  
IHC for, 37  
Gastrointestinal cancer, metastases and, 305  
GB. *See* Glioblastoma  
GBM. *See* Glioblastoma multiforme  
Gd. *See* Gadolinium  
Gd-DTPA. *See* Gadolinium diethylenetriaminepenta-acetic acid  
GeneChip, 26  
Generalized autocalibrating partial parallel acquisition (GRAPPA), 246, 248  
ACS and, 249  
EPI and, 252  
k-space and, 249  
Gene therapy, 105–106  
Genetics, of gliomas, 109–110  
Gestational trophoblastic tumors, metastases and, 305  
GFAP. *See* Glial fibrillary acid protein  
GG. *See* Ganglioglioma  
Glial fibrillary acid protein (GFAP), 33  
astrocytomas and, 35  
AT/RT and, 40  
CPP and, 36  
ependymal tumors and, 36  
EVN and, 37  
gliomas and, 34–35  
oligodendrogliomas and, 35  
PDE4 and, 76  
PXA and, 35  
SEGA and, 35  
Glioblastoma (GB), 192  
ADC and, 284–285  
MIBI and, 205  
pancytokeratin and, 43  
radiolabeled amino acid tracers for, 10  
TMZ for, 172  
Glioblastoma multiforme (GBM), 21, 109  
Avastin for, 115  
FLAIR of, 266  
metastases with, 162–163  
PDE4 and, 71  
PFS with, 115  
Rolipram for, 60  
stereotactic biopsy for, 28–29  
Gliomas. *See also specific types*  
ADC and, 281  
antiangiogenic therapy for, 109–117  
BBB and, 106  
C6, 137–139  
classification of, 192  
EGFR and, 110  
F98, 139–140  
FLAIR for, 319  
genetics of, 109–110  
IHC for, 33–35  
irinotecan for, 99  
lymphoma and, 319  
metastases and, 319  
methionine and, 159–160  
MRI for, 121  
PDGF and, 115  
PDGFR and, 115  
PTEN and, 110  
treatment for, 110–111  
tyrosine kinase growth factors and, 160  
WHO classification of, 110  
Glioma amplified on chromosome 1 (GAC1), 66  
Gliosarcoma, 9L, 136–137  
GLN. *See* Glutamine

- GLU. *See* Glutamate
- Glucose, 9  
 FDG and, 158  
 FDG-PET and, 11
- Glucose regulated protein 78/Binding immunoglobulin protein (GRP78/BiP), 103–104
- Glutamate (GLU), 229
- Glutamine (GLN), 229
- GLX, 229  
 CRE and, 237
- Glycerol, AQP9 and, 55–56
- Glycinamide ribonucleotide formyltransferase, 343
- Gradient echo (GRE), 298, 300, 310
- GRAPPA. *See* Generalized autocalibrating partial parallel acquisition
- GRE. *See* Gradient echo
- Grey matter  
 ADC for, 293  
 sub-cortical, 193–194
- Gross tumor volume (GTV), 166
- Growth factors, 98–99. *See also specific growth factors*
- GRP78/BiP. *See* Glucose regulated protein 78/Binding immunoglobulin protein
- GTV. *See* Gross tumor volume
- HB. *See* Hemangioblastoma
- HD-MTX. *See* High-dose methotrexate
- H&E. *See* Hematoxylin-eosin
- Heat induced epitope retrieval (HIER), 47, 49
- Hemangioblastoma (HB)  
 ADC and, 284  
 IHC for, 41–42  
 metastases and, 319–320  
 VHL and, 319–320
- Hemangiopericytoma (HPC), 44
- Hematoma, metastases and, 319
- Hematoxylin-eosin (H&E), 33, 45  
 for RDD, 368
- Hemorrhage. *See also* Intraparenchymal brain hemorrhage  
 metastases and, 313  
 SAH, 54
- Heparin Sulfate proteoglycan (HSPG), 102
- HERMES, 218
- Heterogeneity, 21–31
- Hexokinase, 158
- HIER. *See* Heat induced epitope retrieval
- High-dose chemotherapy, for PCNSL, 346–347
- High-dose methotrexate (HD-MTX), 337  
 BBB and, 33  
 for NHL, 339  
 for PCNSL, 343–344
- High-grade glioma, 10, 121, 157, 264  
 metastases and, 315
- HIV, lymphoma and, 161
- HMB-45, 35
- Homer-Wright rosettes, 38
- Horseradish peroxidase (HRP), 49
- HPC. *See* Hemangiopericytoma
- HPLC. *See* Performance liquid chromatography
- HRP. *See* Horseradish peroxidase
- HSPG. *See* Heparin Sulfate proteoglycan
- Human herpes virus 6, 365
- Hydrogen isotope (1H), 227
- Hypernephroma, ICH and, 207
- Hypofractionation, 86, 89  
 dosimetry and, 91–92
- Hypothalamus, pilomyxoid astrocytoma in, 1
- IBFBP-7, 105
- Ibritumomab tiuxetan, 345
- IC. *See* Intracellular
- ICH. *See* Intraparenchymal brain hemorrhage
- IELGS. *See* International Extranodal Lymphoma Study Group scoring system
- Ifosfamide, 344
- IGF-binding proteins (IGFBP), 353
- IGFBP. *See* IGF-binding proteins
- IGF-I. *See* Insulin-like growth factor I
- IGF-II. *See* Insulin-like growth factor II
- IGF-IR. *See* Insulin-like growth factor I receptor
- IHC. *See* Immunohistochemistry
- 3-[<sup>123</sup>I]iodo- $\alpha$ -methyl-L-tyrosine (IMT), 9  
 for SPECT, 9
- IL-8. *See* Interleukin-8
- Imaging. *See also specific imaging modalities*  
 European Association of Nuclear Medicine and, 9–18  
 interpretation of, 269–270
- Immunocytochemistry, PDE4 and, 76–78
- Immunohistochemistry (IHC)  
 anaplastic ependymoma for, 36  
 astrocytomas for, 35  
 for AT/RT, 40–41, 354–355  
 for CPP, 36  
 for diagnosis, 33–49

- for differential diagnosis, 42–44
- ependymoma for, 36
- for EVN, 37
- for formalin-fixed paraffin-embedded tissue, 46–49
- ganglioglioma for, 37
- for gliomas, 33–35
- for HB, 41–42
- markers for, 36–37
- for MB, 37–38
- for meningiomas, 37–38
- oligodendroglioma for, 35
- PDE4 and, 75–76
- for RDD, 370
- for tumor grading, 44–46
- Immunoprecipitation, for AT/RT, 355–366
- IMR. *See* Intraoperative magnetic resonance
- IMT. *See* L-3-[123I]-iodo- $\beta$ -methyl tyrosine
- Ingenuity Pathway, 28
- Innovate Therapies for Children with Cancer European Consortium (ITCC), 362
- Insulin-like growth factor I (IGF-I), 353–362
- Insulin-like growth factor II (IGF-II), 353–362
- Insulin-like growth factor I receptor (IGF-IR)
  - AT/RT and, 353–362
  - EGFR and, 362
- Interleukin-8 (IL-8), 98
- International Extranodal Lymphoma Study Group scoring system (IELGS), 338–339
- INTERPRET, 231, 234, 238
- Intra-axial tumors, MRI for, 263–276
- Intracellular (IC), 67–68
- Intraoperative magnetic resonance (IMR), USPIO and, 302
- Intra-operative ultrasound (IOUS)
  - efficacy of, 329–334
  - image characteristics for, 327
  - modes for, 327
  - resection and, 325–334
  - resolution for, 327–329
  - transducers for, 326–327
- Intraparenchymal brain hemorrhage (ICH)
  - BBB and, 210
  - FDG-PET for, 208
  - MET-PET for, 208
  - MIBI-SPECT and, 206–212
- Intrathecal chemotherapy, for PCNSL, 347–348
- L-3-[123I]-iodo- $\beta$ -methyl tyrosine (IMT), 215–216
  - IPA and, 222
  - radiation dosimetry of, 12–13
  - ROI and, 16
  - SPECT and, 14
  - thyroid gland and, 11–12
- p-[123I]iodo-L-phenylalanine (IPA)
  - dosimetry of, 222
  - IMT and, 222
  - retention of, 224
  - ROC and, 224
  - SPECT with, 215–225
    - FLAIR and, 217–218
    - for LGG, 224–225
    - NMR for, 217–218
    - quantitative criteria for, 222
    - results from, 219–222
    - for tumor grading, 224
- IOUS. *See* Intra-operative ultrasound
- IPA. *See* p-[123I]iodo-L-phenylalanine
- Irenat. *See* Sodium perchlorate
- Irinotecan (CPT-11)
  - with bevacizumab, 115
  - for gliomas, 99
- Isodose line, dosimetry and, 90
- ITCC. *See* Innovate Therapies for Children with Cancer European Consortium
- jMRUI, 234
- KAI-1, 65
- Kelly's technique, 192
- Ki-67, 42, 45
  - FLT and, 160
  - MET and, 160
  - MIBI and, 204
- KIR4.1. *See* Potassium inward rectifying channels 4.1
- Klebsiella, 365
- K-space, 245
  - FOV and, 248
  - GRAPPA and, 249
  - MRI and, 247
  - sensitivity maps and, 248
- K-space spatial harmonics (SMASH), 246, 247–248, 250
- LAC. *See* Lactate
- Lactate (LAC), 229
  - abscess and, 273
  - encephalitis and, 274
  - MRS and, 255
  - PMRS and, 269
  - TE and, 232, 311

- Langerhans cell histiocytosis (LCH), 366  
 RDD and, 366, 368
- Large cell/anaplastic (LC/A), 38
- Larmor frequency, 227
- LC/A. *See* Large cell/anaplastic
- LCH. *See* Langerhans cell histiocytosis
- LDH, 338
- Lenalidomide, 115
- Leptomeningeal metastases, 315
- Leucine rich repeat neuronal 2 (LRRN2), 66, 67
- Leukemia, metastases and, 305
- LGG. *See* Low-grade glioma
- LightCycler, 67
- Low-grade glioma (LGG), 192  
 encephalitis and, 274  
 IPA-SPECT for, 224–225
- LRRN2. *See* Leucine rich repeat neuronal 2
- L-transporter, radiolabeled amino acid tracers and, 11
- Lumped constant, 16
- Lung cancer, metastases and, 305
- Lymphoma. *See also* Non-Hodgkin lymphoma;  
 Primary central nervous system lymphoma  
 ADC and, 284–285  
 AIDS and, 291  
 FDG and, 161  
 gliomas and, 319  
 malignant, 284–285  
 metastases and, 305, 319  
 MIBI-SPECT for, 206  
 PET for, 161  
 PMRS and, 272  
 RDD and, 371
- Lymphophagocytosis, 368
- Magnetic resonance imaging (MRI).  
*See also* Diffusion-weighted MRI; Functional MRI; Parallel MRI  
 ADC and, 279–294  
 APT and, 125–127  
 EVN and, 3  
 FDG and, 16  
 FET and, 184–185  
 FLAIR and, 264  
 Gd and, 264, 338  
 for gliomas, 110, 121  
 IMR, 302  
 for intra-axial tumors, 263–276  
 k-space and, 247  
 MBEN and, 5  
 for metastases, 305–321  
 MIBI and, 206  
 PET and, 158  
 pilomyxoid astrocytoma and, 1  
 PMRI, 268  
 PTPR and, 4  
 of pyogenic abscess, 265  
 radiolabeled amino acid tracers and, 10  
 for RDD, 368  
 spiral trajectory, 249  
 stereotactic biopsy and, 23–24  
 USPIO and, 297–303  
 VOI and, 230
- Magnetic resonance spectroscopic imaging (MRSI), 245, 255–259  
 FID and, 255  
 FOV and, 255  
 SENSE and, 257
- Magnetic resonance spectroscopy (MRS), 125  
 antiangiogenic therapy and, 116  
 CHO and, 255  
 CRE and, 255  
 DWI and, 240  
 LAC and, 255  
 MV, and, 267  
 NAA and, 255  
 problems with, 245  
 SV, 227–241  
 TE and, 311  
 WHO classification and, 240–241
- Magnetization transfer contrast (MTC), 123–124
- Magnetization transfer ratio (MTR), 123–124
- Magnetoencephalography (MEG), 167
- Malignant (small) blue cell tumors, 43
- Malignant lymphoma, 284–285
- MAP. *See* Microtubule associated protein
- MASH1, 28
- Matrix metalloproteinases (MMPs), 22, 98, 307
- MB. *See* Medulloblastoma
- MBEI. *See* Model-based expression indexes
- MBEN. *See* Medulloblastoma with extensive nodularity
- MCCRCC. *See* Metastatic clear cell renal cell carcinoma
- MCF-7, 289
- MD. *See* Mean diffusivity
- MDM2, 67
- MDM4. *See* Transformed 3T3 cell double minute 4

- Mean diffusivity (MD), 134, 149, 310  
ADC and, 293
- Mechanical hypothesis, of metastases, 306–307
- Medtronic, 22, 23
- Medulloblastoma (MB), 4–5  
ADC and, 283  
AT/RT and, 41  
FDG and, 161  
IHC for, 37–38  
metastases with, 162–163
- Medulloblastoma with extensive nodularity (MBEN), 5
- MEG. *See* Magnetoencephalography
- Melanoma  
ICH and, 207  
metastases and, 305, 313  
RDD and, 371
- Meningiomas, 44  
ADC and, 281, 285  
IHC for, 37–38  
RDD and, 366, 368  
tumor grading for, 45–46
- Mercaptopurines, for RDD, 371
- Merkel carcinoma, 317
- MET. *See* [Methyl-<sup>11</sup>C]-L-methionine
- Metabolic maps, 312
- Metastases, 308  
ADC and, 281, 284–285  
with anaplastic ependymoma, 162–163  
CT for, 308  
differential diagnosis for, 317–320  
DTI for, 316  
FA and, 316–317  
FDG and, 159  
with GBM, 162–163  
gliomas and, 319  
HB and, 319–320  
hematoma and, 319  
hemorrhage and, 313  
high-grade glioma and, 315  
lymphoma and, 319  
with MB, 162–163  
mechanical hypothesis of, 306–307  
MRI for, 305–321  
PMRS and, 271–272  
QRT-PCR and, 65–69  
radiotherapy for, 307–308  
screening for, 308  
surgery for, 307–308
- Metastatic clear cell renal cell carcinoma (MCCRCC), 41–42
- Metastatic small cell carcinoma, 43
- Methionine PET. *See also* [Methyl-<sup>11</sup>C]-L-methionine  
BBB and, 159  
children and, 161  
DNET and, 161–162  
gliomas and, 159–160  
radiotherapy and, 166, 171–172  
system L amino acid carrier proteins and, 159–160
- Methotrexate (MTX), 33, 337. *See also* High-dose methotrexate  
for RDD, 371
- Methoxyisobutylisonitrile (MIBI)  
ATP and, 203  
BBB and, 203–204, 205–206, 210  
CT and, 206  
GB and, 205  
Ki-67 and, 204  
MRI and, 206  
PET and, 205  
RI of, 206  
ROI and, 204–205  
SPECT with, 203–212  
for AIDS, 206  
chemotherapy and, 206  
ICH and, 206–212  
for lymphoma, 206  
multidrug resistance and, 206  
radiotherapy and, 206  
for toxoplasmosis, 206  
tuberculomas for, 206  
Tc and, 203–212
- Methyl (CH<sub>3</sub>), 229
- [Methyl-<sup>11</sup>C]-L-methionine (MET), 9, 174  
abnormal uptakes of, 192–193  
FET and, 180–181  
Ki-67 and, 160  
PET with, 13–15, 159–161, 174, 215  
for ICH, 208  
for spinal ependymomas, 161  
for tumor grading, 160, 163–164  
radiation dosimetry of, 12–13  
stereotactic biopsy with, 189–199  
sub-cortical grey matter and, 193–194  
for WHO Grade II and III, 10
- O<sup>6</sup>-methylguanine methyltransferase (MGMT), 111



- N-methylnitrosourea (MNU), 136  
 3-methyl-(triazen-1-yl)imidazole-4-carboxamide (MTIC), 111  
 MFs. *See* Mitotic figures  
 MGMT. *See* O<sup>6</sup>-methylguanine methyltransferase  
 MIB-1, 42, 45  
   astrocytomas and, 45  
   meningiomas and, 46  
 MIBI. *See* Methoxyisobutylisonitrile  
 MIC2, 36  
 Microtubule associated protein (MAP), 36  
   synaptophysin and, 38  
 Midazolam, 12  
 Midbrain, RGNT and, 3  
 mI/GLY, 233  
 MION-46, 299  
 Mitotic figures (MFs), 45  
   meningiomas and, 46  
 MMP-9, 22  
   TSP-1 and, 100  
 MMPs. *See* Matrix metalloproteinases  
 MNU. *See* N-methylnitrosourea  
 Model-based expression indexes (MBEI), 26  
 Monoclonal antibodies, for PCNSL, 345–346  
 Movement disorders, FDG for, 9–10  
 MRI. *See* Magnetic resonance imaging  
 MRS. *See* Magnetic resonance spectroscopy  
 MRSI. *See* Magnetic resonance spectroscopic imaging  
 MS. *See* Multiple sclerosis  
 MTC. *See* Magnetization transfer contrast  
 MTIC. *See* 3-methyl-(triazen-1-yl)imidazole-4-carboxamide  
 mTOR, 116  
 MTR. *See* Magnetization transfer ratio  
 Multidrug resistance, MIBI-SPECT and, 206  
 Multiple sclerosis (MS), 184  
   PMRS and, 272–273  
 Multi-voxel (MV), 227  
   metastases and, 315  
   MRS, PMRS and, 267  
   PMRS and, 269  
 MV. *See* Multi-voxel  
 MYC. *See* V-myc myelocytomatosis viral oncogene homolog  
 MYO18B, 65  
 MyoD, AT/RT and, 40  
 Myoinositol, 255  
   PMRS and, 269  
 NAA. *See* N-acetyl aspartate  
 N-acetyl aspartate (NAA), 229, 233, 236–237  
   CHO and, 241  
   encephalitis and, 274  
   metastases and, 315  
   MRS and, 255  
   PMRS and, 269  
   TE and, 311  
 Navigated transcranial magnetic stimulation (nTMS), 168  
 NeuN, 36, 38  
 Neural stem cells (NSCs), 109  
 Neurocytomas  
   central, ADC and, 284  
   EVN, 2–3  
   IHC for, 37  
 Neurofibromatosis, RDD and, 366  
 Neurofilament (NF), 36–37  
   AT/RT and, 40  
 Neuronal tumors, 2–3  
 Neurotrophins, 307  
 Neutropenia, 343, 345  
 NF. *See* Neurofilament  
 NF-1, pilomyxoid astrocytoma and, 1  
 NHL. *See* Non-Hodgkin lymphoma  
 9L gliosarcoma, 136–137  
 90Y. *See* Yttrium-90  
 NMR. *See* Nuclear magnetic resonance  
 Non-Hodgkin lymphoma (NHL), 337  
   HD-MTX for, 339  
   PNHL, 192–194  
 NPA. *See* Asn-Pro-Ala  
 NSCs. *See* Neural stem cells  
 nTMS. *See* Navigated transcranial magnetic stimulation  
 Nuclear/cytoplasmic ratio, 281  
 Nuclear magnetic resonance (NMR), 215  
   for IPA-SPECT, 217–218  
   SPECT and, 218, 223–224  
 NuPage, 74  
 NVP-AEW541, 361  
 Nyquist sampling theorem, 246, 249  
 Obstructive hydrocephalus, RGNT with, 4  
 OCT4, 40  
 OLCs. *See* Oligodendroglia-like cells  
 Oligodendroglia-like cells (OLCs), 42–43

- Oligodendroglioma  
  extraventricular neurocytoma and, 3  
  ICH and, 207  
  IHC for, 35  
  round clear cell (oligodendroglioma-like) tumors,  
    42–43
- Oligonucleotide DNA microarrays, 25
- Ordered-subset expectation maximization  
  (OSEM), 15
- OSEM. *See* Ordered-subset expectation  
  maximization, 53, 42
- Pancytokeratin  
  ependymal tumors and, 36  
  GB and, 43
- Papillary glioneuronal tumor (PGNT), 2
- Papillary tumors of the pineal region (PTPR), 4
- Parallel MRI, 245–259  
  data acquisition, 246–248  
  fMRI and, 252–254  
  mathematical formulation for, 250–253  
  reconstructions with, 248–250  
  SENSE and, 252–254  
  SNR and, 245, 250
- Parasellar tumors, ADC and, 285–286
- Parvovirus B19, 365
- PBS. *See* Phosphate buffered saline
- PCNSL. *See* Primary central nervous  
  system lymphoma
- PCV. *See* Procarbazine, lomustine,  
  vincristine
- PDE4. *See* Phosphodiesterase-4
- PDGF. *See* Platelet-derived growth factor
- PDGFR. *See* Platelet-derived growth factor receptor
- PDGFRA. *See* Platelet derived growth factor  
  receptor alpha polypeptide
- PEComas. *See* Perivascular epithelioid cell  
  differentiation tumors
- Pemetrexed, 343
- PEPSI. *See* Proton-echo-planar-  
  spectroscopic-imaging
- Performance liquid chromatography (HPLC),  
  216–217
- Perfusion magnetic resonance imaging (PMRI), 268
- Periodically Rotated Overlapping Parallel Lines  
  with Enhanced Reconstruction  
  (PROPELLER), 146, 280
- Peritumoral edema, ADC and, 281
- Perivascular epithelioid cell differentiation tumors  
  (PEComas), 35
- PET. *See* Positron emission tomography
- PFS. *See* Progression free survival
- PGF. *See* Placental growth factor
- PGNT. *See* Papillary glioneuronal tumor
- PHH3. *See* Phospho-histone H3
- Phosphate buffered saline (PBS), 49, 73
- Phosphodiesterase-4 (PDE4)  
  cAMP and, 71–80  
  GBM and, 71  
  GFAP and, 76  
  IHC and, 75–76  
  immunocytochemistry and, 76–78  
  PKA-dependent herotrimeric G protein and, 72  
  Western blotting and, 73–75
- Phospho-histone H3 (PHH3), 45
- PIER. *See* Proteolytic induced epitope retrieval
- Pilocytic astrocytoma, extraventricular  
  neurocytoma and, 3
- Pilomyxoid astrocytoma, 1
- Pineal region tumors, 4
- Pituitary tumors, ADC and, 285–286
- PK11195, 175
- PKA-dependent herotrimeric G protein, PDE4  
  and, 72
- Placental alkaline phosphatase (PLAP), 39
- Placental growth factor (PGF), 98  
  BM-EPCs and, 104  
  drugs for, 100
- PLAP. *See* Placental alkaline phosphatase
- Plasma cell granuloma, RDD and, 366
- Plasminogen activators, 307
- Platelet-derived growth factor (PDGF), 98  
  bevacizumab and, 100  
  BM-EPCs and, 104  
  gliomas and, 115  
  TKIs and, 112  
  VEGF-A and, 115
- Platelet-derived growth factor receptor  
  (PDGFR), 101  
  gliomas and, 115  
  sorafenib for, 101
- Platelet derived growth factor receptor alpha  
  polypeptide (PDGFRA), 66–67
- Pleomorphic xanthoastrocytoma  
  (PXA), 35
- P-mode. *See* Power-mode
- PMRI. *See* Perfusion magnetic resonance imaging
- PMRS. *See* Proton magnetic resonance  
  spectroscopy
- PNETs. *See* Primitive neuroectodermal tumors

- PNHL. *See* Primary non-Hodgkin's lymphoma
- Point resolved spectroscopy (PRESS), 228  
TE and, 231
- Positive predictive value (PPV), 206
- Positron emission tomography (PET), 264. *See also* [<sup>18</sup>F]Fluoro-2-deoxyglucose; O-(2-[<sup>18</sup>F]fluoroethyl)-L-tyrosine; [Methyl-<sup>11</sup>C]-L-methionine
- antiangiogenic therapy and, 116
- chemotherapy and, 172
- for children, 161
- CT and, 186
- fMRI and, 169
- for lymphoma, 161
- methionine, 13–15  
BBB and, 159  
children and, 161  
DNET and, 161–162  
gliomas and, 159–160  
system L amino acid carrier proteins and, 159–160
- MIBI and, 205
- for minimizing brain damage, 167–170
- MRI and, 158
- planning and monitoring therapy with, 157–176
- pregnancy and, 11
- reconstruction, 15
- stereotactic biopsy and, 190–192
- temozolomide and, 172
- for tumor grading, 162–166
- Posterior cranial fossa tumors, ADC and, 284
- Post-radiation gliosis (PR), 192
- Potassium inward rectifying channels 4.1 (KIR4.1), 55
- Power-mode (P-mode), for IOUS, 327
- PPV. *See* Positive predictive value
- PR. *See* Post-radiation gliosis; Progesterone receptor
- Pregnancy, PET and, 11
- PRESS. *See* Point resolved spectroscopy
- PRESTO, 252
- Primary central nervous system lymphoma (PCNSL)  
chemotherapy for, 342–345  
combination of agents for, 344–345  
HD-MTX for, 343–344  
intrathecal chemotherapy for, 347–348  
monoclonal antibodies for, 345–346  
radiotherapy for, 340–441  
salvage treatment for, 337–349
- Primary non-Hodgkin's lymphoma (PNHL), 192–194
- Primitive neuroectodermal tumors (PNETs), 40, 192  
ADC and, 283  
FDG and, 161
- Procarbazine, lomustine, vincristine (PCV), 344
- Progesterone receptor (PR), meningiomas and, 38
- Progression free survival (PFS)  
with GBM, 115  
for PCNSL, 343
- PROPELLER. *See* Periodically Rotated Overlapping ParalleL Lines with Enhanced Reconstruction
- Prostate cancer, metastases and, 305
- Protamine, 303
- Proteases, endostatin and, 102
- Protein tyrosine kinase (PTK), 101
- Proteolytic induced epitope retrieval (PIER), 47
- Proton-echo-planar-spectroscopic-imaging (PEPSI), 256–257  
SENSE and, 257–258
- Proton magnetic resonance spectroscopy (PMRS), 227, 263, 268–269  
abscess and, 273  
encephalitis and, 274  
lymphoma and, 272  
metastases and, 271–272  
MS and, 272–273  
MV MRS and, 267  
quantitative, 276  
SV MRS and, 267  
tumefactive demyelinating lesions and, 272–273
- Pseudotumors, 239–240
- PTEN, gliomas and, 110
- PTK. *See* Protein tyrosine kinase
- PTPR. *See* Papillary tumors of the pineal region
- Pulse-Oxymetry, 12
- PXA. *See* Pleomorphic xanthoastrocytoma
- Pyogenic abscess  
DWI and, 240  
MRI of, 265
- Pyruvate, abscess and, 273
- QRT-PCR. *See* Quantitative polymerase chain reaction
- Quantitative PMRS, 276
- Quantitative polymerase chain reaction (QRT-PCR), 26  
for AT/RT, 357–358  
for DNA, 29, 66  
metastases and, 65–69
- QUEST, 236

- RA. *See* Relative anisotropy
- Rac-RhoA, 116
- Radiation dosimetry, 12–13
- Radiation-induced fibrosarcomas (RIF-1), 289
- Radiation necrosis, 10, 152, 207, 280  
recurrence and, 287–288
- Radio frequency (RF), 245
- Radiolabeled amino acid tracers, 10, 159–161.  
*See also specific tracers*  
future development of, 174–175  
L-transporter and, 11  
radiotherapy and, 186  
selection of, 197
- Radiosurgery, 83–95  
dosimetry and, 86–91
- Radiotherapy  
BBB and, 172  
dosimetry for, 12–13  
FDG and, 11, 173  
for metastases, 307–308  
methionine PET and, 166, 171–172  
MIBI-SPECT and, 206  
for PCNSL, 340–441  
radiolabeled amino acid tracers and, 186  
for RDD, 371  
with Rolipram, 80  
with TMZ, 114  
white matter and, 152, 164
- Rathke's cleft cysts (RCCs), 39  
HB and, 42
- rCBV. *See* Relative cerebral blood volume
- RCCs. *See* Rathke's cleft cysts
- rCMRGl. *See* Regional metabolic rate of glucose
- RDD. *See* Rosai-Dorfman disease
- Reactive gliosis, diffuse astrocytoma  
and, 42
- Receptor tyrosine kinases (RTKs), 362
- Recurrence  
radiation necrosis and, 287–288  
resection injury and, 289
- Recycling time (TR), 232
- Regional metabolic rate of glucose  
(rCMRGl), 12  
FDG and, 16
- Regions of interest (ROI), 15  
ADC and, 148, 291–293  
FA and, 150  
IMT and, 16  
MIBI and, 204–205
- Relative anisotropy (RA), DTI and, 146–147
- Relative cerebral blood volume (rCBV), 152, 311  
abscess and, 318  
metastases and, 316, 317
- Renal cancer, metastases and, 305
- Resection  
injury from, recurrence and, 289  
IOUS and, 325–334
- Resolution, for IOUS, 327–329
- Retention index (RI), 204  
of MIBI, 206
- RF. *See* Radio frequency
- RGNT. *See* Rosette-forming glioneuronal tumor of  
the fourth ventricle
- RI. *See* Retention index
- RIF-1. *See* Radiation-induced fibrosarcomas
- Rituximab, 345, 347
- RNA, stereotactic biopsy and, 25, 28
- RNeasy, 24
- ROC  
FET and, 182  
IPA and, 224
- ROI. *See* Regions of interest
- Rolipram, 80
- Rosai-Dorfman disease (RDD), 44, 365–371  
clinical course of, 370–371  
clinical findings with, 366–368  
differential diagnosis for, 366–368  
IHC for, 370  
of spine, 368–369  
treatment for, 370–371
- Rosette-forming glioneuronal tumor of the fourth  
ventricle (RGNT), 3  
with obstructive hydrocephalus, 4
- Round clear cell (oligodendroglioma-like) tumors,  
42–43
- round clear cell (oligodendroglioma-like) tumors,  
42–43
- RTKs. *See* Receptor tyrosine kinases
- S-100  
astrocytomas and, 35  
AT/RT and, 40  
CPP and, 36  
ependymal tumors and, 36  
gliomas and, 34–35  
meningiomas and, 38  
PXA and, 35  
RDD and, 370  
SEGA and, 35
- S100A4, 65

- SAGE, 234
- SAH. *See* Subarachnoid hemorrhage
- Salvage treatment, for PCNSL, 337–349
- Sarcoidosis, 368
- Sarcoma, metastases and, 305
- Schwannomas, ADC and, 285
- SDF-1, BM-EPCs and, 104
- SE. *See* Spin echo
- Sedation, FDG and, 12
- SEGA. *See* Subependymal giant cell astrocytoma
- SENSE. *See* Sensitivity-encoding
- Sensitivity-encoding (SENSE), 146, 246, 248, 250, 257–259, 280
- EPI and, 252–254, 258–259
- MRSI and, 257
- parallel MRI and, 252–254
- PEPSI and, 257–258
- SNR and, 257
- Sensitivity maps, 247–248
- SFT. *See* Solitary fibrous tumor
- SHML. *See* Sinus histiocytosis with massive lymphadenopathy
- Signal to noise ratio (SNR), 246
- DTI and, 135
- FDG-PET and, 169
- parallel MRI and, 245, 250
- SENSE and, 257
- TE and, 233
- VOI and, 230–231
- Significance score algorithm (S-score), 26
- Single photon emission computed tomography (SPECT), 264. *See also* p-[123I]iodo-L-phenylalanine; Methoxyisobutylisonitrile
- CT and, 15
- IMT and, 9, 14
- NMR and, 218, 223–224
- reconstruction, 15
- Single shot radiosurgery, 85
- Single voxel (SV)
- metastases and, 315
- MRS, 227–241
- PMRS and, 267
- PMRS and, 269
- Sinus histiocytosis with massive lymphadenopathy (SHML), 365–371
- siRNA, 103, 106
- SMASH. *See* K-space spatial harmonics
- SNR. *See* Signal to noise ratio
- Sodium [123I]iodide, 216
- Sodium perchlorate (Irenat), 217
- Solitary fibrous tumor (SFT), 44
- Sorafenib, 101
- Space sensitivity-encoding. *See* Sensitivity-encoding
- SPECT. *See* Single photon emission computed tomography
- Spine
- ependymomas of, MET-PET for, 161
- RDD of, 368–369
- Spin echo (SE), 308
- FLAIR and, 308
- SPIO. *See* Superparamagnetic iron oxide
- Spiral trajectory MRI, 249
- S-score. *See* Significance score algorithm
- Standardised uptake value (SUV), 16
- Stealth Neuroimaging Station, 22, 23
- STEAM. *See* Stimulated echo acquisition mode
- Stereotactic biopsy, 10
- with FDG and MET, 189–199
- for GBM, 28–29
- MRI and, 23–24
- PET and, 190–192
- placement for, 28
- results of, 26–29
- technique of, 22–26
- for tumor characterization, 29–30
- Stimulated echo acquisition mode (STEAM), 228, 311
- TE and, 231
- Streptozotocin (STZ), diabetes and, 56
- STZ. *See* Streptozotocin
- SU5416, 101, 105
- Subarachnoid hemorrhage (SAH), AQPs and, 54
- Sub-cortical grey matter, 193–194
- Subependymal giant cell astrocytoma (SEGA), 35
- Subependymomas, ADC and, 284
- Succinate, abscess and, 273
- Sunitinib, 101–102
- Super-aquaporins, 53–54
- Superparamagnetic iron oxide (SPIO), 297–303
- Surgery. *See also* Resection
- BBB and, 172
- for metastases, 307–308
- Survivin, 103
- SUV. *See* Standardised uptake value
- SV. *See* Single voxel
- Synaptophysin, 36–37
- AT/RT and, 40
- CPP and, 36

- EVN and, 37
- MAP and, 38
- metastatic small cell carcinoma and, 43
- System L amino acid carrier proteins, methionine and, 159–160
- T1CE. *See* T1-weighted contrast-enhanced
- T1-weighted contrast-enhanced (T1CE), 218, 220, 223
- Tangier disease, 370
- TAU. *See* Taurine
- Taurine (TAU), 230, 233
- TBR. *See* Tumor to normal brain ratios
- Tc. *See* Technetium
- TE. *See* Echo time
- Technetium (Tc), MIBI and, 203–212
- Temodal. *See* Temozolomide
- Temodar. *See* Temozolomide
- Temozolomide (Temodar, Temodal, TMZ), 60, 101, 111
  - for GB, 172
  - for PCNSL, 342–343
  - PET and, 172
  - radiotherapy with, 114
- Testicular cancer, metastases and, 305
- 1,4,7,10-tetraazacyclododecane-*N,N',N,N'*-tetraacetic-acid-D-Phe<sup>1</sup>-Tyr<sup>3</sup>-octreotide (DOTATOC), 162
- Tetrofosmin, 205
- Thalamus, RGNT and, 3
- Thrombocytopenia, 343, 345
- Thrombospondin-1 (TSP-1), 98
  - BM-EPCs and, 104
  - drugs for, 100
- Thymidylate synthase, 343
- Thyroid cancer, metastases and, 305
- Thyroid gland, IMT and, 11–12
- Thyroid transcription factor-1 (TTF-1), 43
- TII. *See* Tumor Infiltration Index
- TIMPs. *See* Tissue inhibitors of MMPs
- Tissue inhibitors of MMPs (TIMPs), 22
- Tissue-Tek OCT, 24
- TKIs. *See* Tyrosine kinase inhibitors
- TMS. *See* Transcranial magnetic stimulation
- TMZ. *See* Temozolomide
- Topotecan, for PCNSL, 342–343
- Toxoplasmosis
  - AIDS and, 291
  - MIBI-SPECT for, 206
- TR. *See* Recycling time
- Tractography, 140–141
  - DTI and, 169
- Transcranial magnetic stimulation (TMS), 167
- Transducers, for IOUS, 326–327
- Transformed 3T3 cell double minute 4 (MDM4), 66, 67
- Tris-EDTA, 47
- Trizol Reagent, 24
- Tropomyosin, 102
- TSE. *See* Turbo spin echo
- TSENSE, 247
- TSP-1. *See* Thrombospondin-1
- TTF-1. *See* Thyroid transcription factor-1
- Tubercolomas, MIBI-SPECT for, 206
- Tuberculosis, 368
- Tumefactive demyelinating lesions, 318–319
  - PMRS and, 272–273
- Tumor characterization, stereotactic biopsy for, 29–30
- Tumor grading
  - ADC for, 281, 282
  - DTI for, 149–150
  - DWI for, 149–150
  - FDG for, 162–163
  - IHC for, 44–46
  - IPA-SPECT for, 224
  - MET-PET for, 160, 163–164
  - PET for, 162–166
  - WHO and, 44–46
- Tumor infiltration, ADC and, 286–287
- Tumor Infiltration Index (TII), 149
- Tumor to normal brain ratios (TBR), 219
- Turbo spin echo (TSE), 308
- Tyrosine kinase growth factors, gliomas and, 160
- Tyrosine kinase inhibitors (TKIs), 112
- UCR. *See* Upstream conserved regions
- Ultrasmall superparamagnetic iron oxide (USPIO)
  - BBB and, 288–298, 301–302, 303
  - Gd and, 298
  - IMR and, 302
  - MRI and, 297–303
- UNFOLD, 247
- Unfolded protein response (UPR), 103
- UPR. *See* Unfolded protein response
- Upstream conserved regions (UCR), 72, 73
- USPIO. *See* Ultrasmall superparamagnetic iron oxide

- Vandetanib, 114
- Varicella, 365
- Vascular endothelial growth factor (VEGF), 98  
 BM-EPCs and, 104  
 drugs for, 99–100  
 TSP-1 and, 100
- Vascular endothelial growth factor-A (VEGF-A), 110, 115–116  
 angiogenesis and, 111–113  
 PDGF and, 115
- Vascular endothelial growth factor  
 receptor 1 (VEGFR1), 100  
 VEGF-A and, 112
- Vascular endothelial growth factor  
 receptor 2 (VEGFR2), 100–101  
 endostatin and, 102  
 sorafenib for, 101  
 VEGF-A and, 112
- VEGF. *See* Vascular endothelial growth factor
- VEGF-A. *See* Vascular endothelial growth factor-A
- VEGFR1. *See* Vascular endothelial growth factor receptor 1
- VEGFR2. *See* Vascular endothelial growth factor receptor 2
- Vesiculo-vacuolar organelles (VVOs), 112
- Vessel normalization, antiangiogenic therapy and, 114
- VHL. *See* Von Hippel-Lindau syndrome
- Vimentin, 44  
 AT/RT and, 40  
 CPP and, 36  
 gliomas and, 35
- Vinblastine, for RDD, 371
- Virchow-Robin space, 110
- V-myc myelocytomatosis viral oncogene homolog (MYC), 67
- VOI. *See* Volume of interest
- Volume of interest (VOI), 218–219  
 CHO/CRE and, 238  
 MRI and, 230  
 SNR and, 230–231
- Volume ratio (VR), DTI and, 147
- Von Hippel-Lindau syndrome (VHL), 41–42  
 HB and, 319–320
- VR. *See* Volume ratio
- VVOs. *See* Vesiculo-vacuolar organelles
- Water-suppressed (WS), 256
- Western blotting  
 for AT/RT, 356–357  
 PDE4 and, 73–75
- White matter  
 chemotherapy and, 152  
 radiotherapy and, 152, 164
- WHO. *See* World Health Organization
- World Health Organization (WHO)  
 classification by, 1–5  
 ADC and, 281  
 of ependymal tumors, 36  
 of gliomas, 110  
 MRS and, 240–241  
 tumor grading and, 44–46
- WS. *See* Water-suppressed
- Xanthoma, 370
- Xenografts, 113  
 DTI and, 140
- X-ray computed tomography, 264
- Yttrium-90 (90Y), 345
- Zolomide, 345
- Zoster virus, 365